THEORETICAL AND EXPERIMENTAL INVESTIGATIONS OF LARGE AMPLITUDE SHIP MOTIONS AND LOADS IN REGULAR HEAD SEAS

BY

ZHIXIANG TAO, B.Sc. M.Sc.

Submitted as a Thesis for the Degree of Doctor of Philosophy,

Department of Naval Architecture & Ocean Engineering, University of Glasgow.

December 1996

DECLARATION

Except where reference is made to the work of others, this thesis is believed to be original.

DEDICATION

To my wife, my lovely daughter and my parents

ACKNOWLEDGMENTS

I would like to express my appreciation to all those who helped me during my research.

Professor D. Faulkner, former Head of Department, for his help in making my study possible in this department, especially with regard to obtaining financial support from the British Council and the Government of the People's Republic of China.

Professor N. Barltrop, Head of Department, for his kind encouragement and support during my research.

Professor A. Incecik, Lloyd's Register Chair of Offshore Engineering, University of Newcastle, for his supervision, valuable advice, enthusiastic support and encouragement throughout this research.

Mr. J. E. Gillan, for constructing the excellent experimental measurement facilities, modifying the test ship model and kindly helping during my experiments.

Dr. C. C. Fang and Dr. H.S. Chan, for their valuable discussions and help, especially in the experiments.

Mr. D. Percival , for his help in the data acquisition and experimental analysis.

Mr. R. B. Christison (the late Chief Technician), D. J. Sinclair (Acting Chief Technician), Mr. F. Sweeney, Mr. G. Dunning, Mr. D. Nicolson, Mr. B. Reilly, Mr. J. Aitken and Mr. W. Wright, for their help in my experiment.

Mr. A. Mcleary, for his help in the experimental analysis.

Finally, I would like to thank my wife for her continuous encouragement and support.

NOMENCLATURE

Symbols not included in the list below are only used at a specific place and are explained when they occur.

A_0 Sectional area in still water.

a_1, a_3, a_5 Coefficients for conformal mapping of the ship section form up to 1/10 of the design draught.

A_r Instantaneous submerged sectional area.

B_d Width of deck.

B_e Effective beam length.

B_m Breadth of the bottom region at a draught.

C Pressure concentration factor.

c Damping coefficient per unit length.

C_b Coefficient in Payne impact theory.

c_i The ith mode damping coefficient.

$\bar{c}_i$ The ith mode generalized damping.

d Height of water when deck wetness occurs.

EI Bending rigidity.

f External force per unit length.

f_A Ship hull inertia force.

f_b Bottom slamming force.

f_{bf} Bow flare slamming force.

f_H Total hydrodynamic force.

f_{H1} Dynamic restoring force.

f_{H2} Wave damping force.

f_{H3} Fluid momentum force.

f_{pa} Function of coefficient in Payne impact theory.

g Gravitational acceleration.

I_r Mass moment of inertia of hull per unit length with respect to an axis normal

to $x_b - z_b$ plane

K Wave number.

K_1 Nondimensional pressure coefficient.

KAG Shear rigidity.

K_{bsc} Nondimensional pressure coefficient.

$\bar{k}_i$ The ith mode generalized spring constant.

K_{ka} Pressure coefficient of the Karman impact theory.

K_{oc} Dimensional constant depending on section shape.

K_{ocl} Nondimensional K_{oc} values.

K_{pa} Pressure coefficient of the Payne impact theory.

K_s Pressure coefficient of the wave striking impact pressure.

K_{sc} Pressure coefficient of the Stavovy & Chuang's method.

K_w Pressure coefficient of the Wagner impact theory.

L Ship length.

L_a Distance between the longitudinal centre and AP.

L_f Distance between the longitudinal centre and FP.

M Global bending moment.

M_b Bottom slamming bending moment.

M_{bf} Bow flare slamming bending moment.

M_i The ith mode spatial weighting function of bending moment.

m_0 Sectional added mass in still water.

m_r Sectional added mass of instantaneous submerged section.

m_s Unit mass of ship hull.

M_w Wave bending moment.

N Half span of filter.

N_0 Sectional damping coefficient in still water.

N_r Sectional damping coefficient of instantaneous submerged section.

P Total bow flare impact pressure.

P_i Impact pressure due to the normal component to wave surface of the relative velocity between the impact surface and the wave.

P_{ika} Water immersion impact pressure by the Karman impact theory.

P_{iM} Water immersion impact pressure by the momentum slamming theory.

P_{isc} Water immersion impact pressure by the Stavovy & Chuang's method.

P_{iW} Water immersion impact pressure by the Wagner impact theory.

P_p Planing pressure due to the tangential component to wave surface of the relative velocity between the impact surface and the wave.

P_S Wave striking impact pressure.

P_t Total bottom impact pressure.

q_i The ith mode generalized deflection.

$\dot{q}_i$ The ith mode generalized velocity.

$\ddot{q}_i$ The ith mode generalized acceleration.

Q_i The ith mode generalized forcing function.

r Relative motion between the ship and the wave.

$\dot{r}$ Relative velocity between the ship and the wave $(\frac{dr}{dt})$.

$\ddot{r}$ Relative acceleration between the ship and the wave.

$\dot{r}_1$ Relative velocity between the ship and the wave $(\frac{\partial r}{\partial t})$.

S_1, S_2 Absolute motions measured forward and aft.

t Time variable.

T_e Period of encounter.

T_r Instantaneous draught.

u Horizontal water velocity.

U Forward speed.

v Vertical water velocity.

V Global shear force.

V^* Threshold velocity for bottom slamming.

V_b Bottom slamming shear force.

V_{bf} Bow flare slamming shear force.

V_{bh} Horizontal velocity of vehicle.

V_{bhw} Velocity component of impact body parallel to wave surface.

V_{bn} Velocity component of V_{ns} perpendicular to wave surface.

V_{bv} Vertical velocity of vehicle.

V_{bvw} Velocity component of impact body perpendicular to wave surface.

V_{bt} Velocity component of V_{ns} parallel to wave surface.

V_h Horizontal velocity of body at the impact point.

V_{hw} Horizontal velocity of wave particle.

V_i The ith mode spatial weighting function of shear force.

V_n Normal component to the water surface of the relative velocity between the impact body and waves.

V_{ns} Normal velocity to impact surface of vehicle.

V_{nw} Normal velocity component of wave to the water surface at a impact point.

V_o Orbiting velocity of water particle.

V_{on} Orbiting velocity component normal to wave surface.

V_{ot} Orbiting velocity component parallel to wave surface.

V_t Tangential component to the water surface of the relative velocity between the impact body and waves.

V_{tw} Tangential velocity component of wave surface at point A.

V_v Vertical velocity of body at the impact point.

V_{vw} Vertical velocity of wave particle.

V_w Wave celerity.

V_{wa} Wave shear force.

W_n Hamming window.

(x,y,z) Coordinate system moving with ship forward speed.

x' Longitudinal position along the ship.

(x_b,y_b,z_b) Coordinate system fixed in ship.

X_i Dimensionless ith mode shape.

x_m Input signal at m time step.

(x_0,y_0,z_0) Coordinate system fixed in space.

y_m Output filtered signal at m time step.

y_w Half breadth of section in still water.

z_e Vertical elastic deflection, normal to x_b.

z Heave motion.

$\dot{z}$ Heave velocity.

$\ddot{z}$ Heave acceleration.

α Water line angle.

α' Modified water line angle due to pitch motion.

β Body plan angle.

β' Modified body plan angle due to pitch motion.

β_{eh} Angle on wave surface measured from forward longitudinal direction to a plane normal to wave surface and impact surface on hull bottom at a point of concern; see Fig.3.2.

β_{ev} Angle on transverse plane normal to wave surface and measured from impact surface on hull bottom to wave surface; see Fig.3.2.

δ Original wave slope.

δ' Effective wave slope.

δ_j Logarithmic decrement.

δ_{max} Maximum wave slope.

ϕ Deadrise angle of the bow flare slamming pressure.

ϕ_b Deadrise angle of the bottom slamming pressure.

γ Buttock line angle of the bow flare region.

γ' Modified buttock line angle due to pitch motion.

γ_b Buttock angle of the bottom region.

γ_s Component of slope of z_s due to bending only.

η Angle between V_{bhw} and V_{ns}.

λ Wave length.

μ Ship's mass per unit length plus added mass per unit length.

$\bar{\mu}_i$ The ith mode generalized mass.

θ Phase of incident regular wave.

ρ Density of fluid.

ω Wave frequency.

ω_c Cut-off frequency.

ω_e Frequency of encounter.

ω_i Natural frequency of the ith mode.

ξ Water contact angle.

ξ_b Effective impact angle for bottom slamming.

ψ Pitch motion.

$\dot{\psi}$ Pitch velocity.

$\ddot{\psi}$ Pitch acceleration.

ζ Wave elevation.

$\dot{\zeta}$ Vertical wave velocity.

$\ddot{\zeta}$ Vertical wave acceleration.

ζ_a Wave amplitude.

CONTENTS

LIST OF FIGURES

LIST OF TABLES

LIST OF PHOTOGRAPHS

SUMMARY

The aim of this research is to develop computational tools to predict the large amplitude motions and loads on ship travelling with forward speed in waves. An experimental research programme was completed to validate the nonlinear prediction method. In this thesis, the results of theoretical and experimental investigations to predict the nonlinear ship motions, slamming pressures and bending moments in regular head seas are presented.

The practical nonlinear theoretical prediction method described in this research is based on "relative motion hypothesis" in which nonlinear effects, i.e., nonlinear dynamic restoring force, nonlinear damping force and nonlinear fluid momentum force are considered. The motion equations are solved in the time domain by the numerical integration technique, the three points predictor-corrector method (Hamming method). The frequency dependent added mass and damping coefficients are computed at the instantaneous submerged section using the close-fit conformal mapping method. The results by the nonlinear method have very good agreement with the experimental test results for heave and pitch motions, expect overprediction in the resonance region in large waves for the heave motion.

The bottom slamming pressure is calculated by Stavovy & Chuang theory, Ochi & Motter theory, the momentum theory and Payne impact theory. The Ochi & Motter theory predicts a good agreement results with the new experimental data, while other methods predict bigger values than the experimental results.

The momentum slamming theory and Wagner impact theory are used to predict bow flare slamming pressures. The total impact pressure is expressed as the sum of water immersion impact pressure and wave striking impact pressure. The momentum slamming theory and Wagner impact theory can predict a good results of bow flare slamming. The bow flare slamming pressure increases as the wave amplitude and the speed increase.

The wave shear forces and bending moments are calculated using the nonlinear theoretical prediction method and the linear strip theory. Generally, the nonlinear prediction method will give better results than the linear method.

The ship hull is considered to be a Timoshenko beam, where the vibratory elastic response of the ship is calculated by the modal superposition method with the solution represented in terms of a series of normal modes. It is assumed that the mode shapes and natural frequencies can be determined by a separate structural analysis where this modal information is appropriate to the vessel in the equilibrium reference condition when floating in calm water. The global dynamic shear force and bending moment values are predicted using two different methods :

The first method developed is based on the elastic vibratory response due to the total hydrodynamic force;

The other is based on the rigid body response due to the linear force superimposed with the elastic response due to impact forces.

The results by the elastic vibratory response due to the total hydrodynamic force (method 1) have a good agreement with the experimental results and these are much better than the results by the rigid body response superimposed with the elastic response (method 2).

The nonlinear effects due to the change of the hydrodynamic coefficients and the nonlinear restoring force should be considered in the ship motion and load predictions. The nonlinearity of ship motions as well as a significant nonlinearity between the hogging and sagging wave and global bending moments are shown in the results obtained from the nonlinear theoretical predictions and the experimental data.

The nonlinear ship motions and sea loads predicted by the practical computational tools, newly developed in this thesis, can be used to further ship structural strength analysis and guide ship hull design.

CHAPTER 1
INTRODUCTION

As fast ships such as destroyers, container ships and aircraftcarriers travel in rough seas, these ships are subjected to large pitch and heave motions. Their local structures may be damaged and their longitudinal strength may be weakened due to slamming and deck wetness. Therefore, for their safety, a computational tools to estimate nonlinear ship motions and sea loads due to slamming and deck wetness should be developed.

1.1 Ship motions

The linear strip theory has been successfully used to predict ship motions and loads for many years. For example, Korvin Kroukovsky & Jacobs (K.K.J) and Salvesen, Tuck & Faltinsen (S.T.F) methods[1-3].

Bishop et al[4-5] developed a strip theory in which ship motion equations were solved in the frequency domain. This work was based on linear theory. The ship motions were determined by linear forces. The nonlinear instantaneous response of the ship was calculated in the time domain using the convolution integral and then superimposed with the linear response. Finally, the global structural response of the ship hull was obtained. In the study, the ship hull was treated as a nonuniform Timoshenko beam.

Kaplan and Sargent[6] also developed a strip theory in which ship motion equations were solved in the frequency domain. The ship motions were also determined by the linear forces.

However, it should be kept in mind that these methods have limited application due to basic assumptions in the theory. The most obvious limitation is that the theory is linear, that is, both the wave steepness (the wave height divided by the wave length) and motions of the ship (relative to the ship dimensions) are assumed to be small. In large amplitude waves, nonlinear effects will cause the deviation between calculations and the experimental data. In order to develop a more correct and reliable method of predicting wave-induced

motions and loads, nonlinear effects should be included in the simulations[7-16].

The nonlinear hydrodynamic problem of ship motions in regular waves, stated as a mathematical problem with nonlinear boundary conditions, is a formidable task to handle. It was found from investigation of the special important nonlinear effects that it is important to study the nonlinearities arising from the hull section not being wall-sided at the water line. In this investigation, nonlinear incoming waves were not considered.

Juncher Jensen and Terndrup Pedersen[7] calculated the nonlinear vertical bending moment in irregular waves. Their equations of motion were also based on the "relative motion hypothesis" and second-order contributions due to the buoyancy and hydrodynamic forces were obtained by perturbation expansions around the hull's still water position. Their formulation was carried out for a flexible ship.

Results from their calculations for a container ship revealed a distinct difference between the maximum sagging and hogging wave bending moments, the sagging moment being the greater. This nonlinear effect was observed from full scale measurements and the differences between the sagging and hogging bending moments were found to be the same magnitude as those found on measurements. However, their method is limited to rather moderate sea states, since, it is based on series expansions around the still water position.

In order to include the effects of the hull form on the vertical motions and loads in large amplitude waves, it is necessary to solve the motion equations in the time domain. Further, by introducing hydrodynamic coefficients varying with time, it would be possible to include in the formulation rapid fluctuating momentum forces and moments. These are of considerable importance for fast-going ships with large bow flare sections, e.g. container ships.

Meyerhoff and Schlachter[8] developed a strip theory in which ship motion equations are solved in the time domain. The external forces acting on the ship hull were obtained from the instantaneous submerged section of different stations and slamming forces were included. Ship motions and total response of the ship hull in head seas were calculated in the time domain in regular or irregular waves.

Yamamoto et al[9] investigated theoretically the motion and longitudinal strength of a tanker in head seas taking account of the effects of nonlinearities such as the hull shape

nonlinearity, bottom emergence and hydrodynamic impact. A series of tests was carried out in a basin, measuring the heave and pitch angles, the acceleration at the bow and the bottom pressure along the base line. The experimental results were compared with calculations, which showed good agreement. Conclusions obtained are as follows :

The heaving and pitching amplitudes themselves were effected only slightly by slamming, the acceleration at the bow increases due to the effect of nonlinearity. The time history of the calculated pressure and measured were similar in shape. The sagging bending moments became very large in slamming conditions in the fore body in the case of large ships.

Yamamoto et al[10] proposed a theory to predict the behaviour of a ship among rough seas, taking account of impact forces due to slamming and a special version of the theory can be used to determine the rigid-body motions. A series of experiments were conducted with a model of a fast container ship of fine hull form with prominent bow flare, the results obtained were in good accordance with the nonlinear theory even in case of slamming. At $\lambda / L=1.0$, ship motions for five different wave heights were given.

Borresen et al[11] presented a method to predict the nonlinear response of coupled heave and pitch motions and vertical wave loads in regular, head waves based on the strip theory. The nonlinearities arose from the integration of the wave pressure over the wetted part of the hull, and by including the effect of bow flare, bottom slamming and deck wetness. The formulation was based on long waves of ship length order.

The equations were solved in the time domain, and results were presented and compared with those obtained from linear theory and model tests. Generally, good agreement was achieved between the time domain simulations and the model test results.

A nonlinear strip theory for predicting ship motions and loads in the time domain in head seas was presented by J. B. Petersen et al[12]. Hydrostatic, hydrodynamic and impact forces were considered. The added mass and damping coefficients were obtained by different methods, i.e. Lewis form transformation and Boundary Element methods. The simulation results and experimental results of two different models were compared. The results showed that there was a good agreement between the theoretical and experimental results for the container ship model, however, the agreement between the theoretical and

experimental results was not so satisfactory for a fast survey model. There was a slight effect of the hydrodynamic coefficients obtained from different methods on ship motions. However, there was a some effect of the hydrodynamic coefficients obtained from different methods on midship wave bending moment.

A technique of time domain numerical simulation to predict the occurrence of water shipping on board in head waves was presented by Fang et al[13]. The nonlinear effects, which include the effects of large wave amplitude, large ship motions and the change of hull configuration below the free surface and nonlinear resultant wave were taken into account. The instantaneous wave surface around the ship hull was obtained from the complete incident, diffracted and radiated wave system rather than the incident wave only.

The above investigations showed that the results obtained from the nonlinear theoretical prediction methods are more accurate than those obtained from the linear strip theory.

Experimental investigations of ship motions and structural loads were carried out by many researchers.

Two container ship models (2.0 and 3.0 m length models) were used to carry out experiments in head, following and oblique waves by Takezawa et al[17]. Ship motions as well as shear forces and bending moments were measured at four speeds, five encounter angles and ten wave frequencies to investigate different strip theories.

A different container ship model (4.5 m long model) was used to carry out experiments in regular and irregular waves. Ship motions at two speeds, eight wave frequencies were measured to compare experimental results with the results of predictions obtained by theoretical calculations based on the "strip method" by Takaishi et al[18].

Lloyd et al[19] used a destroyer model to carry out experiments in regular oblique waves to measure ship motions and relative motions at two speeds, ten frequencies.

However, the effect of large amplitude ship motions were not investigated in the experiments summarised above.

Only a few examples of two MARINER destroyer models were presented by Borresen et al[11]. The results of the heave, pitch motions and the wave bending moment in the midship at one frequency, two speeds and several wave amplitudes were compared

between the simulations and the experiments.

Y. Yamamoto et al[10] also considered nonlinear effects in rough seas. In their paper, nonlinear effects of heave and pitch motions were investigated at eleven frequencies, two different wave heights (small and large wave heights) and one speed. Only at $\lambda / L = 1.0$, ship motions for five different wave heights were shown. Generally speaking, the response of heave and pitch motions decrease when wave height increases.

A 3.0 m long series 60 ship model was used by Fang et al[13] for the tests to confirm the theoretical predictions. Heave, pitch and relative motions were measured in the tests. However, the experimental results were not given for the heave and pitch motions for three different wave amplitudes (small, medium and large wave heights), only the theoretical calculations were shown in their paper.

1.2 Slamming pressures

When a ship is travelling at high speed in rough sea, the phenomenon of the ship impacting wave occurs. A typical encounter cycle is as follows: at first, the ship's forward bottom emerges from the water and re-enters the water after hitting its surface. This is known as "bottom impact slamming". Then, the bow flare of the ship impacts the wave surface. This is called bow flare slamming. Finally, the ship bow immerses into water and the water impacts the deck, this phenomenon is known as "deck wetness".

The bottom slamming pressure have been investigated by many researchers, The famous methods are the Wagner wedge impact theory[20], the Chuang cone impact theory and the Ochi & Motter's method.

Stavovy and Chuang[21] proposed an analytical method for determining wave impact "slamming" pressure on all types of ship hulls including advanced vehicles that may travel at speeds up to 100 knots and even higher speeds. The method is based on the Wagner wedge impact theory, the Chuang cone impact theory, and experiments were performed at the David W. Taylor Naval Ship Research and Development Center. The prediction of the impact pressure is based on the hypothesis that the impact velocity is equal to the relative velocity normal to the impact surface of the moving body and the wave

surface. The proposed method has been verified by several model tests in waves and by actual ship trials of the catamaran USNS Hayes. Computer programs were developed included for the practical use of the method.

A method to estimate the bottom slamming pressure was developed by Ochi and Motter[22-23]. The bottom slamming pressure is approximately proportional to the square of the relative velocity at the instant of impact. The pressure coefficient depended only on the hull section shape, particularly the shape of the bottom portion below about one tenth of the design draught.

The momentum slamming method[24] is also used to determine the bottom slamming pressure which is defined as the momentum slamming force distributed over the instantaneous breath in the bottom region.

A theoretical method of calculation of the keel pressure and the maximum pressure, which agreed well with measurements developed by Payne[25-26], and this theoretical method was used to predict the impact pressure for the small scale SWATH characteristic model which was used for drop tests by Zhu and Faulkner[27-29].

Several cases of structural damage caused by the bow flare slamming were reported[10,31-32]. In the North Pacific Ocean near Japan, such damage occurred frequently for container ships which are generally characterized by the bow form with prominent flare. It is well known that this particular sea area is usually subjected to heavy seas with high waves in winter seasons due to the seasonal wind from the west. Most damages took place during the voyages from the North and South American Continents to Japan, in heavy head seas with high waves up to 20 m.

The research on the bow flare slamming problems was carried out by many investigators[31-39].

A simplified model and procedure were developed to estimate hydrodynamic forces on a bow with large flare, and the resulting vertical bending moment along a ship hull by Gran et al[33]. The bow flare slamming force was obtained from the conservation law of momentum and the hydrodynamic coefficients were obtained from Lewis' transformations. The dynamic response due to hull flexibility was considered and that was greatest when the force duration matches the natural period of the hull. It was suggested that the short term

distribution of loads and stresses due to the bow flare impact can be described by Weibull probability distributions. The influence of the ship speed and sea state on the loads and responses were investigated to some extent, and it was concluded that the influence of ship speed was relatively much stronger in severe sea states.

The bow flare damage of large full ships due to wave impact was described by Suhara[31]. The investigation of actual damages in full-scale vessels, fundamental concepts regarding the bow flare damage problem, velocity of a ship relative to wave, the bow flare slamming pressures computed using the method proposed by Chuang for impact with water surface and a kind of Bagnold type impact theory for impact with a breaker, and finally, a proposal of design standard of the bow flare were described in his paper.

Bow flare slamming was investigated by Yamamoto et al[34]. Bow flare slamming may become very important for a fast container ship from the structural point of view, because it may result in serious damage in the fore body. The longitudinal vertical bending moment in a container ship was also investigated theoretically.

The problem of fast ships with large bow flare suffering from slamming and damage in the bow region was discussed by Fukasawa et al[35]. The strength rule for the bow longitudinals provided by the classification societies on the basis of their experiences of structural damage to impact pressure was also described. A theory of slamming of ships (Karman's Theory) among regular waves was proposed in this paper. The critical wave heights for collapse of side structure can be obtained for the respective classification societies from the results, and collapsing probability of longitudinals in classification society's rules was also shown.

The structural damage of a fast ship due to bow flare slamming was analysed by Yamamoto et al[32] and the impact pressures were calculated by Karman's theory. The damage was investigated from the viewpoint of ship hydroelasticity with the aid of fracture mechanics. The results obtained suggested the importance of ship handling as well as structural design for preventing damages in large container ships.

Hwang et al[36] described methods to calculate the bow flare impact force and pressure by the momentum slamming theory and the Wagner type impact theory[21], when a ship was travelling in sinusoidal waves with large amplitude. In Hwang's method, the

linear strip theory was used for ship motion calculations and the frequency dependent added mass and restoring forces were computed at the instantaneous submerged sections. However, the damping forces were computed only at the mean position.

A numerical method was developed to simulate the bow flare slamming of fast ships by Arai and Matsunaga[37]. Curved ship body boundary was represented by the Porocity method within the constraints of a rectangular grid system. A numerical simulation was carried out using a cross section of a typical container ship with a large bow flare and the simulations were compared with model experiments.

Faltinsen[38] described various methods (the boundary element method, similarity solution, asymptotic solution and Arai & Matsunaga's theory[37]) to calculate bow flare impact pressure distribution during water entry of a wedge with constant vertical velocity and compared these with drop test pressure measurements.

A theoretical method for determining slamming impact pressure distributions on ship sections was described by Kaplan[39] which provides a means of obtaining average panel slamming pressure distributions, in time history form, as an output associated with vessel motions and loads in a seaway. The theoretical model is based upon using information from a presently existing procedure providing the linear acceleration pressure component, for high frequencies, which is then extended to obtain the total nonlinear pressure distribution inclusive of slamming effects. Comparisons with known analytic solutions, for fixed instantaneous positions of an immersed section (viz. for a circle and semicircular sections) corresponding to the quasi-steady condition, provide a basic validity for this procedure.

Experimental investigations into the bow flare slamming problem were also carried out by various researchers.

Drop tests were conducted with a two-dimensional model which had the same cross section shape of a container ship[32]. Ten pressure gauges were used in the experiments. The time history of slamming pressures was given.

A model test was conducted for models with two kinds of bow flare form in both regular and irregular waves in order to study the effects of the bow flare to the deck wetness and asymmetry of the vertical wave bending moments by Watanabe et al[40].

Motions, impact pressures and vertical wave bending moments were measured. The bow flare slamming pressures only at the stem above LWL for one speed, eleven frequencies and one wave amplitude were given.

Full scale measurement of the bow flare slamming pressure was also carried out by Takemoto et al[41-42].

1.3 Shear forces and bending moments

Wave bending moment of the displacement type ship in waves can be estimated satisfactorily by the linear strip theory [1-3,43].

Calculations were performed of wave induced vertical bending moments using a linear theory of ship motions (S.T.F method[31]) by Soares[44] and the theoretical predictions were compared with various sets of measurements on ship models which are Series 60 C_B=0.7[45], Series 60 C_B=0.8[46], Cargo ship C_B=0.62[47], Dutch container ship C_B=0.60[48], SL-7 Container ship C_B=0.54[49] and a Destroyer model C_B=0.48[19].

The linear theory provided results of good engineering accuracy but perfect results cannot be expected in most cases. The results depended on the block coefficient of the model, heading and speed.

When the wave amplitude becomes large, however, nonlinear characteristics of wave loads become significant. It is important to take account of such nonlinear characteristics.

Some researchers[11-12, 50-52] considered nonlinear effects when they formulated the wave forces. They compared these predictions with the experimental data (as described above).

The results obtained from the nonlinear theoretical predictions methods have better agreement with experimental data than the linear theory.

Chiu and Fujino[53] calculated wave loads considering nonlinear effects, for example, it was possible to calculate the behaviour of the ships in waves even in the case where the submerged portion of the ship's hull varied significantly with time and the nonlinear hydrodynamic forces acting on the ship were considerable. The numerical

prediction values were compared with the model test carried out with two different kinds of semi-displacement craft in head waves, the results were satisfactory.

The large sagging bending moment was illustrated in the theoretical and experimental researches which cannot be obtained from the linear theory.

The vibratory ship response following a slamming impact occurs due to exciting the basic ship structural modes of vibration, which is represented by a sequence of non-continuous high frequency oscillations in accelerations, shears and bending moments for vertical plane response. This type of response follows the occurrence of bow and stern region impact forces, with the dominant response usually that of first - fifth structural bending modes. These oscillations decay due to damping arising from combined structural and hydrodynamic effects. The method of determining these structural response due to slamming is by the use of a modal superposition[24], with the solution represented in terms of a series of normal modes. It is assumed that the mode shapes, as well as the values of the associated frequencies, are determined by a separate structural analysis where this modal information is appropriate to the vessel in the equilibrium reference condition when floating in calm water.

The global bending moment investigated by Kaplan & Sargent[6] and Dai & Song[54] was the wave bending moment induced by linear forces superimposed on the bottom and bow flare slamming bending moments induced by bottom and bow flare slamming force, and these terms were independent among them.

The wave bending moment and slamming bending moment as well as global bending moment of two experimental models in irregular waves were given by Dai & Song[54] . They also found a satisfactory agreement with the theoretical predictions.

The global structural response was treated as the steady state response induced by the linear force and the transient responses induced by the slamming force by Belik et al[55]. The strip theory was used to represent fluid actions and the ship was considered as a nonuniform Timoshenko beam in their study.

The global bending moment consisting of the wave bending moment induced by the linear force and the slamming bending moments induced by slamming forces, which was composed of both a rigid body response and a vibratory response due to the elasticity of the

ship structure, was also studied by Kaplan[56].

The heave, pitch and roll motions as well as vertical and lateral bending moments of a model were measured in irregular waves at one forward speed, one heading angle of the port bow and the same speed and heading in a storm sea condition. The results were also compared with the theoretical predictions which showed a good agreement.

The combination of wave induced response and slamming induced response was also investigated by Hasen[57]. In his study, the non-Gaussian and non-stationary process, Slepian model, was used to solve the combination problem of the low frequency wave induced bending moment and high frequency slamming induced bending moment in ships. He also suggested that the assumption that the time of occurrence and the intensity of a slamming impact are independent of the corresponding quantities of the previous impact, as embedded in the Poisson pulse model, was not valid due to the periodic character of the ship motion.

From above descriptions of ship motions, slamming pressures and wave bending moments as well as global bending moments, some nonlinear methods to predict the large amplitude ship motions and sea loads have been developed by some researchers, however, further investigations of these nonlinear methods and sufficient experimental researches to validate them are needed.

The aim of this research is to develop computational tools to predict the large amplitude motions and loads on ship travelling with forward speed in waves. An experimental research programme was completed to validate the nonlinear prediction method. In this thesis, the results of theoretical and experimental investigations to predict the nonlinear ship motions, slamming pressures and bending moments in regular head seas are presented.

In the chapter 2, the practical nonlinear theoretical prediction method described in this research[58-59] is based on "relative motion hypothesis" in which nonlinear effects, i.e., nonlinear dynamic restoring force, nonlinear damping force and nonlinear fluid momentum force are considered. The motion equations are solved in the time domain by the numerical integration technique, the three points predictor-corrector method (Hamming method). The frequency dependent added mass and damping coefficients are computed at

the instantaneous submerged section using the close-fit conformal mapping method. The results by the nonlinear method have very good agreement with the experimental test results for heave and pitch motions, expect overpredction in the resonance region in large waves for the heave motion.

The bottom and bow flare slamming pressures are described in the Chapter 3.

The bottom slamming pressure is calculated by Stavovy & Chuang theory, Ochi & Motter theory, the momentum theory and Payne impact theory. The Ochi & Motter theory predicts a good agreement results with the experimental data, while other methods predict bigger values than the experimental results.

The momentum slamming theory and Wagner impact theory are used to predict bow flare slamming pressures[61-62]. The total impact pressure is expressed as the sum of water immersion impact pressure and wave striking impact pressure. The momentum slamming theory and Wagner impact theory can predict a good results of bow flare slamming. The bow flare slamming pressure increases as the wave amplitude and the speed increase.

The wave shear forces and bending moments are calculated using the nonlinear theoretical prediction method and the linear strip theory. Generally, the nonlinear prediction method will predict more reasonable good results than the linear method.

The ship hull is considered to be a Timoshenko beam, where the vibratory elastic response of the ship is calculated by the modal superposition method. The global dynamic shear force and bending moment values are predicted using two different methods[63-64] : One is based on the elastic vibratory response due to the total hydrodynamic force; The other is based on the rigid body response due to the linear force superimposed with the elastic response due to impact forces. The results by the elastic vibratory response due to the total hydrodynamic force (method 1) have a good agreement with the experimental results and these are much better than the results by the rigid body response superimposed with the elastic response (method 2). The detailed description can be seen in the Chapter 4.

The experimental researches[59,61-63, 65] are given in the Chapter 5.

The nonlinear ship motions and sea loads predicted by the computational tools developed in this research can be used to further ship structural strength analysis and guide ship hull design.

CHAPTER 2

SHIP MOTIONS

2.1 General description

A nonlinear theoretical prediction method developed described in this research[58] is based on "relative motion hypothesis" in which nonlinear effects, i.e., nonlinear dynamic restoring force, nonlinear damping force and nonlinear fluid momentum force are considered, when the ship motions are calculated and equations are solved in the time domain.

The frequency dependent added mass and damping coefficients are computed at the instantaneous submerged sections by the close-fit conformal mapping method.

The force acting on the ship hull, the derivation and solution of the ship motion equations are discussed and comparisons between the theoretical predictions and experimental data of the heave, pitch and relative motions and acceleration as well as the time history of these motions and the accelerations are also described in this chapter.

2.2 Coordinate systems and assumptions

2.2.1 Coordinate systems

A slender ship moving with constant forward speed U through a train of regular head waves is considered. Let (x,y,z) be a coordinate system moving with the ship relative to a system (x_0,y_0,z_0) fixed in space (see Fig.2.1). The x-axis points in the direction of U, and the (x,y) plane is located at the position of undisturbed water surface (y-axis points to starboard), with the z-axis vertically upward through the centre of gravity. Assume that (x_b,y_b,z_b) is another coordinate system fixed in the ship, and when the ship is moving through the still water, the system (x_b,y_b,z_b) and (x,y,z) coincide.

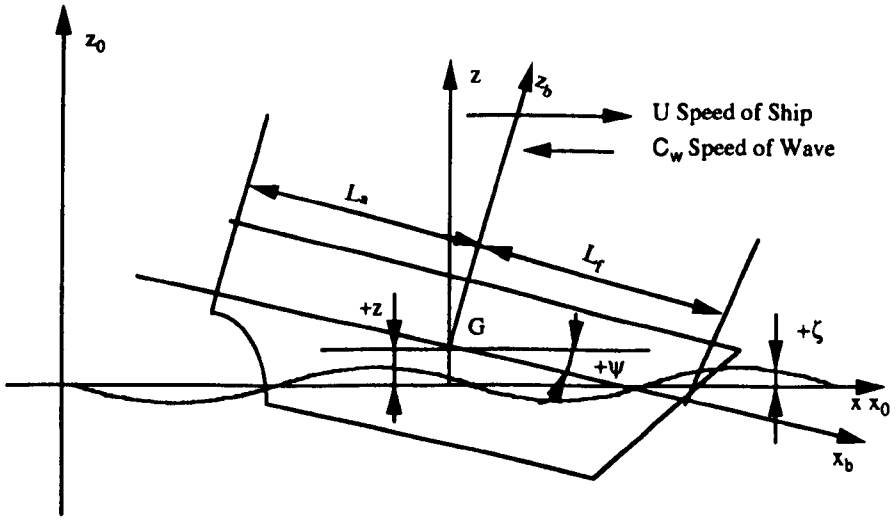

Fig.2.1 Coordinate Systems

2.2.2 Assumptions

1) The fluid is assumed to be inviscid, homogenous and incompressible.

2) The motions in regular, plane waves moving with a constant phase velocity in the x-direction are studied, so the position of the surface (a first - order gravity wave in deep water (sinusoidal wave)) in the moving reference frame (x, y, z) may be written as

$$\zeta(x,t) = \zeta_a \cos(Kx + \omega_e t) \qquad (2\text{-}1)$$

$\zeta(x,t)$ is the wave elevation as a function of x and time t, ζ_a is the wave amplitude, K is the wave number and ω_e is the frequency of encounter in the moving reference frame. The dispersion relation between the wave number and the wave frequency ω for deep water waves :

$$K = \omega^2 / g \qquad (2\text{-}2)$$

The relation between the frequency of encounter and the wave frequency is

$$\omega_e = \omega + KU \qquad (2\text{-}3)$$

3) The ship is long and slender, with the beam and draft small compared to the ship length.

4) The ship has lateral symmetry.

5) This method is based on "relative motion hypothesis", i.e. the wave-exciting forces can be calculated from relative motions between the ship and the wave.

If $z(t), \psi(t)$ are defined as the heave and pitch motions respectively, then the relative motion, the relative velocity ($\dot{r} = \frac{dr}{dt}, \dot{r}_1 = \frac{\partial r}{\partial t}$) and the relative acceleration values are

$$\begin{cases} r = z - x_b\psi - \zeta \\ \dot{r} = \dot{z} - x_b\dot{\psi} + U\psi - \dot{\zeta} \\ \dot{r}_1 = \dot{z} - x_b\dot{\psi} - \dot{\zeta} \\ \ddot{r} = \ddot{z} - x_b\ddot{\psi} + 2U\dot{\psi} - \ddot{\zeta} \end{cases} \qquad (2\text{-}4)$$

2.3 Ship motion equations

2.3.1 Description of external forces

The force $f(x_b, t)$ acting on the ship hull consists of the hydrodynamic force, the hydrostatic force $f_H(x_b, t)$ and the gravity and the ship hull inertia forces (D'Alembert force).

$$f(x_b, t) = f_H(x_b, t) + f_A(x_b, t) \qquad (2\text{-}5)$$

Omitting hydrostatic and gravity forces in still water, the external force can be considered as the sum of the following terms :

1) Dynamic restoring force f_{H1}

2) Wave damping force f_{H2}

3) Fluid momentum force f_{H3}

4) Ship hull inertia force f_A

1) Dynamic restoring force

The dynamic restoring force acting on a two dimensional ship section can be expressed as :

$$f_{H1} = \rho g(A_r - A_0) \qquad (2\text{-}6)$$

ρ Density of fluid.

g Gravitational acceleration.

A_r Instantaneous submerged sectional area.

A_0 Sectional area in still water.

2) Wave damping force

The wave damping force acting on a two dimensional ship section due to surface waves generated from ship oscillations and the deformation of incoming wave field (diffraction effects) can be expressed as :

$$f_{H2}(x_b, t) = -N_r(x_b, t)\dot{r} \qquad (2\text{-}7)$$

N_r Sectional damping coefficient in the heave motion.

3) Fluid momentum force

The hydrodynamic force acting on a two dimensional ship section due to the rate of change of fluid momentum induced by the ship motions relative to the fluid will be :

$$f_{H3} = -\frac{d}{dt}\left[m_r(x_b,t)\dot{r}\right] \qquad (2\text{-}8)$$

d / dt is the substantial derivative given by :

$$\frac{d}{dt} = \frac{\partial}{\partial t} - U\frac{\partial}{\partial x_b} \qquad (2\text{-}9)$$

m_r is the sectional added mass in heave motion which varies as a function of position and time. $\dot{r}$ and $\dot{r}_1$ are the relative velocity between the wave and the ship hull. Therefore :

$$f_{H3} = -m_r(x_b,t)\ddot{r} + \frac{\partial m_r(x_b,t)}{\partial T_r}\dot{r}\dot{r}_1 + U\frac{\partial m_r(x_b,t)}{\partial x_b}\dot{r} \qquad (2\text{-}10)$$

The first term in the integral represents the fluid inertia or "added mass". The second and third terms represent the rate of change of the fluid momentum due to the added mass varying with time and position.

The major contributions to the second and third terms in equation (2-10) will come from the end upper sections with large added mass gradients and high relative velocities, so, these sectional forces will be referred to as "flare " forces.

It is assumed that the force due to momentum impact term is the same, when the ship is moving out of or into water. This would imply that the added mass is reduced during the water exit according to the reduced nominal immersion and that the momentum will be transferred back to the ship. During a fast reduction of the immersed width, such an assumption appears unrealistic[8]. Therefore, in the present study, the momentum impact force term will be ignored when the ship is moving out of the water, but the other terms are not affected. Hence,

$$\frac{\partial m_r}{\partial T_r} = 0 \text{ if } \dot{r} > 0 \qquad (2\text{-}11)$$

4) Ship hull inertia force

In large amplitude and steep waves, the ends of the ship, especially the bow, will become completely submerged during a full oscillation cycle. For ships with flared bow sections some or all of the water will be "splashed" away from the hull. This phenomenon will mainly depend on the relative motion, velocity and acceleration at F.P. and the geometry of the bow flare.

If the relative displacement becomes very large, the bow flare will not prevent water flowing onto the weather deck, and the effect of "green water" on the deck should be included. Due to its hydrodynamic complexity, the water mass due to deck wetness is considered in the ship hull inertia force (D'Alembert force, the gravity of the water mass is ignored) as follows :

$$f_A(x_b,t) = -\left[m_s(x_b) + \rho d(x_b,t) B_d(x_b)\right]\left(\ddot{z}(t) - x_b\ddot{\psi}(t)\right) \qquad (2\text{-}12)$$

$m_s(x_b)$ The unit mass of ship hull.

$\ddot{z}$ Heave acceleration.

$\ddot{\psi}$ Pitch acceleration.

$d(x_b,t)$ Height of water when deck wetness occurs.

$B_d(x_b)$ Width of deck.

2.3.2 Derivation of motion equations

The forces acting on a two dimensional hull section according to the analysis above are

$$f(x_b,t) = f_{H1}(x_b,t) + f_{H2}(x_b,t) + f_{H3}(x_b,t) + f_A(x_b,t) \qquad (2\text{-}13)$$

Since the total of the applied and D'Alembert forces and moments must equal zero :

$$\int_{-L_a}^{L_f} f(x_b,t)dx_b = 0$$
$$\int_{-L_a}^{L_f} f(x_b,t)x_b dx_b = 0 \qquad (2\text{-}14)$$

The motion equations become :

$$\ddot{z}\int_{-L_a}^{L_f}\left(m_r(x_b,t)+m_s(x_b)+\rho d(x_b,t)B_d(x_b)\right)dx_b -$$
$$\ddot{\psi}\int_{-L_a}^{L_f} x_b\left(m_r(x_b,t)+m_s(x_b)+\rho d(x_b,t)B_d(x_b)\right)dx_b =$$
$$\int_{-L_a}^{L_f}\left[\left[\left(\frac{\partial}{\partial T_r}m_r(x_b,t)\right)\left(\dot{z}-x_b\dot{\psi}-\dot{\zeta}\right)+\frac{\partial}{\partial x_b}(m_r(x_b,t))-N_r(x_b,t)\right]\times\right.$$
$$\left.\left(\dot{z}-x_b\dot{\psi}-\dot{\zeta}+U\psi\right)-m_r(x_b,t)\left(2U\dot{\psi}-\ddot{\zeta}\right)+\rho g\left(A_r(x_b,t)-A_0\right)\right]dx_b \qquad (2\text{-}15)$$
$$\ddot{z}\int_{-L_a}^{L_f} x_b\left(m_r(x_b,t)+m_s(x_b)+\rho d(x_b,t)B_d(x_b)\right)dx_b -$$
$$\ddot{\psi}\int_{-L_a}^{L_f} x_b^2\left(m_r(x_b,t)+m_s(x_b)+\rho d(x_b,t)B_d(x_b)\right)dx_b =$$
$$\int_{-L_a}^{L_f} x_b\left[\left[\left(\frac{\partial}{\partial T_r}m_r(x_b,t)\right)\left(\dot{z}-x_b\dot{\psi}-\dot{\zeta}\right)+\frac{\partial}{\partial x_b}(m_r(x_b,t))-N_r(x_b,t)\right]\times\right.$$
$$\left.\left(\dot{z}-x_b\dot{\psi}-\dot{\zeta}+U\psi\right)-m_r(x_b,t)\left(2U\dot{\psi}-\ddot{\zeta}\right)+\rho g\left(A_r(x_b,t)-A_0\right)\right]dx_b$$

2.4 Solutions

2.4.1 Numerical solutions

The motion equations given in (2-15) are solved by the use of numerical integration technique in the time domain.

A computer program has been developed for this purpose and a three-point predictor-corrector technique (Hamming's method[66], which can save computational time) is employed to integrate the equations.

2.4.2 Added mass and damping coefficients

The solution was obtained by numerical integration in the time domain. This is a method well suited to deal with nonlinear problems, but it creates some difficulties concerning the hydrodynamic sectional added mass and damping. In linear theory, where the solution is obtained in the frequency domain, these hydrodynamic quantities are calculated only at still water position and as a function of the frequency of encounter.

In the analysis presented, a section may be given a large displacement from the equilibrium position, and therefore, added mass and damping coefficients will depend on the instantaneous position of the wave relative to the hull. Strictly speaking, in a nonlinear formulation the classical definition of frequency dependent added mass and damping coefficients is no longer valid. The added mass and damping forces are then replaced by a single nonlinear hydrodynamic force, obtained from the integration of the nonlinear hydrodynamic pressure around the hull, this pressure could be calculated by first solving the corresponding nonlinear boundary value problem for the velocity potential, which is an extremely complicated task.

Faltinsen[67] applied Green's function boundary integral technique to solve this nonlinear problem in the simple case of forced oscillations in otherwise calm water. But the method was verified only by small amplitude motions.

In this study, the added mass and damping coefficients vary with the instantaneous draught, i.e. these quantities are calculated as if a section undergoes small (linear) oscillations about this position at a given frequency. There are several methods to calculate the hydrodynamic coefficients, i.e. infinite frequency method, Lewis's transformation method, close-fit conformal mapping method and Frank Close-Fit method[68]. In this study, hydrodynamic coefficients at 24 drafts, 21 stations and 30 encounter frequencies are calculated using the close-fit conformal mapping method and the conformal mapping coefficients are used as many as necessary in order to get the desired close-fit accuracy[69-71].

2.5 Correlation studies

The nonlinear theoretical prediction method had been described in the previous sections. Small wave height validation of the theoretical method was carried out by comparing the results with published experimental data from a destroyer model[19] and a container ship model[18].

2.5.1 Motion response of a destroyer model in small wave heights

A series of experimental tests on a destroyer model were carried out by Lloyd[19].

Comparisons of the results obtained from the nonlinear theoretical prediction method, the linear strip theory and the experimental data (model test and full scale trial) carried out by Lloyd[19] at Fn=0.21, ten wave frequencies and one wave height (1/50 wave length) in head seas are shown in Fig.2.2-2.3.

The motion responses of heave and pitch by the nonlinear theoretical prediction method (wave amplitude is 1/100 wave length) and the linear strip theory show the same results and there is a very good agreement between the predictions and the model test measurements, except for a discrepancy in $\lambda / L = 1.4 - 2.0$ region (Fig.2.2) and also a reasonably good agreement between the predictions and the full scale trial results (Fig.2.3).

2.5.2 Motion response of a container ship model in small wave heights

A series of experimental tests on a container ship model was carried out by Takaishi[18].

Comparisons of the results obtained from the nonlinear theoretical prediction method, the linear strip theory and the experimental data carried out by Takaishi[18] at Fn=0.20, ten wave frequencies and one wave height (1/50 wave length) in head seas are shown in Fig.2.4.

The motion response of heave and pitch by the nonlinear theoretical prediction method (wave amplitude is 1/100 wave length), the linear strip theory show the same

results except for a little difference in the resonance region and there is an excellent agreement between the predictions and the experimental data (pitch motion response Fig.2.4).

2.5.3 Summary of comparisions in small wave heights

The validation of the nonlinear theoretical prediction method in small wave heights and the linear strip theory had been carried out by comparing with the experimental data (a destroyer model test and full scale trail and a container ship model test). There is a reasonably good agreement between the theoretical predictions and the experimental test results.

2.6 Comparisons between the theoretical predictions and experiments

The theoretical motion responses in larger waves were compared with model tests undertaken in the Hydrodynamics Laboratory, University of Glasgow.

The model tests are described in Chapter 5.

2.6.1 Heave and pitch motions

1) Nondimensional values of heave and pitch motions obtained from predictions and measurements due to different wave frequencies at three different wave amplitudes (2.5, 4.0, 7.5 cm), two speeds Fn=0.15 and 0.25, are shown in Figs.2.5-2.6 and Figs.A.2.1-A.2.6.

For Fn=0.15, there is a good agreement between the theoretical results which take into account the nonlinear effects and experimental measurements shown in Fig.2.5 and Figs.A.2.1-A.2.3.

The influence of the wave amplitude can be seen from Fig.2.5. A large wave will cause large ship motions and the nonlinear effects become significant. In this figure, three different wave amplitudes are considered. The results show that while the wave amplitude

decreases, the results approach the values of the linear methods, which are based on the small-amplitude motion assumptions. When the large waves is considered, the motion response becomes different, normally, the nondimensional motion response values decrease when the wave amplitude increases.

For Fn=0.25, there is also a good agreement between the theoretical results which take into account the nonlinear effects and the experimental data shown in Fig.2.6 and Figs.A.2.4-A.2.6. However, there are some differences (overestimation) in the heave resonance region.

The influence of the wave amplitude can be seen from Fig.2.6. The large waves cause large ship motions and the nonlinear effects becomes significant. In this figure, three different wave amplitudes are considered. The results show that while the waves become small, the response values approach the values obtained from the linear methods based on the small-amplitude assumptions. When the large waves are considered, the motion response values become different, normally, the nondimensional motion response values decrease when the wave amplitudes increase.

2) The nondimensional heave and pitch motion values obtained from predictions and measurements due to different wave heights at three different wave frequencies (λ / L=1.0, 1.2, 1.4), two speeds Fn=0.15 and 0.25, are shown in Figs.2.7-2.12.

For Fn=0.15, there is an excellent agreement between the experimental data and the nonlinear theoretical results for the pitch motions, there is a satisfactory agreement between the experimental data and the nonlinear theoretical results for the heave motion except some differences when the wave amplitudes are large.

For Fn=0.25, there is also an excellent agreement between the experimental data and the nonlinear theoretical results for the pitch motions, there are some differences between the experimental data and the nonlinear theoretical results for the heave motions at large waves.

The theoretical results which take into account the nonlinear effects are more accurate than linear results, especially in large waves.

At low speeds and wave frequencies and small wave amplitudes, the linearity of

heave and pitch motions becomes more apparent i.e. in these conditions, the nonlinear effects are insignificant.

2.6.2 Relative motions and accelerations

Nondimensional relative motion and acceleration values obtained from predictions and measurements at different wave frequencies and for three different wave amplitudes (1.0, 4.0 and 7.5 cm), and two speeds Fn=0.15 and 0.25, are shown in Figs.2.13-2.14 and Figs.A.2.7-A.2.12.

The theoretical results which take into account the nonlinear effects agree better with the experimental data than those obtained from the the linear theory as shown in these Figures. There are differences between the relative motion predictions and measurements in large waves, this is because the water level exceeds the freeboard and it was not possible to measure the height of water over deck (Figs.2.24 and 2.26).

The influence of wave height can be seen from Figs.2.13 and 2.14. The large waves will cause large relative ship motions and accelerations. Normally, the relative motions and acceleration decrease as the wave height increases due to nonlinear effects. In the region of resonance, there are some differences between the theoretical results and the experimental data.

2.6.3 Time history analysis

Time history of the heave, pitch, relative motions and accelerations obtained from measurements and predictions at $\lambda / L=1.0$, Fn=0.15 ; $\lambda / L=1.3$, Fn=0.25 for two wave amplitudes are shown in Figs.2.15-2.28 (The time history of the accelerations as obtained from the experiments was not given because the values were recorded in the chart recorder).

The theoretical results agree with the experimental ones generally well. The positive amplitude and negative amplitudes are of different magnitude, which are different from the general harmonic results in the frequency domain, as shown in these Figures. This

phenomena are due to the change of hydrodynamic coefficients and the nonlinear restoring force which results from significant changes in cross-section areas.

2.7 Conclusions

1) The results predicted by the nonlinear theoretical methods are approaching the values obtained by the linear strip theory for small waves. For large waves, the nonlinearity of motion responses has been clearly shown. Generally, the nondimensional values of heave and pitch motions decrease as wave amplitudes increase.

2) The results by the nonlinear method show very good agreement with the experimental test results for heave and pitch motions, expect for overestimation in the resonance region in large waves for the heave motion. As the forward speed increases, the more the overprediction in the resonance region has been shown in the heave motion response.

3) As the wave amplitude increases, the heave and pitch motions increase.

4) The positive and negative amplitude values obtained by the time domain analysis and the experimental tests are generally different from each other while they have equal values above and below the at-rest water line by the frequency domain (linear theory) calculations.

5) The resistance type wave probe is not suitable for measuring the relative motions in large waves. This is because the height of water over deck can not be measured.

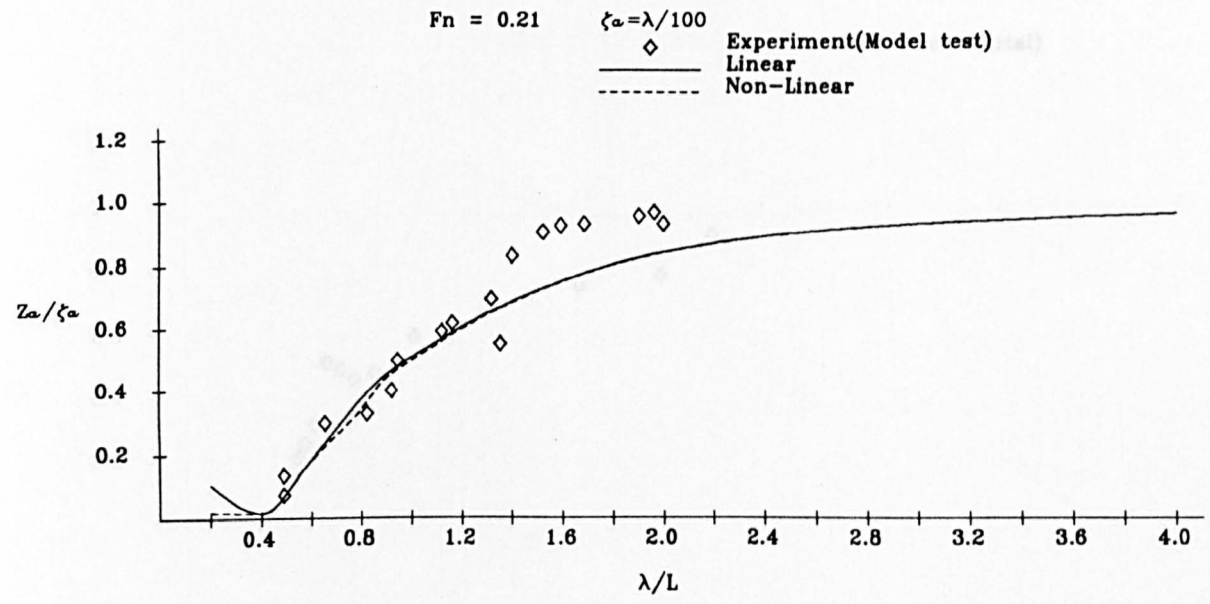

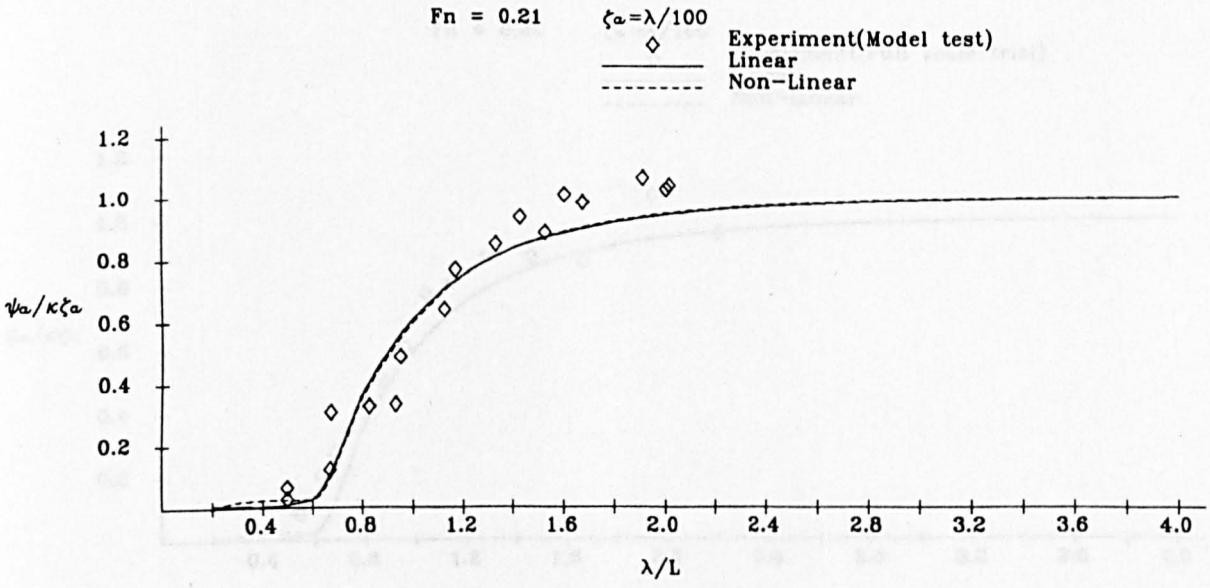

Fig.2.2 Heave and Pitch in Regular Head Seas

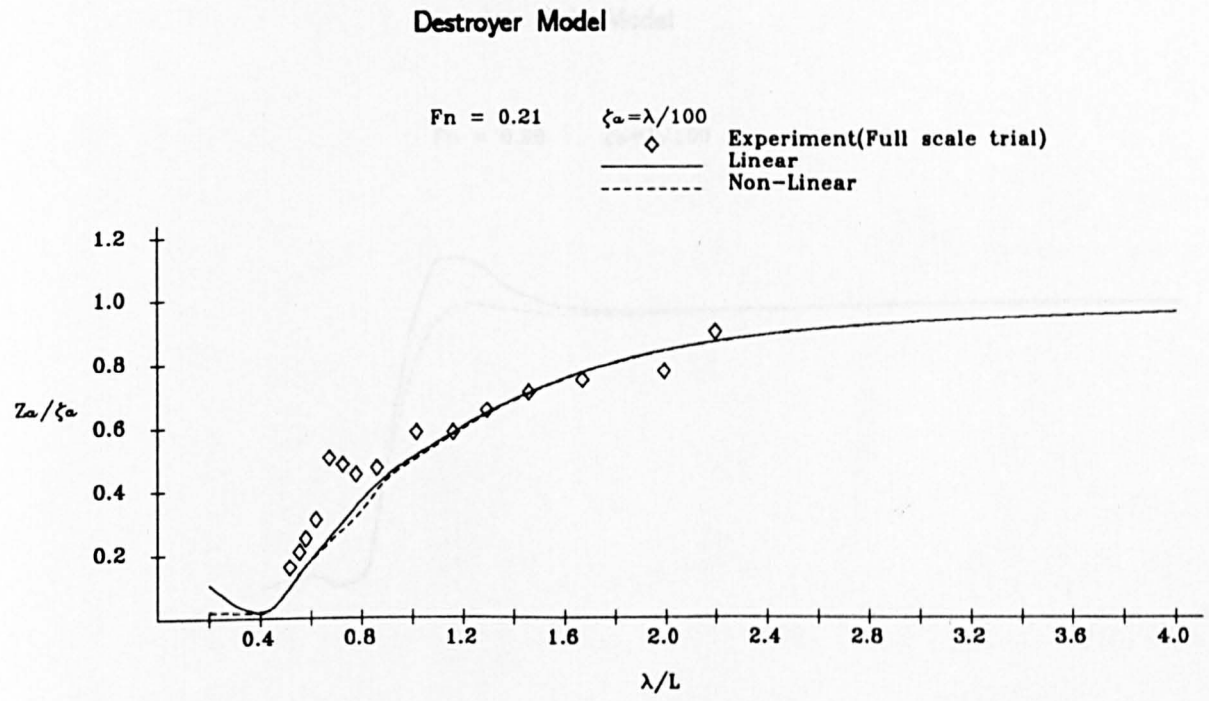

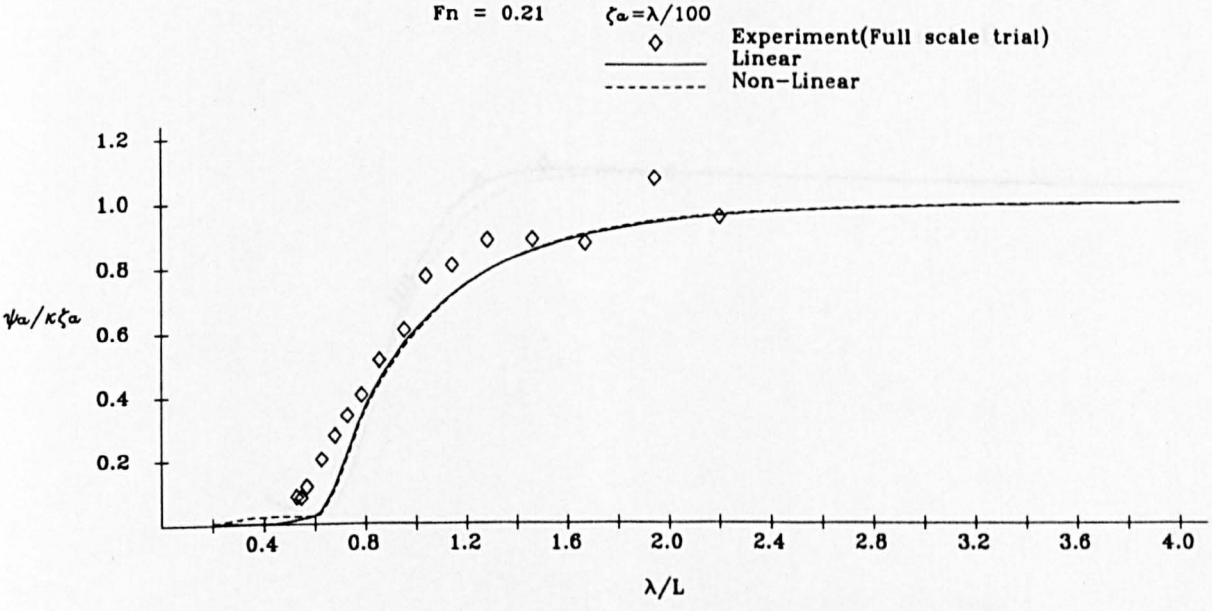

Fig.2.3 Heave and Pitch in Regular Head Seas

Container Ship Model

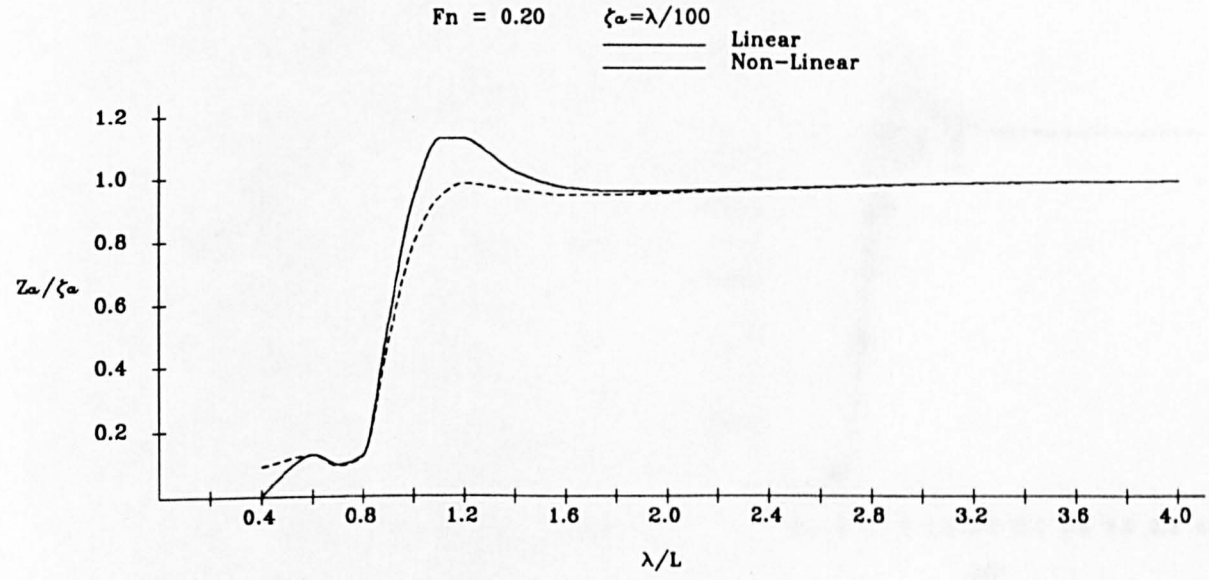

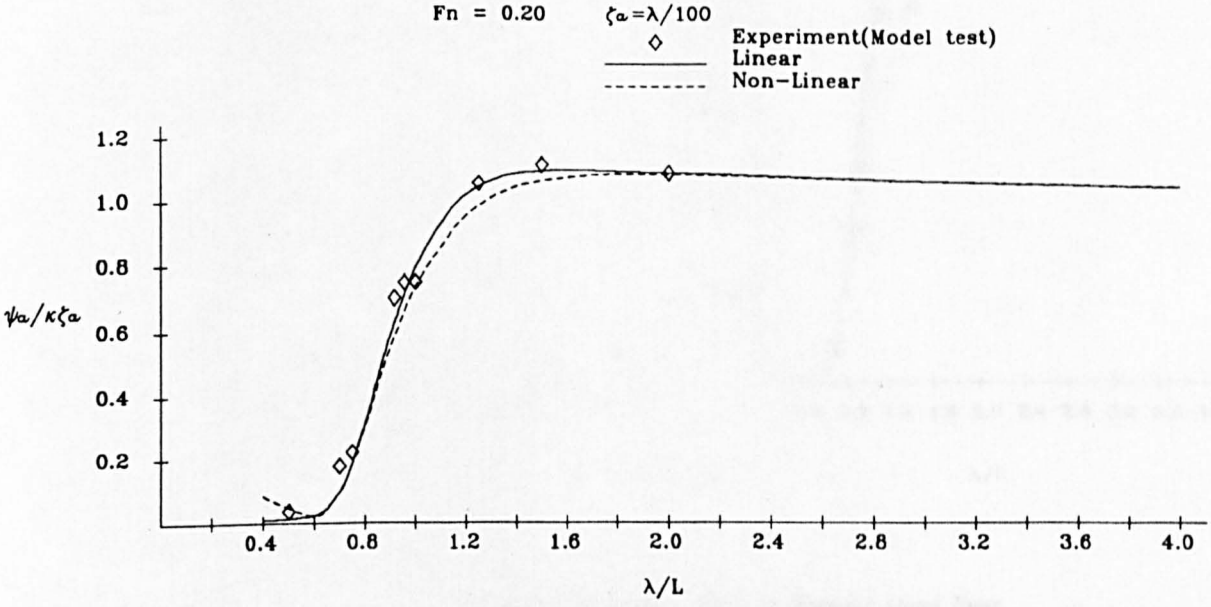

Fig.2.4 Heave and Pitch in Regular Head Seas

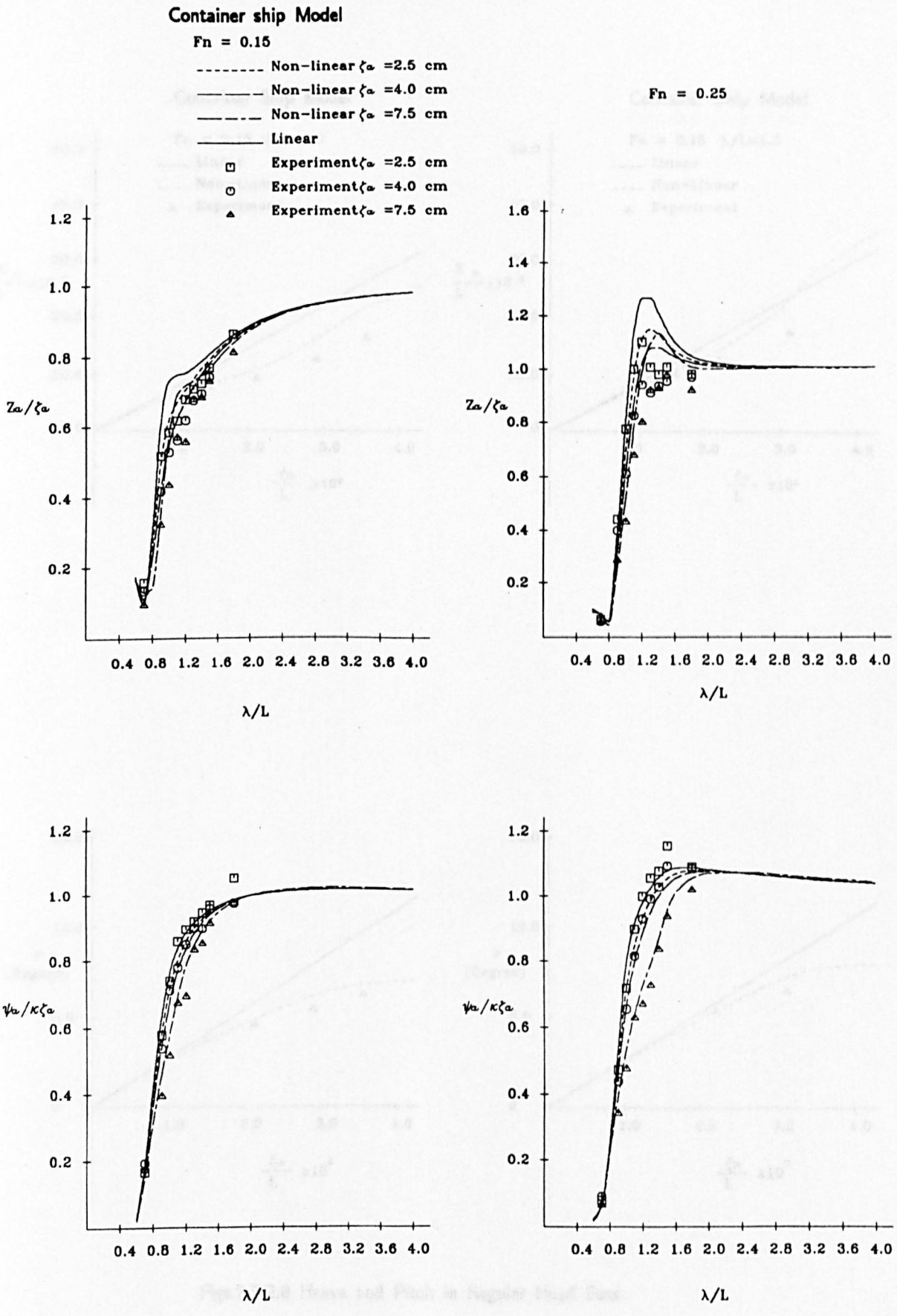

Figs.2.5-2.6 Heave and Pitch in Regular Head Seas

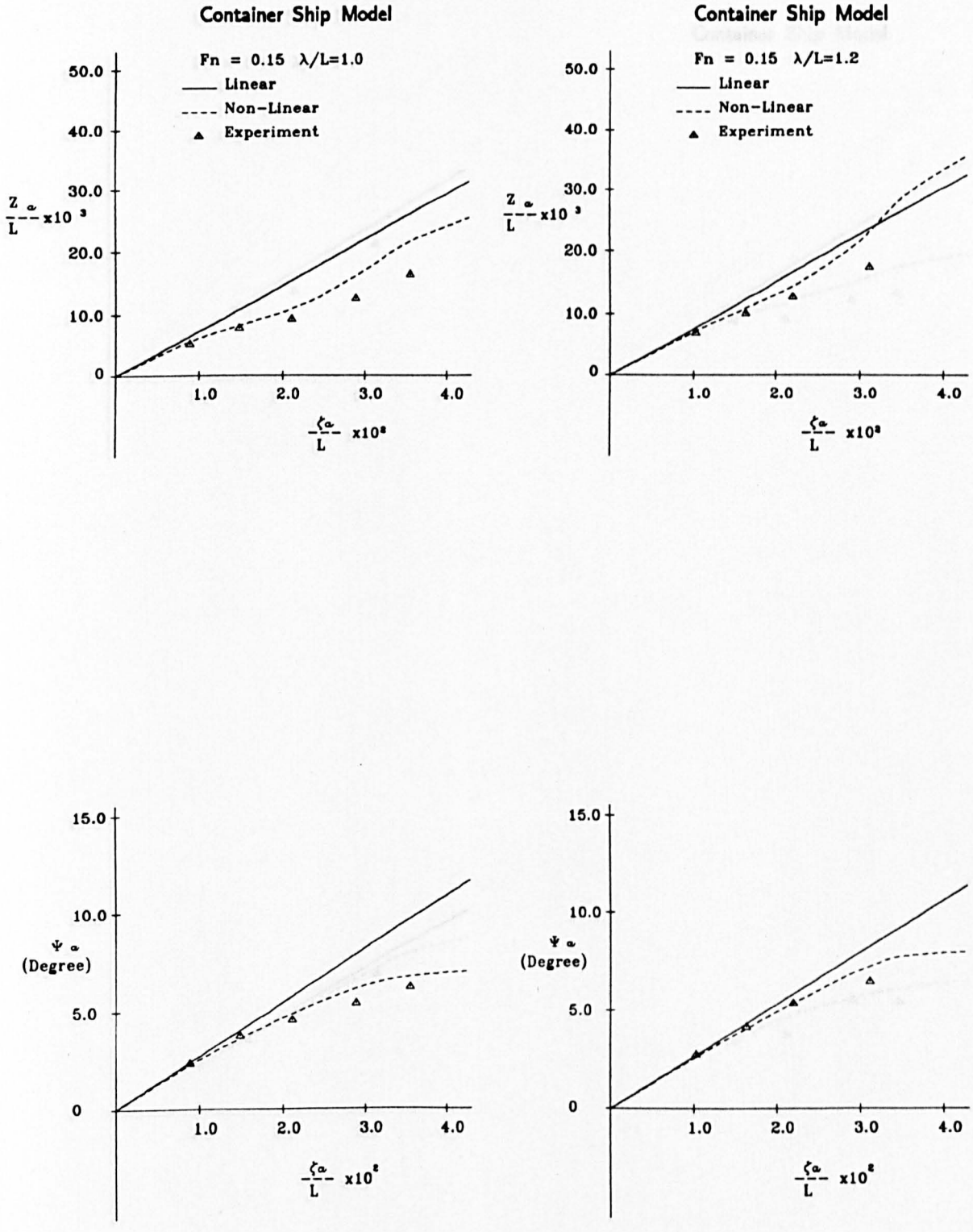

Figs.2.7-2.8 Heave and Pitch in Regular Head Seas

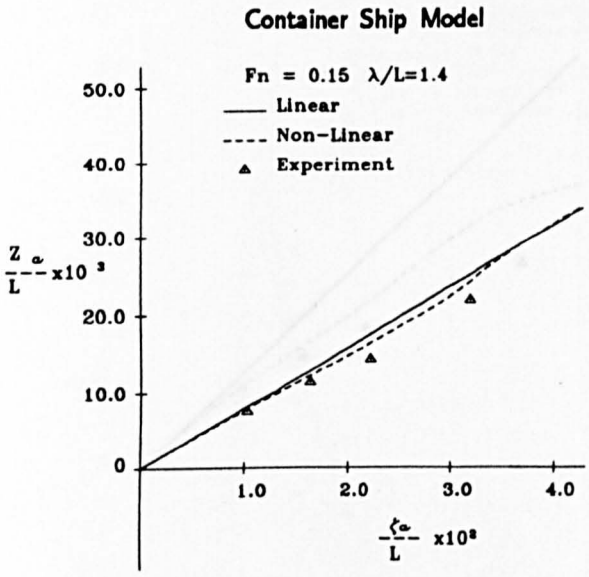

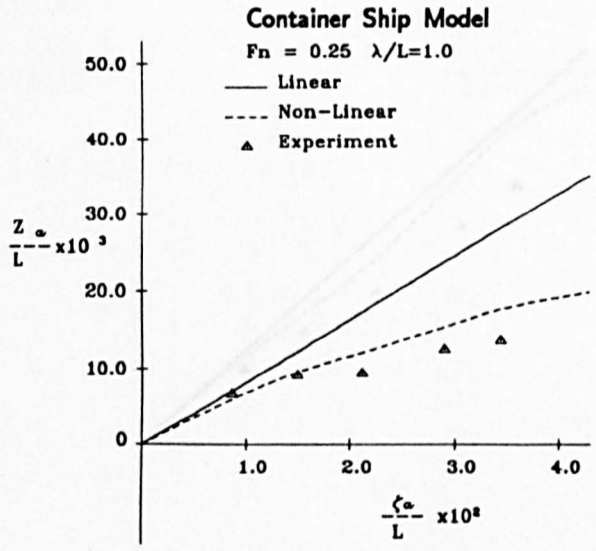

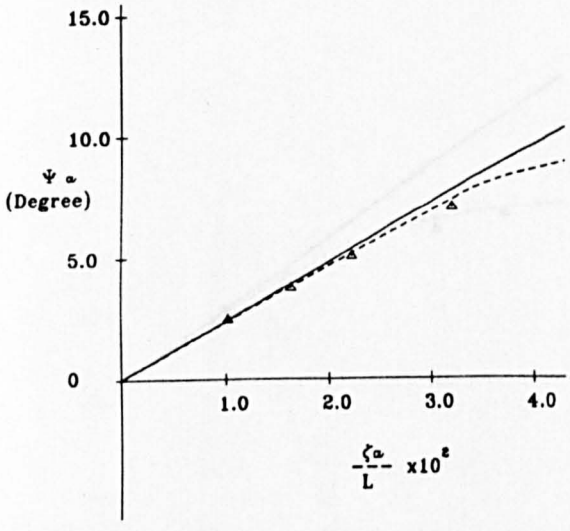

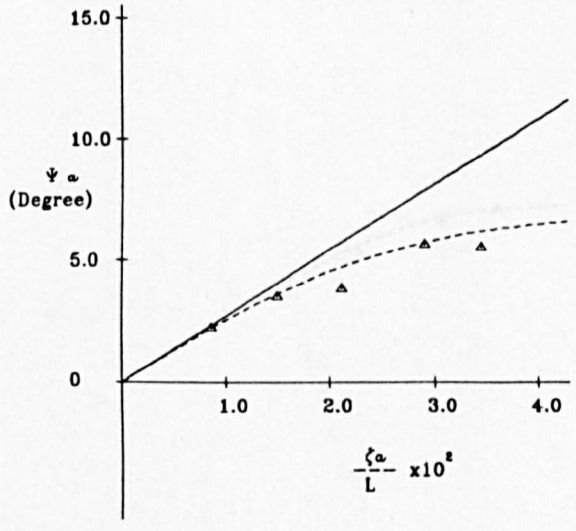

Figs.2.9-2.10 Heave and Pitch in Regular Head Seas

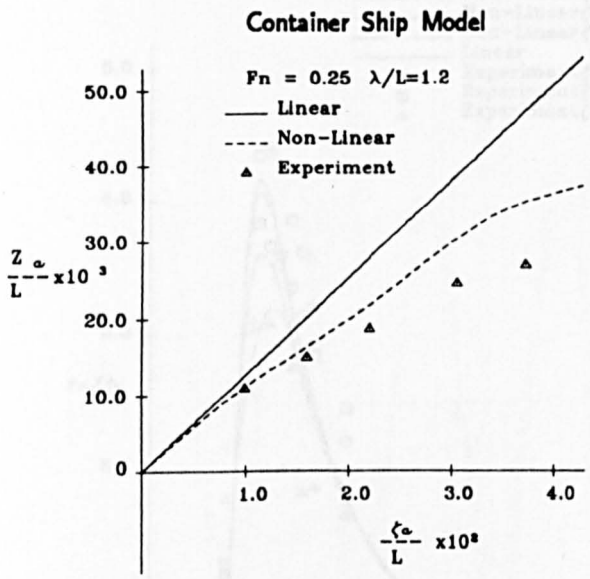

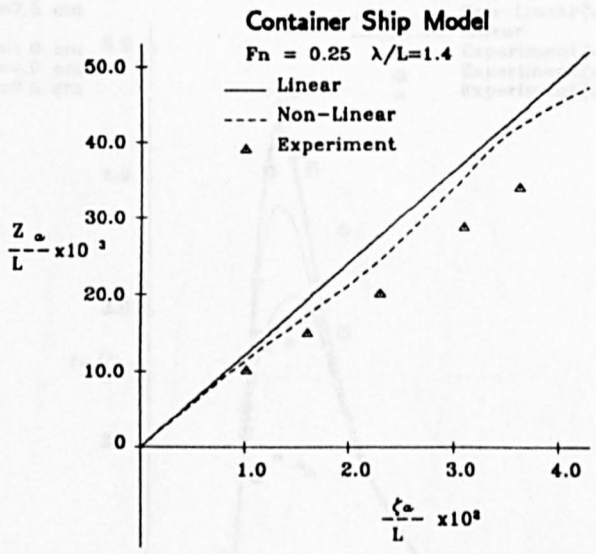

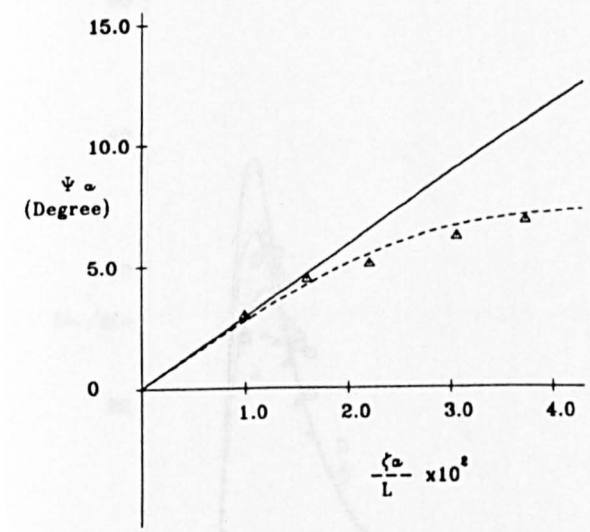

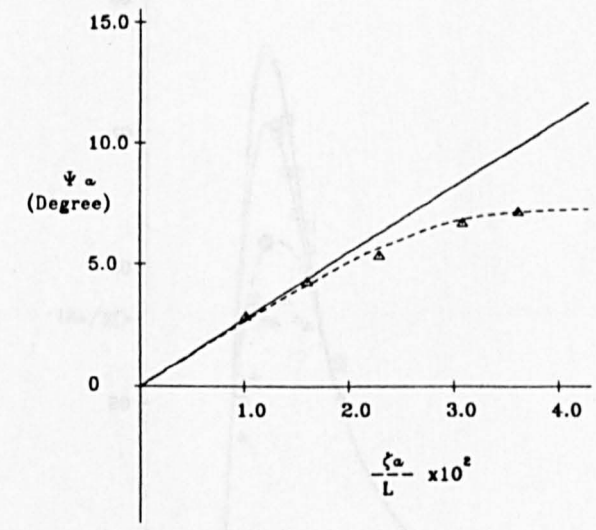

Figs.2.11-2.12 Heave and Pitch in Regular Head Seas

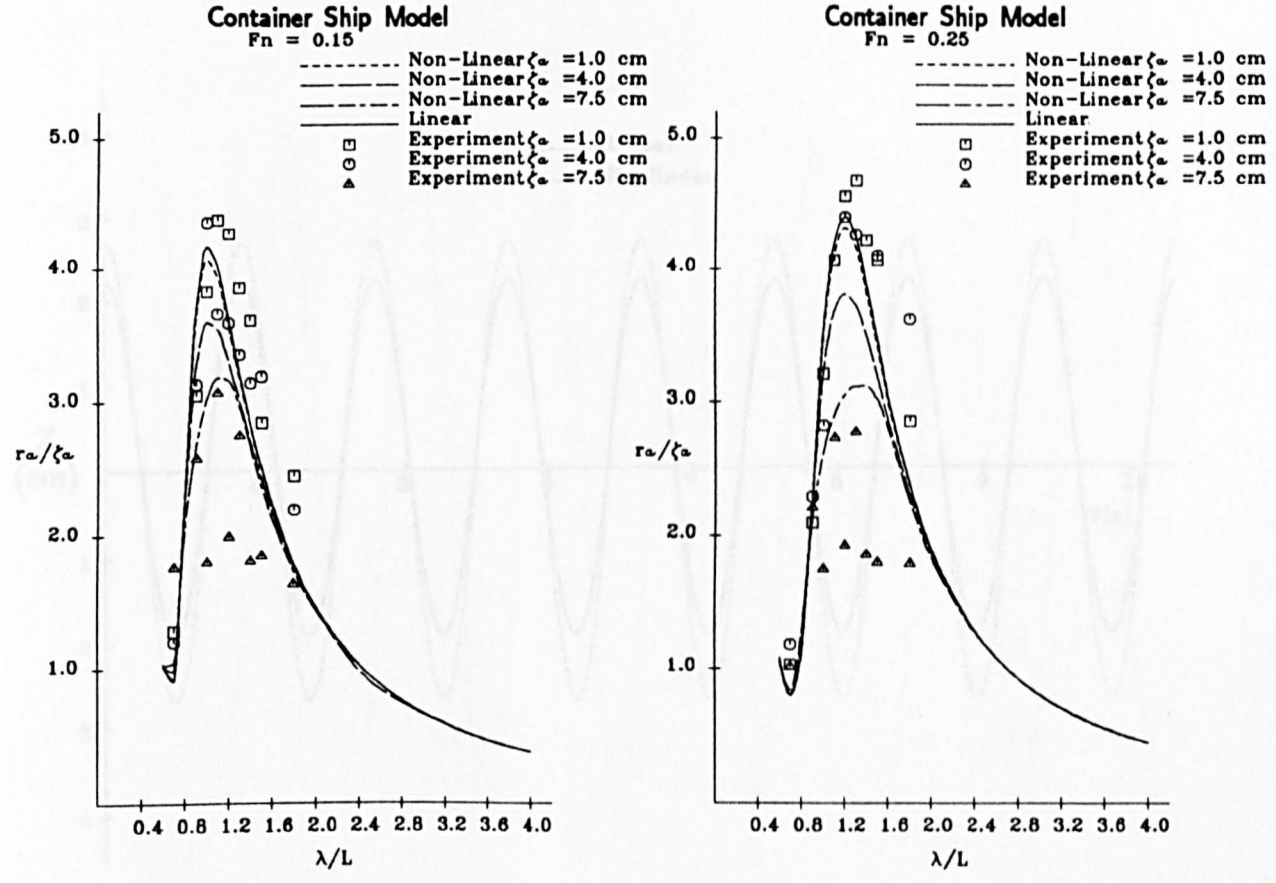

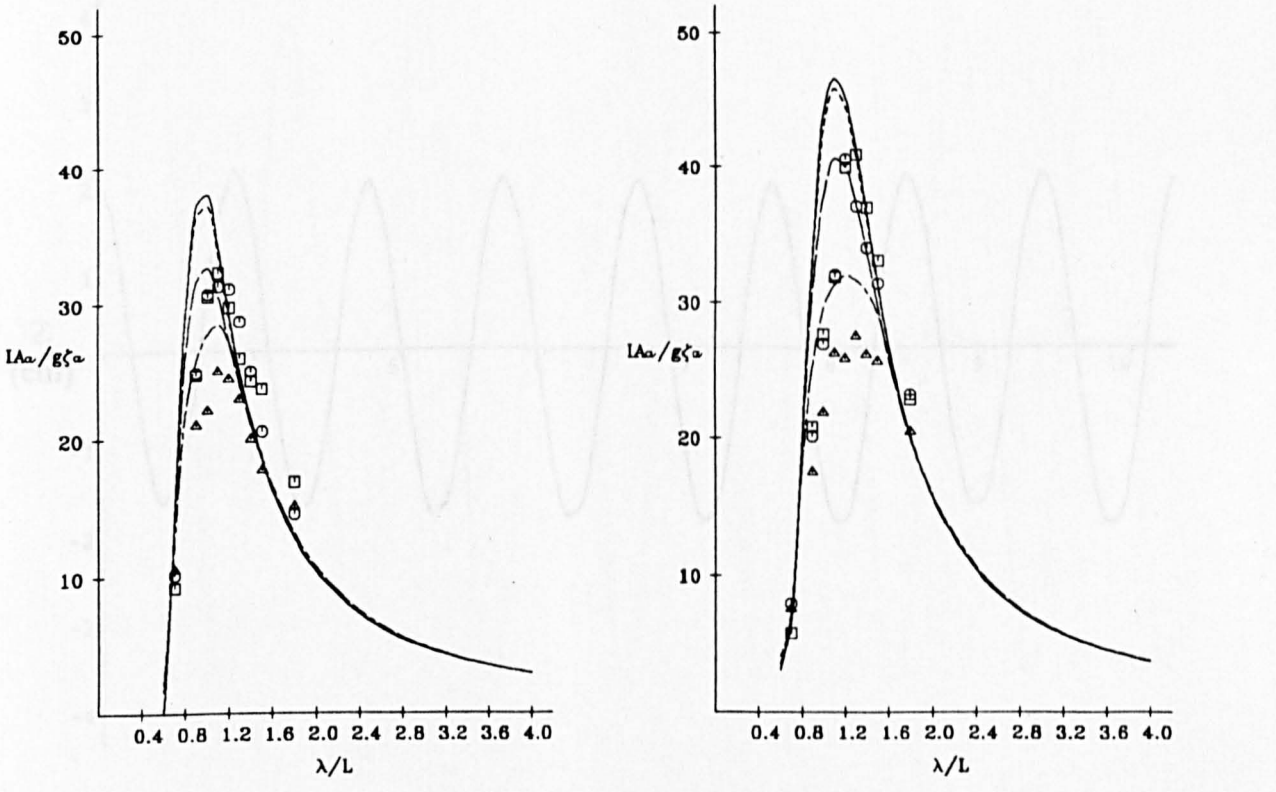

Figs.2.13-2.14 Relative Motion and Acceleration in Regular Head Seas at FP

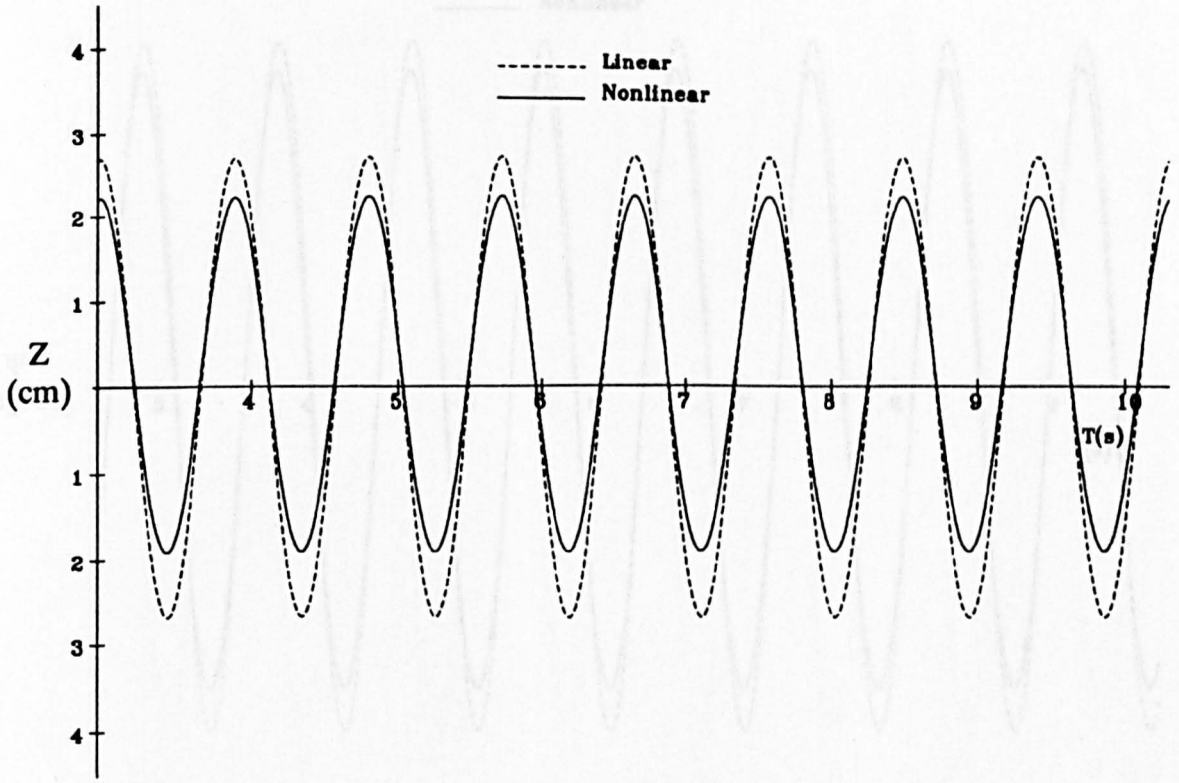

Fig.2.15 Heave Time History in Theory Fn=0.15 $\lambda / L = 1.0$ $\zeta_a = 3.70$ cm

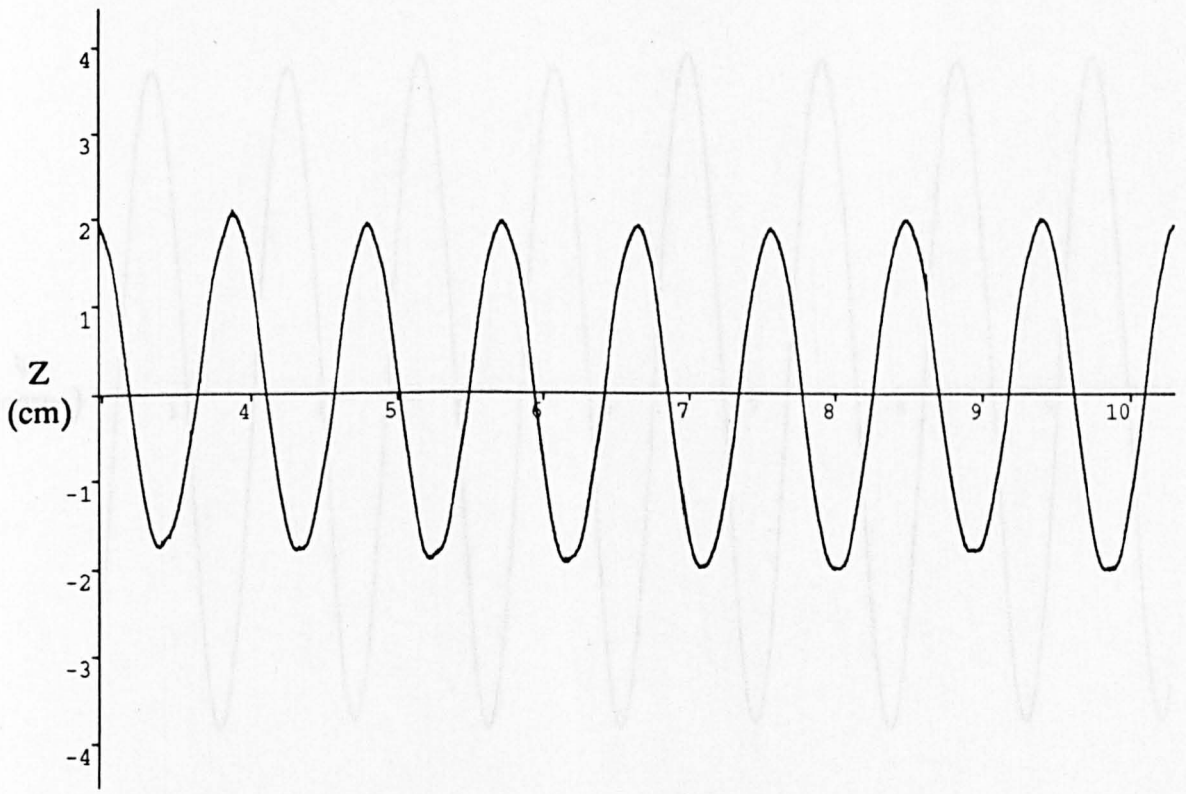

Fig.2.16 Heave Time History in Experiment Fn=0.15 $\lambda / L = 1.0$ $\zeta_a = 3.70$ cm

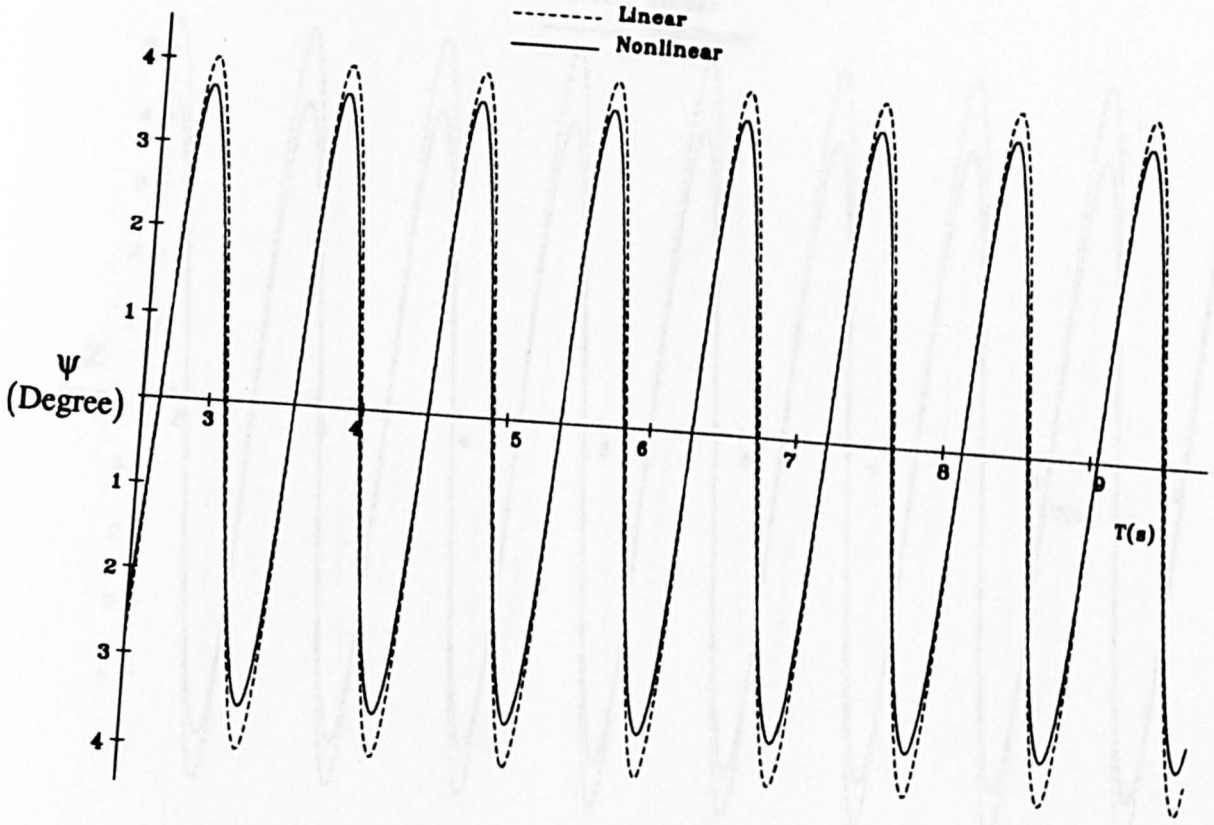

Fig.2.17 Pitch Time History in Theory Fn=0.15 $\lambda / L=1.0$ $\zeta_a=3.70$ cm

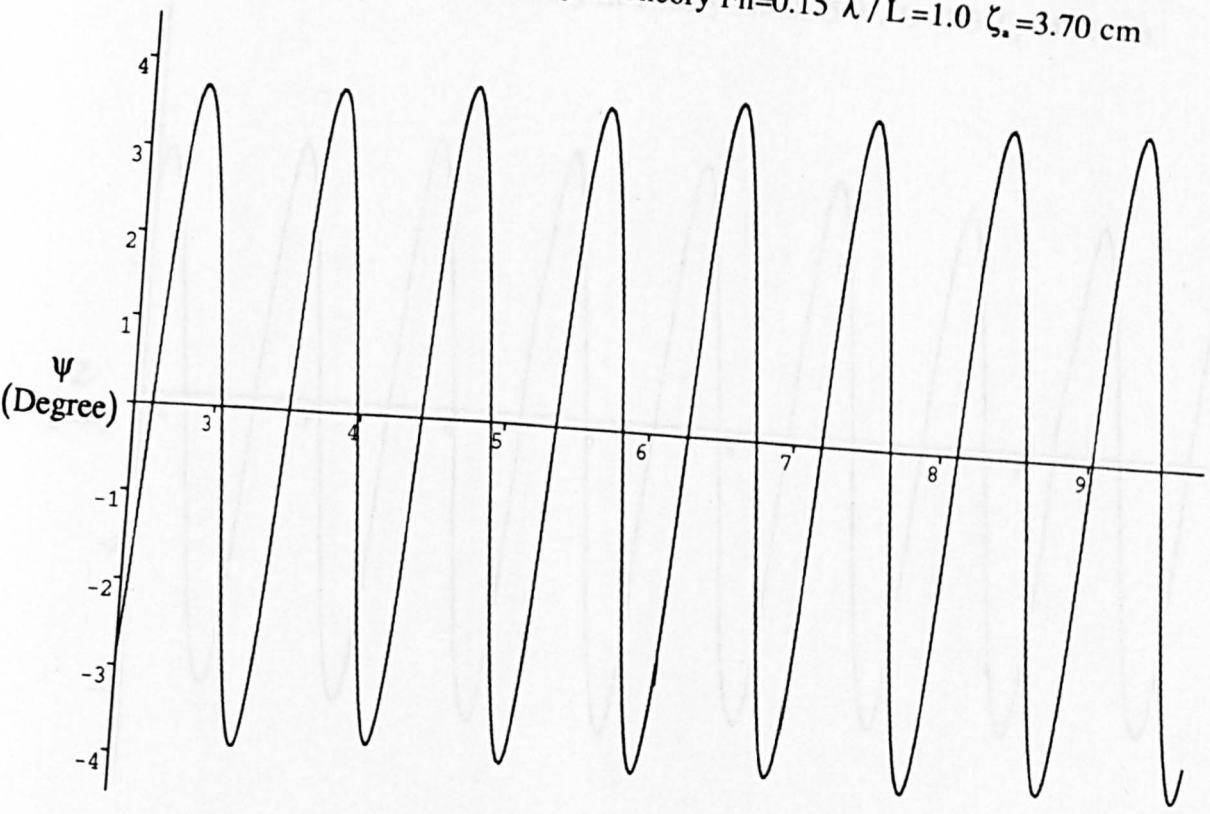

Fig.2.18 Pitch Time History in Experiment Fn=0.15 $\lambda / L=1.0$ $\zeta_a=3.70$ cm

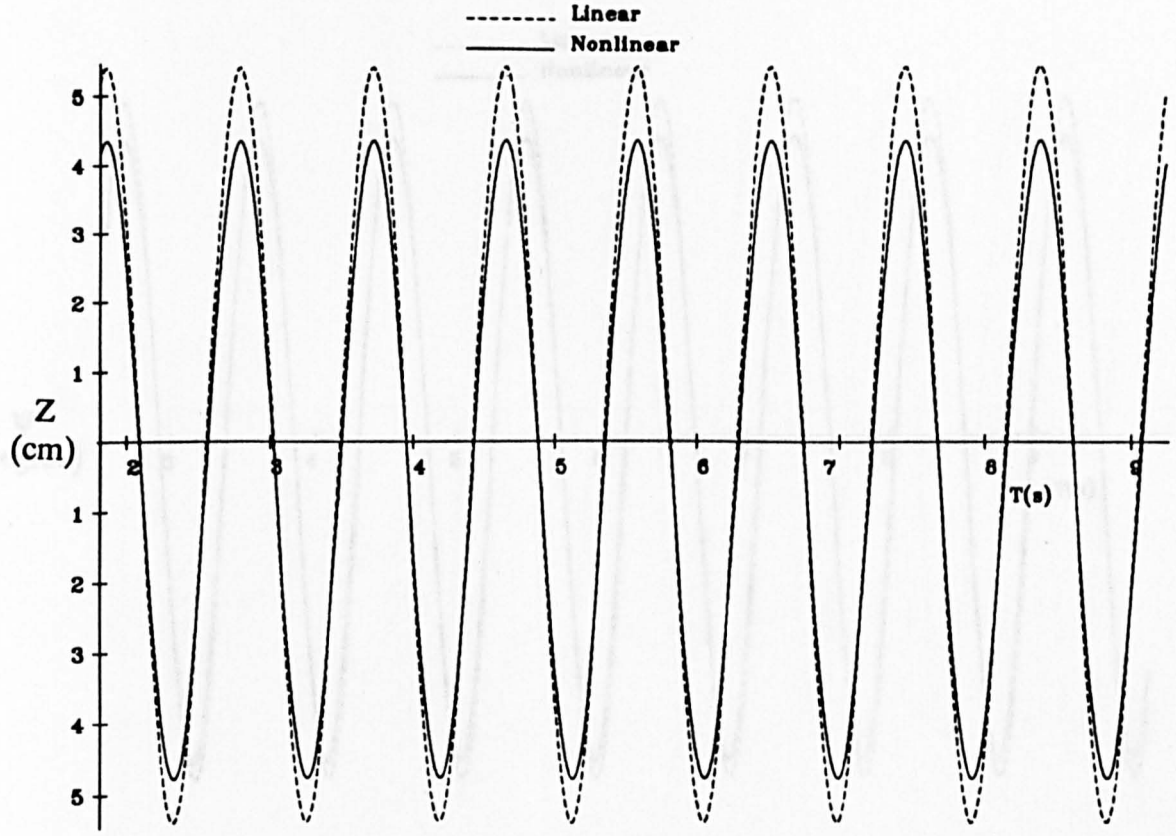

Fig.2.19 Heave Time History in Theory Fn=0.25 $\lambda / L = 1.3$ $\zeta_a = 4.26$ cm

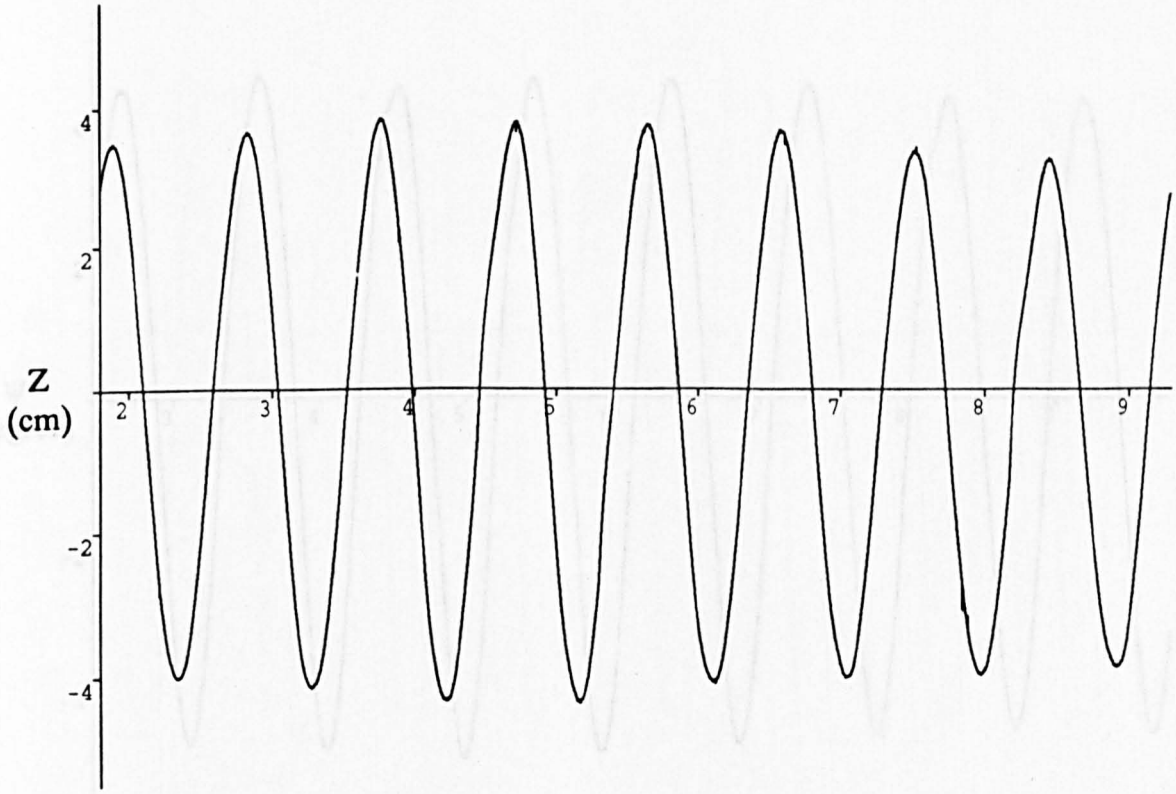

Fig.2.20 Heave Time History in Experiment Fn=0.25 $\lambda / L = 1.3$ $\zeta_a = 4.26$ cm

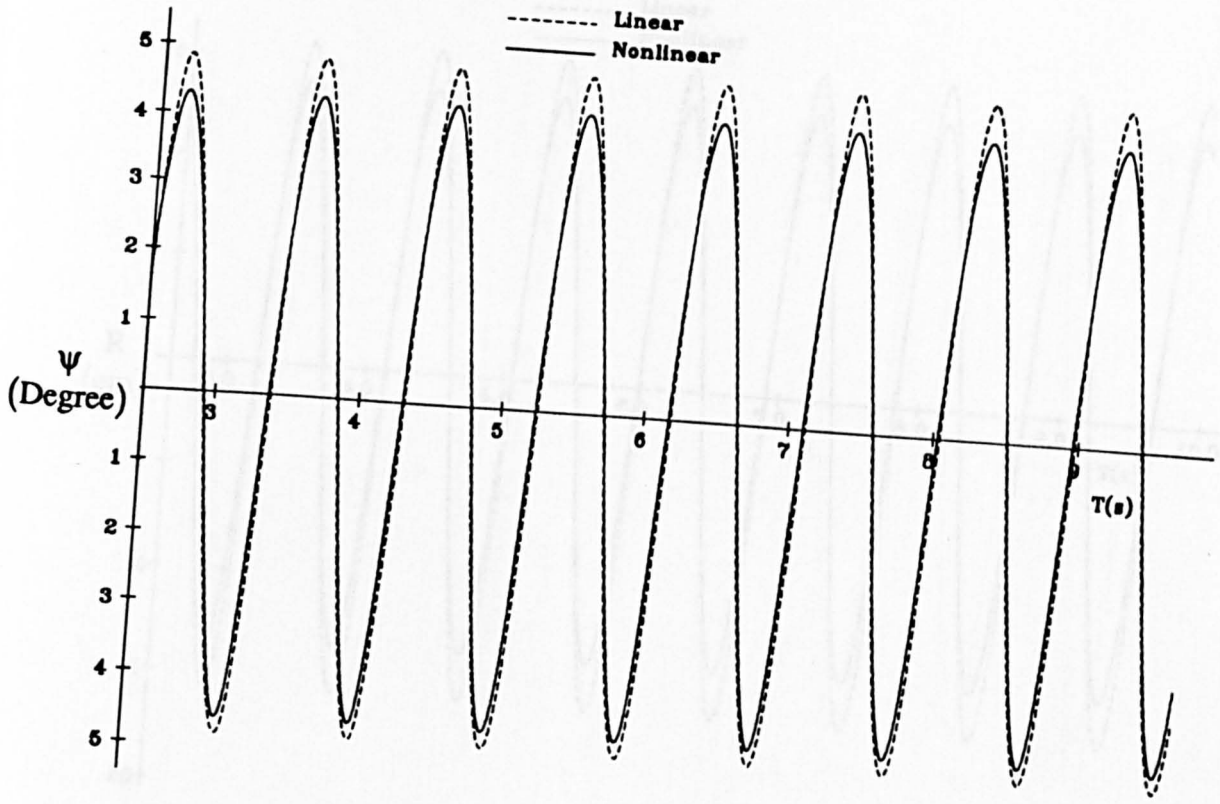

Fig.2.21 Pitch Time History in Theory Fn=0.25 $\lambda / L = 1.3$ $\zeta_a = 4.26$ cm

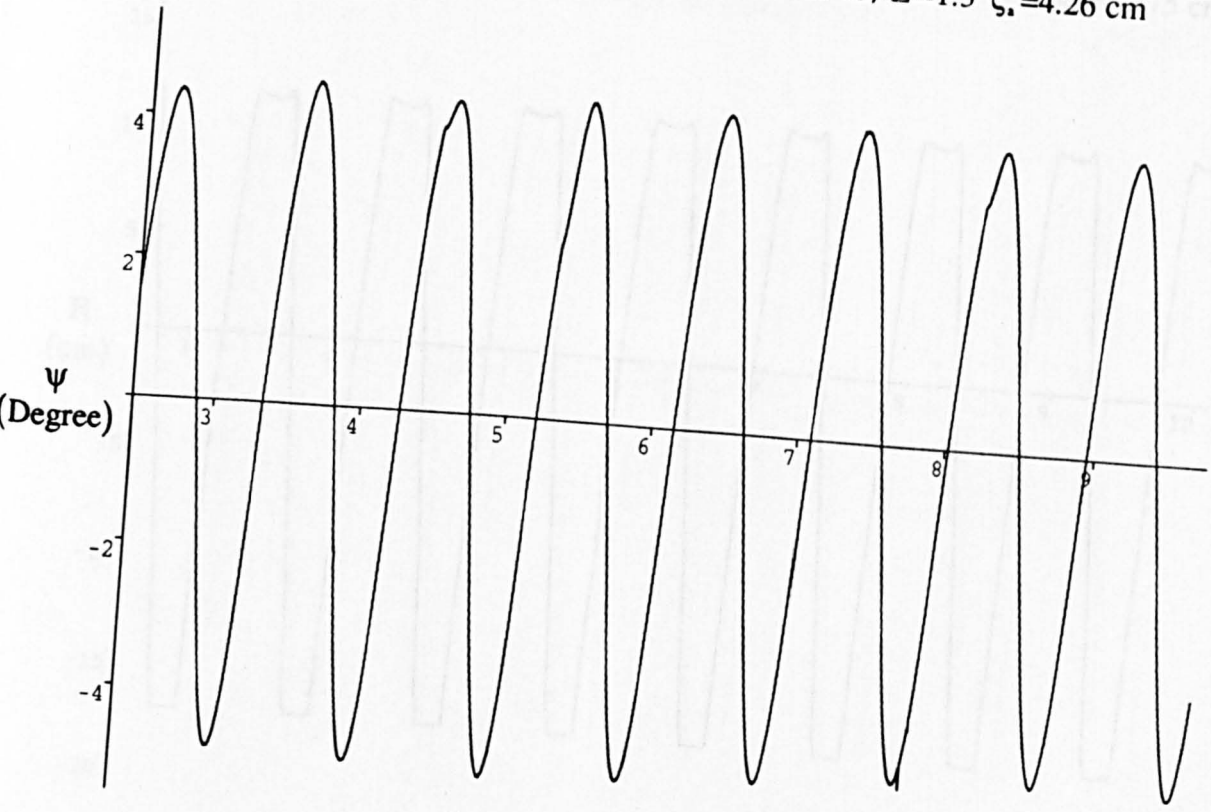

Fig.2.22 Pitch Time History in Experiment Fn=0.25 $\lambda / L = 1.3$ $\zeta_a = 4.26$ cm

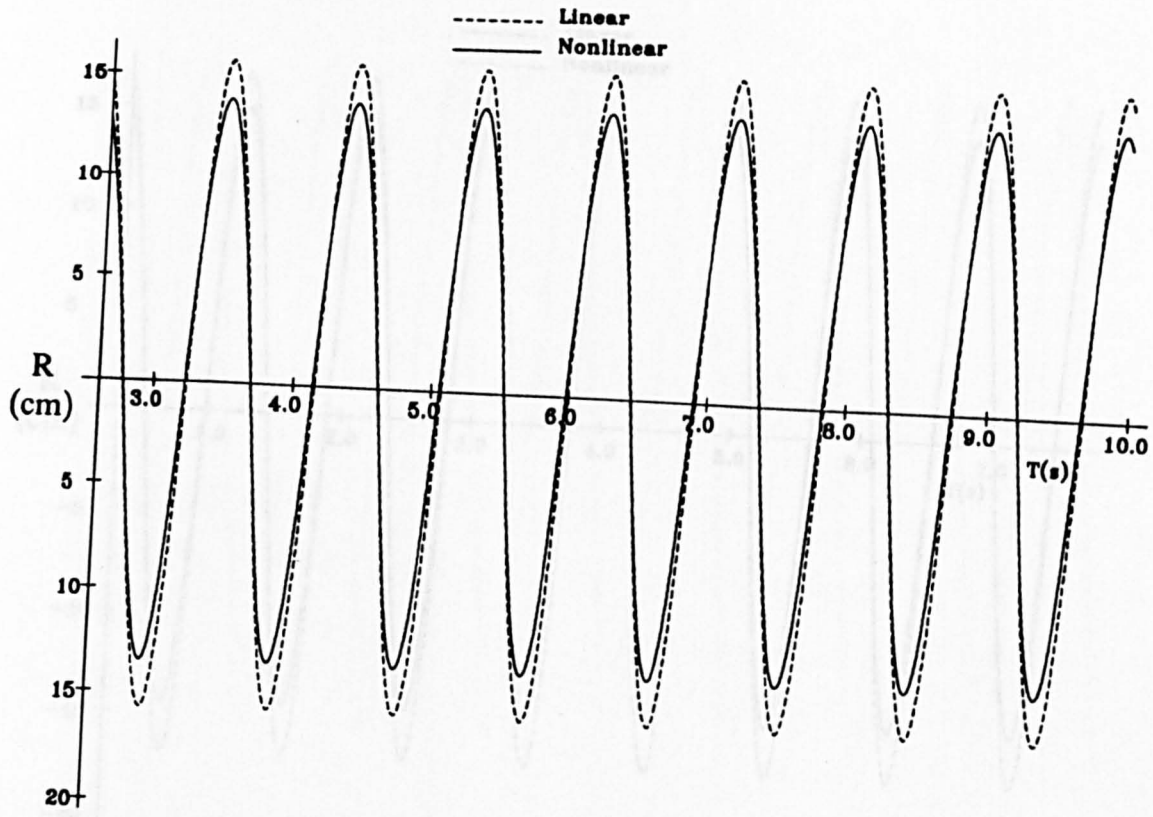

Fig.2.23 Relative Motion Time History in Theory Fn=0.15 $\lambda / L = 1.0$ $\zeta_a = 3.775$ cm

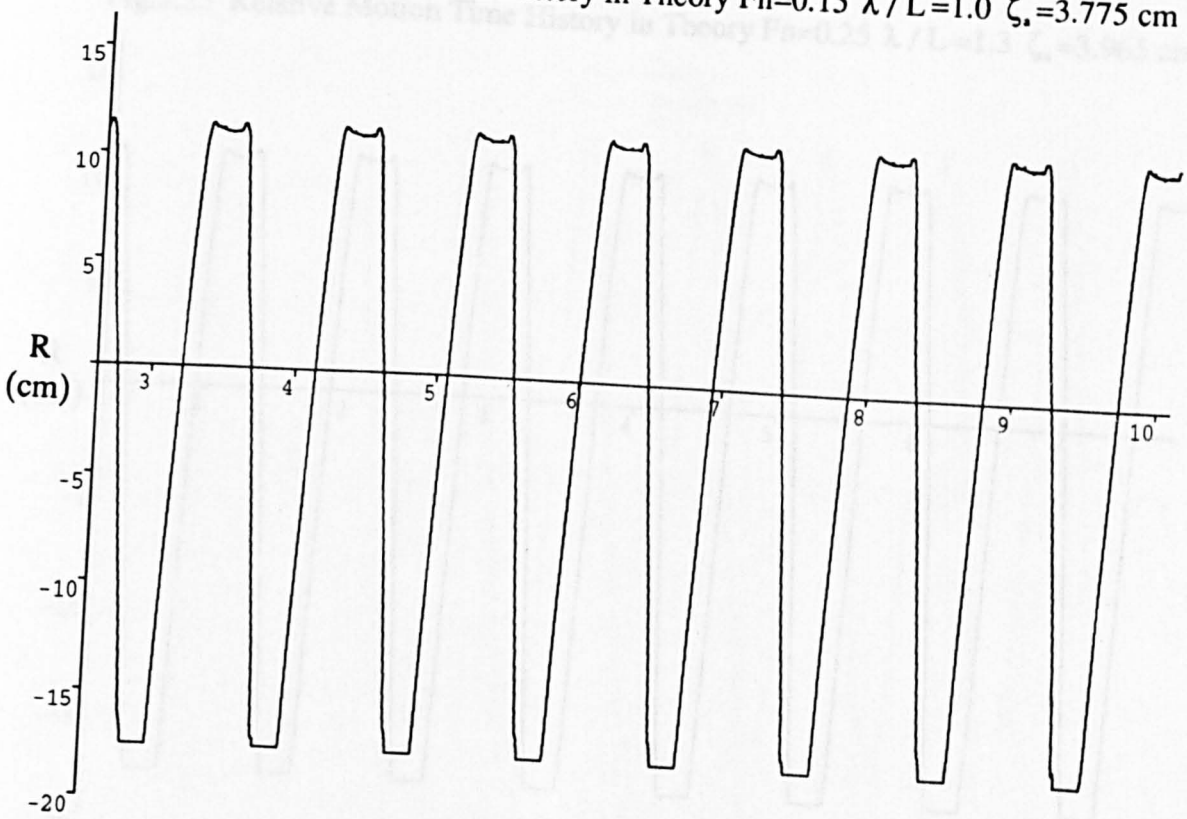

Fig.2.24 Relative Motion Time History in Experiment Fn=0.15 $\lambda / L = 1.0$ $\zeta_a = 3.775$ cm

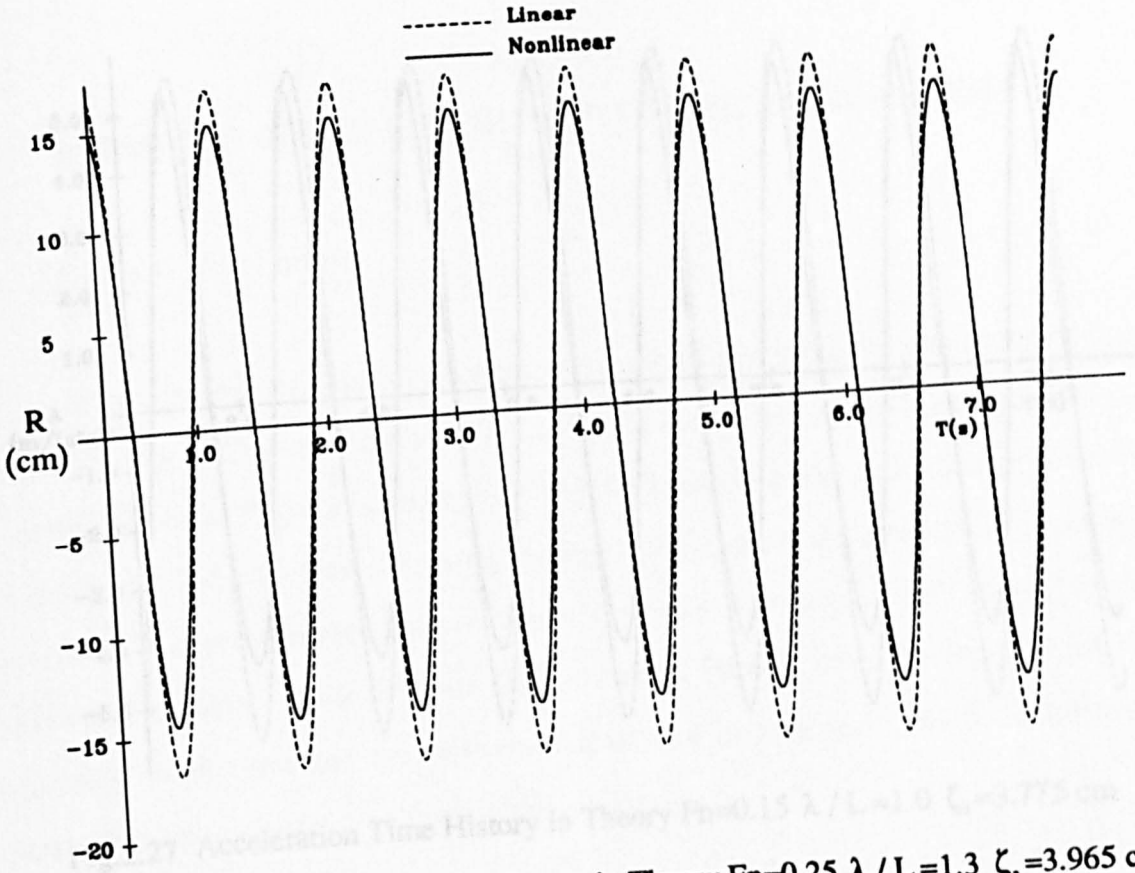

Fig.2.25 Relative Motion Time History in Theory Fn=0.25 $\lambda / L = 1.3$ $\zeta_a = 3.965$ cm

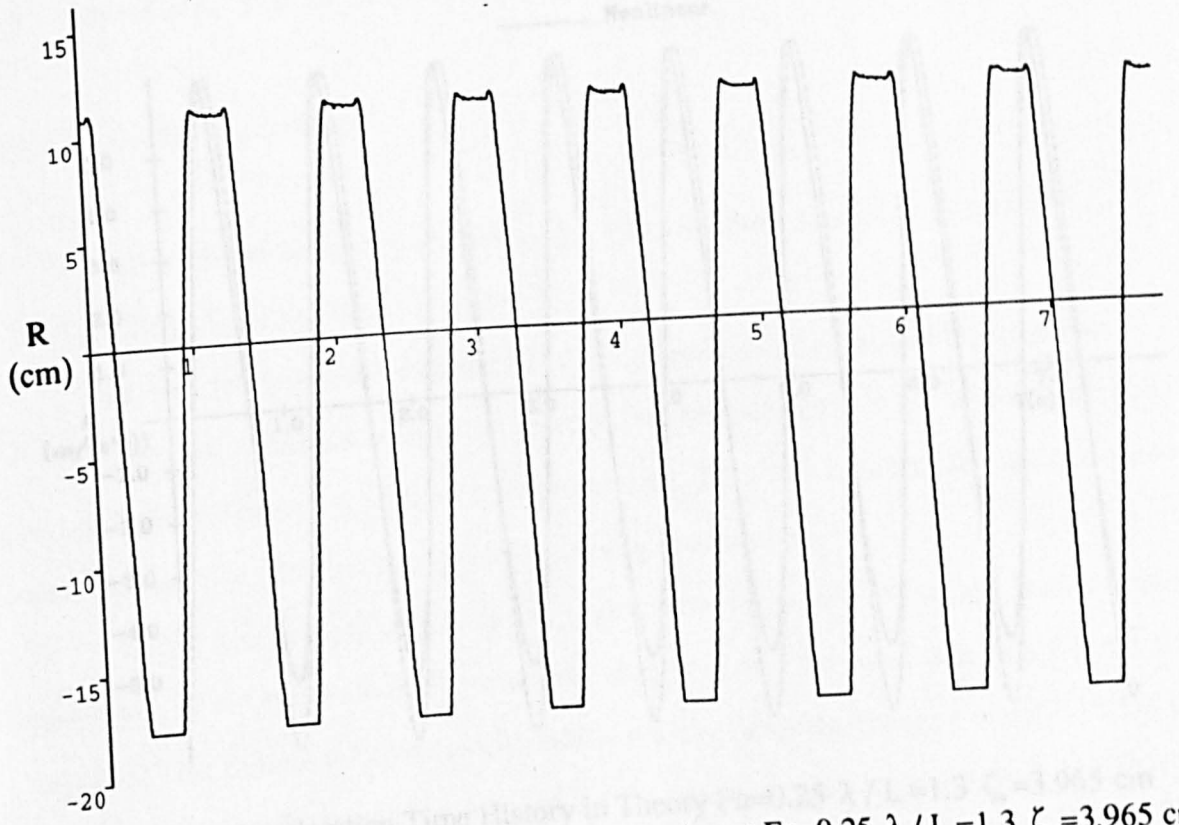

Fig.2.26 Relative Motion Time History in Experiment Fn=0.25 $\lambda / L = 1.3$ $\zeta_a = 3.965$ cm

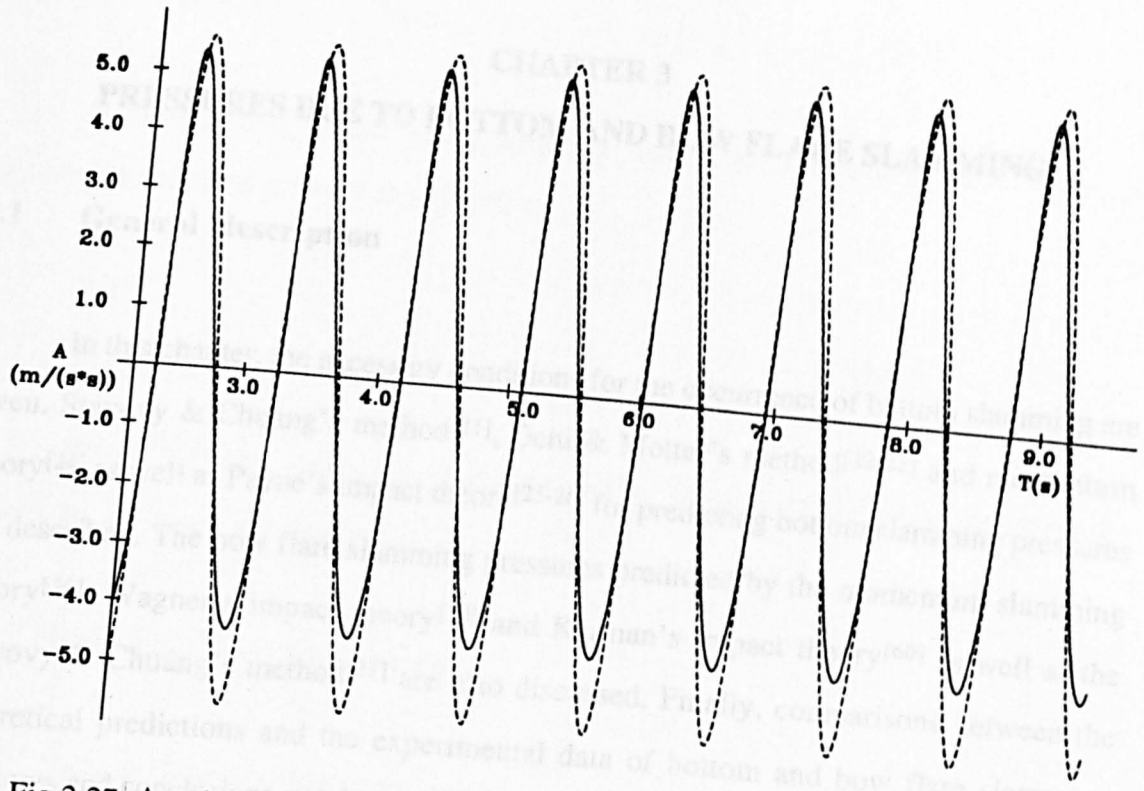

Fig.2.27 Acceleration Time History in Theory Fn=0.15 λ / L=1.0 ζ_a=3.775 cm

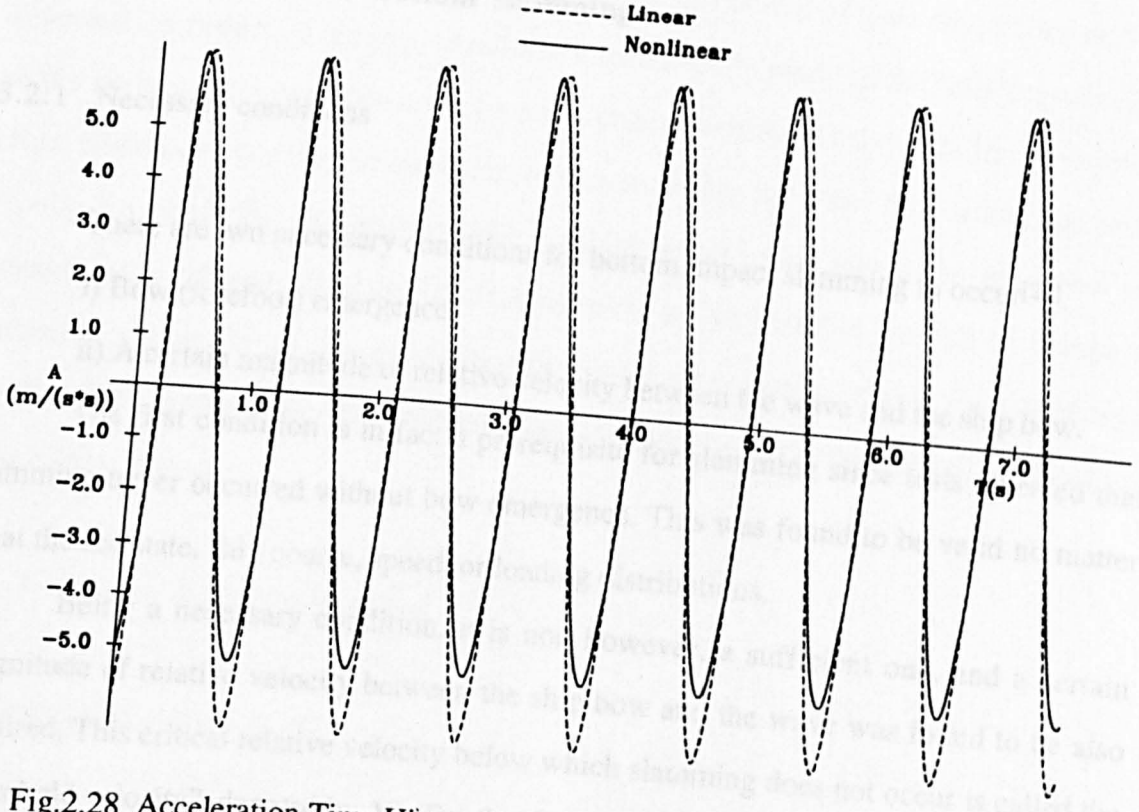

Fig.2.28 Acceleration Time History in Theory Fn=0.25 λ / L=1.3 ζ_a=3.965 cm

CHAPTER 3

PRESSURES DUE TO BOTTOM AND BOW FLARE SLAMMING

3.1 General description

In this chapter, the necessary conditions for the occurrence of bottom slamming are given. Stavovy & Chuang's method[21], Ochi & Motter's method[22-23] and momentum theory[24] as well as Payne's impact theory[25-26] for predicting bottom slamming pressures are described. The bow flare slamming pressures predicted by the momentum slamming theory[36], Wagner's impact theory[20] and Karman's impact theory[60] as well as the Stavovy & Chuang's method[21] are also discussed. Finally, comparisons between the theoretical predictions and the experimental data of bottom and bow flare slamming pressures and conclusions are shown in this chapter.

3.2 Pressures due to bottom slamming

3.2.1 Necessary conditions

There are two necessary conditions for bottom impact slamming to occur[24].

i) Bow (forefoot) emergence.

ii) A certain magnitude of relative velocity between the wave and the ship bow.

The first condition is in fact a prerequisite for slamming since tests revealed that slamming never occurred without bow emergence. This was found to be valid no matter what the sea state, ship course, speed, or loading distributions.

Being a necessary condition, it is not, however, a sufficient one, and a certain magnitude of relative velocity between the ship bow and the wave was found to be also required. This critical relative velocity below which slamming does not occur is called the "threshold velocity", denoted by V^*. For S -175 container ship (ship length, L is 175.0 m) using the Froude Scaling Law, the "threshold velocity" is :

$$V^* = 0.293\sqrt{L} \qquad (3\text{-}1)$$

Corresponding to the bow emergence and threshold velocity conditions, the necessary conditions are written as follows:

$$\begin{aligned} r &\geq T_r \\ |\dot{r}| &\geq V^* \end{aligned} \qquad (3\text{-}2)$$

Where T_r is the ship's draught at the section where investigated if the necessary conditions are or are not satisfied.

3.2.2 Bottom slamming phenomenon

Bottom slamming has been investigated by various researchers. There are three main phases in bottom slamming[24]. In phase I, the body is approaching the free surface until the moment the first contact is made. During this period of time, the airflow and the wave surface deflection are of predominant importance. In phase II, the body impacts fully on the surface and penetrates it until a more-or-less wetting is achieved. The cushioning effect of air and spray may be important factors, as well as the water flow around the body. Finally, in phase III, the fully wetted problem is described where the pressures are considered to be relatively static and the forces to be the result of the rate of change of momentum. Three kinds of impact phenomena were also observed during the experiments by Watanabe et al[72]. One was oblique impact, another was trapped air impact and the third was normal impact.

3.2.3 Stavovy & Chuang's method

1) Description of the method

The method used here is based on the calculation of the impact pressure on an infinitesimal area of the hull bottom. In that area, the deadrise, buttock, trim, and heel

angles are determined from ship lines, body plan, ship motions and wave profile. The ship section does not necessarily have to have a straight-line bottom with constant deadrise angle. The deadrise angle can vary along the hull bottom of the ship section, as is typical for conventional hull forms with curved sections. Further, only the ship motion at that infinitesimal area is considered, regardless of how complicated the wave surface profile is.

Slamming of a ship at high speed results in pressures acting normal to the hull bottom in the slamming area that may be separated into two components :

i) The impact pressure, P_i, due to the normal component to wave surface of the relative velocity between the impact surface and the wave.

ii) The planing pressure, P_p, due to the tangential component to wave surface of the relative velocity between the impact surface and the wave.

To estimate the maximum impact pressure, the pressure-velocity relation can be written in general form as

$$P_i = \frac{1}{2}\rho K_{bsc} V_{bn}^2 \qquad (3\text{-}3)$$

Where

K_{bsc} Nondimensional pressure coefficient.

V_{bn} Relative normal velocity of impact body to wave surface.

The K_{bsc} values are as follows:

$$K_{bsc} = 2K_1 / \cos^4 \xi_b \qquad (3\text{-}4)$$

ξ_b is the effective impact angle on a plane normal to the wave surface and the impact surface on the hull bottom measured from the wave surface to the impact surface of the hull bottom, and K_1 can be determined from the Wagner wedge impact theory, the Chuang cone impact theory, and DTNSRDC drop tests of wedges and cones shown in equation (3-5) and Fig.3.1.

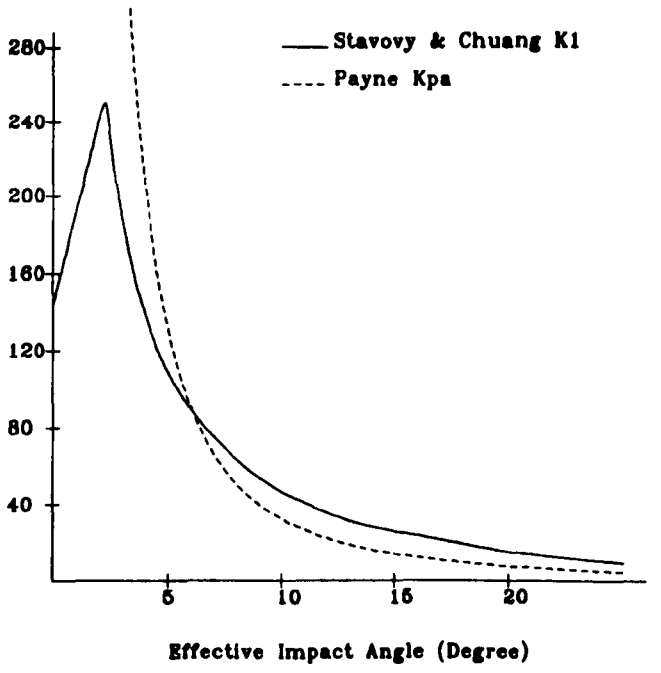

Fig.3.1 Pressure Coefficients

$$K_1 = 24.218\xi_b + 72.0$$

when $0^0 \le \xi_b < 2.2^0$

$$K_1 = 314.22087 - 136.1064\xi_b + 29.34059\xi_b^2 - 3.3681\xi_b^3$$
$$+0.19552\xi_b^4 - 0.00451\xi_b^5$$

when $2.2^0 \le \xi_b < 11^0$

(3-5)

$$K_1 = 683.81885 - 193.6841\xi_b + 22.70183\xi_b^2 - 1.3385\xi_b^3$$
$$+0.03938\xi_b^4 - 0.0004606\xi_b^5$$

when $11^0 \le \xi_b < 20^0$

$$K_1 = (1 + 2.4674 / \tan^2 \xi_b) \cdot 0.3842824$$

when $20^0 \le \xi_b$

The planing pressure acting normal to the hull bottom is

$$P_p = \frac{1}{2}\rho V_{bt}^2 \qquad (3\text{-}6)$$

V_{bt} Relative tangential velocity of impact body to water particles on wave surface.

The planing pressure is usually small and insignificant as compared with the impact pressure.

The total pressure due to the normal velocity component of the vehicle both the normal and tangent to the wave surface is therefore :

$$P_t = P_i + P_p \qquad (3\text{-}7)$$

2) V_{bn}, V_{bt} Calculations

The determination of V_{bn}, V_{bt} is based on the hypothesis that only the velocity component of the moving body normal to the impact surface and the velocity component of the wave normal to its surface generate the impact pressure.

If one considers first that the vehicle moves with a horizontal velocity V_{bh} and a vertical velocity V_{bv} at the impact area which can be formulated from the motion equations as follows:

$$\begin{aligned} V_{bh} &= -x_b\dot{\psi}\sin\psi + U\cos\psi \\ V_{bv} &= -\dot{z} + x_b\dot{\psi}\cos\psi + U\sin\psi \end{aligned} \qquad (3\text{-}8)$$

At the time of impact, the vehicle has a deadrise angle ϕ_b, a trim angle ψ, and a buttock angle γ_b , and the wave surface makes an angle of δ with the horizontal axis. If the vehicle has a heel angle, ϕ_b is the sum of deadrise and heel angles.

At the point of impact, let V_{bhw} be the velocity component of the impact body parallel to the wave surface, and V_{bvw} the velocity component of the impact body perpendicular to the wave surface, then as shown in Fig.3.2.

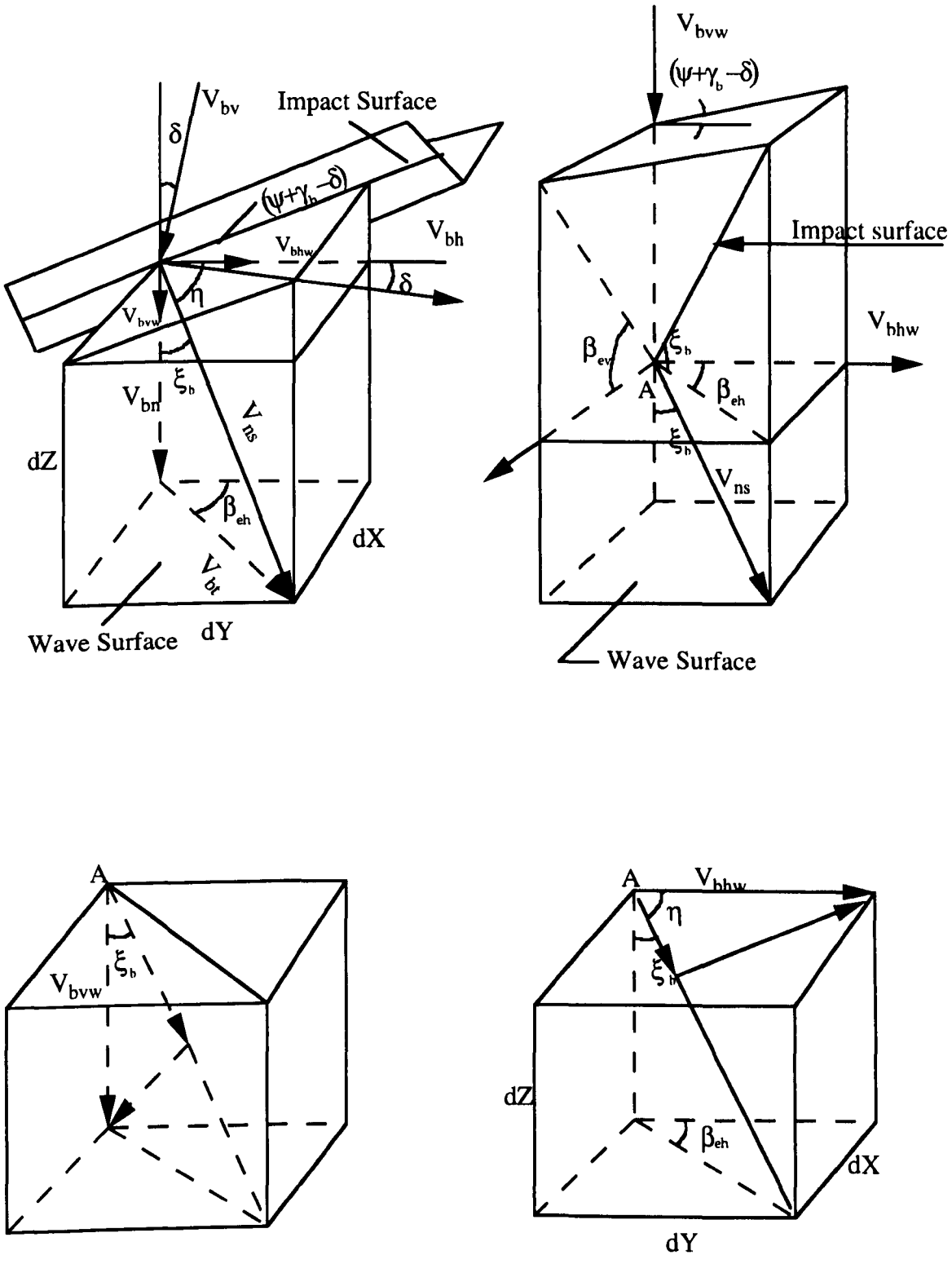

Fig.3.2 Velocity Diagram for Impact Surface[21]

$$V_{bhw} = V_{bh}\cos\delta - V_{bv}\sin\delta$$
$$V_{bvw} = V_{bh}\sin\delta + V_{bv}\cos\delta \qquad (3\text{-}9)$$

To include the water-orbiting velocity, these equations become:

$$V_{bhw} = V_{bh}\cos\delta - V_{bv}\sin\delta - V_{ot}$$
$$V_{bvw} = V_{bh}\sin\delta + V_{bv}\cos\delta + V_{on} \qquad (3\text{-}10)$$

V_{ot}, V_{on} are defined in the next section.

Both V_{bhw} and V_{bvw} can be separated into two velocity components, one normal and one tangential to the impact surface of the vehicle. The tangential velocity produces a resistance or drag force. Since this force is parallel to the impact surface, it does not generate a slamming pressure. Only the velocity component V_{ns}, which is normal to the impact surface, will generate the slamming pressure as the vehicle strikes the wave surface. This normal velocity V_{ns} is :

$$V_{ns} = V_{bhw}\cos\eta + V_{bvw}\cos\xi_b \qquad (3\text{-}11)$$

With

$$\cos\eta = \cos\beta_{eh}\sin\xi_b \qquad (3\text{-}12)$$

So

$$V_{ns} = V_{bhw}\cos\beta_{eh}\sin\xi_b + V_{bvw}\cos\xi_b \qquad (3\text{-}13)$$

Therefore

$$V_{bn} = V_{ns}\cos\xi_b$$
$$V_{bt} = V_{ns}\sin\xi_b \qquad (3\text{-}14)$$

Where

$$\beta_{ch} = \tan^{-1}\left(\frac{\tan\phi_b}{\sin(\psi-\delta)+\tan\gamma_b\cos(\psi-\delta)}\right)$$
$$\beta_{cv} = \tan^{-1}\left(\frac{\tan\phi_b}{\cos(\psi-\delta)-\tan\gamma_b\sin(\psi-\delta)}\right) \qquad (3\text{-}15)$$

$$\xi_b = \tan^{-1}\left(\cos\beta_{ch}\tan(\psi+\gamma_b-\delta)+\sin\beta_{ch}\tan\beta_{cv}\right) \qquad (3\text{-}16)$$

3) Definition of V_{ot} and V_{on}

Consider the wave movement of the sea. It is a well-known phenomenon that although the surface waves propagate at a certain celerity V_w , the movement of water particles oscillates back and forth only within an orbiting circle.

The relations between the orbiting motion of water particles and the wave surface are shown in Fig.3.3. Since the time dt is considered infinitesimal, the wave within a small portion of the slamming area (in fact, this portion is considered infinitesimal also) can be approximated as a flat surface. The unknown velocities can then be determined as follows:

$$V_w = (g/K)^{1/2} \qquad (3\text{-}17a)$$

So

$$V_{on} = V_{nw} = V_w \sin\delta \qquad (3\text{-}17b)$$

The maximum wave slope is

$$\delta_{max} = K\zeta_a \qquad (3\text{-}17c)$$

and

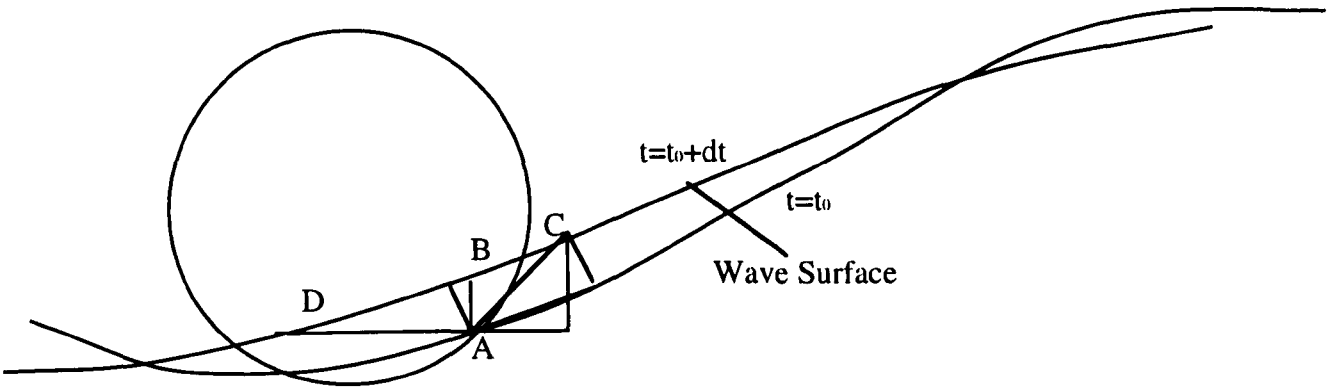

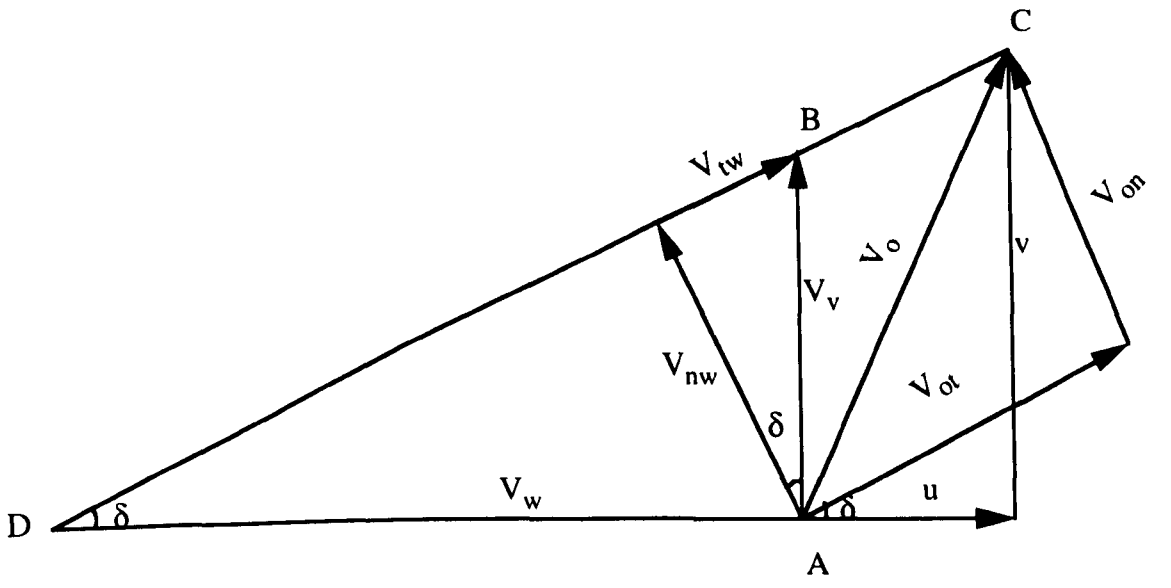

Fig.3.3 Velocity Diagram for Wave Surface[21]

$$V_0 = \delta_{max} V_w \qquad (3\text{-}17d)$$

So

$$V_{0t} = \pm\left(V_0^2 - V_{0n}^2\right)^{1/2} \qquad (3\text{-}17e)$$

(The +/- signs should agree with those of $-\sin Kx_b$)

3.2.4 Ochi & Motter's method

In this method[22-23], the slamming pressure at the keel is approximately proportional to the square of the relative velocity at the instant of impact. In other words, the pressure is expressed by

$$P_t = K_{oc}\dot{r}^2 = \frac{1}{2}\rho K_{ocl}\dot{r}^2 \qquad (3\text{-}18)$$

Where:

K_{oc} Dimensional constant depending on section shape.

K_{ocl} Nondimensional K_{oc} values.

The K_{oc} and K_{ocl} values are a function only of the hull section shape, particularly the shape of the bottom portion below about one tenth of the design draught. If the bottom of the section is above or below the baseline, then the distance between the level of water line and the bottom is substituted for the design draught.

Normally, the accurate K_{oc} and K_{ocl} values should be obtained from the model tests, but , if there is not enough model test data available, the best regression equation selected after a comprehensive search for the best fit to the available model test data by Ochi can be used to decide K_{oc} K_{ocl} values shown in the following :

$$K_{oc} = \exp\{-3.599 + 2.419a_1 - 0.873a_3 + 9.624a_5\} \qquad (3\text{-}19)$$

For the nondimensional expression, only the first term should be changed. That is,

$$K_{ocl} = \exp\{1.377 + 2.419a_1 - 0.873a_3 + 9.624a_5\} \qquad (3\text{-}20)$$

a_1, a_3, a_5 are the coefficients for conformal mapping of the ship section form up to 1/10 of the design draught.

At the station 2 (0.05L from FP), the values of a_1, a_3, a_5 are 0.237273, 0.086751 and -0.0095455 and the value of K_{ocl} is 5.95.

3.2.5 Momentum theory

The hydrodynamic forces f_H acting on a two dimensional ship section will be :

$$f_H = f_{H1} + f_{H2} + f_{H3} \qquad (3\text{-}21)$$

The impact force of bottom will take the following form[24] :

$$f_b = \rho g A_r - N_r \dot{r} - \frac{d}{dt}[m_r \dot{r}] \qquad (3\text{-}22)$$

So, the bottom slamming pressure by the momentum method is as follows :

$$P_t = f_b / B_m \qquad (3\text{-}23)$$

Where:

B_m Breadth of the bottom at any draught.

3.2.6 Payne impact theory

The bottom slamming pressure is the sum of the impact pressure and the planing pressure as described in Stavovy & Chuang's method.

The impact pressure predicted by the Payne impact theory as follows[25-26] :

$$P_i = \frac{1}{2}\rho K_{pa} V_{bn}^{\ 2} \qquad (3\text{-}24)$$

Where

$$K_{pa} = \left(\frac{1}{\tan\xi_b}\right)^2 + \left(\frac{4\pi C_b f_{pa}(\xi_b)}{\cos\xi_b}\right)^2 + \frac{8\pi C_b f_{pa}(\xi_b)}{\tan\xi_b \cos\xi_b} \qquad (3\text{-}25)$$

and

$f_{pa}(\xi_b)$ may be approximated by $1 - \frac{\xi_b}{\pi}$

C_b taken as 0.05

The planing pressure is also predicted as equation (3-6), so, the total bottom slamming pressure by the Payne impact theory is :

$$P_t = \frac{1}{2}\rho K_{pa} V_{bn}^{\ 2} + \frac{1}{2}\rho V_{bt}^{\ 2} \qquad (3\text{-}26)$$

3.3 Pressures due to bow flare slamming

3.3.1 Impact force by the momentum slamming theory

The hydrodynamic force f_H acting on a two dimensional ship section consists of the dynamic restoring force f_{H1}, the wave damping force f_{H2} and the fluid momentum force f_{H3} (see equation (3-21)).

The hydrodynamic force consists of linear and nonlinear terms, the nonlinear forces are due to the bow form with prominent flare. The impact force of bow flare will take the following form :

$$f_{bf} = \rho g(A_r - A_0 + 2y_w r) - (N_r - N_0)\dot{r} - \frac{d}{dt}[(m_r - m_0)\dot{r}] \qquad (3\text{-}27)$$

y_w Half breadth of section in the still water.

N_0 Sectional damping coefficient in the still water.

m_0 Sectional added mass in the still water.

3.3.2 Bow flare impact pressure

The actual mechanism of bow flare impact is extremely complicated. In the present research, two different generating mechanisms of the bow flare impact pressures are assumed : One is the water immersion impact pressure, due to the normal component of the relative velocity to the water surface between the impact surface and the wave; The other is the wave striking impact pressure, P_S, due to the tangential component of the relative velocity to the water surface between the impact surface and the water particle.

These two components of impact pressure are perpendicular to the impact surface, and the total bow flare impact pressure is the sum of these two components.

To investigate the water immersion impact pressure, two prediction methods are used as follows :

i) The impact pressure by the momentum slamming theory, P_{iM}.

The impact force is assumed to be distributed over a certain length of the beam with the introduction of local correction factors near the water line contact region.

ii) The impact pressure by the Wagner impact theory , P_{iW}.

In the case of wave striking impact, the striking velocity of the water particle is considered to be the tangential component of the relative velocity.

From the above impact pressure definition, the total bow flare impact pressure by the momentum slamming theory, P, is given by

$$P = P_{iM} + P_S \qquad (3\text{-}28)$$

and that by the Wagner impact theory, P, is given by

$$P = P_{iW} + P_S \tag{3-29}$$

For the purpose of comparing different theories for bow flare slamming pressure prediction, the Stavovy & Chuang's method and Karman's impact theory are also used to calculate the bow flare slamming pressure in some wave frequencies, amplitudes and speeds. The bow flare slamming pressure by the Stavovy & Chuang's method :

$$P = P_{iSC} + P_S \tag{3-30}$$

and by Karman impact theory :

$$P = P_{iKa} + P_S \tag{3-31}$$

3.3.3 Impact pressure by the momentum slamming theory

The impact force in Equation (3-27) is the force acting on a strip of unit length. This force is thought to be the sum of impact pressure distributed on the hull surface. For a general ship section, it is difficult to find the shape of pressure distribution. A previous study [73] showed that the peak value of impact pressure appears near the water surface contact part. The peak value seems to be influenced mainly by the local factor near the water contact part. Therefore, in the study, the pressure concentration factor C (Fig.3.4) which is evaluated from the pressure distribution on the wedge shaped section is introduced, and the impact pressure is assumed to be distributed uniformly over the effective beam length B_e defined by

$$B_e = A_r / (T_r \times C) \tag{3-32}$$

where A_r is the instantaneous submerged sectional area and T_r is the instantaneous

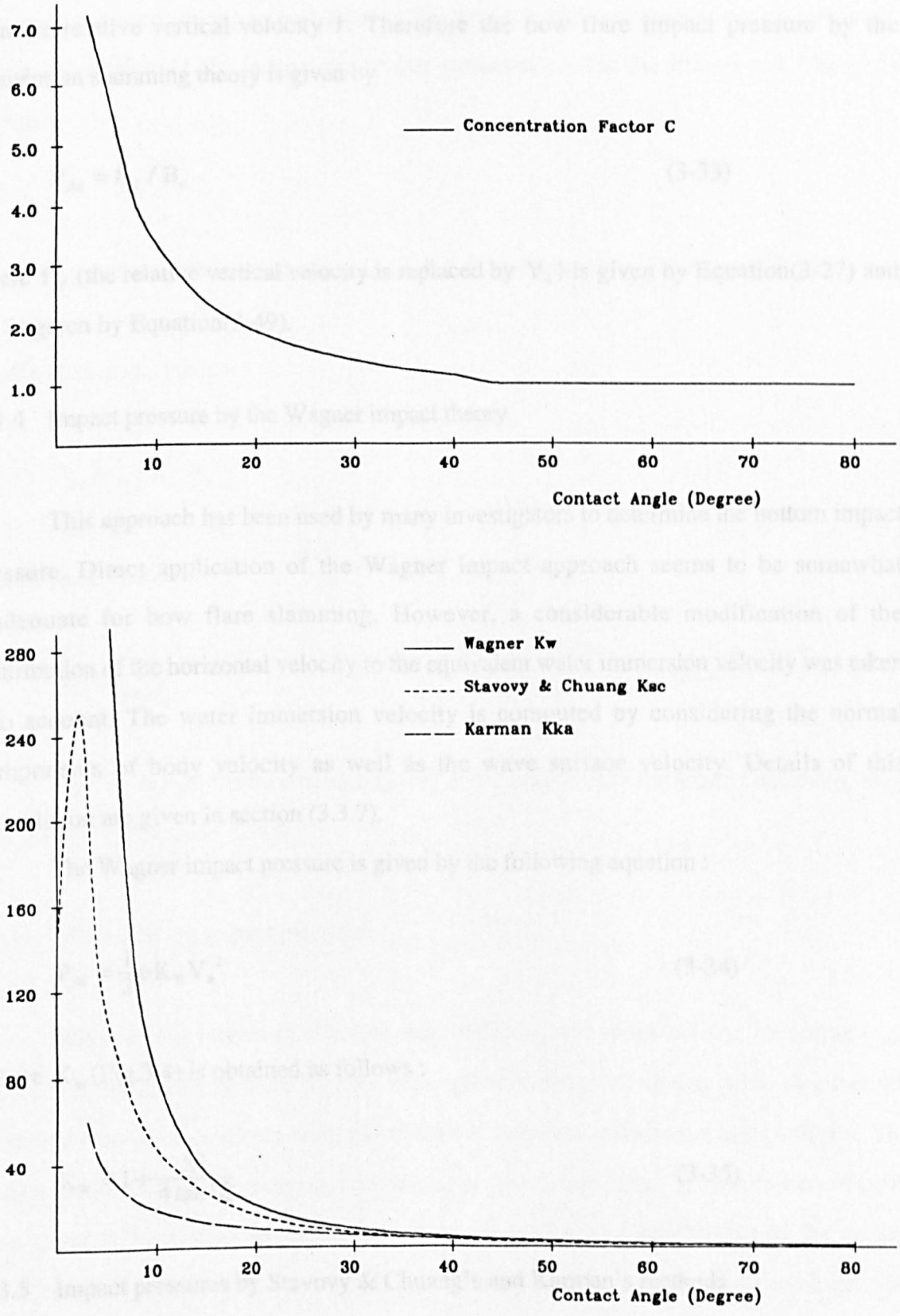

Fig.3.4 Concentration Factor and Pressure Coefficients

submerged draught. It can be assumed that the peak pressure is influenced by the local water immersion velocity, i.e., the normal component V_n of the relative velocity rather than the relative vertical velocity $\dot{r}$. Therefore the bow flare impact pressure by the momentum slamming theory is given by

$$P_{iM} = f_{bf} / B_e \qquad (3\text{-}33)$$

where f_{bf} (the relative vertical velocity is replaced by V_n) is given by Equation(3-27) and V_n is given by Equation(3-49).

3.3.4 Impact pressure by the Wagner impact theory

This approach has been used by many investigators to determine the bottom impact pressure. Direct application of the Wagner impact approach seems to be somewhat inadequate for bow flare slamming. However, a considerable modification of the contribution of the horizontal velocity to the equivalent water immersion velocity was taken into account. The water immersion velocity is computed by considering the normal components of body velocity as well as the wave surface velocity. Details of this formulation are given in section (3.3.7).

The Wagner impact pressure is given by the following equation :

$$P_{iw} = \frac{1}{2}\rho K_w V_n^2 \qquad (3\text{-}34)$$

Where K_W(Fig.3.4) is obtained as follows :

$$K_w = 1 + \frac{\pi^2}{4\tan^2\xi} \qquad (3\text{-}35)$$

3.3.5 Impact pressures by Stavovy & Chuang's and Karman's methods

Stavovy & Chuang's method based on the Wagner wedge impact theory, the

Chuang cone impact theory, and DTNSRDC drop tests as used in bottom slamming pressure calculation. In this study, this method is extended to calculation of the bow flare slamming pressure and the impact velocity V_n which is different from the impact velocity in the calculation of the bottom slamming pressure, so, for the Stavovy & Chuang's method :

$$P_{isc} = \frac{1}{2}\rho K_{sc} V_n^2 \qquad (3\text{-}36)$$

K_{sc} is the same as in equation (3-5), but ξ_h is replaced by ξ (also see Fig.3.4)

For Karman impact theory :

$$P_{ika} = \frac{1}{2}\rho K_{ka} V_n^2 \qquad (3\text{-}37)$$

Where (see Fig.3.4)

$$K_{ka} = \frac{\pi}{\tan\xi} \qquad (3\text{-}38)$$

The V_n is decided by equation (3-49) and ξ(degrees) is the water contact angle of hull surface in Equation (3-46).

3.3.6 Wave striking impact pressure

When a ship travels in a severe sea condition, it is observed that incoming high waves become steeper because they are superposed on the swell up due to the ship motion. Eventually the water particles strike the surface of bow flare with a very large velocity. The phenomenon is usually superposed on the water immersion impact phenomenon of bow. The actual striking velocity of wave particles as well as the distribution of the impact pressure are extremely difficult to obtain theoretically. The peak pressure on breakwater by a partial breaking wave is equal to twice the hydrodynamic pressure of jet flow on a wall perpendicular to the jet as shown by Nagai[74]. The bow flare impact pressure due to the

wave striking phenomenon is assumed to be proportional to the square of tangential relative velocity between the impact surface and the water particle in the present research. The constant K_S is taken to be 4, while Hayashi and Hattori[75] suggest 2 to 5 for K_S as found from the measurements. Then the striking impact pressure on the vertical wall can be written as follows :

$$P_S = \frac{1}{2}\rho K_S V_t^2 \qquad (3\text{-}39)$$

where V_t is defined by Equation (3-51) in section 3.3.7.

Since the above equation is valid for a vertical wall, the following modification is made[31] .

$$P_S = \frac{1}{2}\rho K_S V_t^2 \left(\frac{150-\xi}{60}\right) \qquad (3\text{-}40)$$

where ξ (degrees) is the water contact angle of the hull surface in Equation (3-46)

3.3.7 V_n, V_t Calculation

The lateral motion of a ship and the deformation of incident wave caused by ship motions are ignored in this research. The water line angle, the body plan angle and the buttock line angle α, β, γ respectively, are shown in Fig.3.5.

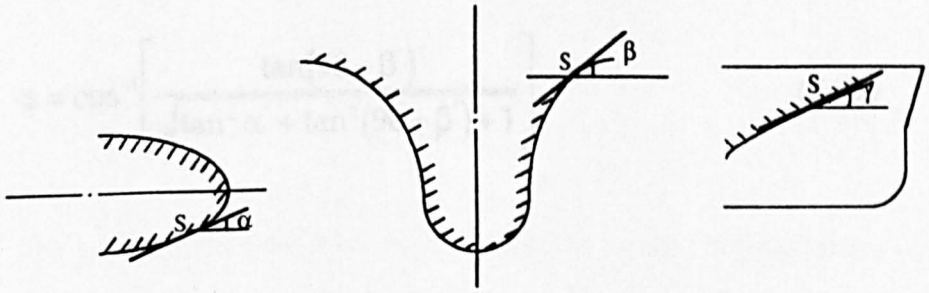

Water line angle Body plan angle Buttock line angle

Fig.3.5 Angles of Hull Surface

The above angles are changed by the pitch motion in waves. We assume that the water line angle, α is not changed, then the modified angles become :

$$\begin{aligned} \alpha' &= \alpha \\ \gamma' &= \gamma - \psi \\ \beta' &= 90 - \tan^{-1}\left[\tan\alpha' \tan(90-\gamma')\right] \end{aligned} \tag{3-41}$$

where ψ is pitch angle. Because the tangential velocity to the hull surface does not generate any impact force, we define the vertical normal plane which is normal to the hull surface and normal to the still water plane, as shown in Fig.3.6 and hereafter only the velocity components in this plane are considered to generate the impact.

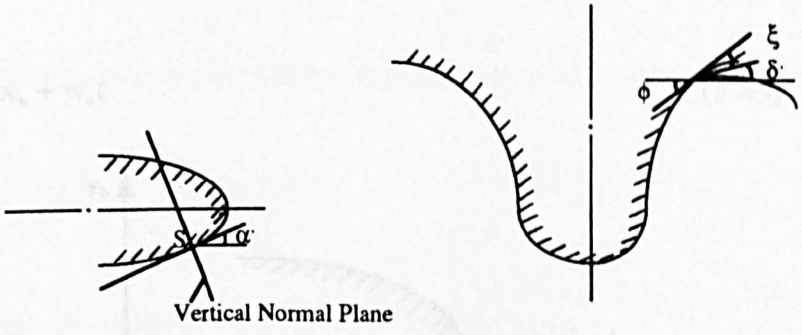

Water plane Vertical normal plane

Fig.3.6 Vertical Normal Plane

From the geometrical relation in Fig.3.7, the deadrise angle, ϕ, of the hull surface in the vertical normal plane is given by the equation

$$\phi = \cos^{-1}\left[\frac{\tan(90-\beta')}{\sqrt{\tan^2\alpha' + \tan^2(90-\beta')+1}}\right] \tag{3-42}$$

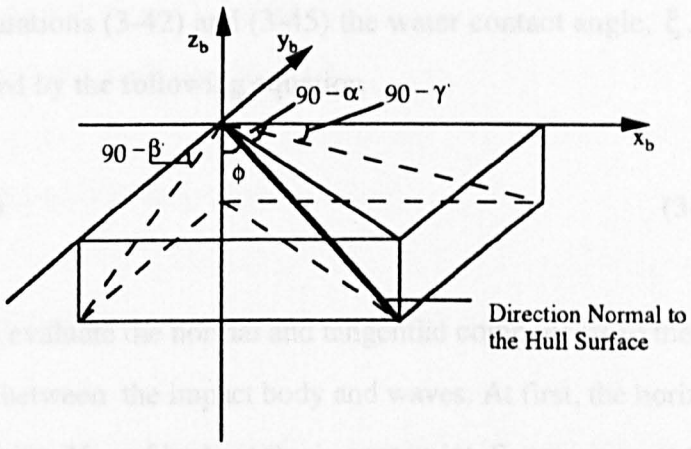

Fig.3.7 Deadrise Angle, ϕ, in the Vertical Normal Plane

The phase of incident regular wave at the impact point, S, as shown in Fig.3.8, is

$$\theta = Kx_b + w_e t \qquad (3\text{-}43)$$

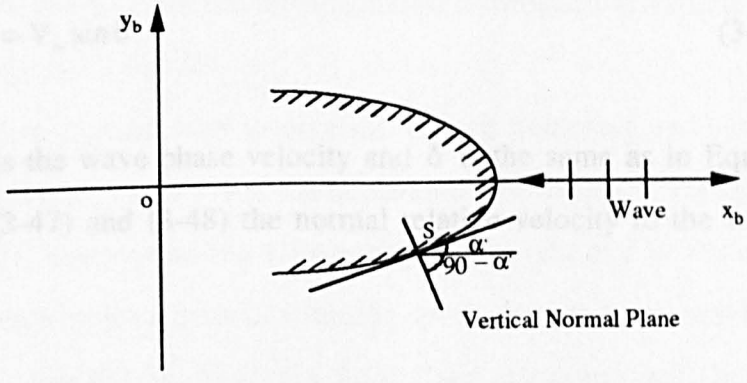

Fig.3.8 Relative Direction of Wave with Respect to Vertical Normal Plane

The original wave slope, δ is

$$\delta = -K\zeta_a \sin\theta \qquad (3\text{-}44)$$

The angle between the wave direction and the vertical normal plane is $(90-\alpha')$

So, the effective wave surface angle, δ', in the vertical normal plane is

$$\delta' = \delta\cos(90-\alpha') \qquad (3\text{-}45)$$

From Equations (3-42) and (3-45) the water contact angle, ξ, which is shown in Fig.3.6 is obtained by the following equation

$$\xi = \phi - \delta' \tag{3-46}$$

Now, we evaluate the normal and tangential components to the water surface of the relative velocity between the impact body and waves. At first, the horizontal velocity, V_h , and vertical velocity, V_v , of body at the impact point, S, are given as follows :

$$\begin{aligned} V_h &= -x_h \dot{\psi} \sin\psi + U\cos\psi \\ V_v &= \dot{z} - x_h \dot{\psi} \cos\psi - U\sin\psi \end{aligned} \tag{3-47}$$

and the rising velocity of wave normal to the water surface is approximately

$$V_{nw} = V_w \sin\delta \tag{3-48}$$

where V_w is the wave phase velocity and δ is the same as in Equation (3-44). From Equations (3-47) and (3-48) the normal relative velocity to the water surface, V_n is obtained by

$$V_n = V_h \cos(90 - \alpha')\sin\delta' - V_v \cos\delta' + V_{nw} \tag{3-49}$$

where V_n is positive for body going into the water.

The horizontal and vertical velocities of wave particles in the direction of wave propagation are

$$\begin{aligned} V_{hw} &= \omega\zeta_a \cos\theta \\ V_{vw} &= \omega\zeta_a \sin\theta \end{aligned} \tag{3-50}$$

Then, from Equation (3-47) and (3-50), the tangential relative velocity to the water surface, V_t is obtained by

$$V_t = V_v \sin\delta' + V_h \cos\delta' \cos(90-\alpha') + (V_{hw}\cos\delta - V_{vw}\sin\delta)\cos(90-\alpha') \quad (3\text{-}51)$$

where V_t is positive for bow striking.

3.4 Comparisons between the theoretical predictions and experiments

An experimental description of bottom and bow flare slamming pressures is given in Chapter 5.

3.4.1 Bottom slamming pressure

1) Ship behaviour

The ship behaviour and the lengthwise distribution of vertical relative velocity are shown in Figs.A.3.1-A.3.20

In these Figures, bow emergence, bottom slamming and bow flare slamming as well as deck wetness are shown. The maximum bow emergence is shown at the time near t=0.0 T_e. The bottom touches the waves progressively and finally several stations near F.P. plunge into water almost simultaneously, the bottom slamming occurring in the bow region (See Fig.A.3.3). Next the bow flare slamming will occur (Fig.A.3.5 and Fig.A.3.7), followed by the phenomenon of deck wetness (Fig.A.3.9, Fig.A.3.11 and Fig.A.11.13), after that, the bow will continue to move out of the water (Fig.A.3.15, Fig.A.3.17 and Fig.A.3.19). All of these phenomena will be repeated at the next period.

2) Bottom slamming pressure due to different wave frequencies

The bottom slamming pressure predicted by the Stavovy & Chuang's method, Ochi & Motter's method and the momentum theory as well as Payne impact theory according to different wave frequencies and comparisons between the theoretical predictions and experimental data at Fn=0.15 and 0.25, ζ_a=7.5 cm and station 2 are shown in Figs.3.9-3.10.

From these figures, there is a good agreement between the results predicted by the Ochi & Motter's method and the experimental data. The results by the other three methods are several times larger than the experimental data. This phenomenon is more clearly shown in Fn=0.25 than in Fn=0.15.

This is because the Ochi & Motter's method is based on a large number of the bottom slamming test results of the ship model. The Stavovy & Chuang's method, Payne impact theory are based on the drop test results. The momentum theory is not quite suitable to predict the bottom slamming pressure, but it is better than the Stavovy & Chuang's method and Payne impact theory.

3) Bottom slamming pressure due to different wave amplitudes

The bottom slamming pressure predicted by the Stavovy & Chuang's method, Ochi & Motter's method and the momentum theory as well as Payne impact theory according to different wave amplitudes and comparisons between the theoretical predictions and the experimental data at Fn=0.15 and 0.25, λ / L=1.0, 1.2 and 1.4 are shown in Figs.3.11-3.15.

From these figures, the bottom slamming pressure increases as the wave amplitude increases. The results by the Ochi & Motter's method again agree well with the experimental data. The results by the other methods give a greater value (in some cases by several times) than the experimental data.

3.4.2 Bow flare slamming pressure

1) Ship behaviour and impact force

i) The ship behaviour and the lengthwise distribution of vertical relative velocity are shown in Figs.A.3.1-A.3.20 (see section 3.4.1).

ii) Time duration of slamming

Time duration at bottom slamming and bow flare slamming is different, for example, for Fn=0.25, Sta.=2, $\lambda / L=1.2$ and $\zeta_a=7.5$ cm, the time duration in the bottom area is 0.0111 seconds, while the time duration in the bow flare region is 0.1741 seconds, the latter is 15.7 times longer than the former. So, the time duration in the bow flare slamming is much longer than the time duration in the bottom slamming.

iii) Contribution of different nonlinear terms to impact force

The main contribution to the bow flare slamming force is nonlinear fluid momentum force. The contribution of the nonlinear restoring force, nonlinear damping force and nonlinear fluid momentum force at Fn=0.15 and 0.25, Sta.=3, $\lambda / L=1.2$ and $\zeta_a=8.75$ cm can be described as follow :

For Fn=0.15, when the draught is nearly 14.50 cm (still water draught is 13.5 cm), the ratio of contribution to the bow flare slamming force for the three nonlinear terms is 0.85%, 13.15% and 86.00%.

When the draught is nearly 17.15 cm , the ratio of contribution to the bow flare slamming force for the three nonlinear terms is 5.60%, 24.60% and 69.80%.

When the draught is 20.0 cm , the ratio of contribution to the bow flare slamming force for the three nonlinear terms is 11.50%, 31.50% and 57.00%.

For Fn=0.25, when the draught is nearly 14.50cm (still water draught is 13.5 cm), the ratio of contribution to the bow flare slamming force for the three nonlinear terms is 0.93%, 14.06% and 85.01%.

When the draught is nearly 17.15 cm, the ratio of contribution to the bow flare slamming force for the three nonlinear terms is 6.10%, 25.70% and 68.20%.

When the draught is 20.0 cm , the ratio of contribution to the bow flare slamming force for the three nonlinear terms is 12.50%, 32.60% and 54.90%.

Therefore, the contributions of the nonlinear restoring force and damping force should not be neglected.

2) Bow flare slamming pressures according to different frequencies

The nondimensional values of bow flare slamming pressures obtained from predictions by the momentum slamming theory and the Wagner impact theory and measurements according to different wave frequencies at two wave amplitudes, two speeds and three stations (0.05L, 0.01L and 0.15L from FP) and draught of 20 cm are shown in Figs. 3.17-3.24.

For Fn=0.15, there is very good agreement between the predictions and the measurements for Sta.=2 and 3, when ζ_a=4.0 cm (Figs. 3.17 and 3.19) and there is good agreement between the predictions and the measurements for Sta.=2 and 3, when ζ_a=7.5 cm (Figs. 3.18 and 3.20). The Wagner impact theory seems to predict more accurate results than the momentum slamming theory in the resonance region in large waves.

When λ / L is nearly 1.0, the pressures get to maximum due to the resonance phenomenon.

For Fn=0.25, there is also good agreement between the predictions and the measurements for Sta.=2 and 3, when ζ_a=4.0 cm (Figs. 3.21 and 3.23) and there is satisfactory agreement between the predictions and the measurements for Sta.=2 and 3, when ζ_a=7.5 cm (Figs. 3.22 and 3.24). The Wagner impact theory seems to predict more accurate results than the momentum slamming theory in the resonance region in large waves.

When λ / L is nearly 1.2, the pressures reach a maximum due to the resonance phenomenon .

3) Bow flare slamming pressures according to different wave amplitudes

The theoretical and experimental results of the bow flare slamming pressures by two methods for different wave amplitudes are illustrated in Figs. 3.25-3.36 at Fn=0.15 and 0.25, λ / L=1.0, 1.2 and 1.4, Sta.=2 and 3.

For Fn=0.15, comparisons between the predictions and the measurements show very good agreement (Figs. 3.25-3.30). The bow flare slamming pressures increase while the wave amplitude increases.

For Fn=0.25, the predictions and the measurements agree very well (Figs.3.31-

3.36) and the bow flare slamming pressures increase while the wave amplitude increases.

There are nearly same results between the predictions by the momentum slamming theory and the Wagner type impact theory at the low wave amplitude region, but, when the wave amplitude increases the difference between them also increases.

4) Bow flare slamming pressures according to different speeds

The bow flare slamming pressures by the momentum slamming theory for different speeds are shown in Fig. 3.37-3.42.

For $\lambda / L=1.0$, at Sta.=2 and 3, the bow flare slamming pressures for the three speeds are nearly the same in the small wave amplitude region. In the large wave amplitude region, there are some differences among them and the results at Fn=0.15 are the maximum. This is because the motion responses become maximum, when Fn=0.15, $\lambda / L=1.0$.

For $\lambda / L=1.2$ and 1.4, Sta.=2 and 3, the impact pressures increase as the Froude Number increases.

5) Bow flare slamming pressures according to different draughts

In Figs. 3.43-3.50, the variation of impact pressures due to different draught and wave striking pressures are shown at Sta.=2 and 3, for Fn=0.15 and 0.25, ζ_a=4.0 and 7.5 cm. The wave striking pressures, which are the difference between P_{iM} and P decrease as the wave amplitude increases. This is because the bow flare part contacts the trough of waves and does not meet the crest in the case of large amplitude regular waves. This phenomenon can be seen more clearly for Fn=0.25 than for Fn=0.15.

6) Comparisons between the different theoretical methods

The results by the four methods and the experiments are compared with each other at Fn=0.15 and 0.25, Sta.=2 and ζ_a=4.0 and 7.5 cm are shown in Figs.A.3.21-A.3.24.

From these Figures, when ζ_a=4.0 cm, the results by the four theoretical methods show good agreement with the experimental data and the results by the momentum slamming theory seem to be the best (Figs.A.3.21 and A.3.23); When ζ_a=7.5 cm, nearly

the same results are obtained by the four methods and the results have a satisfactory agreement with the experimental data except in the resonance region where the results by the Wagner impact theory have the best agreement with the experimental data (Figs.A.3.22 and A.3.24).

3.5 Conclusions

3.5.1 Bottom slamming pressure

1) The bottom slamming pressure may be predicted by the Ochi & Motter's method.

2) The Stavovy & Chuang's method, the momentum theory and Payne impact theory will predict bigger values than the experimental data in the bottom slamming pressure calculation.

3) The bottom slamming pressure increases as the wave amplitude increases.

3.5.2 Bow flare slamming pressure

1) The momentum slamming theory can be used to predict the bow flare slamming pressures in moderate and large waves (except in the resonance region in large waves). In the resonance region in large waves, the Wagner impact theory will predict better results.

2) The bow flare impact pressures increase as the wave amplitude increases.

3) Generally, the bow flare impact pressures increase as Froude Number increases.

4) The contribution of the wave striking pressures to the total impact pressures is relatively small, but noticeable in the small wave amplitude region.

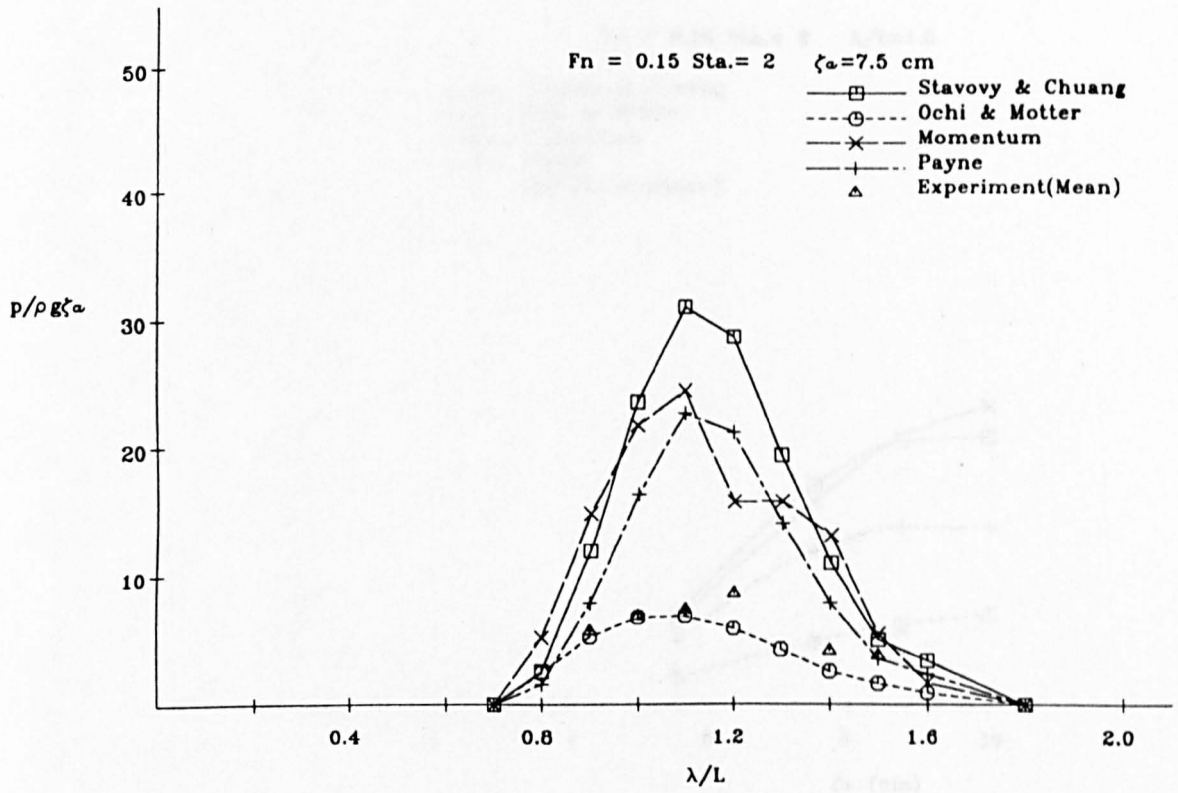

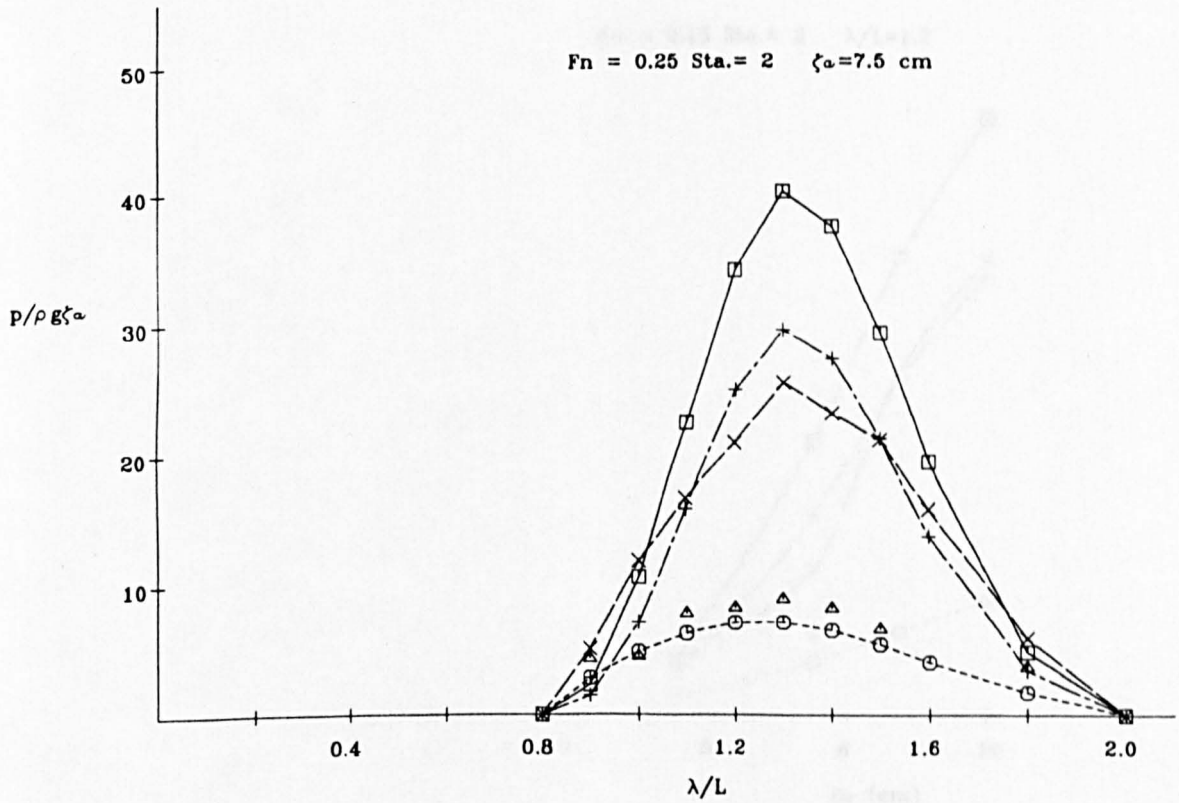

Figs.3.9-3.10 Bottom Slamming Pressure

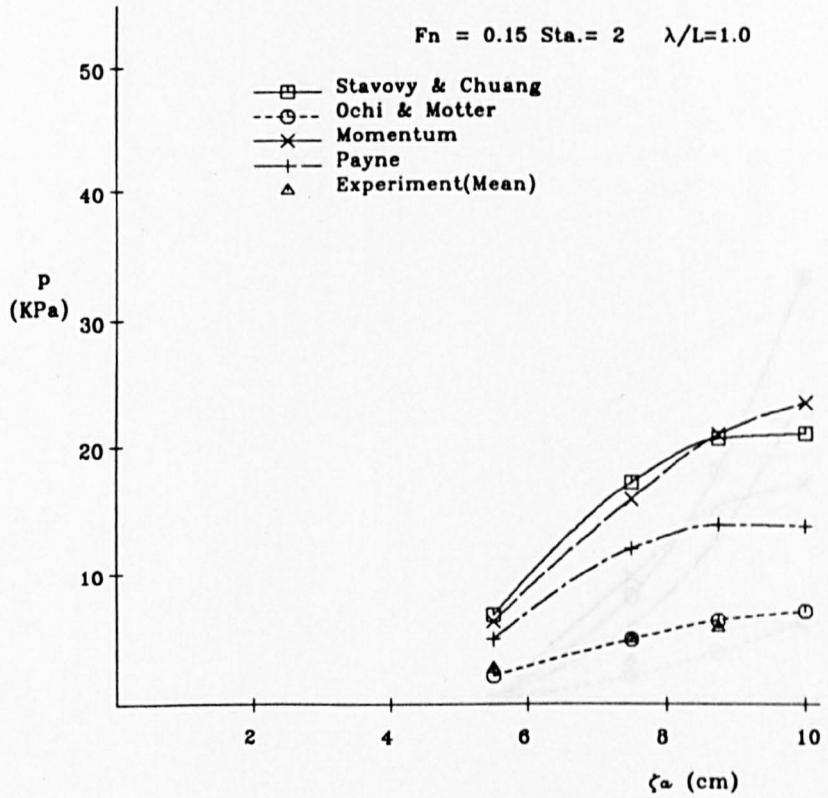

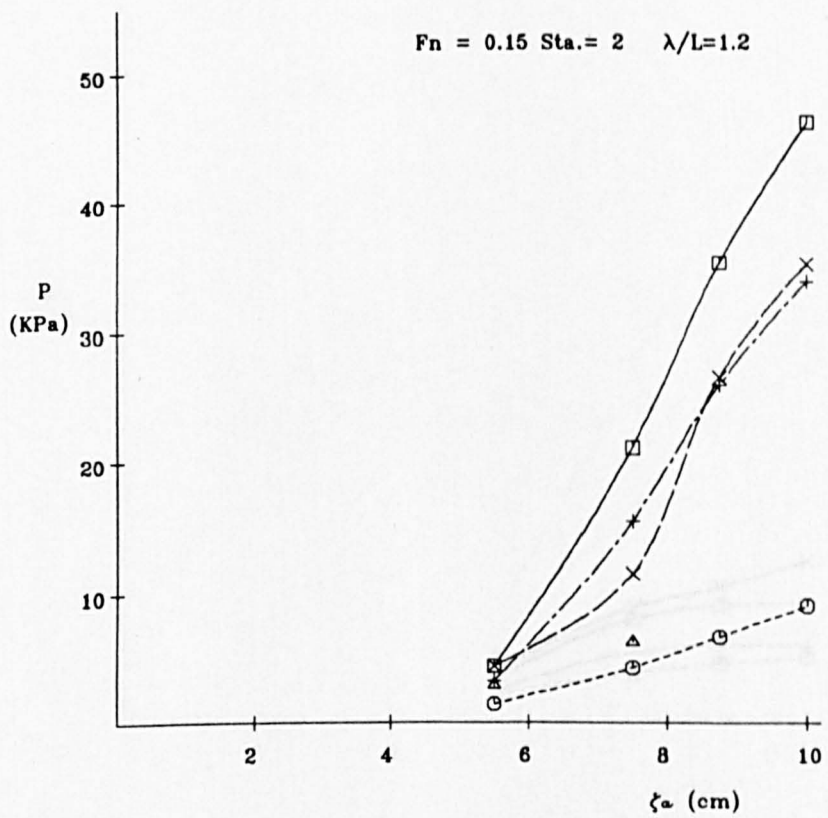

Figs.3.11-3.12 Bottom Slamming Pressure

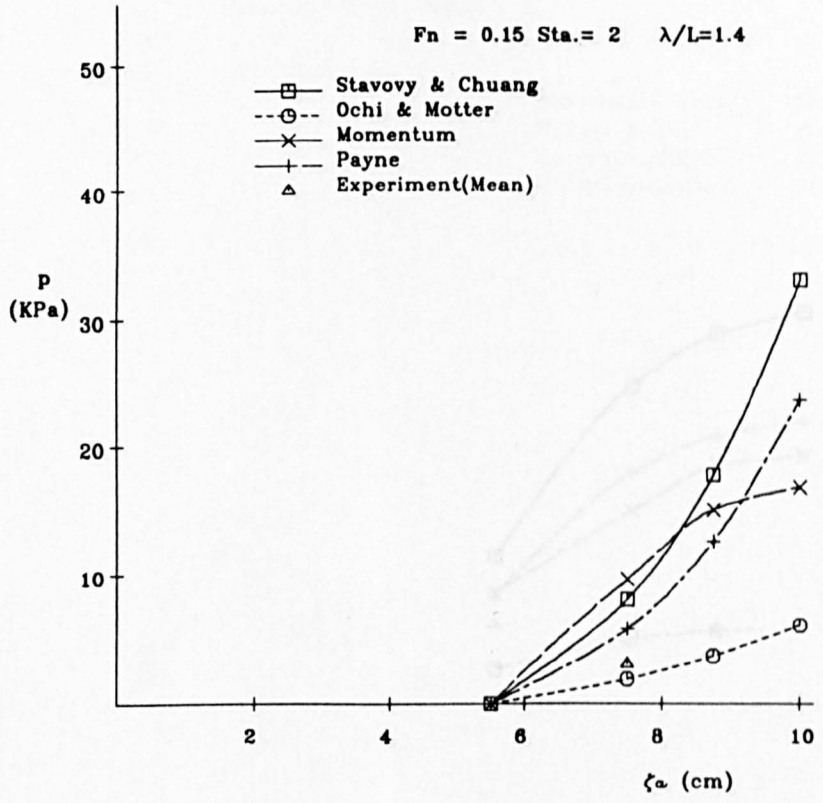

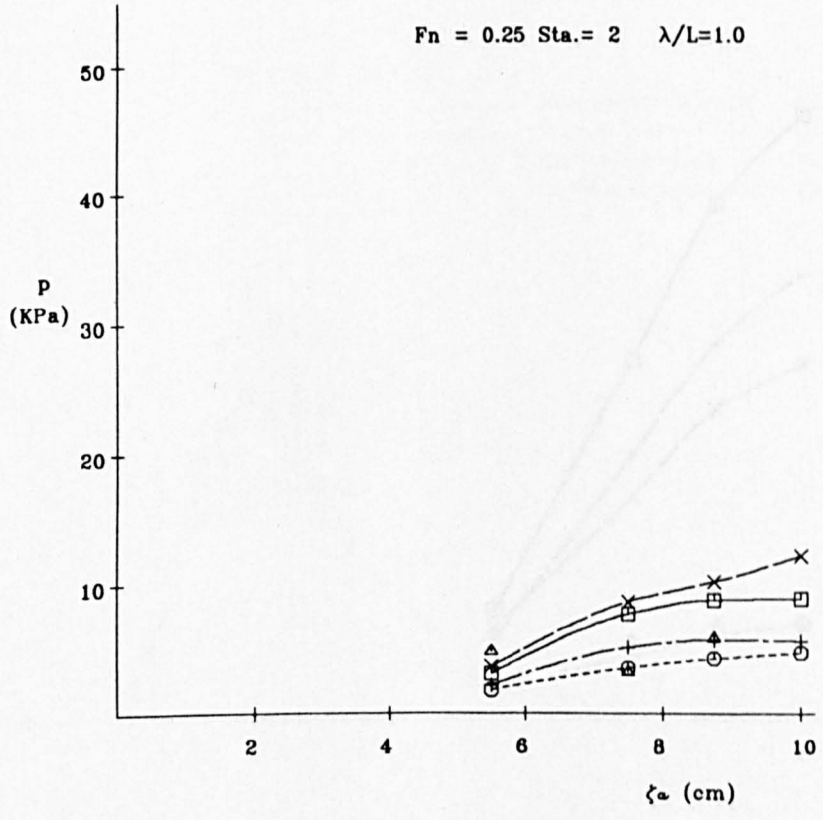

Figs.3.13-3.14 Bottom Slamming Pressure

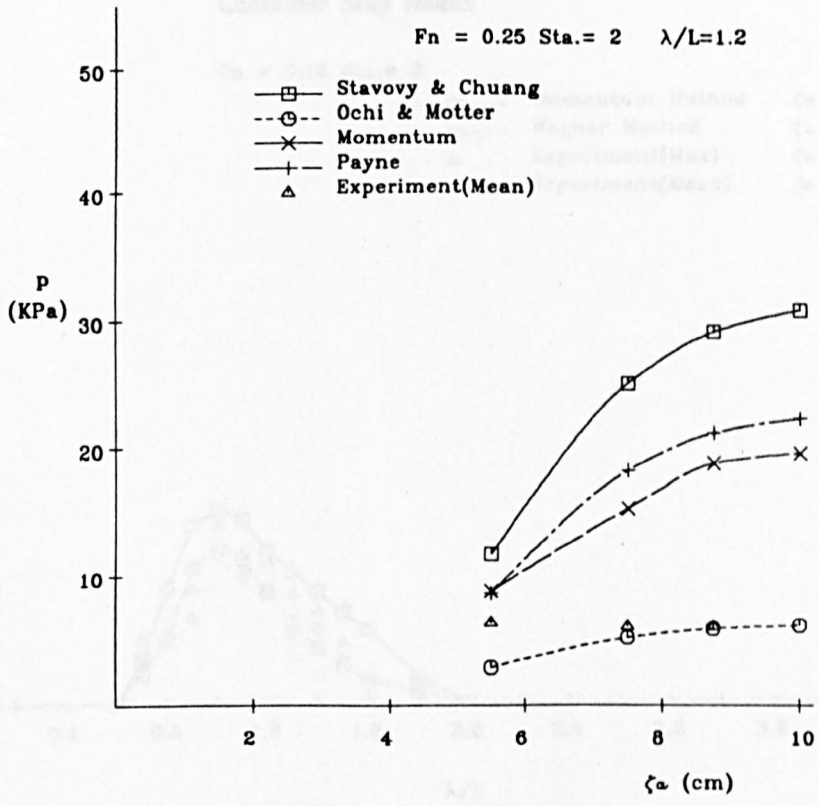

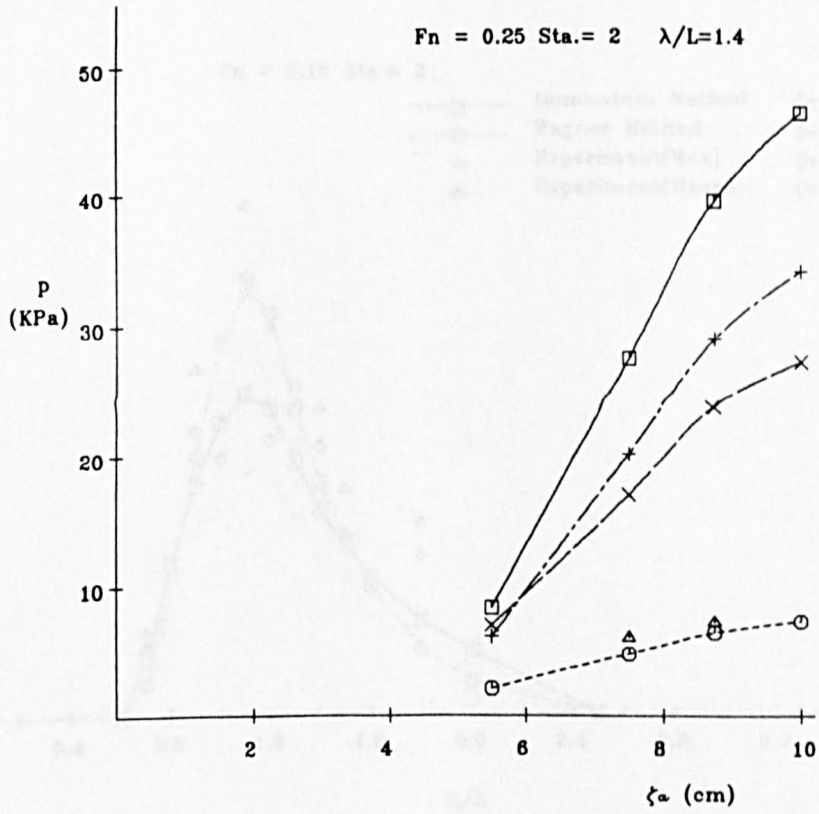

Figs.3.15-3.16 Bottom Slamming Pressure

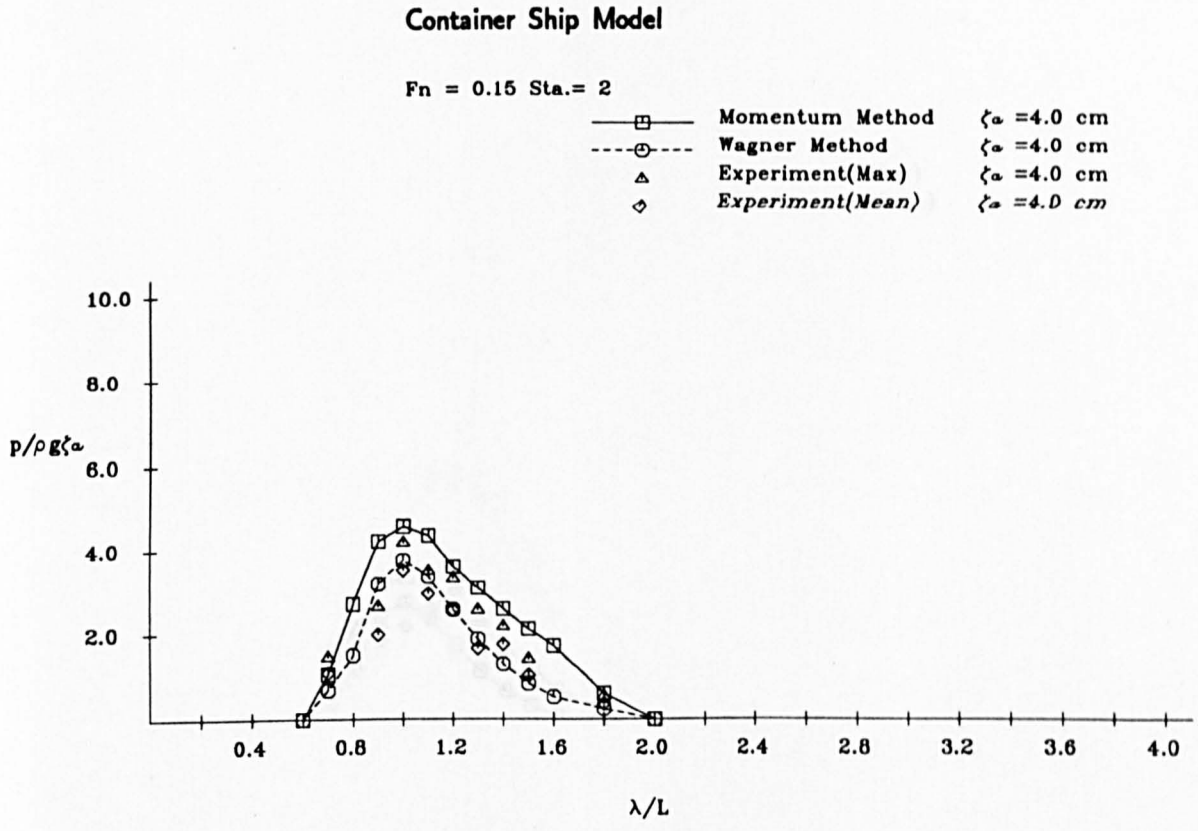

Fig.3.17 Bow Flare Impact Pressure Draught 20 cm

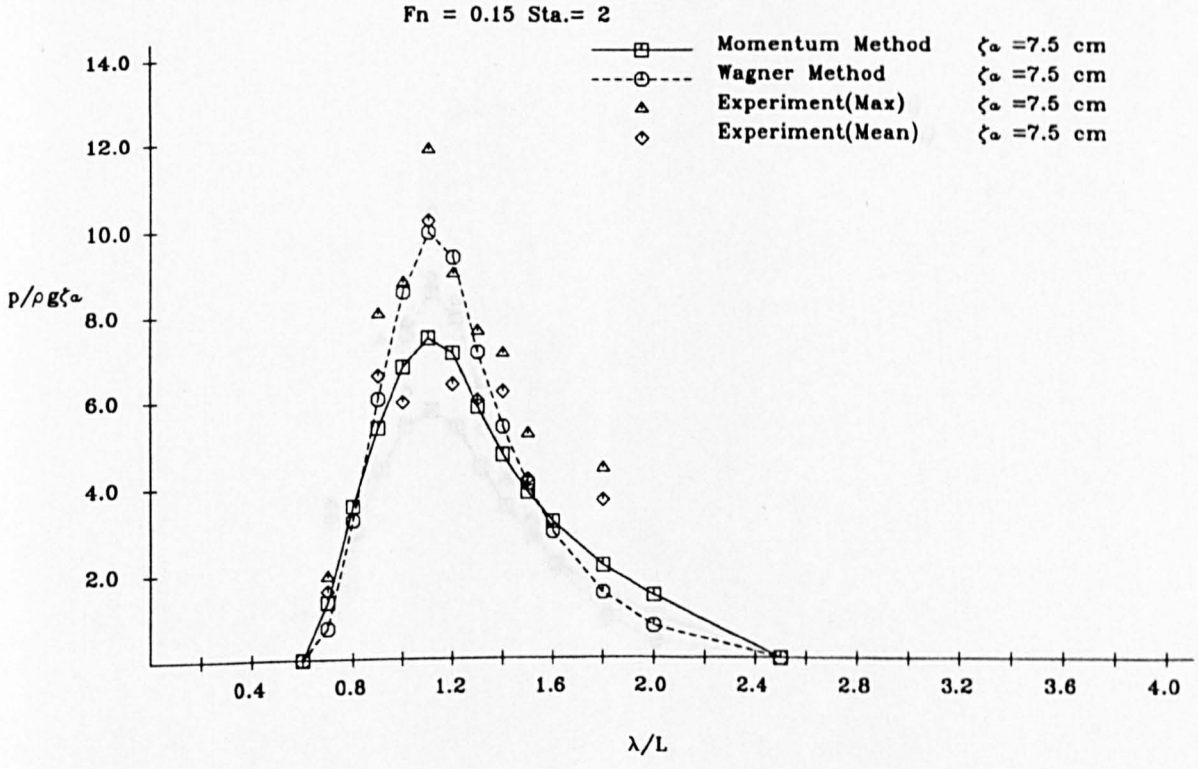

Fig.3.18 Bow Flare Impact Pressure Draught 20 cm

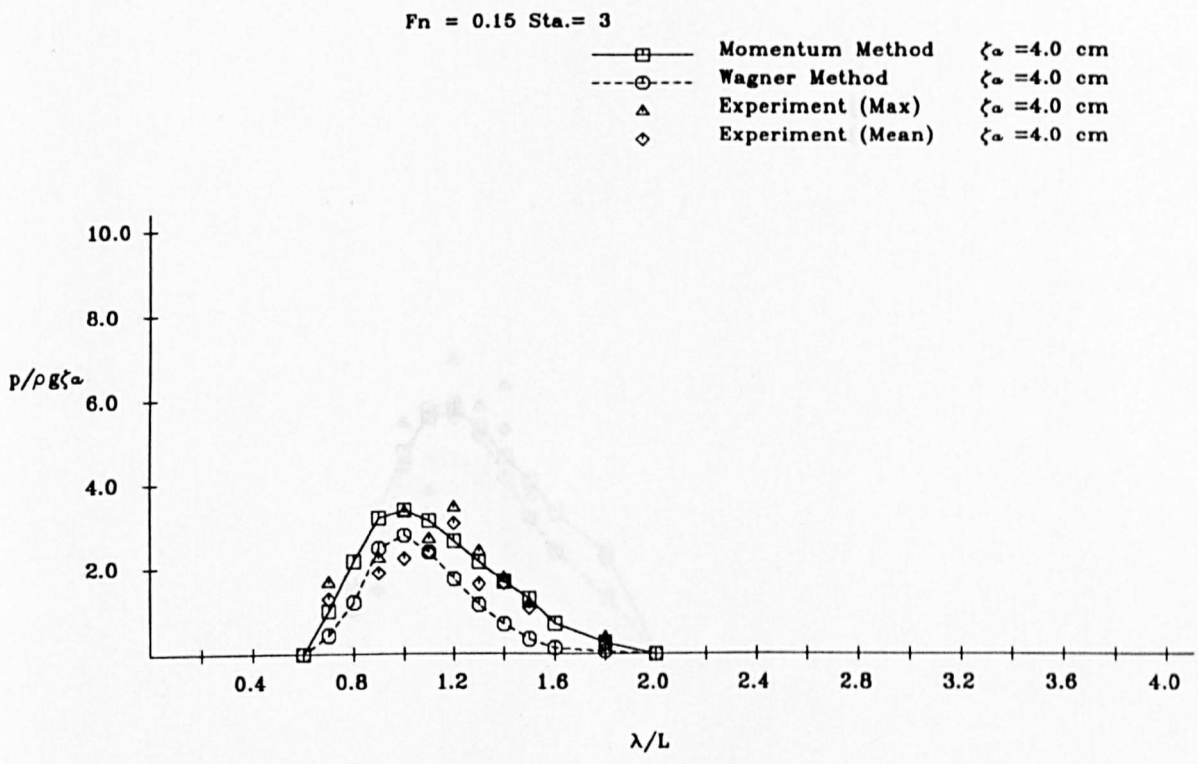

Fig.3.19 Bow Flare Impact Pressure Draught 20 cm

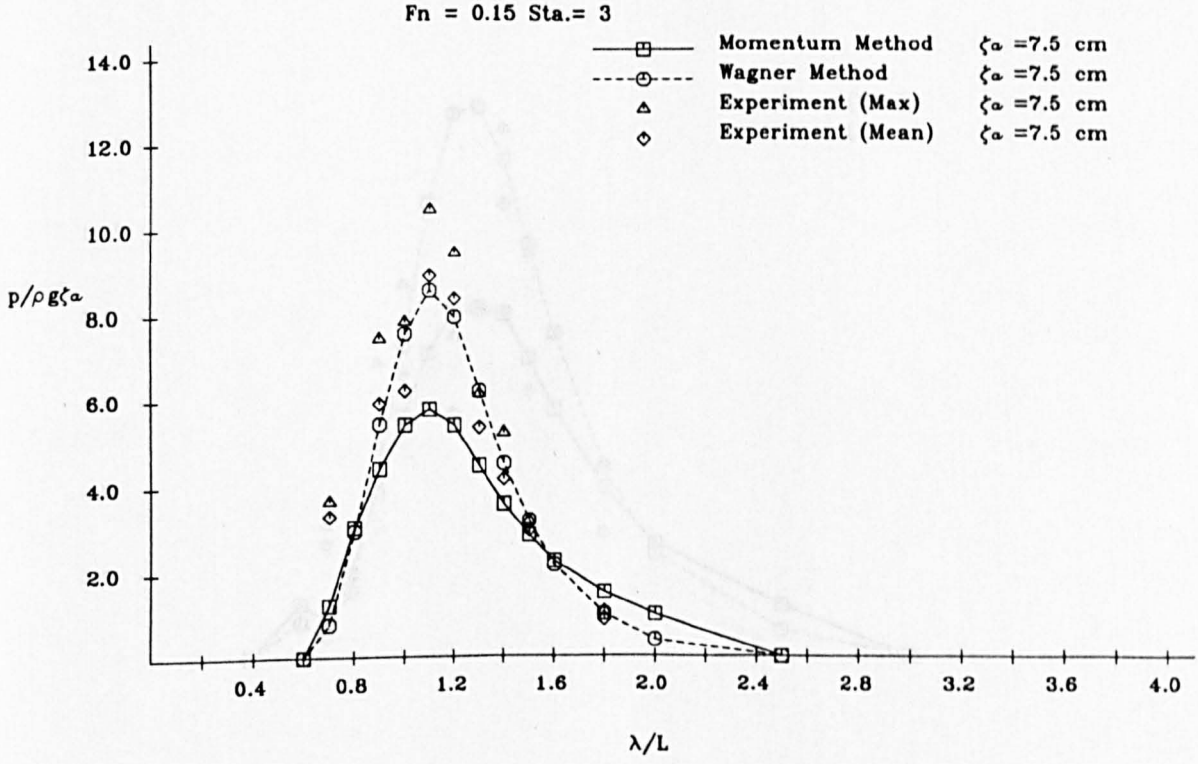

Fig.3.20 Bow Flare Impact Pressure Draught 20 cm

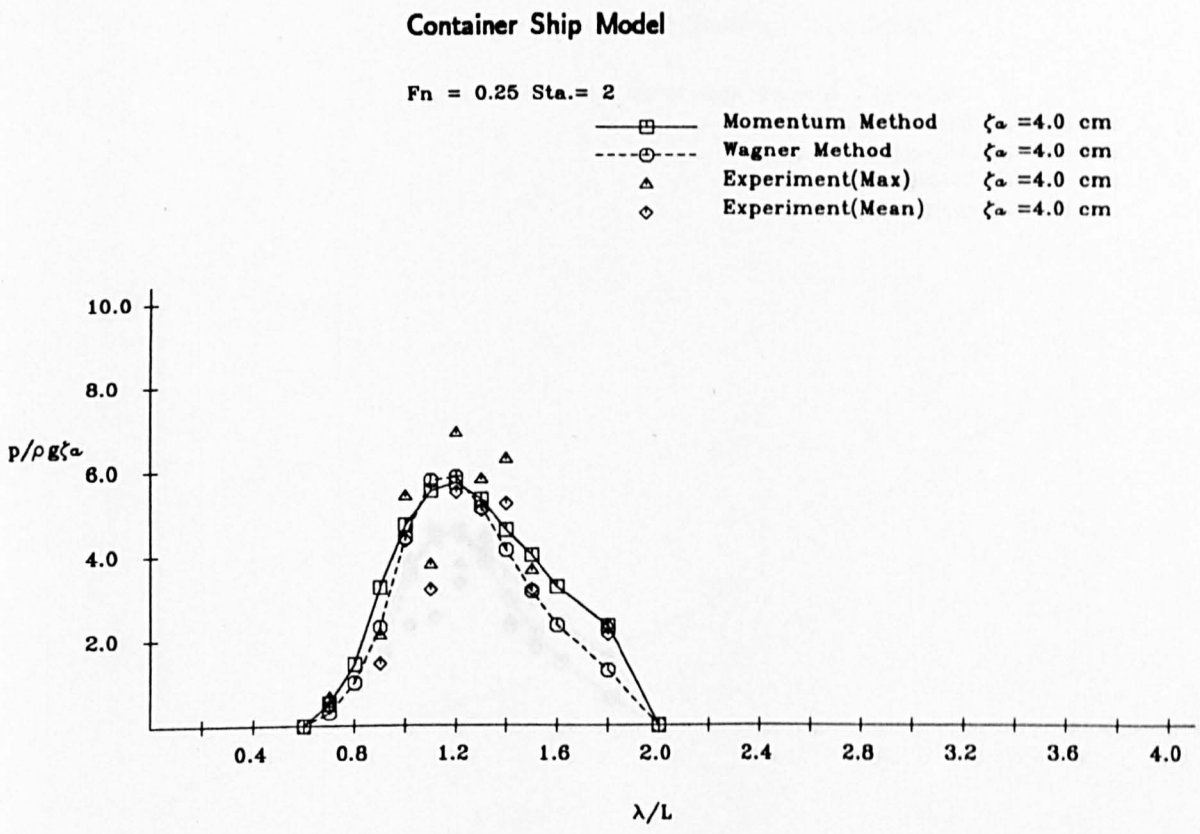

Fig.3.21 Bow Flare Impact Pressure Draught 20 cm

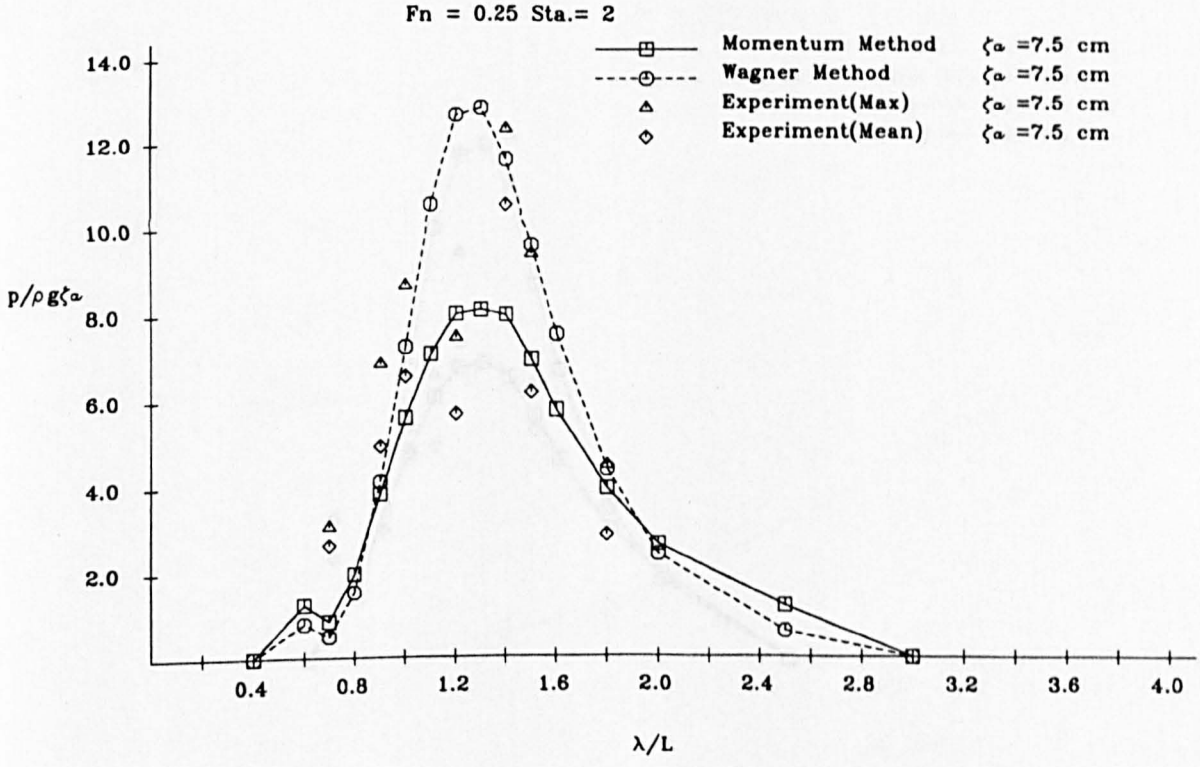

Fig.3.22 Bow Flare Impact Pressure Draught 20 cm

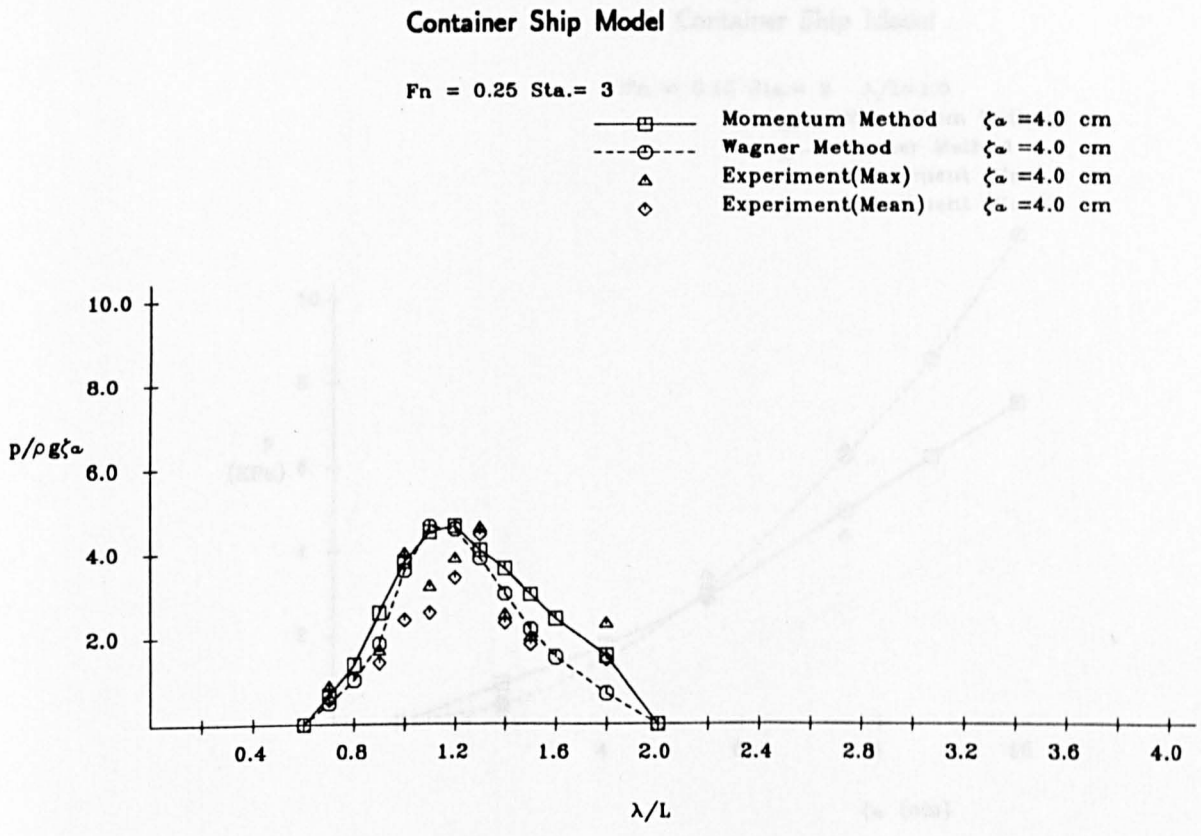

Fig.3.23 Bow Flare Impact Pressure Draught 20 cm

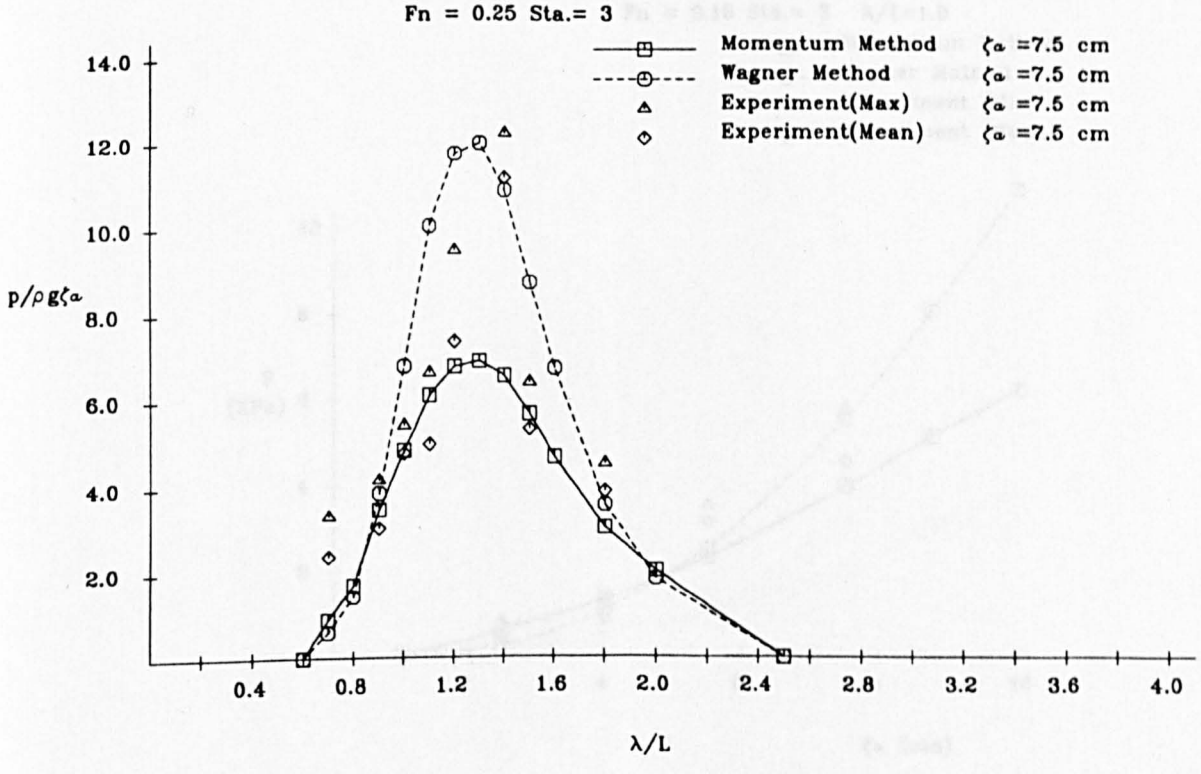

Fig.3.24 Bow Flare Impact Pressure Draught 20 cm

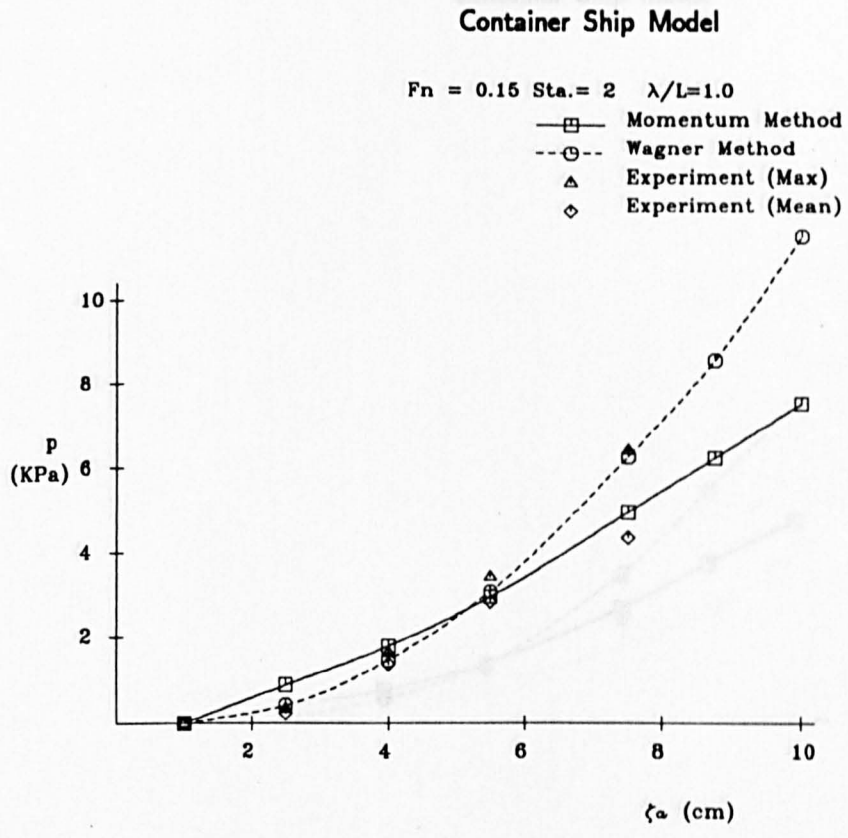

Fig.3.25 Bow Flare Impact Pressure Draught 20 cm

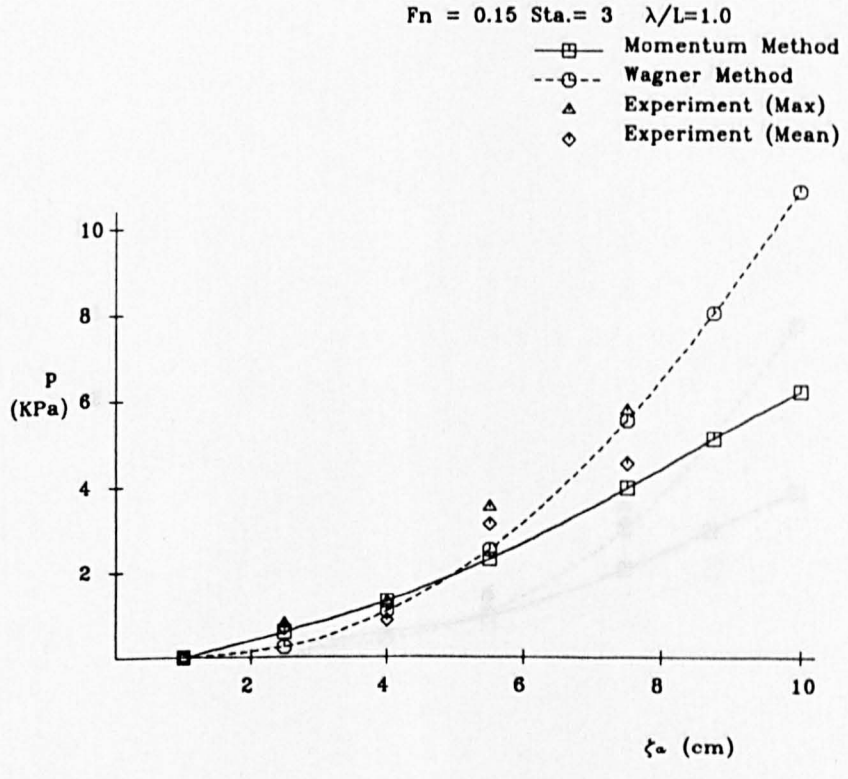

Fig.3.26 Bow Flare Impact Pressure Draught 20 cm

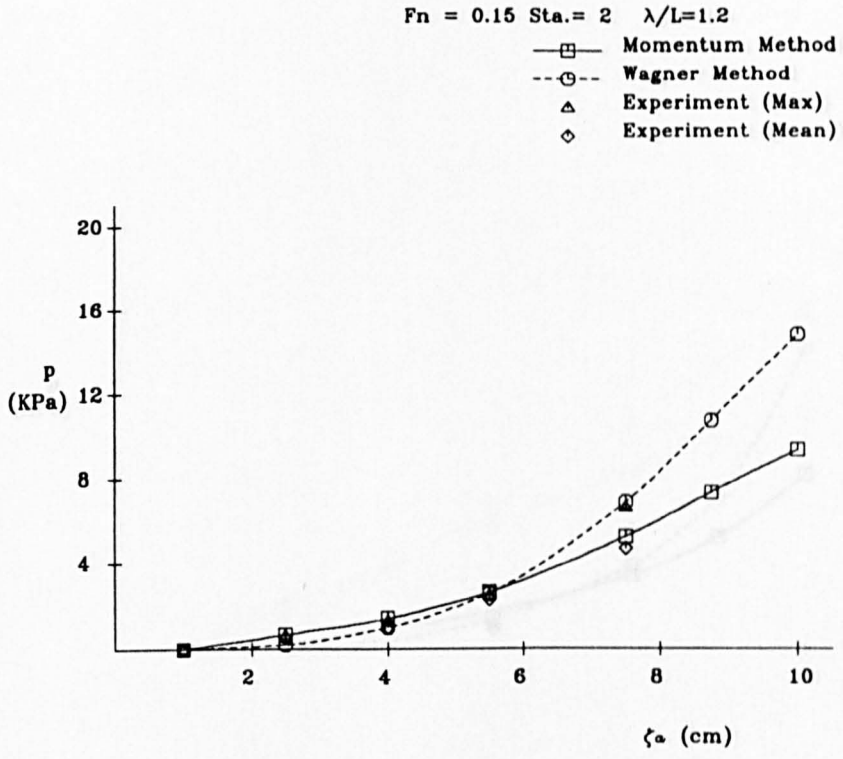

Fig.3.27 Bow Flare Impact Pressure Draught 20 cm

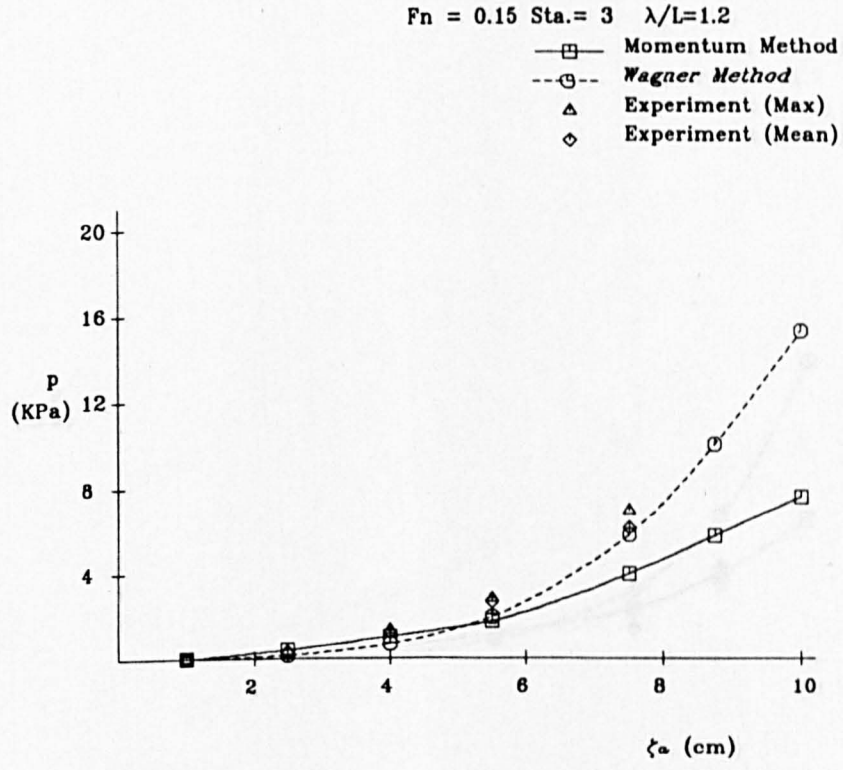

Fig.3.28 Bow Flare Impact Pressure Draught 20 cm

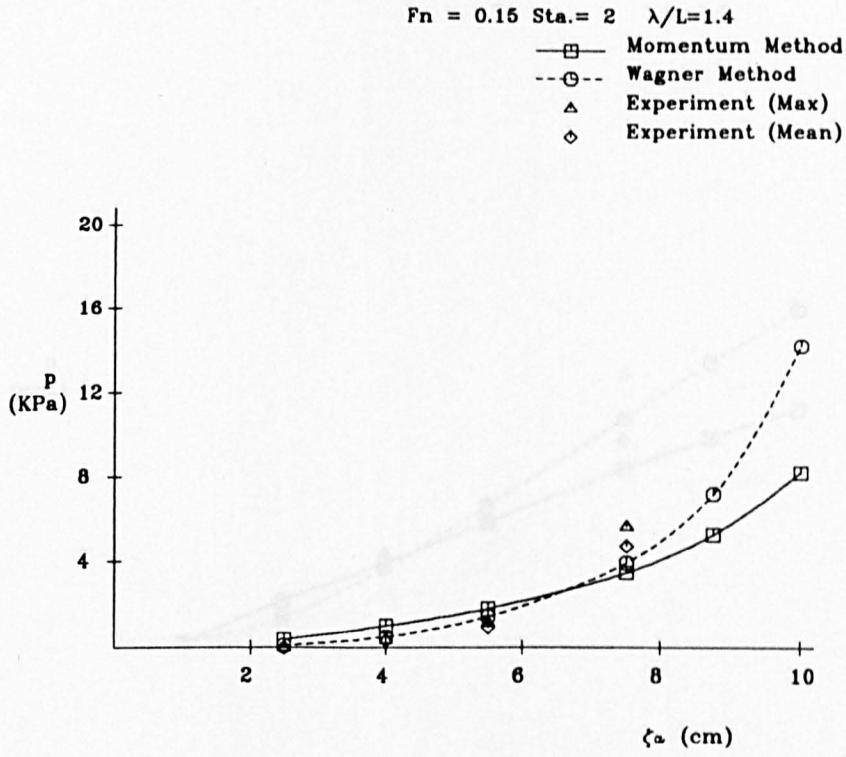

Fig.3.29 Bow Flare Impact Pressure Draught 20 cm

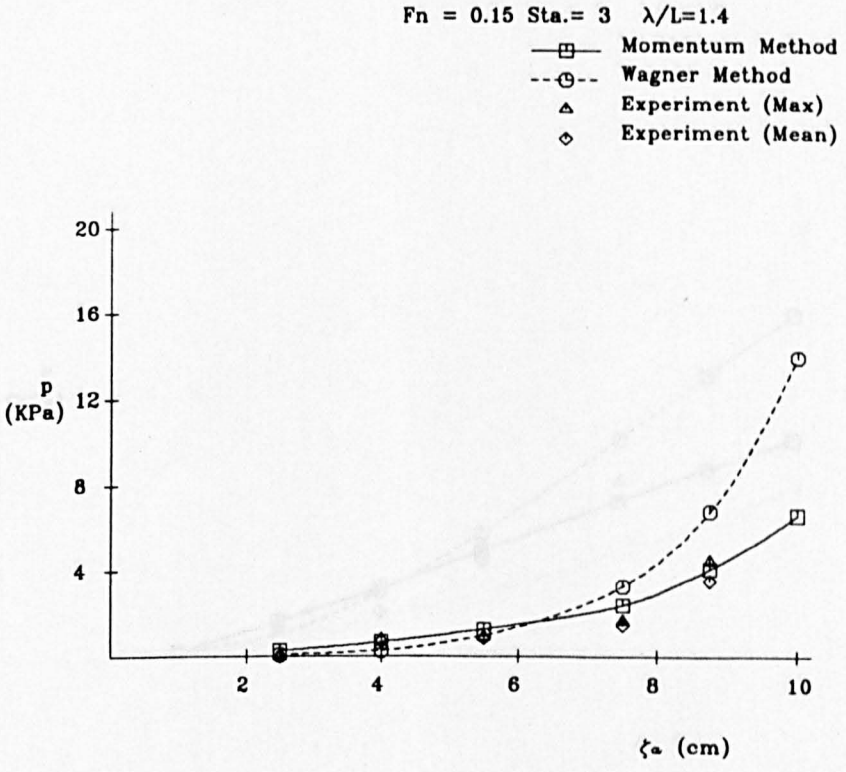

Fig.3.30 Bow Flare Impact Pressure Draught 20 cm

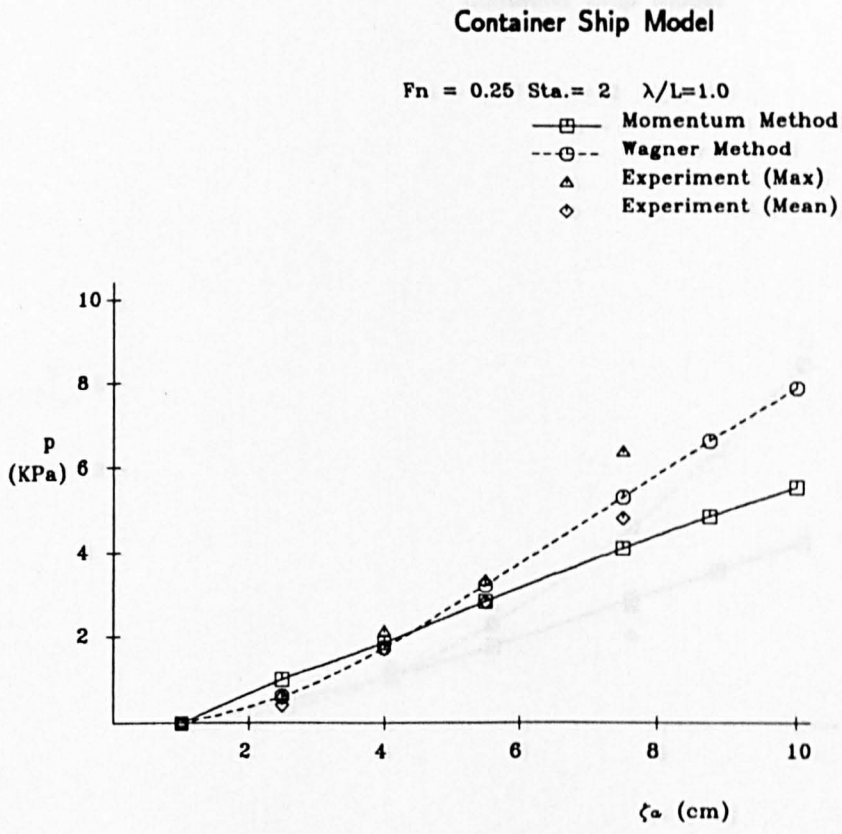

Fig.3.31 Bow Flare Impact Pressure Draught 20 cm

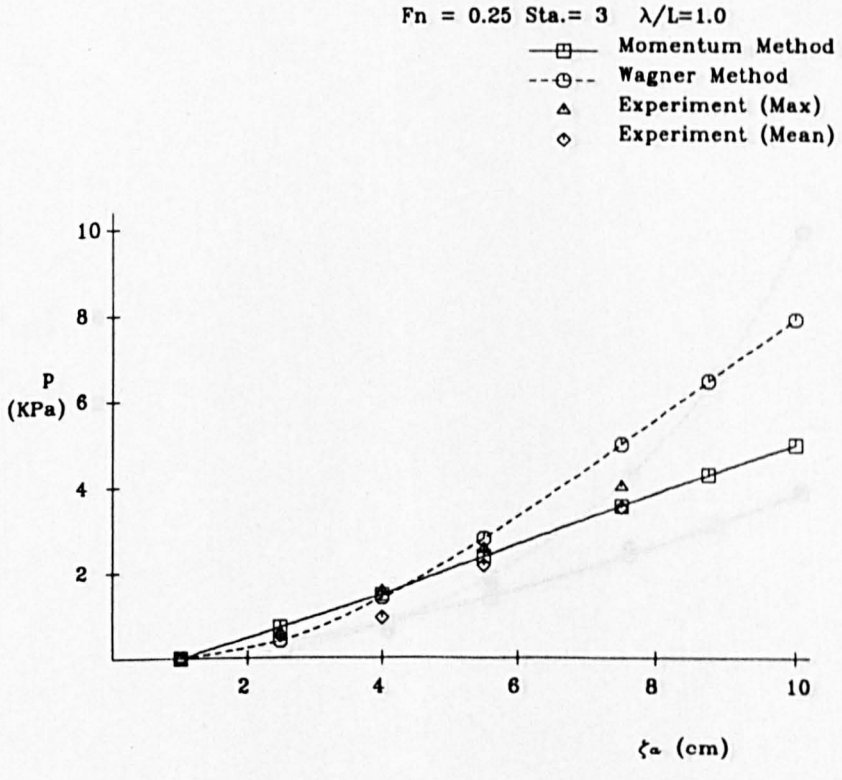

Fig.3.32 Bow Flare Impact Pressure Draught 20 cm

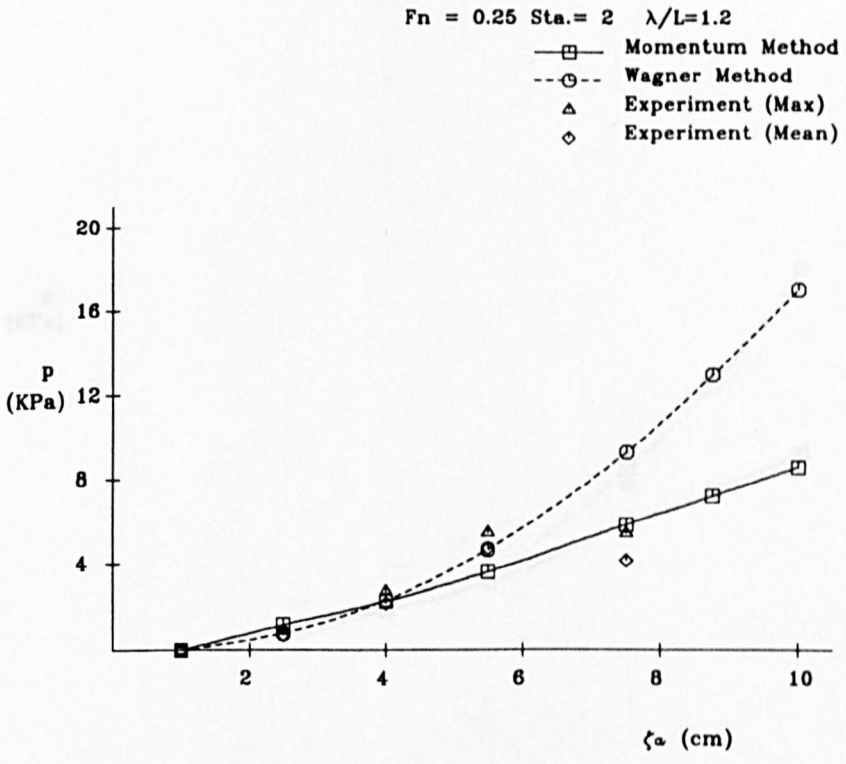

Fig.3.33 Bow Flare Impact Pressure Draught 20 cm

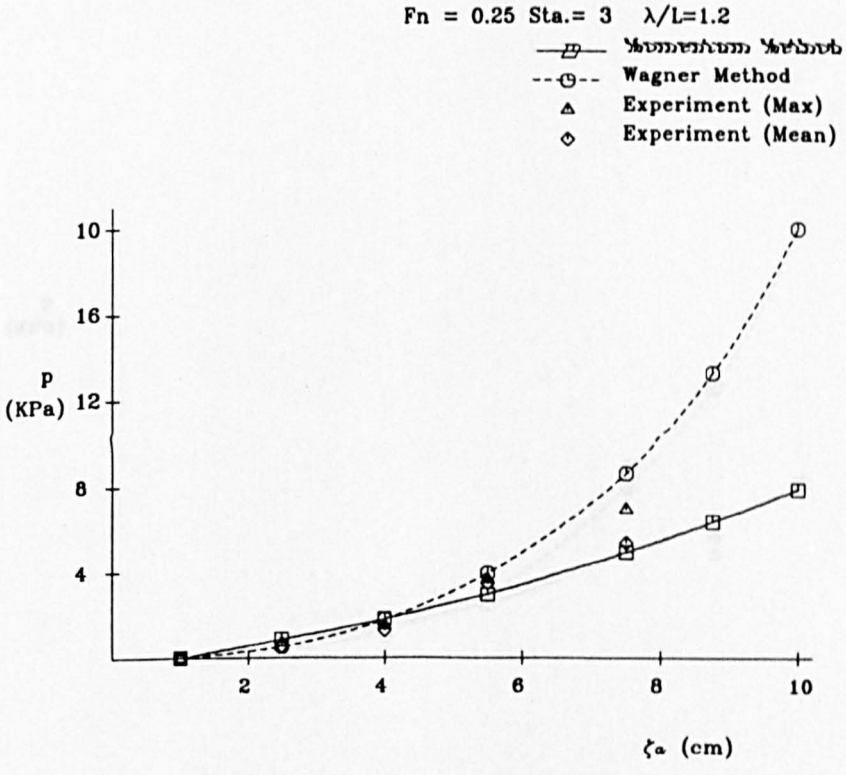

Fig.3.34 Bow Flare Impact Pressure Draught 20 cm

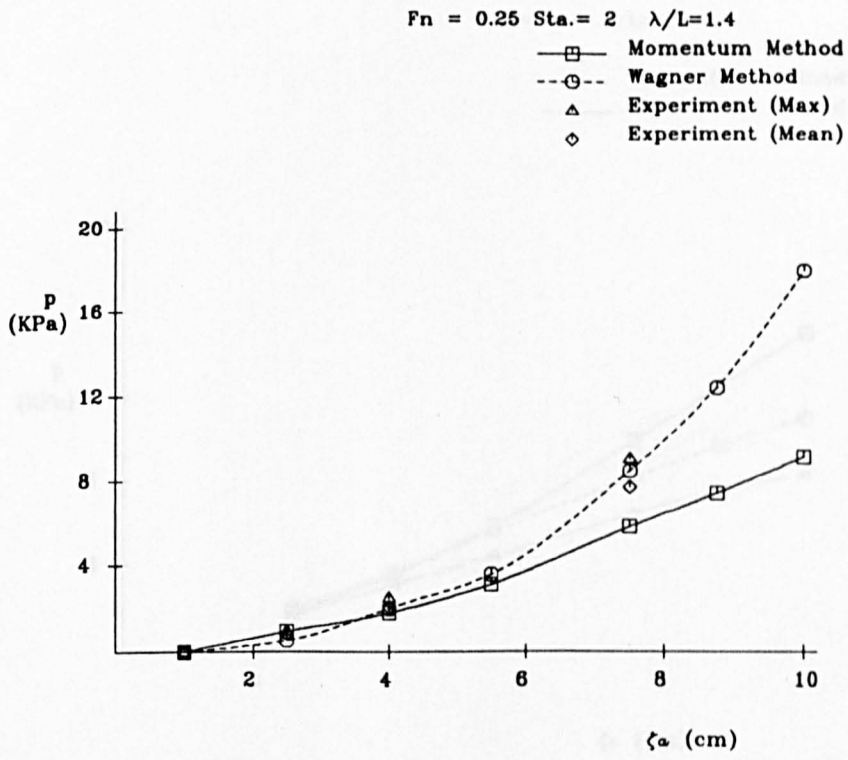

Fig.3.35 Bow Flare Impact Pressure Draught 20 cm

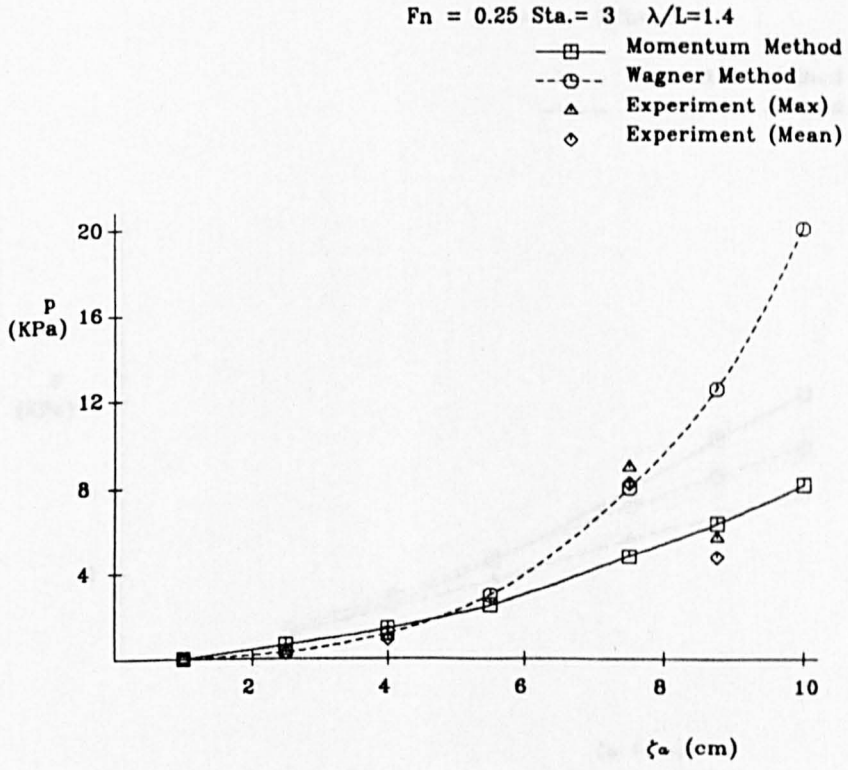

Fig.3.36 Bow Flare Impact Pressure Draught 20 cm

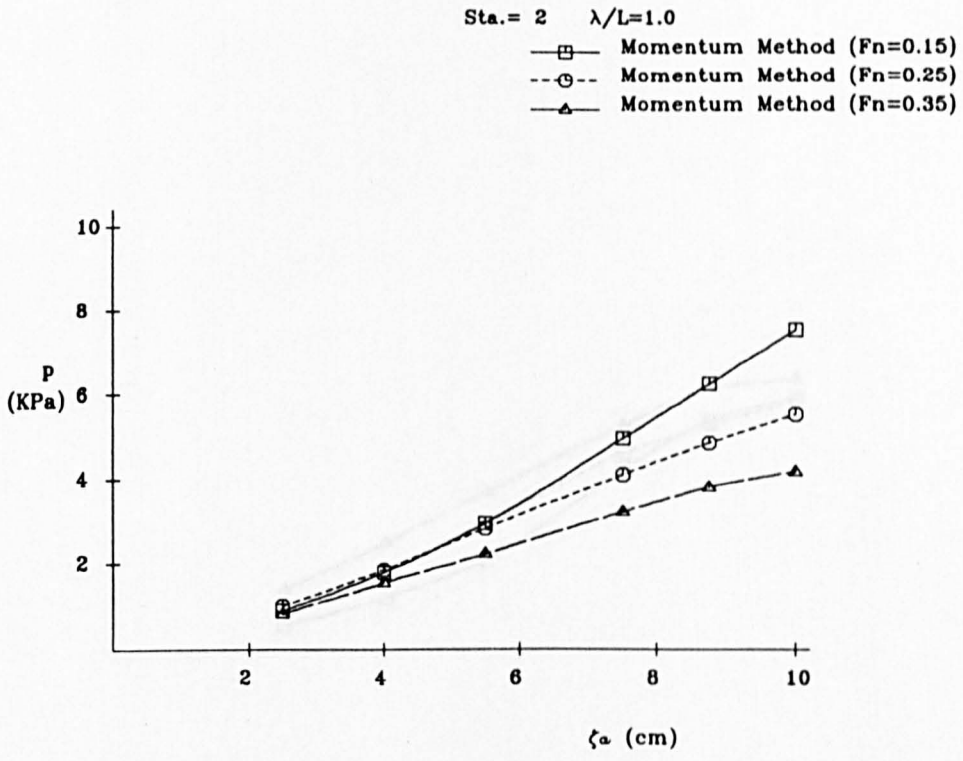

Fig.3.37 Bow Flare Impact Pressure Draught 20 cm

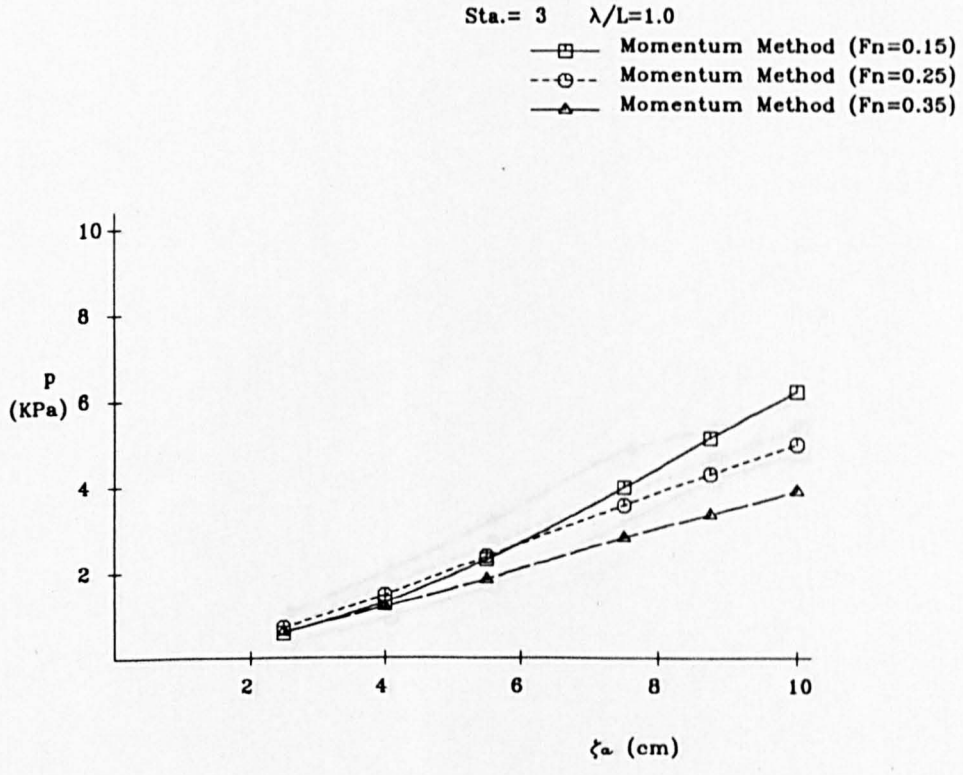

Fig.3.38 Bow Flare Impact Pressure Draught 20 cm

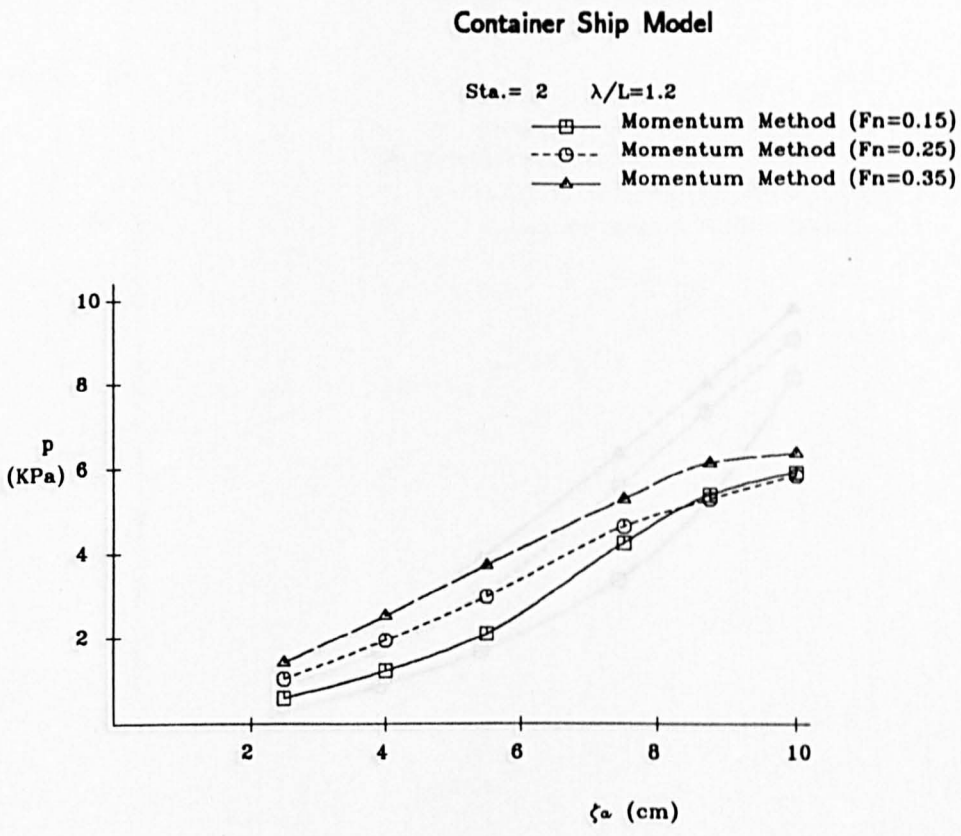

Fig.3.39 Bow Flare Impact Pressure Draught 20 cm

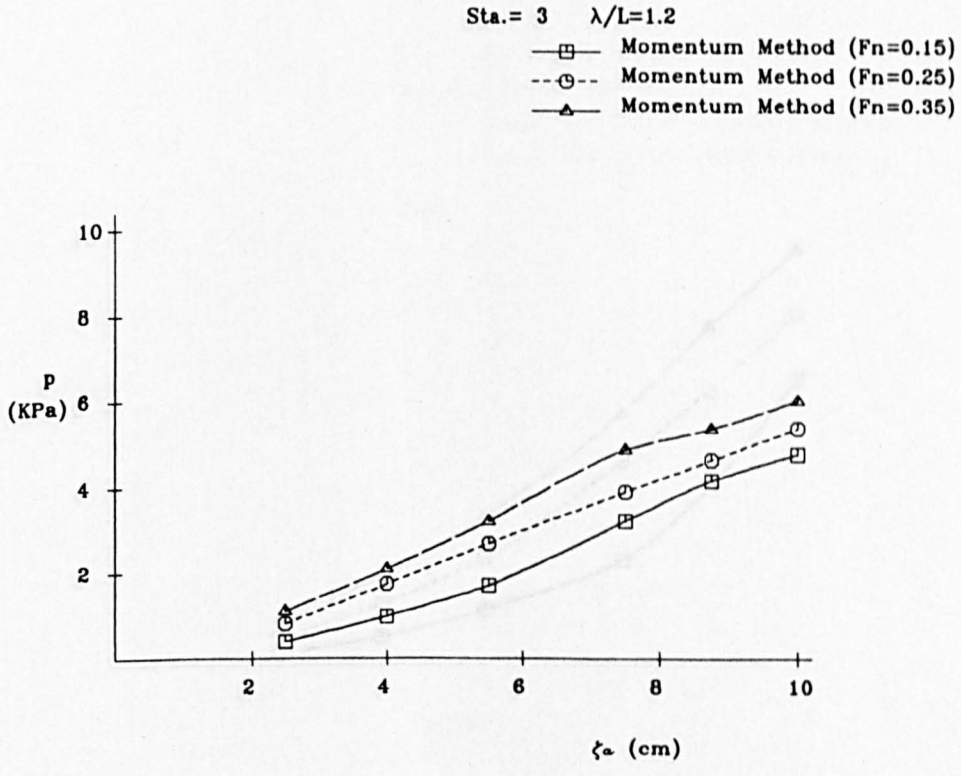

Fig.3.40 Bow Flare Impact Pressure Draught 20 cm

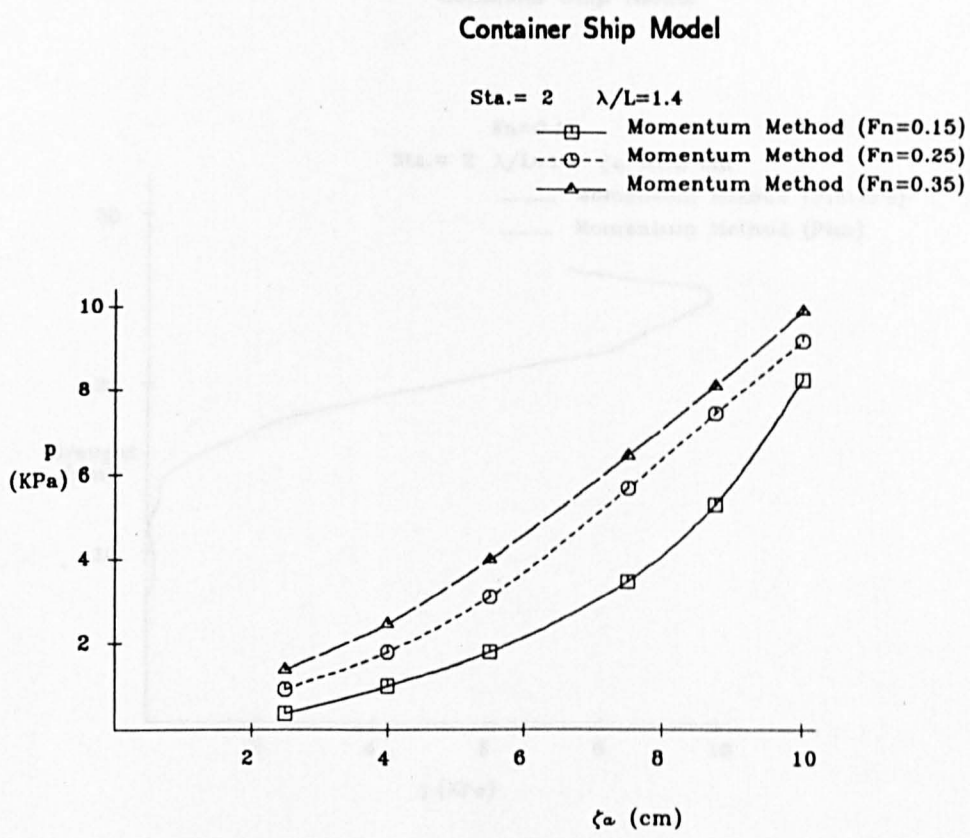

Fig.3.41 Bow Flare Impact Pressure Draught 20 cm

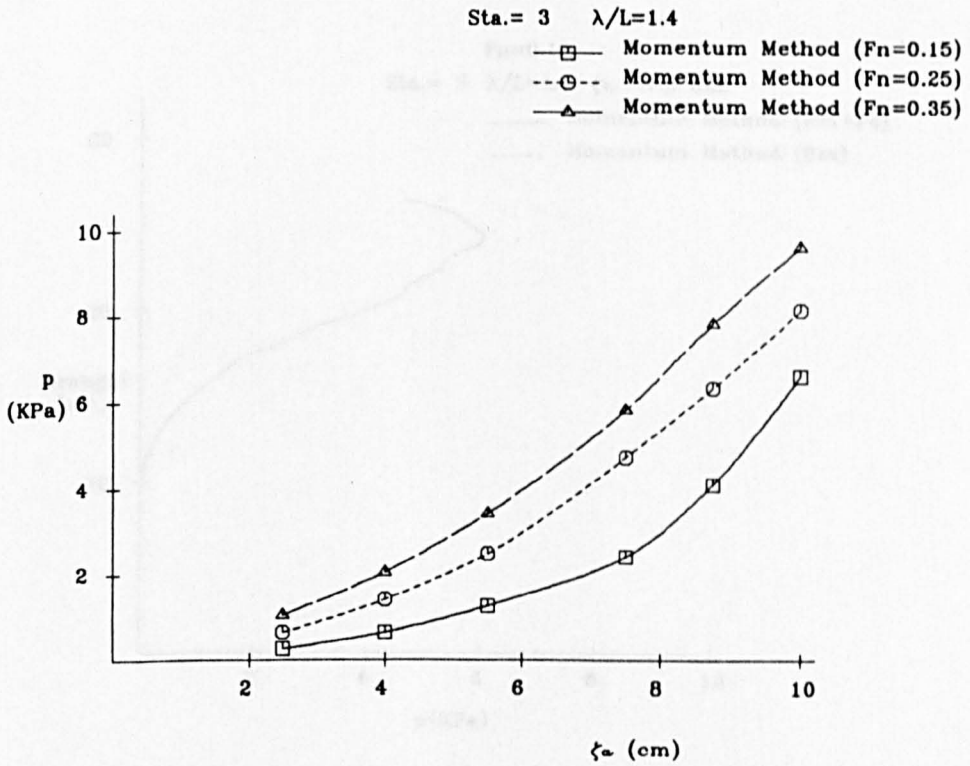

Fig.3.42 Bow Flare Impact Pressure Draught 20 cm

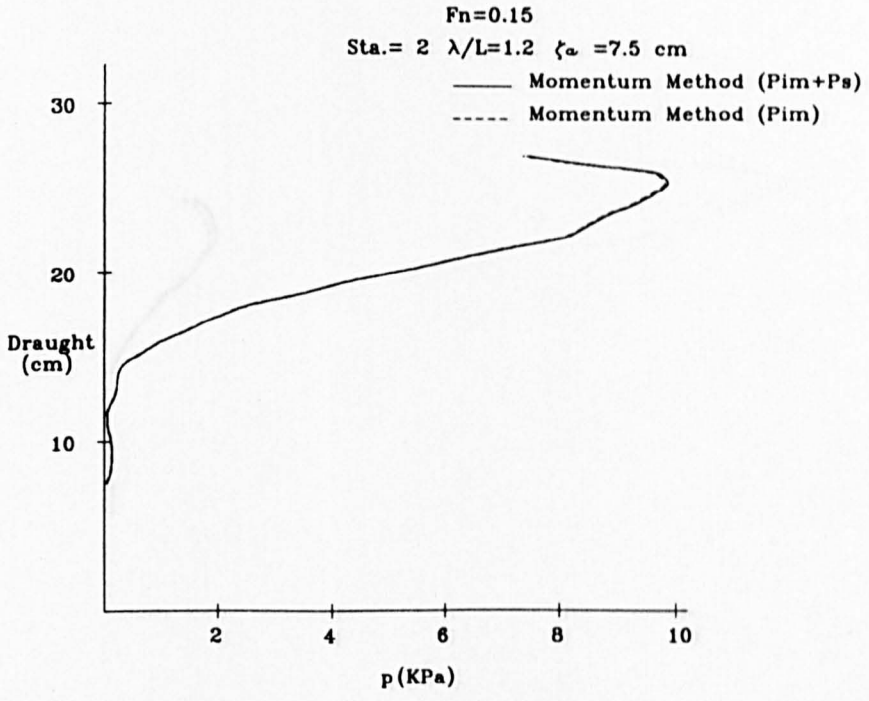

Fig.3.43 Impact Pressure Variation due to Draught

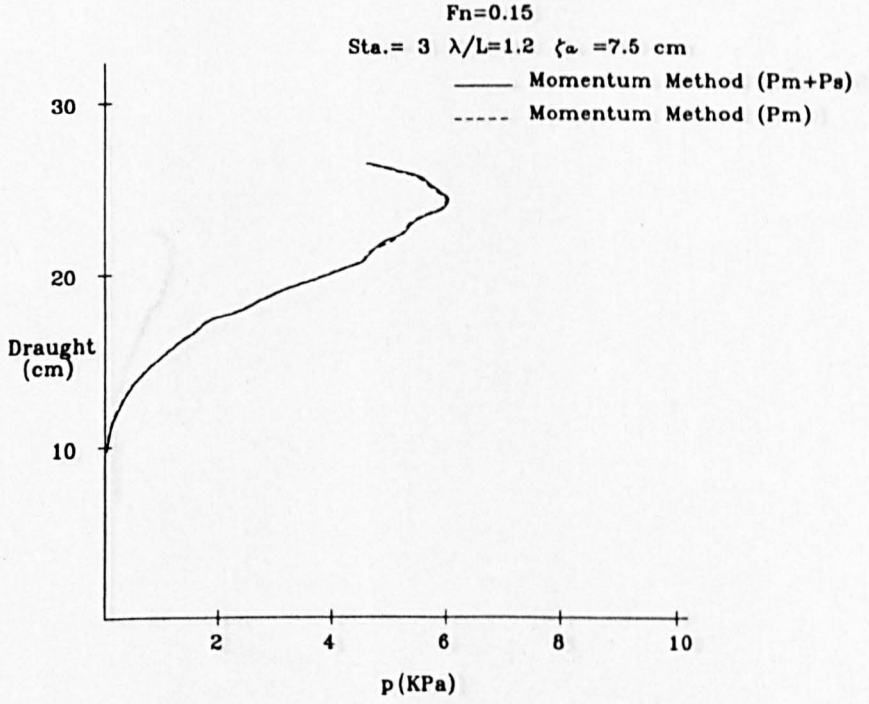

Fig.3.44 Impact Pressure Variation due to Draught

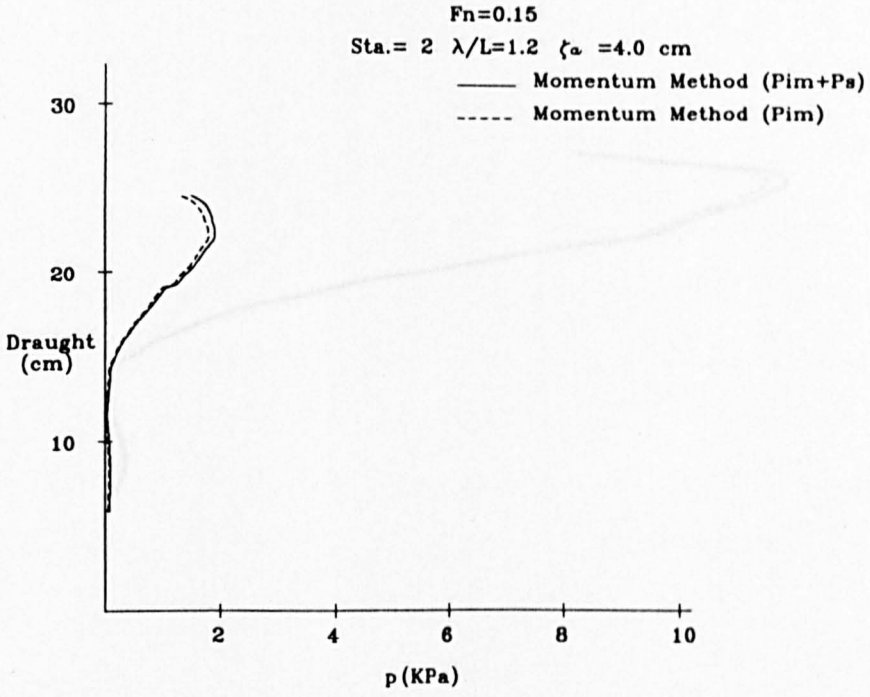

Fig.3.45 Impact Pressure Variation due to Draught

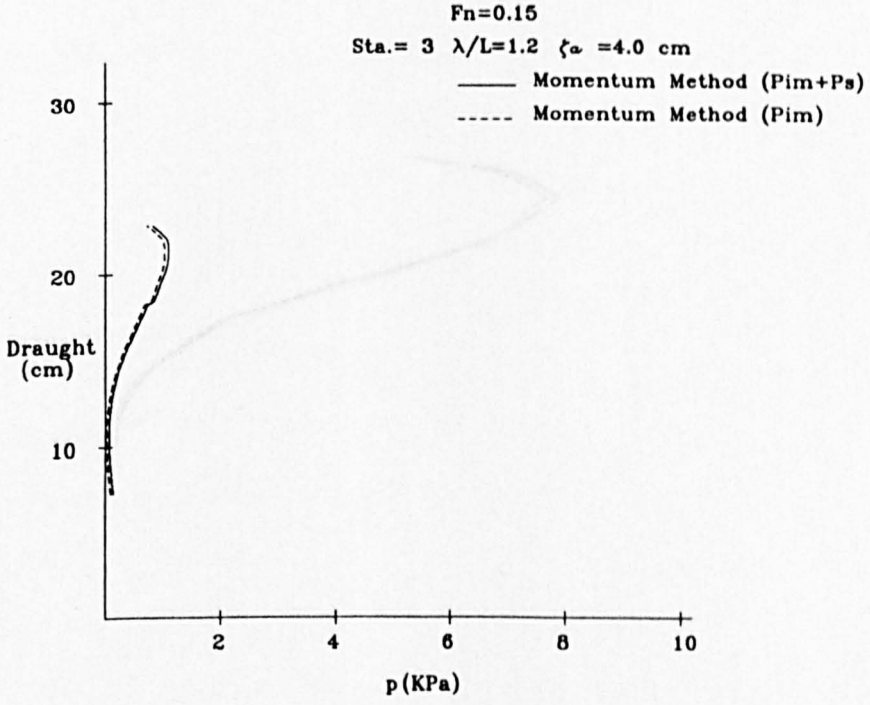

Fig.3.46 Impact Pressure Variation due to Draught

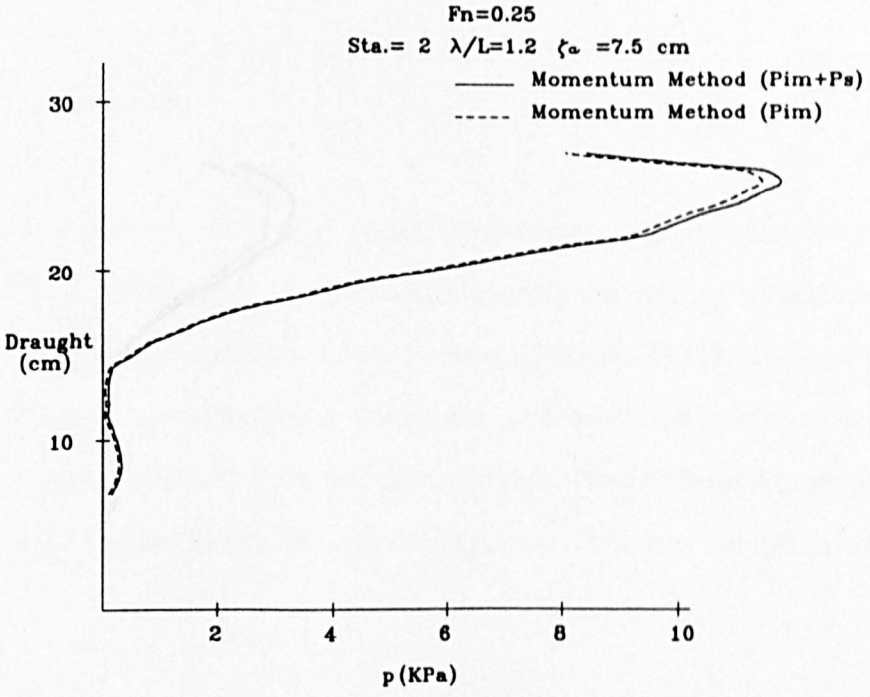

Fig.3.47 Impact Pressure Variation due to Draught

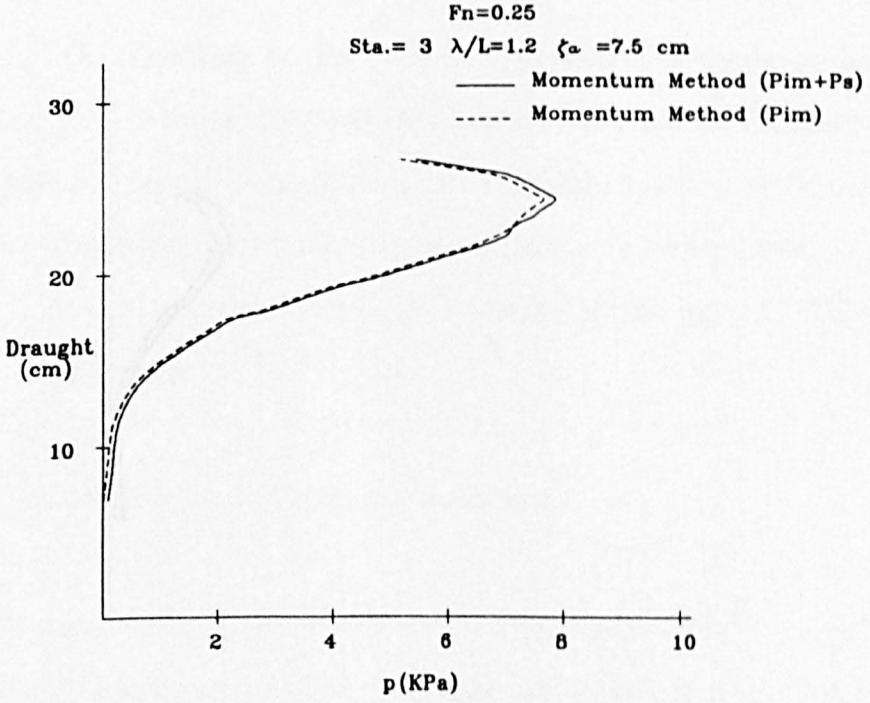

Fig.3.48 Impact Pressure Variation due to Draught

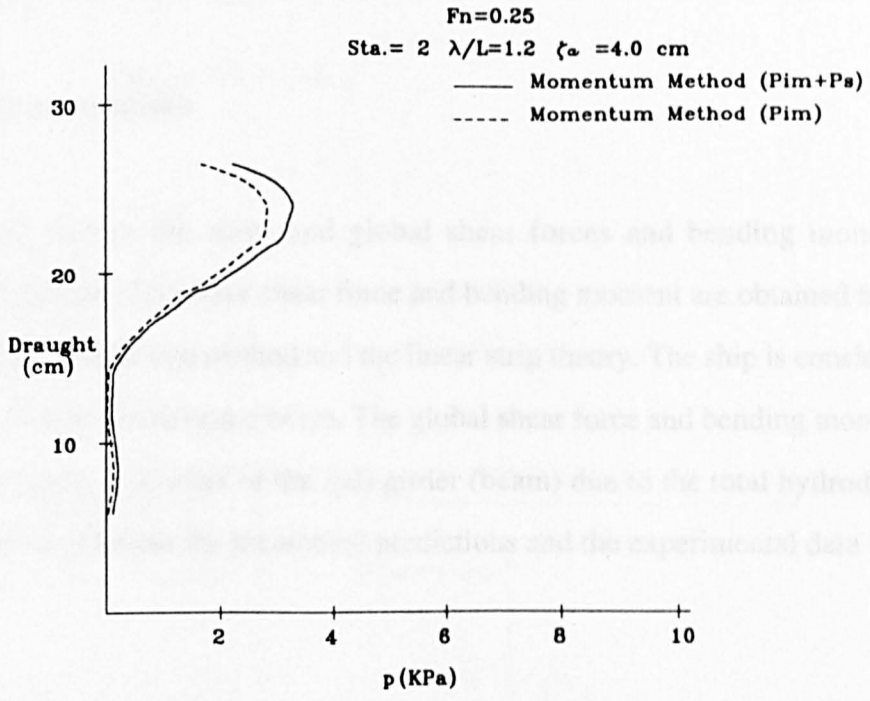

Fig.3.49 Impact Pressure Variation due to Draught

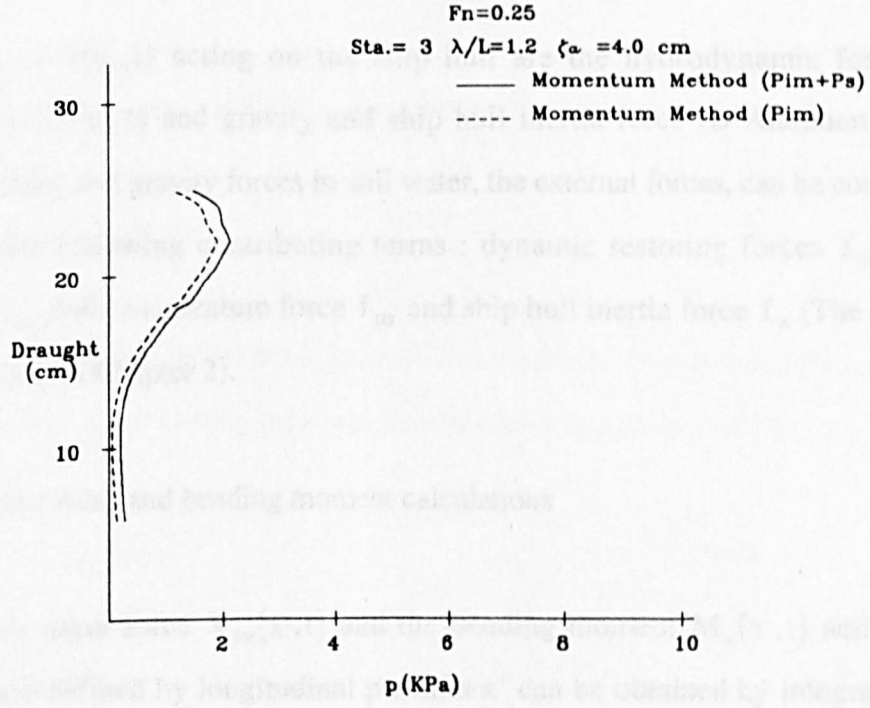

Fig.3.50 Impact Pressure Variation due to Draught

CHAPTER 4

SHEAR FORCE AND BENDING MOMENT CALCULATIONS

4.1 General description

The prediction of the wave and global shear forces and bending moments is described in this chapter. The wave shear force and bending moment are obtained from the nonlinear theoretical prediction method and the linear strip theory. The ship is considered as a free-free nonuniform Timoshenko beam. The global shear force and bending moment are treated as the dynamic responses of the hull girder (beam) due to the total hydrodynamic force. Comparisions between the theoretical predictions and the experimental data are also described.

4.2 Wave shear force and bending moment calculations

4.2.1 Description of forces

The forces $f(x_b,t)$ acting on the ship hull are the hydrodynamic force, the hydrostatic force $f_H(x_b,t)$ and gravity and ship hull inertia force (D'Alembert force). Omitting hydrostatic and gravity forces in still water, the external forces, can be considered as the sum of the following contributing terms : dynamic restoring forces f_{H1}, wave damping force f_{H2}, fluid momentum force f_{H3} and ship hull inertia force f_A (The detailed description is given in Chapter 2).

4.2.2 Wave shear force and bending moment calculations

The wave shear force $V_{wa}(x',t)$ and the bending moment $M_w(x',t)$ acting on a transverse section defined by longitudinal position x' can be obtained by integrating the force and moment values aft of the section considered (see Fig.4.1) in the following form :

form :

$$\begin{cases} V_{ws}(x',t) = \int_{-L_a}^{x'} f(x_b,t)dx_b \\ M_w(x',t) = \int_{-L_a}^{x'} f(x_b,t)(x'-x_b)dx_b \end{cases} \tag{4-1}$$

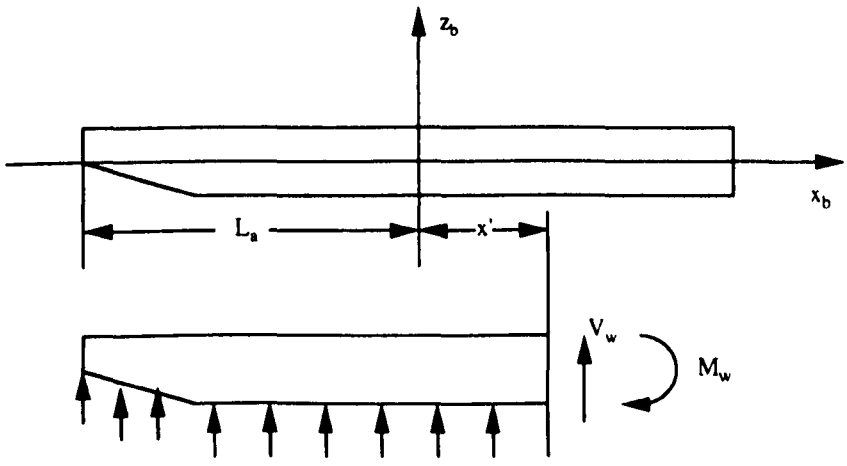

Fig.4.1 Shear Force and Bending Moment Induced by Waves

4.3 Global shear force and bending moment calculations

4.3.1 Description of forces

The hydrodynamic force (the dynamic restoring force, the wave damping force and the fluid momentum force) acting on a two dimensional ship section will be :

$$f_H = f_{H1} + f_{H2} + f_{H3} \tag{4-2}$$

and further written as

$$f_H = \rho g(A_r - A_0) - N_r \dot{r} - \frac{d}{dt}(m_r \dot{r}) \qquad (4\text{-}3)$$

4.3.2 Global shear force and bending moment calculations

1) Mathematical formulation of shear force and bending moment

The damped vertical response of a ship's hull to the global hydrodynamic force, assuming it behaves like a free-free nonuniform beam of length L, is governed by the following system of partial differential equations[24]:

$$\begin{aligned}
&\mu(x_b)\frac{\partial^2 z_e}{\partial t^2} + c(x_b)\frac{\partial z_e}{\partial t} + \frac{\partial V(x_b,t)}{\partial x_b} = f_H(x_b,t) \\
&\frac{\partial M(x_b,t)}{\partial x_b} = V(x_b,t) + I_r(x_b)\frac{\partial^2 \gamma_s}{\partial t^2} \\
&M(x_b,t) = EI(x_b)\frac{\partial \gamma_s(x_b,t)}{\partial x_b} \\
&\frac{\partial z_e}{\partial x} = -\frac{V(x_b,t)}{KAG} + \gamma_s(x_b,t)
\end{aligned} \qquad (4\text{-}4)$$

Where

x_b Distance in longitudinal direction measured from origin of coordinate system

t Time variable

z_e Vertical elastic deflection, normal to x_b

μ Ship's mass per unit length plus added mass per unit length

c Damping coefficient per unit length

V Shear force in z_b -- direction

f_H Total hydrodynamic force per unit length

M Global bending moment

I_r Mass moment of inertia of hull per unit length with respect to an axis normal to $x_b - z_b$ plane

γ_s Component of slope of z_s due to bending only

EI Bending rigidity.

KAG Shear rigidity.

The ship is assumed to have free ends, so that the boundary conditions are :

$$\begin{cases} V(-L_a,t) = V(L_f,t) = 0 \\ M(-L_a,t) = M(L_f,t) = 0 \end{cases} \qquad (4\text{-}5)$$

If the rotary inertia term is neglected, the dynamic behaviour of the beam can be treated in terms of a series of responses in each of its normal modes i , which retain the important property of orthogonality with respect to the effective mass per unit length :

$$\int_{-L_a}^{L_f} \mu(x_b) X_i(x_b) X_j(x_b) dx_b = 0 \qquad (i \neq j) \qquad (4\text{-}6)$$

Here $X_i(x_b)$ is the normal mode function in arbitrary dimensionless units, and it simply represents a pattern of relative displacement along the length of the beam for a particular mode i.

A generalized coordinate with the dimensions of length $q_i(t)$ is used to define the displacement time history of the system in its ith normal mode. Then the motion in a particular mode i is given by multiplying $q_i(t)$ by the dimensionless normal mode function $X_i(x_b)$, and the total response is finally given by summing the contributions from all the modes :

$$z_c(x_b,t) = \sum_{i=1}^{\infty} q_i(x_b,t) X_i(x_b) \qquad (4\text{-}7)$$

Similarly, $M(x_b,t)$ and $V(x_b,t)$ may be represented as the product of $q_i(t)$ by a spatial weighting function $M_i(x_b)$ or $V_i(x_b)$, respectively, and the form of these functions will be determined from the analysis :

$$M(x_b,t)=\sum_{i=1}^{\infty} q_i(t)M_i(x_b)$$
$$V(x_b,t)=\sum_{i=1}^{\infty} q_i(t)V_i(x_b) \qquad (4\text{-}8)$$

It is assumed that $f_H(x_b,t)$ can be written in the following series form :

$$f_H(x_b,t)=\sum_{i=1}^{\infty}\frac{\mu(x_b)Q_i(t)X_i(x_b)}{\int_{-L_a}^{L_f}\mu(x_b)X_i^2(x_b)dx_b} \qquad (4\text{-}9)$$

Multiplying both sides of (4-9) by $X_i(x_b)$, integrating over the ship's length, and using the orthogonality property (4-6) lead to an explicit form for the function $Q_i(t)$:

$$Q_i(t)=\int_{-L_a}^{L_f} f_H(x_b,t)X_i(x_b)dx_b \qquad (4\text{-}10)$$

Neglecting the term involving I_r and substituting in equations (4-4) the series representations for $M(x_b,t)$, $V(x_b,t)$ and $f_H(x_b,t)$, (4-7) to (4-9), the following three equations are obtained :

$$\sum_{i=1}^{\infty}(\mu\ddot{q}_iX_i+c\dot{q}_iX_i+q_i\frac{dV_i}{dx_b}-\frac{\mu Q_iX_i}{\int_{-L_a}^{L_f}\mu X^2{}_i dx_b})=0$$
$$\sum_{i=1}^{\infty}(q_iV_i-q_i\frac{dM_i}{dx_b})=0 \qquad (4\text{-}11)$$
$$\sum_{i=1}^{\infty}[q_i\frac{d^2X_i}{dx^2{}_b}+q_i\frac{d}{dx_b}(\frac{V_i}{KAG})-\frac{q_iM_i}{EI}]=0$$

These equations are satisfied if each term in the summation is set equal to zero. Combining the resulting equations :

$$\mu\ddot{q}_iX_i+c\dot{q}_iX_i+q_i\frac{d^2}{dx^2{}_b}[EI\frac{d^2X_i}{dx^2{}_b}+EI\frac{d}{dx_b}(\frac{V_i}{KAG})]=\frac{\mu Q_iX_i}{\int_{-L_a}^{L_f}\mu X^2{}_i dx_b} \qquad (4\text{-}12)$$

Consider the free motion of the beam with no forcing function acting, the right-hand side of (4-12) becomes zero and, after rearranging the equation, for any normal mode

$$\frac{\ddot{q}_i + (c/\mu)\dot{q}_i}{q_i} = -\frac{1}{\mu X_i}\frac{d^2}{dx^2_b}[EI\frac{d^2X_i}{dx^2_b} + EI\frac{d}{dx_b}(\frac{V_i}{KAG})] = -\frac{1}{\mu X_i}\frac{d^2M_i}{dx_b{}^2} \tag{4-13}$$

Since the left-hand side is just a function of time and the right-hand side just a function of space, it is concluded that both must be equal to a constant $-\omega_i{}^2$, where ω_i is the natural frequency of the ith mode. This leads to

$$\ddot{q}_i + (c/\mu)\dot{q}_i + \omega_i{}^2 q_i = 0 \tag{4-14}$$

$$\frac{d^2M_i}{dx_b{}^2} = \frac{d^2}{dx^2_b}[EI\frac{d^2X_i}{dx^2_b} + EI\frac{d}{dx_b}(\frac{V_i}{KAG})] = \mu\omega_i{}^2X_i \tag{4-15}$$

Integrating (4-15) along the length of the beam, we get

$$\begin{aligned} M_i &= \int_{-L_a}^{x_b}\int_{-L_a}^{x_b}\mu\omega_i{}^2X_i dx^2{}_b \\ V_i &= \int_{-L_a}^{x_b}\mu\omega_i{}^2X_i dx_b \end{aligned} \tag{4-16}$$

The following integral gives a more convenient representation for M_i :

$$\begin{aligned} M_i &= \int_{-L_a}^{x_b}\mu\omega_i{}^2X_i(x_b - s)ds \\ V_i &= \int_{-L_a}^{x_b}\mu\omega_i{}^2X_i ds \end{aligned} \tag{4-17}$$

Substituting (4-15) in (4-12), multiplying both sides by X_i, and taking the space integral of both sides from $-L_a$ to L_f , we get :

$$\bar{\mu}_i \ddot{q}_i + \bar{c}_i \dot{q}_i + \bar{k}_i q_i = Q_i \tag{4-18}$$

Where $\bar{\mu}_i$, the generalized mass, is defined by

$$\bar{\mu}_i = \int_{-L_a}^{L_f} \mu X_i^2 dx_b \tag{4-19}$$

and $\bar{c}_i$, the generalized damping, is

$$\bar{c}_i = \int_{-L_a}^{L_f} c X_i^2 dx_b \tag{4-20}$$

and $\bar{k}_i$, the generalized spring constant, is

$$\bar{k}_i = \omega_i^2 \bar{\mu}_i \tag{4-21}$$

Since the effective mass per unit length μ is only a function of x_b, it follows that $\bar{\mu}_i$ is a constant for a particular mode i and it has dimensions of mass. The generalized damping $\bar{c}_i$, which is discussed in more detail in the next section, is for similar reasons also a constant. Since ω_i or the natural frequency of the ith mode has a certain fixed value, we conclude that (4-18) is a simple constant coefficient linear second-order differential equation where the unknown is $q_i(t)$ and the forcing function is $Q_i(t)$. The solution of such an equation is simple if initial conditions are given. Assuming that at time t=0 the beam is at rest so that $q_i(0) = \dot{q}_i(0) = 0$, the solution is then given in a closed convolution integral form as

$$q_i(t) = \int_0^t \frac{Q_i(\tau)}{\lambda_i \bar{\mu}_i} \exp[-(\bar{c}_i / 2\bar{\mu}_i)(t-\tau)] \sin[\lambda_i (t-\tau)] d\tau \tag{4-22}$$

$$\lambda_i = \sqrt{\omega_i^2 - \frac{1}{4}(\bar{c}_i / \bar{\mu}_i)^2} \tag{4-23}$$

Knowing $q_i(t)$ as well as the normal mode shapes and natural frequencies, it is possible to compute V_i, M_i from (4-17) and finally to obtain the shear force and the bending moment from (4-8) for any location x_b along the ship.

2) Definition of the required parameters

The solution for the elastic response of the ship structure to the total hydrodynamic force, as given by the normal mode approach to the beam theory, requires the knowledge of a certain number of parameters. These are ship mass and added mass distribution, damping coefficient, normal mode shapes, and natural frequencies.

The ship's mass or weight distribution may be determined from the ship model hull mass and internal arrangements.

The close-fit conformal mapping method is used to calculate the added mass based on the ship's calm water waterline sections and correction factors of three dimensional flow are considered.

Normal mode shapes, natural frequencies of ship hull are obtained from the transfer matrix method.

Experimental data and empirical formula are used to determine the damping coefficient of ship hull vibration.

The logarithmic decrement of vertical hull vibration of the 2 node mode δ_2 was obtained from the experiments (For the S-175 container ship model, δ_2 is 0.1904). The logarithmic decrement of the j node mode is estimated as follows[76] :

$$\delta_j = \delta_2(\omega_i / \omega_1)^{0.75} \qquad (4\text{-}24)$$

Where, j=3, 4, 5 and 6; *i* is *i*th normal mode *i*=j-1.

The damping coefficient for vertical vibration of the ship hull is given by[34]

$$c_i = \frac{\bar{c}_i}{\bar{\mu}_i} = \delta_j \cdot \omega_i / \pi \qquad (4\text{-}25)$$

3) Natural frequencies and damping coefficients

The natural frequencies, the logarithmic decrement and the damping coefficients for the S-175 container ship model are shown in Table 1.

Table 1 Natural Frequency,
Logarithmic Decrement and Damping Coefficient

Modal	1	2	3	4	5
ω_i(Hz)	8.952	18.545	29.985	41.954	54.569
δ_{i+1}	0.1904	0.3287	0.4715	0.6066	0.7389
c_i	3.409	12.192	28.276	50.900	80.642

If the ship motions are calculated by linear forces (neglecting nonlinear forces), i.e. the relative motion, velocity and acceleration are based on linear forces, the global shear forces and bending moments are described as the sum of wave shear forces and bending moments induced by the linear wave forces in equation (4-1), the shear forces and bending moments induced by the bottom slamming force in equation (4-4) (in the bottom region, the f_H replaced by f_b given in equation(3-22)) and by the bow flare slamming force given in equation (4-4) (in the bow flare region, f_H is replaced by f_{bf} (equation (3-27)) as follows :

$$V = V_{wa} + V_b + V_{bf}$$
$$M = M_w + M_b + M_{bf} \qquad (4\text{-}26)$$

Therefore, in this chapter, there are two methods: method 1 calculation from equation (4-4), the dynamic response due to the global hydrodynamic forces, and method 2 calculation from equation (4-26), linear wave shear force and bending moment

superimposing slamming shear force and bending moment, used to predict the global shear force and bending moment values.

4.4 Comparisons between the theoretical predictions and experiments

A description of the experiment is given in section 5.3 (Chapter 5).

4.4.1 Wave shear forces and bending moments

1) Wave shear forces and bending moments for different wave frequencies

Average and hogging as well as sagging wave shear force and bending moment according to different frequencies at two forward speeds, two wave amplitudes and two stations are shown in Figs.A.4.1-A.4.16 (Due to problems associated with the strain gauges mounted to measure shear forces, the results of the experimental measurement for wave shear forces are not included).

i) Wave bending moments

For Fn=0.15 (6.21 m/s for full scale case), at stations 10 and 7 (0.45L and 0.3L from FP), when ζ_a=4.0 cm (2.8 m for full scale case), for the average and hogging wave bending moment (Figs.A.4.1-A.4.4), the results by the nonlinear theoretical prediction method and the linear strip theory show good agreement with the experiment. The results by the nonlinear theoretical prediction method show excellent agreement with the experimental data for the sagging wave bending moment (Figs.A.4.2 and A.4.4).

When ζ_a=7.5 cm (5.25 m for full scale case), for the average wave bending moment, the results by the nonlinear theoretical prediction method and the linear strip theory show some difference in the resonance region, and the results by the linear strip theory show better agreement with the experimental data than the nonlinear theoretical prediction method at station 10 (Fig.A.4.5). The results by the nonlinear theoretical prediction method show better agreement with the experimental data than the linear strip

theory at station 7 (Fig.A.4.7). For the hogging wave bending moment, the results by the nonlinear theoretical prediction method and the linear strip theory show some difference in the resonance region, and the results by the nonlinear theoretical prediction method show excellent agreement with the experimental data (Figs.A.4.6 and A.4.8); For the sagging wave bending moment, the results by the nonlinear theoretical prediction method and the linear strip theory show a big difference in the resonance region, and the results by the linear strip theory show better agreement with the experimental data than the nonlinear theoretical prediction method at station 10 (Fig.A.4.6). The results by the nonlinear theoretical prediction method show better agreement with the experimental data than the linear strip theory at station 7 (Fig.A.4.8).

For Fn=0.25 (10.35 m/s for full scale case), at stations 10 and 7 (0.45L and 0.3L from FP), when ζ_a=4.0 cm (2.8 m for full scale case), the results by the nonlinear theoretical prediction method show very good agreement with the experimental data for the average, hogging and sagging wave bending moments (Figs.A.4.9-A.4.12).

At station 10, ζ_a=7.5 cm (5.25 m for full scale case), the results by the nonlinear theoretical prediction method and the linear strip theory show a large difference in the resonance region (Figs.A.4.13 and A.4.14). The results by the linear strip theory show better agreement with experimental data than the nonlinear theoretical prediction method;

At station 7, ζ_a=7.5 cm, the results by the nonlinear theoretical prediction method and the linear strip theory differ considerably in the resonance region (Figs.A.4.15 and A.4.16), the results by the nonlinear theoretical prediction method show much better agreement with the experimental data than the linear strip theory.

ii) Wave shear forces

For Fn=0.15, at stations 10 and 7, ζ_a=4.0 cm, the results by the nonlinear theoretical prediction method and the linear strip theory are the same (Figs.A.4.1-A.4.4);

At stations 10 and 7, ζ_a=7.5 cm, The results by the nonlinear theoretical prediction method and the linear strip theory are nearly same (Figs.A.4.5-A.4.8), although, there is a small difference between them in the resonance region.

For Fn=0.25, at stations 10 and 7, ζ_a=4.0 cm, the results by the nonlinear theoretical prediction method and the linear strip theory are nearly the same (Figs.A.4.9-A.4.12);

At stations 10 and 7, ζ_a=7.5 cm, the results by the nonlinear theoretical prediction method and the linear strip theory show some difference in the resonance region (Figs.A.4.13-A.4.16).

2) Wave shear forces and bending moments for different wave amplitudes

Hogging, sagging and average wave shear force and bending moment values for different wave amplitudes at two forward speeds, three wave frequencies and two stations are shown in Figs.A.4.17-A.4.44.

i) Wave bending moments

There is very good agreement among the results by the nonlinear theoretical prediction method, the linear strip theory and the experimental data in all conditions with small waves.

For Fn=0.0, at two stations (λ / L=1.0), At station 7, the results by the nonlinear theoretical prediction method show very good agreement with the experimental data for the hogging and sagging as well as average wave bending moments (Fig.A.4.19-A.4.20), at station 10, the results by the nonlinear theoretical prediction method show better agreement with the experimental data than the linear strip theory for the hogging wave bending moment, while the results by the linear strip theory show a little bit better agreement with the experimental data than the nonlinear theoretical prediction method for the sagging wave bending moment in the large waves (Figs.A.4.17 and A.4.18).

For Fn=0.15 (6.21 m/s for full scale case), at station 10, there are different results by the nonlinear theoretical prediction method and the linear strip theory in large waves when λ / L=1.0 and the results by the nonlinear theoretical prediction method show better agreement with the experimental data than the linear strip theory for the hogging wave bending moment, while the results by the linear strip theory show better agreement with the

experimental data than the nonlinear theoretical prediction method for the sagging and average wave bending moment in large waves (Figs.A.4.21 and A.4.22); The results by the nonlinear theoretical prediction method show better agreement with the experimental data than the linear strip theory when $\lambda / L=1.2$ and 1.4 (Figs.A.4.25, A.4.26 and A.4.29, A.4.30);

At station 7, different results are given by the nonlinear theoretical prediction method and the linear strip theory in large waves and the results by the nonlinear theoretical prediction method have a satisfactory agreement with experimental data, when $\lambda / L=1.0$ (Figs.A.4.23 and A.4.24), show good agreement with the experimental data, when $\lambda / L=1.2$ (Figs.A.4.27 and A.4.28) and very good agreement with the experimental data when $\lambda / L=1.4$ (Figs.A.4.31 and 4.32).

The significant difference between hogging and sagging bending moment are illustrated in these Figures.

At $\lambda / L=1.0$, station 10, $\zeta_a=7.5$ cm (Fig.A.4.21), for the nonlinear theoretical prediction method, the sagging bending moment is 2.54 times the hogging bending moment, for the linear strip theory, the sagging bending moment is equal to the hogging bending moment.

For Fn=0.25 (10.35 m/s for full scale case), at station 10, different results are given by the nonlinear theoretical prediction method and the linear strip theory in large waves, when $\lambda / L=1.0$ and 1.2, and the results by the nonlinear theoretical prediction method show better agreement with the experimental data than the linear strip theory for the hogging wave bending moment, while, the results by the linear strip theory show better agreement with the experimental data than the nonlinear theoretical prediction method for the sagging and average wave bending moment in large waves (Figs.A.4.33, A.4.34 and A.4.37, A.4.38); The results by the nonlinear theoretical prediction method show good agreement with the experimental data, when $\lambda / L=1.4$ (Figs.A.4.41 and A.4.42).

At station 7, there are different results by the nonlinear theoretical prediction method and the linear strip theory in large waves and results by the nonlinear theoretical prediction method show satisfactory agreement with experimental data when $\lambda / L=1.0$ and 1.2 (Figs.A.4.35, A.4.36 and A.4.39, A.4.40), show good agreement with the experimental

data, when $\lambda / L=1.4$ (Figs.A.4.43 and A.4.44).

The significant difference between the hogging and sagging bending moment are also illustrated in these Figures.

At $\lambda / L=1.2$, station 10, $\zeta_a=7.5$ cm (Fig.A.4.37), the nonlinear theoretical method predicts the sagging bending moment as 2.98 times the hogging bending moment, the linear strip theory predicts the sagging bending moment as equal to the hogging bending moment.

ii) Wave shear forces

Fn=0.0, $\lambda / L=1.0$, results obtained from the the nonlinear theoretical prediction method are identical to those obtained from the linear strip theory (Figs.A.4.17-A.4.20).

For Fn=0.15, results obtained by the nonlinear theoretical prediction method are nearly identical to those by the linear strip theory (Figs.A.4.21-A.4.32), although, there are some differences for large waves.

For Fn=0.25, at station 10 when $\lambda / L=1.0$, 1.2 and 1.4, there is a small difference between the results obtained from the nonlinear theoretical prediction method and those obtained from the linear strip theory in large waves (Figs.A.4.33, A.4.34, A.4.37, A.4.38, A.4.41, A.4.42); However, at station 7, when $\lambda / L=1.0$, there is a large difference between the results obtained by the nonlinear theoretical prediction method and those obtained by the linear strip theory for large waves (Figs.4.35).

4.4.2 Global shear forces and bending moments

1) Global shear forces and bending moments for different wave frequencies

Average as well as hogging and sagging global shear force and bending moment values according to different wave frequencies at two forward speeds, two wave amplitudes and two stations are shown in Figs.A.4.45-A.4.88 (Due to problems associated with strain gauges mounted to measure shear forces, the results of the experimental measurement for global shear forces are not included).

i) Global bending moments

For Fn=0.15 (6.21 m/s for full scale case), at stations 10 and 7 (0.45L and 0.3L from FP), ζ_a=4.0 cm (2.8 m for full scale case) (Figs. A.4.45-A.4.52). The results by the two theoretical prediction methods and the experiment show good agreement. The difference between the hogging and sagging global bending moment values can be more clearly seen in Figs.A.4.46 and A.4.48;

At stations 10 and 7, ζ_a=7.5 cm (5.25 m for full scale case), the results by the two theoretical prediction methods show big difference in the resonance region, and results by method 1 show satisfactory agreement with the experimental data at station 10 (Fig.A.4.49 and A.4.50), and very good agreement with the experimental data at station 7 (Figs. A.4.51 and A.4.52).

For Fn=0.25 (10.35 m/s for full scale case), at stations 10 and 7, ζ_a=4.0 cm (Figs.A.4.53 - A.4.56), the results by the two theoretical prediction methods and the experiments show good agreement. The difference between the hogging and sagging global bending moment can be more clearly seen in Figs.A.4.54, and A.4.56;

At stations 10 and 7, ζ_a=7.5 cm (5.25 for full scale case), the results by the two theoretical prediction methods show a large difference in the resonance region (Figs.A.4.57-A.4.60), and very good agreement between the results by method 1 and the experimental data for average global bending moment ; However, comparisons between the results by method 1 and the experimental data for hogging and sagging global bending moments show some difference in the resonance region.

ii) Global shear forces

For Fn=0.15, when ζ_a=4.0 cm, at station 10, the results by the two theoretical prediction methods are nearly the same (Figs.A.4.45-A.4.46). However, at station 7, the results by two theoretical prediction methods show somewhat difference, especially, in the resonance region (Figs.A.4.47 and A.4.48);

When ζ_a=7.5 cm, at station 10, the results by the two theoretical prediction methods are the same (Figs.A.4.49 and A.4.50), However, at stations 7, the results by the two theoretical prediction methods are different, especially, in the resonance region

(Figs.A.4.51-A.4.52).

For Fn=0.25, at station 10, ζ_a=4.0 cm, the results by the two theoretical prediction methods are nearly the same (Figs.A.4.53-A.4.54). However, at station 7, the results by the two theoretical prediction methods are different, especially, in the resonance region (Figs.A.4.55 and A.4.56);

When ζ_a=7.5 cm, at station 10, , the results by the two theoretical prediction methods are nearly the same (Figs.A.4.57 and A.4.58), However, at station 7, the results by the two theoretical prediction methods are significant different, especially, in the resonance region (Figs.A.4.59 and A.4.60).

2) Global shear forces and bending moments for different wave amplitudes

Hogging, sagging and average global shear force and bending moment values for different wave amplitudes at two forward speeds, three wave frequencies and three stations are shown in Figs.A.4.61-A.4.88.

i) Global bending moments

There is excellent agreement among the results by the two theoretical prediction methods and the experimental data in all conditions in small waves.

For Fn=0.0, at two stations, when λ / L=1.0, the two theoretical prediction methods yield nearly the same results and satisfactory agreement was obtained with the experimental data, although in large waves, there is a small difference between them. This is because the nonlinear effect is small when the forward speed is zero (Figs.A.4.61 - A.4.64).

For Fn=0.15 (6.21 m/s for full scale case), at station 10, two theoretical prediction methods yield different results in large waves when λ / L=1.0 and results by method 1 show good agreement with the experimental data. Although, at large waves, there is some differences between them (Figs.A.4.65 and A.4.66); the results by the two theoretical prediction methods show a small difference in large waves and very good agreement with the experiments when λ / L=1.2 (Figs.A.4.69 and A.4.70);

At station 7, there are different results by two theoretical prediction methods when $\lambda / L=1.0$ in large waves and results by method 1 show very good agreement with the experiments (Figs.A.4.67 and A.4.68); the results by the two theoretical prediction methods show small difference in large waves and the results by method 1 show very good agreement with the experiments when $\lambda / L=1.2$ (Figs.A.4.71 and A.4.72);

The significant difference between the hogging and sagging global bending moment are illustrated in these Figures.

When $\lambda / L=1.0$, at station 10, for $\zeta_a=7.5$ cm (Fig.A.4.65), method 1 gives the sagging global bending moment as 3.16 times the hogging global bending moment, method 2 gives the sagging global bending moment as 2.36 times the hogging global bending moment.

For Fn=0.25 (10.35 m/s for full scale case), at station 10, there is a big difference between results by the two theoretical prediction methods when $\lambda / L=1.0$ and 1.2 in large waves (Figs.A.4.77, A.4.78 and A.4.81, A.4.82) and results by method 1 show a satisfactory agreement with the experiments for the hogging and average global bending moment. Although, at large waves, there is some differences between the sagging global bending moment values; when $\lambda / L=1.4$, there is small differences between the results by the two theoretical prediction methods and the results by method 1 show a more satisfactory agreement with experiments than those by method 2 (Figs.A.4.85 and A.4.86);

At station 7, there is a large difference between results by the two theoretical prediction methods when $\lambda / L=1.0$ and 1.2 in large waves and results by method 1 show good agreement with experiments for the hogging and sagging global bending moment (Figs.A.4.79 and A.4.83), and excellent agreement with experiments for the average bending moment (Figs.A.4.80 and A.4.84); when $\lambda / L=1.4$, there is a small different between the two theoretical prediction methods and results by method 1 show good agreement with experiments for the hogging and sagging global bending moment (Fig.A.4.87), and very good agreement with experiments for the average global bending moment values (Fig.A.4.88).

The significant difference between the hogging and sagging global bending moments can also be illustrated in these Figures.

When $\lambda / L=1.2$, at station 10, for $\zeta_a=7.5$ cm (Fig.A.4.81), method 1 yields the sagging global bending moment as 3.36 times the hogging global bending moment, method 2 yields the sagging global bending moment as 2.50 times the hogging global bending moment.

ii) Global shear forces

Fn=0.0, $\lambda / L=1.0$, results between the two theoretical prediction methods at station 10 are similar (Figs.A.4.61 and A.4.62), there is a small difference between the two theoretical prediction methods at station 7 in large waves (Figs.A.4.63 and A.4.64).

For Fn=0.15, at station 10 when $\lambda / L=1.0$ and 1.2, the two theoretical prediction methods yields similar results (Figs.A.4.65, A.4.66, A.4.69, A.4.70); at station 7, there is a large difference in the results by the two theoretical methods in large waves when $\lambda / L=1.0$ (Figs.A.4.67 and A.4.68); there are some differences in the results obtained from the two theoretical methods in large waves when $\lambda / L=1.2$ (Figs.A.4.71 and A.4.72).

For Fn=0.25, at station 10 when $\lambda / L=1.0$, 1.2 and 1.4, the two theoretical prediction methods give the same results (Figs.A.4.77, A.4.78, A.4.81, A.4.82, A.4.85 and A.4.86); at station 7, there are significant differences in the results obtained by the two theoretical methods in large waves, when $\lambda / L=1.0$ and 1.2 (Figs.A.4.79, A.4.80 and A.4.83, A.4.84); there is some difference in the results by the two theoretical methods in large waves, when $\lambda / L=1.4$ (Figs.A.4.87 and A.4.88).

4.4.3 Time history of wave and global bending moments

1) Time history of the wave bending moments

The time history of the wave bending moment obtained from predictions and experiments at Fn=0.15, $\lambda / L=1.2$, $\zeta_a=4.083$ and 7.786 cms; Fn=0.25, $\lambda / L=1.4$, $\zeta_a=4.050$ and 7.720 cms, stations 10, 7 and 15 are shown in Figs.A.4.89-A.4.100.

For Fn=0.15, $\lambda / L=1.2$, $\zeta_a=4.083$ cm; Fn=0.25, $\lambda / L=1.4$, $\zeta_a=4.050$ cm,

stations 10, 7 and 15, the time history of the predicted wave bending moment and the measurements show very good agreement (Figs.A.4.89-A.4.94). The shape of the time history is identical between the predictions and measurements, although the peak values obtained from the predictions are a little larger than those obtained from the measurements.

The hogging and sagging wave bending moment values are quite different and those can be clearly seen in the time history of the wave bending moments obtained from predictions and measurements. This indicates a major weakness in the linear strip theory which cannot predict the different values for the hogging and sagging bending moments.

For Fn=0.15, $\lambda / L=1.2$, $\zeta_a=7.786$ cm; Fn=0.25, $\lambda / L=1.4$, $\zeta_a=7.720$ cm, at stations 10, 7 and 15, the time history of the wave bending moment values obtained from predictions and measurements show good agreement (Figs.A.4.95-A.4.100). The shape of the theoretical and experimental time history shows good similarity, although the peak values of the theoretical predictions are different from those obtained from the experiments.

The hogging and sagging wave bending moments obtained from predictions and measurements are quite different which can be clearly seen in the time history of the wave bending moment curves.

The effect of the bottom, bow flare slamming and deck wetness on the wave bending moment can be seen from the time history curves obtained from the predictions and measurements(Figs.A.4.95 and A.4.98).

The first peak is induced by the bottom slamming effect (1), the second peak is the bow flare slamming effect (2), and the third peak is induced by the deck wetness effect (3).

2) Time history of the global bending moments

The time history of the global bending moments obtained from the predictions and measurements at Fn=0.15, $\lambda / L=1.2$, $\zeta_a=4.083$ cm; Fn=0.25, $\lambda / L=1.4$, $\zeta_a=4.050$ cm, at stations 10, 7 and 15, at Fn=0.15, $\lambda / L=1.2$, $\zeta_a=7.786$ cm; Fn=0.25, $\lambda / L=1.4$, $\zeta_a=7.72$ cm, station 10 are shown in Figs.A.4.101-A.4.108.

For Fn=0.15, $\lambda / L=1.2$, $\zeta_a=4.083$ cm; Fn=0.25, $\lambda / L=1.4$, $\zeta_a=4.050$ cm, at

stations 10, 7 and 15, the time history of the global bending moment obtained from predictions and measurements show very good agreement (Figs.A.4.101-A.4.106). The shape of the predicted time history is identical to that of measured, although the peak values given by the theory are a little larger than those obtained from the experiments.

For Fn=0.15, $\lambda / L=1.2$, $\zeta_a=7.786$ cm; Fn=0.25, $\lambda / L=1.4$, $\zeta_a=7.720$ cm, station 10, the time history of the global bending moment obtained from the predictions and measurements also show a good agreement (Figs.A.4.107-A.4.108). The shape between the theoretical and experimental time history show a similarity , although the peak values obtained from the predictions are larger than those given by the experiments.

The hogging and sagging global bending moment values are quite different which can also be clearly seen in the time history of the global bending moment obtained from the predictions and measurements.

4.5 Conclusions

4.5.1 Wave bending moments

1) The wave bending moment values predicted by the nonlinear method have a generally good agreement with the experimental test results, although, in large waves and the resonance region, the results obtained by the nonlinear theoretical prediction method will overestimate, especially for the sagging wave bending moment.

2) The time history of the wave bending moments obtained by the nonlinear theoretical method and the experiments shows a good agreement, and the effect of the bottom, bow flare slamming and deck wetness effect can be clearly seen in these curves.

3) The significant difference between the hogging and sagging wave bending moment can be seen clearly from the results of predictions and measurements and should be considered in ship design.

4.5.2 Global bending moments

1) The global bending moment results obtained by the vibratory elastic response due to total hydrodynamic force (method 1) have a much better agreement with the experimental data than the wave bending moment superimposed on the slamming bending moment (method 2). This is a very useful tools to determine the global sea loads.

2) The predicted time history of the global bending moments obtained from the vibratory elastic response due to the total hydrodynamic force and the experimental measurements also shows a good agreement.

3) The significant difference between the hogging and sagging global bending moments can also been seen in this analysis and should be considered in ship design.

CHAPTER 5

EXPERIMENTS

5.1 General description

The two experimental tests carried out in January and October 1995, in which each test lasted four weeks and more than 100 runs were carried out, will be described in this chapter. The test model, test conditions and facilities will be discussed.

In the first series of experimental tests, the ship heave, pitch and the relative motions as well as the accelerations at bow; the bottom and bow flare slamming pressures at nine different wave frequencies, six wave amplitudes, two speeds and several bow stations were measured.

In the second series of experimental tests, the ship heave and pitch motions, shear forces and bending moments at nine different wave frequencies, five wave amplitudes, two speeds and three stations were measured.

5.2 Experiment - I Ship motions and pressures

5.2.1 Description of the model

A 1/70 scale model of the S-175 container ship was constructed from glass reinforced plastic (GRP) (Fig.5.1) and its principal characteristics are shown in Table 2[77].

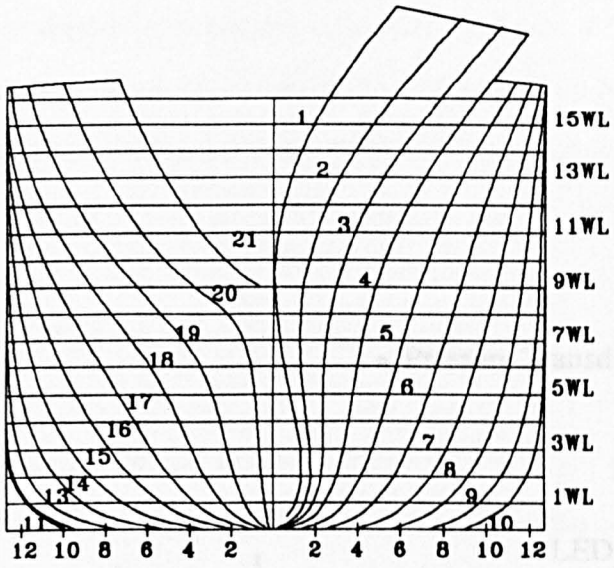

Fig.5.1 Body Plan of Container Ship Model

Table 2 Principal Characteristics of S -- 175 for Model Test I

Symbol	Items	Ship	Model
L (m)	Length	175.0	2.500
B (m)	Breadth	25.40	0.363
D (m)	Depth	15.40	0.220
T (m)	Draught	9.50	0.136
∇ (m^3)	Volume	24138.5	0.07038
C_b	Block Coefficient	0.5716	0.5716
$C_{\text{⊠}}$	Section Coefficient	0.970	0.970
LCG	Longitudinal Centre of Gravity from Midship	-2.48	-0.0354
VCG	Centre of Gravity from Base Line	9.52	0.1355
K_{yy}	Radius of Pitch Gyradius	42.0	0.613

5.2.2 Test conditions

In these experiments, the heave, pitch, bow relative motions and the bow

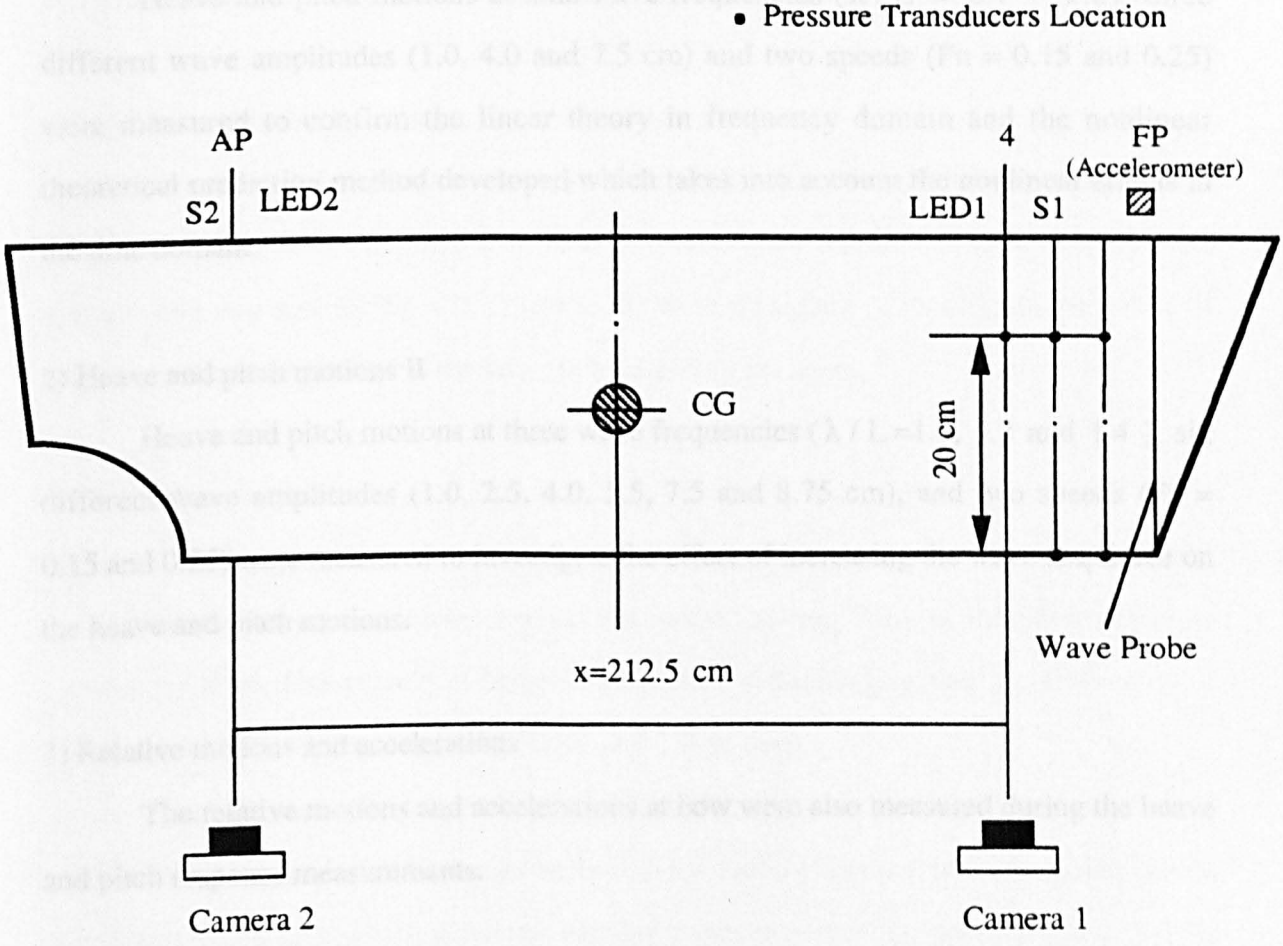

Fig.5.2 Profile of Model (Experiment I)

accelerations; the bottom slamming pressures at stations 2 and 3 at the centre line of the bottom and the bow flare slamming pressures at stations 2, 3 and 4 (0.05L, 0.10L and 0.15L from FP), at draught level of 20 cm were measured in head seas (Fig.5.2). The model set-up in the carriage and model in waves are shown in photographs 1 - 4.

1) Heave and pitch motions I

Heave and pitch motions at nine wave frequencies (λ / L = 0.7 -- 1.8), three different wave amplitudes (1.0, 4.0 and 7.5 cm) and two speeds (Fn = 0.15 and 0.25) were measured to confirm the linear theory in frequency domain and the nonlinear theoretical prediction method developed which takes into account the nonlinear effects in the time domain.

2) Heave and pitch motions II

Heave and pitch motions at three wave frequencies (λ / L=1.0, 1.2 and 1.4), six different wave amplitudes (1.0, 2.5, 4.0, 5.5, 7.5 and 8.75 cm), and two speeds (Fn = 0.15 and 0.25) were measured to investigate the effect of increasing the wave amplitude on the heave and pitch motions.

3) Relative motions and accelerations

The relative motions and accelerations at bow were also measured during the heave and pitch response measurements.

4) Pressures due to bottom slamming I

Bottom slamming pressures at two stations (2 and 3), nine wave frequencies (λ / L = 0.7 -- 1.8), two different wave amplitudes (4.0 and 7.5 cm) and two speeds (Fn = 0.15 and 0.25) were measured to validate the prediction methods.

5) Pressures due to bottom slamming II

Bottom slamming pressures at two Stations (2 and 3), three wave frequencies (λ / L = 1.0, 1.2 and 1.4), four different wave amplitudes (2.5, 4.0, 5.5 and 7.5 cm) and

two speeds (Fn = 0.15 and 0.25) were measured to investigated the effect of increasing the wave amplitude on the bottom slamming.

6) Bow flare slamming pressures I

Bow flare slamming pressures at three Stations (2, 3 and 4), nine frequencies (λ / L = 0.7 -- 1.8), two different wave amplitudes (4.0 and 7.5 cm) and two speeds (Fn = 0.15 and 0.25) were measured to validate prediction methods.

7) Bow flare slamming pressures II

Bow flare slamming pressures at three Stations (2, 3 and 4), three wave frequencies (λ / L=1.0, 1.2 and 1.4), four different wave amplitudes (2.5, 4.0, 5.5, and 7.5 cm) and two speeds (Fn = 0.15 and 0.25) were measured to investigate the effect of increasing wave amplitude on the bow flare slamming pressures.

5.2.3 Facilities and tests

All the experiments were carried out in the Towing Tank of the Hydrodynamic Laboratory at the Department of Naval Architecture & Ocean Engineering, University of Glasgow, which is 77 m long, 4.6 m wide and 2.4 m deep.

This Laboratory is equipped with an electronically controlled towing carriage which has a maximum speed of 6.4 m/s and an electro-hydraulic plunger type wave maker placed at one end of the tank which generates regular waves in frequency range of 0.4 to 1.4 Hz and in the wave height range of 1.6 cm to 22 cm. Waves are absorbed by a beach at the other end of the tank.

The general arrangement of the towing tank is shown in Fig.5.3.

1) Measurement devices

The model was towed by a vertical post which allows freedom in heave and pitch motions with restraints in other directions. The towing point was positioned at the centre of gravity of the model which was free to pitch around a hinge pin at its centre of gravity. The

TEXT BOUND CLOSE TO THE SPINE IN THE ORIGINAL THESIS

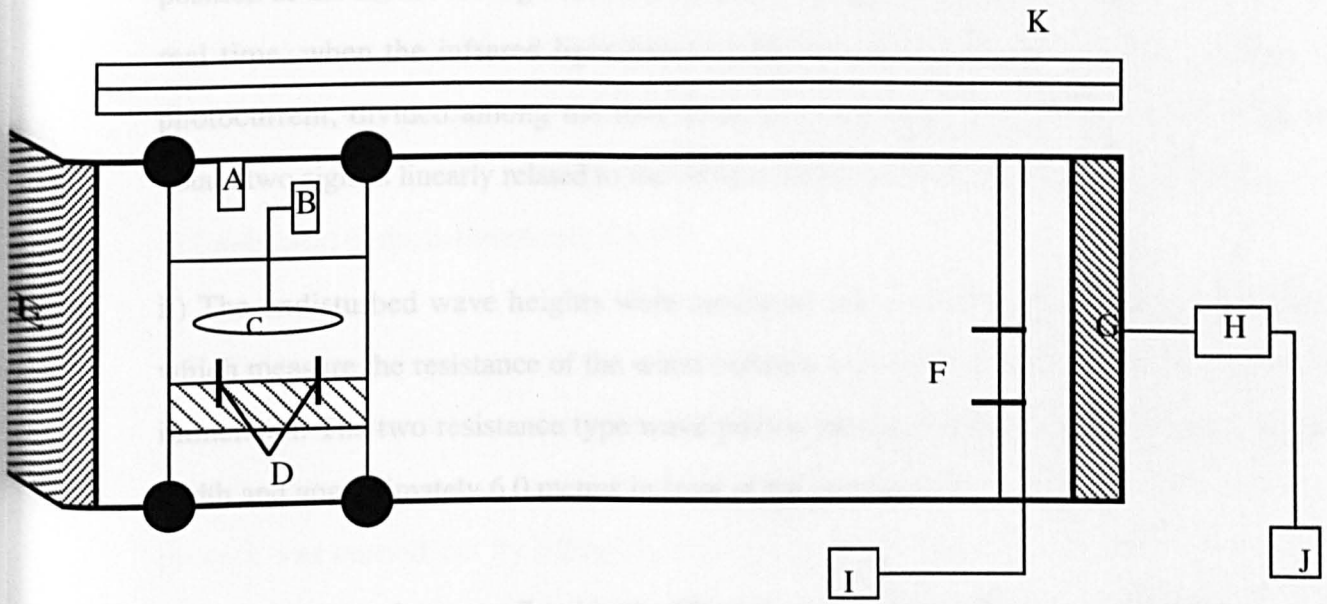

C Control Desk of Towing Carriage
D Data-Acquisition System
C Container Ship Model
S Selspot System
W Wave Absorbing Beach
R Resistance Type Wave Probes

G: Wave Maker
H: Hydraulic Unit
I: Chart - recorder
J:Dell-200 Microcomputer
(Digital-to-Analog Converter)
K: Current Conductor Rails

Fig.5.3 General Arrangement of Towing Tank

pitch pivot was mounted at the end of the vertical heave rod which slides in linear bearings leaving the model free to heave.

i) The heave and pitch motions of the model were measured with a pair of small light emitting diodes (LED selspot system) positioned on the deck of the model. The selspot system was used to measure the coordinates of multiple points, small light emitting diodes were used to identify the selected points. A versatile photoelectric camera detected the position of the diodes for registration and analysis of static as well as dynamic processes in real time, when the infrared light from a LED was focused on the detector surface, a photocurrent, divided among the four electrodes occurred. The current can be used to obtain two signals linearly related to the vertical and horizontal coordinates of the LED.

ii) The undisturbed wave heights were measured with two resistance type wave probes which measure the resistance of the water between two wires as a function of the depth of immersion. The two resistance type wave probes were placed at B/2, B/4 across the tank width and approximately 6.0 metres in front of the wavemaker.

iii) Two wave probes were fitted in the FP of the model (both sides) to pick up the relative motion signal.

iv) A gravity type accelerometer was used to measure the vertical bow acceleration at FP.

v) Two dynamic pressure transducers ENDEVCO Model 8510B-200, were used to measure the bottom slamming pressures.

vi) Two dynamic pressure transducers ENDEVCO Model 8510B-200, and one static pressure transducer were used to measure the bow flare slamming pressures.

The ENDEVCO Model 8510B is a rugged, miniature and high sensitivity piezoresistive pressures transducer. It has a 10-32 mounting thread, 3.8 mm face diameter and is available in ranges from 1 psi to 200 psi. Its high sensitivity combined with high

resonance makes it ideal for measuring dynamic pressures.

ENDEVCO pressure transducers feature a four-active arm strain gauge bridge diffused into a unique sculptured silicon diaphragm for maximum sensitivity and wide band frequency response. Self-contained hybrid temperature compensation provides stable performance over the temperature range 0^0 of to 200^0F. ENDEVCO transducers also feature excellent linearity, high shock resistance, and negligible sensitivity to temperature transients.

All the signals are collected by the Data Collecting System (32 channels analogue to digital converter, AMUX--64 System) after passing through multi - channel amplifiers and filters and are then recorded into the Macintosh -- IIci micro computer system.

2) Calibration of the measurement devices

i) Calibration of selspot system

To measure the linearity of the selspot system, one LED was mounted on a vertical rod. The distance between the LED and the cameras was about 150.0 cm. The calibration process was carried out by lifting the LED gradually at 1.0, 2.0, 3.0, 4.0, 5.0, 7.0 and 10.0 cm and the new positions of the LEDs were recorded in the computer at each time step. The calibration results shown a linear relationship for the selspot system. The accuracy of the measurement was within ± 0.01 cm.

ii) Calibration of accelerometer

The accelerometer was rotated 90 degrees and the position of the pen corresponding to 9.81 m/s was marked on the Chart - recorder.

iii) Calibration of wave probe

The calibration process was carried out by lifting the wave probe from 2 cm up to 10 cm and at each time step the new positions of the pens were marked on the chart - recorder and new positions signals were also sent to the computer. The calibration results show a linear relationship. The accuracy of the measurement was within ± 0.015 cm.

iv) Calibration of dynamic pressure transducer

The calibration values stated on the dynamic pressure transducers were used as the calibration values. The accuracy of the measurement was within ±0.004 Psi.

v) Calibration of static pressure transducer

A hand held test pump was used for calibration. The pressure was increased to 1psi, 2psi and 3psi. A linear relationship between the pressure and the voltage was obtained. The accuracy of the measurement was within ±0.01 Psi.

3) Process of experiment

The Process of experiments is shown in Fig.5.4. Details are described as follows :

i) S-175 container ship model was connected to the carriage as shown in Fig.5.5. The towing point was at the LCG position. The plastic covers were used on the deck of the model for waterproofing during the experiment.

ii) The longitudinal ballast distribution was adjusted to satisfy the design longitudinal centre of gravity.

iii) The height of the ballast weights was adjusted to satisfy the vertical centre of gravity from the model inclination test.

iv) The Selspot system, accelerometer and wave probes were calibrated to identify the linearity of transducers and to measure the calibration coefficients in order to relate an output voltage to a physical quantity being measured.

v) The radius of gyration of the model in pitch motion was measured by the Bifilar Suspension method (see photo 5).

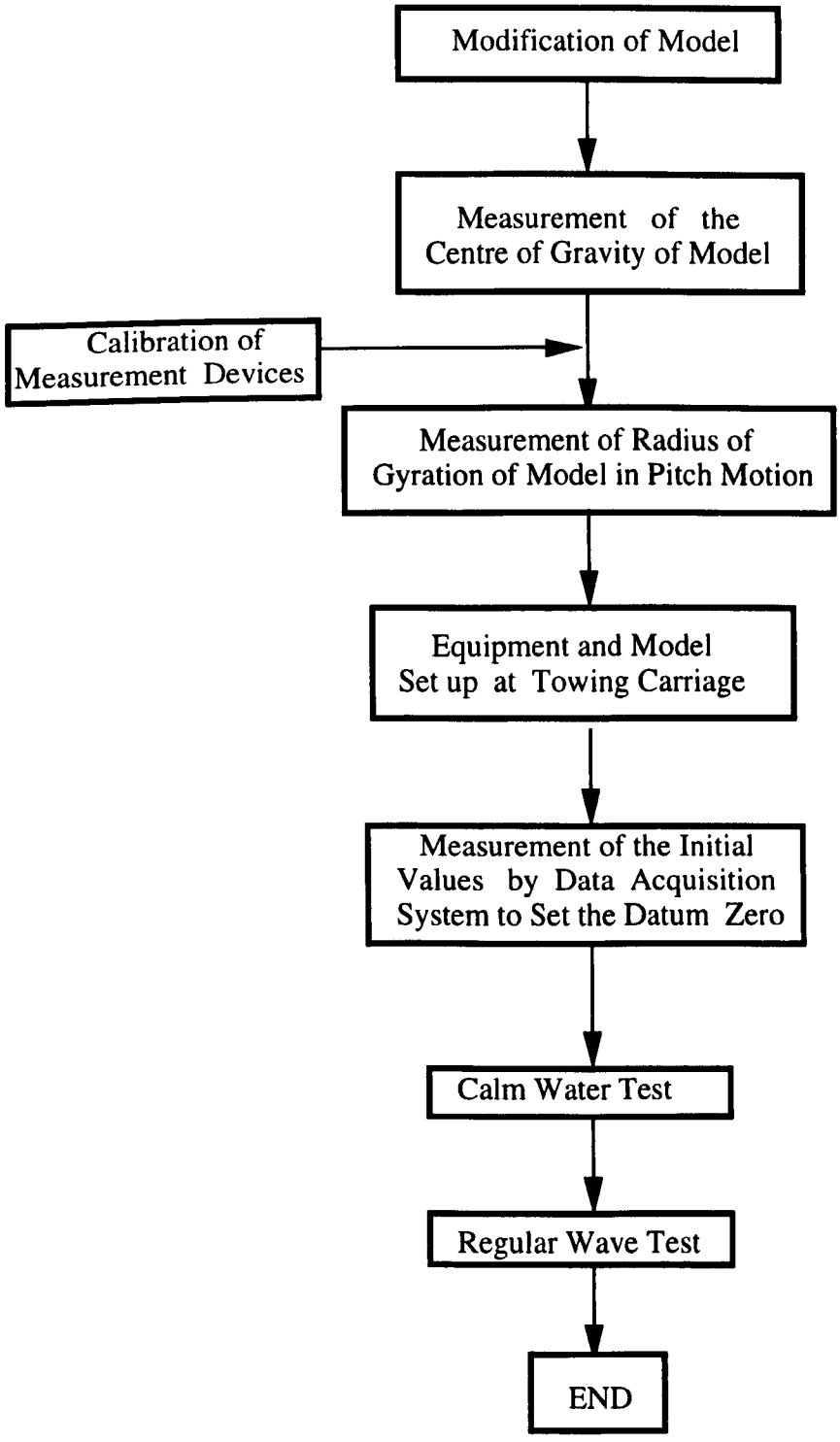

Fig. 5.4 A Flowchart of Experiment I

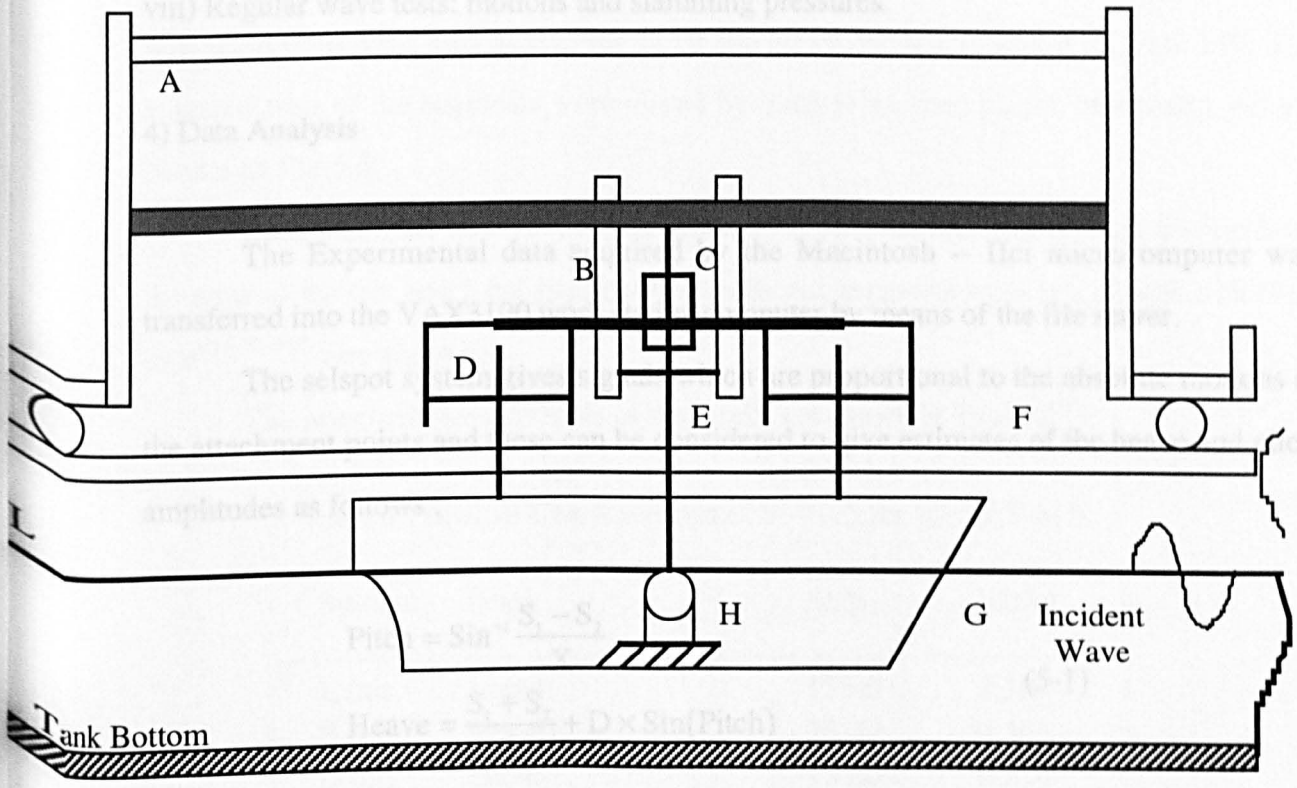

A: Main Carriage

B: Measurement Frame

C: Towing Post Frame

D: Yaw Restraint Rod

E: Heave Rod

F: Rail Track

G: Container Ship Model

H: Free Pitch Pivot

Fig.5.5 Measurement System on the Towing Carriage

vi) The initial values were measured by data acquisition system and were set to zero.

vii) Calm water tests

viii) Regular wave tests: motions and slamming pressures.

4) Data Analysis

The Experimental data acquired by the Macintosh -- IIci microcomputer was transferred into the VAX3100 work station computer by means of the file server.

The selspot system gives signals which are proportional to the absolute motions at the attachment points and these can be considered to give estimates of the heave and pitch amplitudes as follows :

$$\text{Pitch} = \text{Sin}^{-1}\frac{S_1 - S_2}{X}$$
$$\text{Heave} = \frac{S_1 + S_2}{2} + D \times \text{Sin}(\text{Pitch}) \qquad (5\text{-}1)$$

where S_1 and S_2 are the absolute motions measured forward and afterward, X=212.5 cm is the longitudinal separation of the two measurement locations and D=15.21 cm is the half difference of longitudinal distances between the LCG and the each measuring point.

The test results of motions are given in nondimensional values, Z_a / ζ_a for heave, $\psi_a / K\zeta_a$ for pitch, r_a / ζ_a for relative motion, $LA_a / g\zeta_a$ for acceleration. The peak to peak amplitude defined by the average value of the distance between maximum and minimum is used in the analysis.

The test results of pressures are also given in nondimensional values, $P / \rho g\zeta_a$, for the bottom and bow flare slamming pressures.

5.3 Experiment - II Ship motions, shear forces and bending moments

5.3.1 Description of the model

A 1/70 scale model of the S-175 container ship was divided into four segments by 5 mm wide transverse cuts at stations 7, 10 and 15 (0.3L, 0.45L and 0.7L from FP). The exposed ends of the segments were closed by glass reinforced plastic bulkheads. All are shown in Fig.5.6.

Each bulkhead was fixed on the model by fibre-glass and was set back 60 mm from the edge of the cut, and 5 cm gaps between adjacent segments were sealed with a flexible tape[45,78-79] (see photo 6).

The principal characteristics of the model are shown in Table 2[77].

Table 3 Principal Characteristics of S -- 175 for Model Test II

Symbol	Items	Ship	Model
L (m)	Length	175.0	2.500
B (m)	Breadth	25.40	0.363
D (m)	Depth	15.40	0.220
T (m)	Draught	9.50	0.136
∇ (m^3)	Volume	24138.5	0.07038
C_b	Block Coefficient	0.5716	0.5716
C_o	Section Coefficient	0.970	0.970
LCG	Longitudinal Centre of Gravity from Midship	-2.48	-0.0354
VCG	Centre of Gravity from Base Line	9.52	0.136
K_{yy}	Radius of Pitch Gyradius	42.0	0.510

5.3.2 Test conditions

In these experiments, the heave and pitch motions, shear forces and bending moments at three stations were measured.

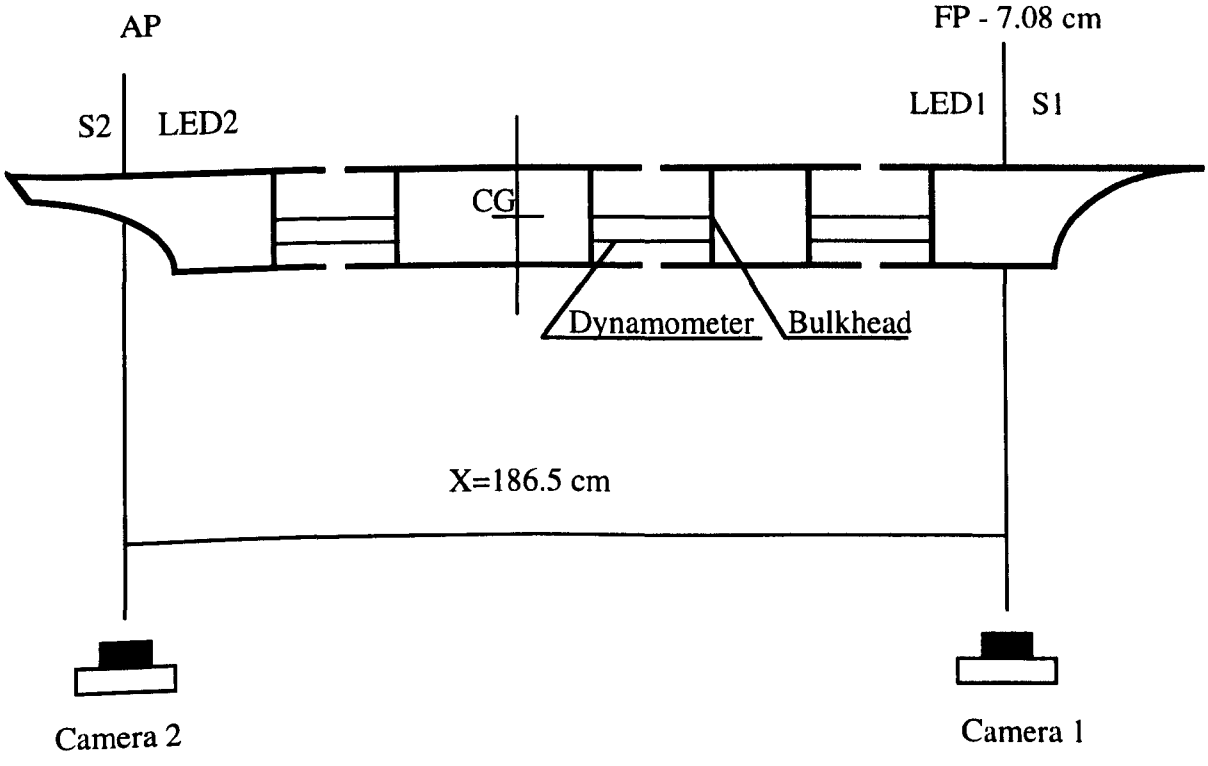

Fig. 5.6 Profile of Model (Experiment II)

1) Calm water test

Heave and pitch motions, shear forces and bending moments at five speeds 0.7, 0.7428, 1.0, 1.238 and 1.4 m/s in the still water were measured to study the effect of different speeds.

2) Heave and pitch motions I

Heave and pitch motions at zero speed, one frequency ($\lambda / L = 1.0$), and five different wave amplitudes (2.5, 4.0, 5.5, 7.5 and 8.75 cm) were measured to get the effect of the different wave amplitudes at zero speed.

3) Heave and pitch motions II

Heave and pitch motions at nine frequencies ($\lambda / L = 0.7$ -- 1.8), three different wave amplitudes (2.5, 4.0 and 7.5 cm) and two speeds (Fn = 0.15 and 0.25) were measured to confirm the linear theory in the frequency domain and the nonlinear theoretical prediction method developed which takes into account nonlinear effects in the time domain.

4) Heave and pitch motions III

Heave and pitch motions at three frequencies (λ / L=1.0, 1.2 and 1.4), five different wave amplitudes (2.5, 4.0, 5.5, 7.5 and 8.75 cm), and two speeds (Fn = 0.15 and 0.25) were measured to investigate the effect of increasing wave height on the heave and pitch motions.

5) Shear forces and bending moments

Shear forces and bending moments were also measured during heave and pitch response measurements at stations 7, 10 and 15.

5.3.3 Facilities and tests

All the experiments were carried out in the Towing Tank of the Hydrodynamics Laboratory at the Department of Naval Architecture & Ocean Engineering, University of

Glasgow, which is 77 m long, 4.6 m wide and 2.4 m deep.

This Laboratory is equipped with an electronically controlled towing carriage which has a maximum speed of 6.4 m/s and an electro-hydraulic plunger type wave maker placed at one end of the tank which generates regular waves in the frequency range of 0.4 to 1.4 Hz and in the wave height range of 1.6 cm to 22 cm. Waves are absorbed by a beach at the other end of the tank.

The general arrangement of the towing tank is shown in Fig.5.3, but there are three wave probes fixed in the front of the wave maker to measure the wave heights.

1) Measurement devices

The model was towed by a vertical post which allows freedom in heave and pitch motions with restraints in other directions. The towing point is positioned at the centre of gravity of the model which is free to pitch around a hinge pin at its centre of gravity. The pitch pivot is mounted at the end of the vertical heave rod which slides in linear bearings leaving the model free to heave.

i) A description of the LED selspot system is given in section 5.2.3.

ii) A description of the resistance type wave probe is also given in section 5.2.3.

iii) Three Dynamometers were used to measure shear forces and bending moments

The four segments of the model were joined by three strain gauge dynamometers[19,80].

The strain gauge dynamometer was made of mild steel and consisted of two plates connected by a rectangular strain bar. The plate was 10 cm ×10 cm ×1.0 cm (height ×width ×thickness). The strain bar was 10 cm long, the section was 4.961 cm × 2.940 cm ×0.30 cm (height ×width ×thickness).

The shear force was measured by two strain gauges (half bridge circuit[81]) bonded to the front face and back face of the strain bar which was 45 degrees to the centre line of

the front and back face.

The bending moment was measured by a pair of strain gauges (still half bridge circuit) bonded to the top face and bottom face of the strain bar which was in the centre line of the top and bottom face. The measurement by two strain gauges on the centre of the bar (in the top and bottom face) was confirmed by another two strain gauges on the side of the strain bar (still in the top and bottom face).

The location of the strain gauges is shown in Fig. 5.7.

The strain gauges used here was 2 mm gauge L. 6 W. 2.5

These gauges have a negligible effect on the test object but allow measurement of both static and dynamic strain. Both surfaces of these gauges are laminated thus fully protecting the copper nickel alloy foil grid.

All gauges are complete with integral wire for simple installation. Available in single or rosette styles with temperature compensation for use with either aluminium or mild steel.

The technical specification is shown in Table 4.

Table 4 Technical Specification of Strain Gauge*

Gauge Length	2 mm
Measurable strain	2 to 4 % max.
Temperature Range	-30 ^0C to + 180^0C
Gauge Resistance	120 $\Omega \pm$ 0.5%
Gauge Factor	2.00(nominal)
Gauge Factor Temperature Coefficient	$\pm$0.015%/^0C
Fatigue Life	10^5Reversals at 1000 Micro Strain
Foil Material	Copper Nickel Alloy
Base Material	Polyimide

* 1 micro strain is equal to an extension of 0.0001%

All the signals were collected by the Data Collecting System (32 channels analogue to digital converter, AMUX--64 System) after passing through multi - channel amplifiers

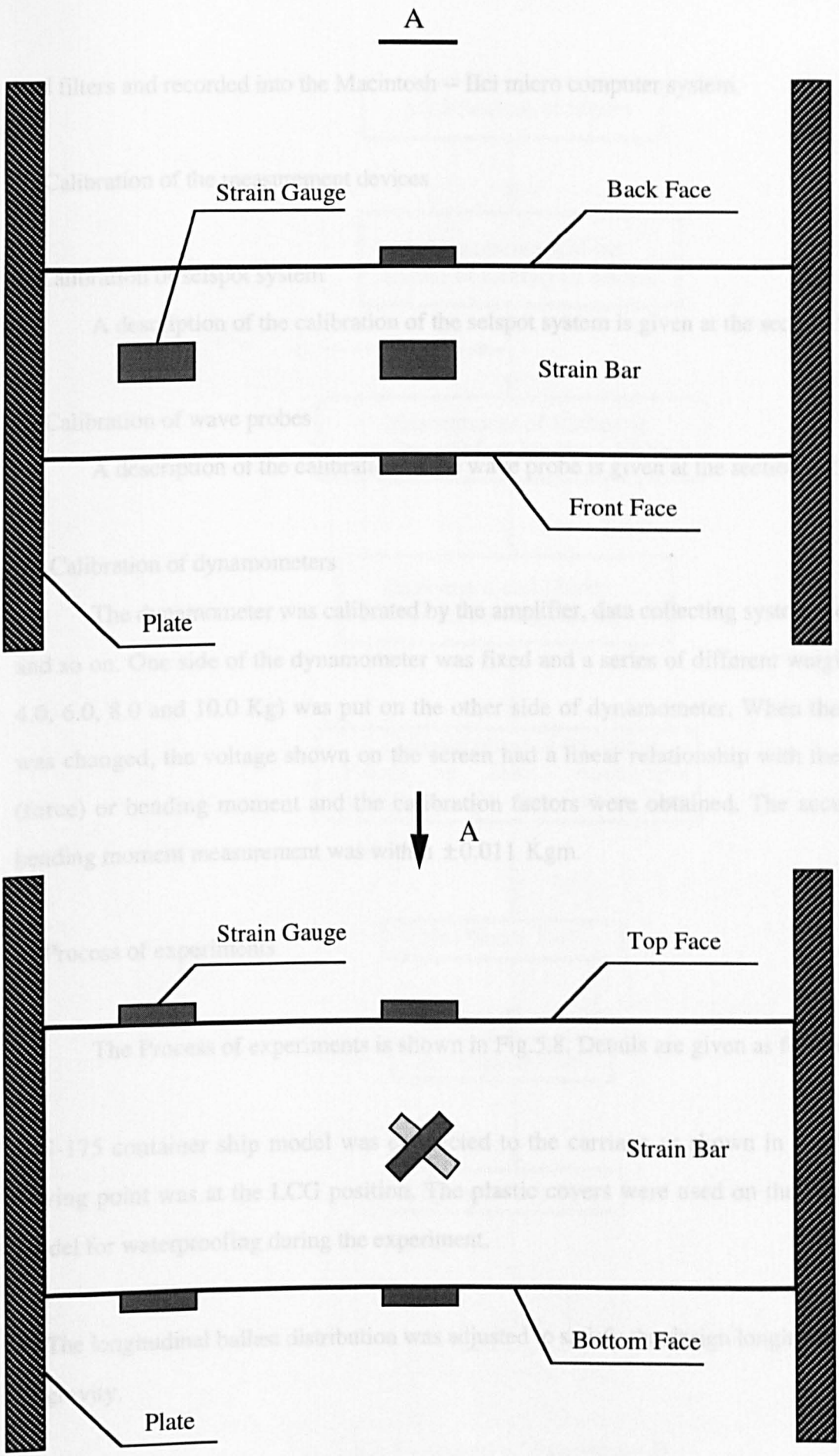

Fig. 5.7 Dynamometer

and filters and recorded into the Macintosh -- IIci micro computer system.

2) Calibration of the measurement devices

i) Calibration of selspot system

A description of the calibration of the selspot system is given at the section 5.2.3.

ii) Calibration of wave probes

A description of the calibration of the wave probe is given at the section 5.2.3.

iii) Calibration of dynamometers

The dynamometer was calibrated by the amplifier, data collecting system, computer and so on. One side of the dynamometer was fixed and a series of different weights (2.0, 4.0, 6.0, 8.0 and 10.0 Kg) was put on the other side of dynamometer. When the weight was changed, the voltage shown on the screen had a linear relationship with the weight (force) or bending moment and the calibration factors were obtained. The accuracy of bending moment measurement was within ± 0.011 Kgm.

3) Process of experiments

The Process of experiments is shown in Fig.5.8. Details are given as follows :

i) S-175 container ship model was connected to the carriage as shown in Fig.5.5. The towing point was at the LCG position. The plastic covers were used on the deck of the model for waterproofing during the experiment.

ii) The longitudinal ballast distribution was adjusted to satisfy the design longitudinal centre of gravity.

iii) The height of ballast weights was adjusted to satisfy the vertical centre of gravity from

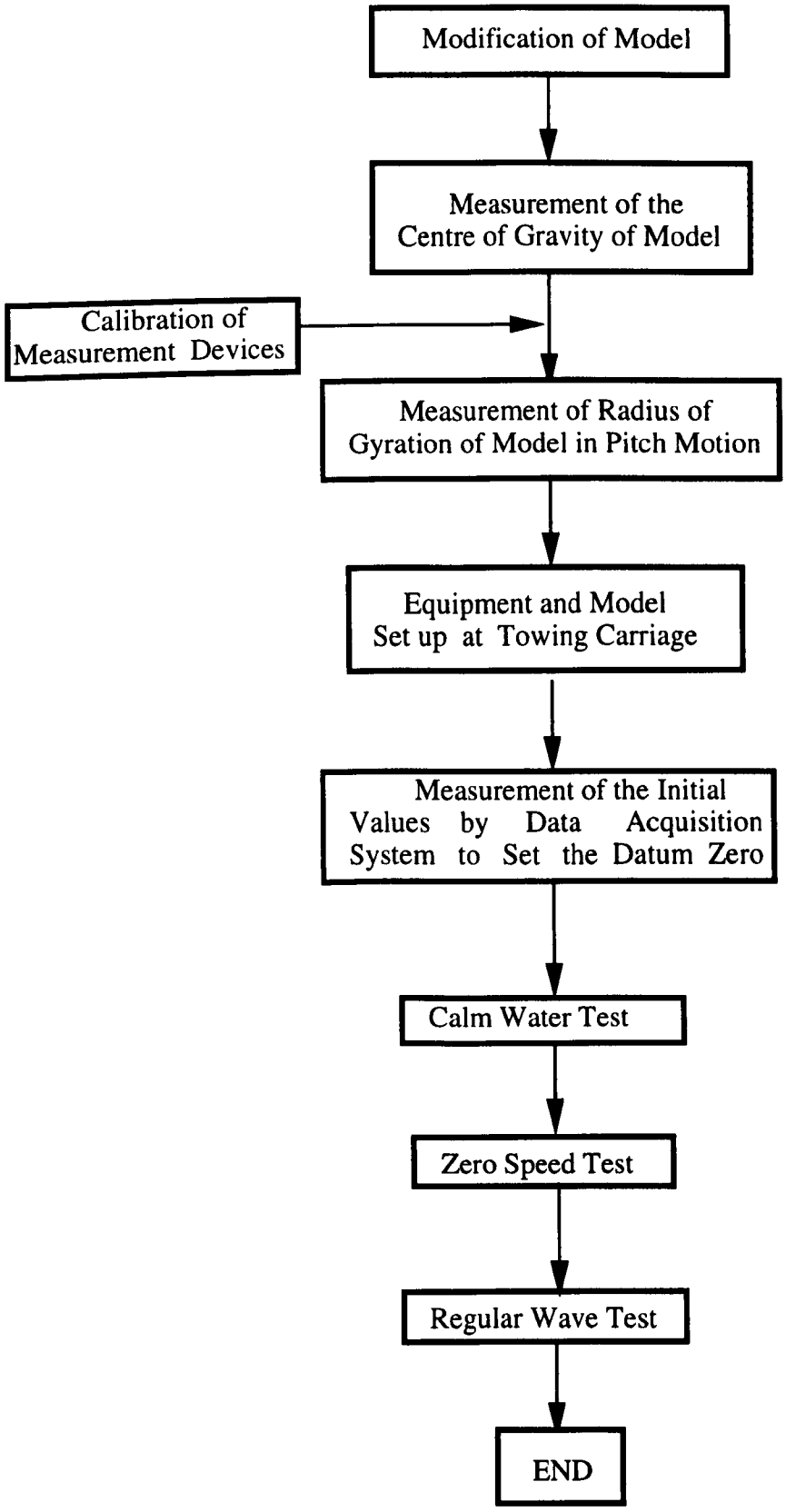

Fig. 5.8 A Flowchart of Experiment II

the model inclination test.

iv) Selspot system, dynamometers and wave probes were calibrated to identify the linearity of transducers and to measure the calibration coefficients in order to relate an output voltage to a physical quantity being measured.

v) The radius of gyration of the model in pitch motion was also measured by the Bifilar Suspension method.

vi) The initial values were measured by the data acquisition system and were set to zero.

vii) Calm water tests

viii) Zero speed tests

ix) Regular wave tests

4) Data Analysis

During these sets of experiments, the signals from the selspot system were analysed using the following equations for estimating the heave and pitch motions :

$$\text{Heave} = \frac{S_1 + S_2}{2}$$
$$\text{Pitch} = \text{Sin}^{-1}\frac{S_1 - S_2}{X} \qquad (5\text{-}2)$$

where S_1 and S_2 are the absolute motions measured forward and afterward, X=186.50 cm is the longitudinal separation of the two measurement locations.

The test results of motions are also given in the nondimensional values, Z_a / ζ_a for heave, $\psi_a / K\zeta_a$ for pitch, $M / \rho g L^3 B$ for bending moment. The peak to peak values as

well as hogging and sagging values were measured in the bending moment measurement.

For analysing the wave bending moment (Low frequency component of the bending moment signal), the filter technique[82-83] was used in the analysis, this filter is a non-recursive digital filter with a Hamming window and can be expressed as follows:

$$y_m = \frac{dt\omega_c}{\pi} \sum_{n=-N}^{N} W_n \frac{\sin ndt\omega_c}{ndt\omega_c} x_{m-n} \qquad (5\text{-}3)$$

Where

x_m Input signal at m time step.

y_m Output filtered signal at m time step.

dt Sampling rate.

ω_c Cut - off frequency.

W_n Hamming window.

N Half span of filter.

With

$$W_n = 0.54 + 0.46\cos\frac{n\pi}{N} \qquad (5\text{-}4)$$

5.4 Time history of experiments

The time history of the heave motion, pitch motion and relative motion; the bow flare slamming pressures; the wave and global bending moments are shown in Figs.A.5.1-A.5.22.

5.5 Test result analysis

In two cases, λ / L=1.0 and 1.5, the experimental tests are repeated, the error is 5%-10%. So, this experimental tests have a good repeatability. The experimental setup and facilities is a very suitable system to investigate the motion responses, slamming pressures and bending moments

CHAPTER 6
CONCLUSIONS

The aims of the research on nonlinear ship motions and sea loads have been met :

- The computational tools required to predict the large amplitude motions and sea loads of ship travelling with forward speed in waves have been developed.
- An experimental research programme design to complement and validate this nonlinear prediction method has been completed.
- The results of theoretical and experimental investigations to quantify the nonlinear ship motions, slamming pressures and bending moments in regular head seas have been presented.

6.1 Ship motions (Chapter 2)

The practical nonlinear theoretical prediction method described in this research is based on "relative motion hypothesis" in which nonlinear effects, i.e., nonlinear dynamic restoring force, nonlinear damping force and nonlinear fluid momentum force are considered. The motion equations are solved in the time domain by the numerical integration technique, the three points predictor-corrector method (Hamming method). The frequency dependent added mass and damping coefficients are computed at the instantaneous submerged section using the close-fit conformal mapping method.

(1) Generally, when using the nonlinear theory, the nondimensional values of heave and pitch motions decrease as the wave amplitudes increase. This is in-line with the experimental results but there is a tendency to overestimate heave motion in the resonance region. This indicates that the linear theory is very conservative and the resonance damping is still to low.

(2) The nonlinear method is a much superior predictor than the linear model in that it has much better agreement with the experimental test results for the heave and pitch motions. The contribution of different nonlinear terms to the

total external force depends on the encounter wave frequency.

(3) As expected, the nonlinear time domain analysis and the experimental are generally give values for crests and troughs which are different from each other whereas they equal values above and below the at-rest water line by the frequency domain (linear theory) calculations.

(4) The resistance type wave probe has limitation for measuring the relative motions in large waves. This is because it is vulnerable to splashing, and if the crest height exceeds the freeboard, the excess height of water over deck can not be measured. So, an additional probe to measure green water on deck should have been installed.

6.2 Bottom slamming pressures (Chapter 3)

The bottom slamming pressure was calculated by Stavovy & Chuang theory, Ochi & Motter theory, the momentum theory and Payne impact theory.

(1) The Ochi & Motter theory is strongly recommended for use in predicting the bottom slamming pressure for ships travelling in a seaway. Other methods will predict good bottom slamming pressure results for drop test cases. The Ochi & Motter method was based on whole ship test data and it is only through further tests of this type that the experimental database and hence the slamming model can be improved.

(2) The bottom slamming pressure increases as the wave amplitude increases because of the larger relative velocity.

6.3 Bow flare slamming pressures (Chapter 3)

The momentum slamming theory and Wagner impact theory were used to predict bow flare slamming pressures. The total impact pressure is expressed as the sum of water immersion impact pressure and wave striking impact pressure.

(1) The momentum slamming theory and Wagner impact theory are recommended

to predict the bow flare slamming.

(2) The bow flare slamming pressure increases as the wave amplitude and the speed increase because of the larger relative velocity.

(3) The relative contribution of the wave striking pressures to the total impact pressures decreases as the wave amplitude increases. This is because the ship's bow flare contacts between the trough and the crest of waves in the case of large amplitude regular waves.

6.4 Wave shear forces and bending moments (Chapter 4)

The wave shear forces and bending moments were calculated using the nonlinear theoretical prediction method and the linear strip theory.

(1) Generally, the nonlinear prediction method give better results than linear method, although, in large waves and the resonance region, midship wave bending moment will be overestimated by the nonlinear method because the damping is too low in the resonance region.

(2) The time history of the wave bending moments obtained by the nonlinear theoretical method and the experiments shows good agreement. The effect of the bottom, bow flare slamming and deck wetness effect can be clearly identified by characteristics features in these curves. This phenomenon shows that the nonlinear method has significant advantages over the linear theory.

(3) The significant nonlinearity of the hogging and sagging wave bending moment can be seen clearly from the results of predictions and measurements. It is important to be considered in ship hull design.

6.5 Global shear forces and bending moments (Chapter 4)

The ship hull is considered to be a Timoshenko beam, where the vibratory elastic response of the ship is calculated by the modal superposition method.

(1) Method 1 based on the elastic vibratory response due to the total hydrodynamic

force and these are much better than the results by the rigid body response superimposed with the elastic response (method 2), and have a good agreement with the experimental results. The method 1 are strongly recommended to predict the global dynamic shear force and bending moment values

(2) The predicted time history of the global bending moments obtained from the vibratory elastic response due to the total hydrodynamic force and the experimental measurements shows good agreement. The significant nonlinearity of the hogging and sagging global bending moments can also been seen in this analysis. It must also be considered in ship hull design.

6.6 Recommendation for future work

The quasi-nonlinear time domain technique has been shown to provide more reasonable predictions for the large amplitude motions and sea loads of ship travelling in waves than the linear frequency domain theory. The sea loads predicted by this nonlinear method can be used in further ship structural strength analysis and guiding ship hull design. However, the nonlinear strip method is a kind of practical tool for investigating the large amplitude motions and sea loads. It is worthwhile to devote continuous efforts in this line of research :

- The predictions will be improved by incorporating the viscous damping, nonlinear wave profile and incident wave deformation into the time domain simulations.
- The heave and pitch motions in irregular head seas, regular and irregular head seas including surge motion will be necessary to carry out for more practical sea case.
- The amplitude of heave and pitch motions in regular and irregular following seas with or without surge motion is also a very interesting project.
- Motions and sea loads of the six degrees of freedom (heave, pitch, surge and roll, sway and yaw) in the time domain will be the ultimate research aim.

REFERENCES

1. Korvin Kroukovsky, B. V., "*Investigation of Ship Motions in Regular Waves*" Trans. SNAME, Vol. 55, 1955.

2. Korvin Kroukovsky, B. V. and Jacobs, W. R., "*Pitching and Heaving Motions of a Ship in Regular Waves*", Trans. SNAME, Vol. 65, 1957.

3. Salvesen, N., Tuck, E. O. and Faltinsen, O., " *Ship Motions and Sea Loads*" Trans. SNAME, Vol. 78, 1970.

4. Bishop, R. E. D., Price, W. G. and Tam, P. K. Y., "*A Unified Dynamic Analysis of Ship Response to Waves*", Trans. RINA, Vol. 119, 1977.

5. Bishop, R. E. D., Price, W. G. and Tam, P. K. Y., "*On the Dynamic of Slamming*", Trans. RINA, Vol. 120, 1978.

6. Kaplan, P. and Sargent, T. P., "*Further Studies of Computer Simulation of Slamming and other Wave-induced Vibratory Structural Loadings on Ships in Waves*", SSC - 231, Ship Structure Committee, Washington D.C., 1972.

7. Jensen, J. J. and Pedersen, P. T., "*Wave - Induced Bending Moments in Ships - A Quadratic Theory*", Trans. RINA, Vol.121, 1979.

8. Meyerhoff, W. K. and Schlachter, G., "*An Approach for the Determination of Hullgirder Loads in a Seaway Including Hydrodynamic Impacts*", Ocean Engineering, Vol. 7, 1980.

9. Yamamoto, Y., Fujino, M. and Fukasawa T., "*Motion and Longitudinal Strength of a Ship in Head Sea and the Effects of Non-Linearities (1st Report)*", Journal of Society of Naval Architects of Japan, Vol. 143, 1978.

10. Yamamoto, Y., Fukasawa, T., Arai, M. and Kajita, E., "*Nonlinear Effects for Ship Motions in Heavy Seas*", International Shipbuilding Progress, Vol. 29, No. 333, 1982.

11. Borresen, R. and Tellsgard, F., "*Time History Simulation of Vertical Motions and Loads on Ships in Regular, Head Waves of Large Amplitude*", Norwegian Maritime Research, No.2/1980.

12. Petersen, J. B. and Marnas, L., "*Comparison of Nonlinear Strip Theory Predictions and Model Experiments*", Department of Ocean Engineering, The Technical University of Denmark, January, 1989.

13. Fang, M. C., Lee, M. L. and Lee, C. K., "*Time Simulation of Water Shipping for a Ship Advancing in Large Longitudinal Waves*", Journal of Ship Research, Vol. 37, No.2, June 1993.

14 Chiu, F. C. and Fujino, M. "*Nonlinear Prediction of Vertical Motions of a Fishing Vessel in Head Sea*", Journal of Ship Research, Vol. 35, No.1, March 1991.

15 MacFarlane, G. J. and Renilson, M. R., "*A Note on the Effect of Nonlinearity on the Prediction of the Vertical Motions of a Small High Speed Craft*", Proceeding of International Conference on Seakeeping and Weather, 28 February & 1 March 1995 London.

16 Boyd, J., Klaka, K and Thomas, G., "*Analysis of Nonlinear Vessel Motions: Experiments and Predictions*", Proceeding of International Conference on Seakeeping and Weather, 28 February & 1 March 1995 London.

17. Takezawa, S., Hirayama, T., Nishimoto, K. and Kolayashi, K., "*Strip Methods for Motions and Wave Loads in Following and Oblique Seas and Comparison with Experiments*", The Proceeding of International Workshop on Ship and Platform Motions, October 1983, University of California, Berkeley.

18. Takaishi. Y, Yoshino. T, Takagi. M and Saito. K , "*On the Motion of a High-Speed Container Ship with a Single Screw in Oblique Waves*", Journal of the Society of Naval Architects of Japan, Vol. 129, June, 1971.

19. Lloyd, A. R. J. M., Brown, J. C. and Anslow, J. F. W., "*Motions and Loads on Ship Models in Regular Oblique Waves*", Trans. RINA, Vol.122, 1980.

20. Wagner, H., "*Uber Stoss-Gleitvorgange an der Oberflache von Flussigkeiten*", ZAMM, Bd.12, 1932.

21. Stavovy, A. B. and Chuang, S. L., "*Analytical Determination of Slamming Pressures for High-Speed Vehicles in Waves*", Journal of Ship Research , Vol. 20, No.4, 1976.

22. Ochi, M. K. and Motter L. E., "*A Method to Estimate Slamming Characteristics for Ship Design*", Marine Technology, Vol.8, No.2, 1971.

23. Ochi, M. K. and Motter L. E., "*Prediction of Slamming Characteristics and Hull Response for Ship Design*", Trans. SNAME, Vol.81, 1973.

24. Mansour, A. and d'Oliveira, J. M., "*Hull Bending Moment due to Ship Bottom Slamming in Regular Waves*", Journal of Ship Research, Vol. 19, No.2, June 1975.

25. Payne, P. R., "*Technical Note, The Vertical Impact of a Wedge on a Fluid*", Ocean Engineering, Vol.8, No.4, 1981.

26. Payne, P. R., "*The Normal Force on a Flat Planning Plate Including Low Length to Beam Ratios*", Ocean Engineering, Vol.8, No.3, 1981.

27. Zhu, L. and Faulkner, D., "*Slamming Drop Tests for Small Scale SWATH Characteristic Model*", Departmental Report, NAOE-94-34, Department of Naval Architecture & Ocean Engineering, University of Glasgow.

28. Zhu, L., "*Structural Response of Ship Plate in Slamming-Drop Test Results and Analysis*", Departmental Report, NAOE-95-20, Department of Naval Architecture & Ocean Engineering, University of Glasgow.

29. Zhu, L. and Faulkner D., "*Design Pressure for the Wet-Deck Structure of Twin-Hull Ships*", Proceeding of Third International Conference on Fast Sea transportation, Fast'95, Tranvemunde, Germany, September 25-27, 1995.

30. Colwell, J., Datta, I. and Rogers, R., "*Head Seas Slamming Tests on a Fast Surface Ship Hull Form Series*", Proceeding of International Conference on Seakeeping and Weather, 28 February & 1 March 1995, London.

31. Suhara, T., "*Bow Flare Damages of Large Full Ships due to Wave Impact*" International Shipbuilding Progress, Vol.23, No.261, May 1976.

32. Yamamoto, Y., Iida, K., Fukasawa, T., Murakami, T., Arai, M. and Ando, A., "*Structural Damage Analysis of a Fast Ship due to Bow Flare Slamming*", International Shipbuilding Progress, Vol. 32, No. 369, 1985.

33. Gran, S., Olsen, H. and Tellsgard, F., "*Hull Responses to Hydrodynamic Forces on Bow Flare*", Norwegian Maritime Research, No.3, 1976.

34. Yamamoto, Y., Fujino, M. and Fukasawa, T., "*Motion and Longitudinal Strength of a Ship in Head Sea and the Effects of Non-linearities (3rd Report)*", Journal of Society of Naval Architects of Japan, Vol. 145, 1979.

35. Fukazawa, T. and Yamamoto, Y., "*Some Considerations on Bow Form and Handling of Fast Cargo/Containerships from the Viewpoint of Slamming*", Journal of the Society of Naval Architects of Japan, Vol. 148, 1980.

36. Hwang, J. H., Kim, Y. J., Min, K. S. and Ahn, S. I., "*Prediction of Bow Flare Impact Pressure by Momentum Slamming Theory*", The Proceedings of International Workshop on Ship and Platform Motions, University of California, Berkeley, U.S.A., October 1983.

37. Arai , M. and Matsunaga, K., "*A Numerical and Experimental Study of Bow Flare Slamming*", Journal of the Society of Naval Architects of Japan, No.166, 1989.

38. Faltinsen, M., "*On Seakeeping of Conventional and High-Speed Vessels*" Journal of Ship Research, Vol.37, No.2, 1993.

39. Kaplan, P., "*A Theoretical Method for Determining Slam Impact Pressure Distributions on Ship Sections*", Proceeding of OMAE, 1996, Vol. I, Part A, Florence, Italy.

40. Watanabe, I., Ueno, M. and Sawada, H., "*Effects of Bow Flare Shape to the Wave Loads of a Container Ship*", Journal of Society of Naval Architects of Japan, No.166, 1989.

41. Takemoto, H., Hashizume, Y. and Oka, S., "*Full-Scale Measurement of Wave Impact Loads and Hull Response of a Ship in Waves (1st Report)*", Journal of Society of Naval Architects of Japan, Vol.158, 1985.

42. Takemoto, H., Hashizume, Y. and Oka, S., "*Full-Scale Measurement of Wave Impact Loads and Hull Response of a Ship in Waves (2st Report)*", Journal of Society of Naval Architects of Japan, Vol.159, 1986.

43. Kaplan, P., Sargent, T. P. and Cilmi, J., "*Theoretical Estimates of Wave Loads on the SL-7 Container Ship in Regular and Irregular Seas*", Ship Structure Committee, SSC-246, 1974.

44. Soares, C. G., "*Comparison of Measurements and Calculations of Wave Induced Vertical Bending Moments in Ship Models*", International Shipbuilding Progress, Vol. 37, No. 412, 1990.

45 Vossers, G., Swaan, W. A. and Rijken, H., "*Vertical and Lateral Bending Moment Measurements on Series 60 Models*", International Shipbuilding Progress, Vol.8, No.3, 1961.

46 Wahab, R., "*Amidship Forces and Moments on a C_B=0.80 Series 60 Model in Wave from Various Directions*", Netherlands Ship Research Centre TNO, Report No. 100s, November 1967.

47 Chiocco, M. J. and Numata, E., "*Midship Wave Bending Moments in a Model of the Cargo Ship 'Wolverine State' running at Oblique Headings in Regular Waves*", Report No. SSC-201, Ship Structure Committee, Washington D.C., 1969.

48 Gie, T. S., "*Wave Load Measurements on a Model of a Large Container Ship*", Netherlands Ship Research Centre, Report No. 173S, 1972.

49. Dalzell, J. F. and Chiocco, M. J., "*Wave Loads in a Model of the SL-7 Container Ship Running at Oblique Headings in Regular Waves*", Report No. SSC-239, Ship Structure Committee, Washington, D. C., 1973.

50. Fujino, M., Yoon, B. S., Kawada, J and Yoshino, I., "*A Study on Wave Loads Acting on a Ship in Large Amplitude Waves (1st Report)*", Journal of Society of Naval Architects of Japan, Vol.156, 1984.

51. Fujino, M., Yoon, B. S., Kawada, J and Yoshino, I., "*A Study on Wave Loads Acting on a Ship in Large Amplitude Waves (2nd Report)*", Journal of Society of Naval Architects of Japan, Vol.157, 1985.

52. Fujino, M., Yoon, B. S., Kawada, J and Yoshino, I., "*A Study on Wave Loads Acting on a Ship in Large Amplitude Waves (3rd Report)*", Journal of Society of Naval Architects of Japan, Vol.158, 1985.

53. Chiu, F. and Fujino, M., "*Nonlinear Prediction of Vertical Motions and Wave Loads of High-Speed Craft in Head Sea*", International Shipbuilding Progress, Vol. 36, No. 406, 1989.

54. Dai, Y. S. and Song, J. Z., "*Hull Bending Moment in a Seaway*", Shipbuilding of China, No.3, 1980.

55. Belik, O., Bishop, R. E. D. and Price, W. G., "*On the Slamming Response of Ships to Regular Head Waves*", Trans. RINA, Vol. 122, 1980.

56. Kaplan, P., "*Computer Simulation/Prediction of Ship Motions and Loads in a Seaway*", International Conference on Seakeeping and Weather, 28 February & 1 March, 1995 London.

57. Hansen, P. F., "*On Combination of Slamming - and Wave - Induced Response*", Journal of Ship Research, Vol.38, No.2, 1994.

58. Tao, Z. X., "*Time Domain Simulation of Vertical Motions and Loads on Monohull Ships in Regular Head Waves*", Departmental Report, NAOE-94-23, Department of Naval Architecture & Ocean Engineering, University of Glasgow.

59. Tao, Z. X., "*Experimental and Theoretical Investigations of Large Amplitude Motions of a Container Ship Model in Head Seas*" Departmental Report NAOE-95-18, Department of Naval Architecture & Ocean Engineering, University of Glasgow.

60. Karman, V. T., "*The Impact of Seaplane Floats During Landing*", NACA TN. No.321, 1929.

61. Tao. Z. X., "*Experimental and Theoretical Investigations of Bow Flare Slamming Pressures in Regular Head Seas*", Departmental Report NOAE-95-25, Department of Naval Architecture & Ocean Engineering, University of Glasgow.

62. Tao. Z. X. and Incecik, A., "*Large Amplitude Ship Motions and Bow Flare Slamming Pressure in Regular Head Seas*", Proceeding of OMAE, Vol. I, Part A, June 16-20, 1996, Florence, Italy.

63. Tao. Z. X. and Incecik, A., "*Nonlinear Ship Motion and Global Bending Moment Predictions in Regular Head Seas* ", Sent to the Journal of International Shipbuilding Progress.

64. Tao. Z. X. and Incecik, A., "*Nonlinear Ship Motion and Bending Moment Calculations in Time Domain*", For comparative study of nonlinear ship motion response in time domain in 13th International Ship and Offshore Structure Conference, Load Committee, August 1997, Trondheim.

65.. Fang, C. C., "*Experimental Investigation of Large Amplitude Motions of a Catamaran in Waves*", Departmental Report, NAOE-94-15, Department of Naval Architecture & Ocean Engineering, University of Glasgow.

66. Hamming, R. W., "*Numerical Methods for Scientists and Engineers*", 2nd Ed., McGraw-Hill Kogakusha, 1973.

67. Faltinsen, O. M., "*Numerical Free Surface Motion Outside or Inside Moving Bodies*", Proc. of the 2nd Int. Conf. on Numerical Ship Hydrodynamics, Univ. of California, Berkeley 1977.

68. Frank, W., "*Oscillation of Cylinders in or Below the Free Surface of Deep Fluids*", DTNSRDC Report No. 2375, Washington D. C., 1967.

69 Tasai, F., "*On the Damping Force and Added Mass of Ships Heaving and Pitching*", Report of Research Institute for Applied Mechanics, Kyuchu University, Vol. VII, No.26, 1959.

70 Smith, W. E., "*Computation of Pitch and Heave Motions for Arbitrary Ship Forms*", International Shipbuilding Progress, Vol.14, No. 155, 1967.

71 Landweber, L. and Macagno, M. C., "*Added Mass of Two-Dimensional Forms Oscillating in a Free Surface*", Journal of Ship Research, Vol., No.4, November, 1957.

72. Watanabe I., Tanizawa, K. and Sawada, H., "*An Observation of Bottom Impact Phenomena by means of High Speed Video and Transparent Model*", Journal of Society of Naval Architecture of Japan, No.164, 1988.

73. Ferdinande, I. V. , "*Theoretical Consideration on the Penetration of a Wedge into the Water*", International Shipbuilding Progress, Vol. 13, April, 1966.

74. Nagai, S., "*Shock Pressure Exerted by Breaking of Breakwaters*", Journal of Waterways and Harbours Division, Pro. of the ASCE, Vol. 86, No. WW2, 1960.

75. Hayashi, T. and Hattori, S., " *On the Pressures of Breaking Waves*", Proceeding of 4th Japan Coastal Engineering Conference, 1957.

76. Clarke, J. D., "*Measurement of Hull Stresses in Two Frigates During a Severe Weather Trial*", The Naval Architect, No. 3, 1982.

77. Murdey, D. C., "*Specification for a Comparative of Computed Ship Motions in Six Degrees of Freedom*", NRC, Marine Dynamics and Ship Laboratory, Report LTR-SH-228, 1978.

78. Fain, R. A., "*Design and Installation of a Ship Response Instrumentation System aborad the SL-7 Class Container Ship S.S. Sea-Land Mclean*", Ship Structure Committee, SSC-238, 1973.

79. Toki, N., Hatatenaka, K., Takahashi, T. and Fujii, H., "*Experimental and Theoretical Approach to the Estimation of Nonlinear Vertical Wave Loads*", Journal of Society of Naval Architects of Japan, Vol. 154, 1983.

80. Bingham, R. H. and Tapper, J. E. "*A Five Component Balance*", Admiralty Experiment Works, TM7565, December, 1975.

81. Holister, G. S., "*Experimental Stress Analysis : Principles and Methods*", Cambridge at the University Press, 1967.

82. Bozic, S. A., "*Digital and Kalman Filtering*", Edward Aenold, 1979.

83. Mcleary, A., Cornut, S. and Incecik, A., "*Wave Drift and Viscous Damping Forces Acting on TLPS : Some Experimental Results*", Proceeding ISOPE, 1996, Los Angeles, USA, 26-31 May, 1996.

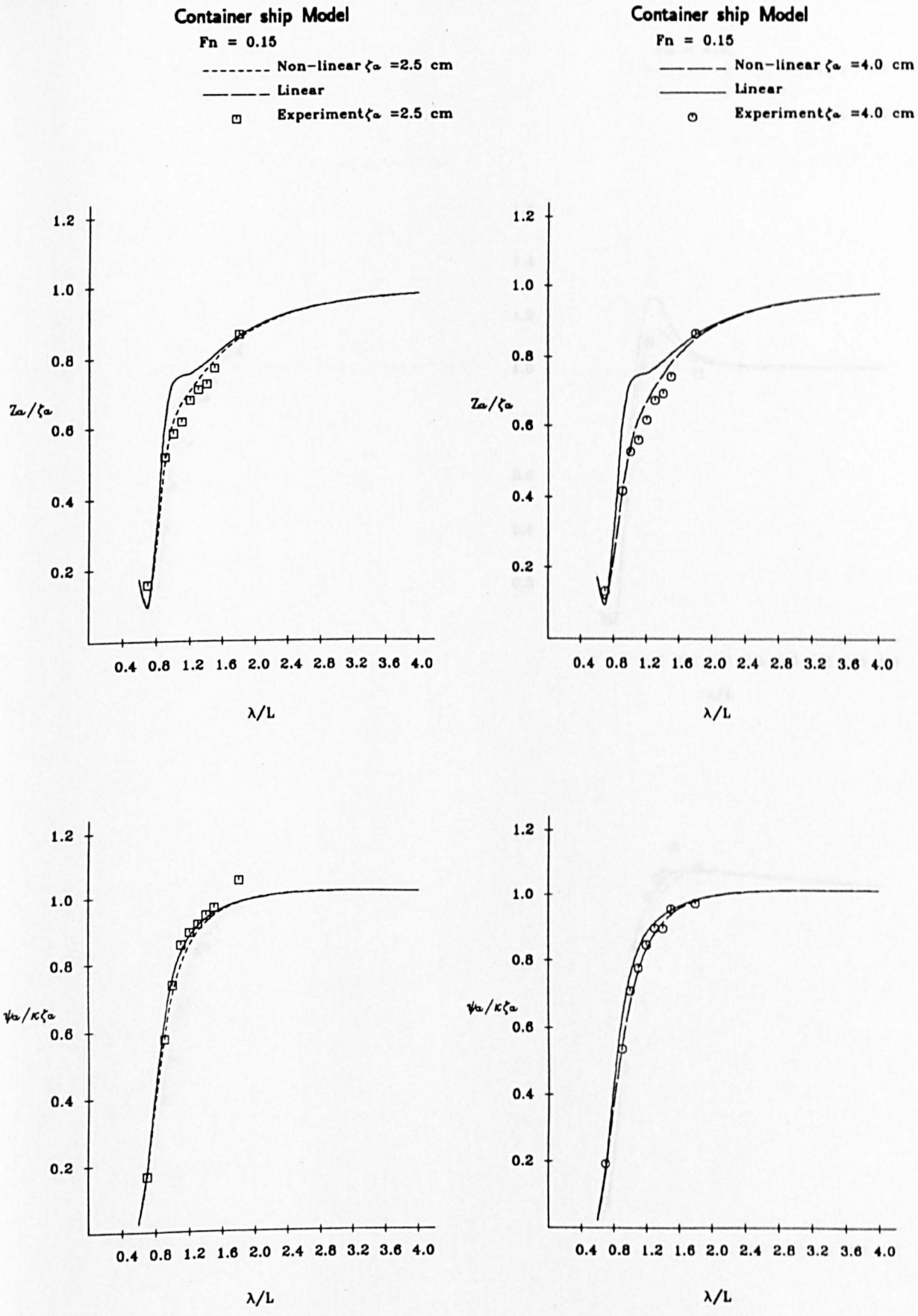

Figs.A.2.1-A.2.2 Heave and Pitch in Regular Head Seas

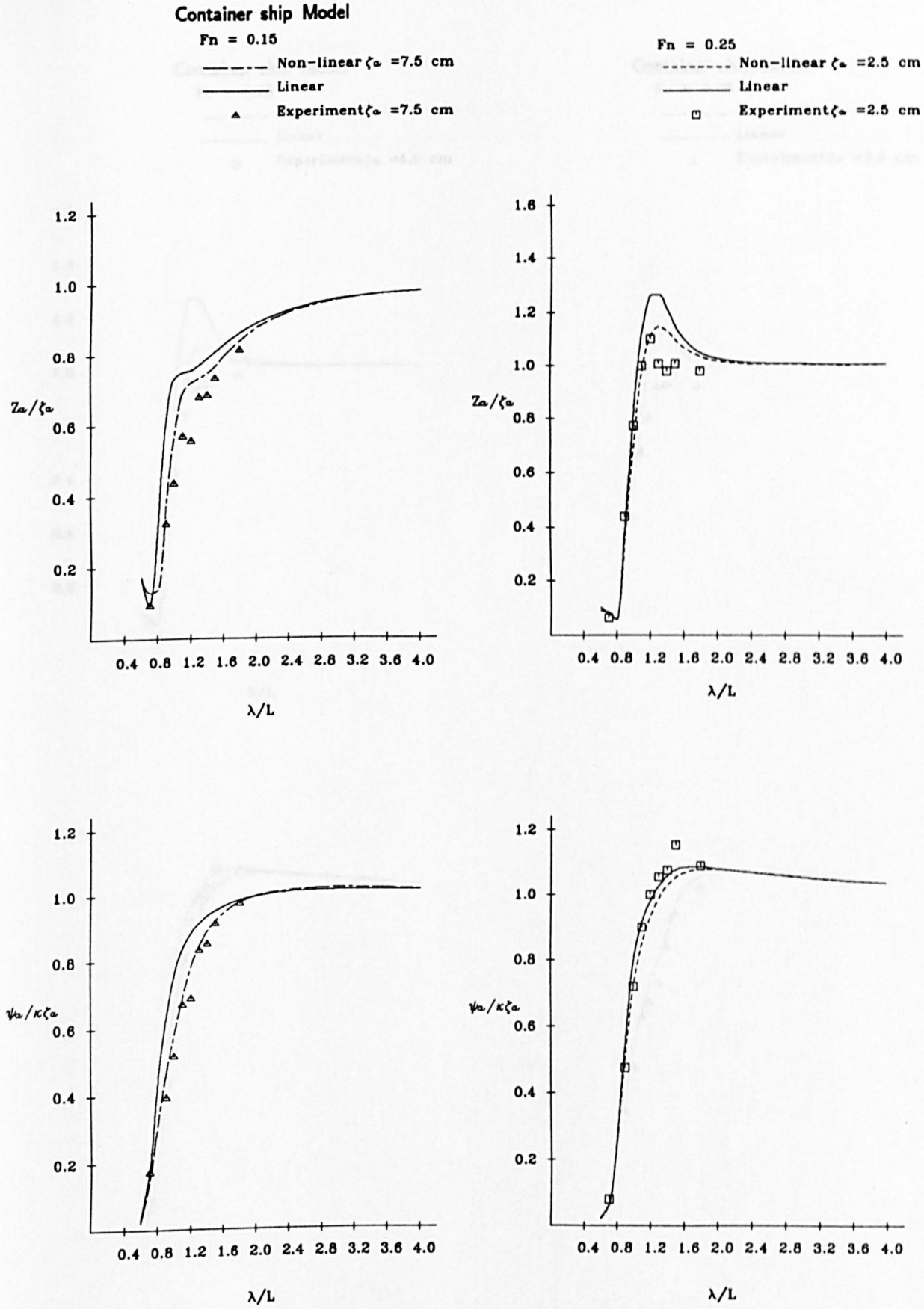

Figs.A.2.3-A.2.4 Heave and Pitch in Regular Head Seas

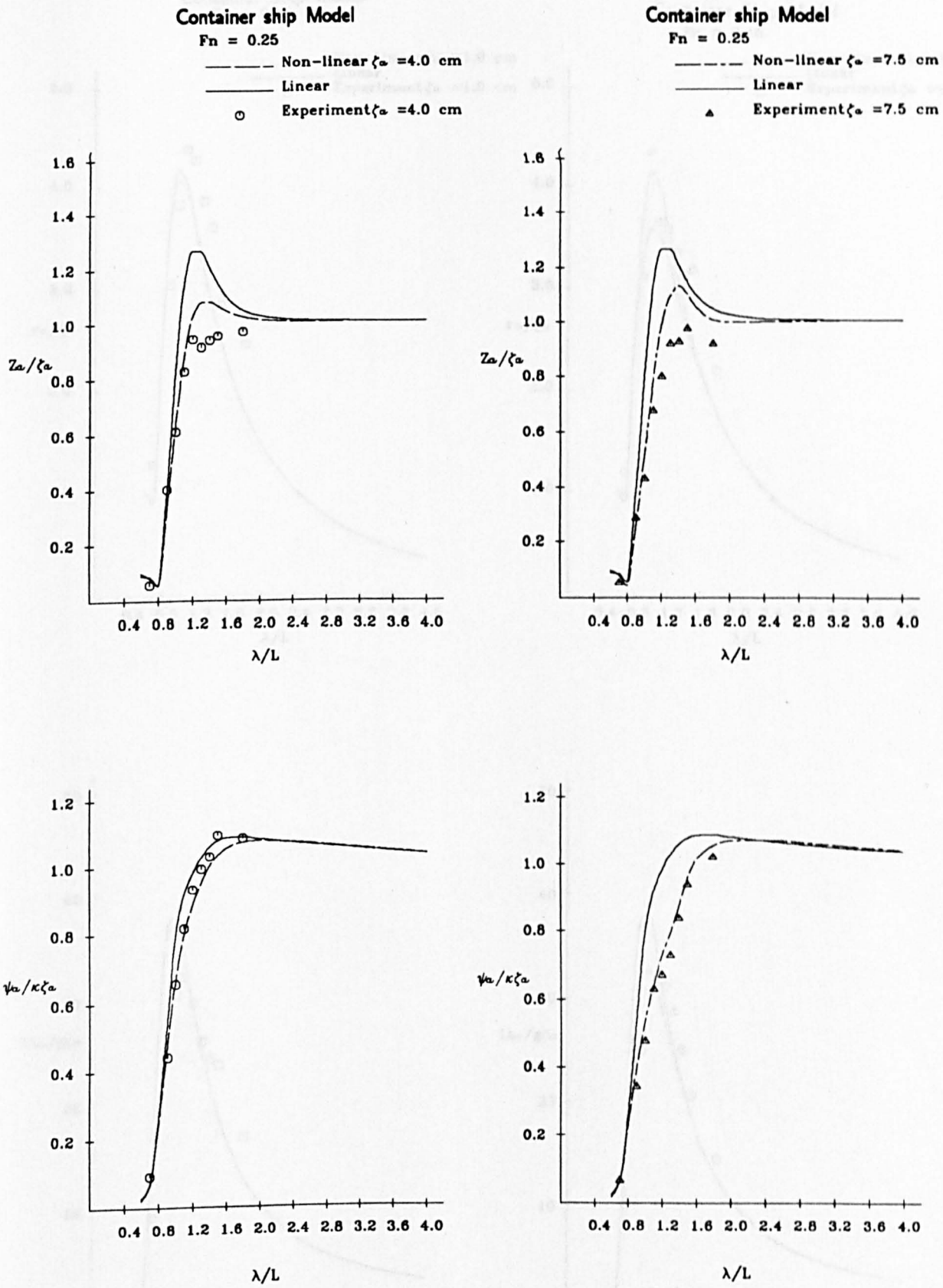

Figs.A.2.5-A.2.6 Heave and Pitch in Regular Head Seas

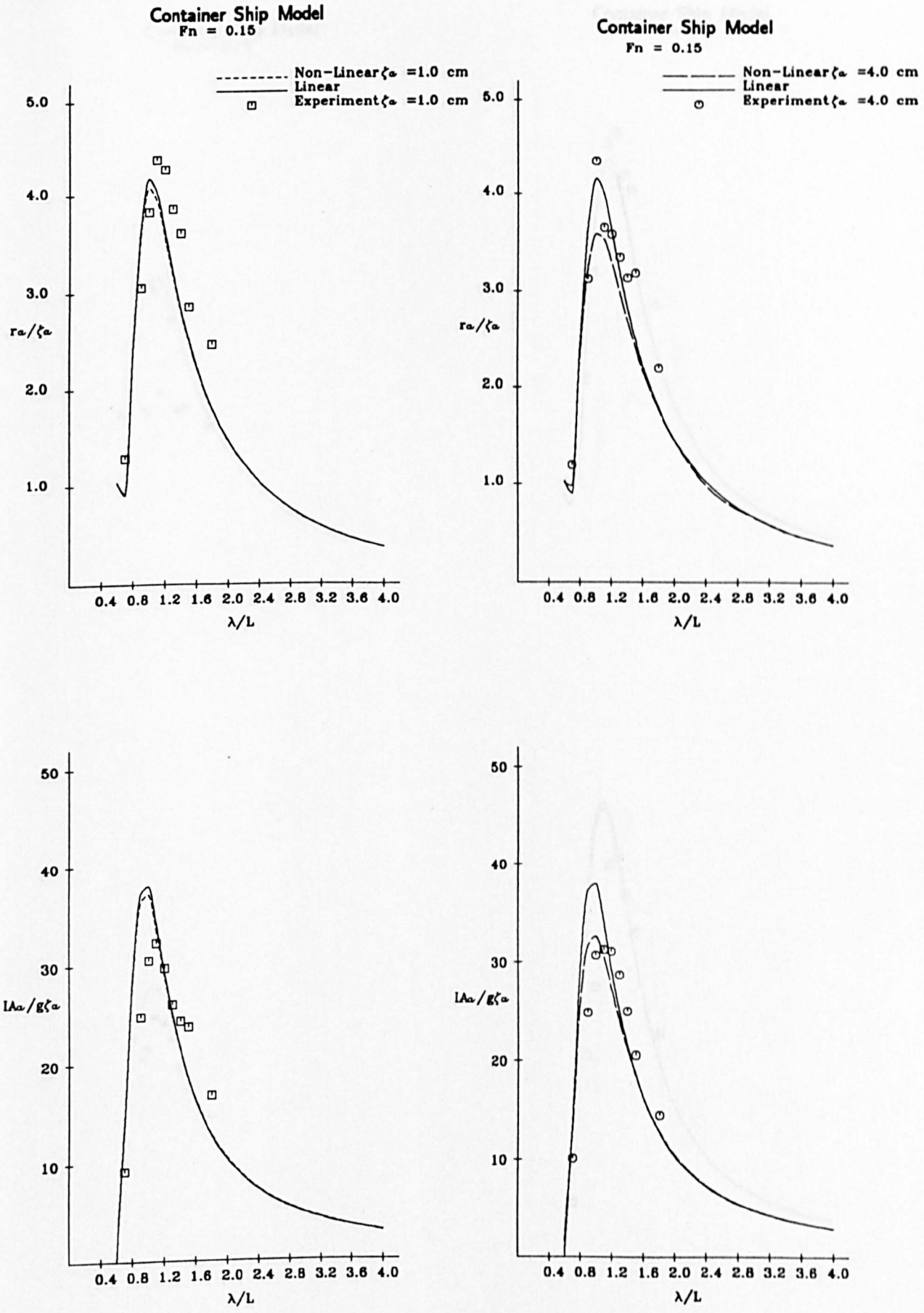

Figs.A.2.7-A.2.8 Relative Motion and Acceleration in Regular Head Seas at FP

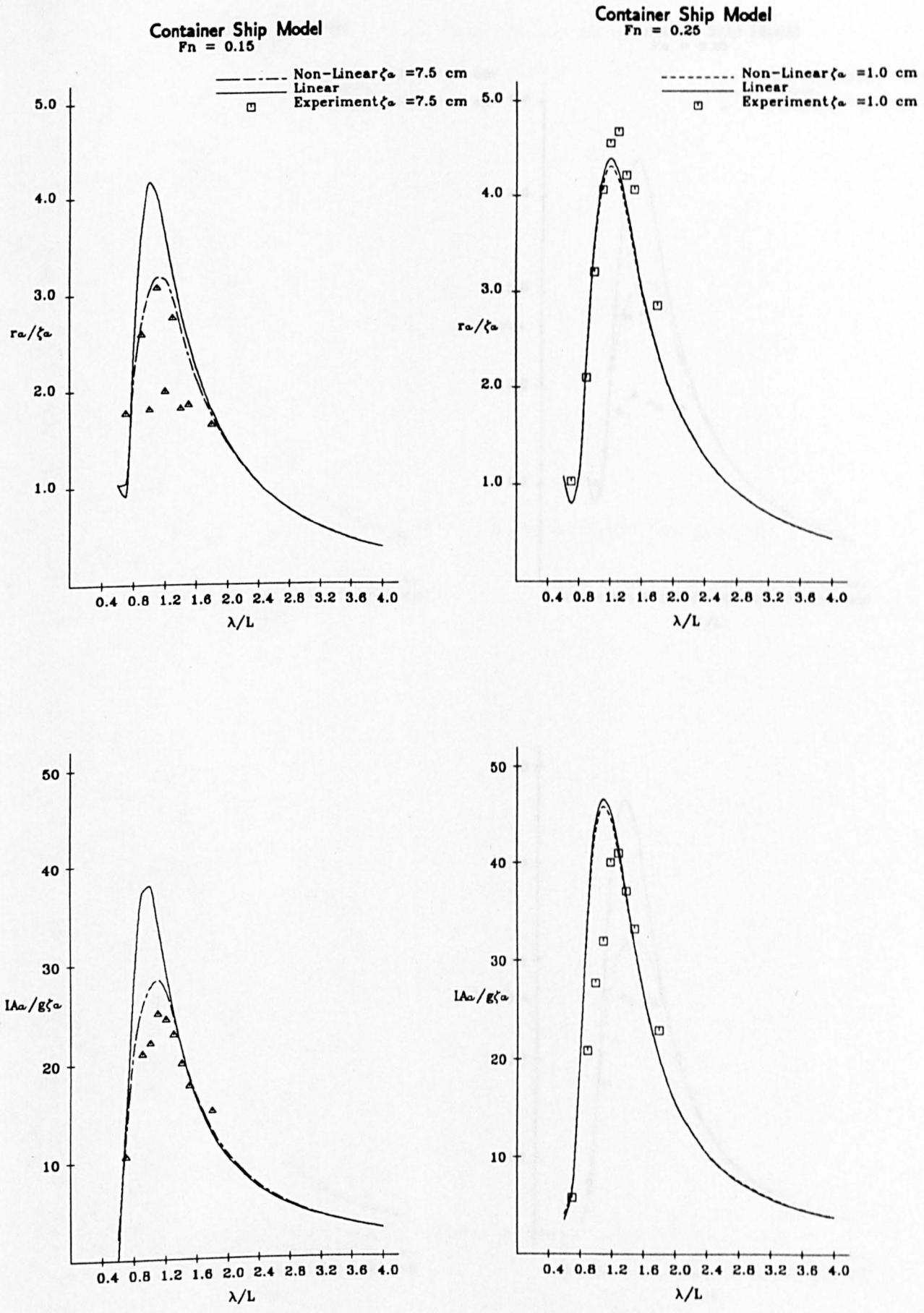

Figs.A.2.9-2.10 Relative Motion and Acceleration in Regular Head Seas at FP

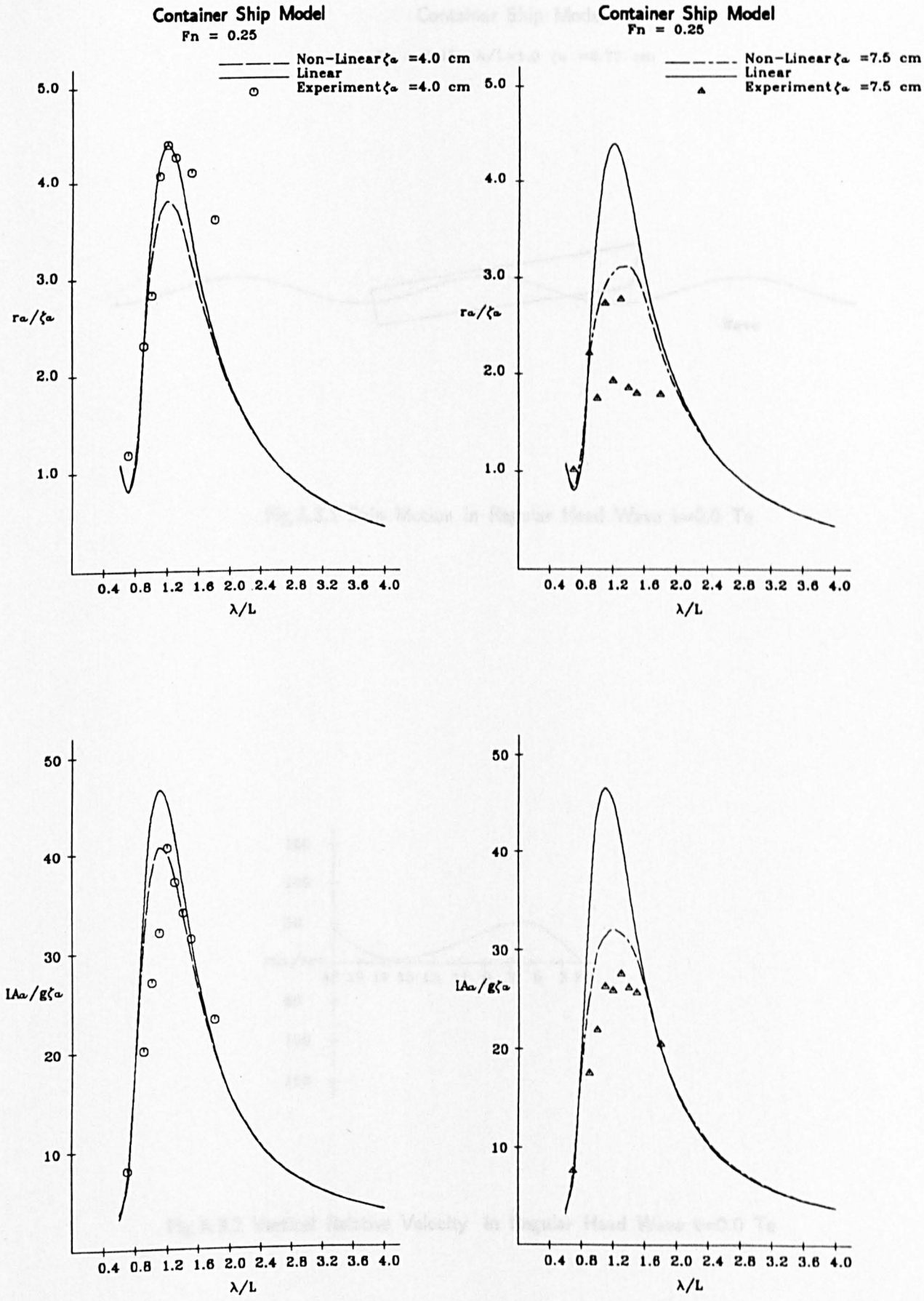

Figs.A.2.11-2.12 Relative Motion and Acceleration in Regular Head Seas at FP

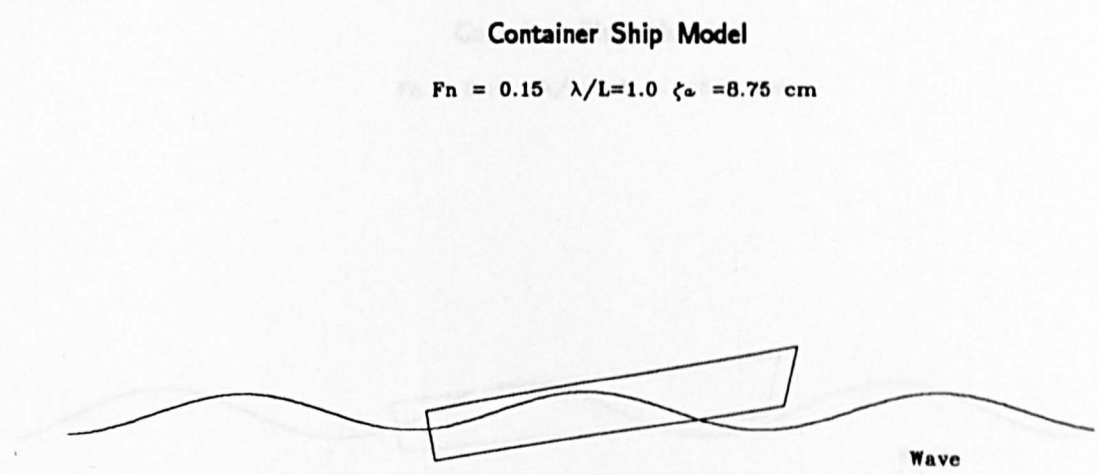

Fig.A.3.1 Ship Motion in Regular Head Wave t=0.0 Te

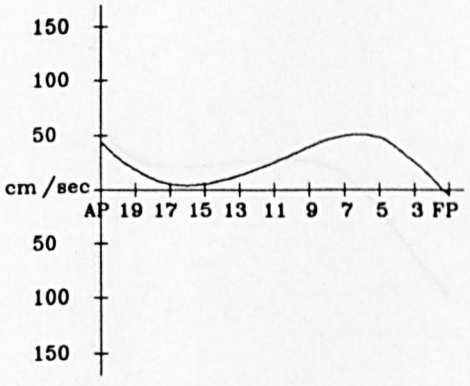

Fig.A.3.2 Vertical Relative Velocity in Regular Head Wave t=0.0 Te

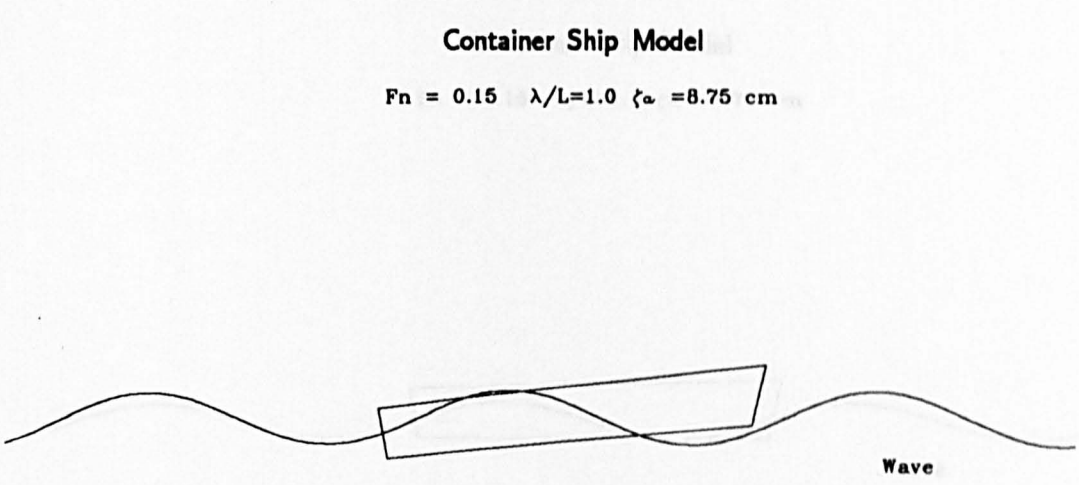

Fig.A.3.3 Ship Motion in Regular Head Wave t=0.1 Te

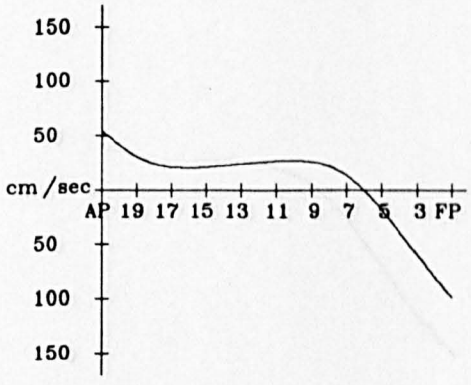

Fig.A.3.4 Vertical Relative Velocity in Regular Head Wave t=0.1 Te

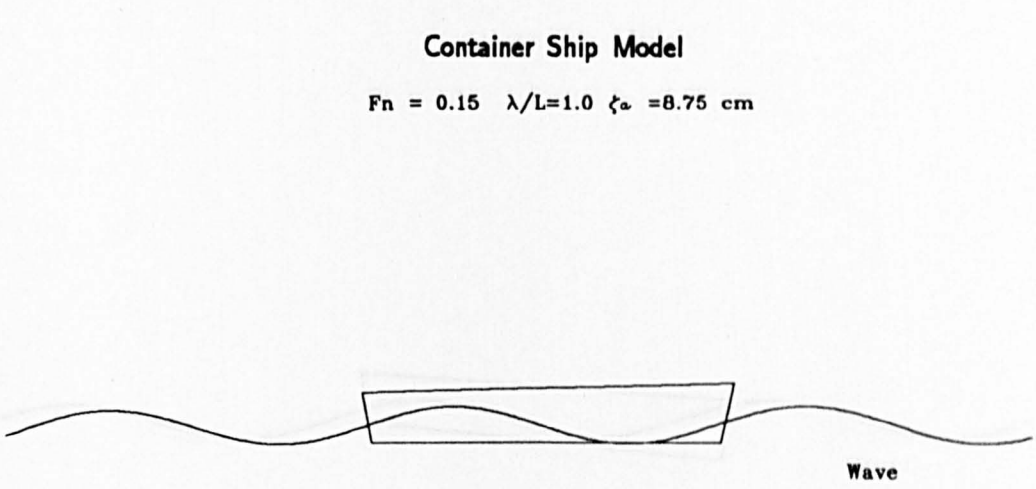

Fig.A.3.5 Ship Motion in Regular Head Wave t=0.2 Te

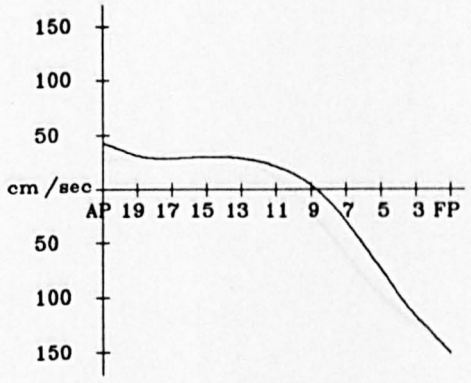

Fig.A.3.6 Vertical Relative Velocity in Regular Head Wave t=0.2 Te

Container Ship Model

Fn = 0.15 λ/L=1.0 ζ_a =8.75 cm

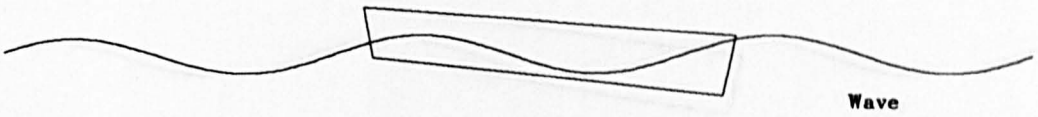

Fig.A.3.7 Ship Motion in Regular Head Wave t=0.3 Te

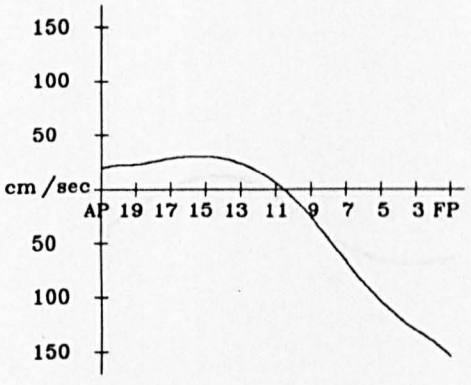

Fig.A.3.8 Vertical Relative Velocity in Regular Head Wave t=0.3 Te

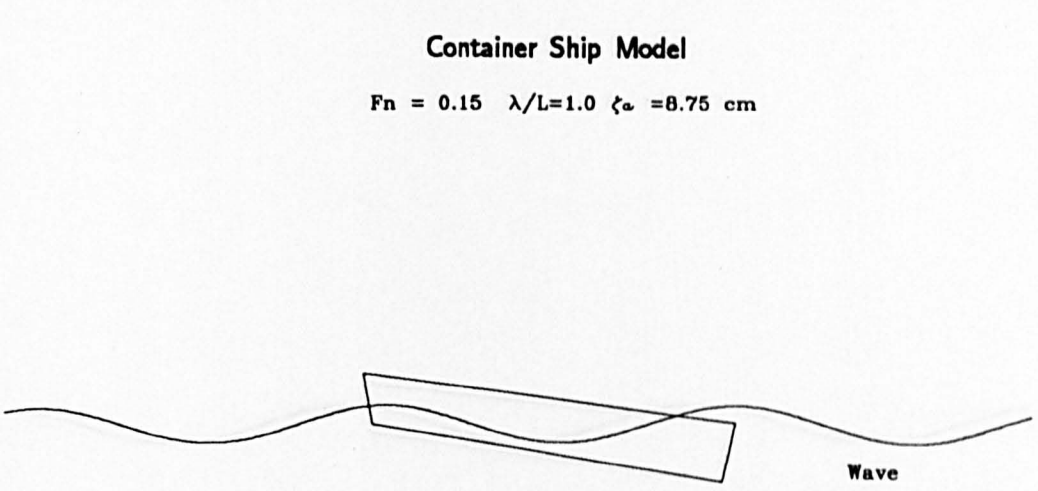

Fig.A.3.9 Ship Motion in Regular Head Wave t=0.4 Te

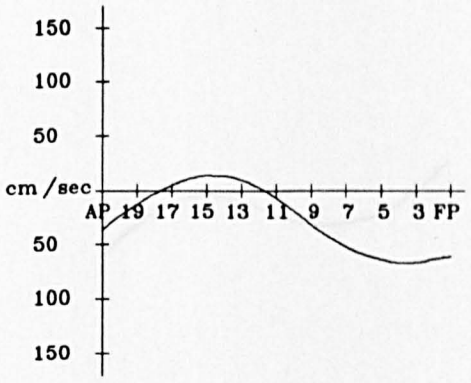

Fig.A.3.10 Vertical Relative Velocity in Regular Head Wave t=0.4 Te

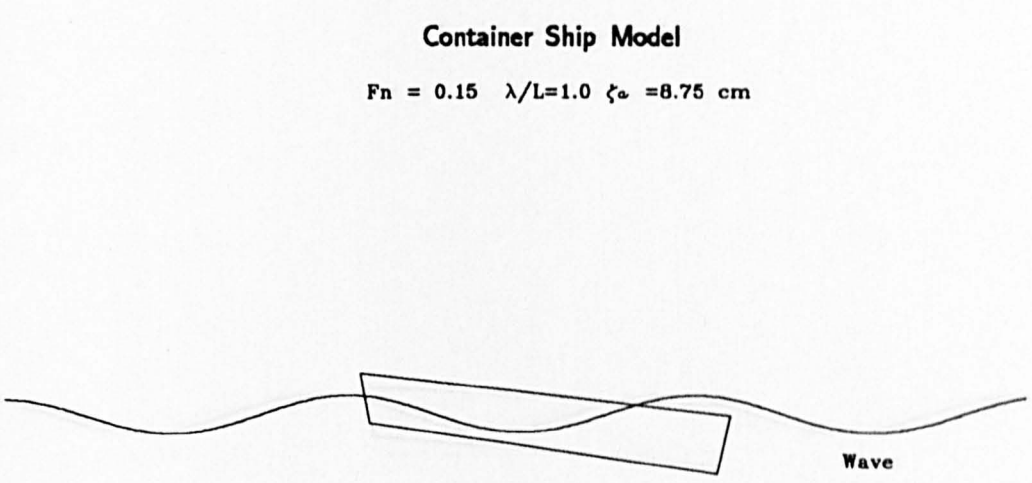

Fig.A.3.11 Ship Motion in Regular Head Wave t=0.5 Te

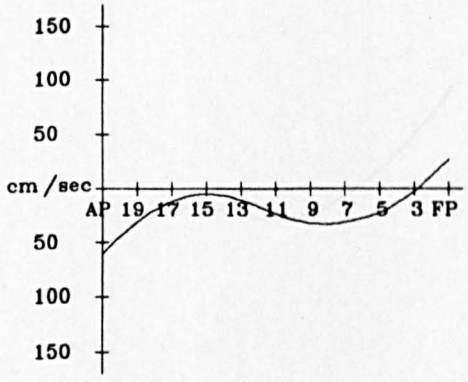

Fig.A.3.12 Vertical Relative Velocity in Regular Head Wave t=0.5 Te

Container Ship Model

Fn = 0.15 λ/L=1.0 ζ_a =8.75 cm

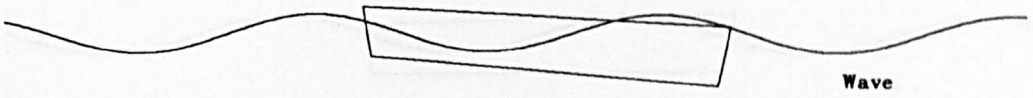

Fig.A.3.13 Ship Motion in Regular Head Wave t=0.6 Te

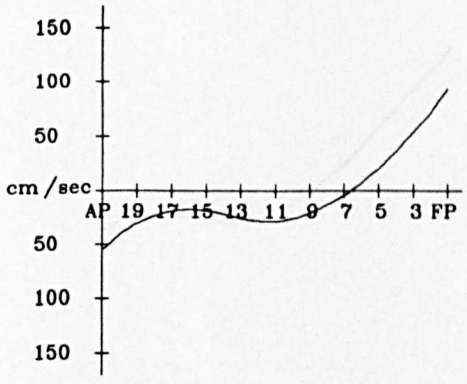

Fig.A.3.14 Vertical Relative Velocity in Regular Head Wave t=0.6 Te

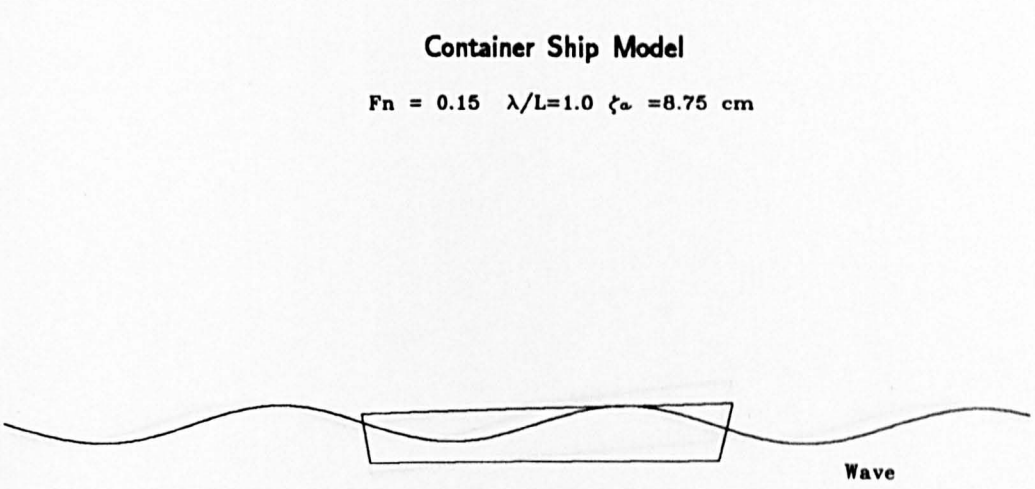

Fig.A.3.15 Ship Motion in Regular Head Wave t=0.7 Te

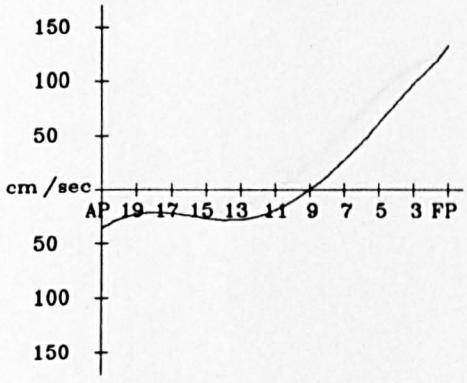

Fig.A.3.16 Vertical Relative Velocity in Regular Head Wave t=0.7 Te

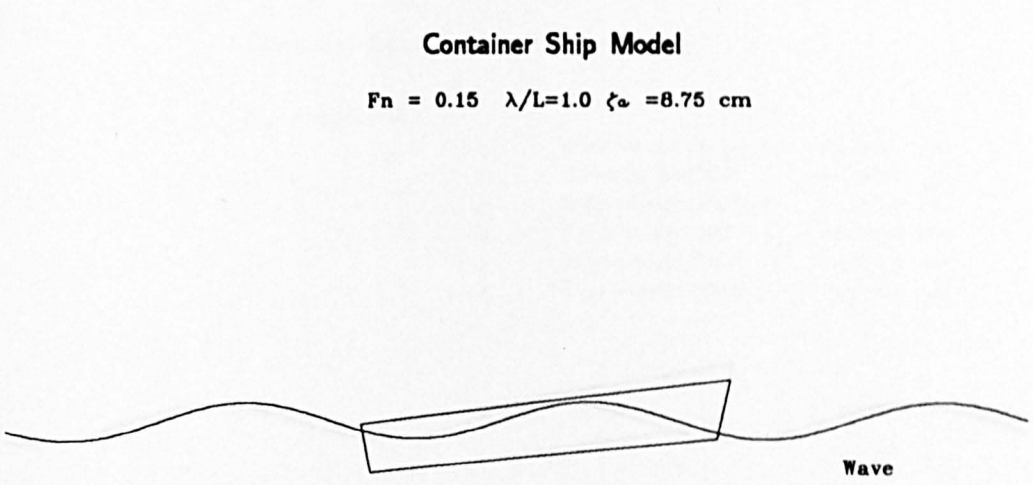

Fig.A.3.17 Ship Motion in Regular Head Wave t=0.8 Te

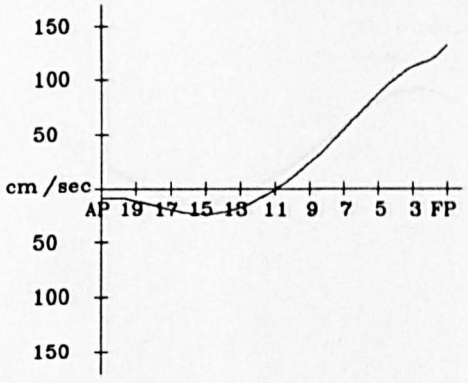

Fig.A.3.18 Vertical Relative Velocity in Regular Head Wave t=0.8 Te

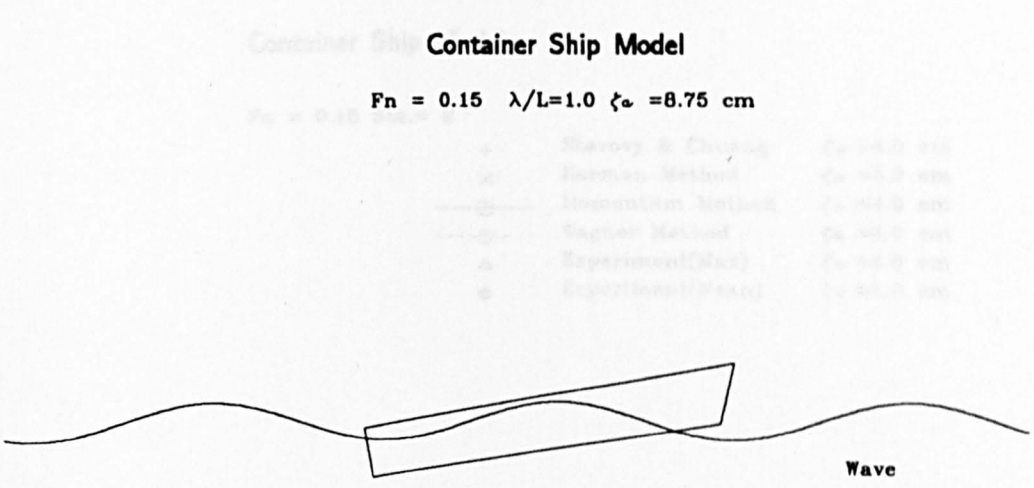

Fig.A.3.19 Ship Motion in Regular Head Wave t=0.9 Te

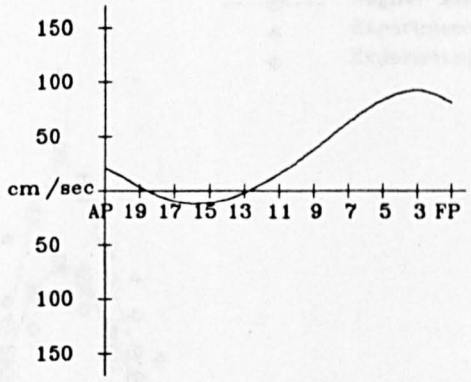

Fig.A.3.20 Vertical Relative Velocity in Regular Head Wave t=0.9 Te

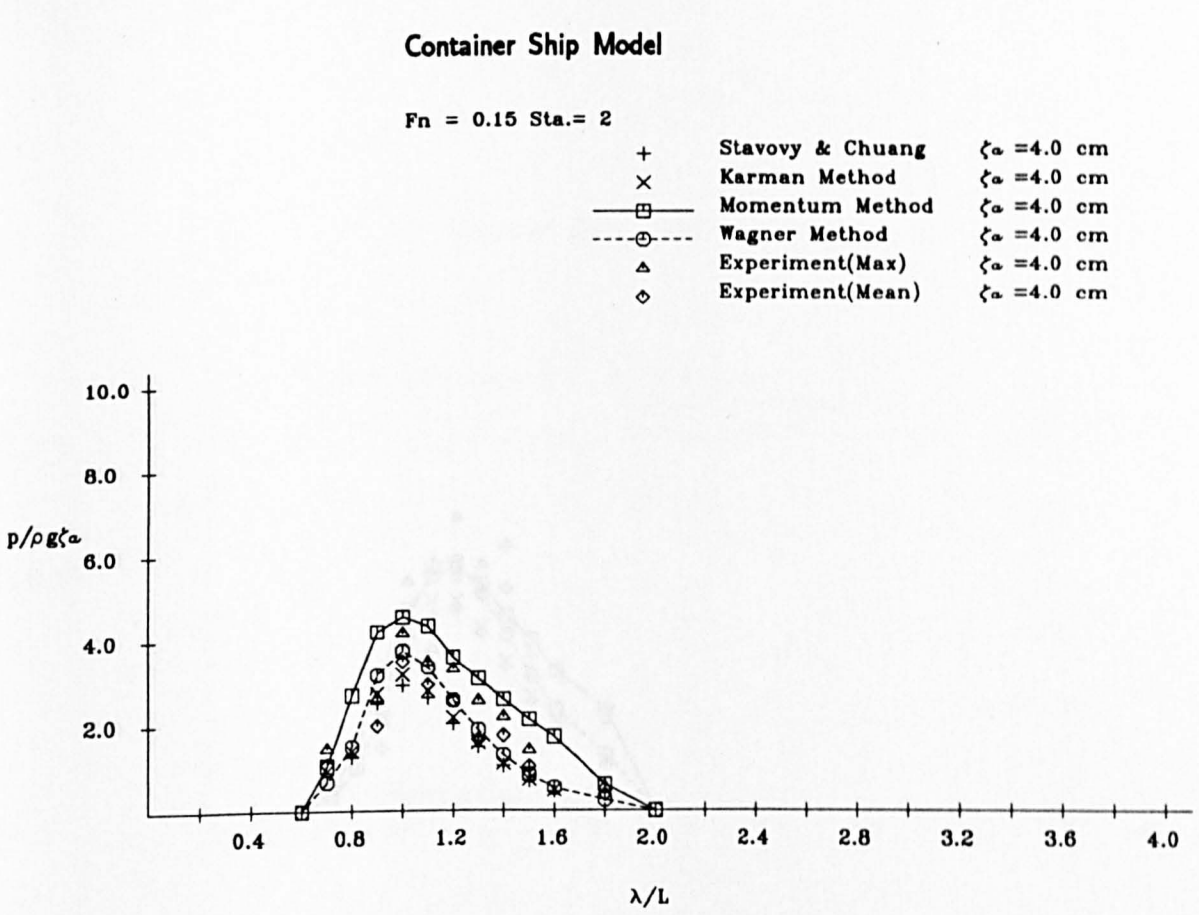

Fig.A.3.21 Bow Flare Impact Pressure Draught 20 cm

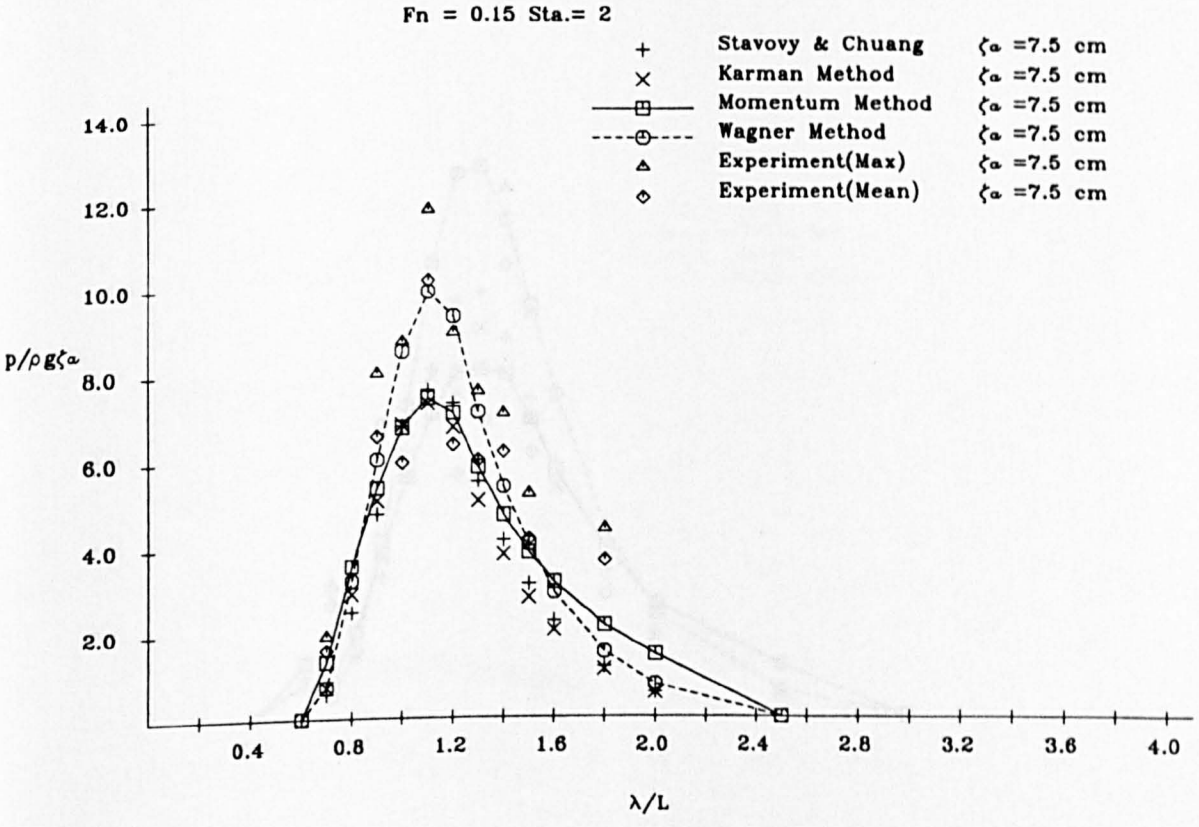

Fig.A.3.22 Bow Flare Impact Pressure Draught 20 cm

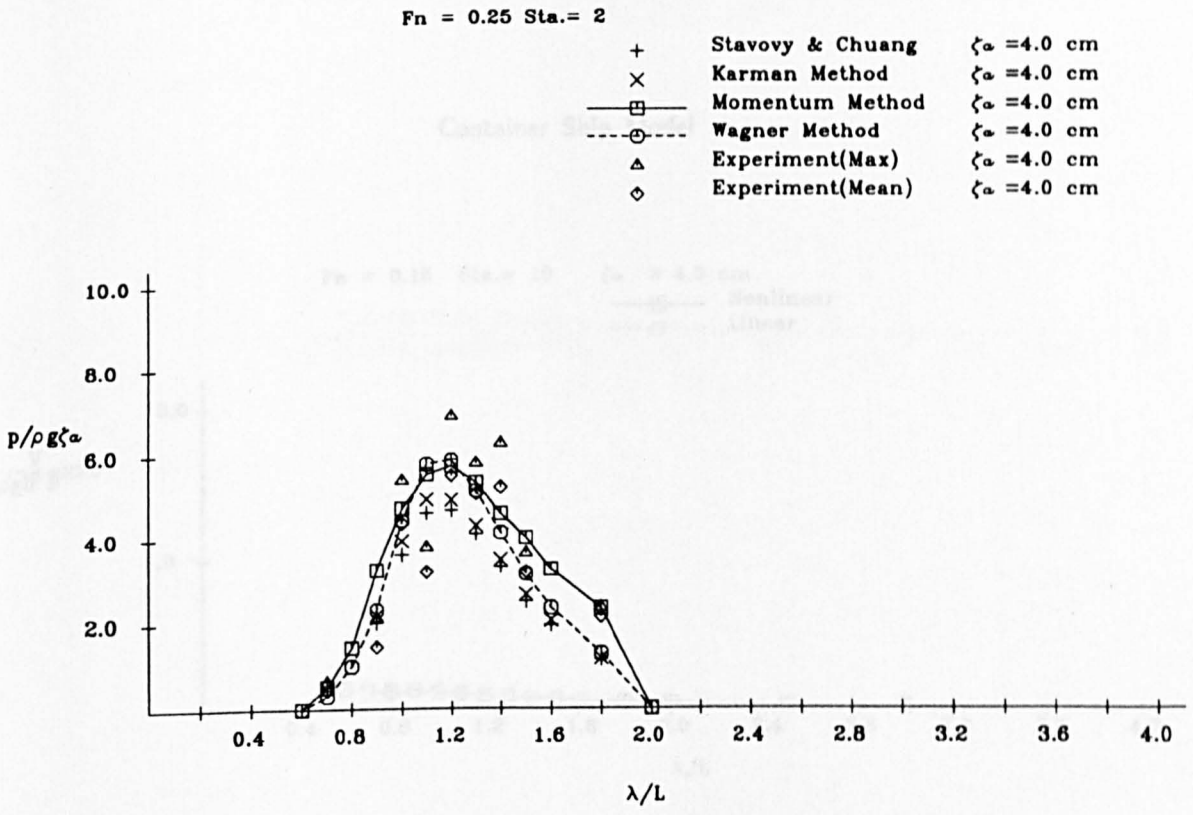

Fig.A.3.23 Bow Flare Impact Pressure Draught 20 cm

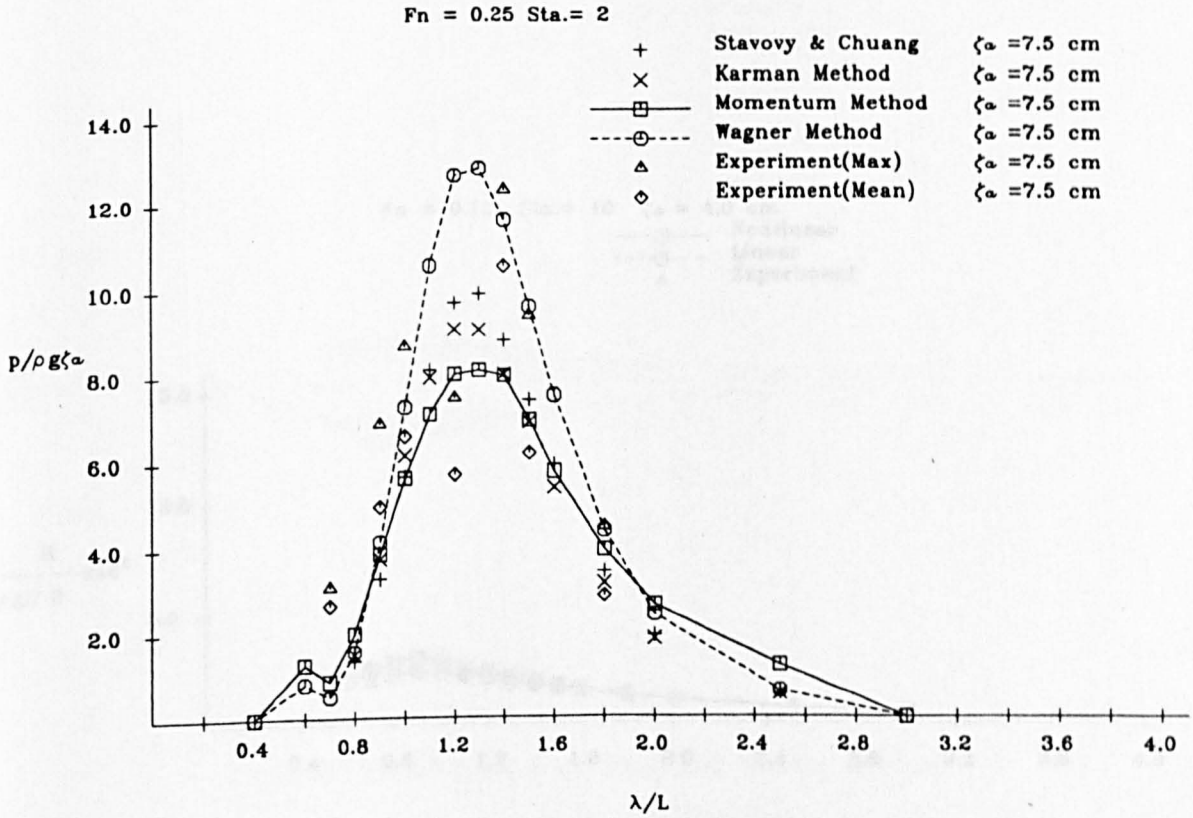

Fig.A.3.24 Bow Flare Impact Pressure Draught 20 cm

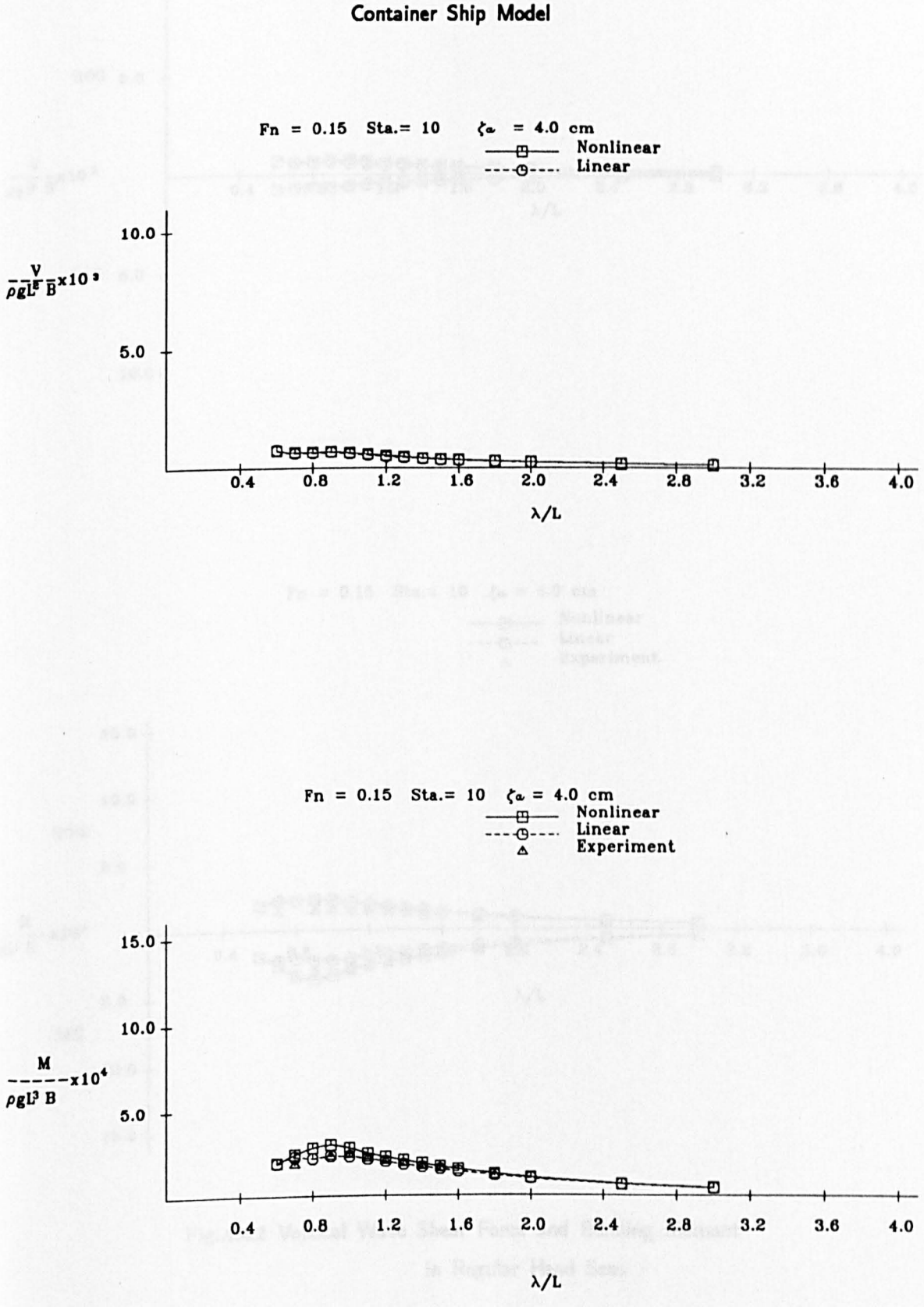

Fig.A.4.1 Vertical Wave Shear Force and Bending Moment in Regular Head Seas

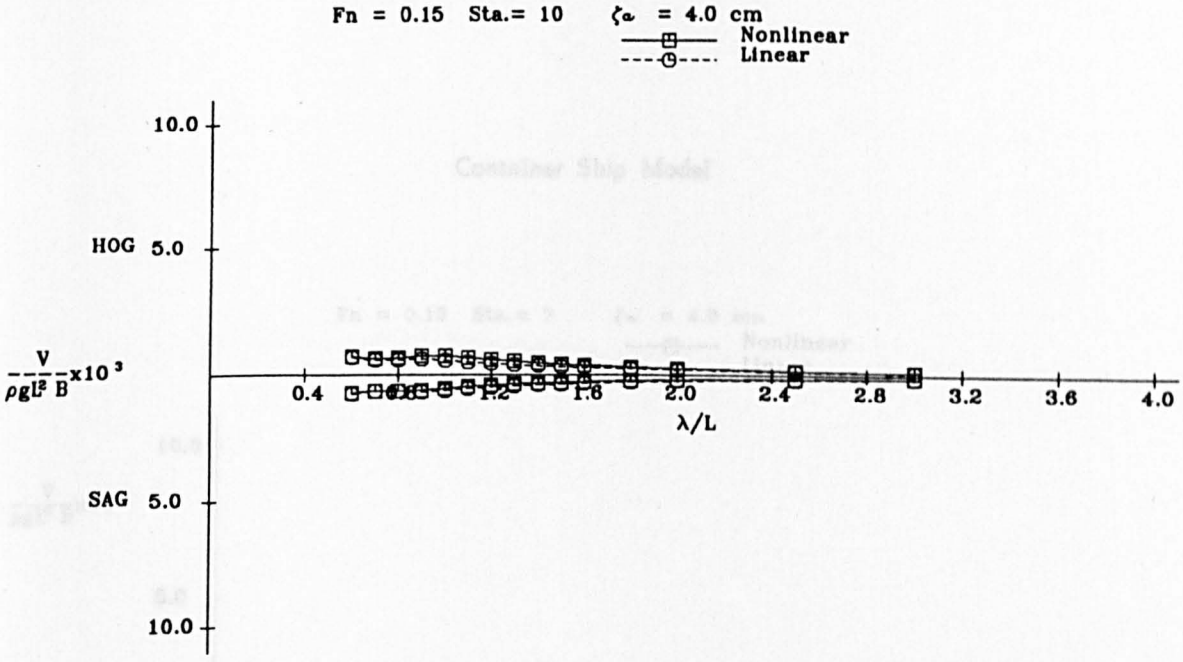

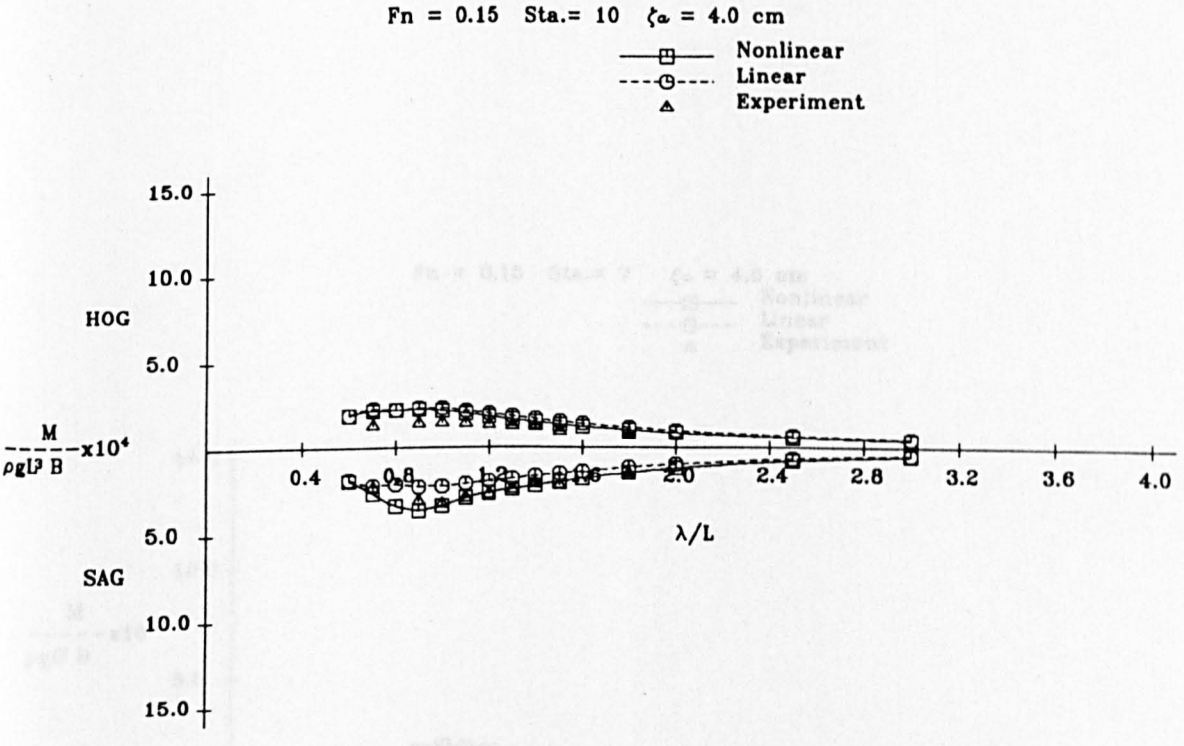

Fig.A.4.2 Vertical Wave Shear Force and Bending Moment in Regular Head Seas

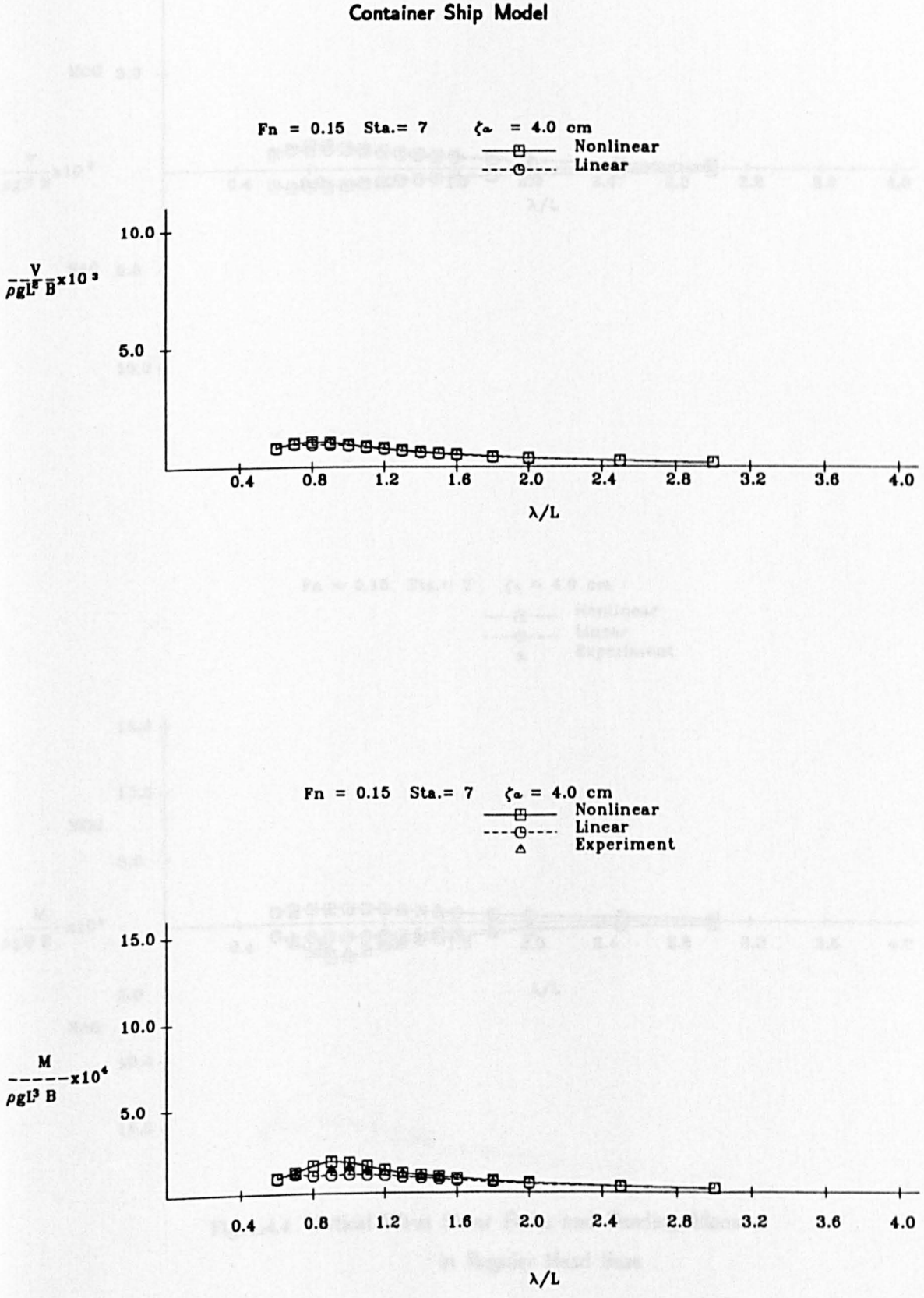

Fig.A.4.3 Vertical Wave Shear Force and Bending Moment in Regular Head Seas

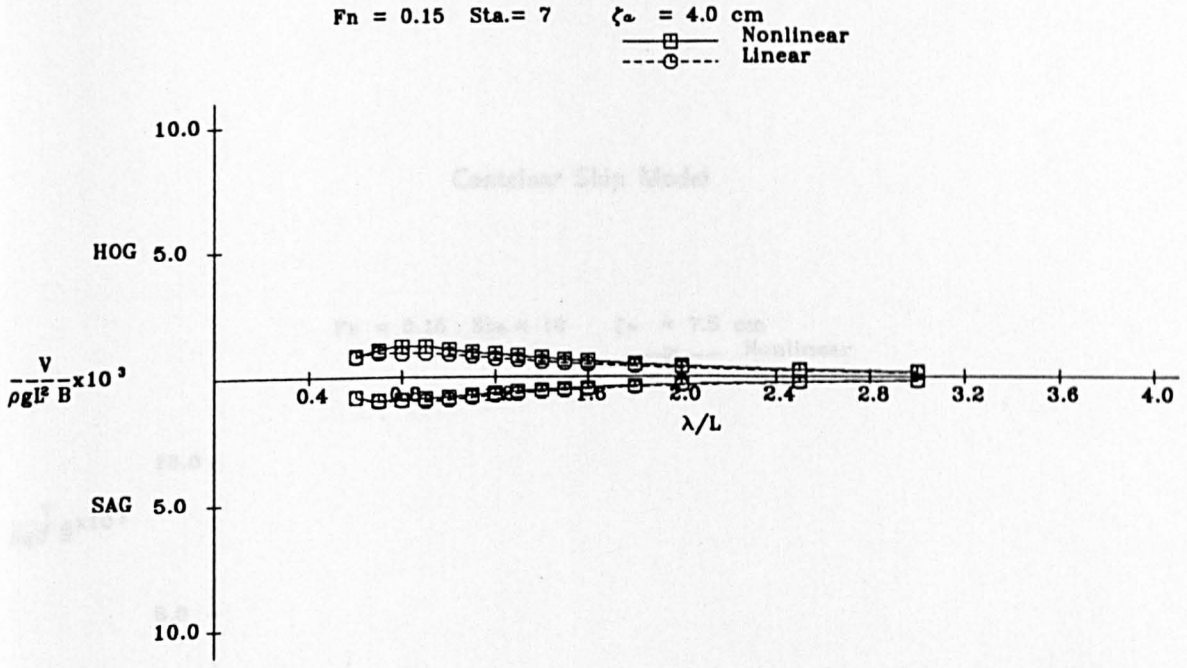

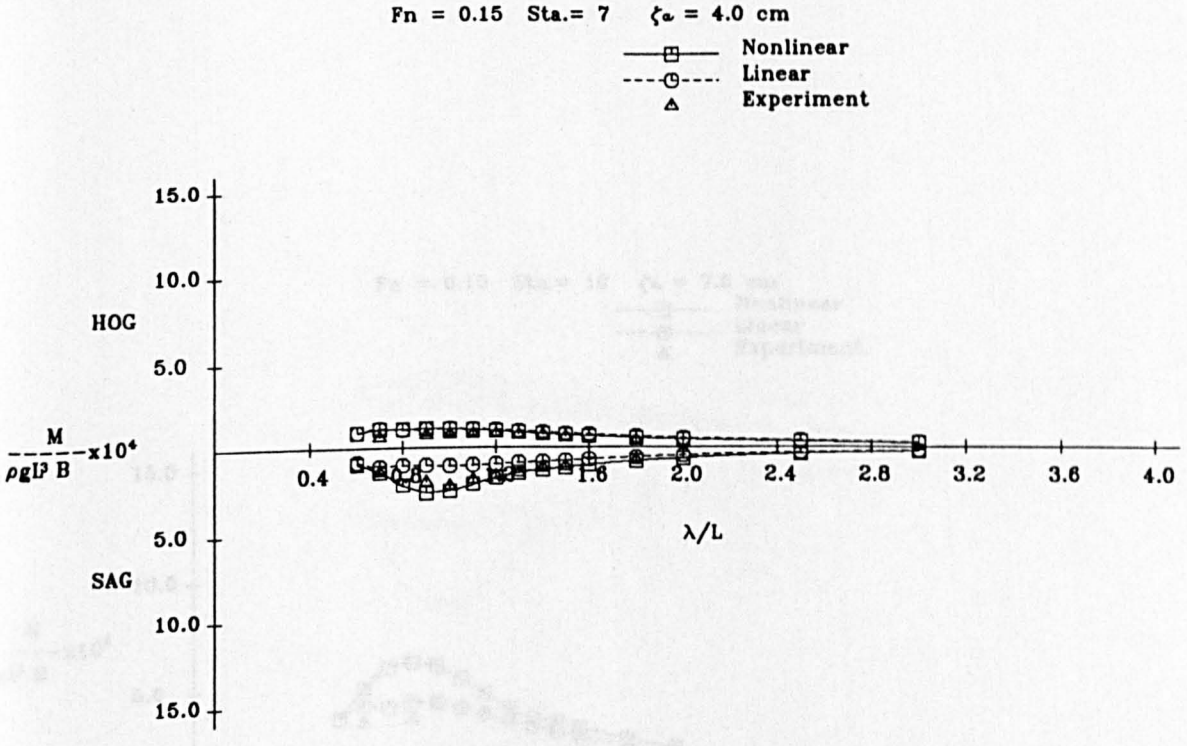

Fig.A.4.4 Vertical Wave Shear Force and Bending Moment in Regular Head Seas

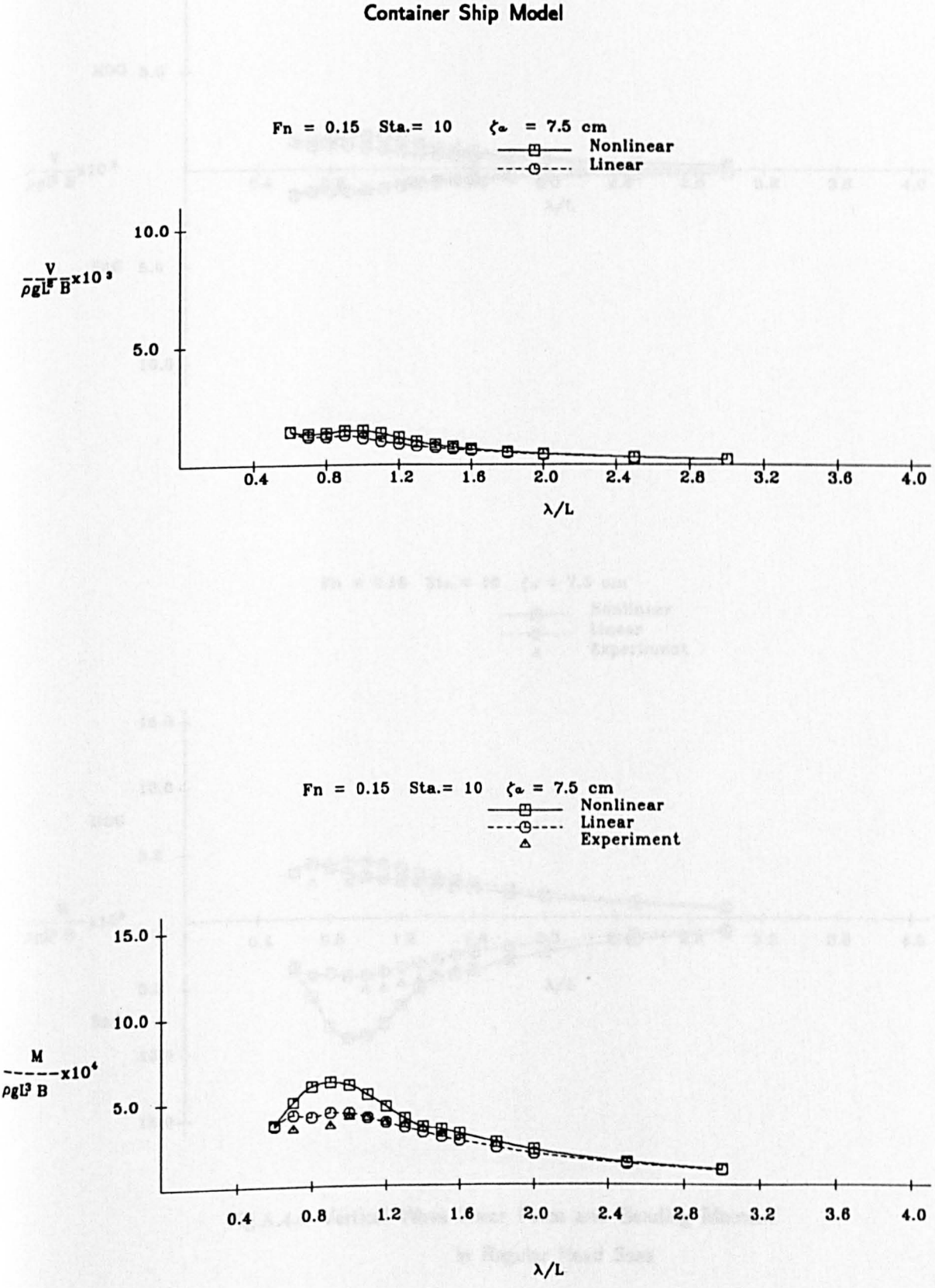

Fig.A.4.5 Vertical Wave Shear Force and Bending Moment in Regular Head Seas

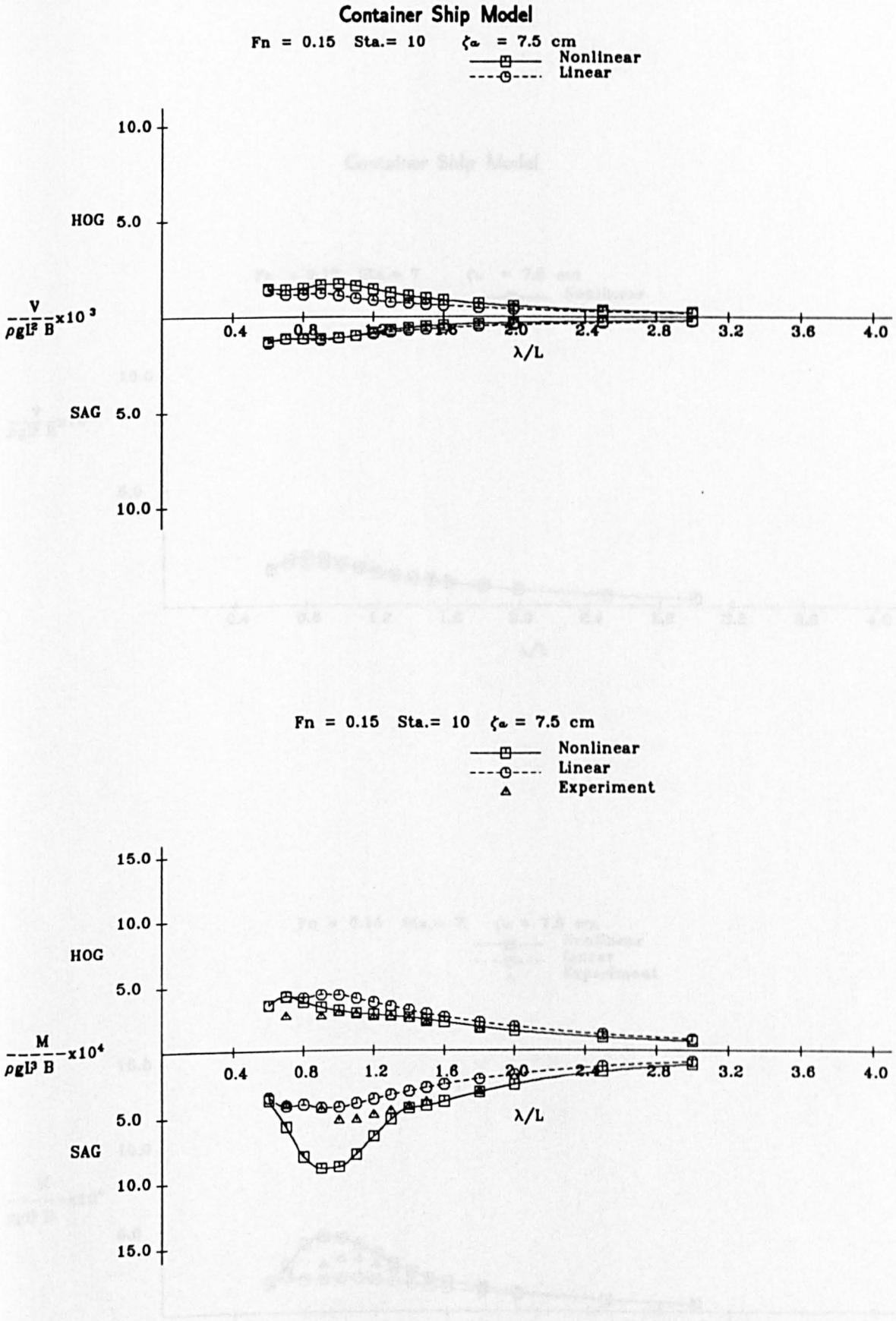

Fig.A.4.6 Vertical Wave Shear Force and Bending Moment in Regular Head Seas

Container Ship Model

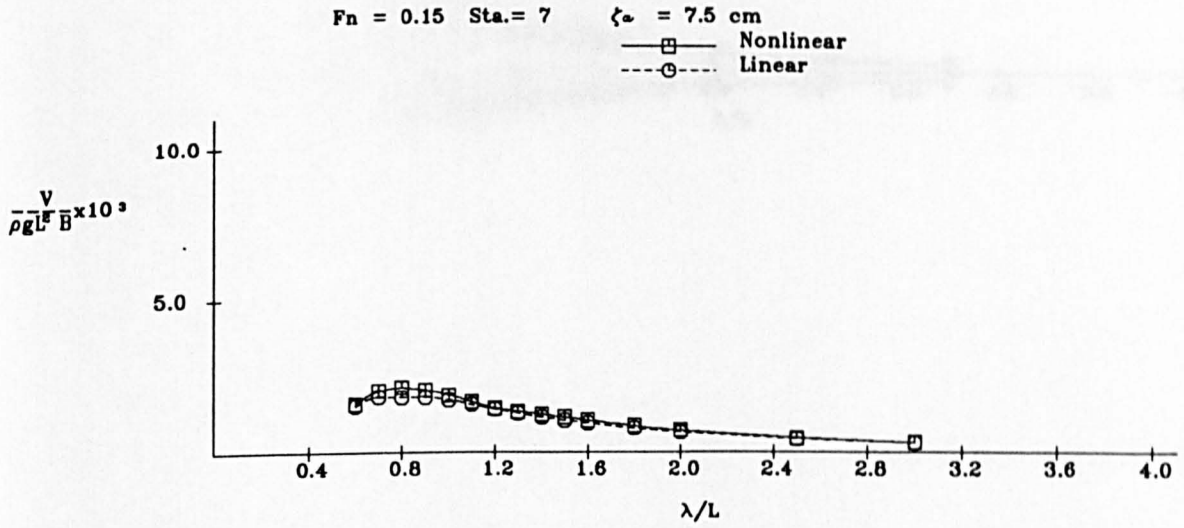

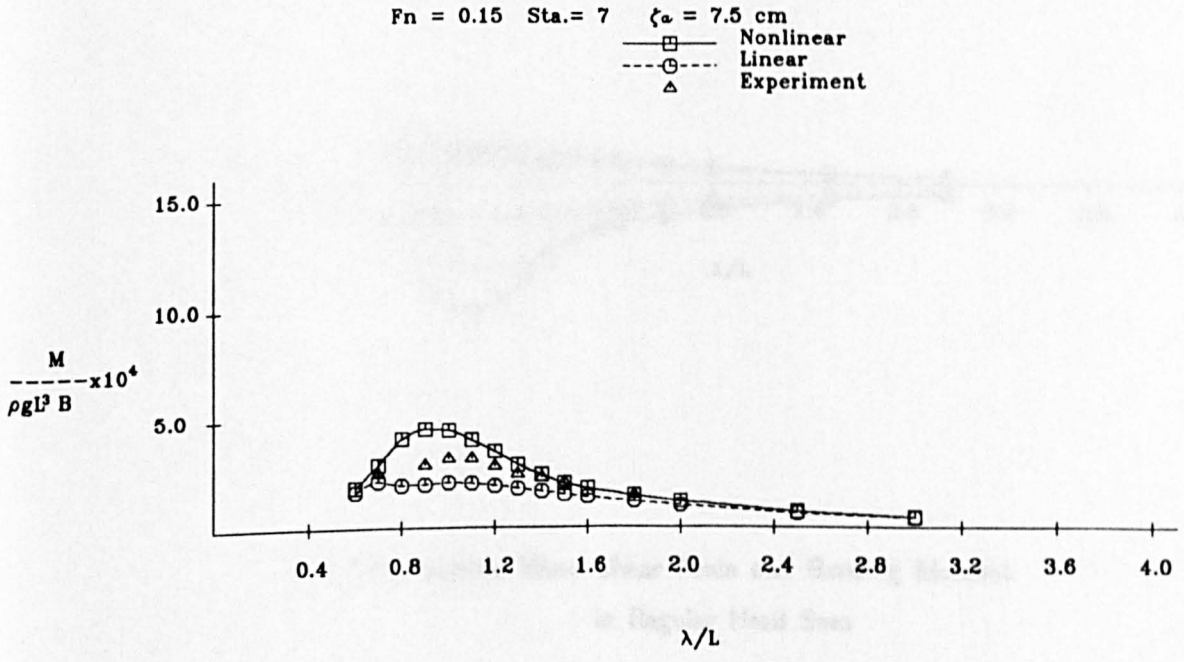

Fig.A.4.7 Vertical Wave Shear Force and Bending Moment in Regular Head Seas

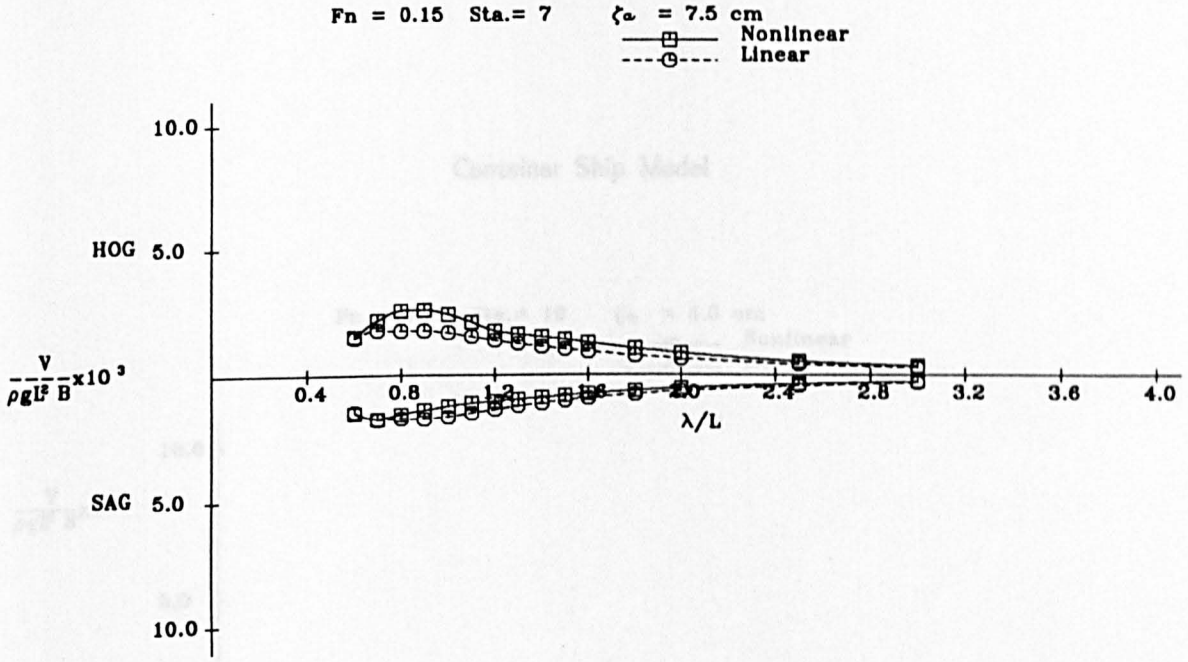

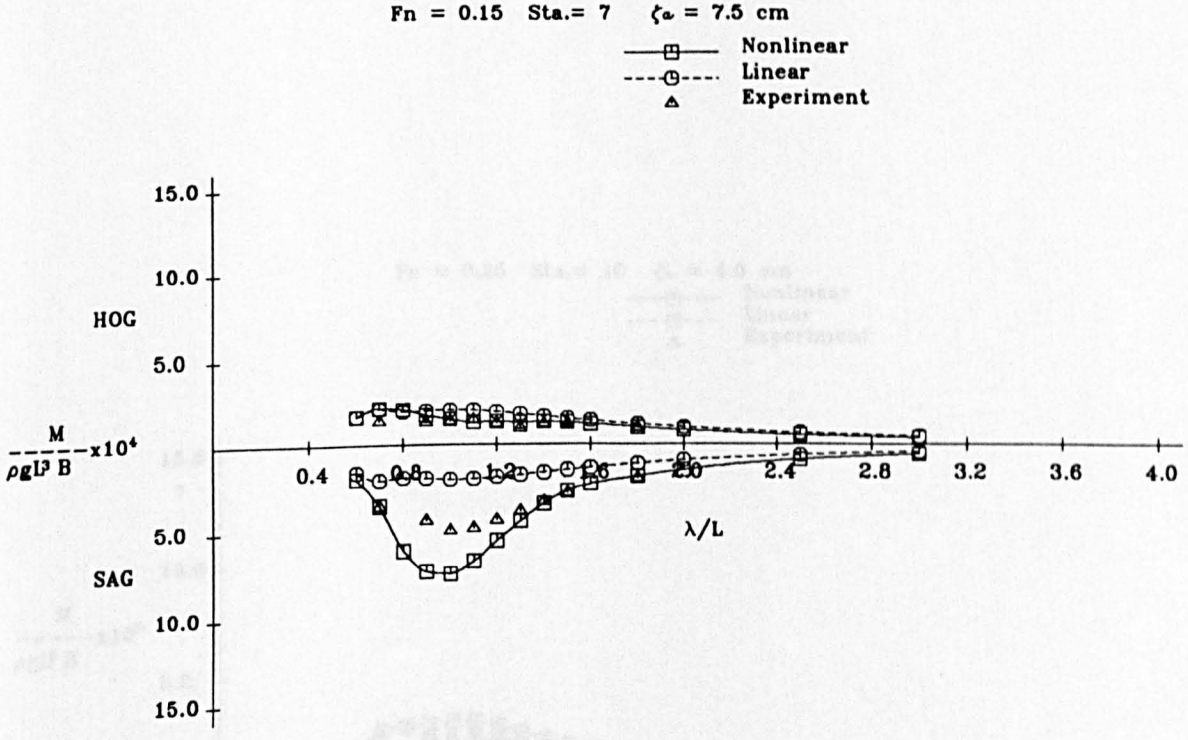

Fig.A.4.8 Vertical Wave Shear Force and Bending Moment in Regular Head Seas

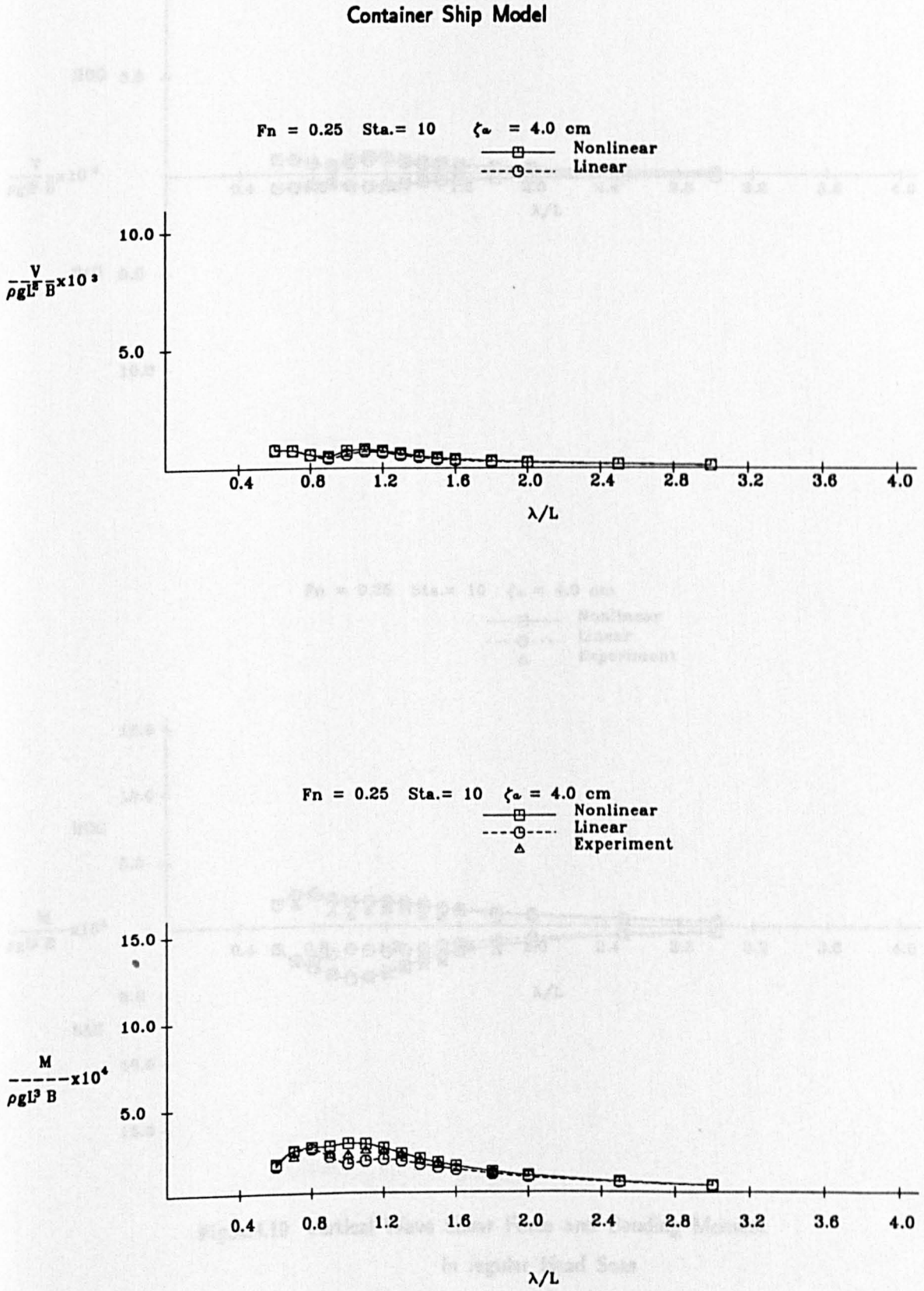

Fig.A.4.9 Vertical Wave Shear Force and Bending Moment in Regular Head Seas

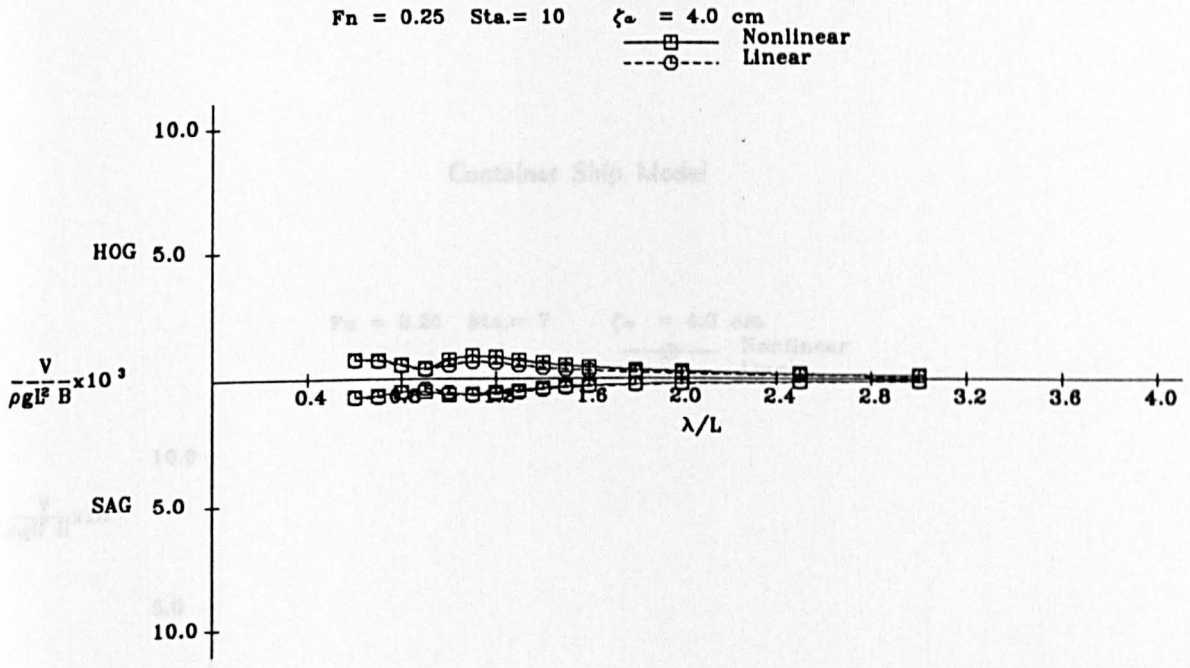

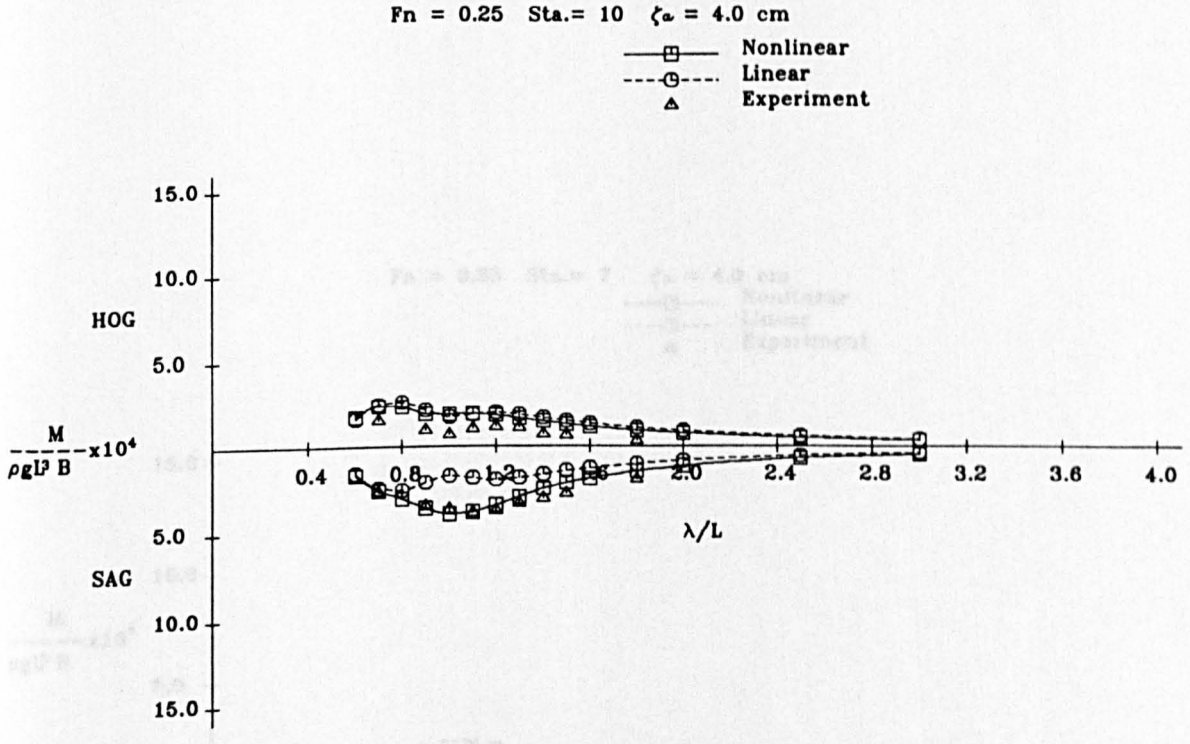

Fig.A.4.10 Vertical Wave Shear Force and Bending Moment in regular Head Seas

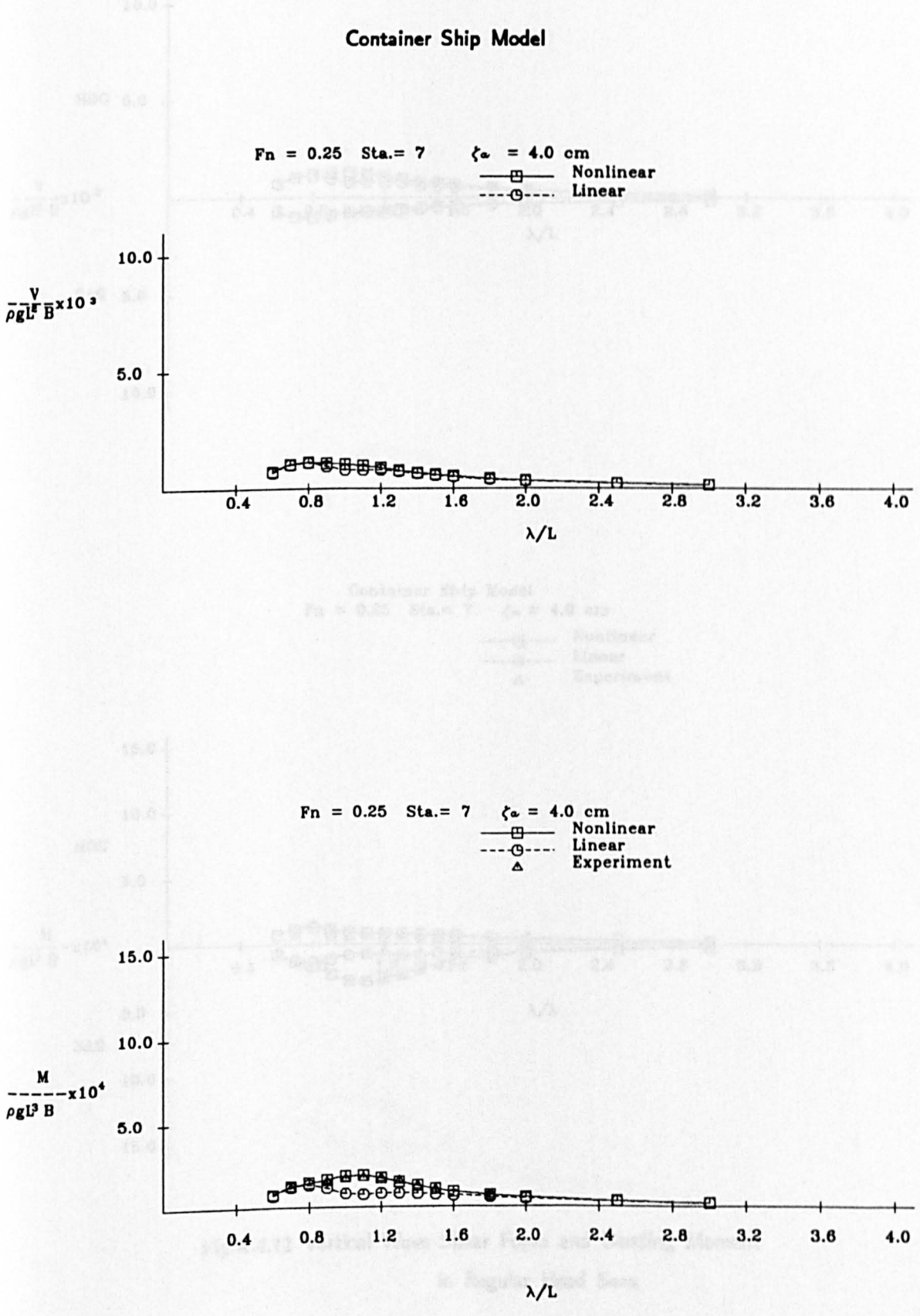

Fig.A.4.11 Vertical Wave Shear Force and Bending Moment in Regular Head Seas

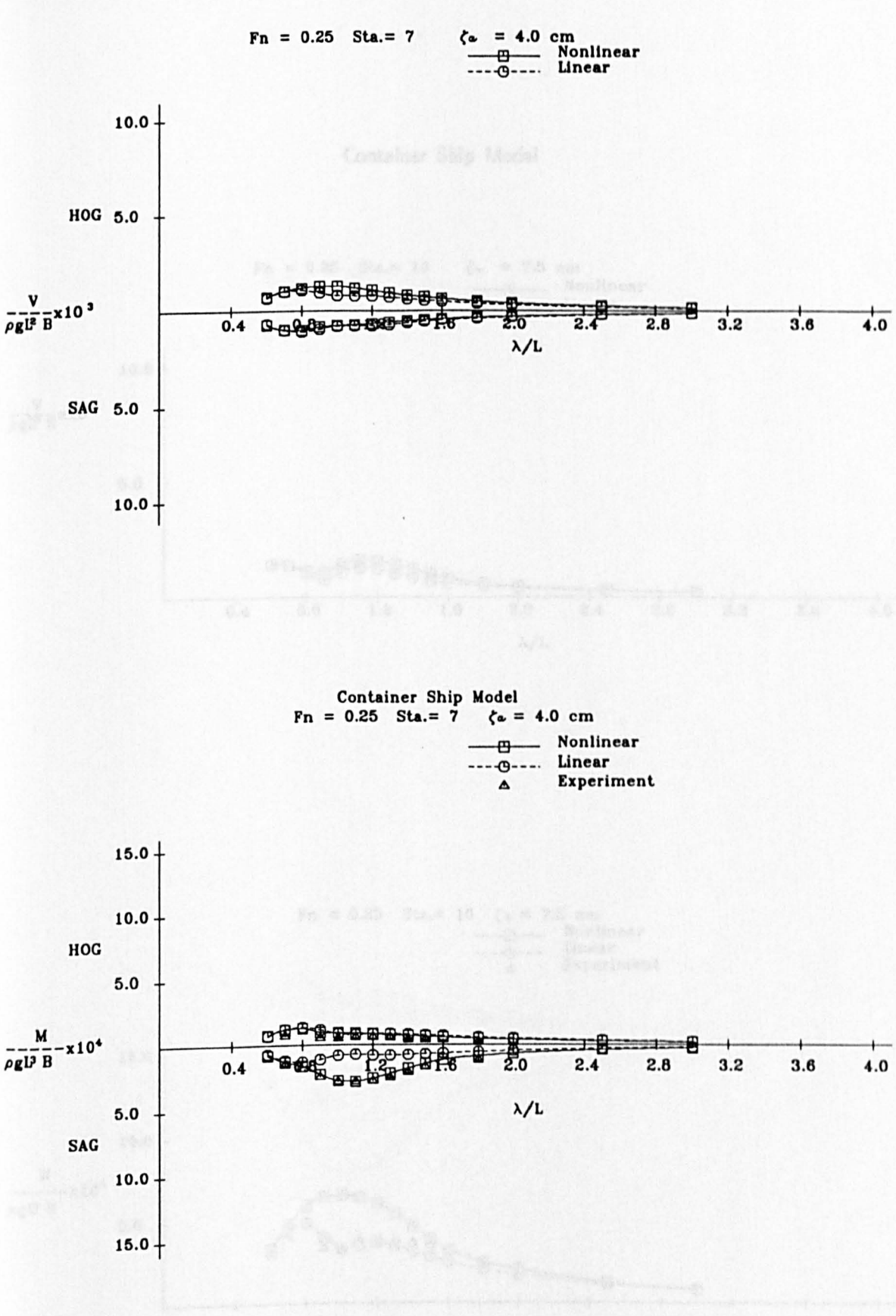

Fig.A.4.12 Vertical Wave Shear Force and Bending Moment in Regular Head Seas

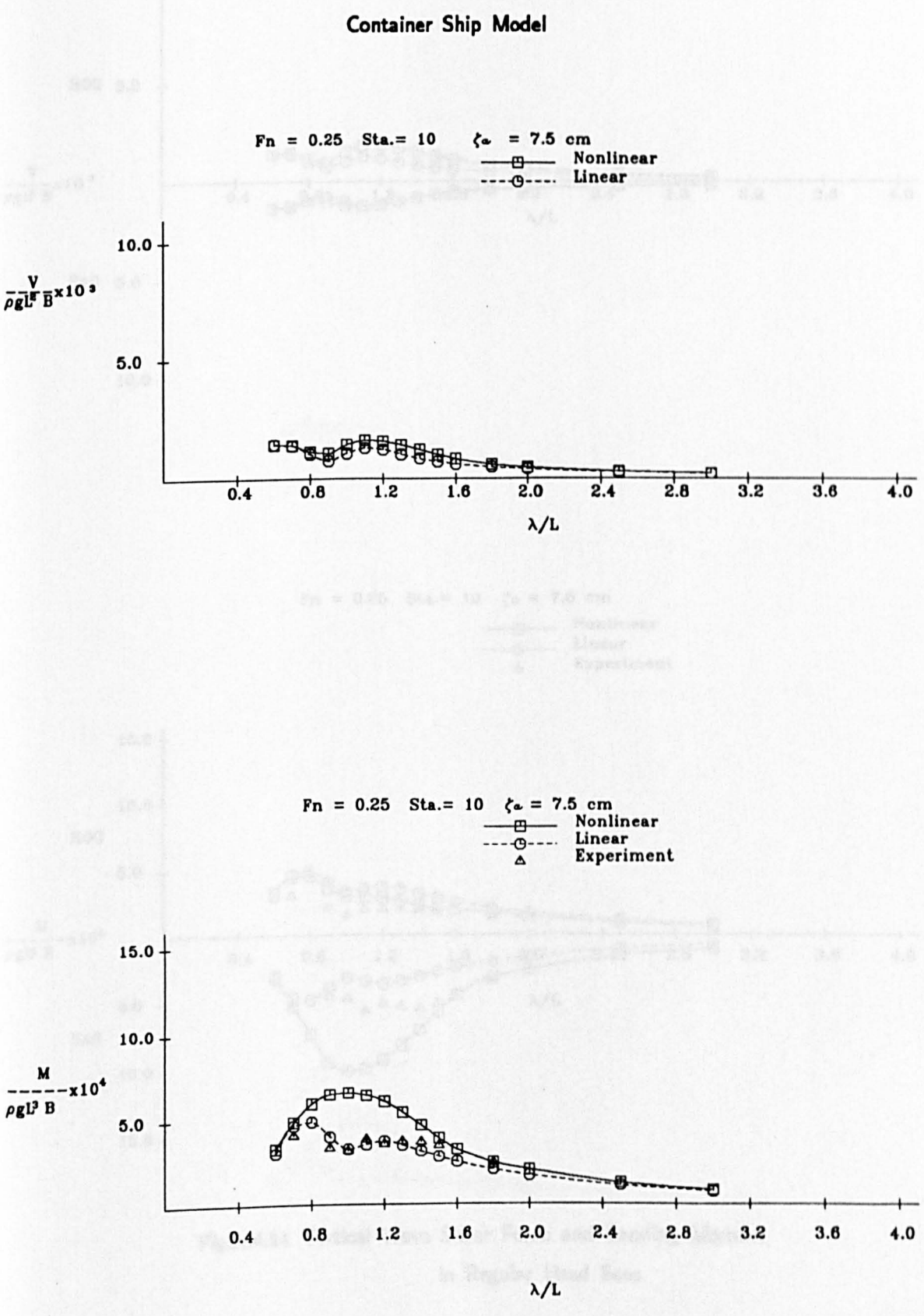

Fig.A.4.13 Vertical Wave Shear Force and Bending Moment in Regular Head Seas

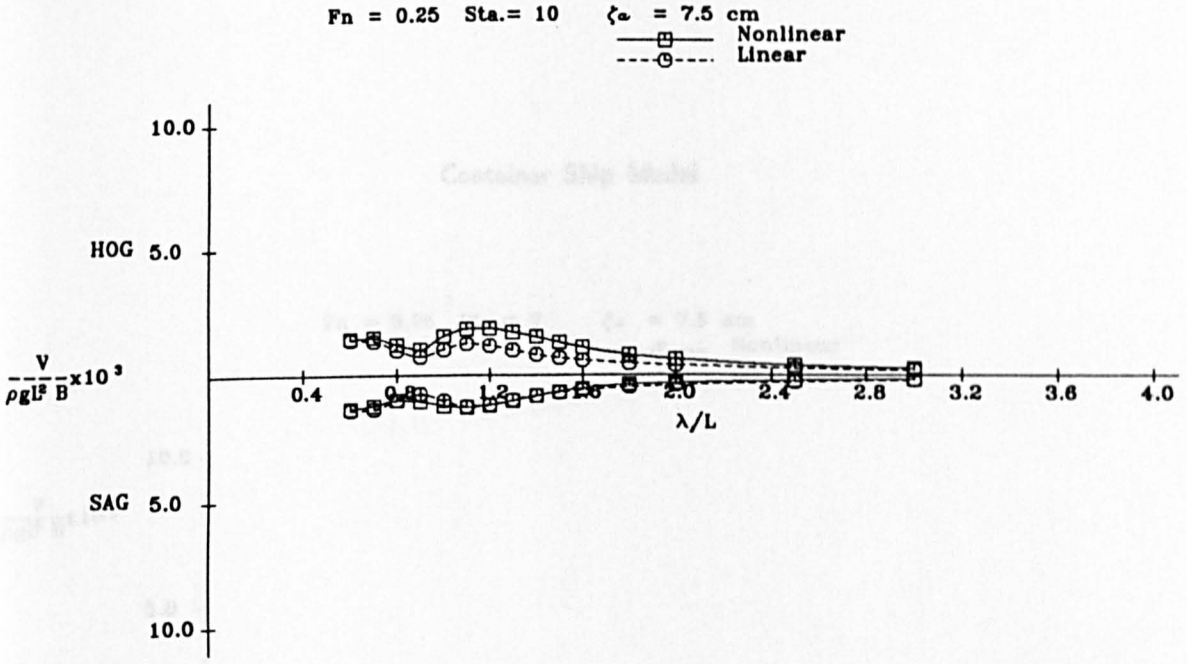

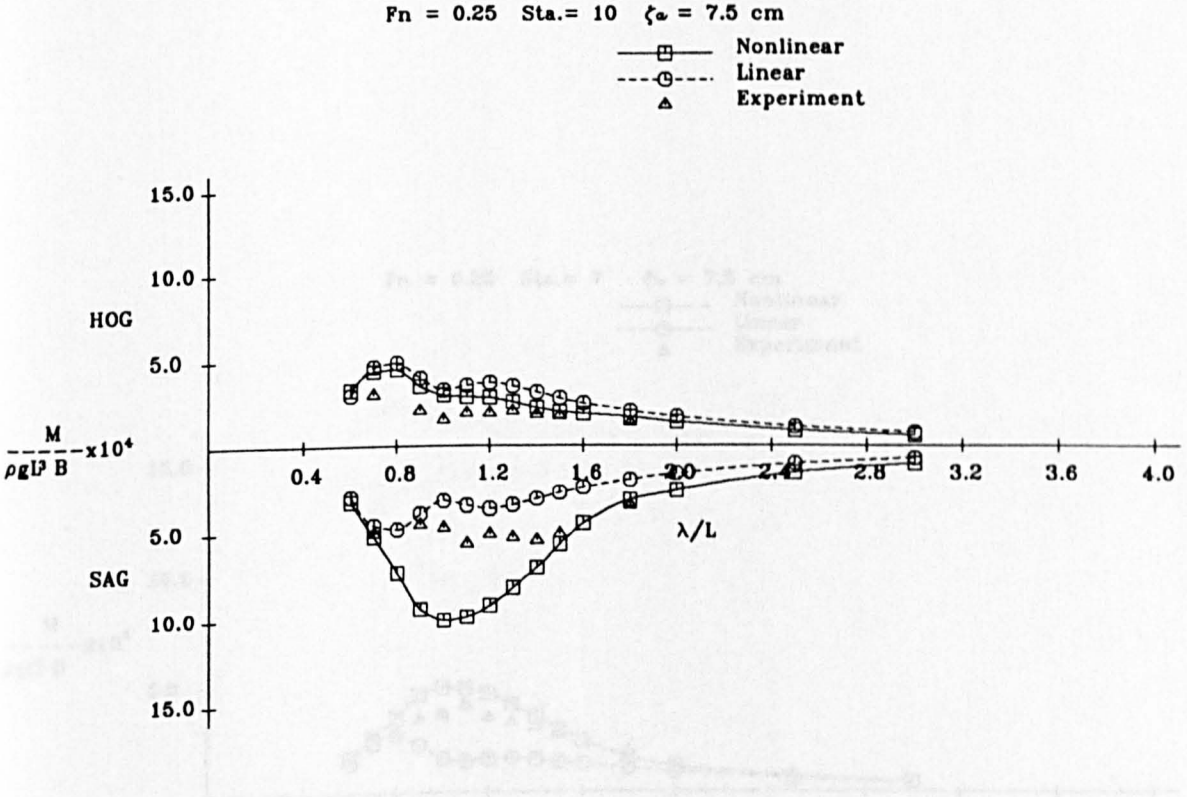

Fig.A.4.14 Vertical Wave Shear Force and Bending Moment in Regular Head Seas

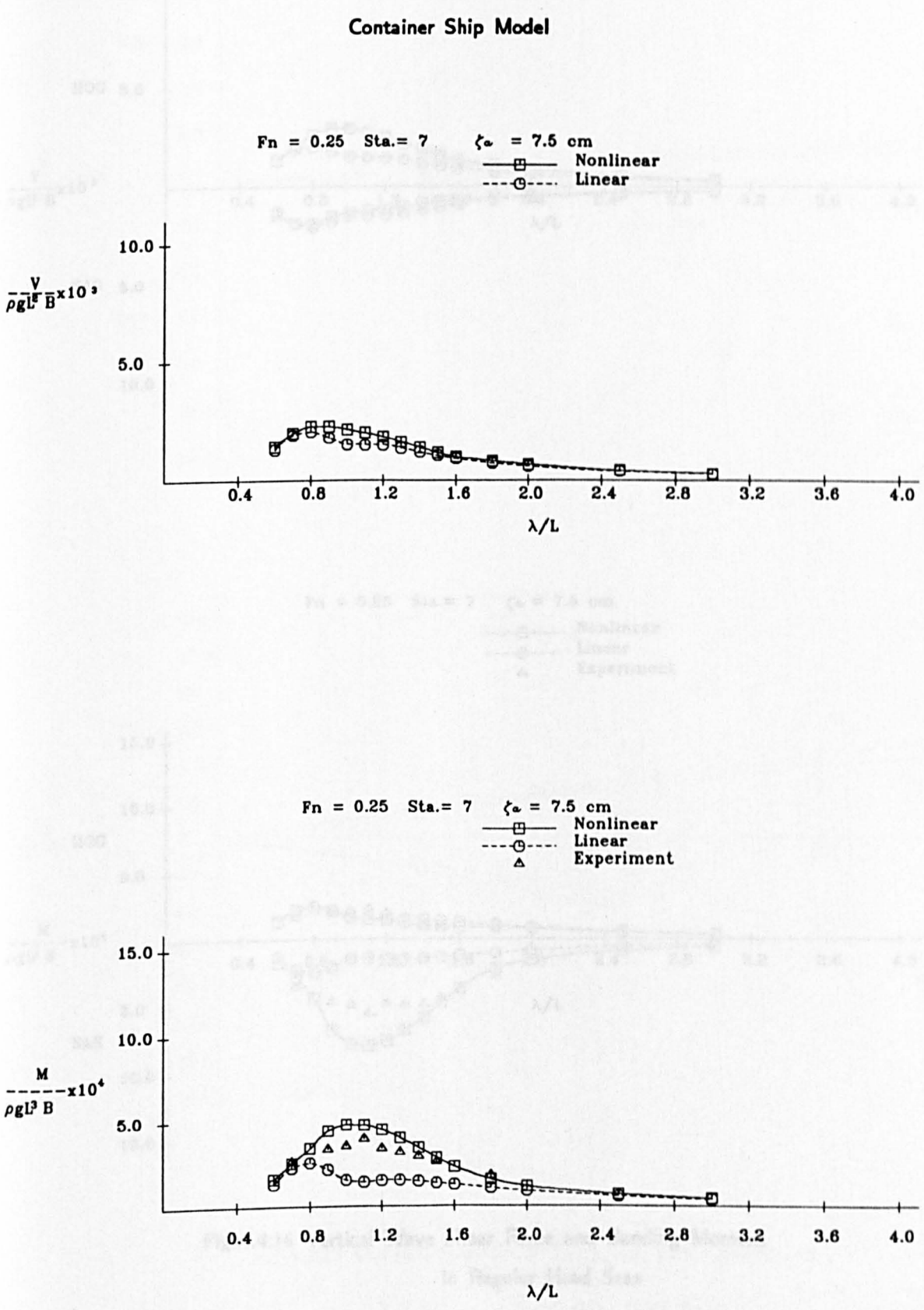

Fig.A.4.15 Vertical Wave Shear Force and Bending Moment in Regular Head Seas

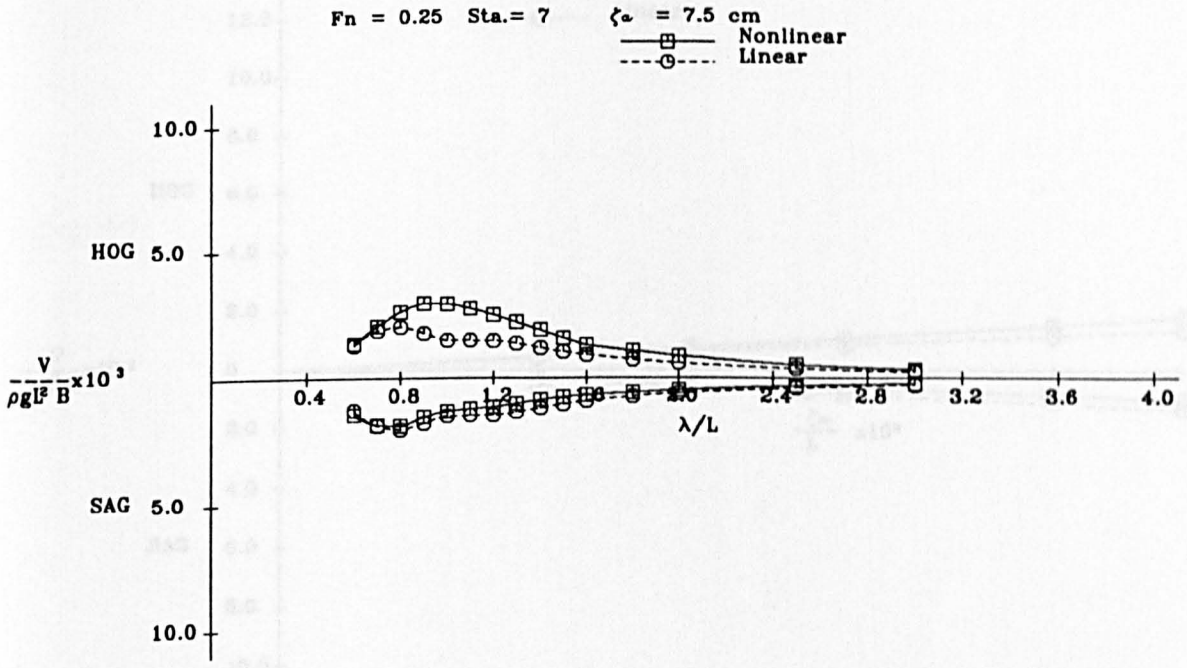

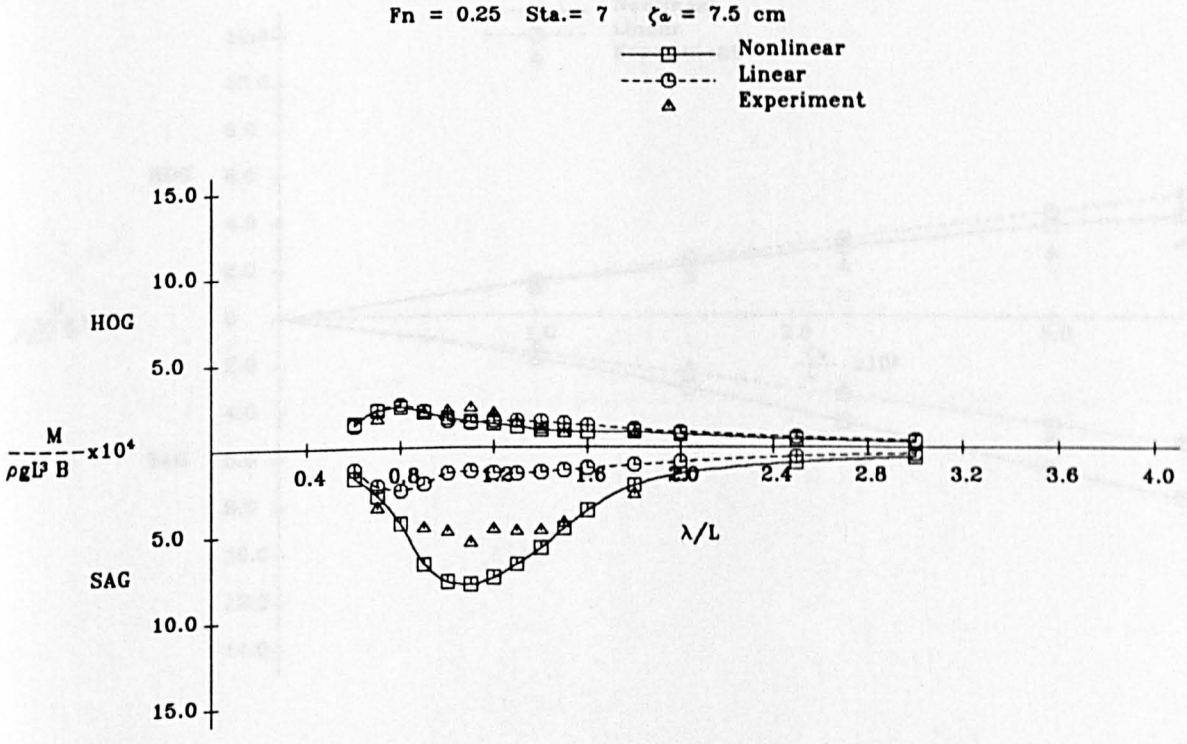

Fig.A.4.16 Vertical Wave Shear Force and Bending Moment in Regular Head Seas

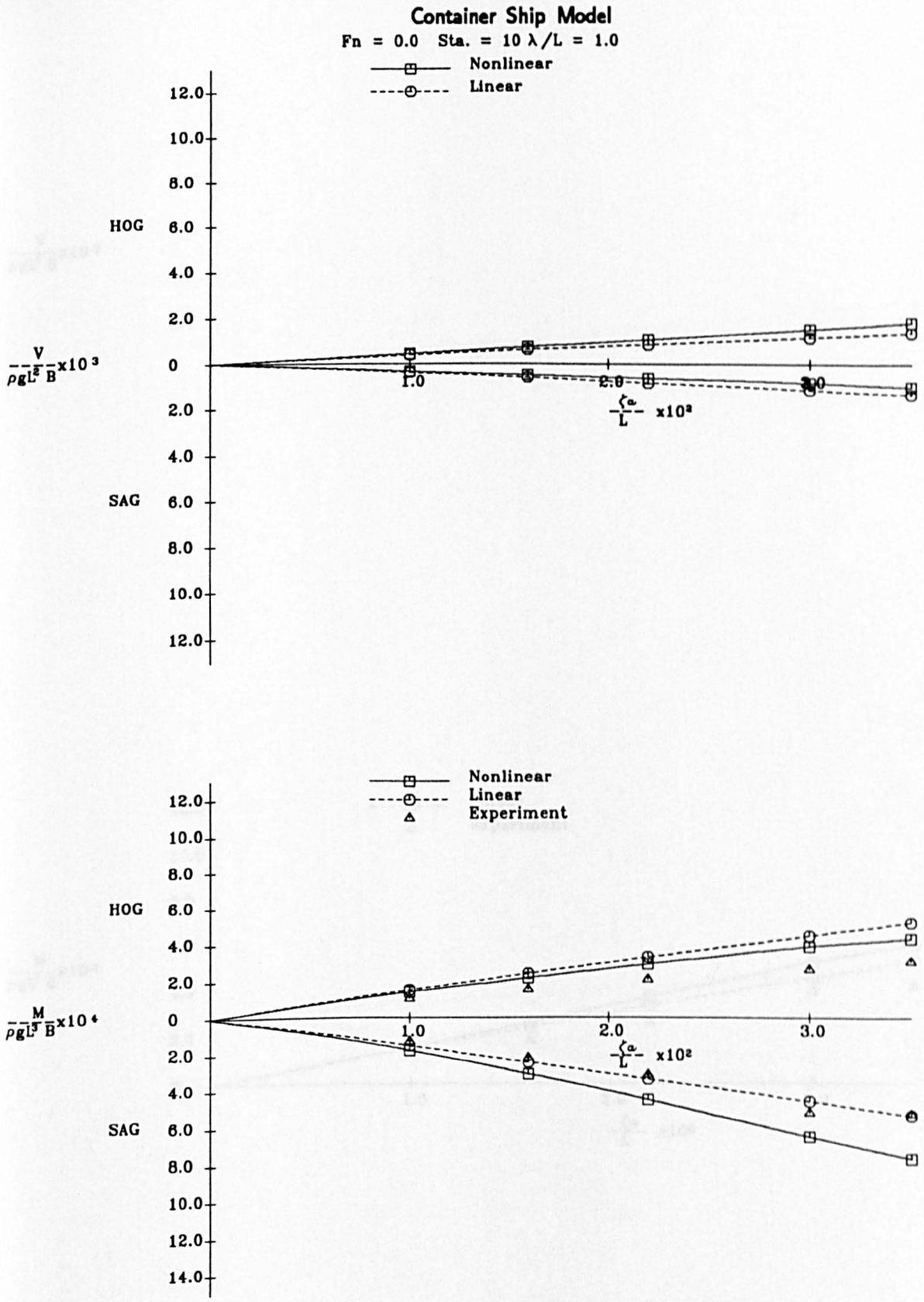

Fig.A.4.17 Vertical Wave Shear Force and Bending Moment in Regular Head Seas

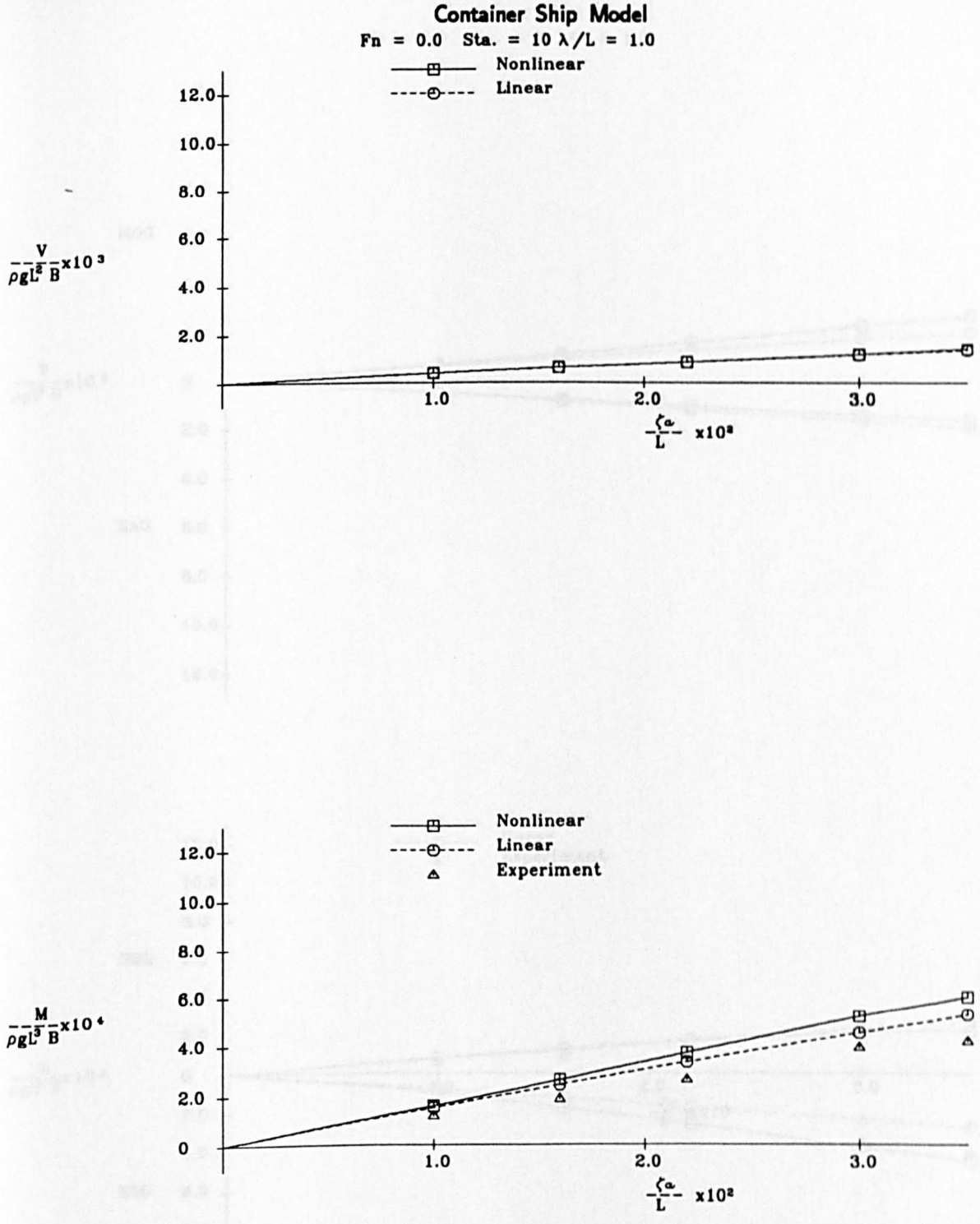

Fig.A.4.18 Vertical Wave Shear Force and Bending Moment in Regular Head Seas

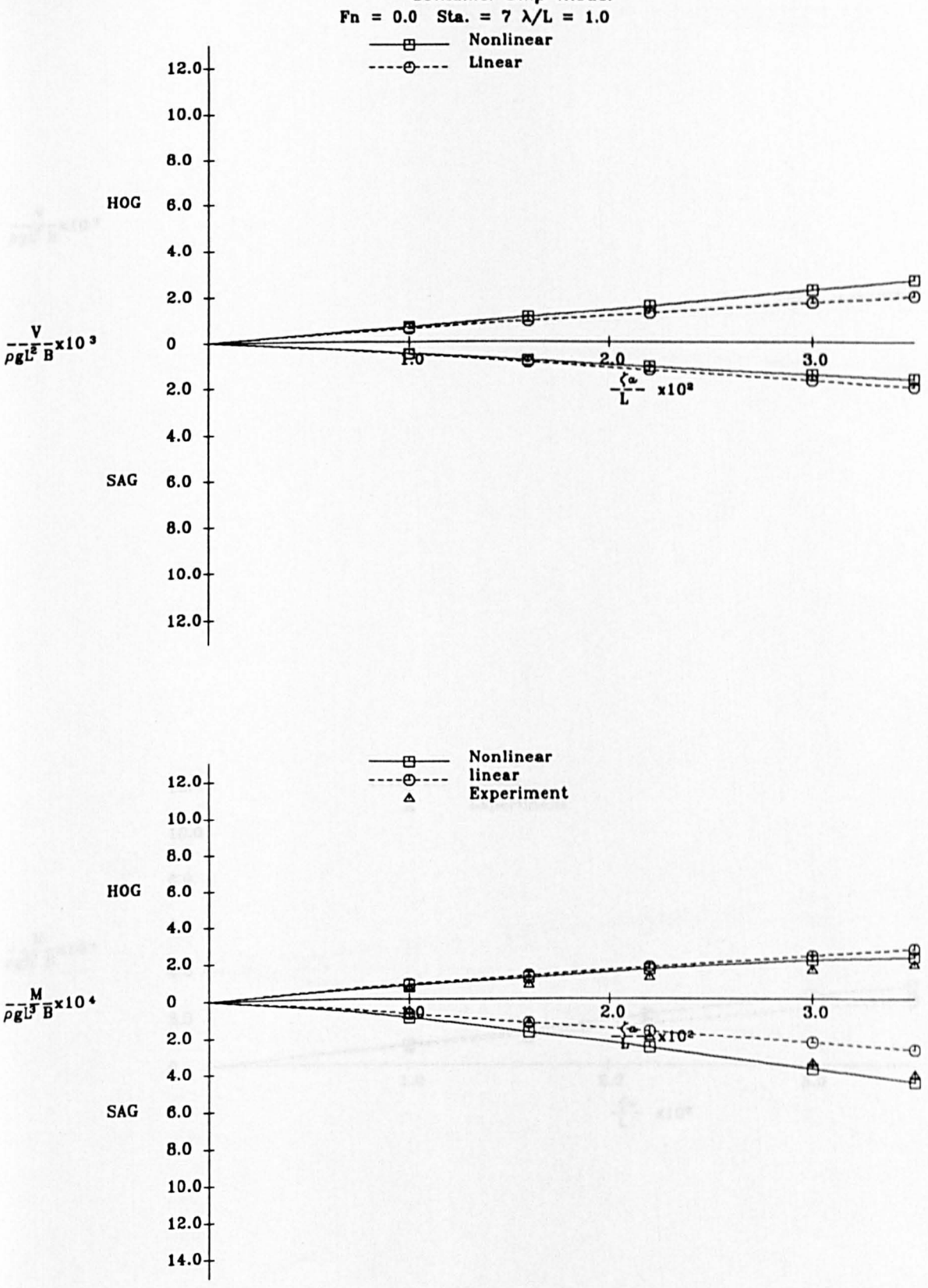

Fig.A.4.19 Vertical Wave Shear Force and Bending Moment in Regular Head Seas

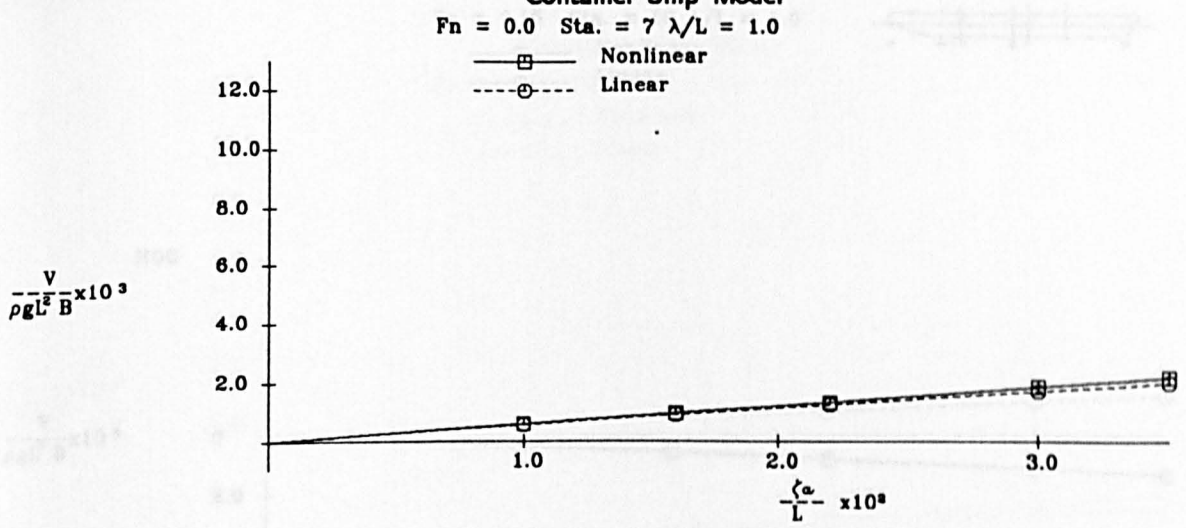

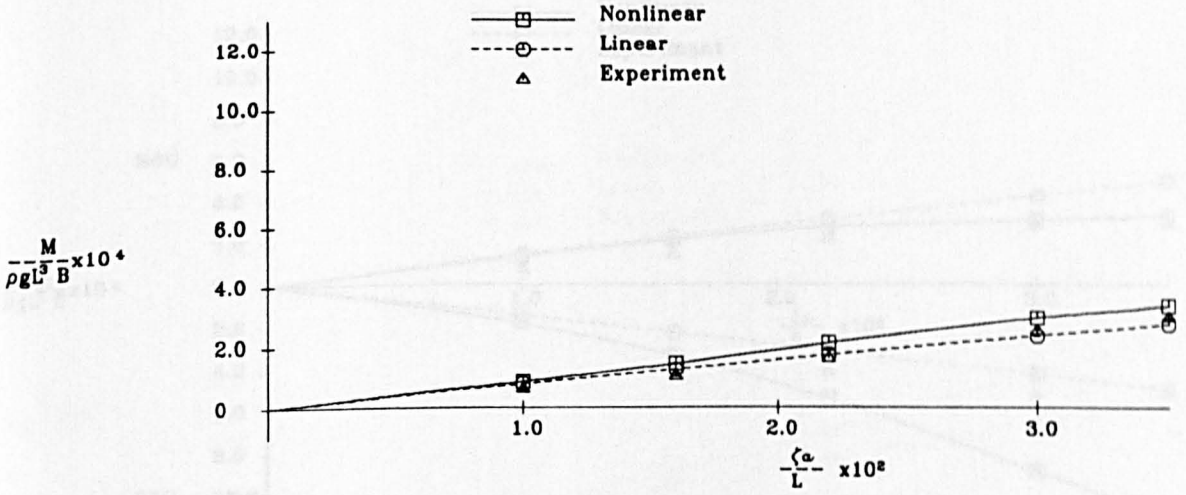

Fig.A.4.20 Vertical Wave Shear Force and Bending Moment in Regular Head Seas

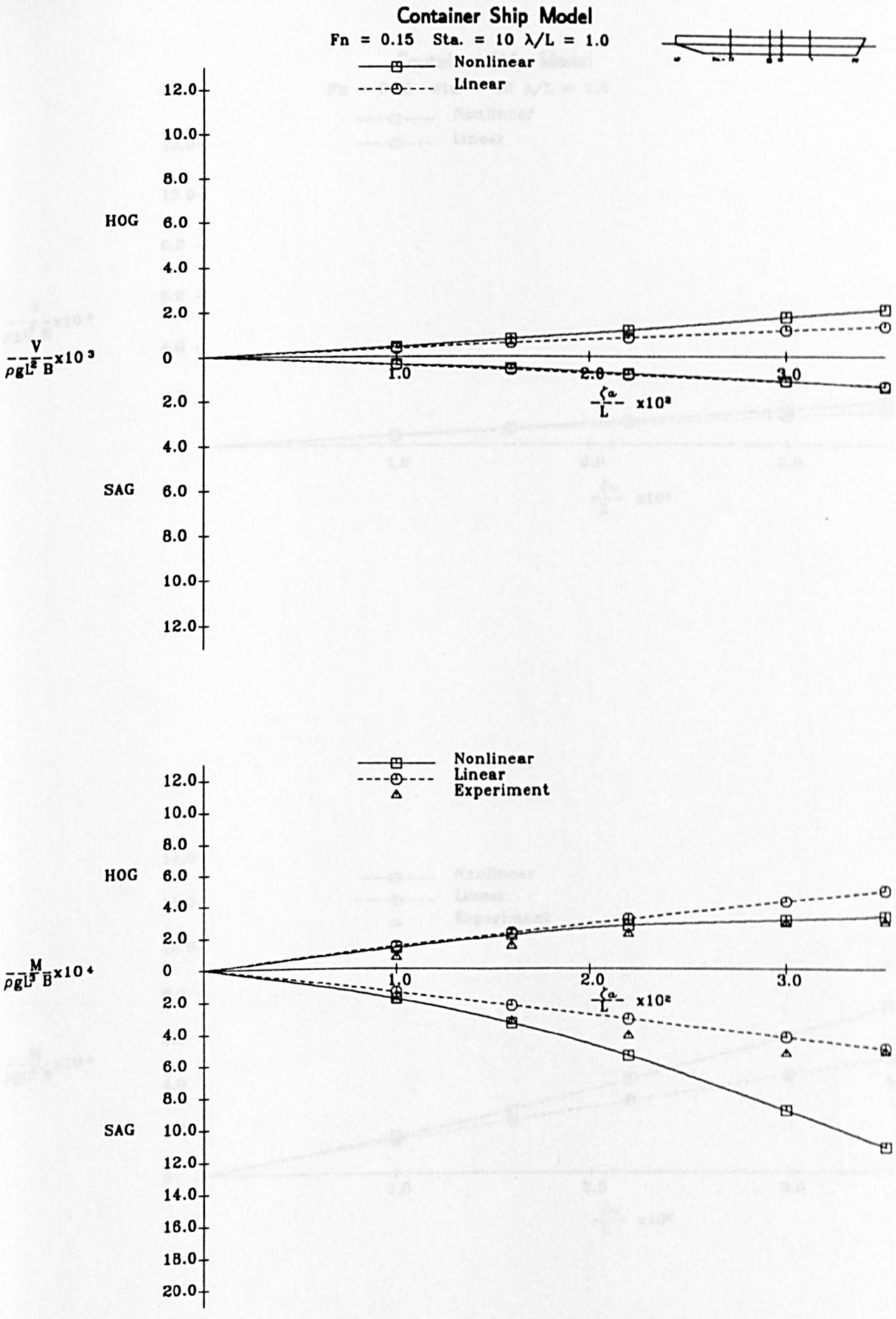

Fig.A.4.21 Vertical Wave Shear Force and Bending Moment in Regular Head Seas

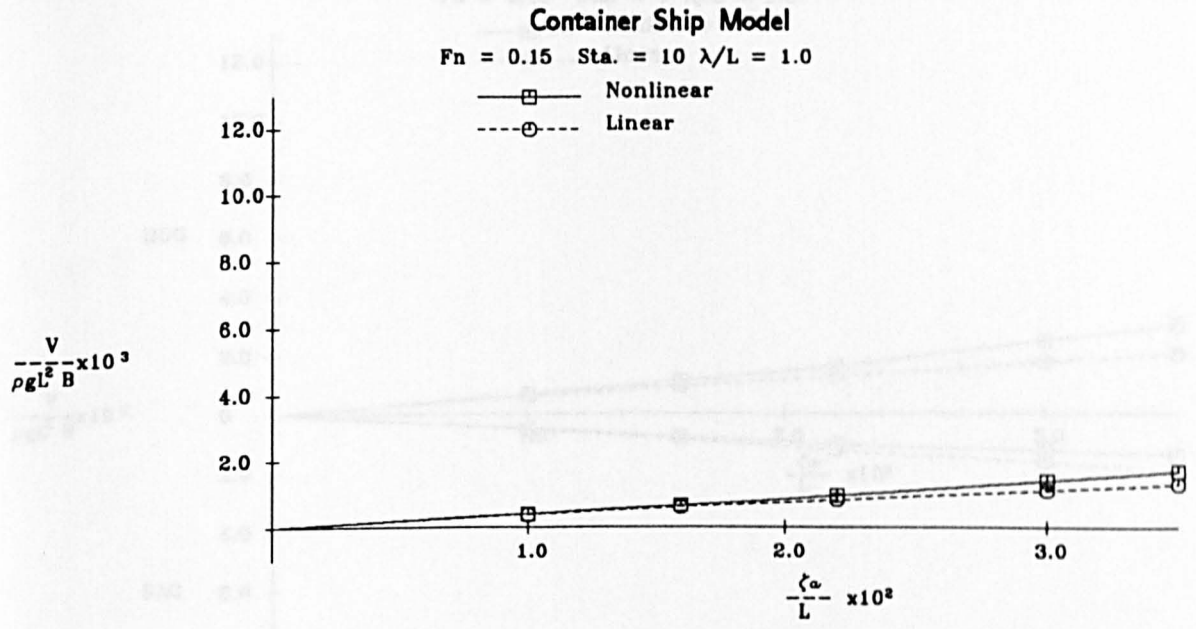

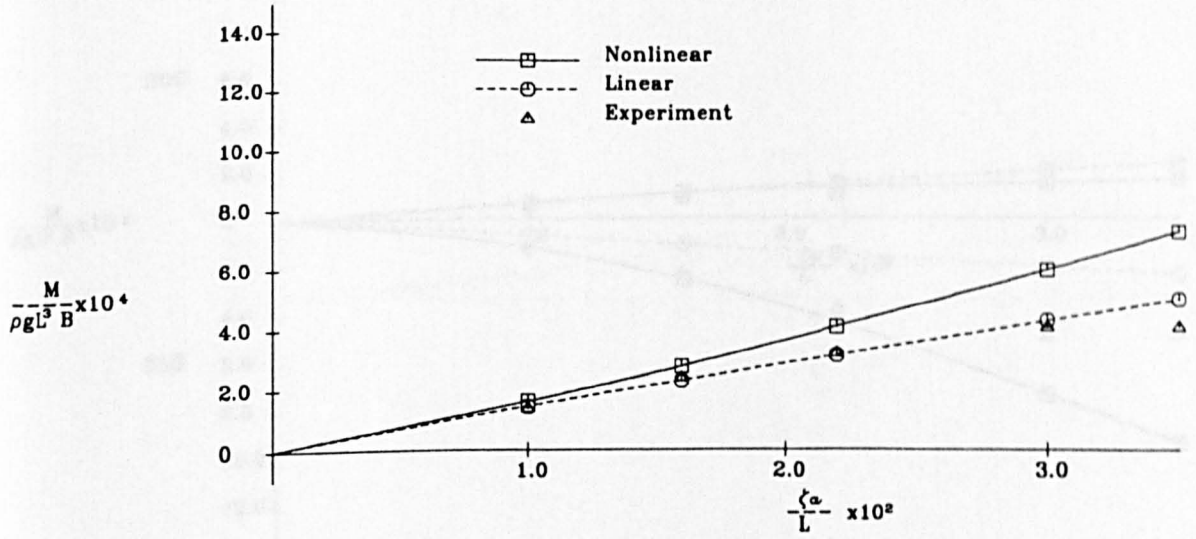

Fig.A.4.22 Vertical Wave Shear Force and Bending Moment in Regular Head Seas

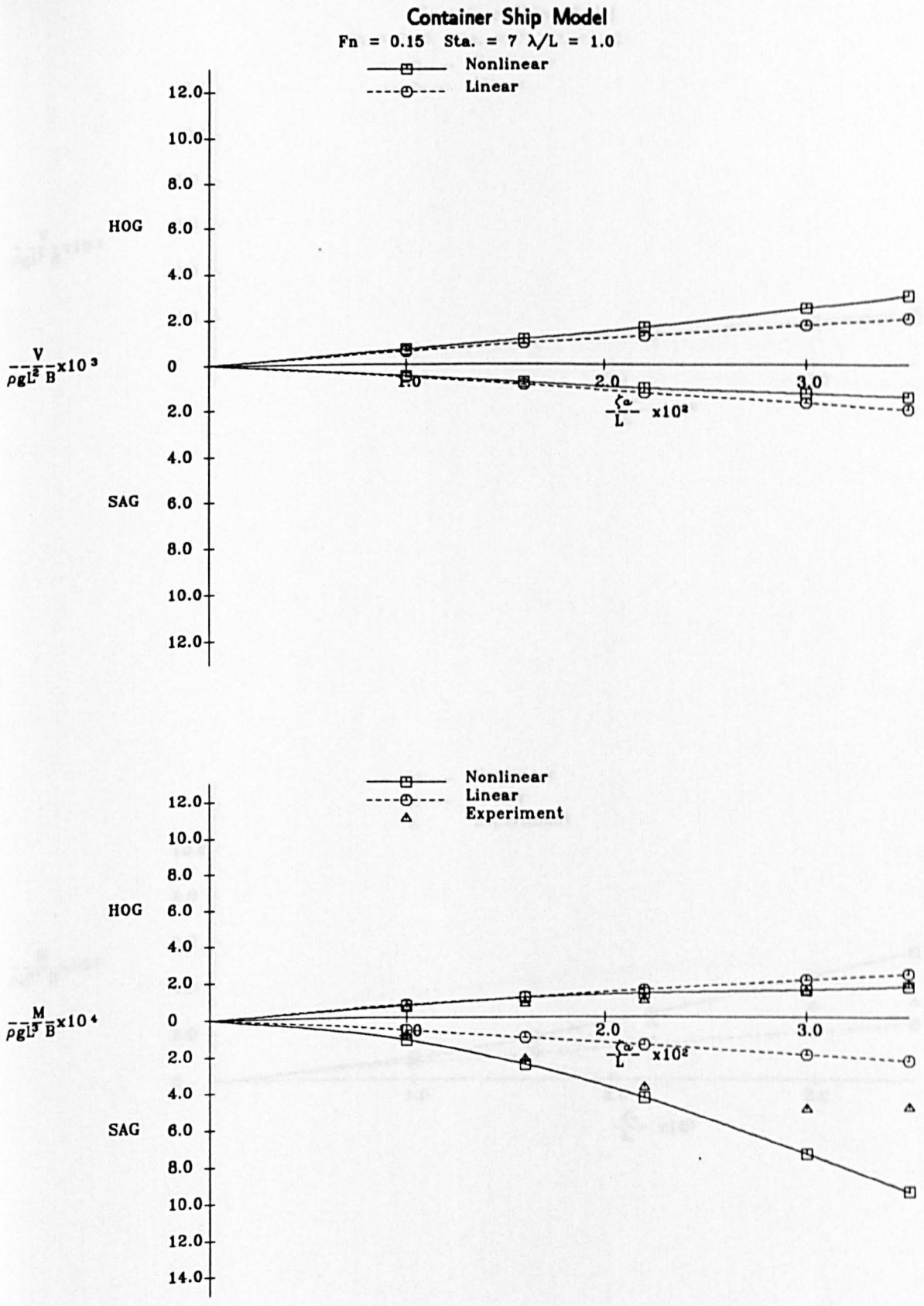

Fig.A.4.23 Vertical Wave Shear Force and Bending Moment

in Regular Head Seas

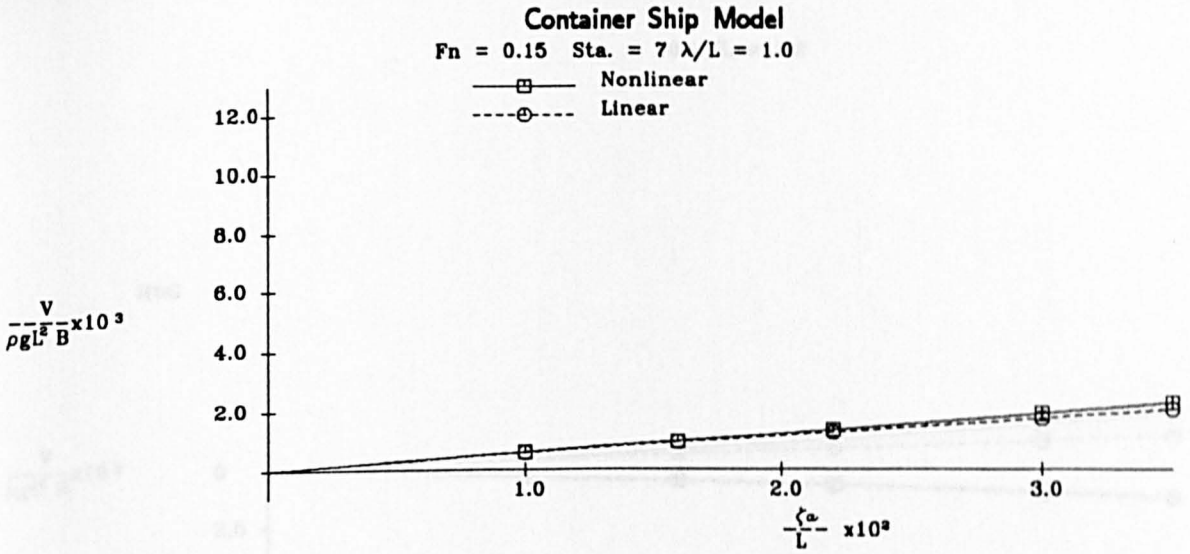

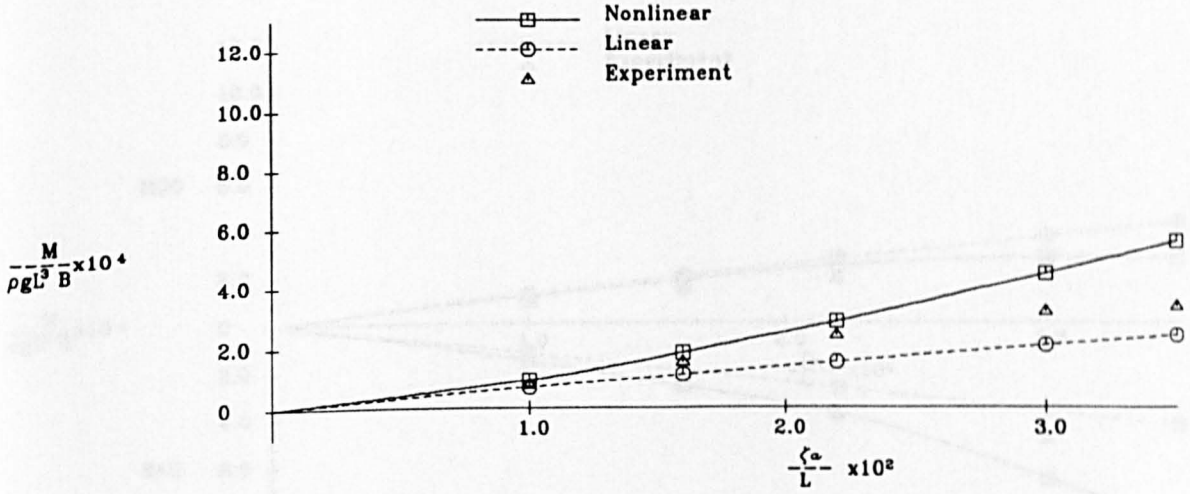

Fig.A.4.24 Vertical Wave Shear Force and Bending Moment in Regular Head Seas

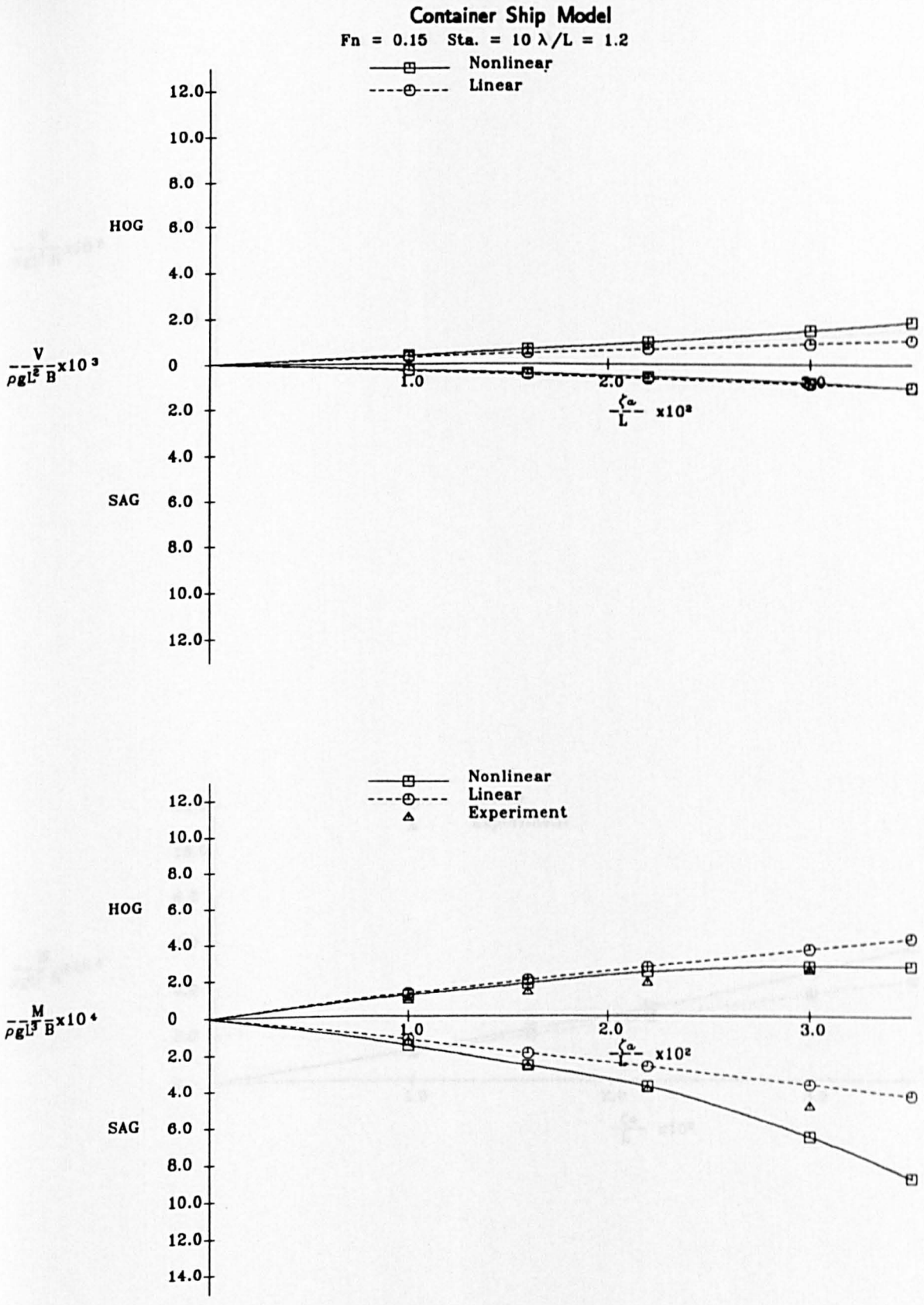

Fig.A.4.25 Vertical Wave Shear force and bending Moment in Regular Head Seas

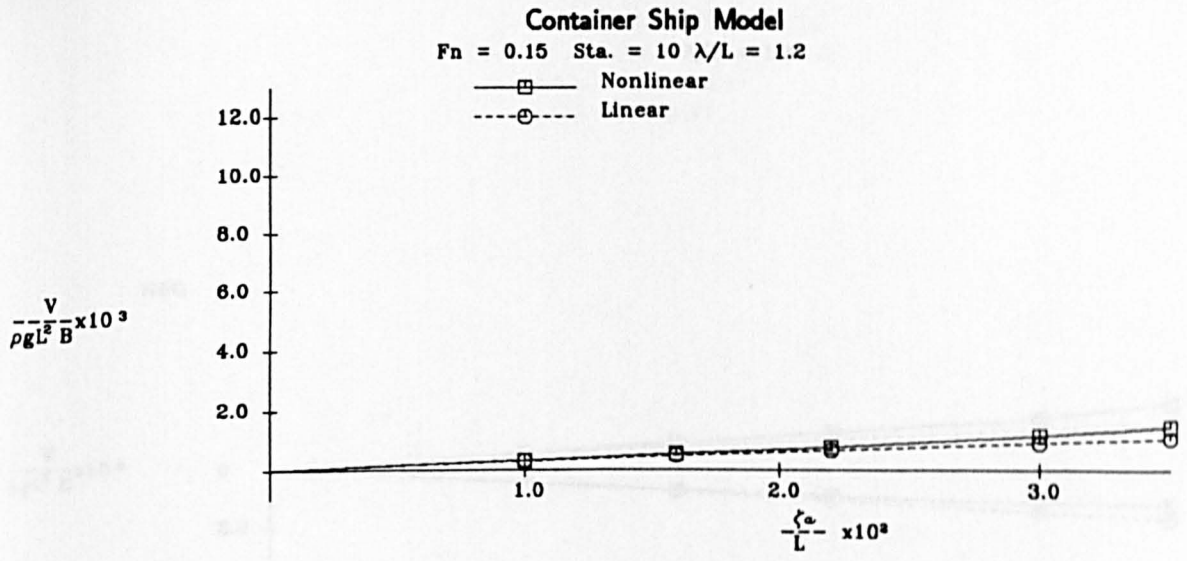

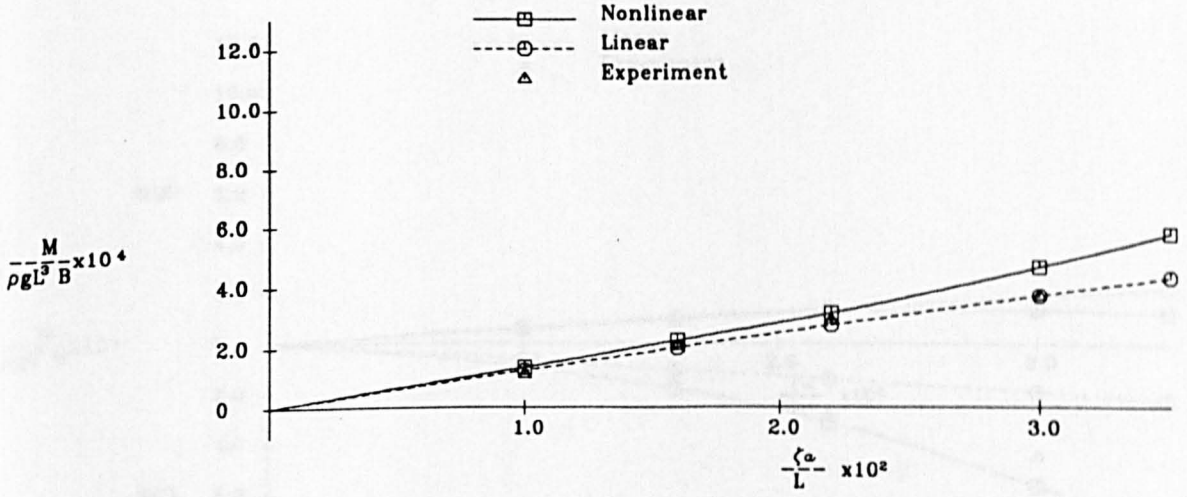

Fig.A.4.26 Vertical Wave Shear Force and Bending Moment in Regular Head Seas

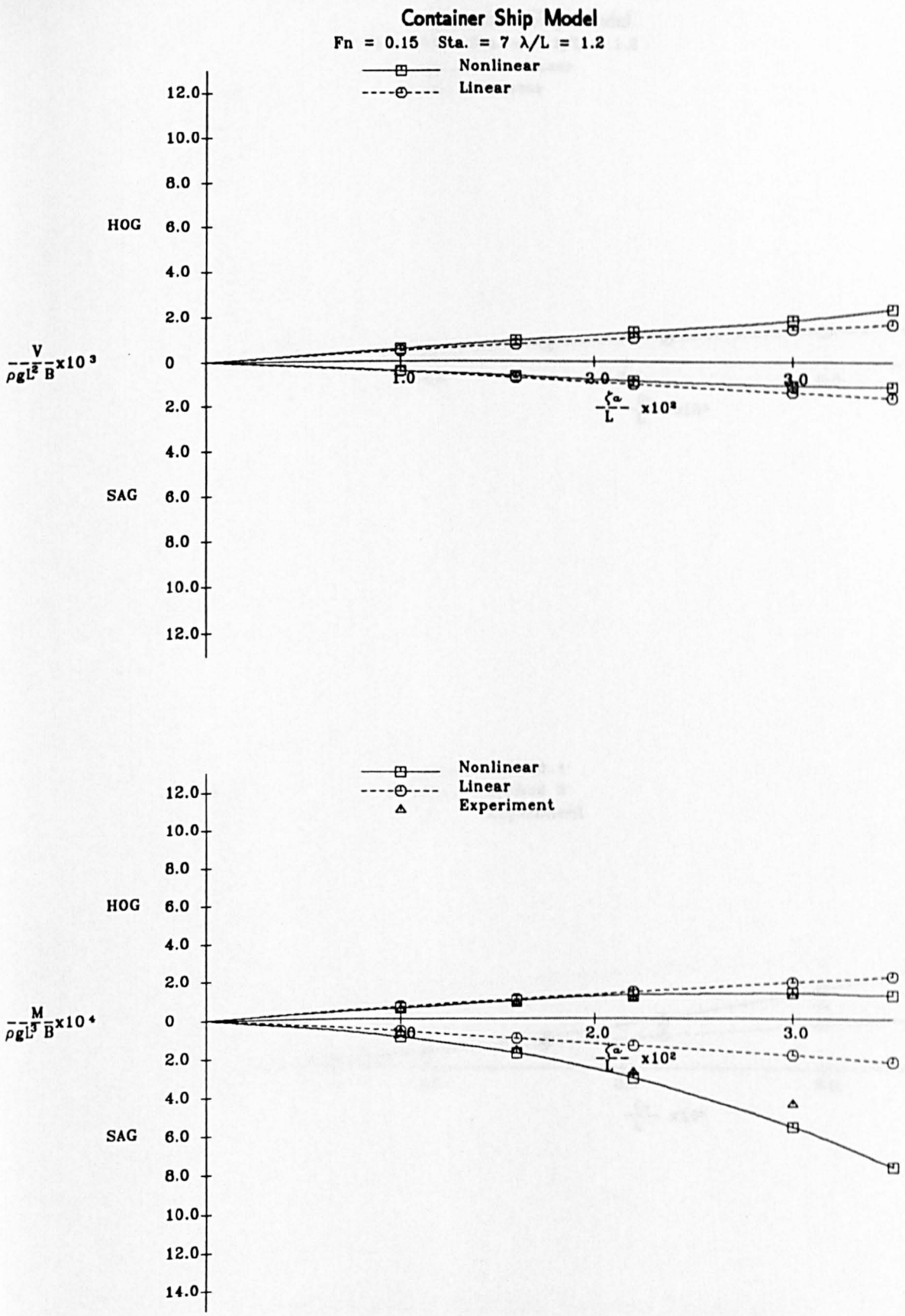

Fig.A.4.27 Vertical Wave Shear Force and Bending Moment in Regular Head Seas

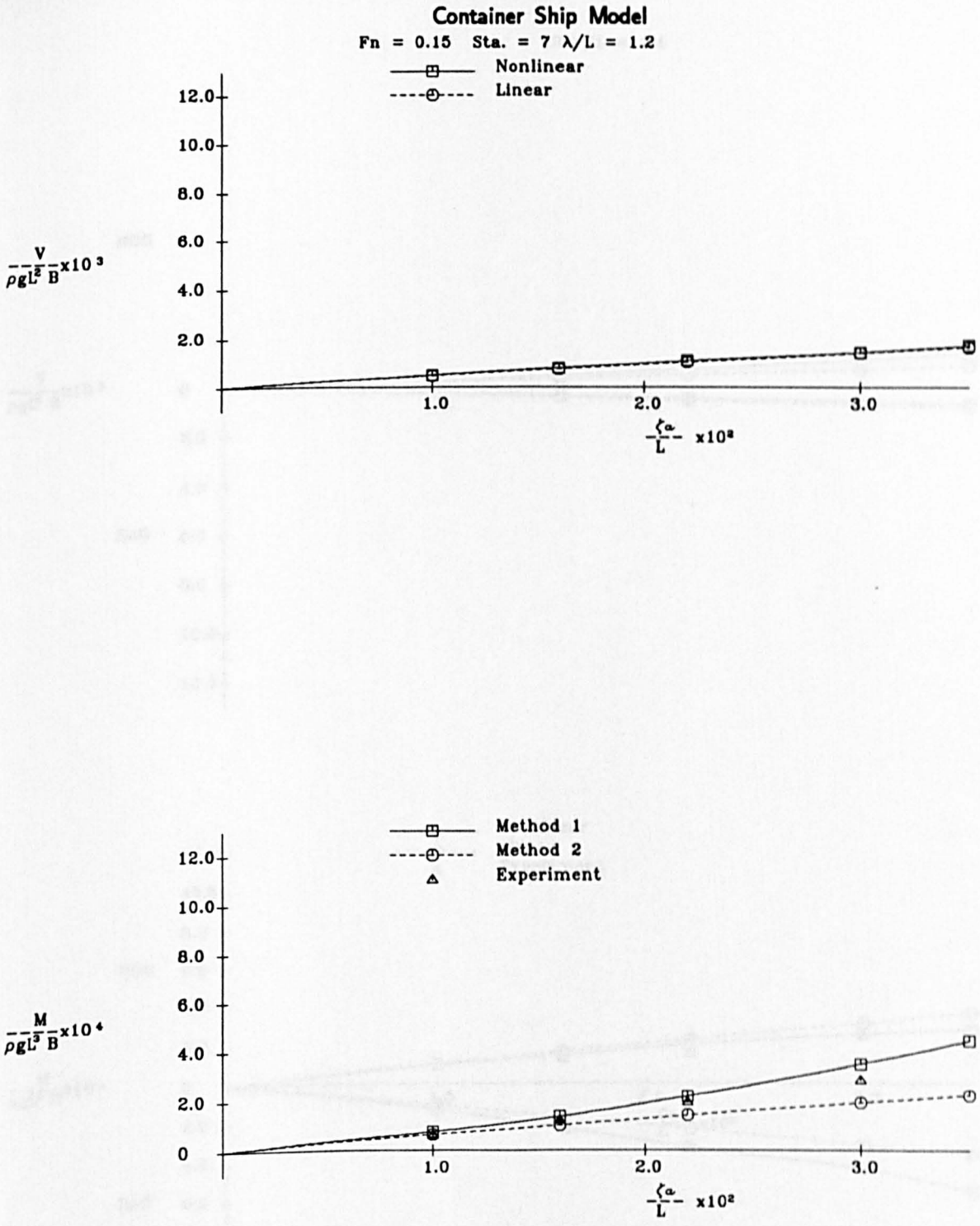

Fig.A.4.28 Vertical Wave Shear Force and Bending Moment in Regular Head Seas

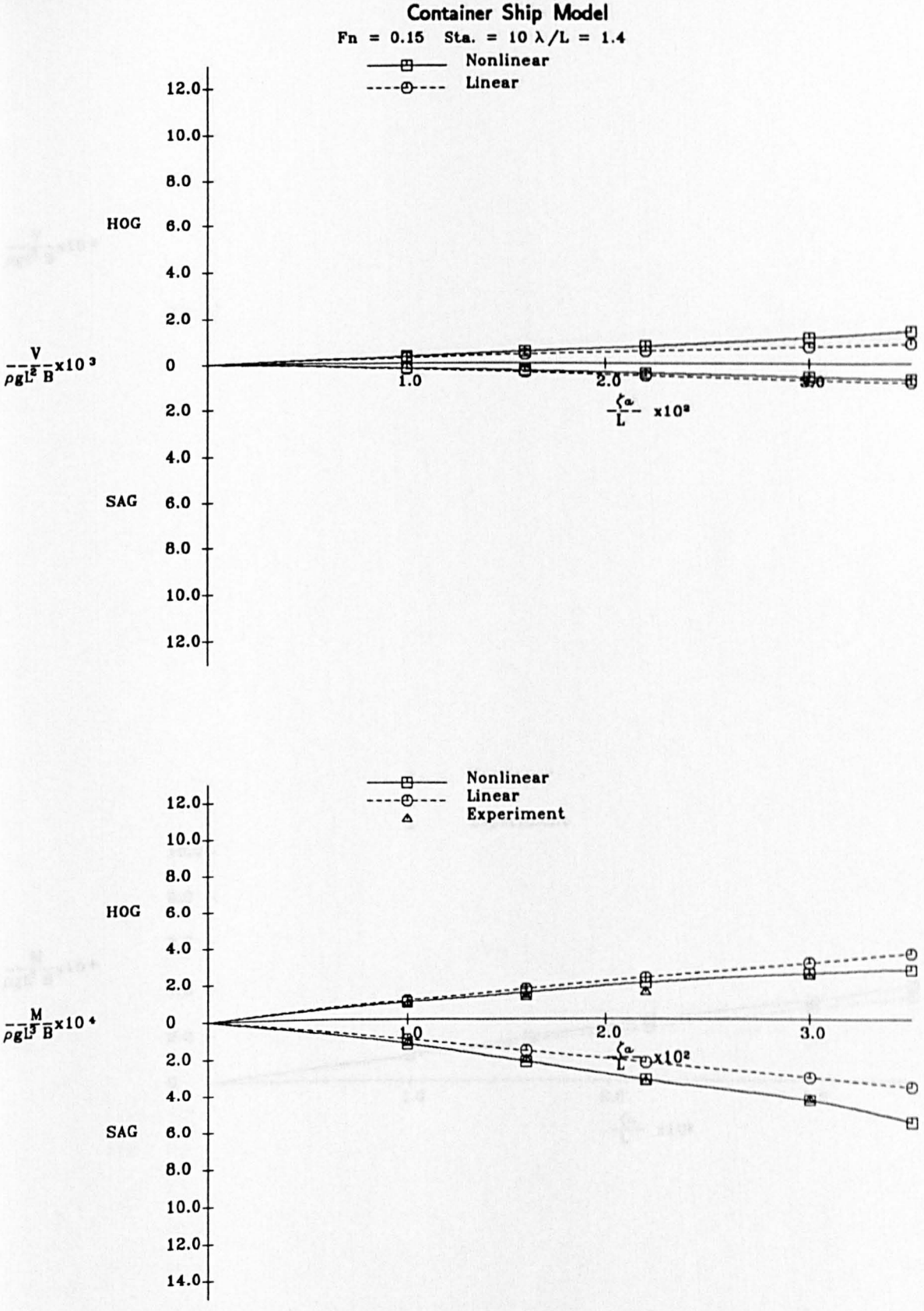

Fig.A.4.29 Vertical Wave Shear Force and Bending Moment in Regular Head Seas

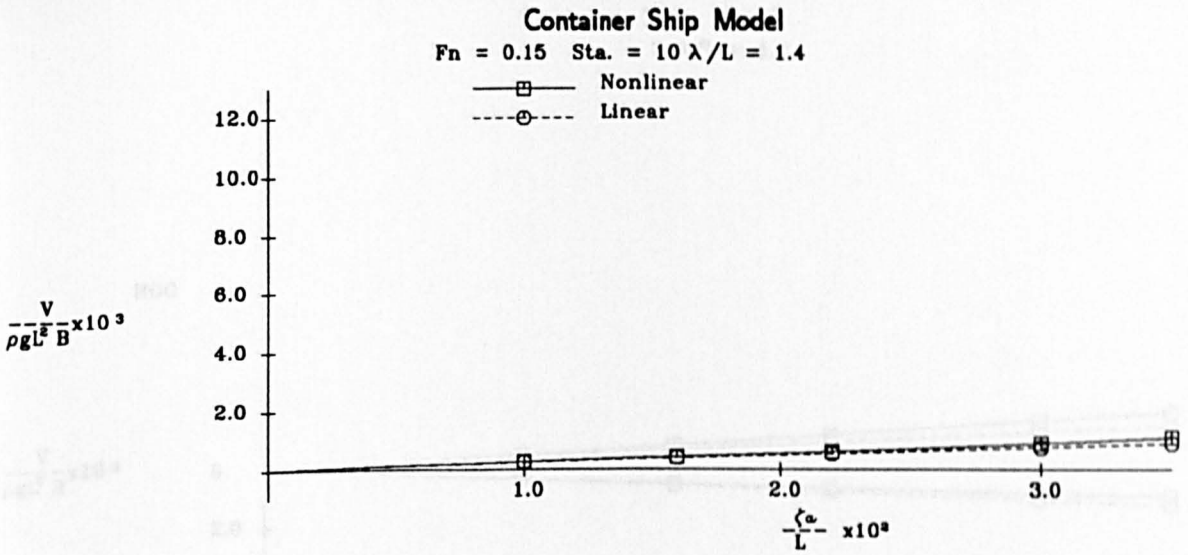

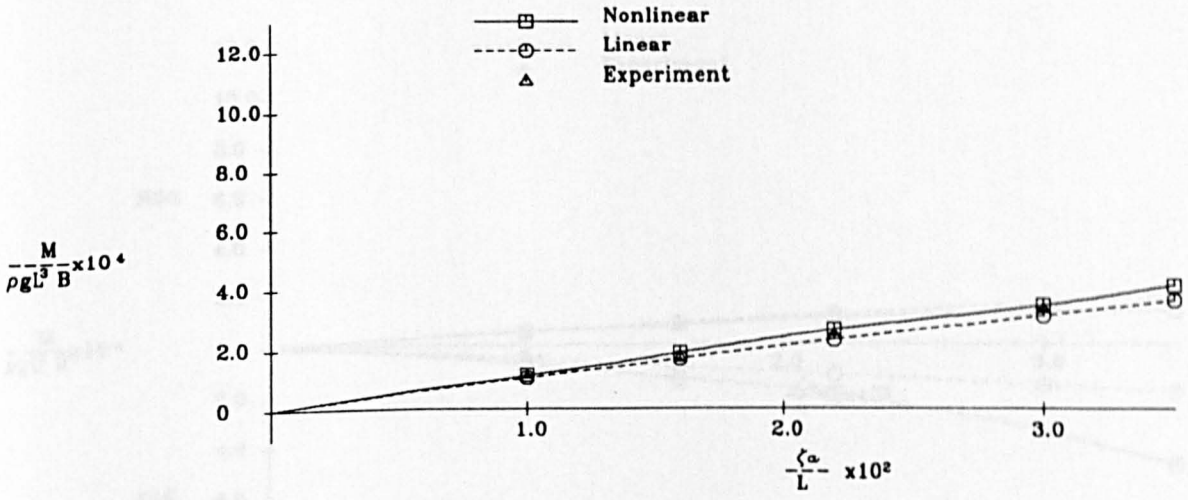

Fig.A.4.30 Vertical Wave Shear Force and Bending Moment in Regular Head Seas

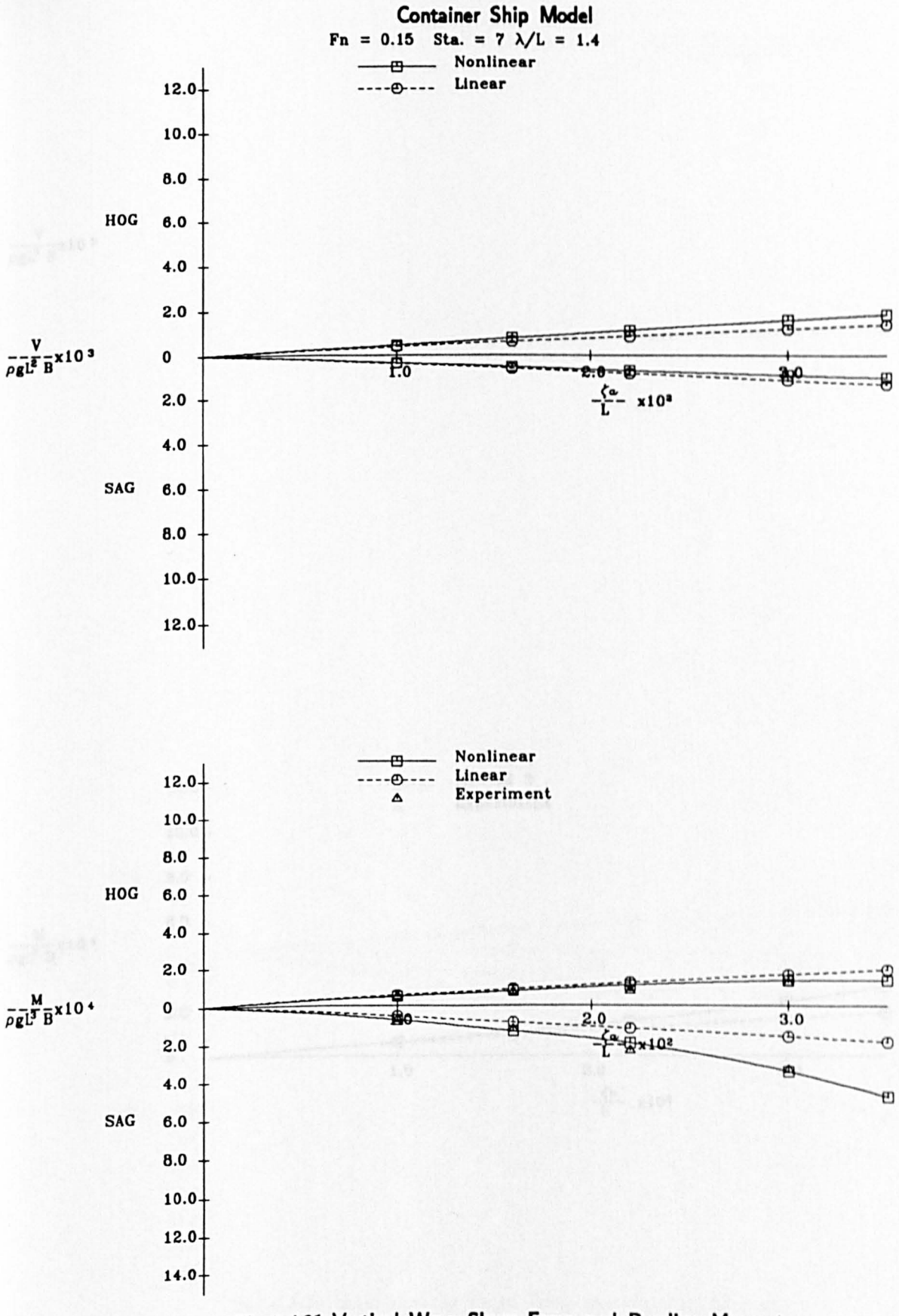

Fig.A.4.31 Vertical Wave Shear Force and Bending Moment in Regualr Head Seas

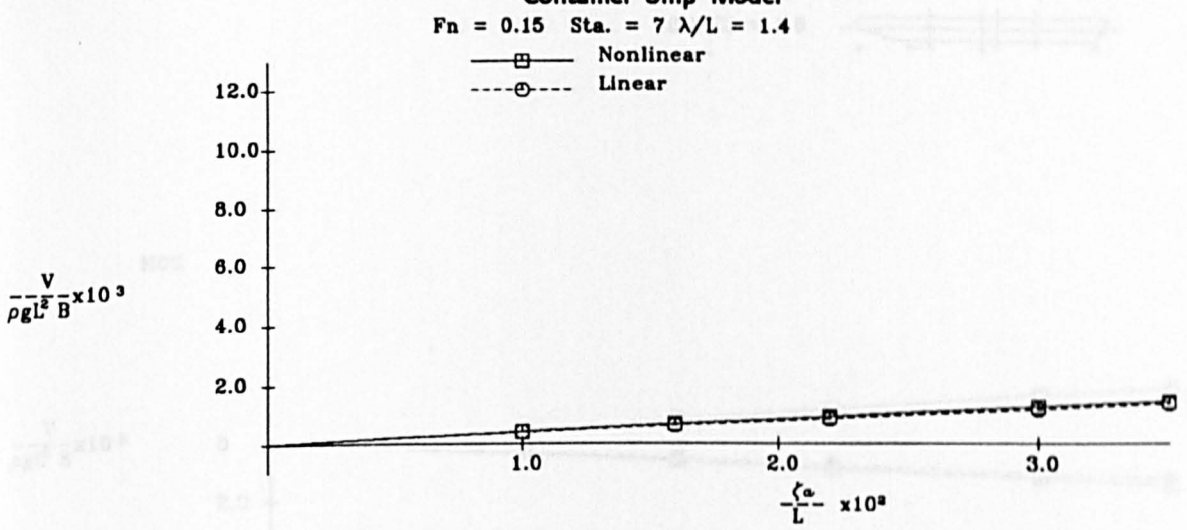

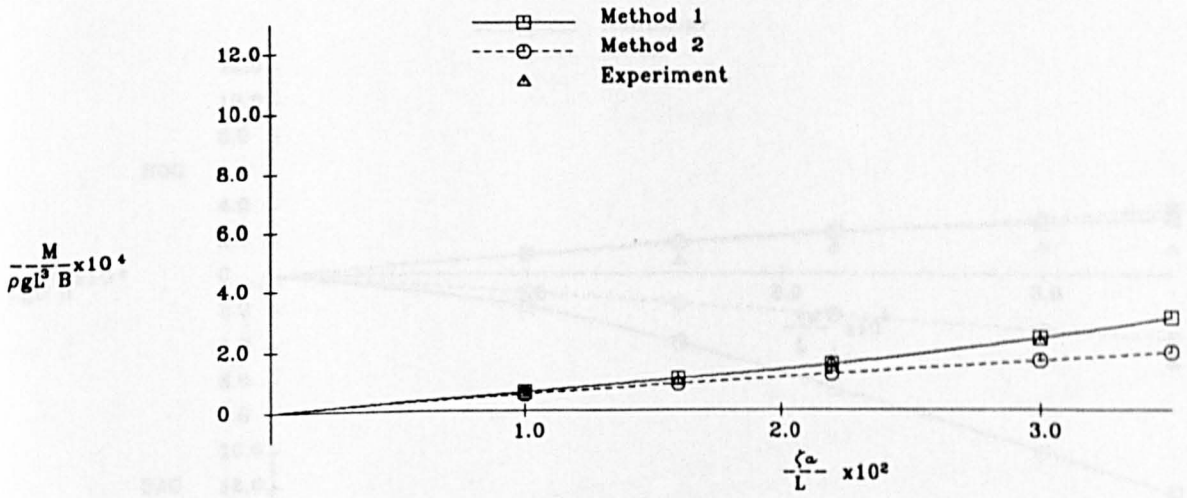

Fig.A.4.32 Vertical Wave Shear Force and Bending Moment in Regular Head Seas

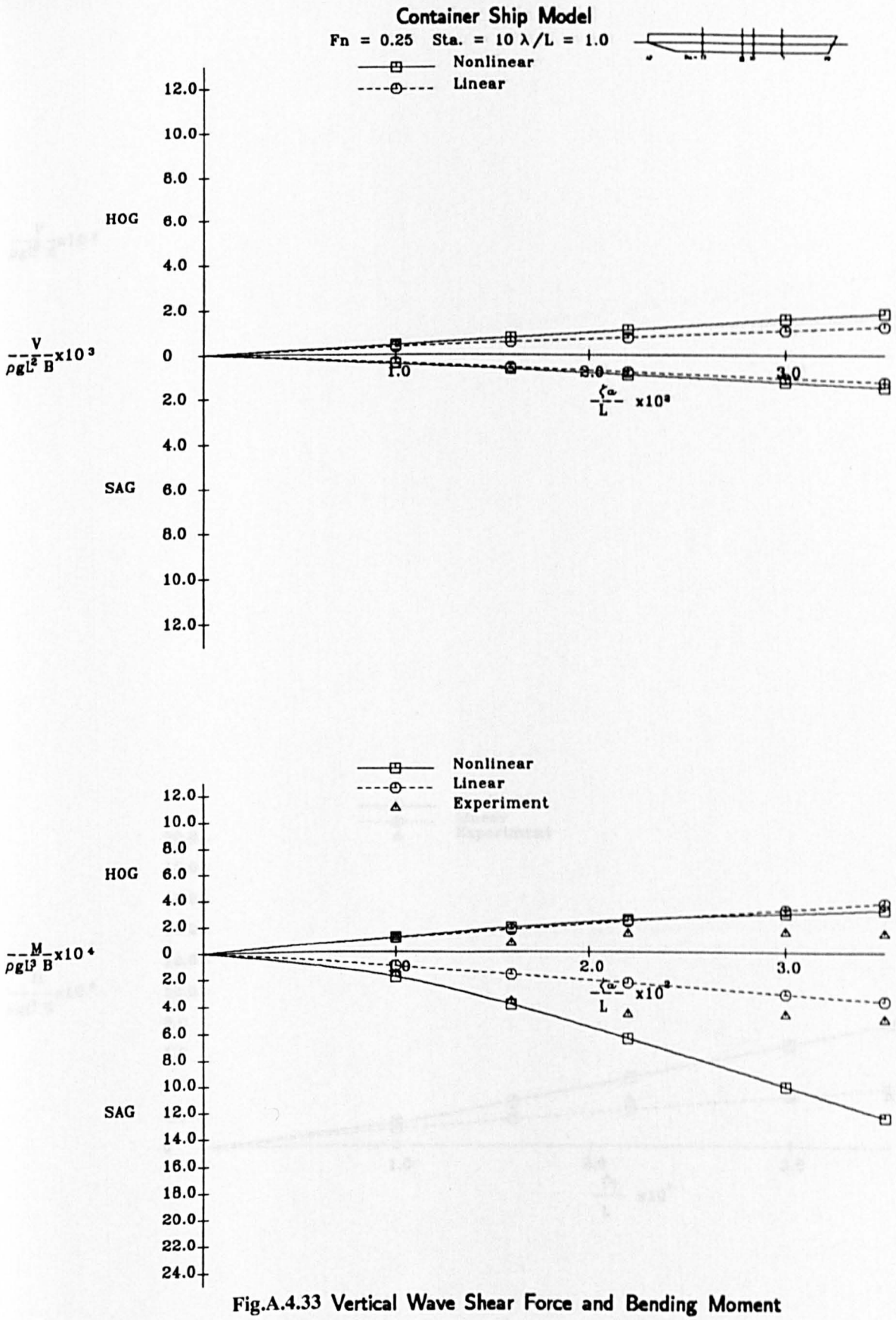

Fig.A.4.33 Vertical Wave Shear Force and Bending Moment in Regular Head Seas

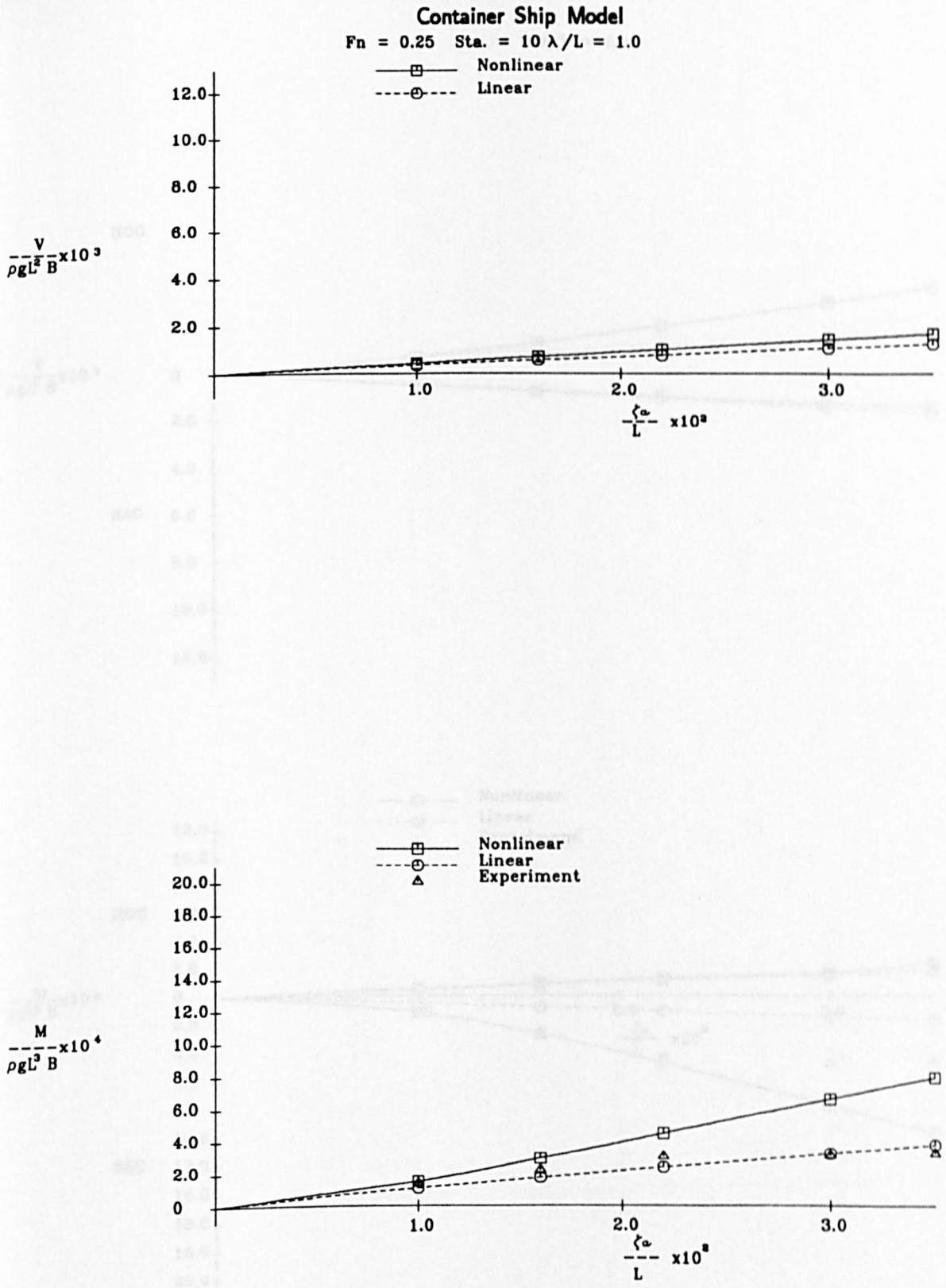

Fig.A.4.34 Vertical Wave Shear Force and Bending Moment in Regular Head Seas

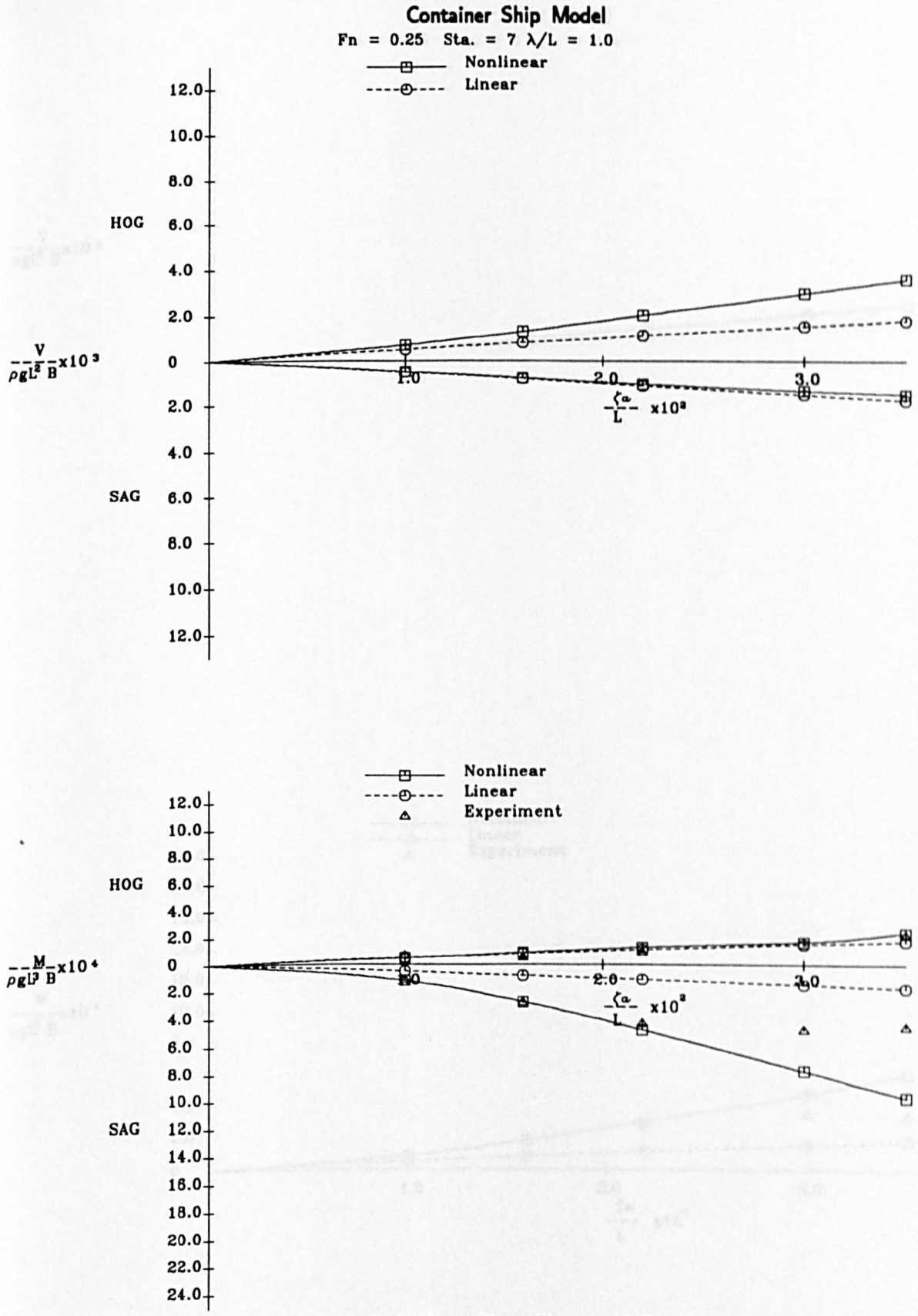

Fig.A.4.35 Vertical Wave Shear Force and Bending Moment in Regular Head Seas

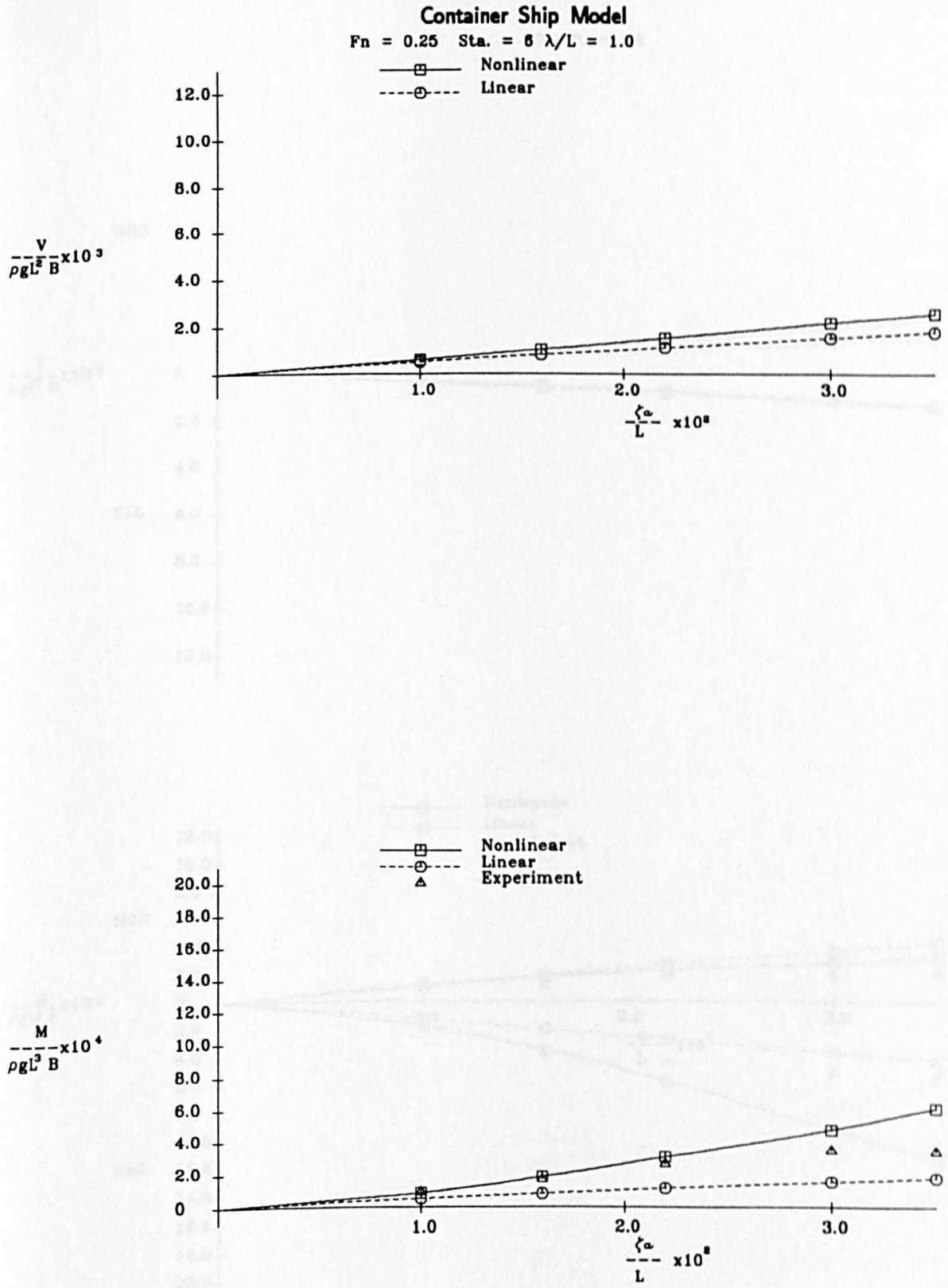

Fig.A.4.36 Vertical Wave Shear Force and Bending Moment in Regular Head Seas

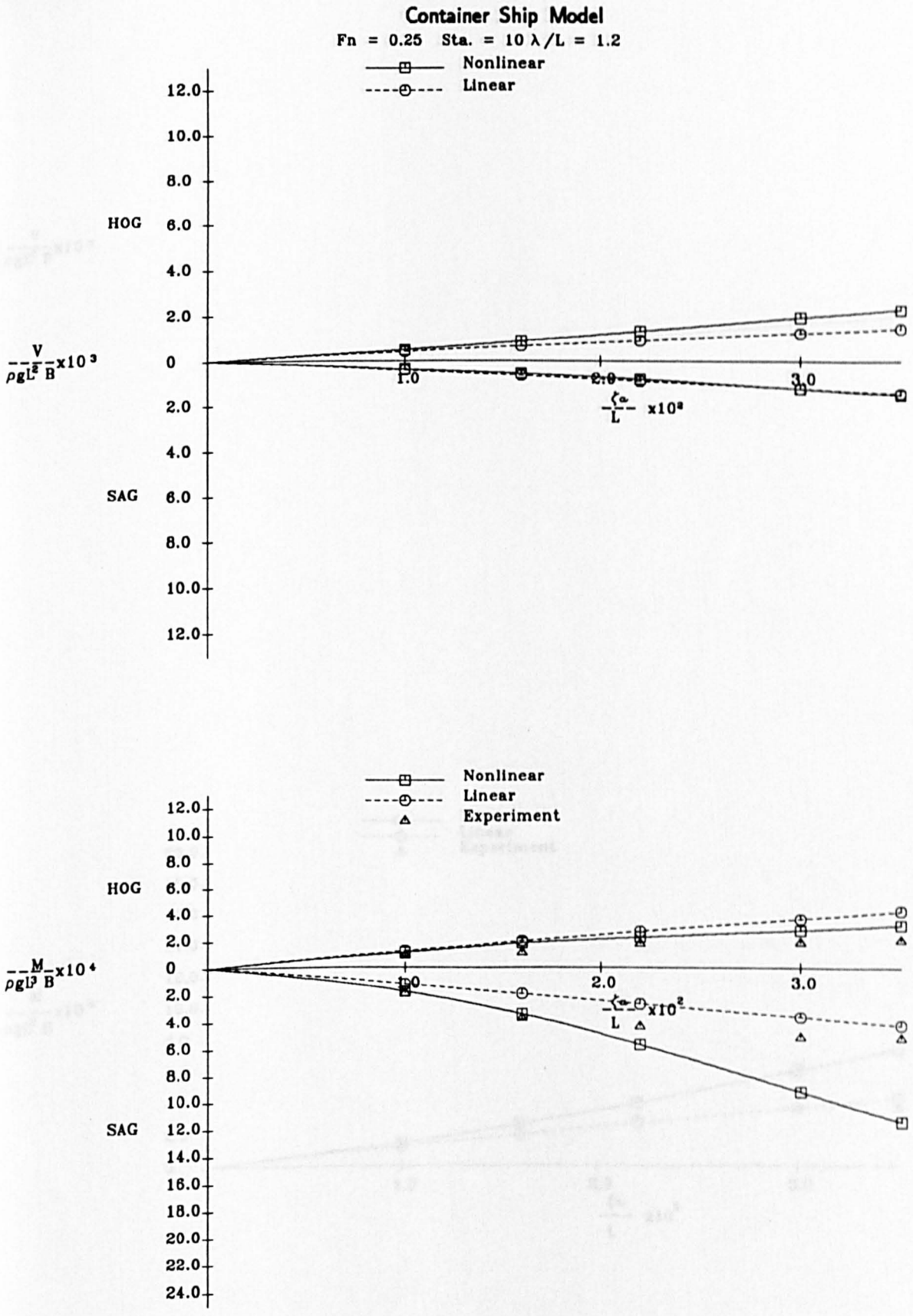

Fig.A.4.37 Vertical Wave Shear Force and Bending Moment in Regular Head Seas

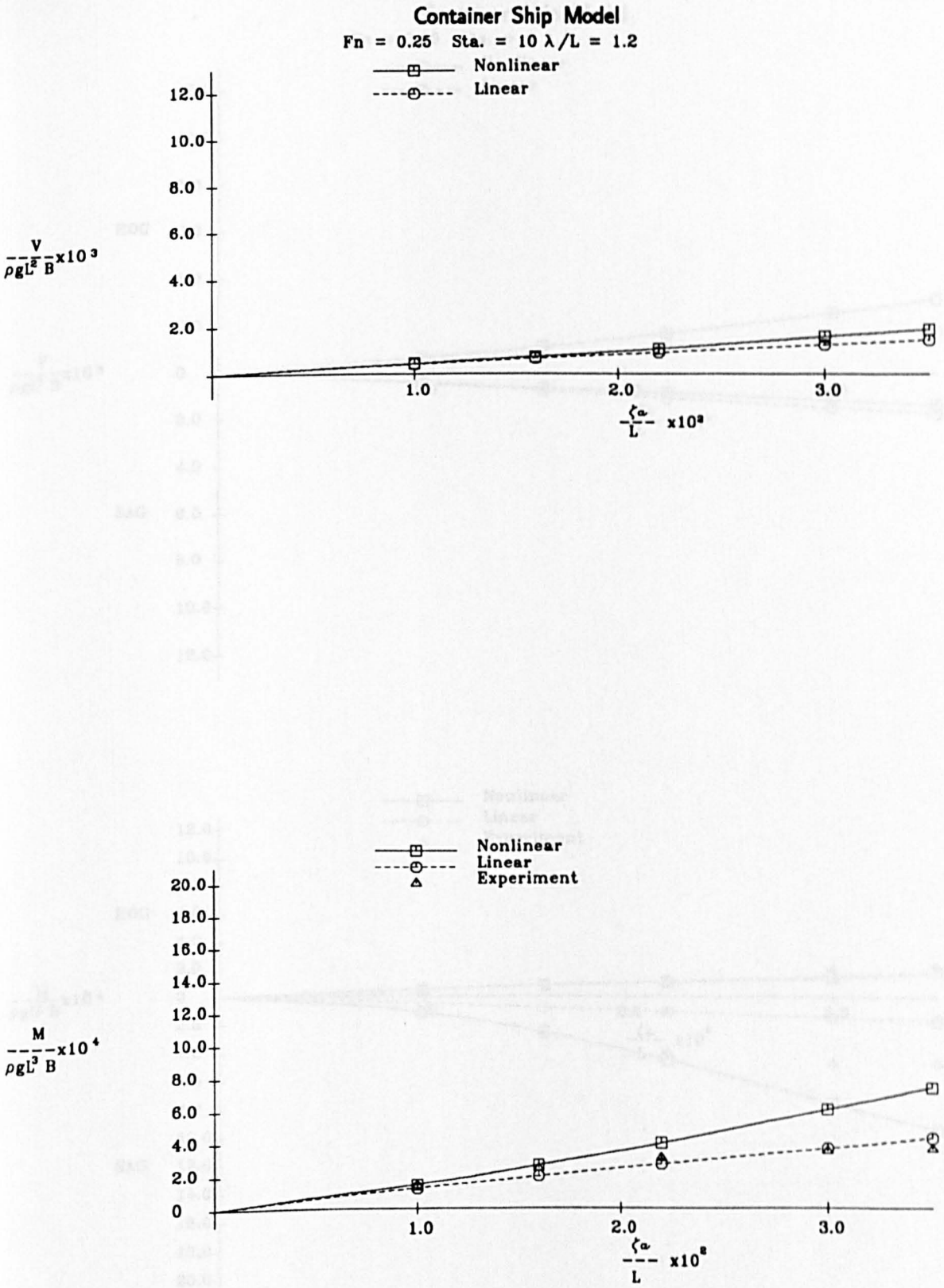

Fig.A.4.38 Vertical Wave Shear Force and Bending Moment in Regular Head Seas

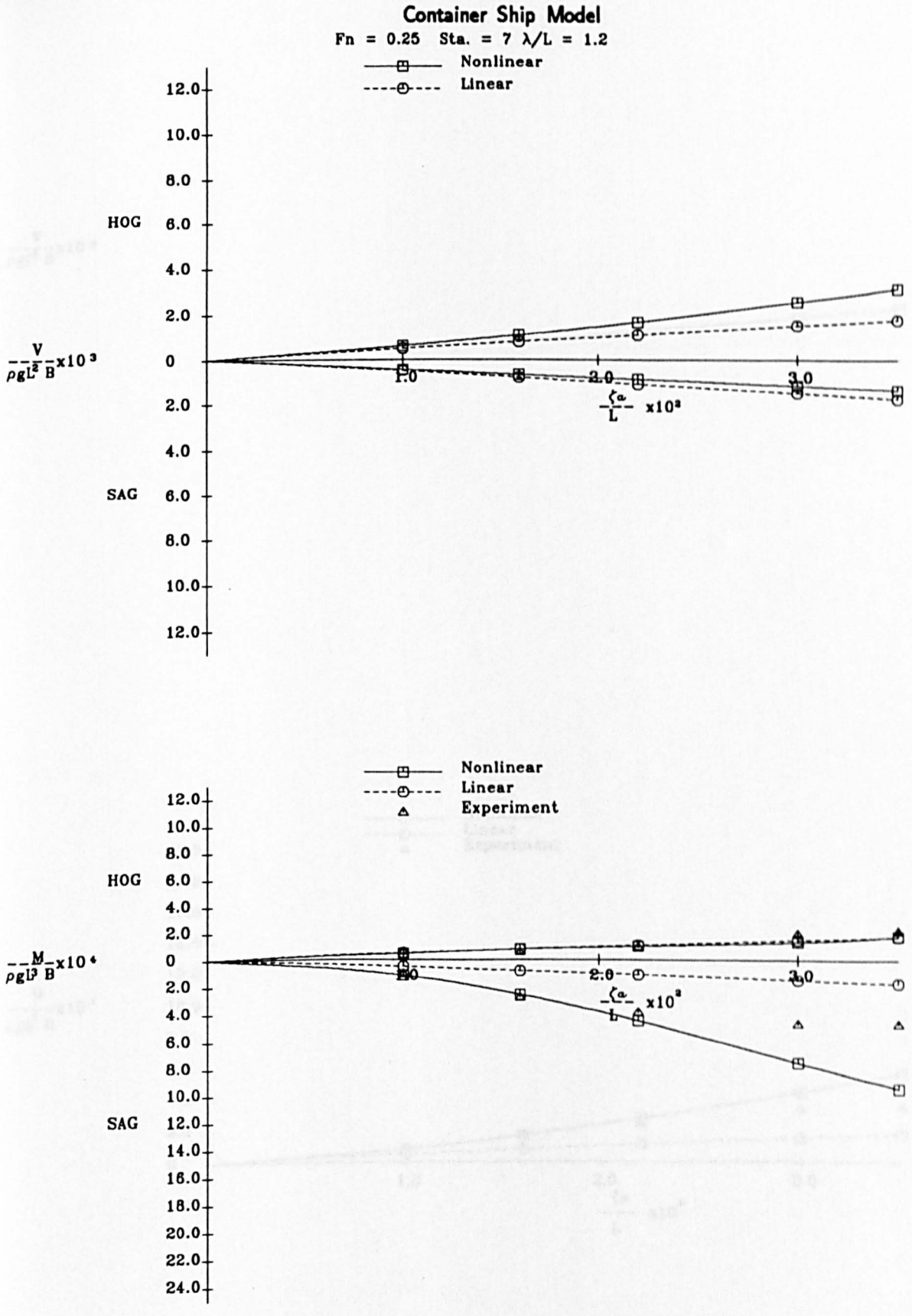

Fig.A.4.39 Vertical Wave Shear Force and Bending Moment in Regular Head Seas

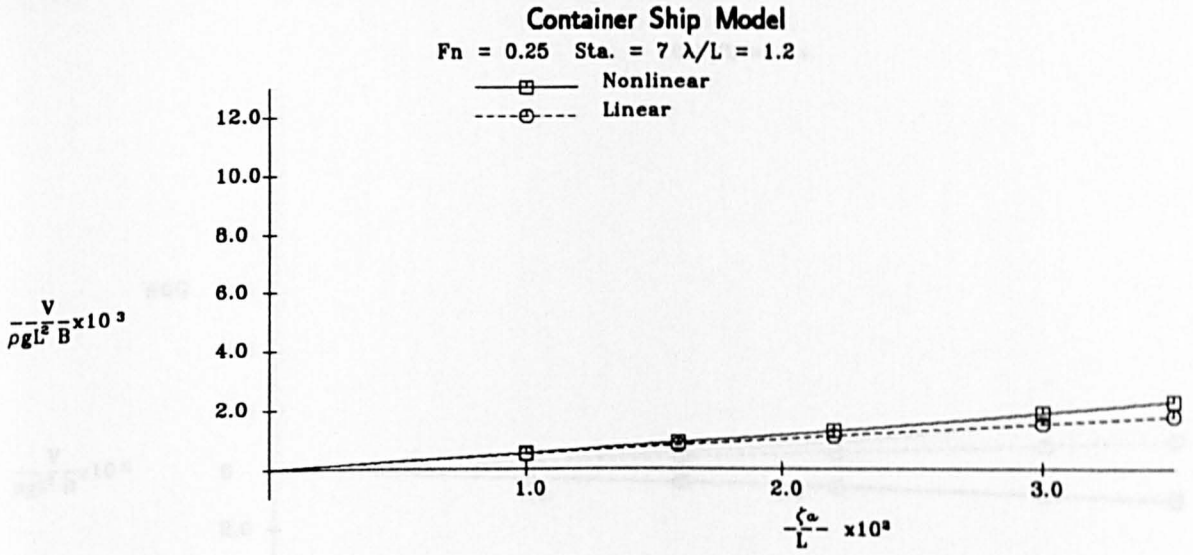

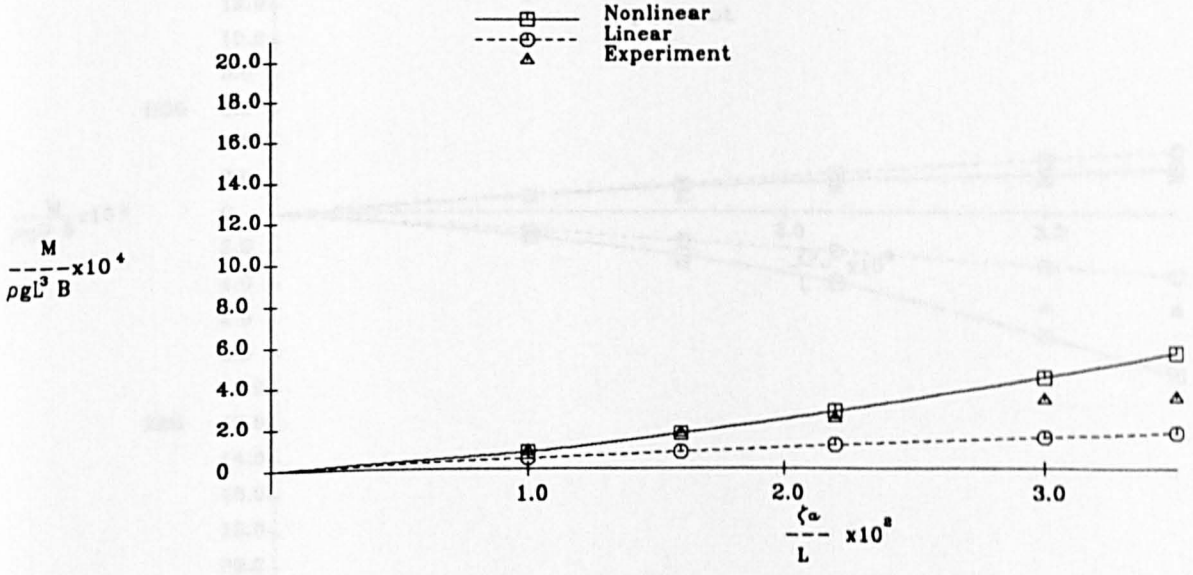

Fig.A.4.40 Vertical Wave Shear Force and Bending Moment

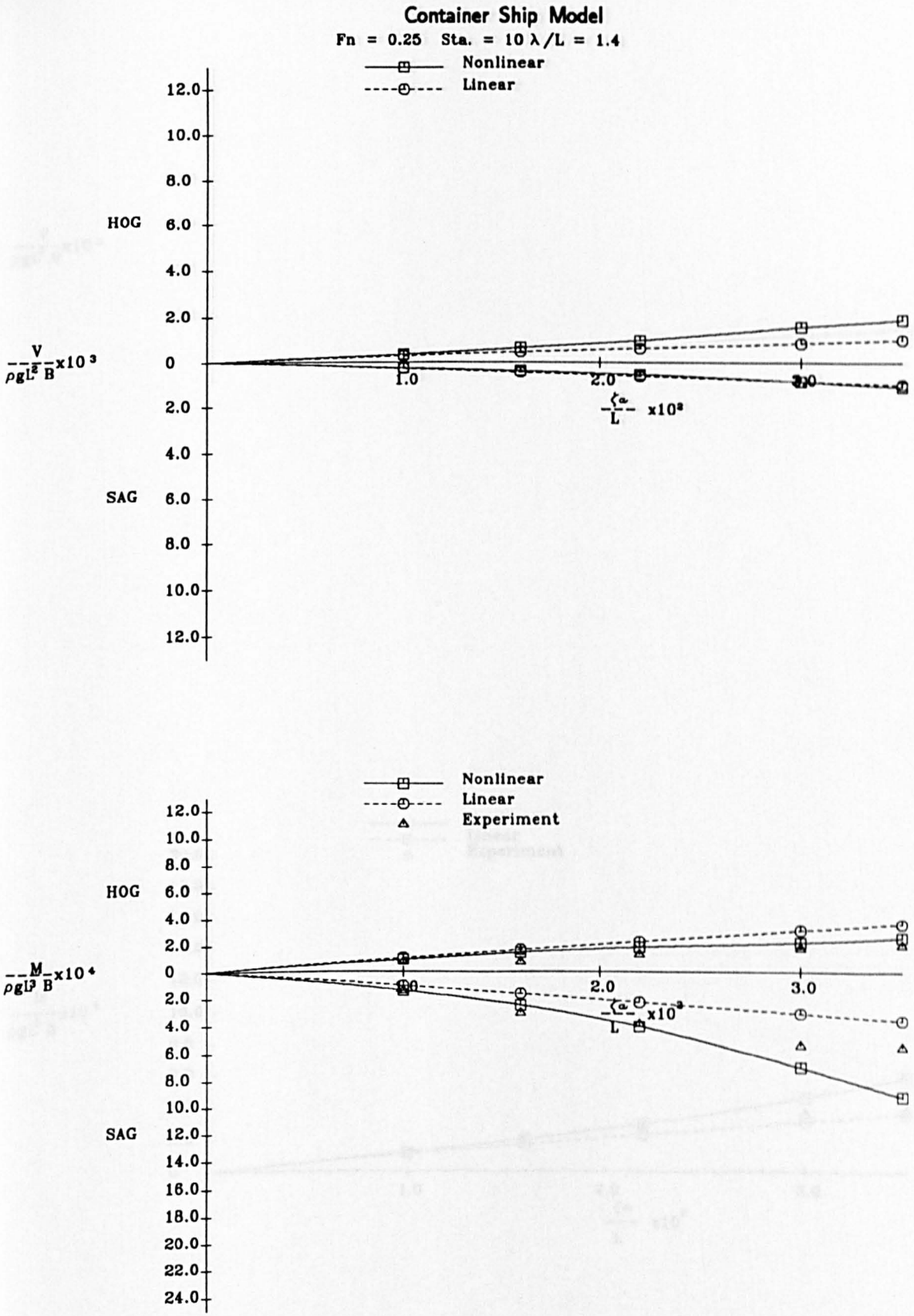

Fig.A.4.41 Vertical Wave Shear Force and Bending Moment in Regular Head Seas

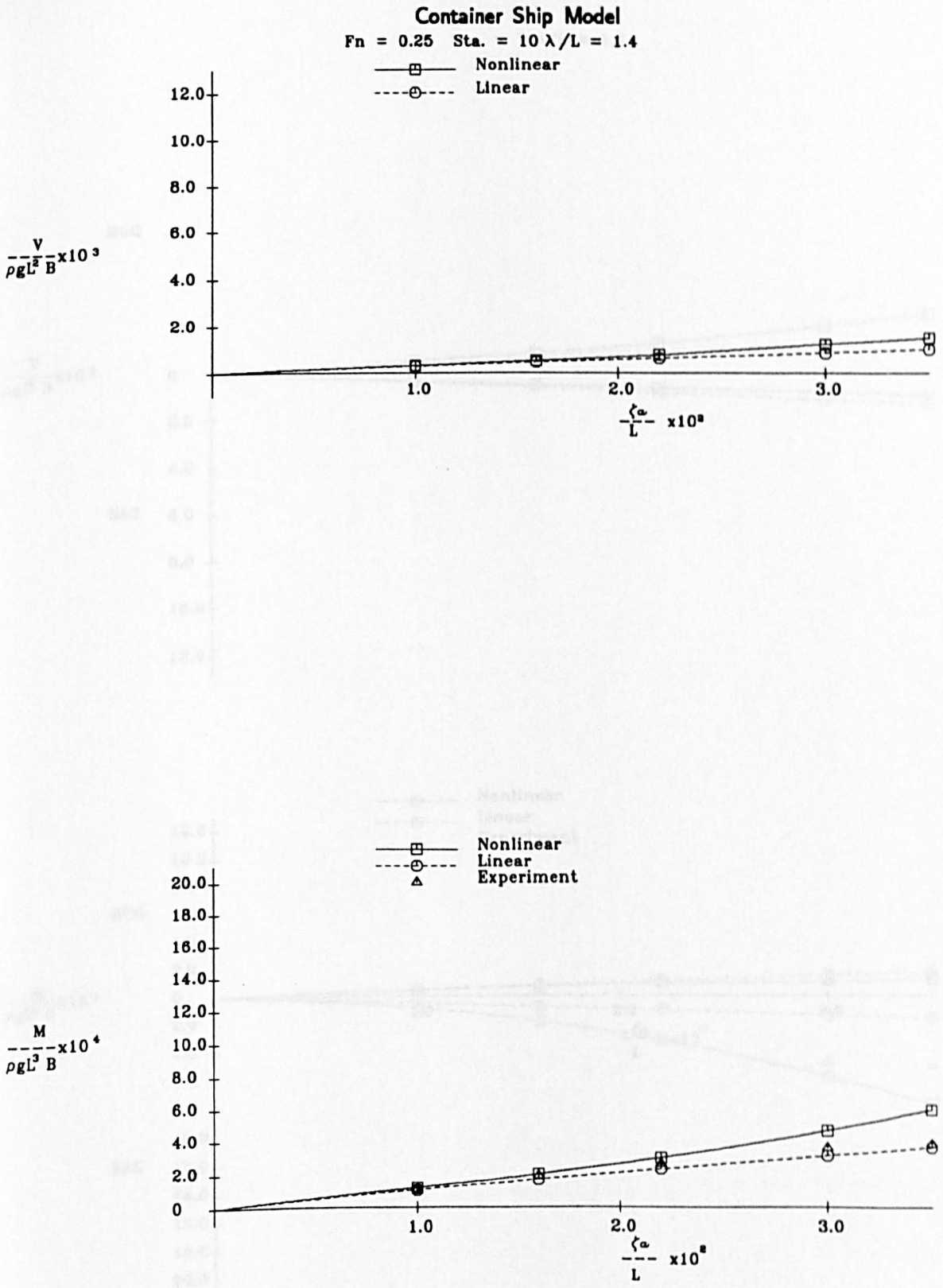

Fig.A.4.42 Vertical Wave Shear Force and Bending Moment in Regular Head Seas

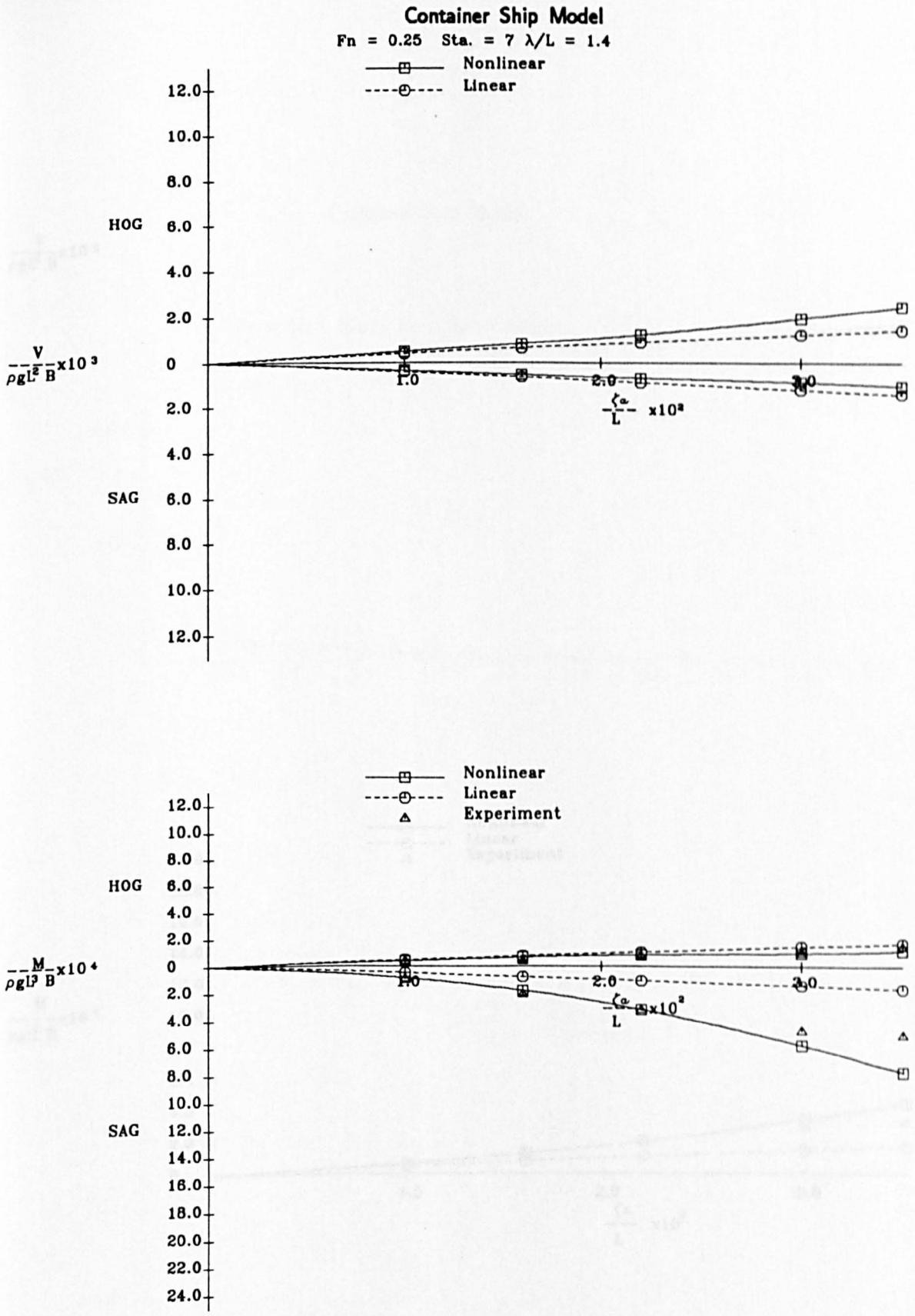

Fig.A.4.43 Vertical Wave Shear Force and Bending Moment in Regular Head Seas

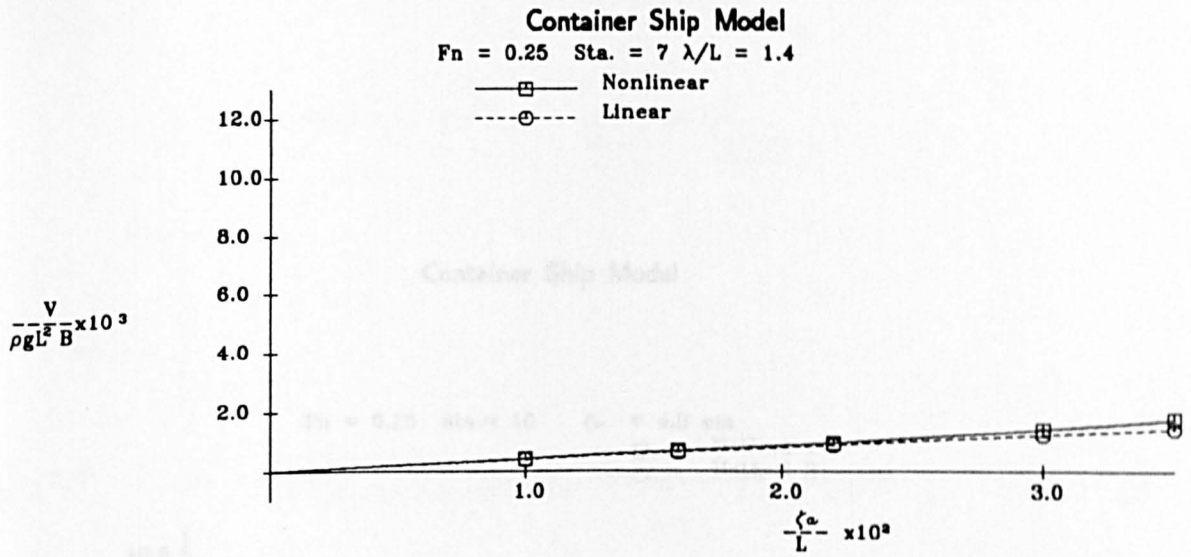

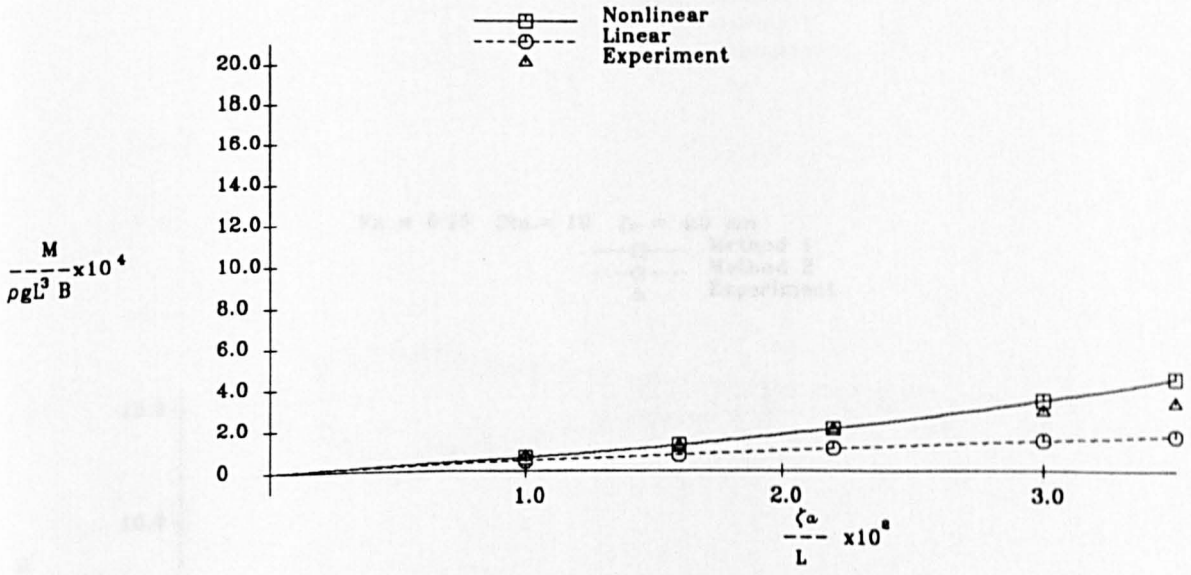

Fig.A.4.44 Vertical Wave Shear Force and Bending Moment in Regular Head Seas

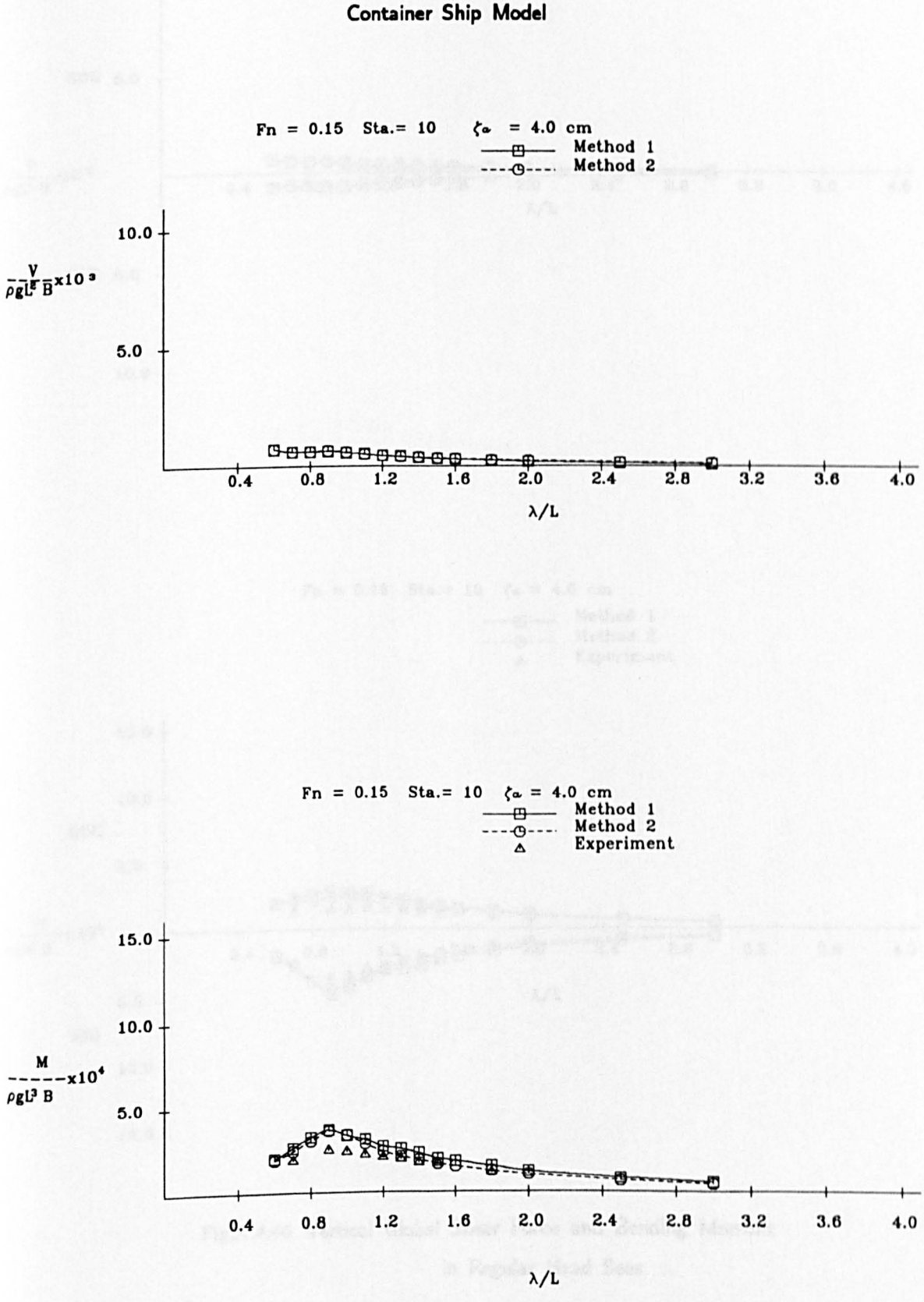

Fig.A.4.45 Vertical Global Shear Force and Bending Moment in Regular Head Seas

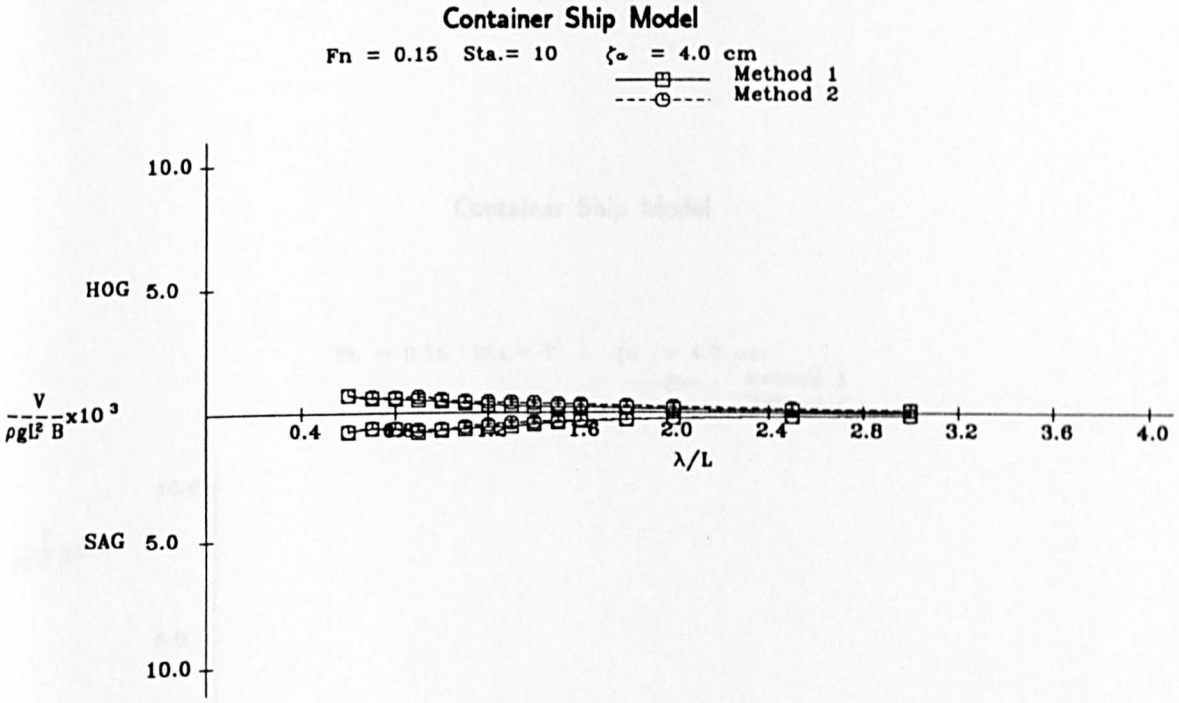

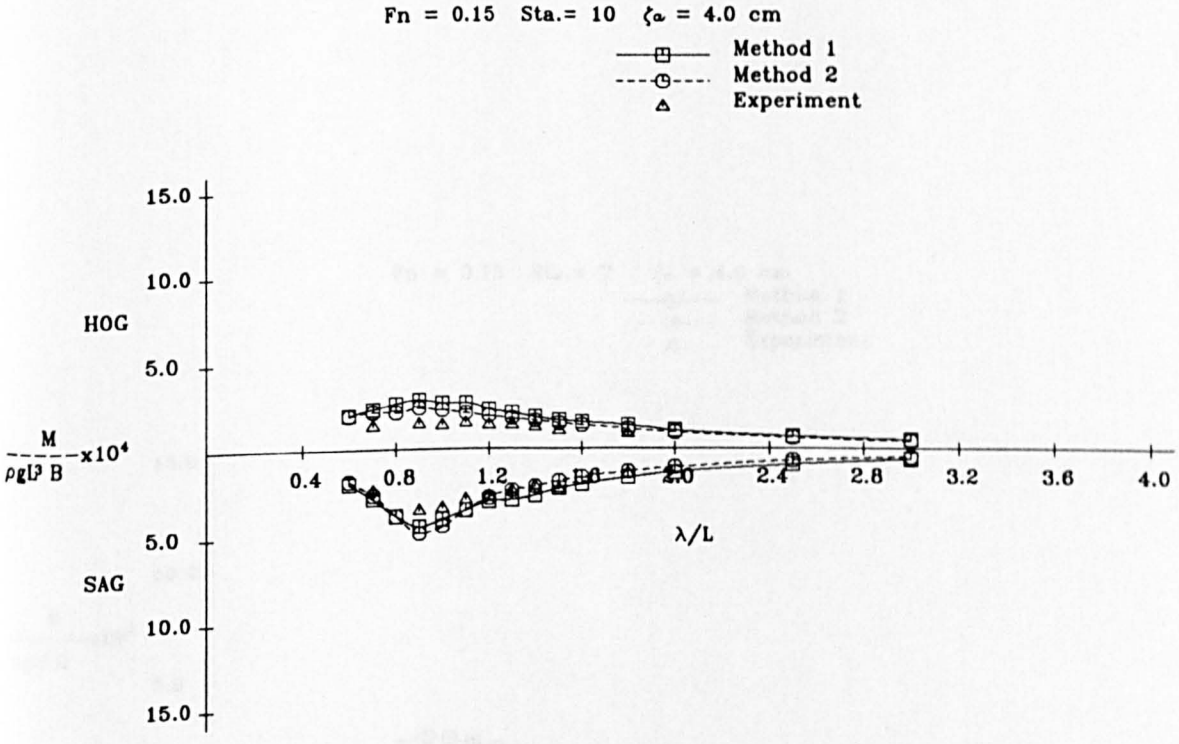

Fig.A.4.46 Vertical Global Shear Force and Bending Moment in Regular Head Seas

Container Ship Model

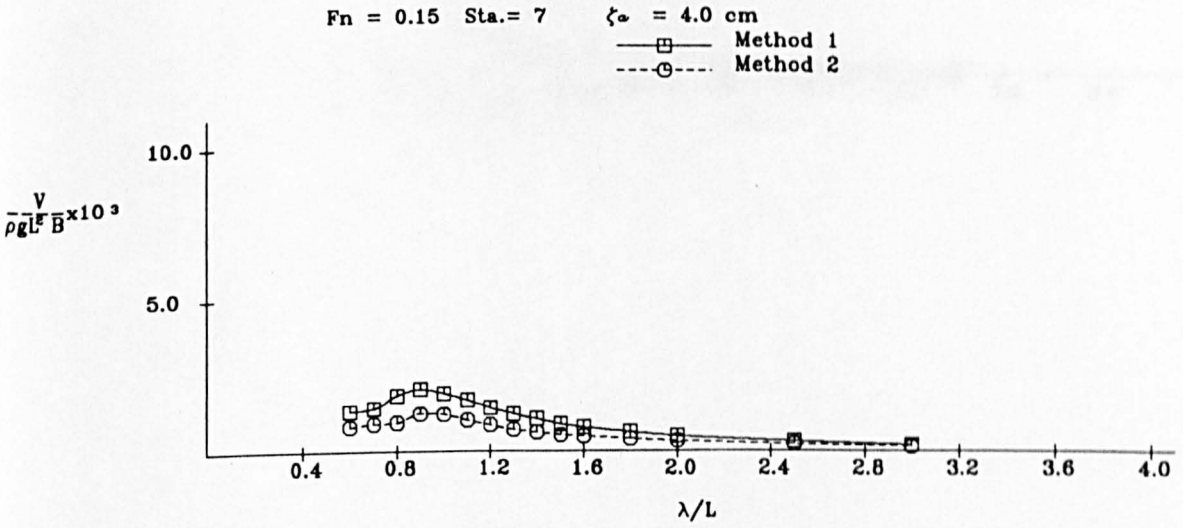

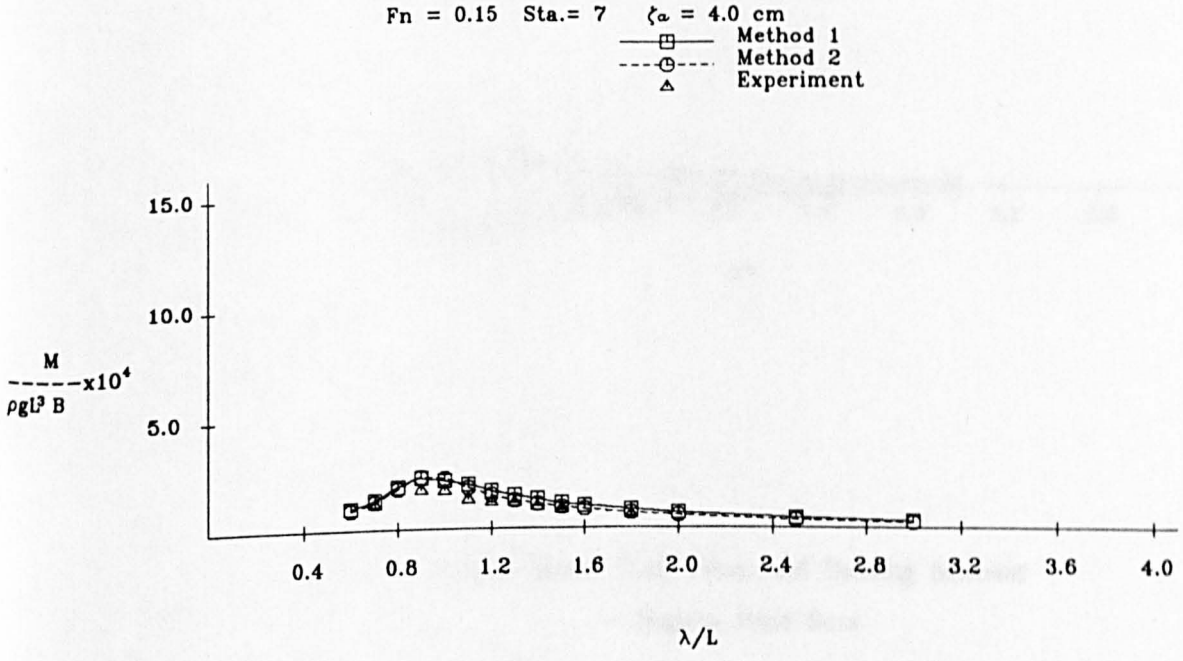

Fig.A.4.47 Vertical Global Shear Force and Bending Moment in Regular Head Seas

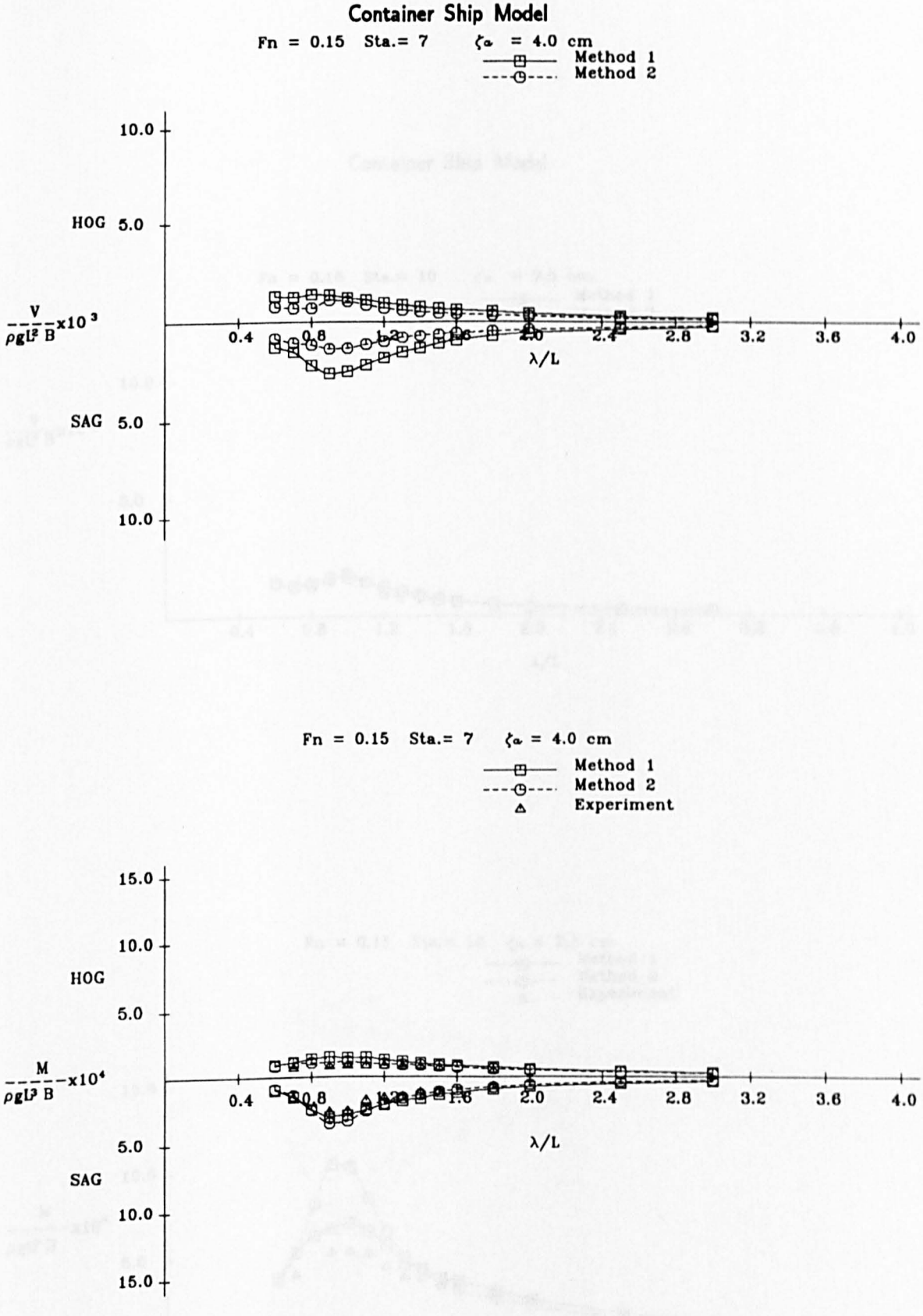

Fig.A.4.48 Vertical Global Shear Force and Bending Moment in Regular Head Seas

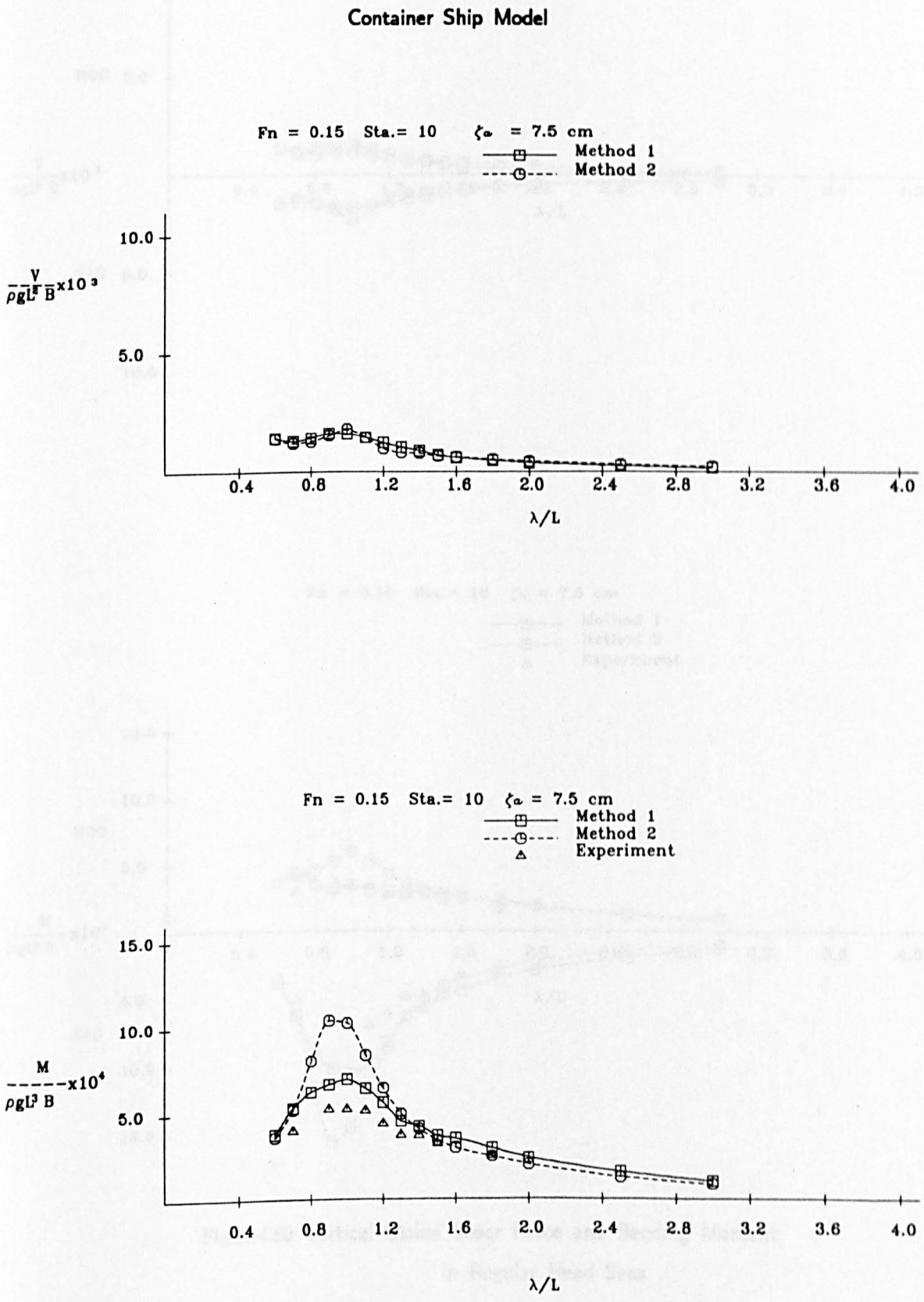

Fig.A.4.49 Vertical Global Shear Force and Bending Moment in Regular Head Seas

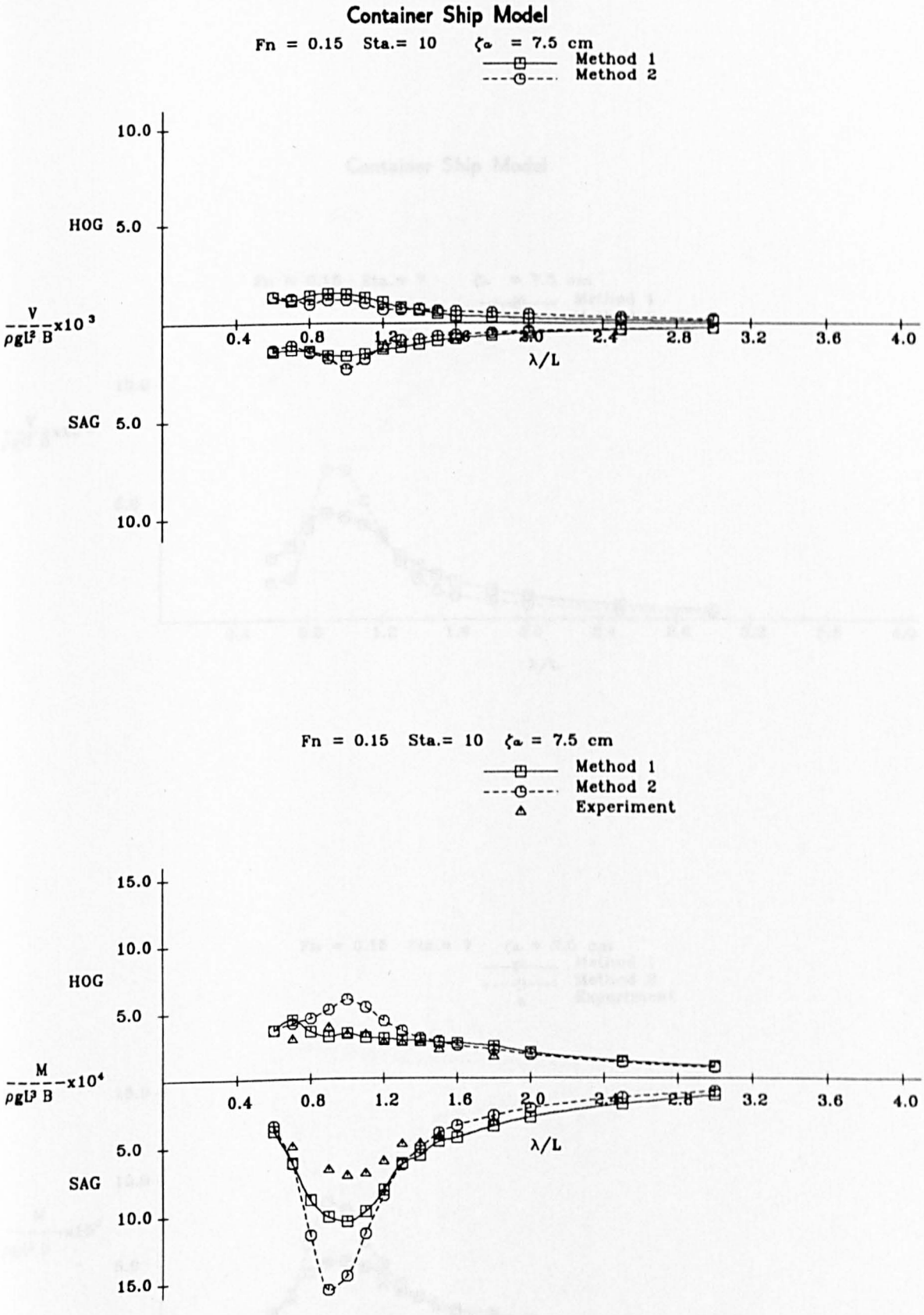

Fig.A.4.50 Vertical Global Shear Force and Bending Moment in Regular Head Seas

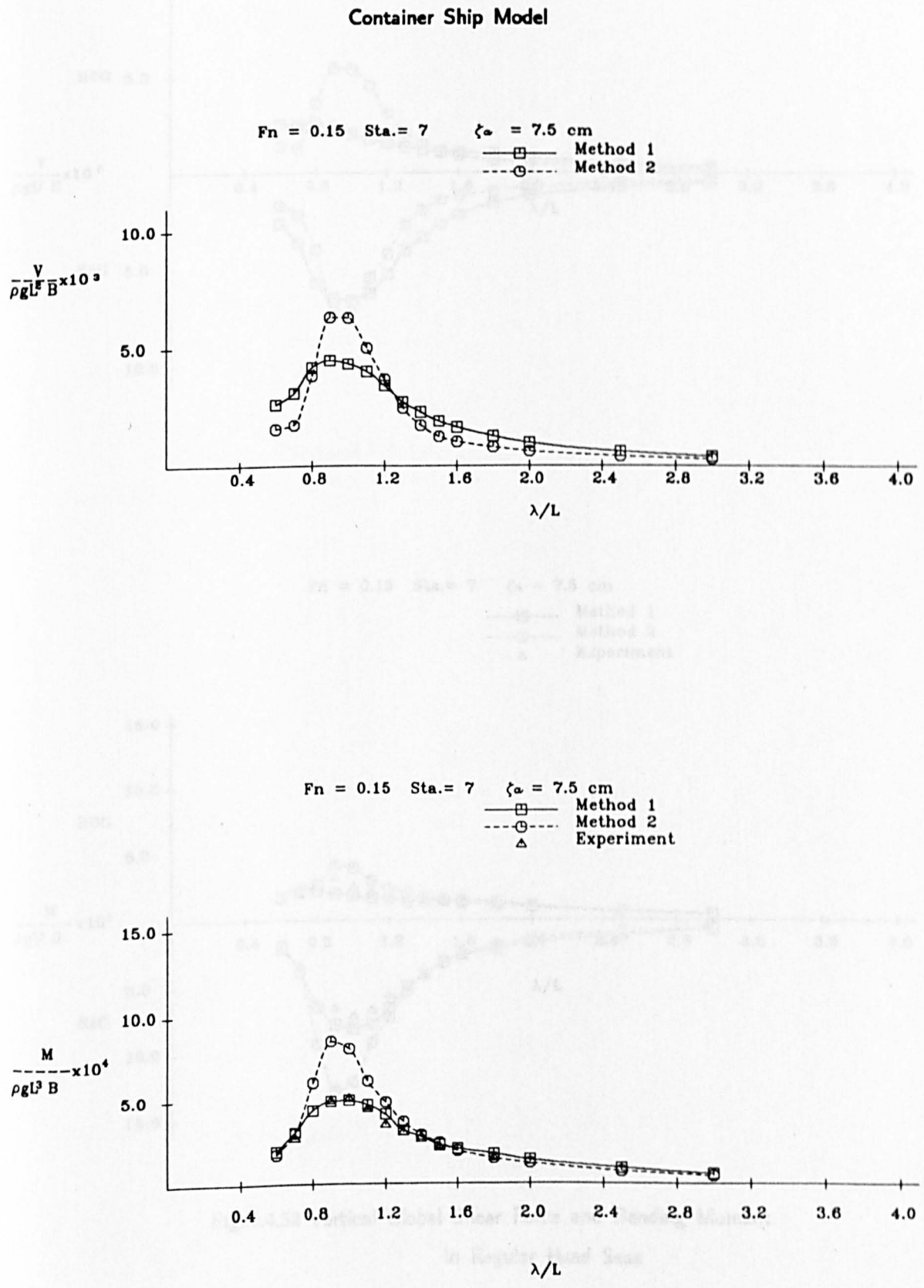

Fig.A.4.51 Vertical Global Shear Force and Bending Moment in Regular Head Seas

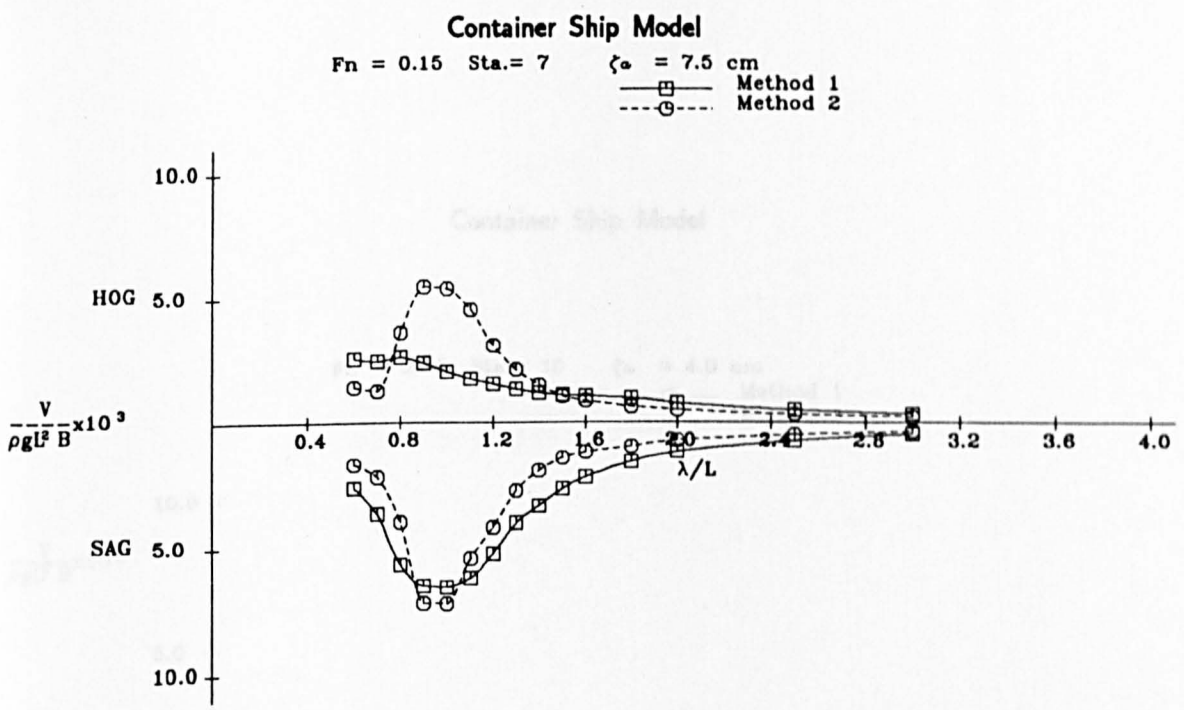

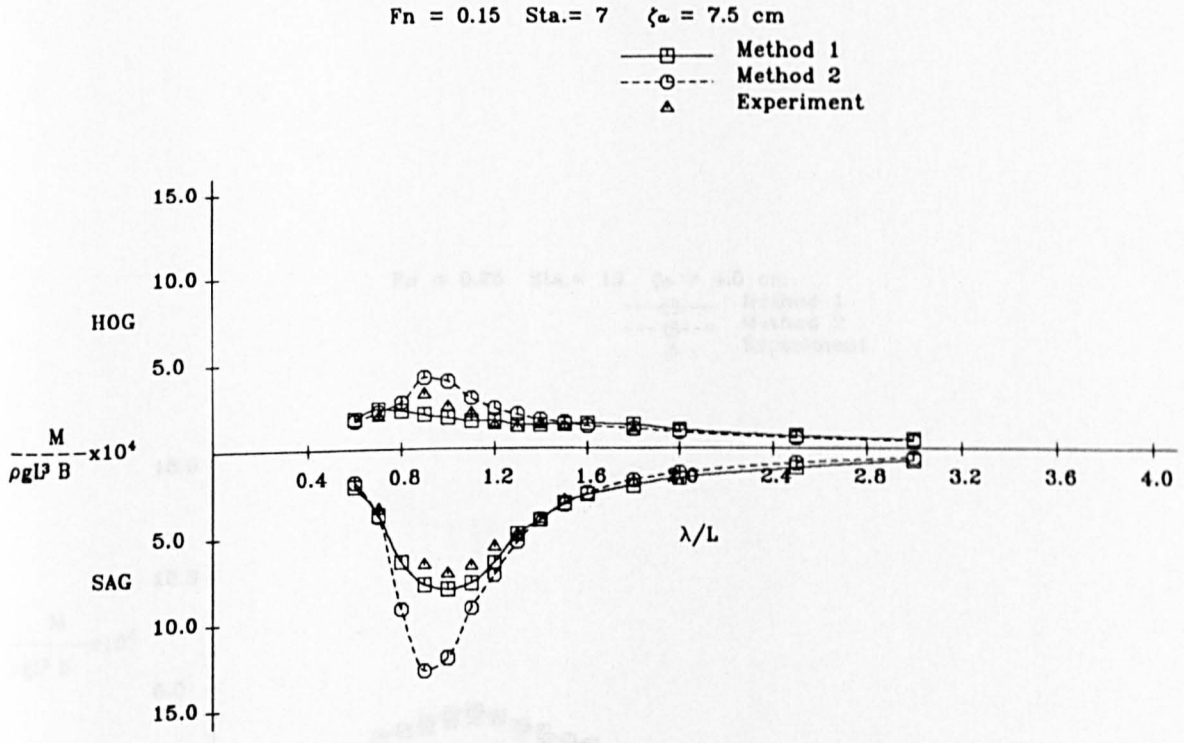

Fig.A.4.52 Vertical Global Shear Force and Bending Moment in Regular Head Seas

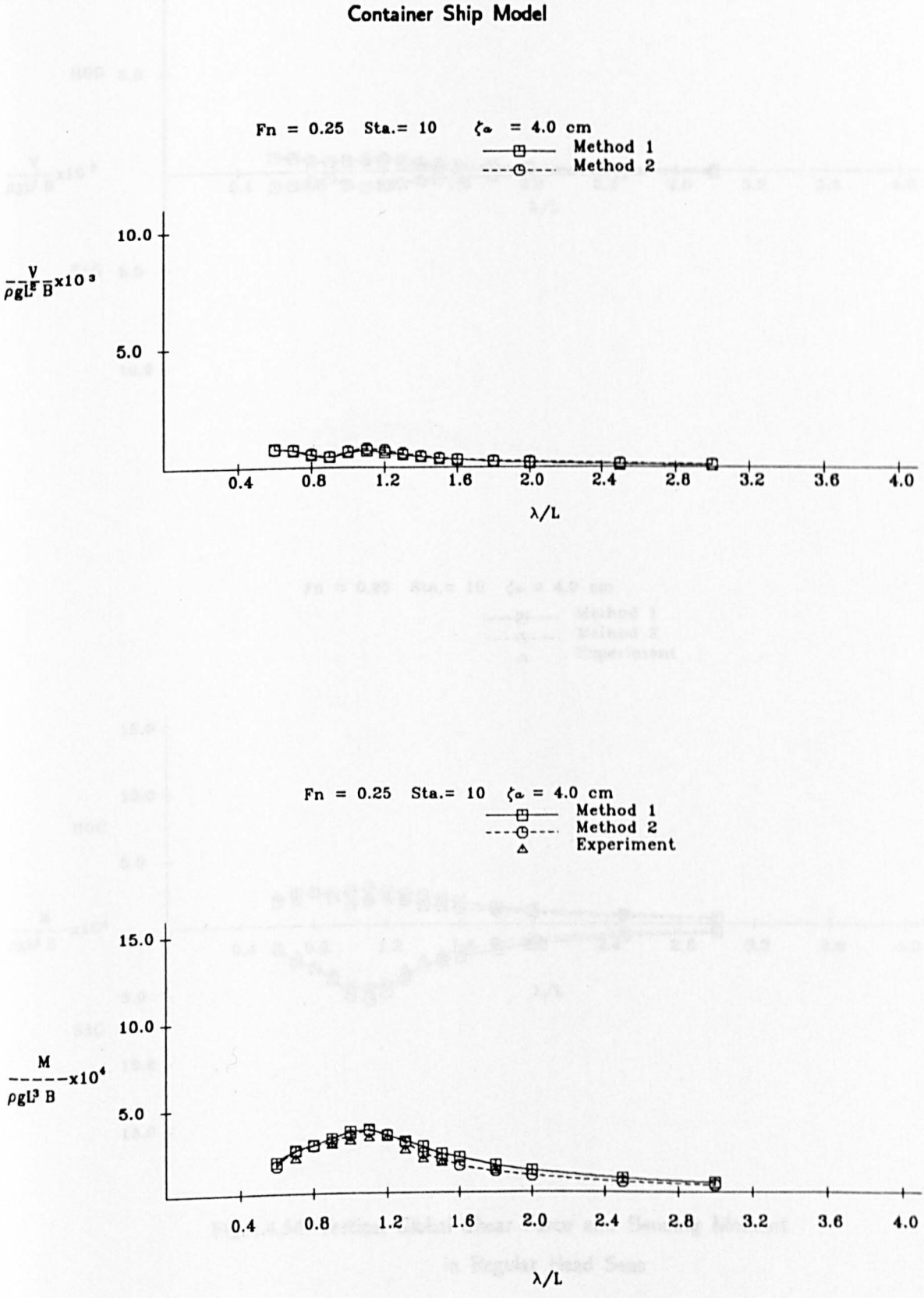

Fig.A.4.53 Vertical Global Shear Force and Bending Moment in Regular Head Seas

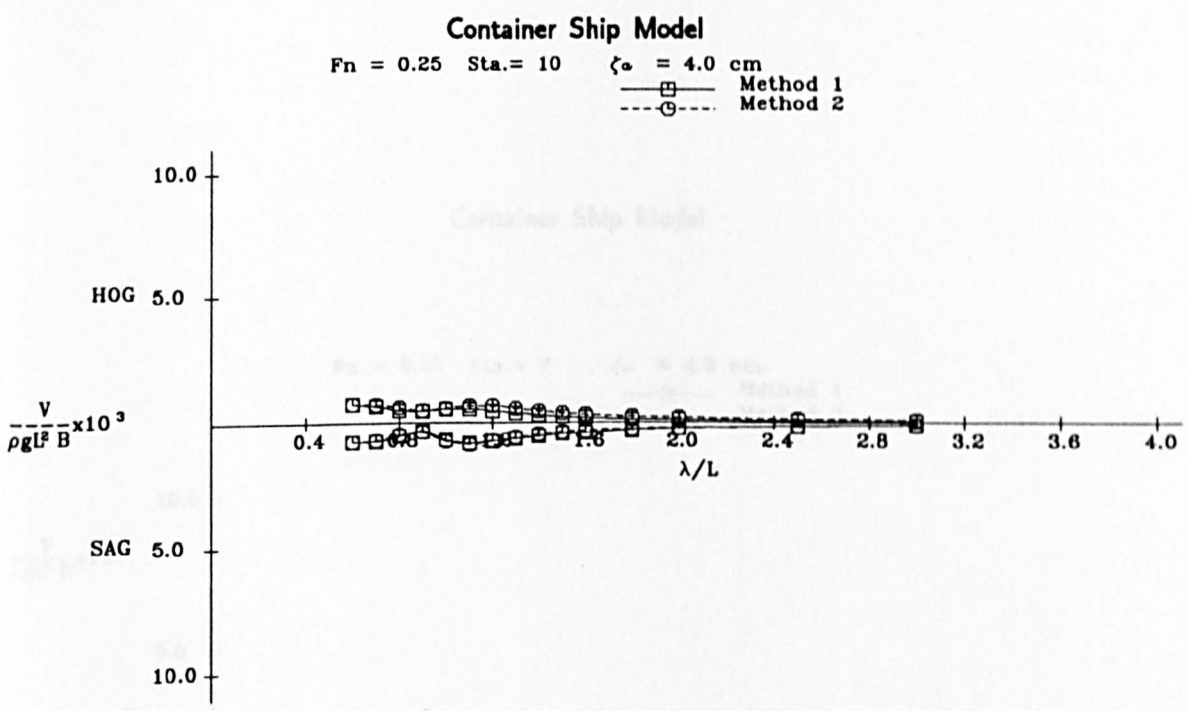

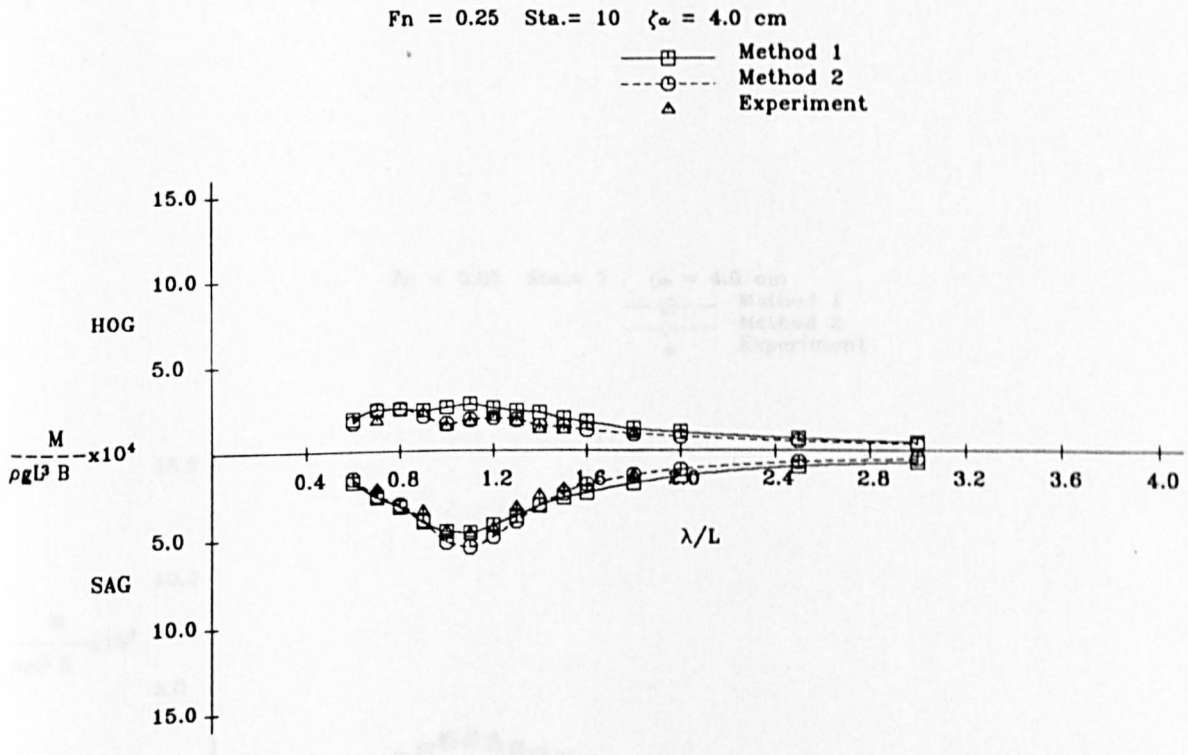

Fig.A.4.54 Vertical Global Shear Force and Bending Moment in Regular Head Seas

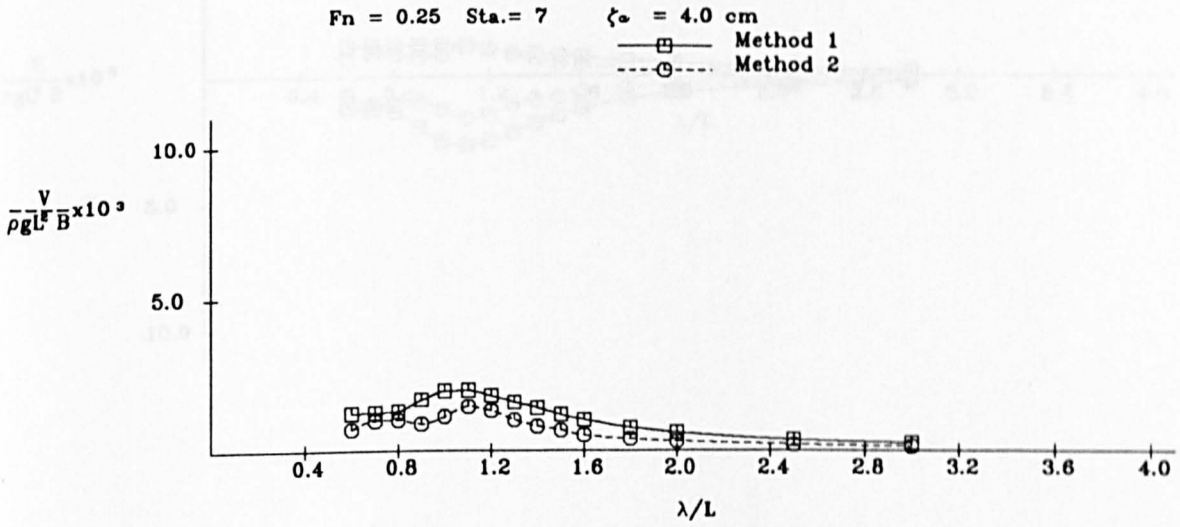

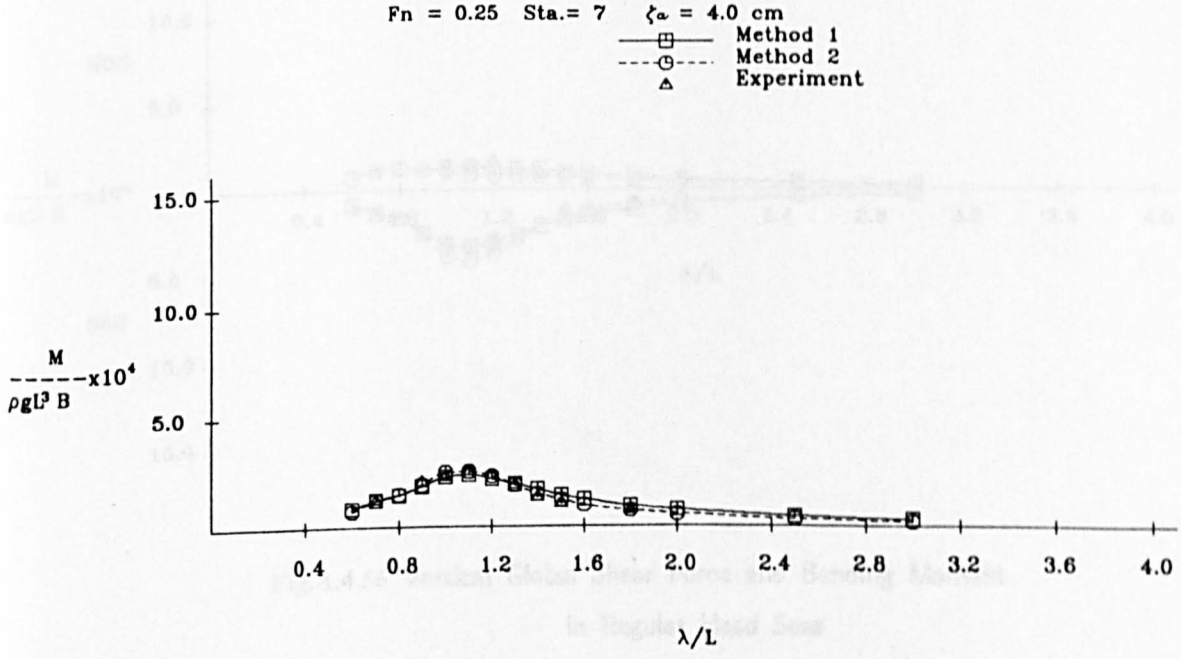

Fig.A.4.55 Vertical Global Shear Force and Bending Moment in Regular Head Seas

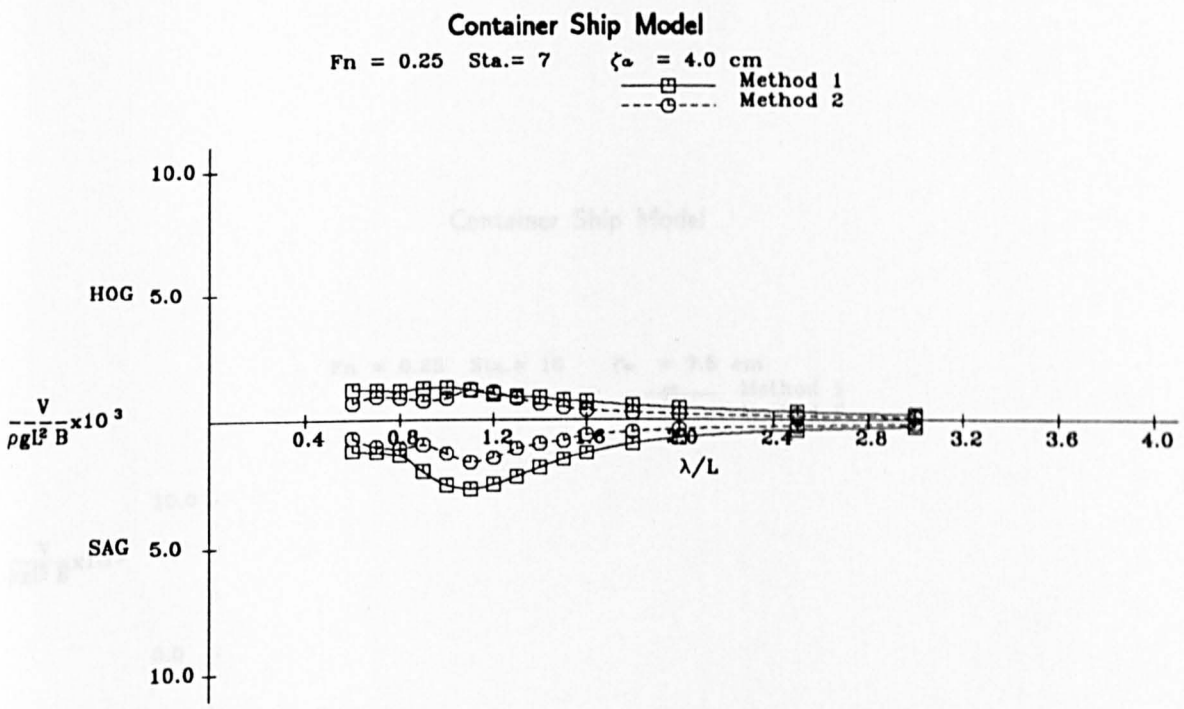

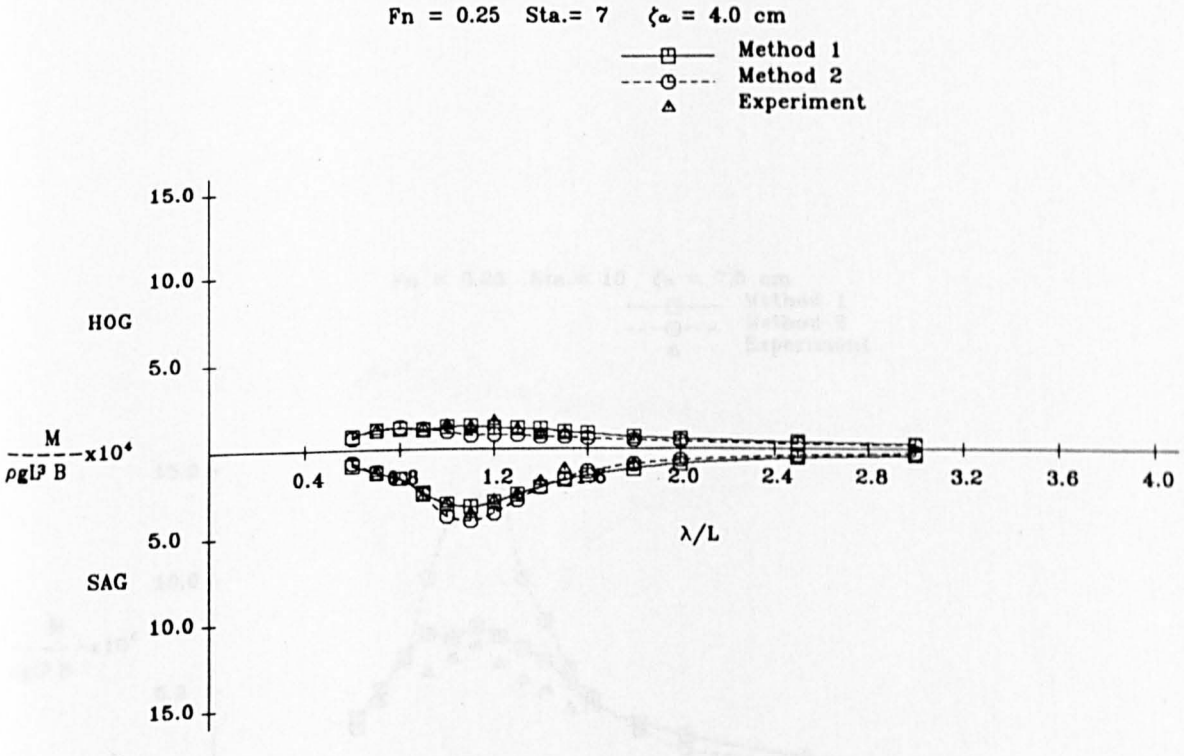

Fig.A.4.56 Vertical Global Shear Force and Bending Moment in Regular Head Seas

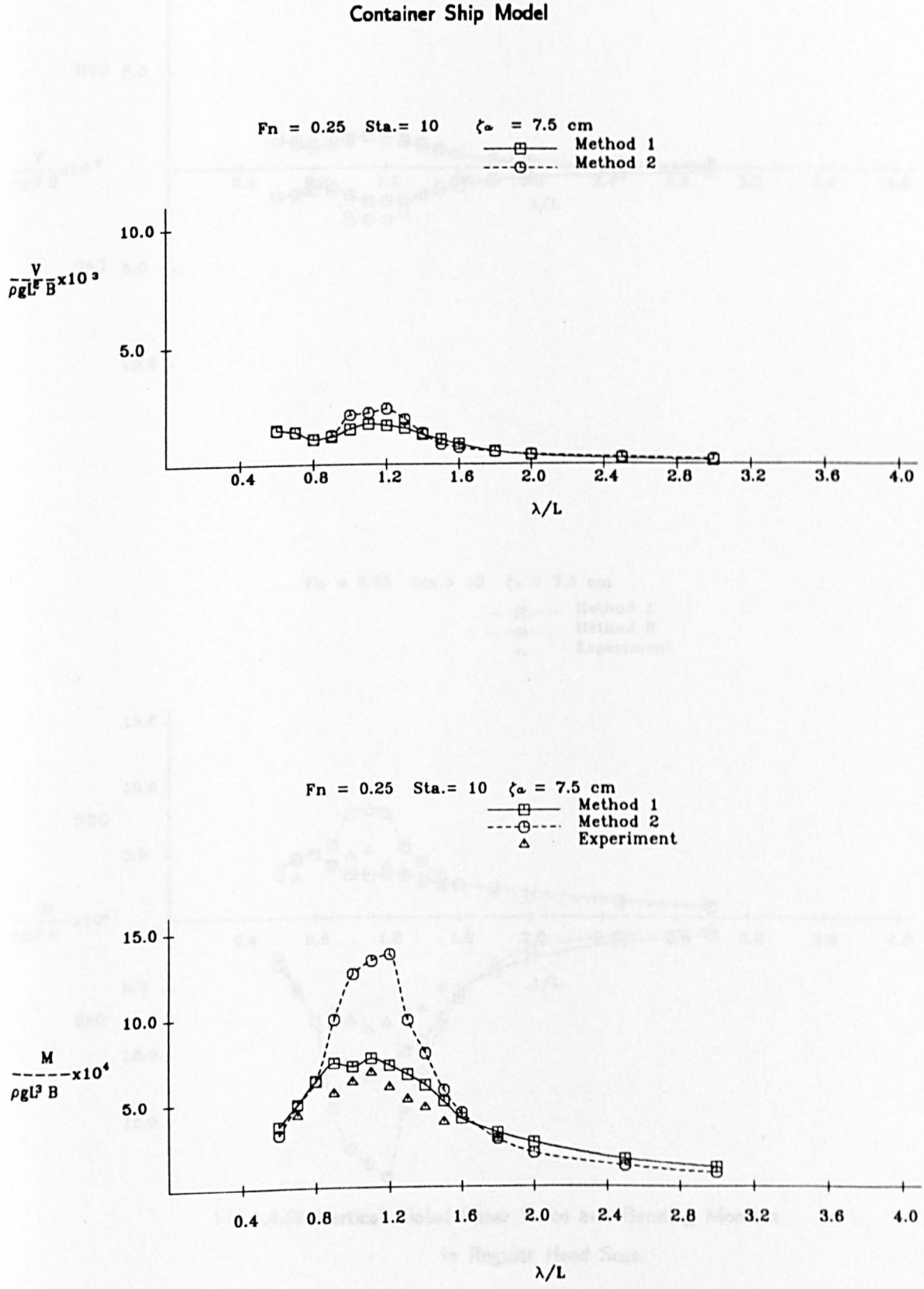

Fig.A.4.57 Vertical Global Shear Force and Bending Moment in Regular Head Seas

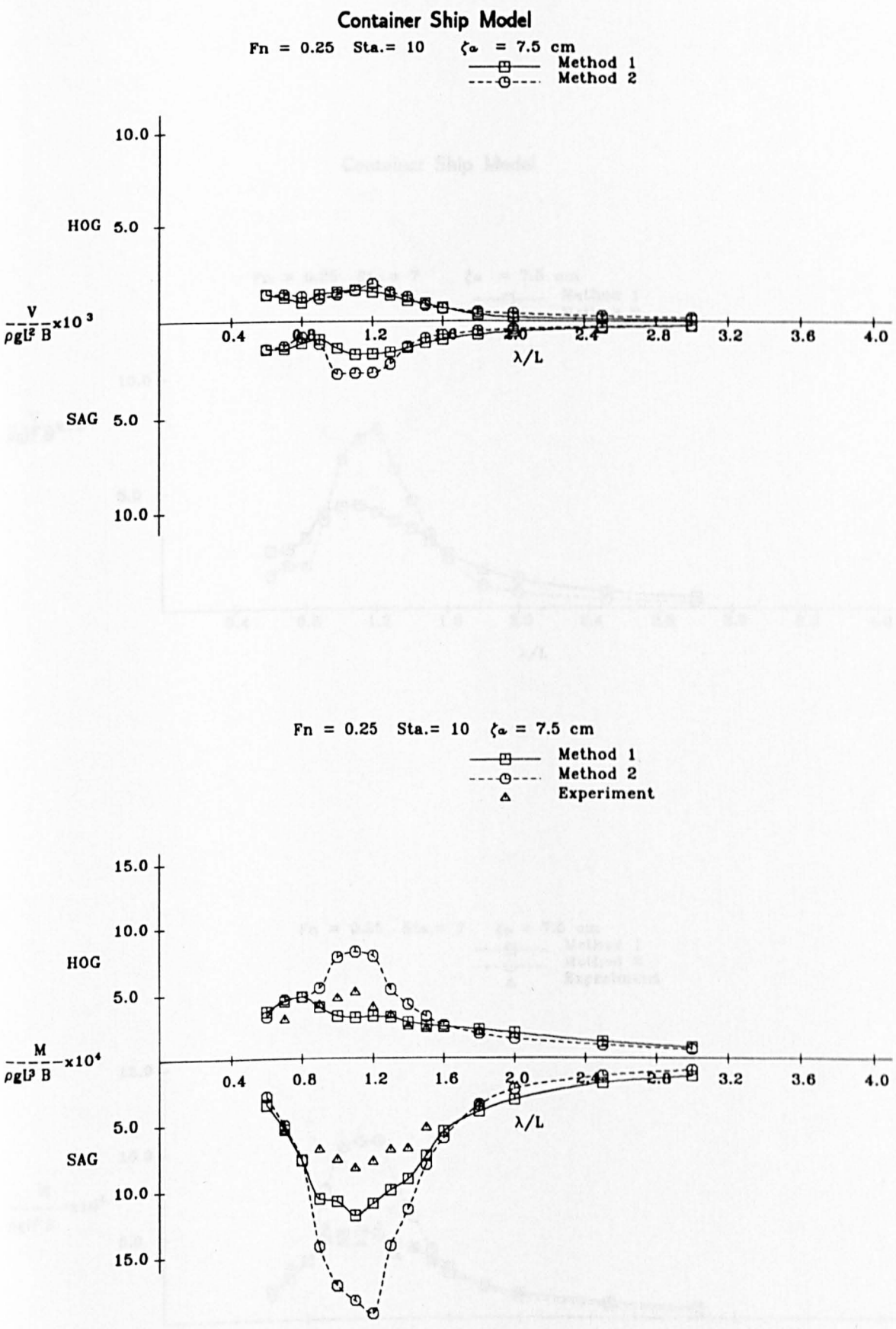

Fig.A.4.58 Vertical Global Shear Force and Bending Moment in Regular Head Seas

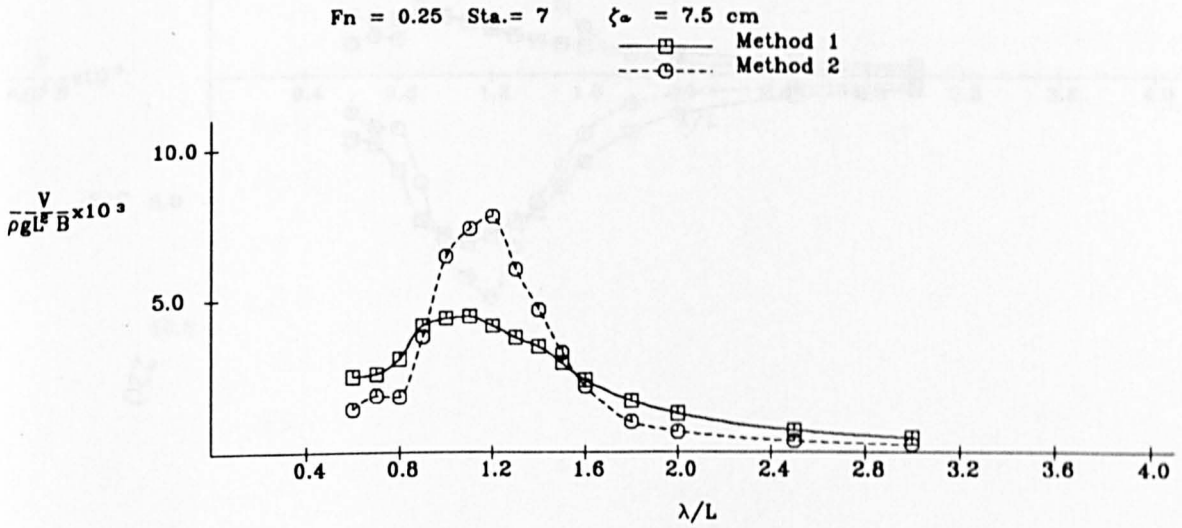

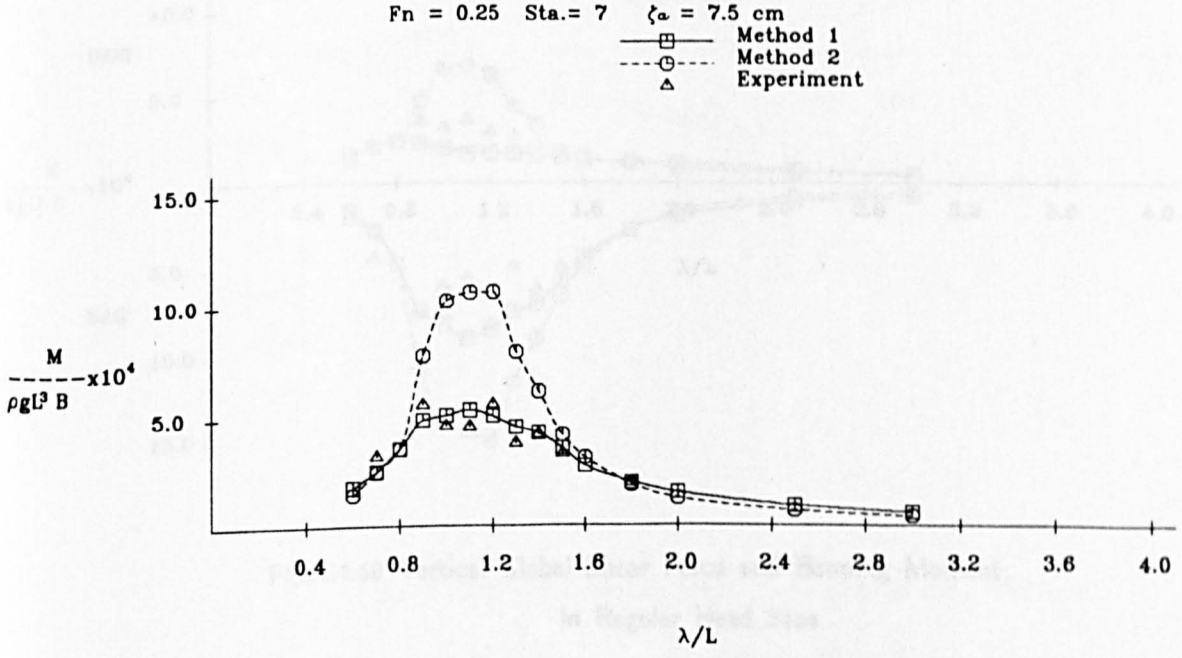

Fig.A.4.59 Vertical Global Shear Force and Bending Moment in Regular Head Seas

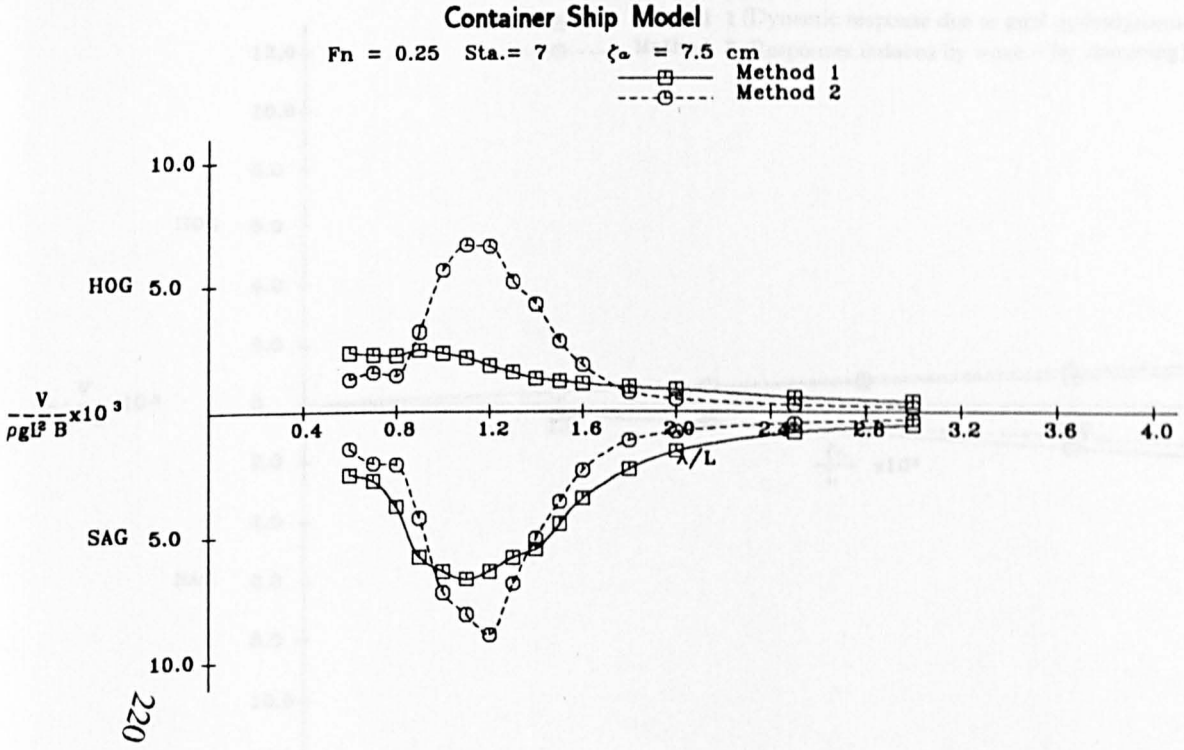

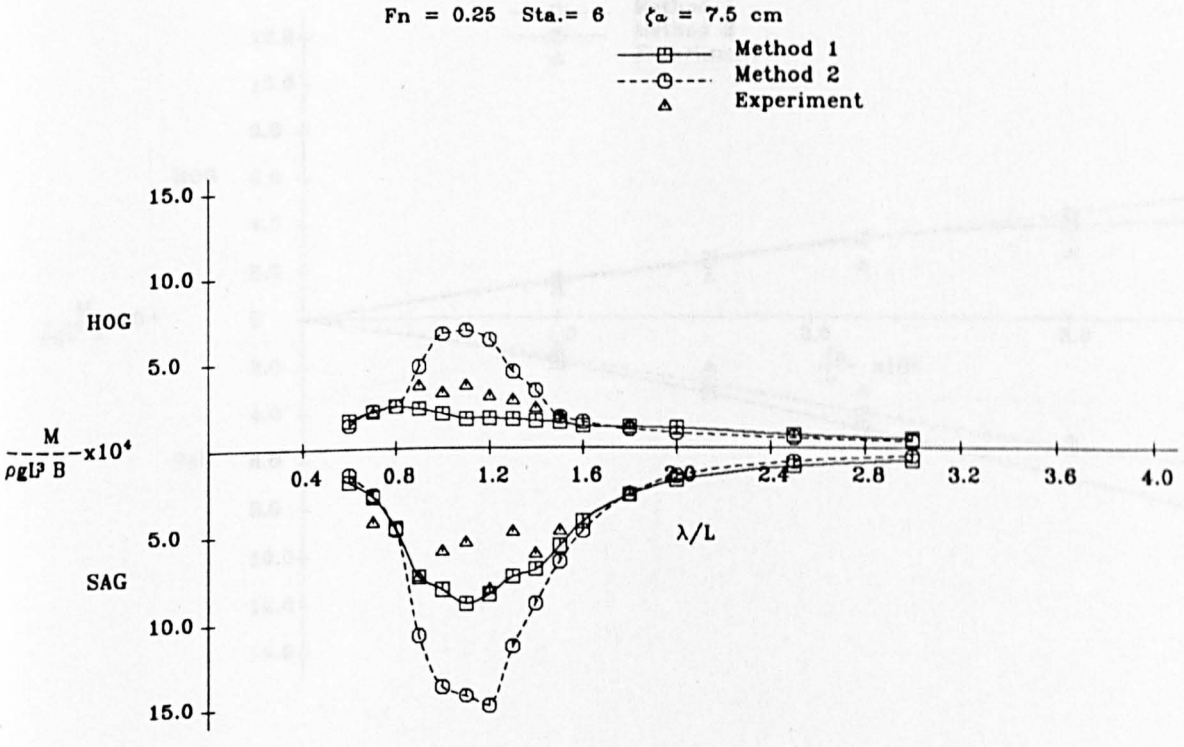

Fig.A.4.60 Vertical Global Shear Force and Bending Moment in Regular Head Seas

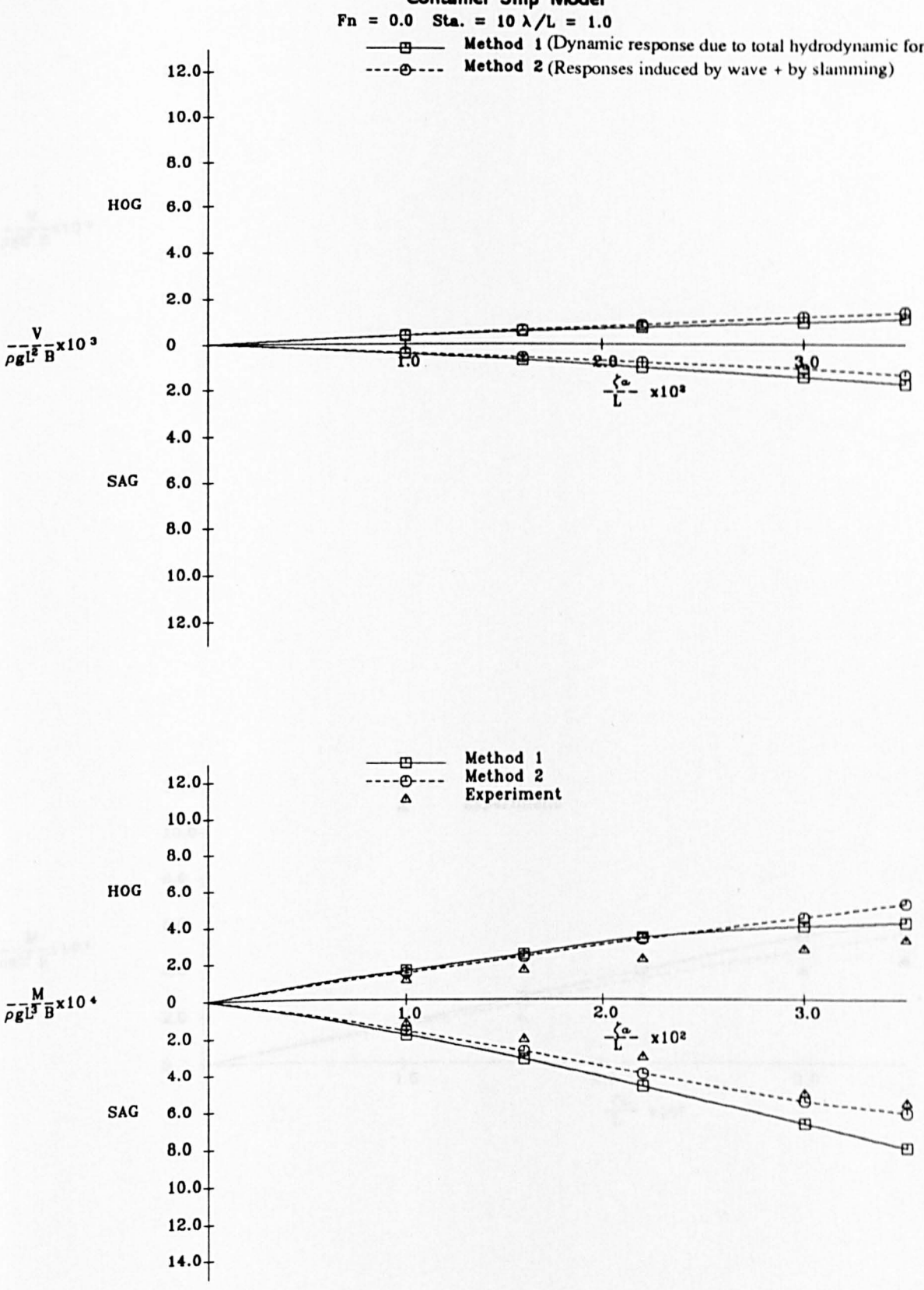

Fig.A.4.61 Vertical Global Shear Force and Bending Moment

in Regular Head Seas

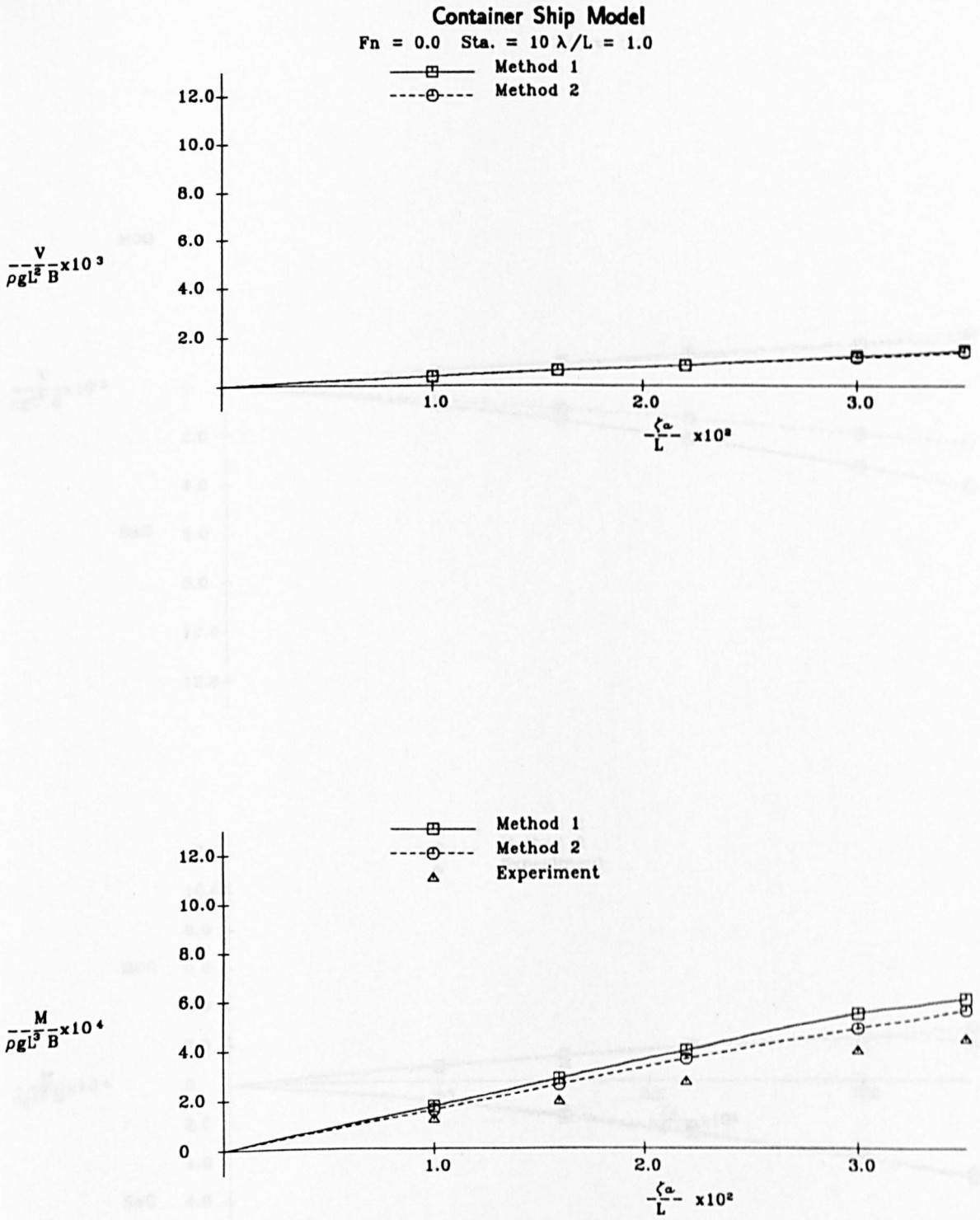

Fig.A.4.62 Vertical Global Shear Force and Bending Moment in Regular Head Seas

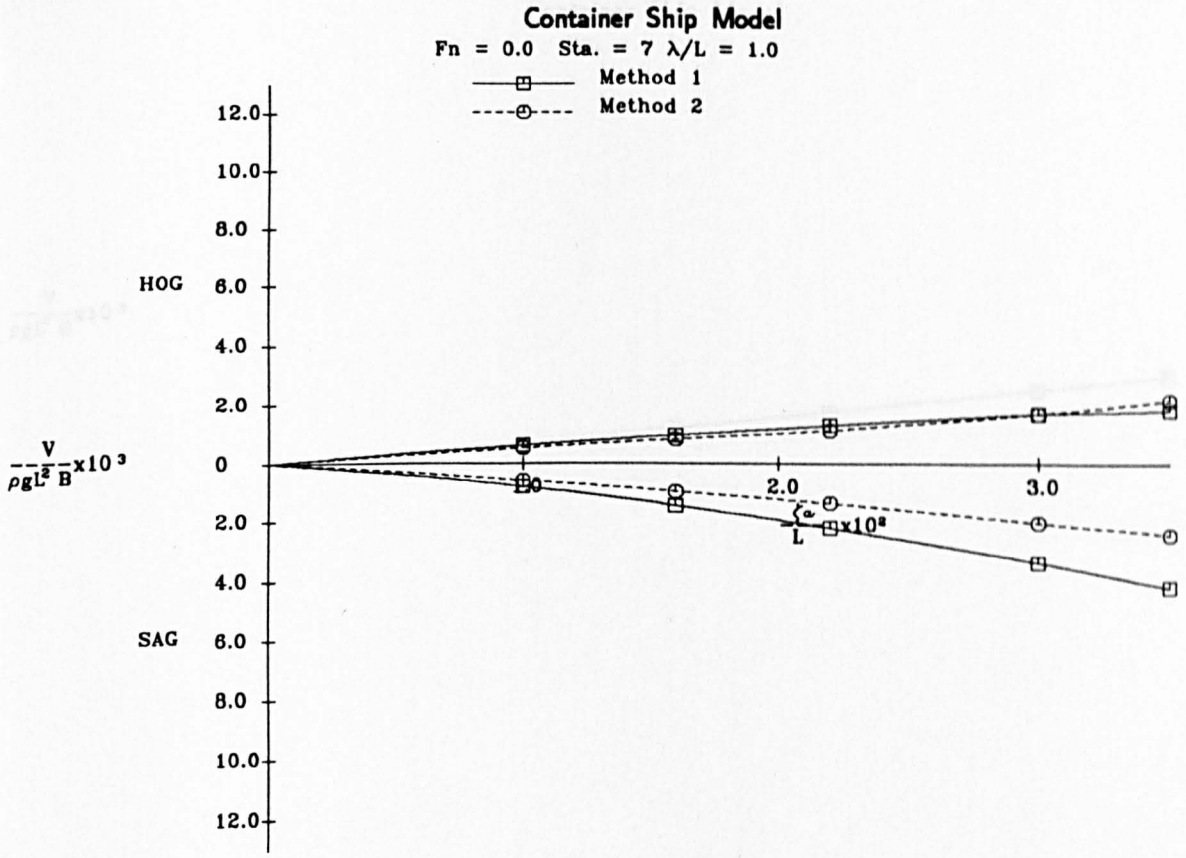

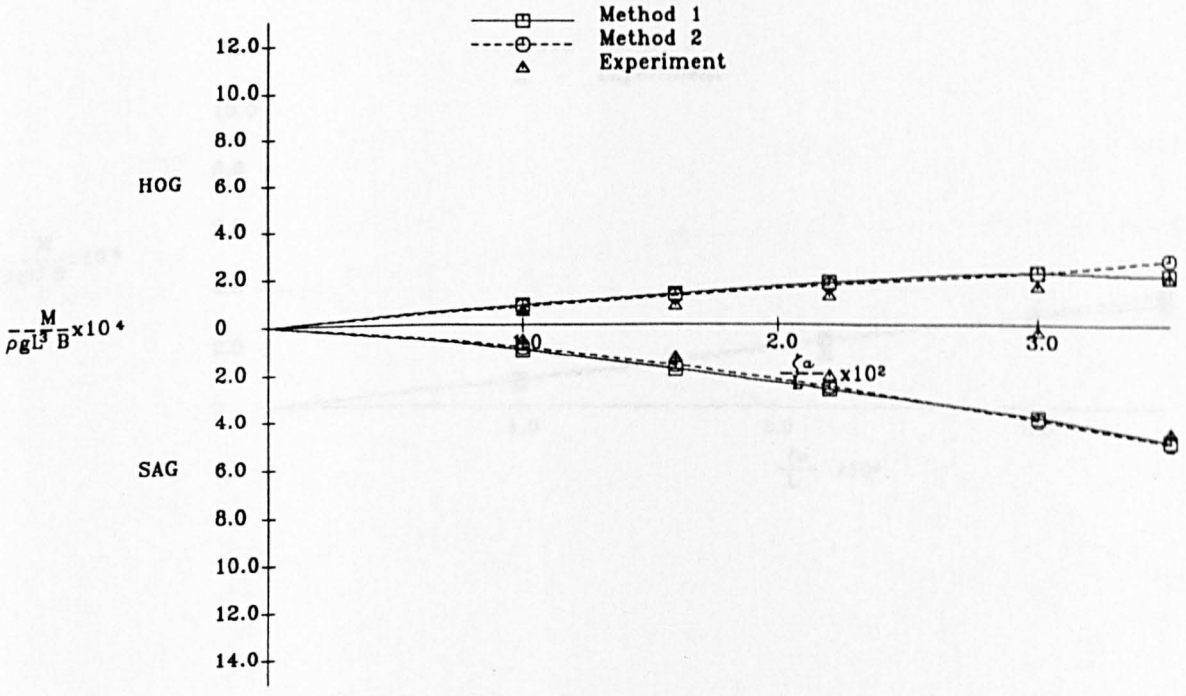

Fig.A.4.63 Vertical Global Shear Force and Bending Moment in Regular Head Seas

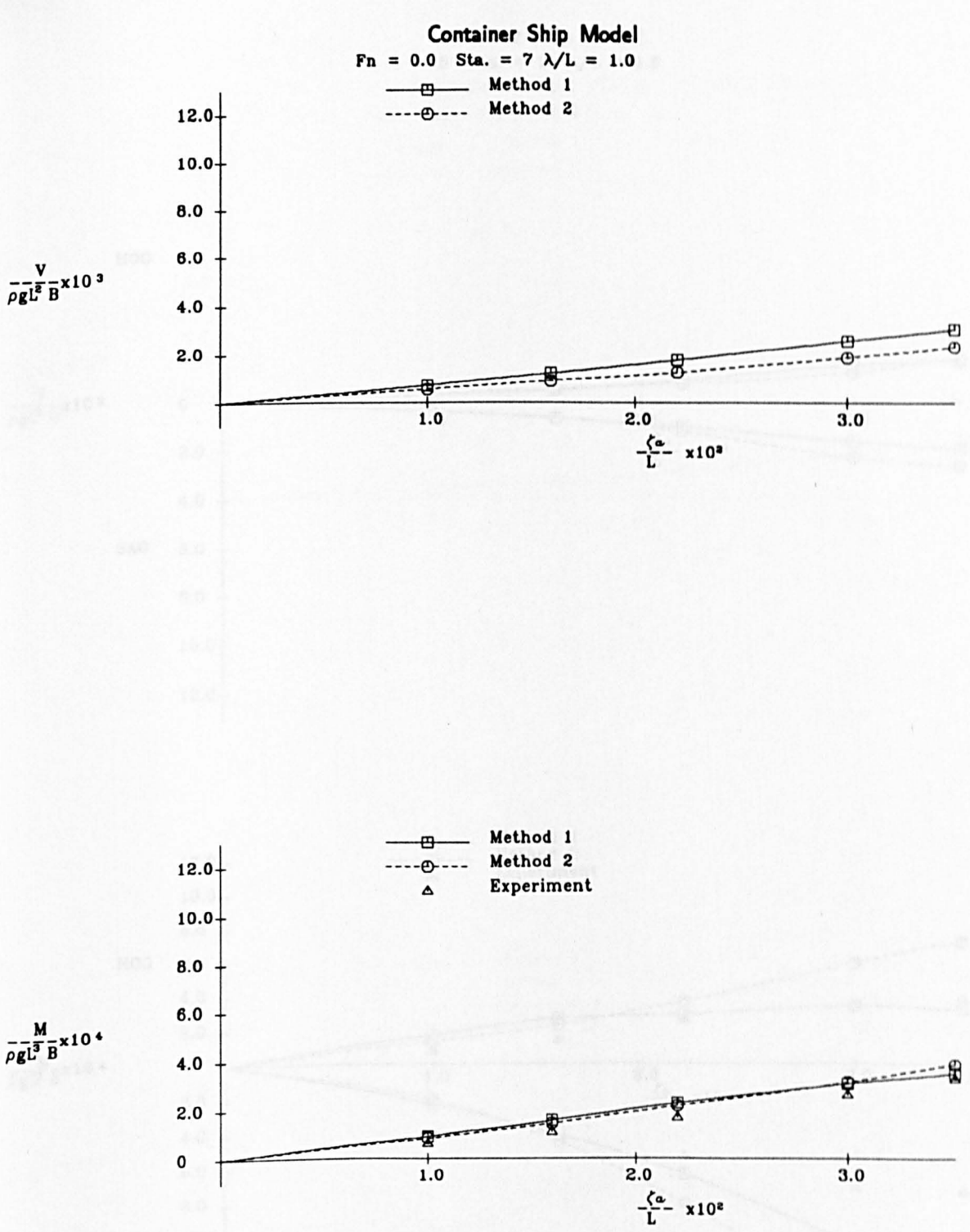

Fig.A.4.64 Vertical Global Shear Force and Bending Moment in Regular Head Seas

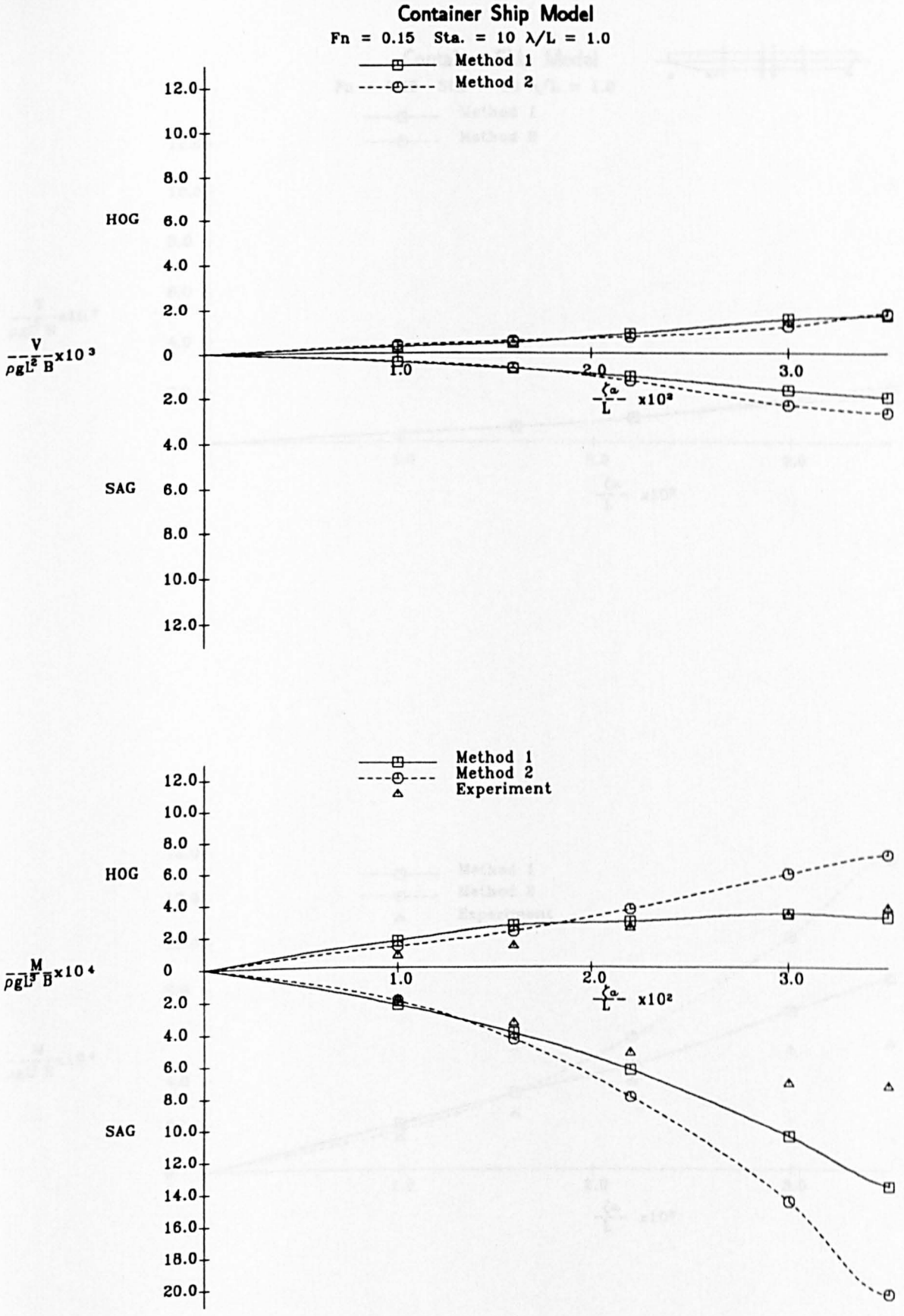

Fig.A.4.65 Vertical Global Shear Force and Bending Moment in Regular Head Seas

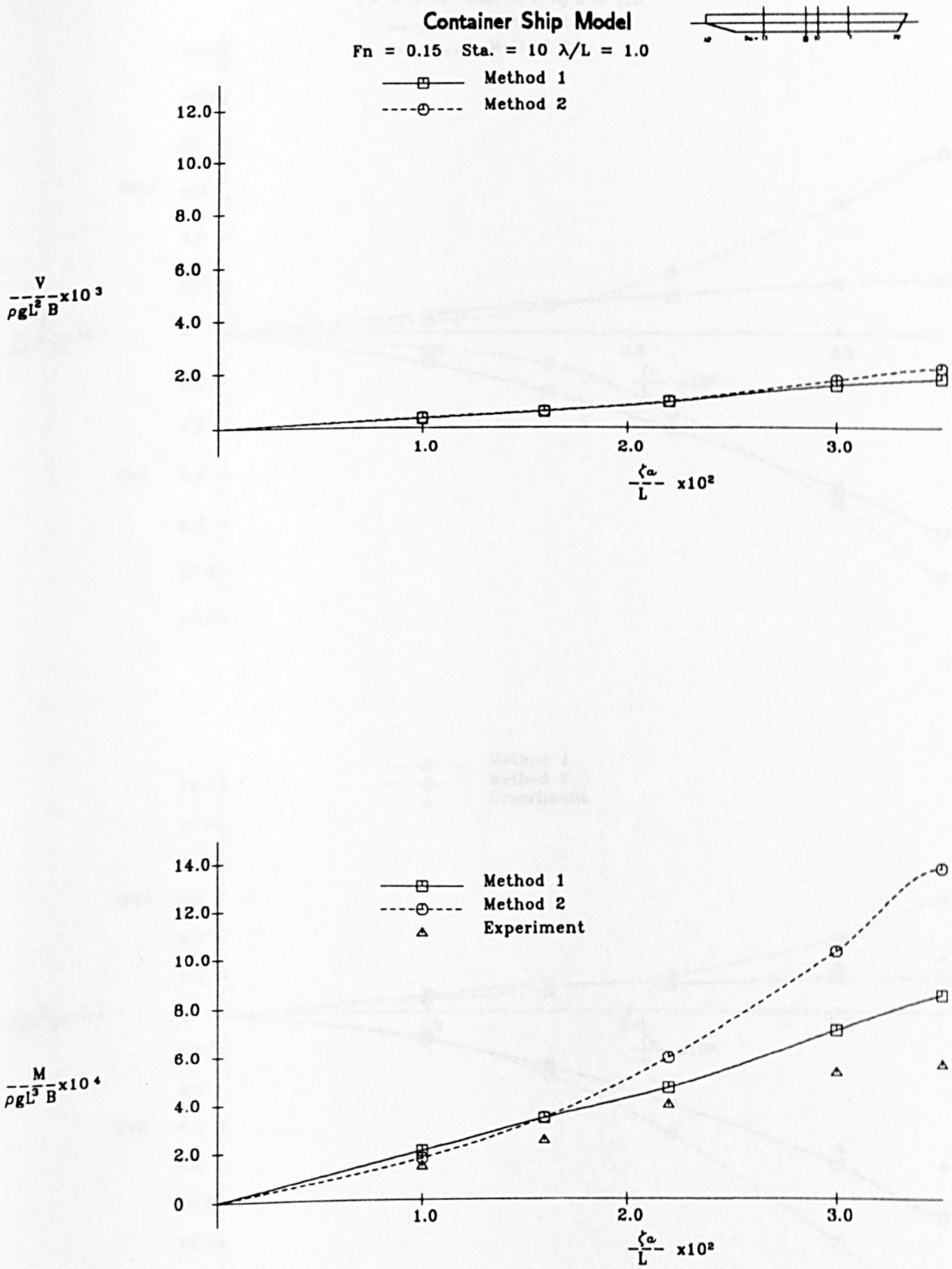

Fig.A.4.66 Vertical Global Shear Force and Bending Moment in Regular Head Seas

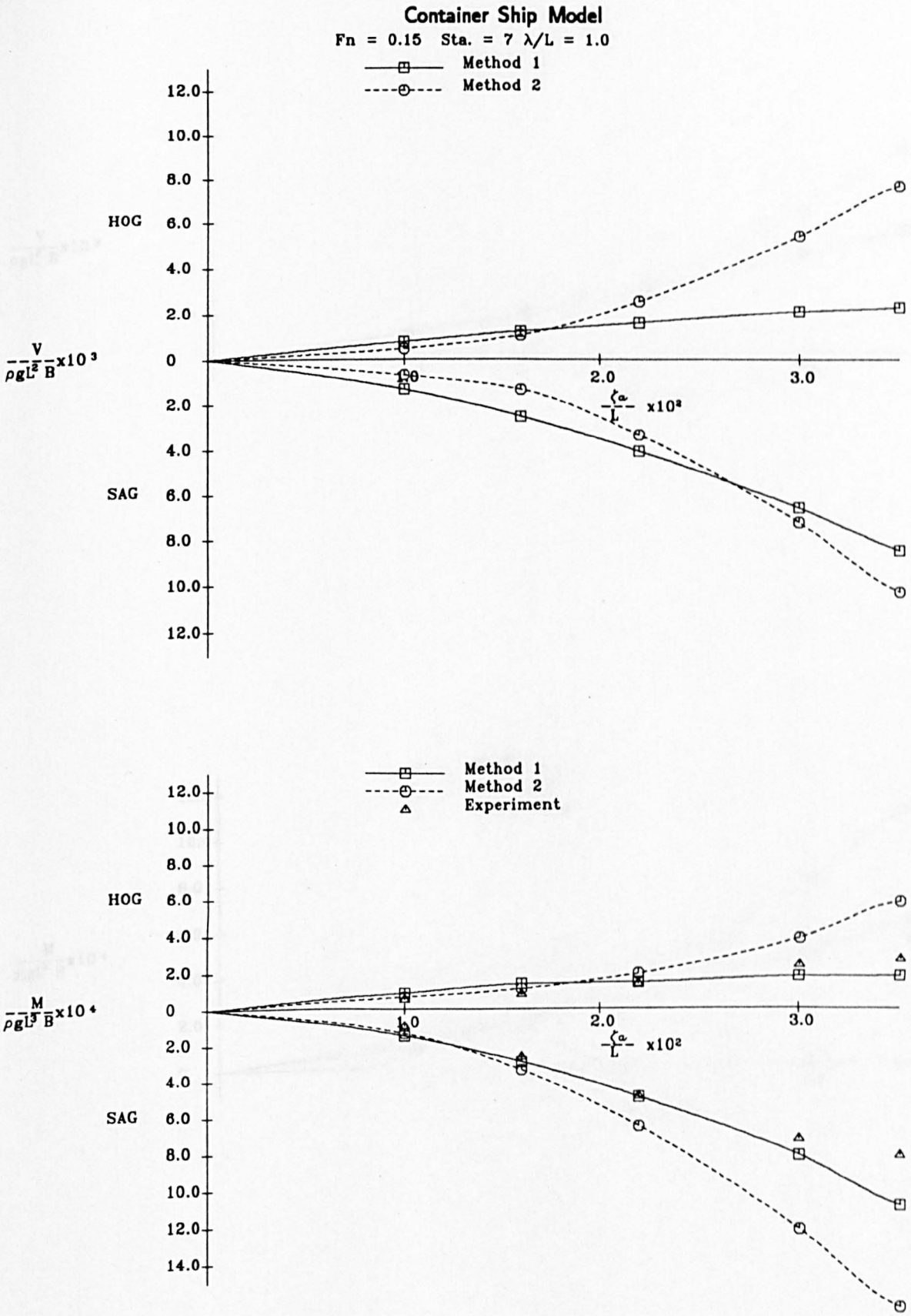

Fig.A.4.67 Vertical Global Shear Force and Bending Moment in Regular Head Seas

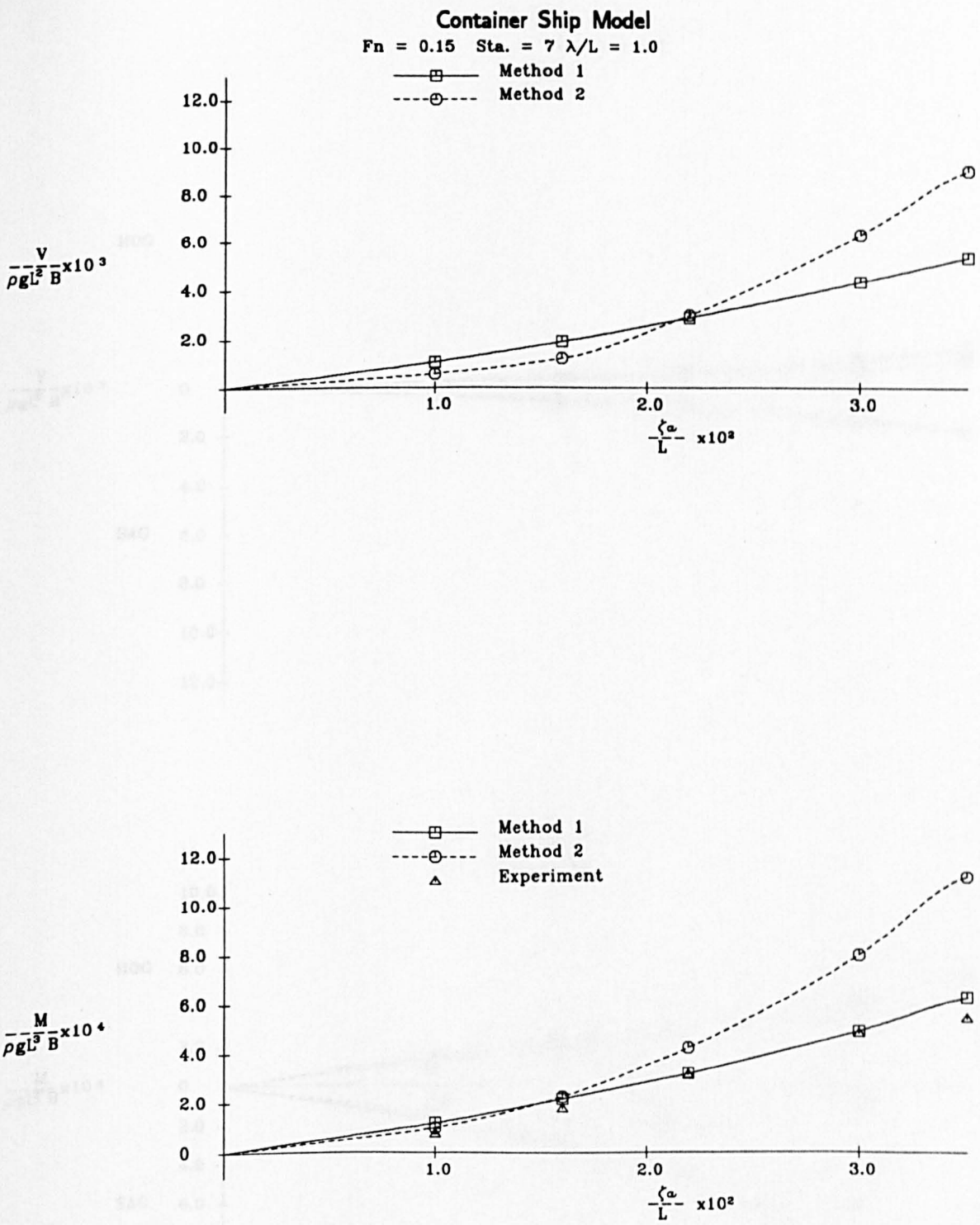

Fig.A.4.68 Vertical Global Shear Force and Bending Moment in Regular Head Seas

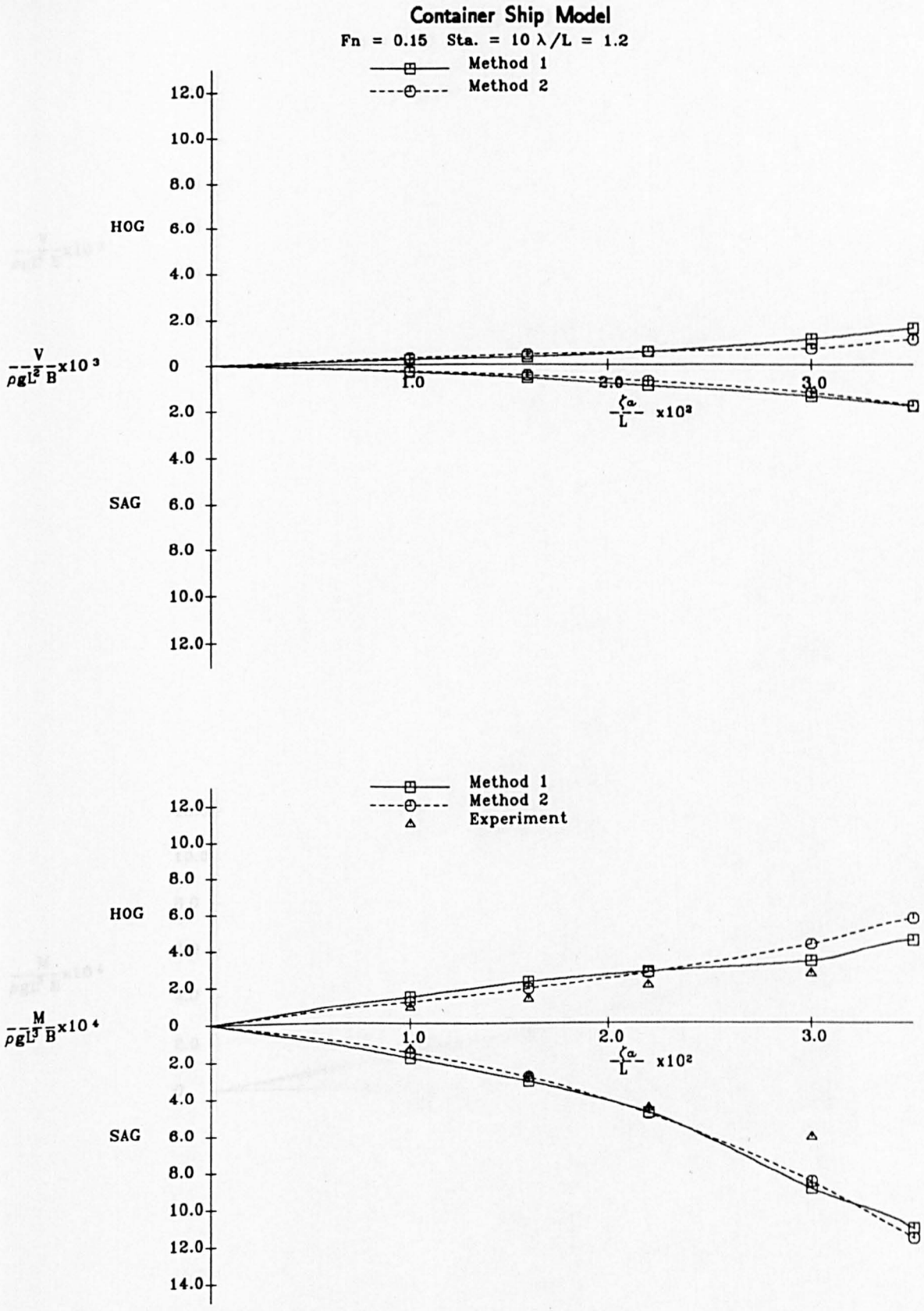

Fig.A.4.69 Vertical Global Shear force and bending Moment

in Regular Head Seas

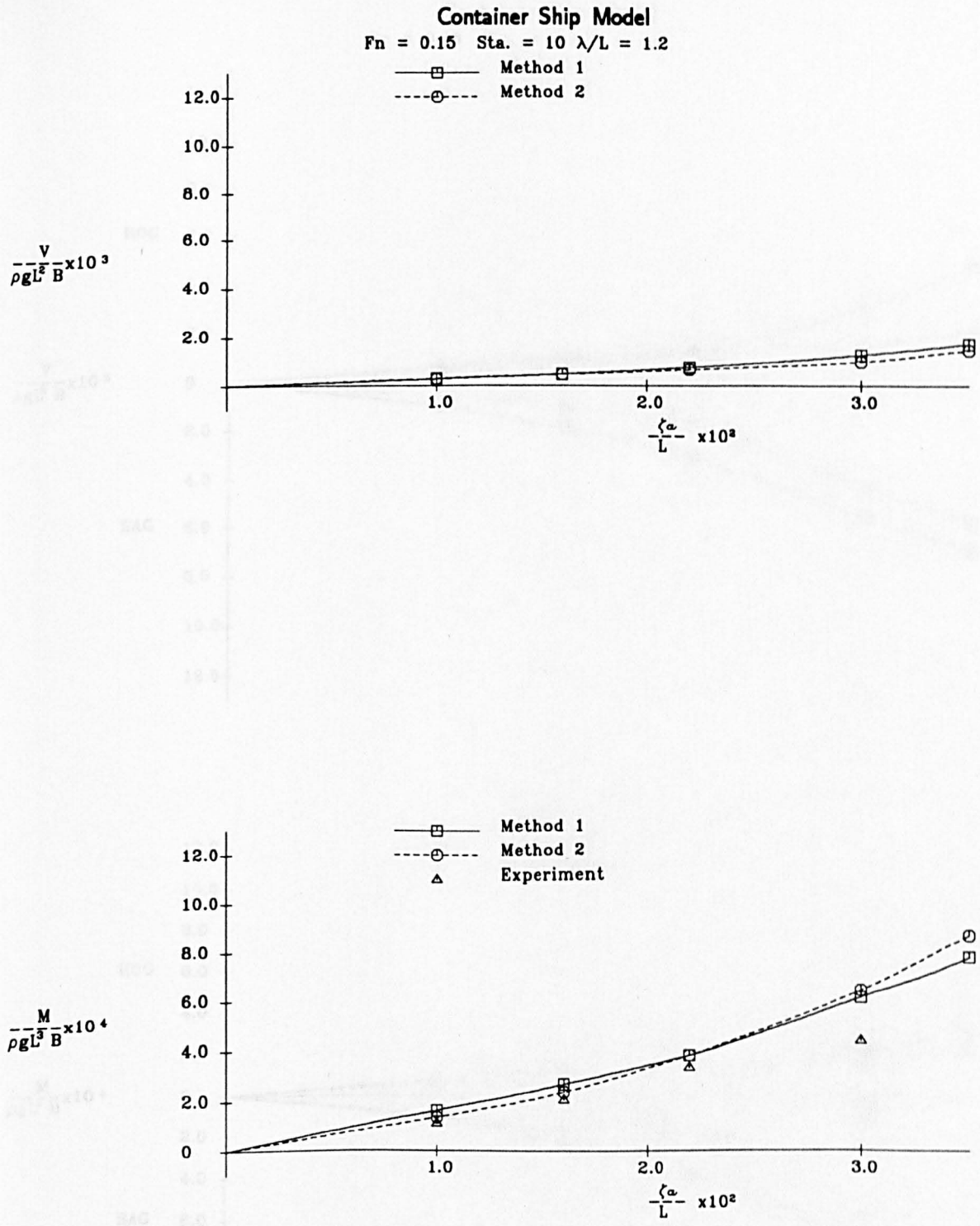

Fig.A.4.70 Vertical Global Shear Force and Bending Moment in Regular Head Seas

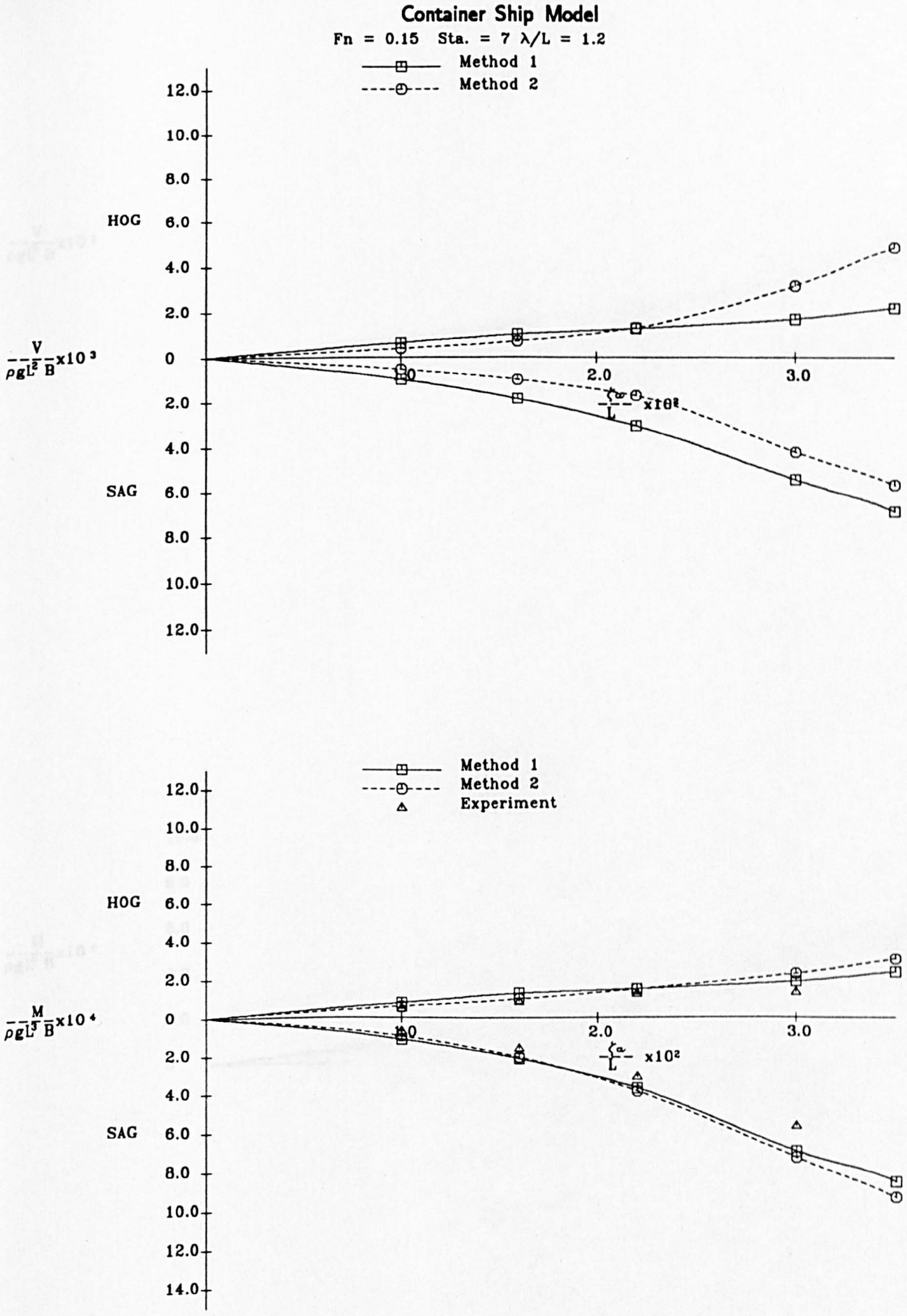

Fig.A.4.71 Vertical Global Shear Force and Bending Moment

in Regular Head Seas

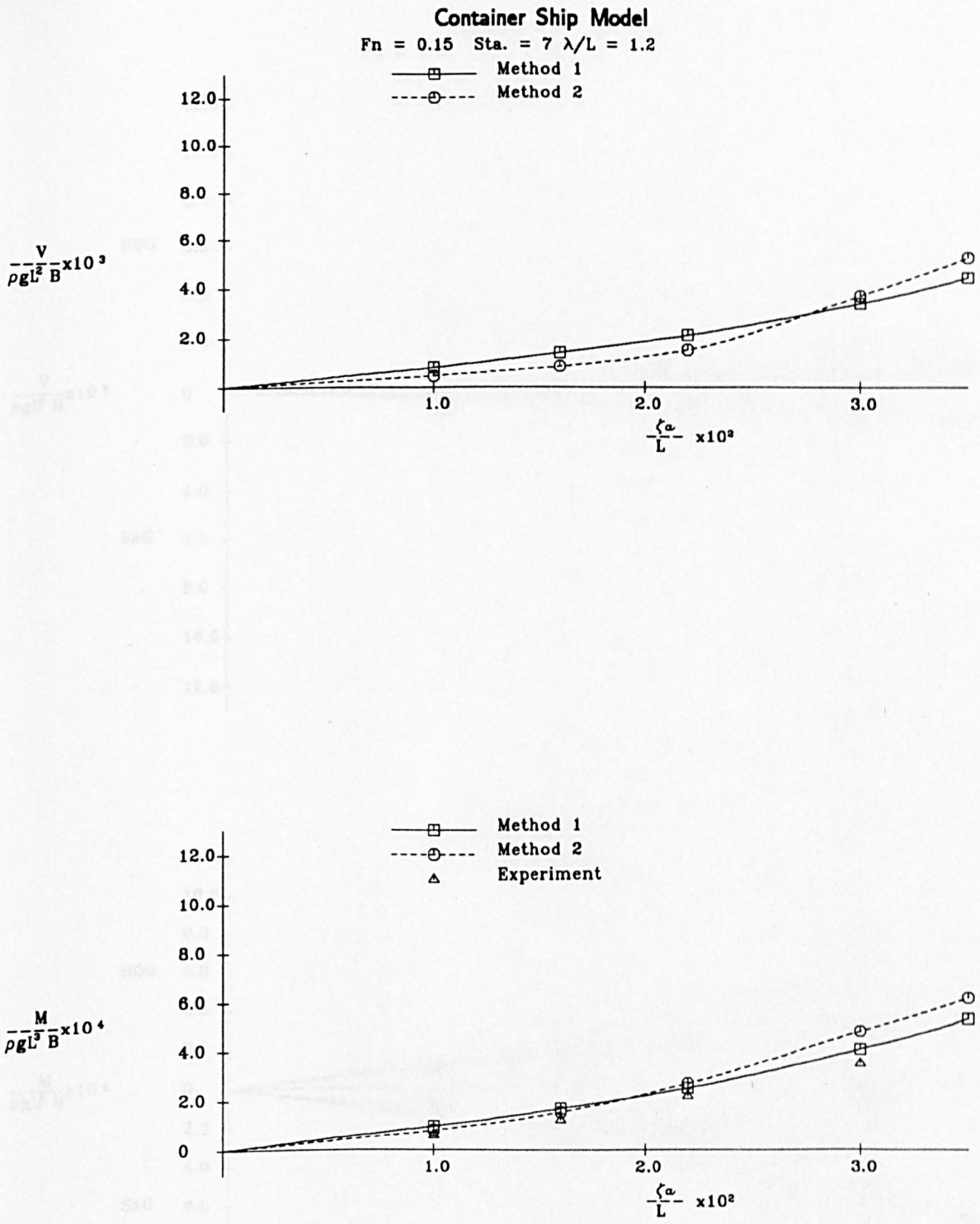

Fig.A.4.72 Vertical Global Shear Force and Bending Moment in Regular Head Seas

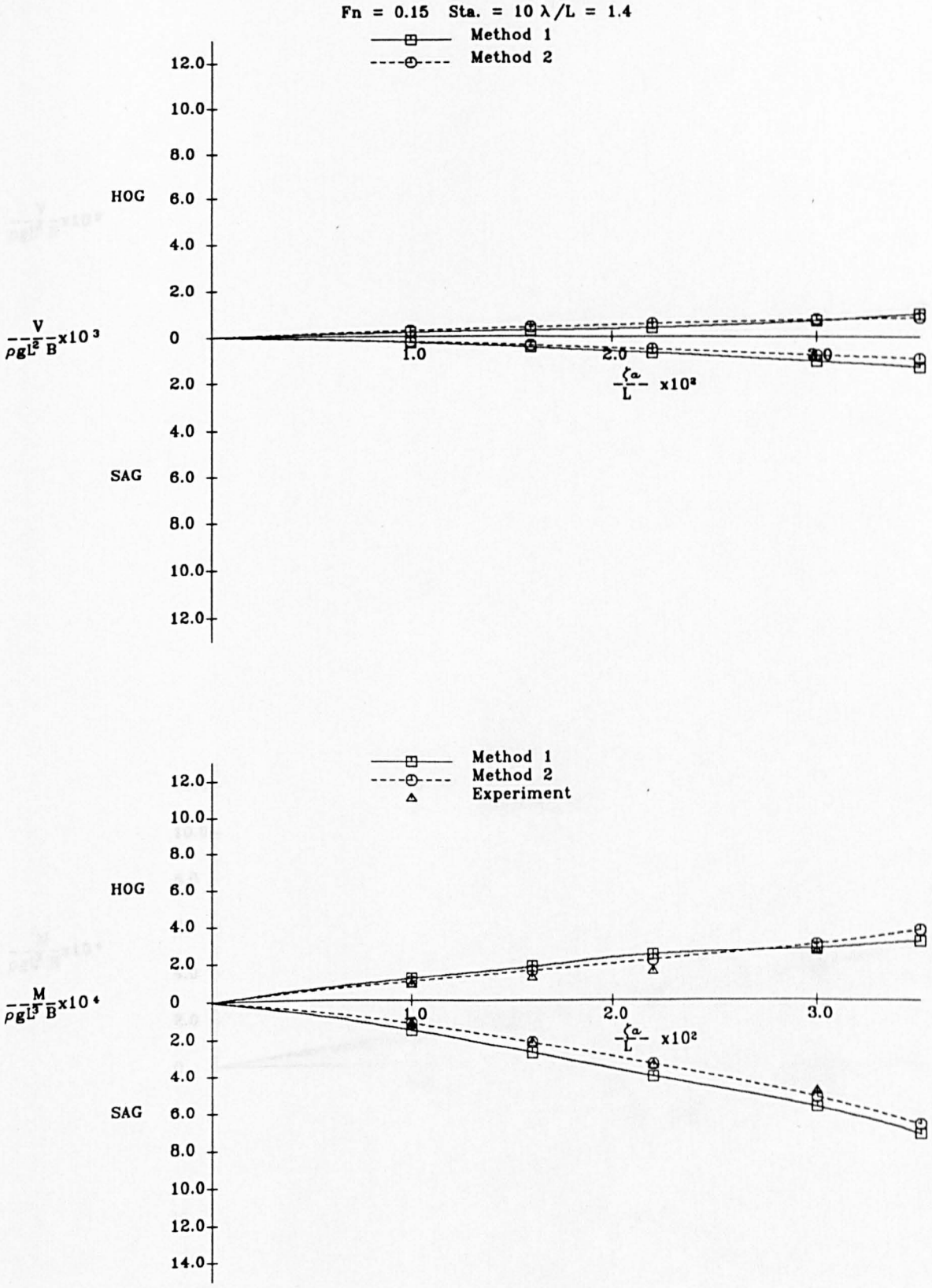

Fig.A.4.73 Vertical Global Shear Force and Bending Moment in Regular Head Seas

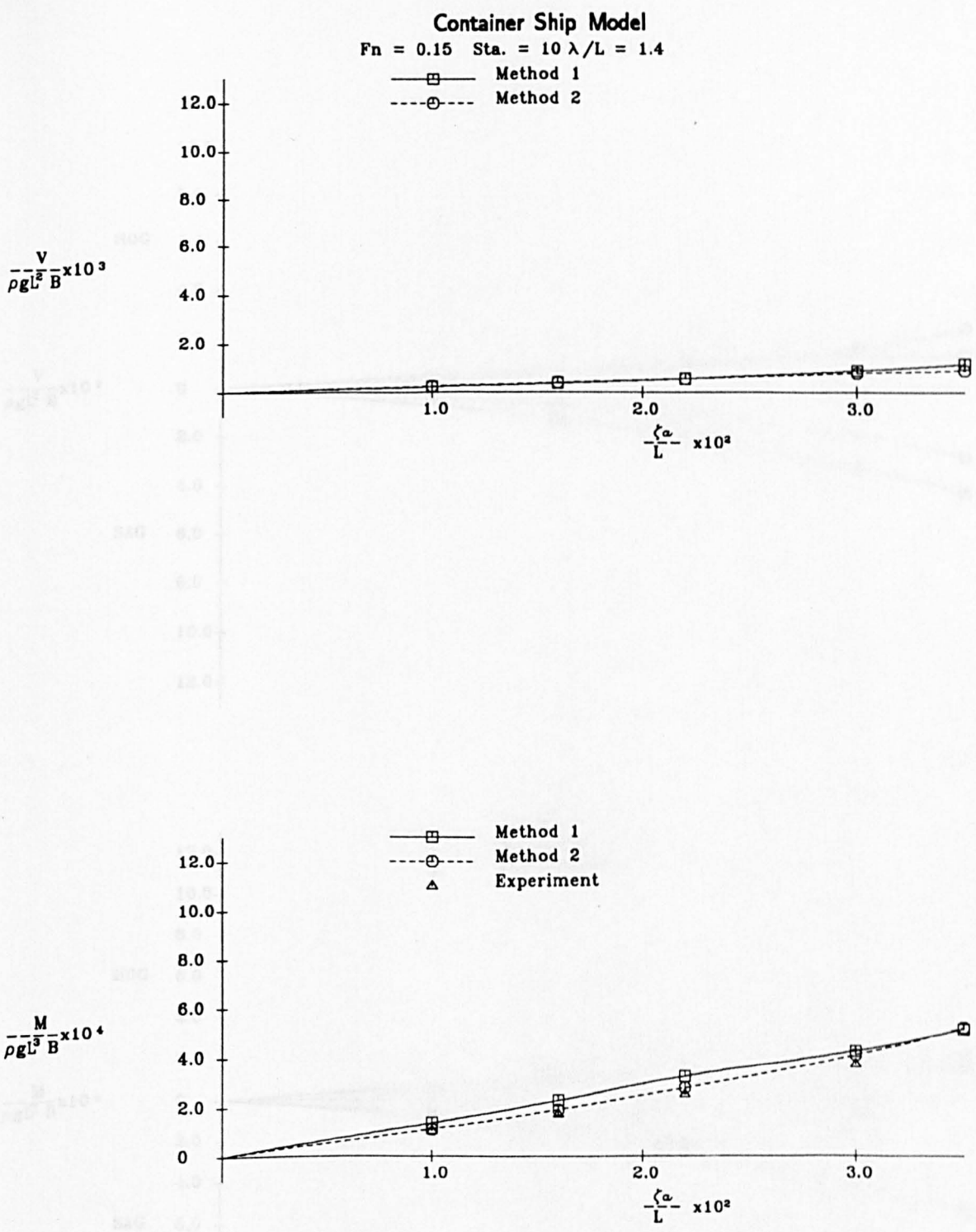

Fig.A.4.74 Vertical Global Shear Force and Bending Moment in Regular Head Seas

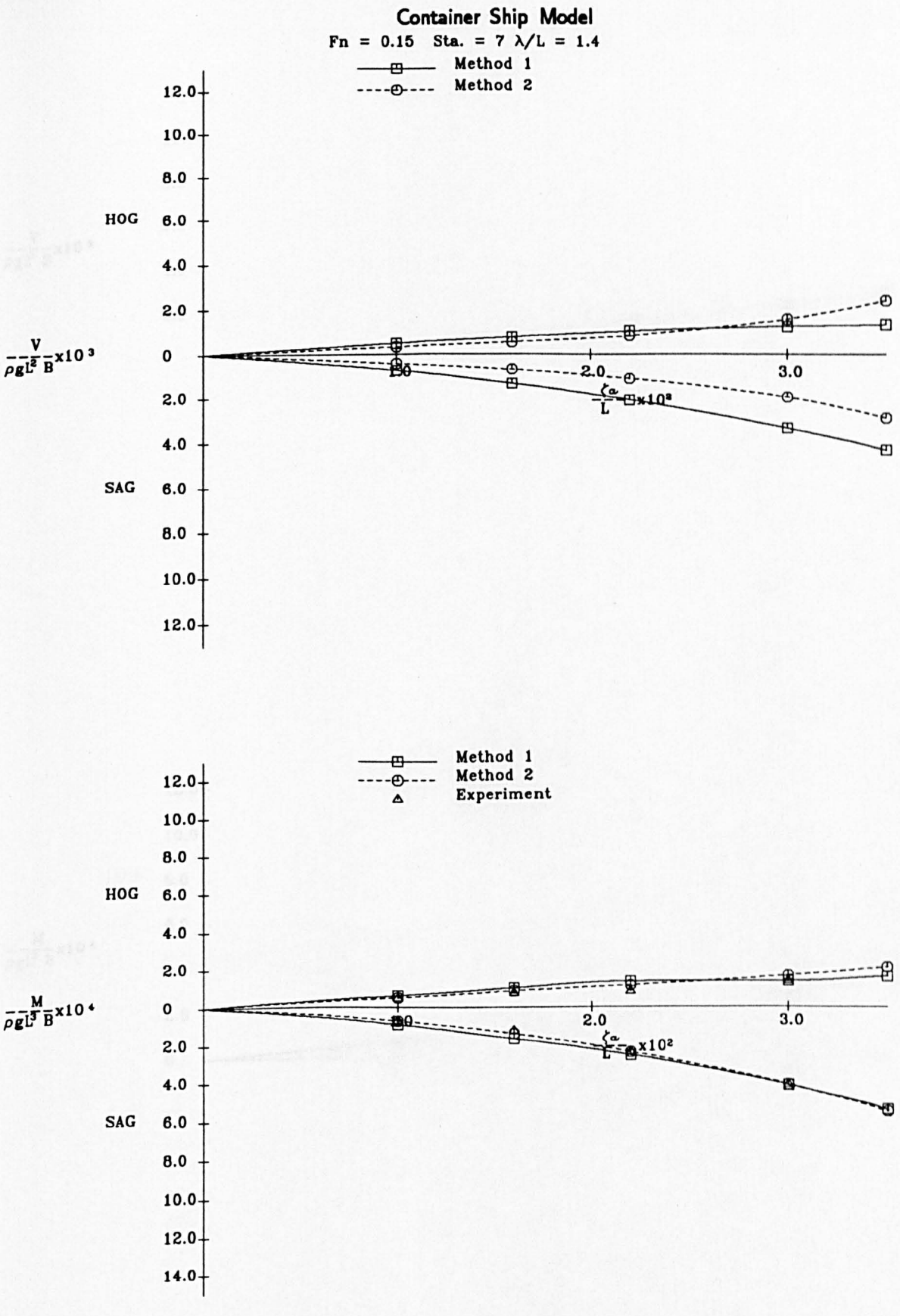

Fig.A.4.75 Vertical Global Shear Force and Bending Moment in Regular Head Seas

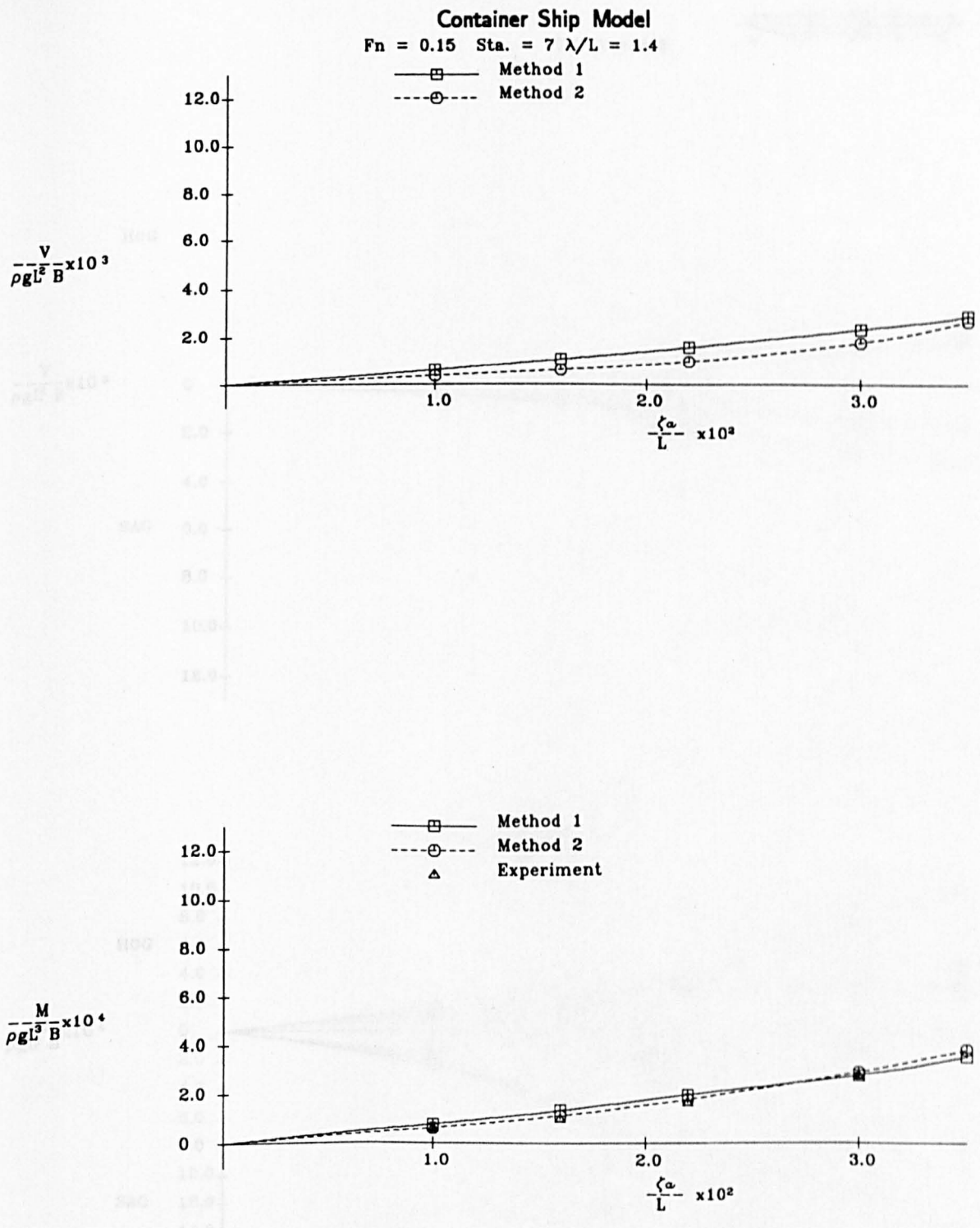

Fig.A.4.76 Vertical Global Shear Force and Bending Moment in Regular Head Seas

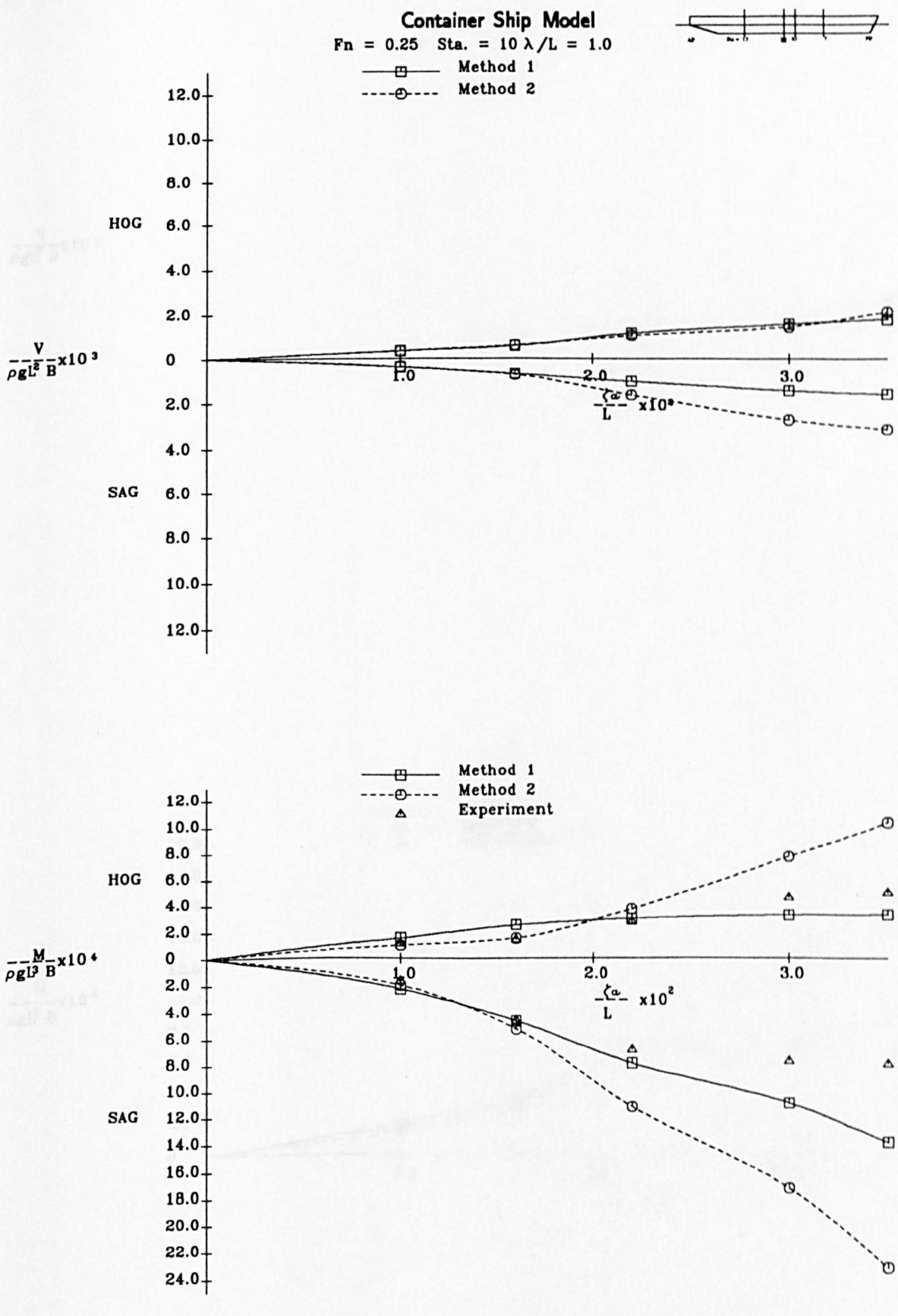

Fig.A.4.77 Vertical Global Shear Force and Bending Moment in Regular Head Seas

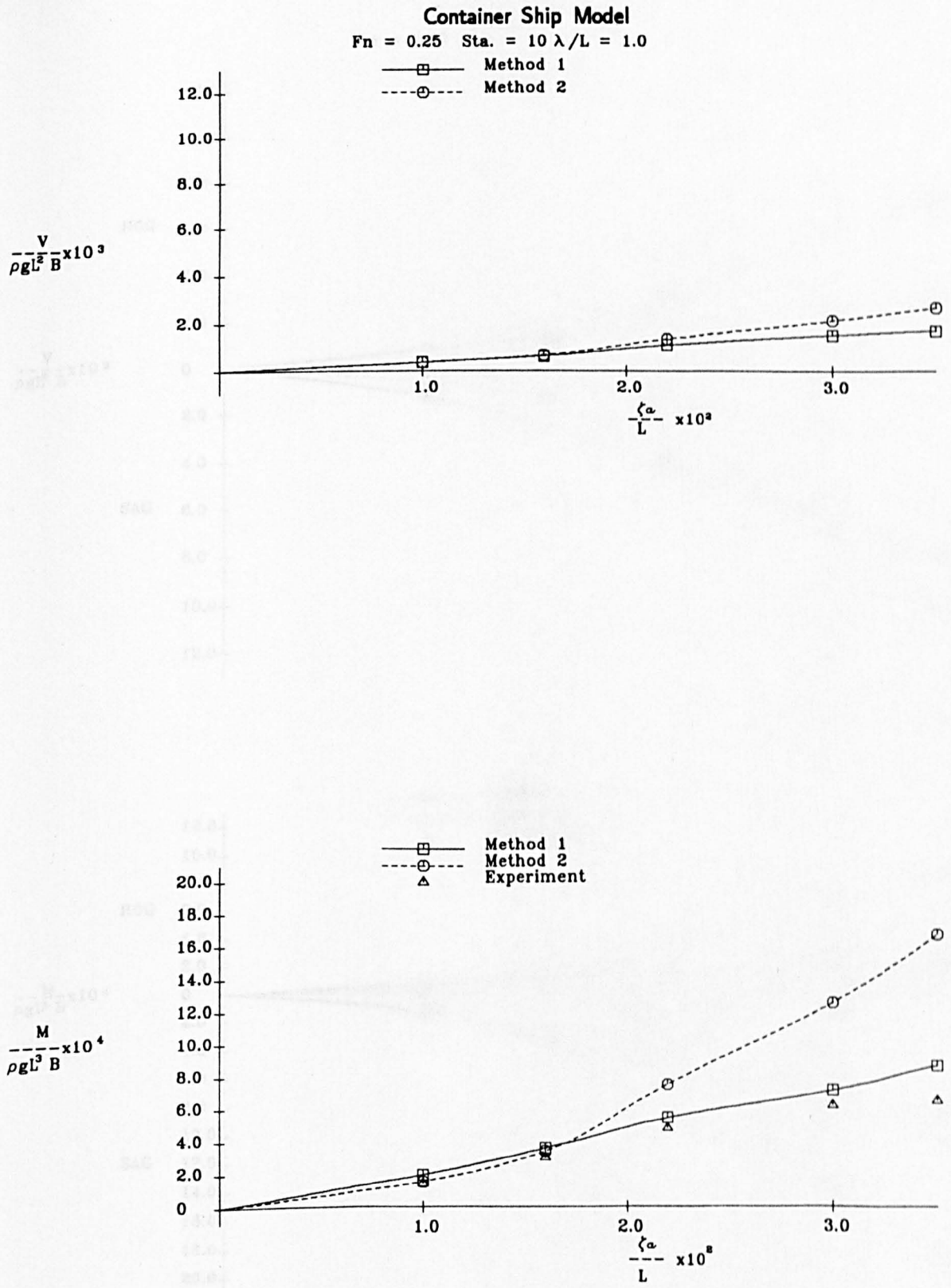

Fig.A.4.78 Vertical Global Shear Force and Bending Moment in Regular Head Seas

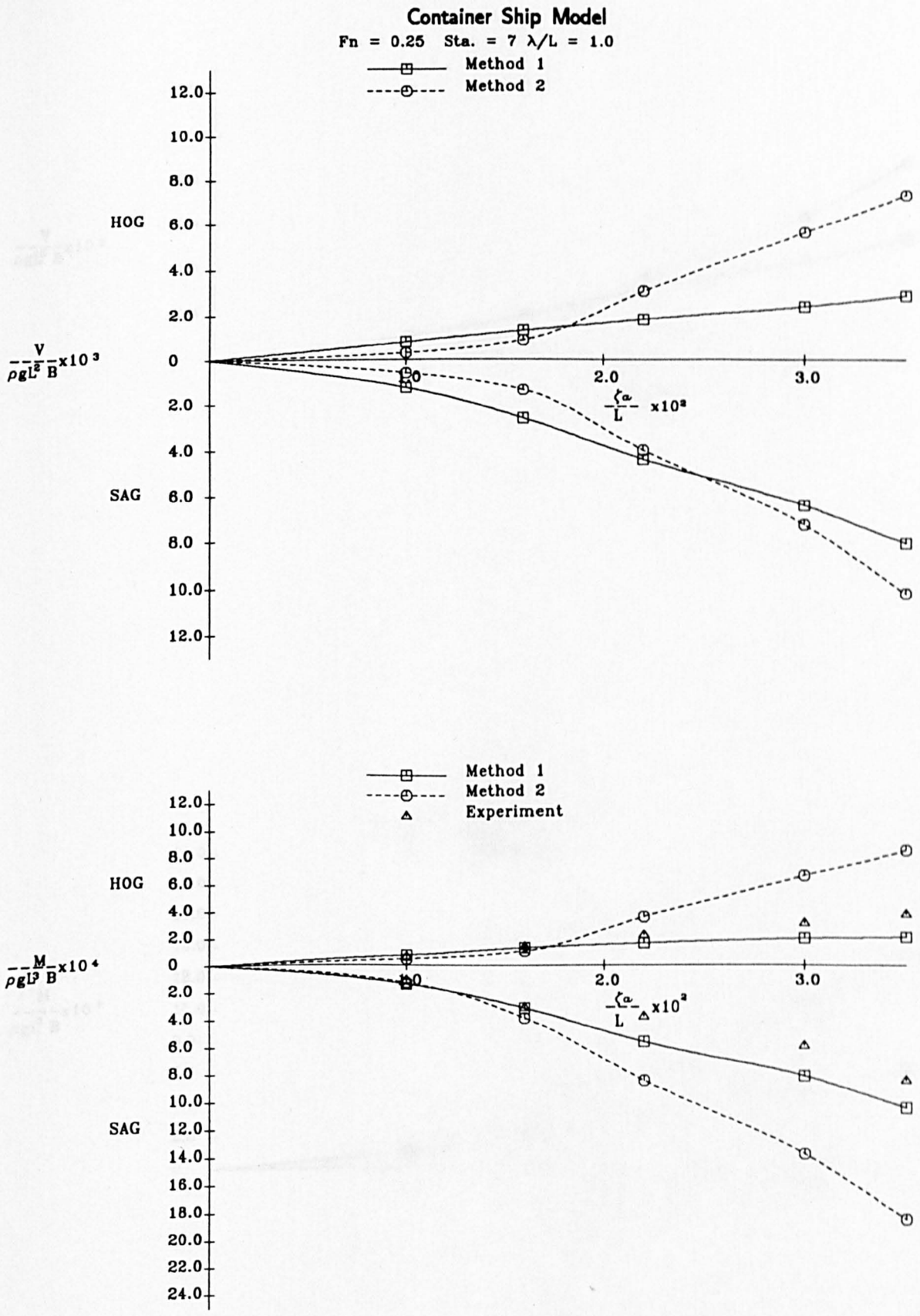

Fig.A.4.79 Vertical Global Shear Force and Bending Moment in Regular Head Seas

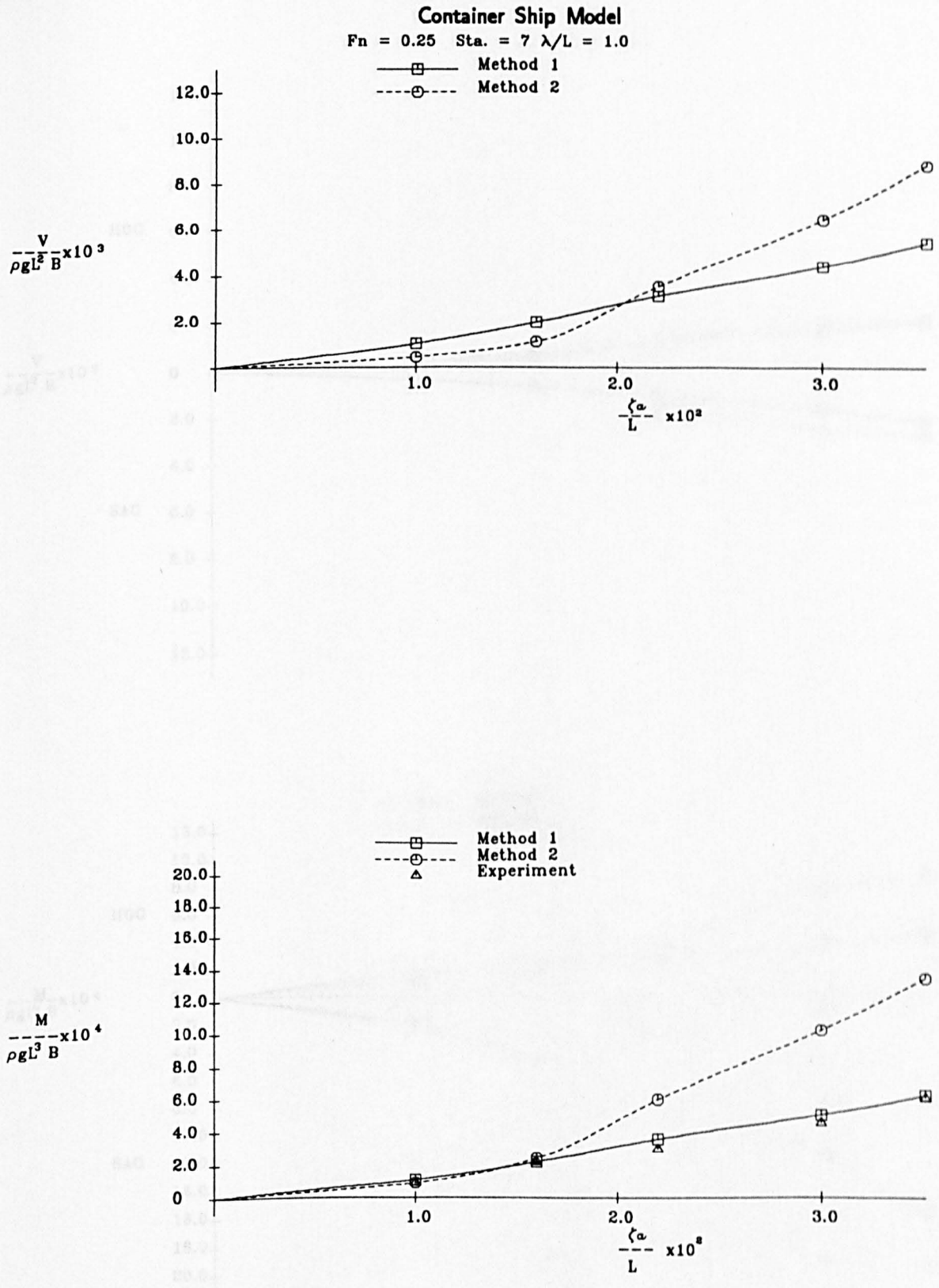

Fig.A.4.80 Vertical Global Shear Force and Bending Moment in Regular Head Seas

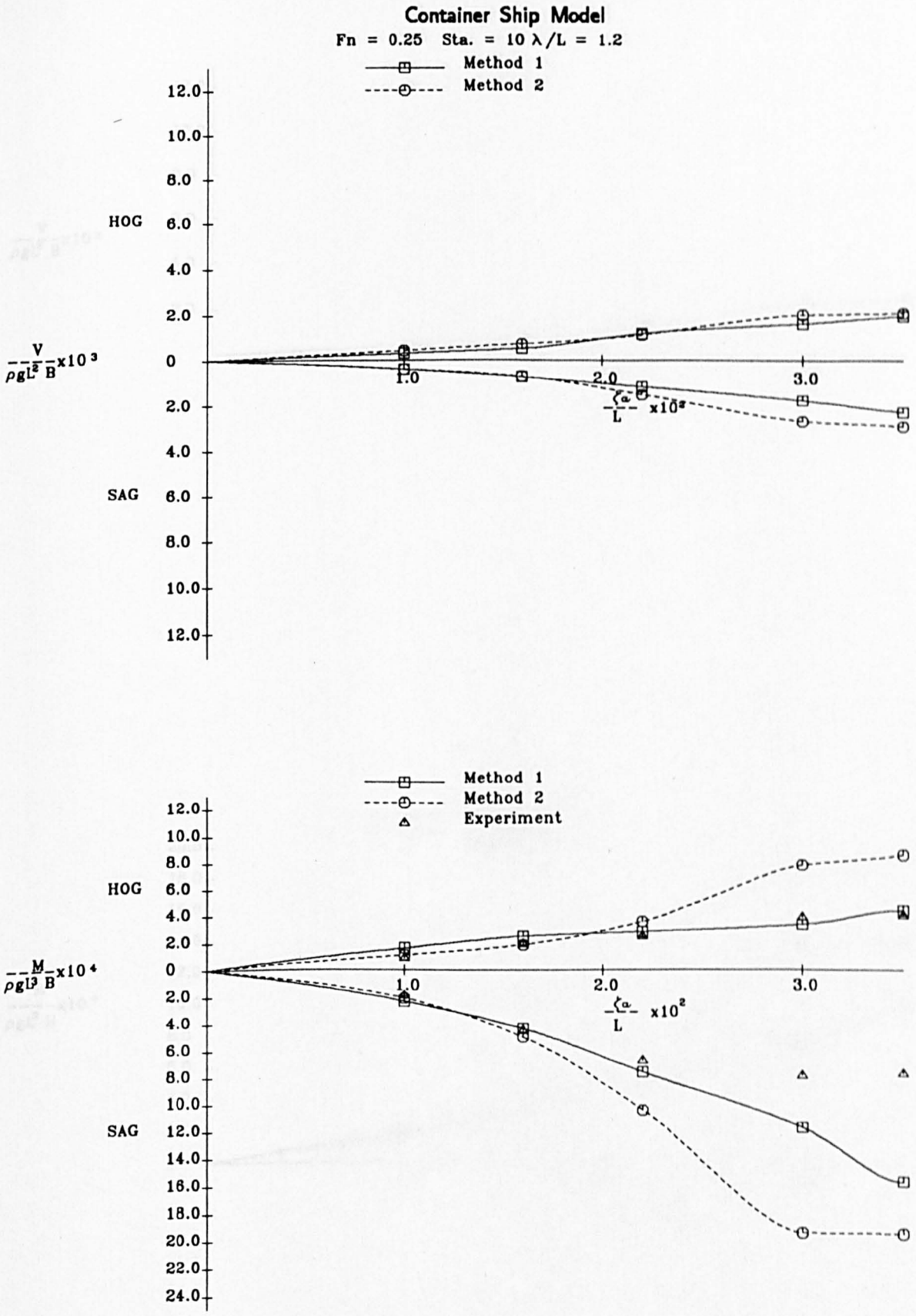

Fig.A.4.81 Vertical Global Shear Force and Bending Moment in Regular Head Seas

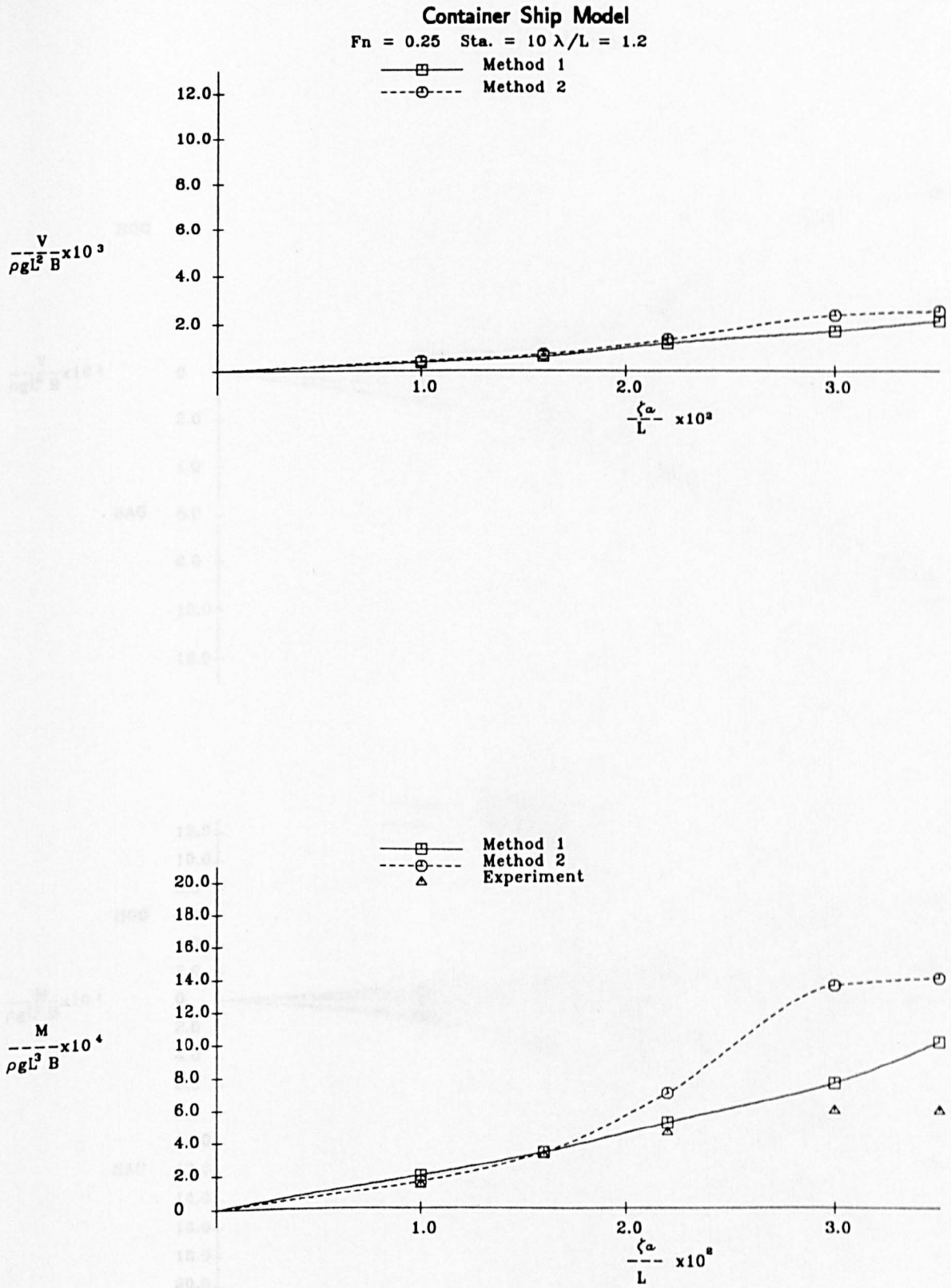

Fig.A.4.82 Vertical Global Shear Force and Bending Moment in Regular Head Seas

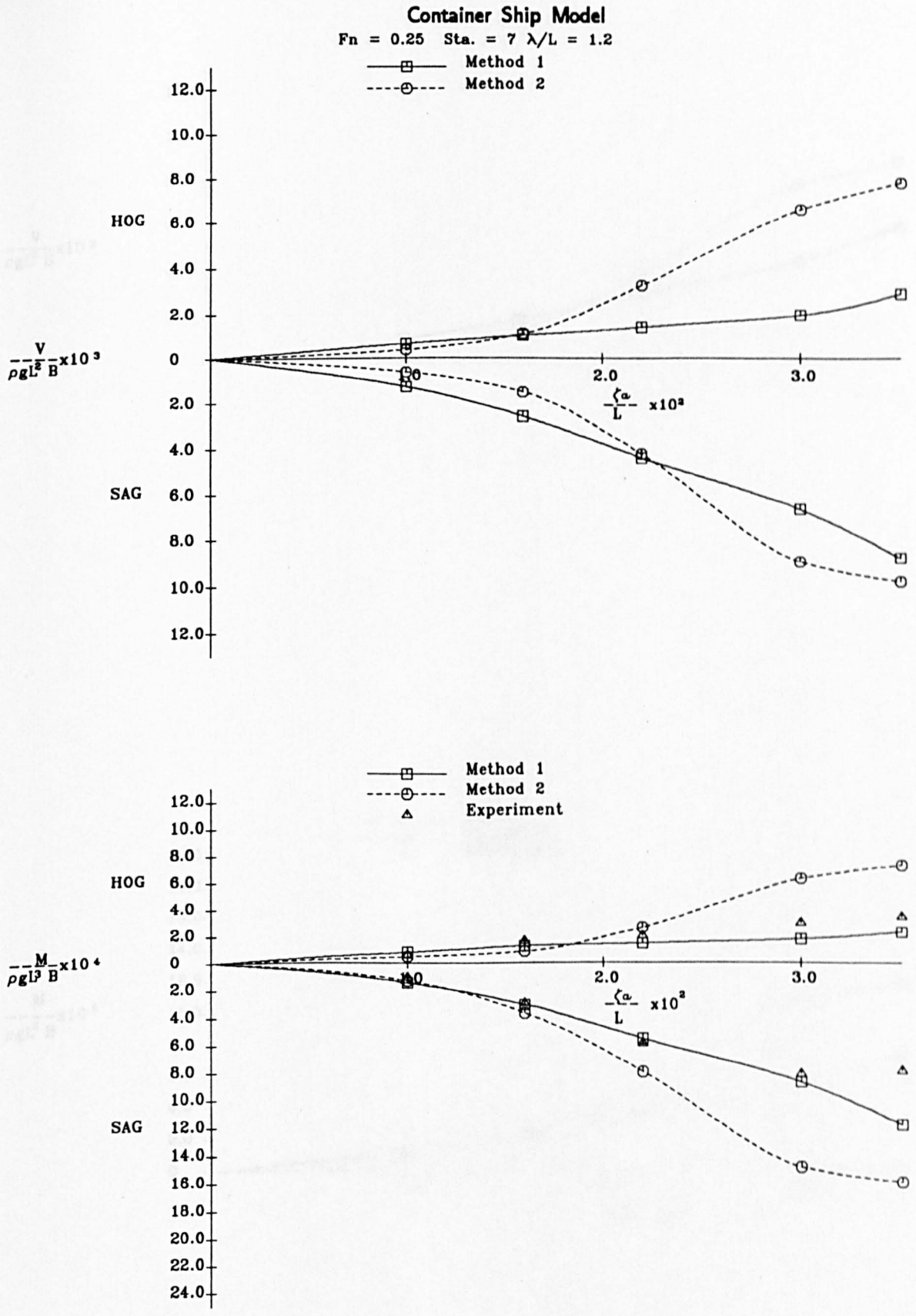

Fig.A.4.83 Vertical Global Shear Force and Bending Moment in Regular Head Seas

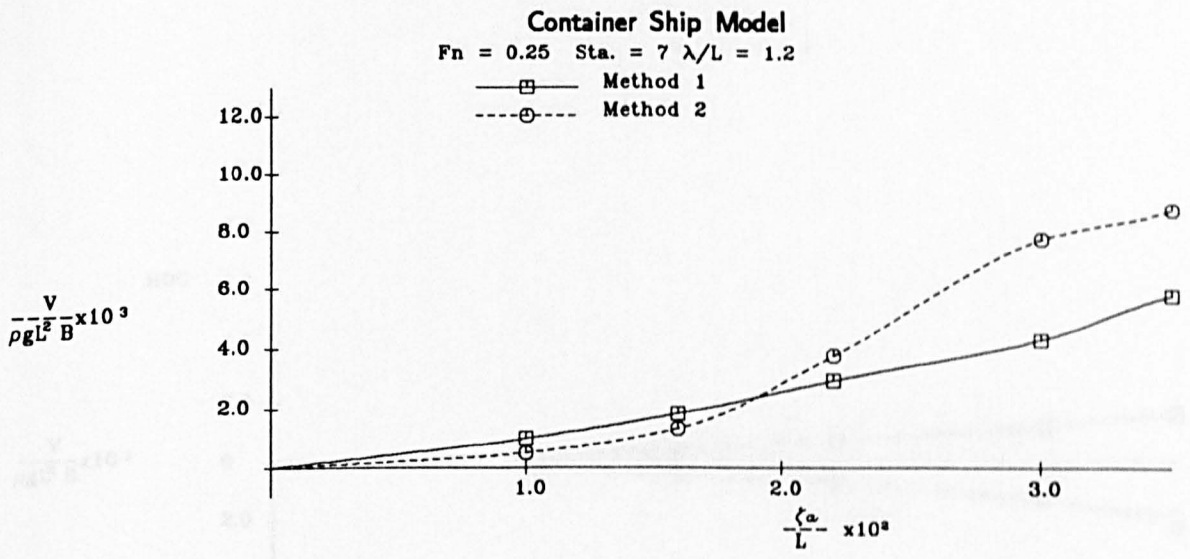

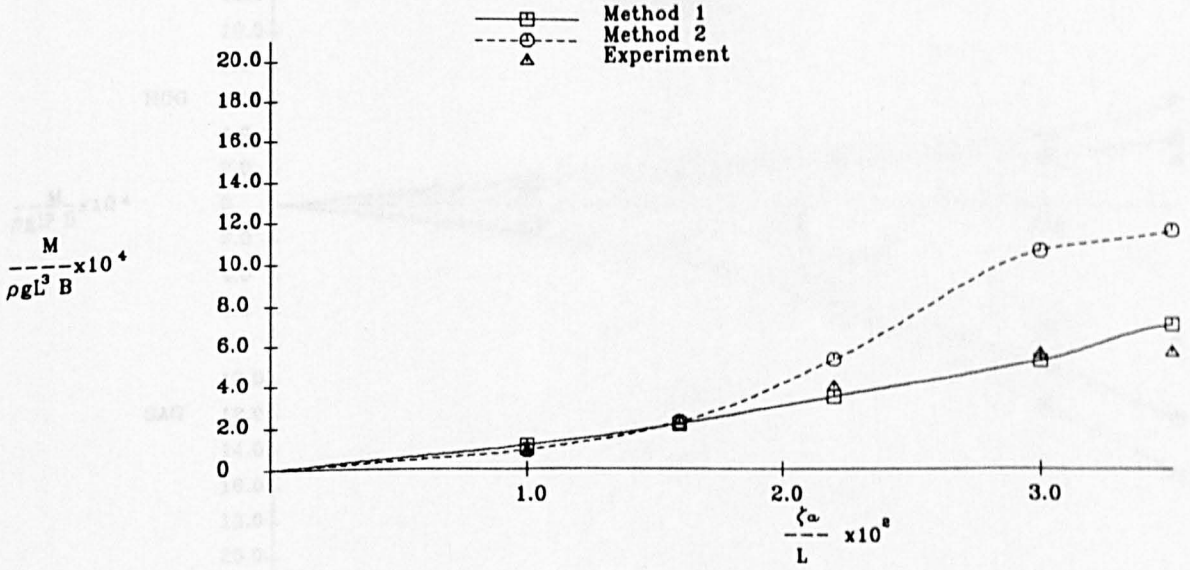

Fig.A.4.84 Vertical Global Shear Force and Bending Moment in Regular Head Seas

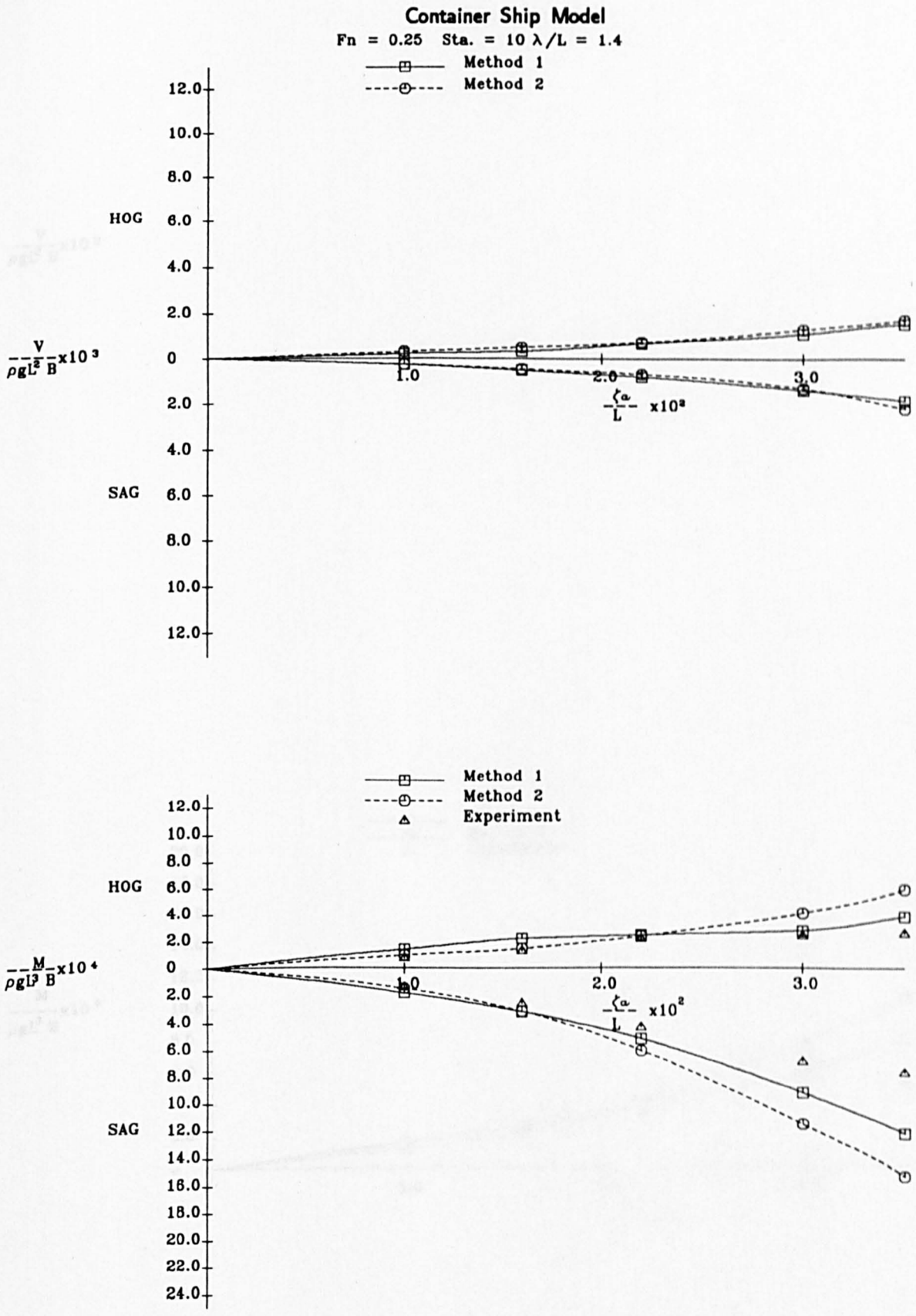

Fig.A.4.85 Vertical Global Shear Force and Bending Moment in Regular Head Seas

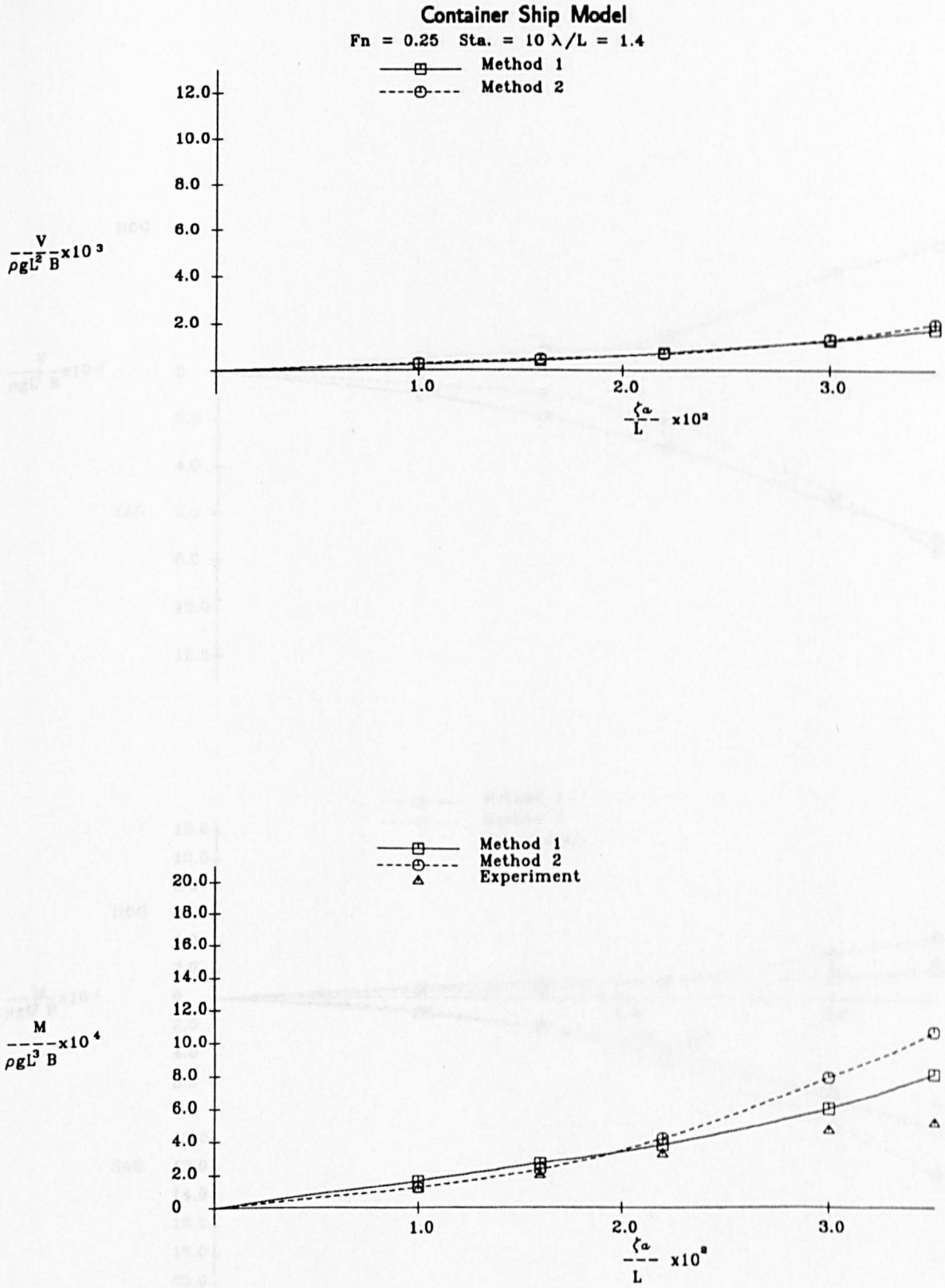

Fig.A.4.86 Vertical Global Shear Force and Bending Moment in Regular Head Seas

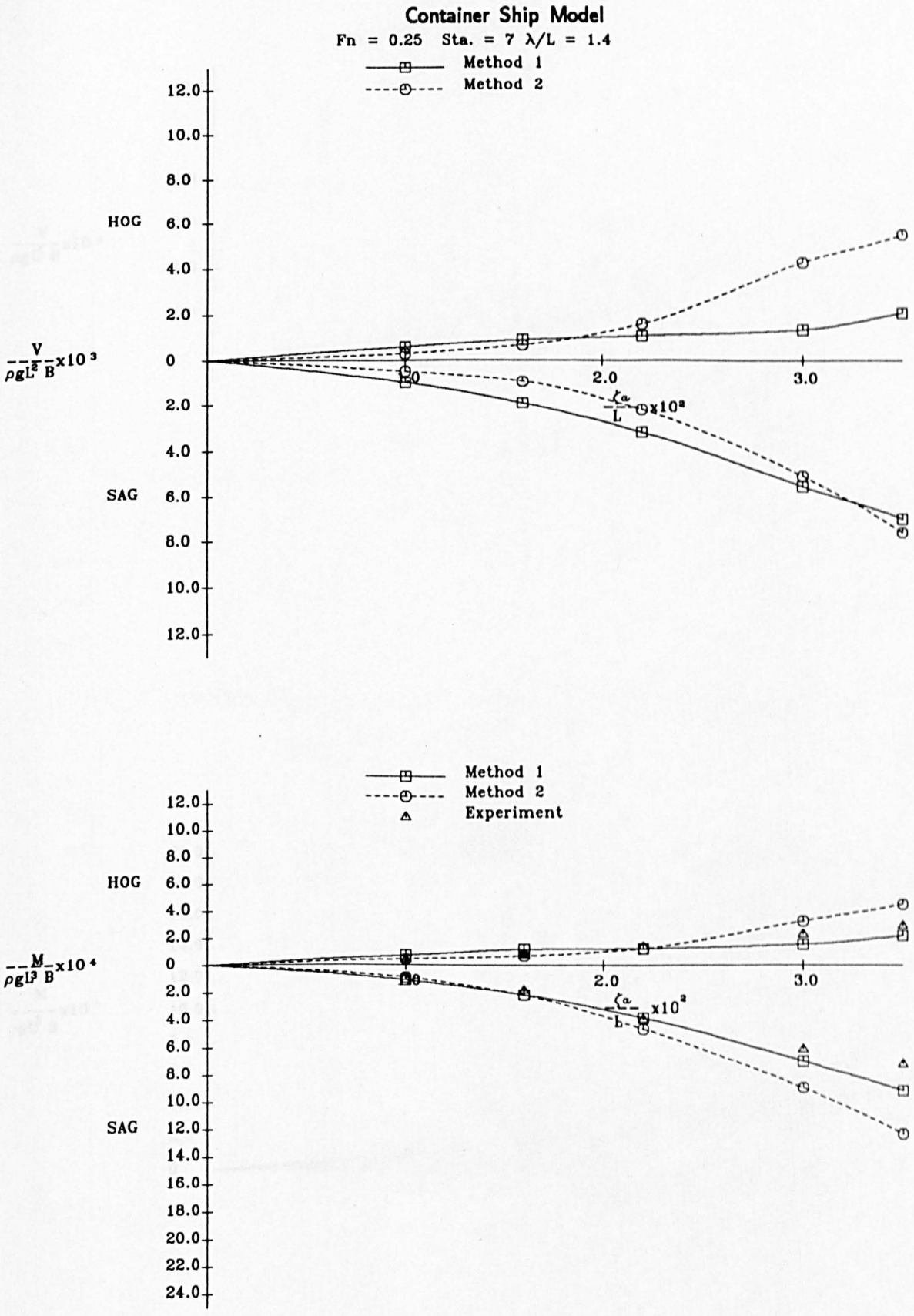

Fig.A.4.87 Vertical Global Shear Force and Bending Moment in Regular Head Seas

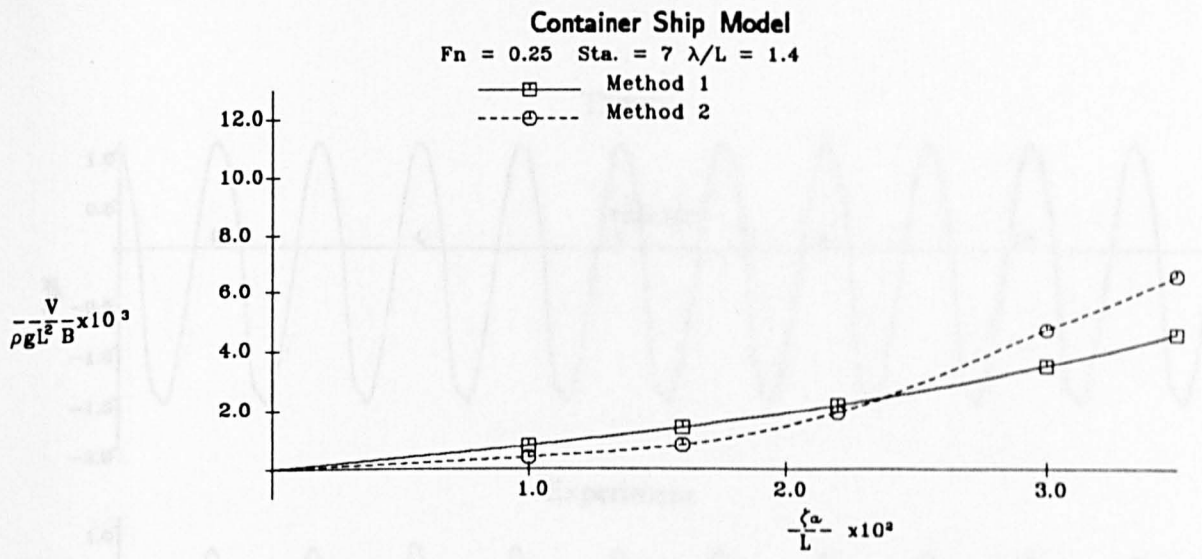

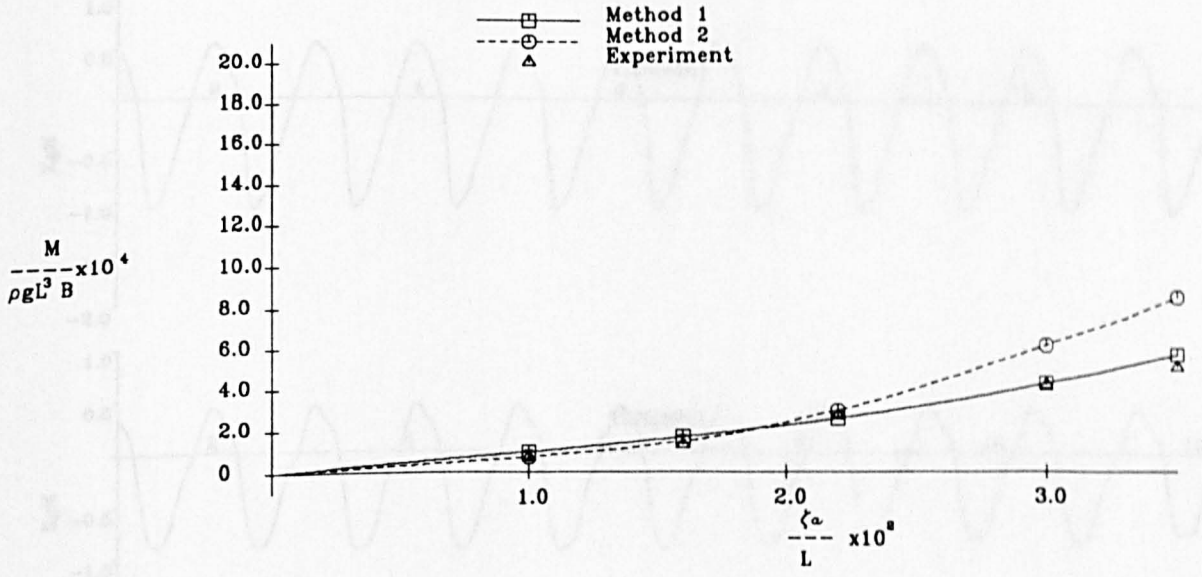

Fig.A.4.88 Vertical Global Shear Force and Bending Moment in Regular Head Seas

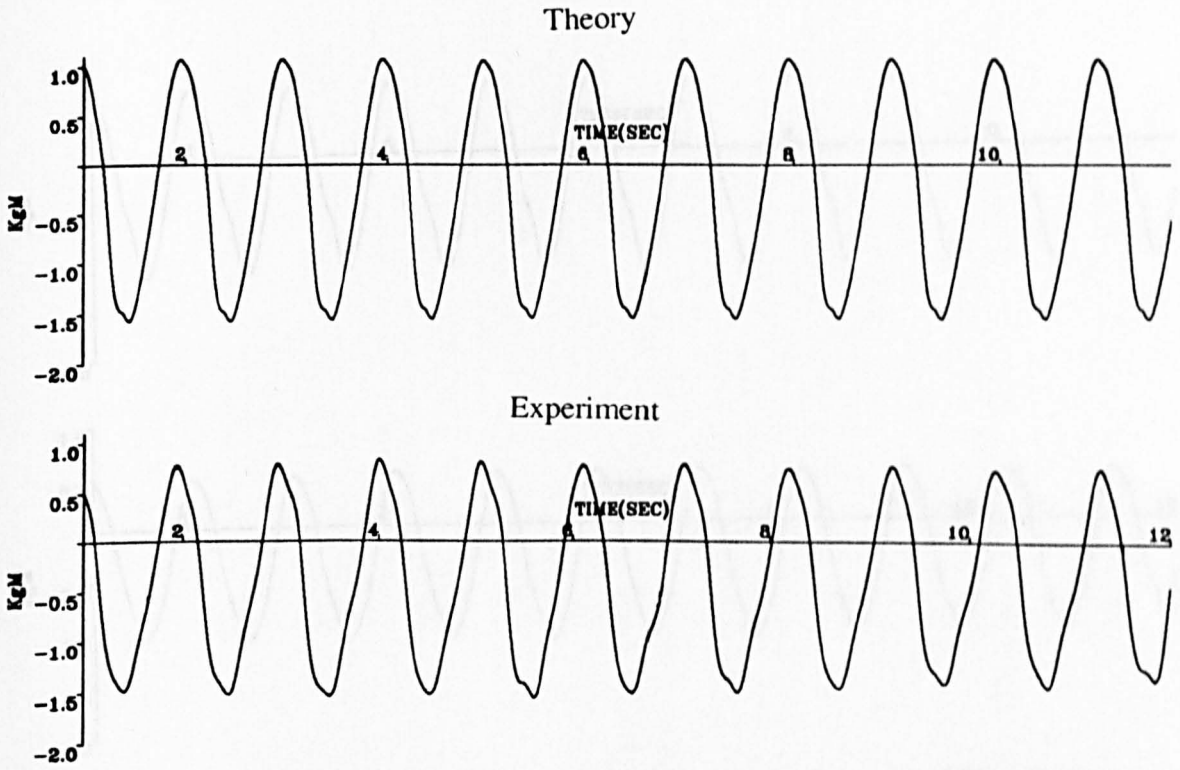

Fig.A.4.89 Time History of Wave Bending Moment in Theory and Experiment

Fn=0.15 Sta.= 10 λ / L=1.2, ζ_a=4.083 cm

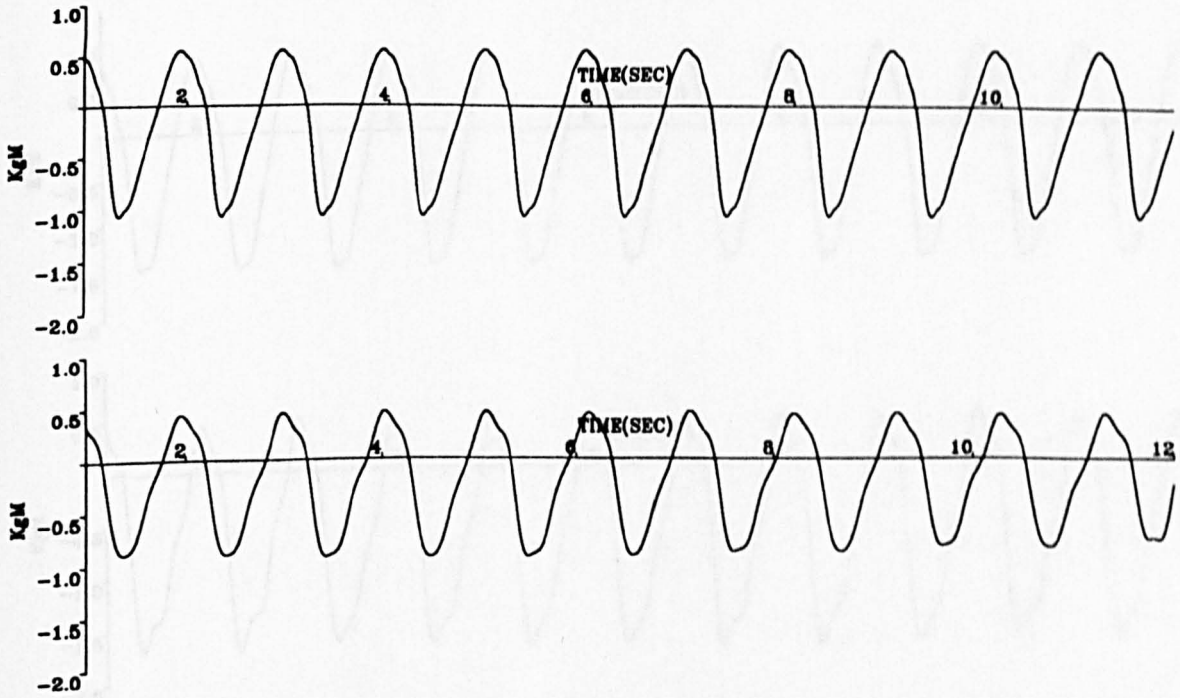

Fig.A.4.90 Time History of Wave Bending Moment in Theory and Experiment

Fn=0.15 Sta.= 7 λ / L=1.2, ζ_a=4.083 cm

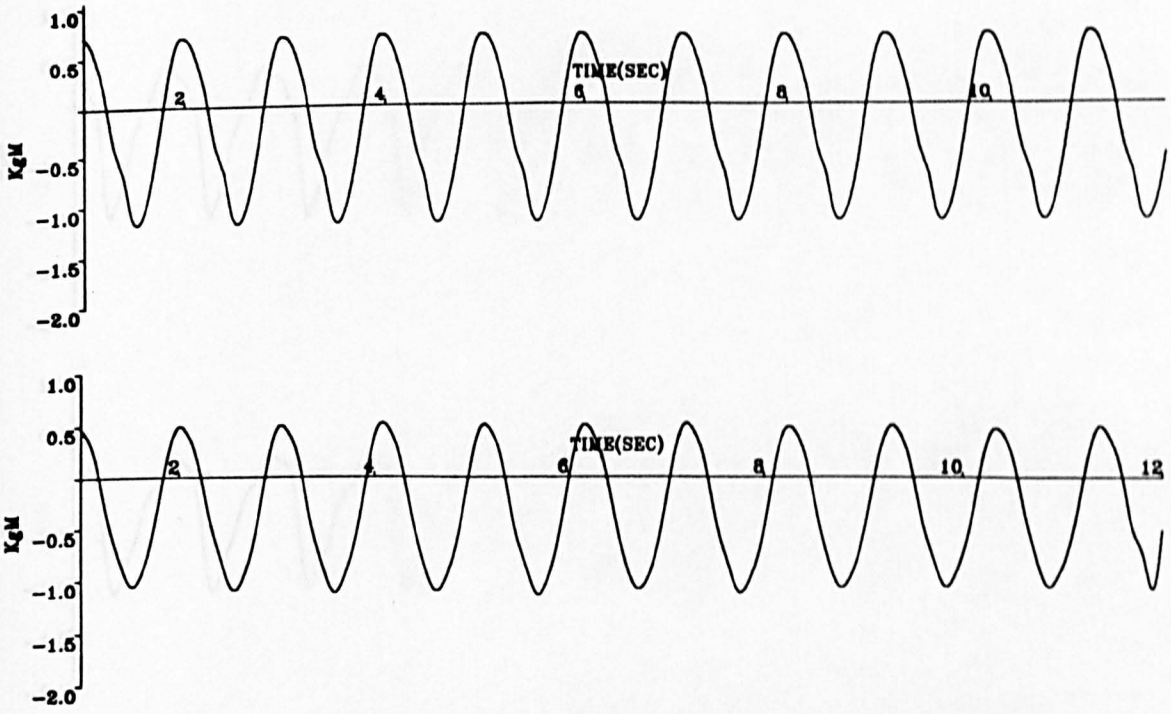

Fig.A.4.91 Time History of Wave Bending Moment in Theory and Experiment

Fn=0.15 Sta.= 15 λ / L=1.2, ζ_a=4.083 cm

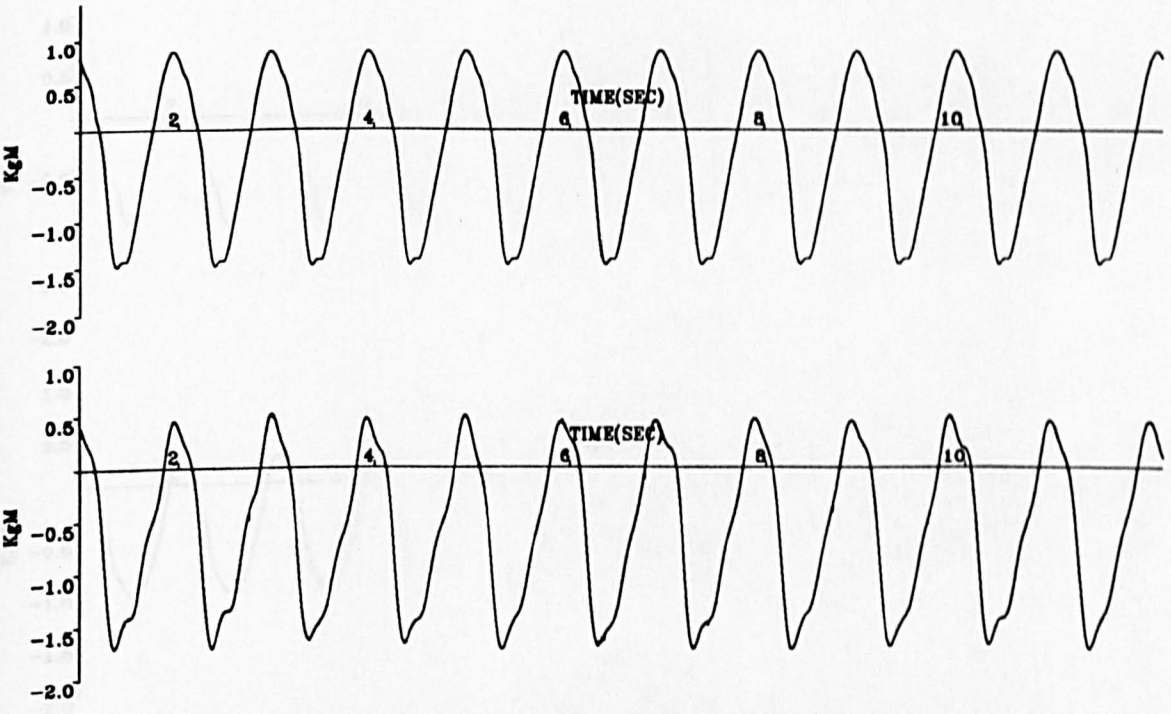

Fig.A.4.92 Time History of Wave Bending Moment in Theory and Experiment

Fn=0.25 Sta.= 10 λ / L=1.4, ζ_a=4.050 cm

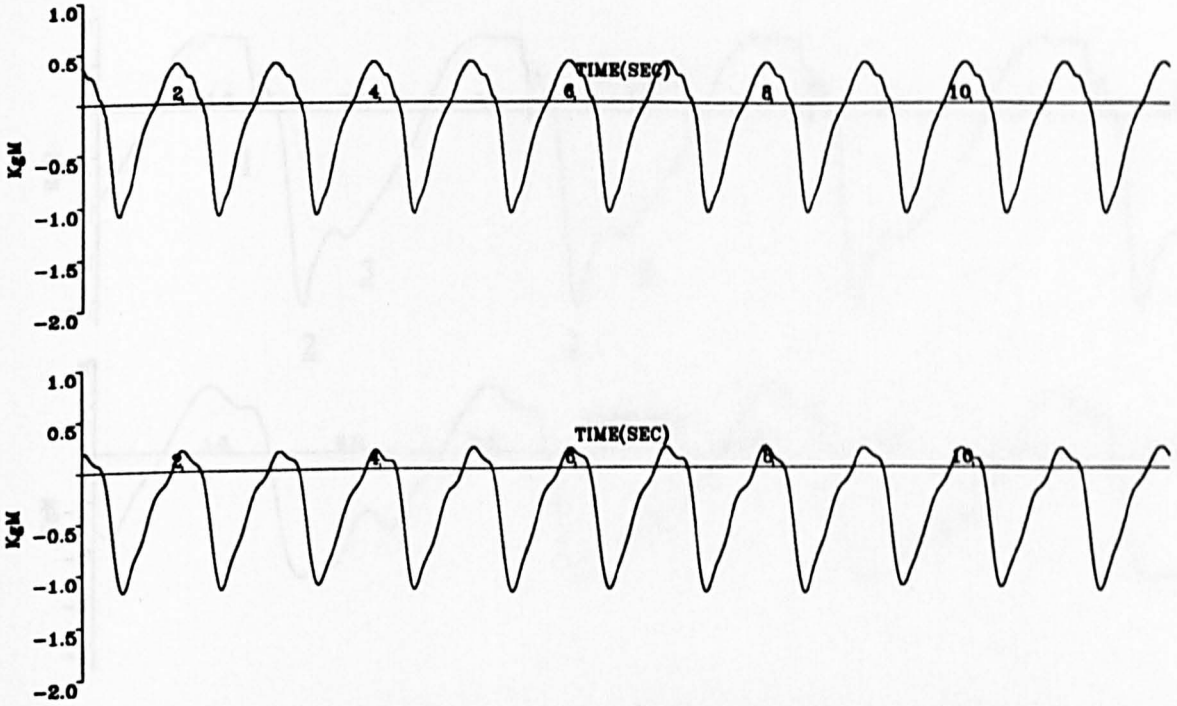

Fig.A.4.93 Time History of Wave Bending Moment in Theory and Experiment

Fn=0.25 Sta.= 7 $\lambda / L = 1.4$, $\zeta_a = 4.050$ cm

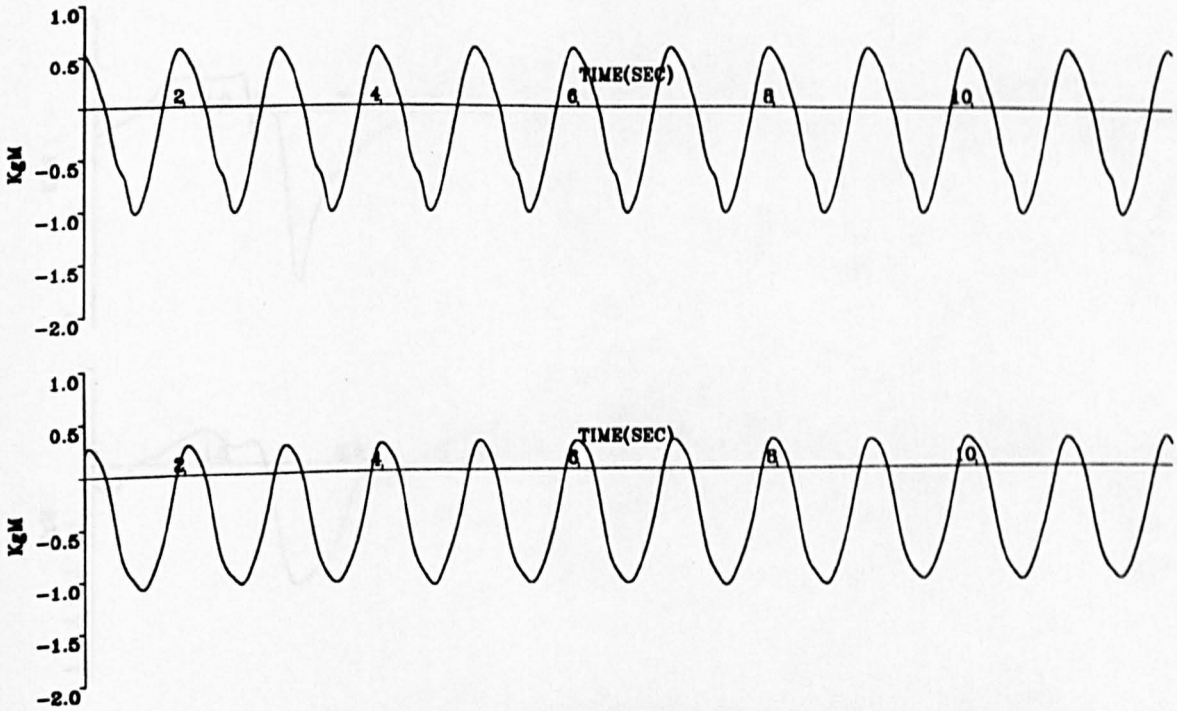

Fig.A.4.94 Time History of Wave Bending Moment in Theory and Experiment

Fn=0.25 Sta.= 15 $\lambda / L = 1.4$, $\zeta_a = 4.050$ cm

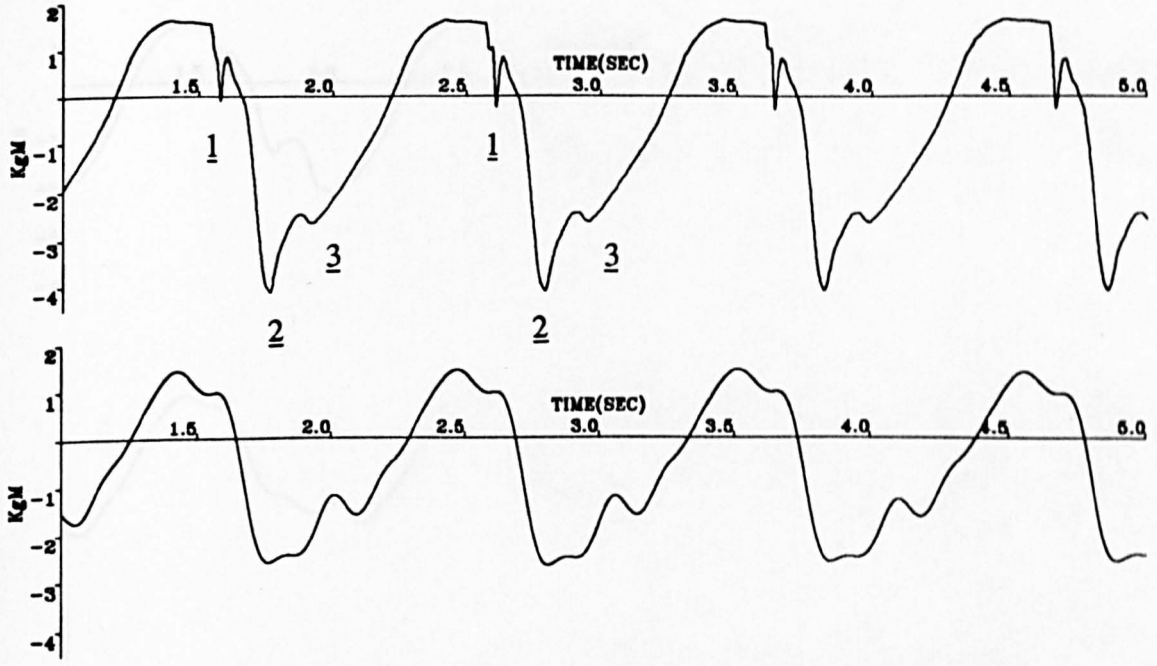

Fig.A.4.95 Time History of Wave Bending Moment in Theory and Experiment

Fn=0.15 Sta.= 10 λ / L=1.2, ζ_a=7.786 cm

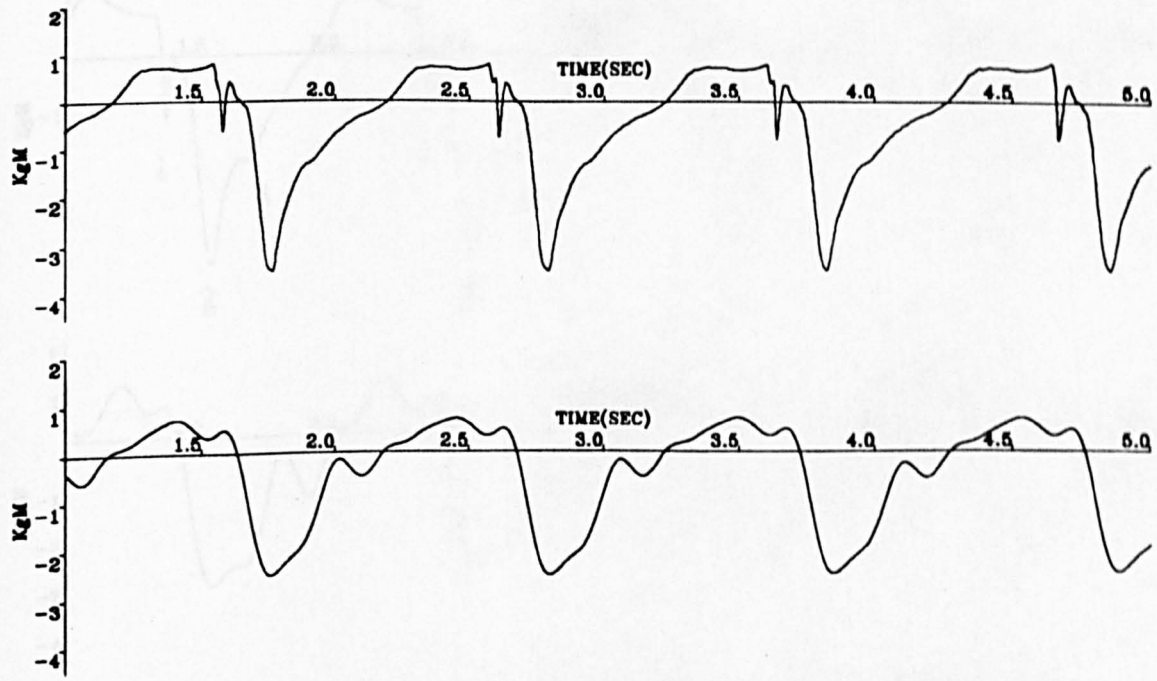

Fig.A.4.96 Time History of Wave Bending Moment in Theory and Experiment

Fn=0.15 Sta.= 7 λ / L=1.2, ζ_a=7.786 cm

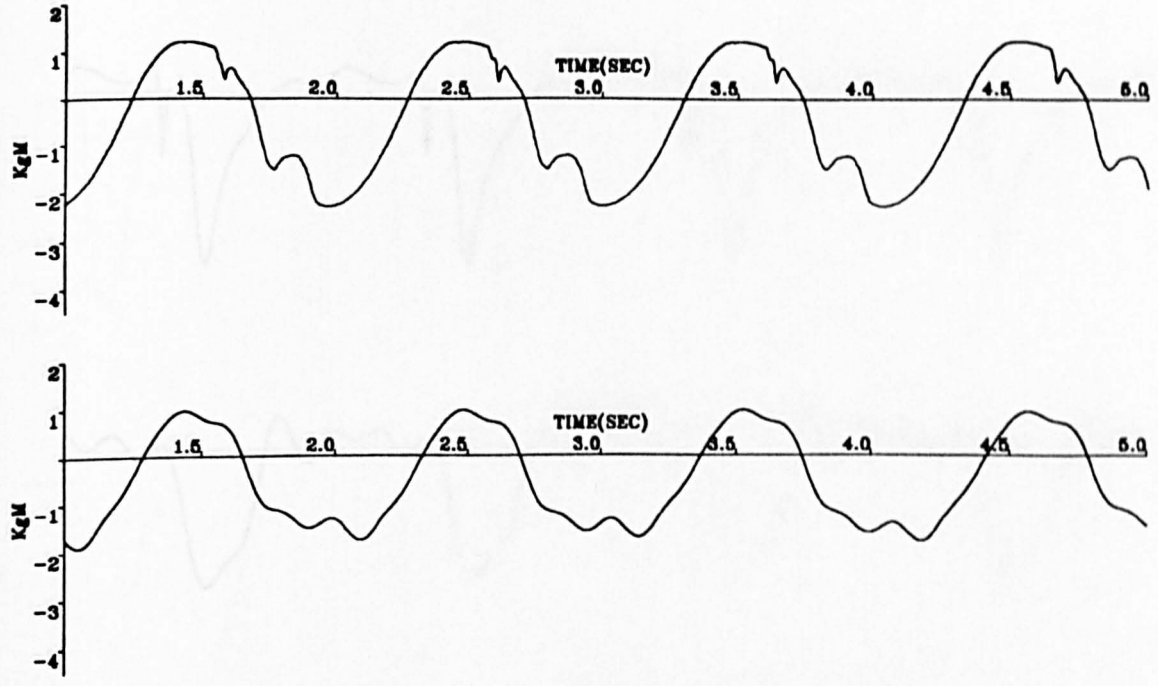

Fig.A.4.97 Time History of Wave Bending Moment in Theory and Experiment

Fn=0.15 Sta.= 15 λ / L=1.2, ζ_a=7.786 cm

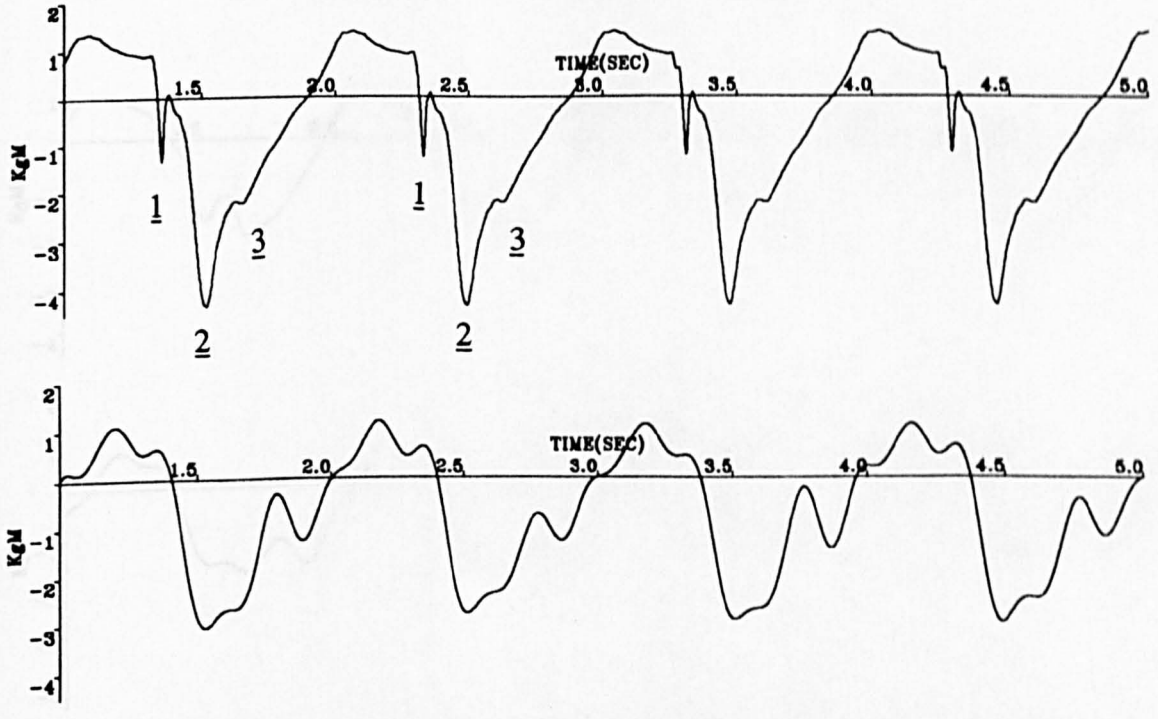

Fig.A.4.98 Time History of Wave Bending Moment in Theory and Experiment

Fn=0.25 Sta.= 10 λ / L=1.4, ζ_a=7.720 cm

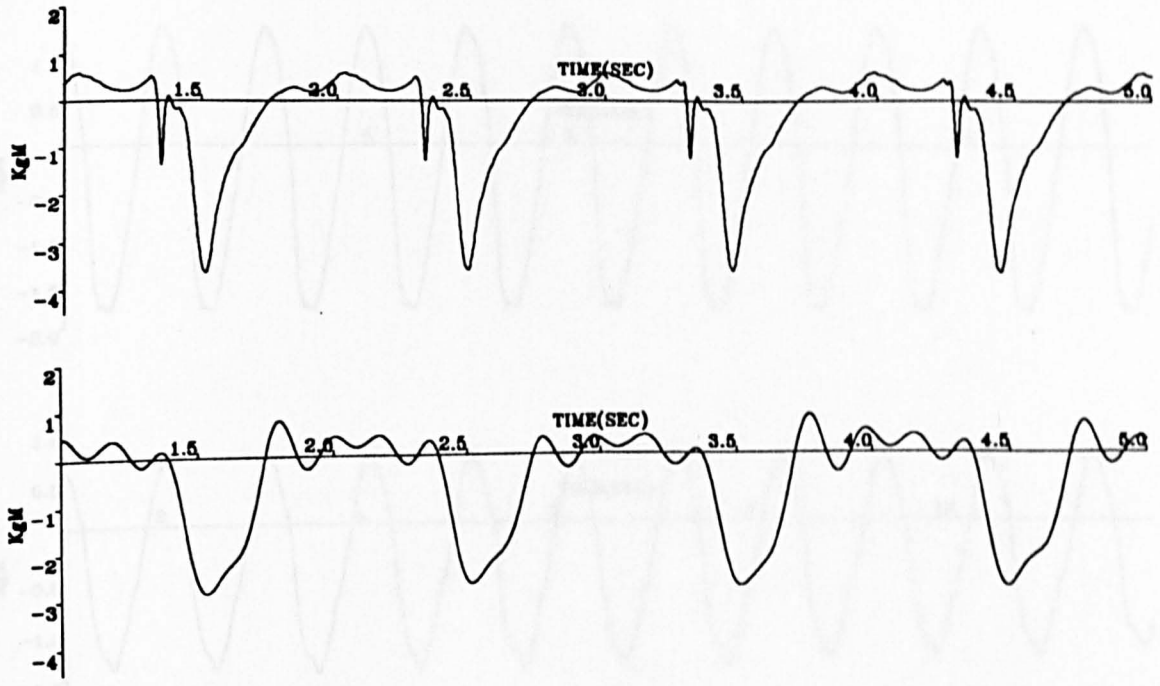

Fig.A.4.99 Time History of Wave Bending Moment in Theory and Experiment

Fn=0.25 Sta.= 7 λ / L=1.4, ζ_a=7.720 cm

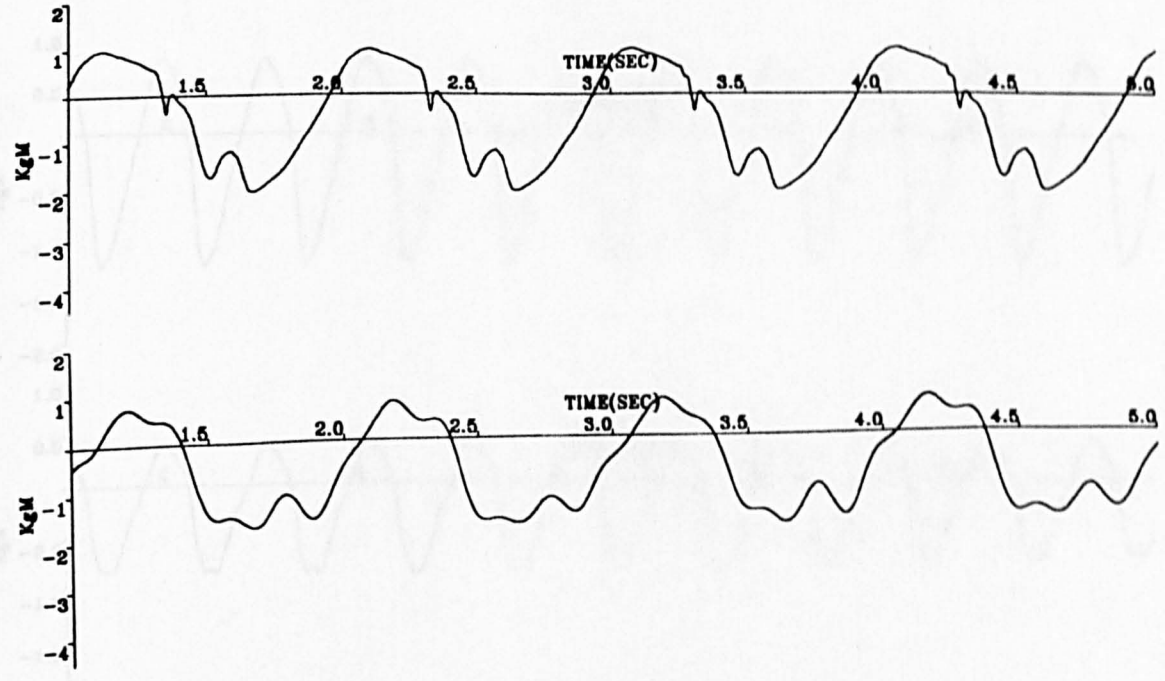

Fig.A.4.100 Time History of Wave Bending Moment in Theory and Experiment

Fn=0.25 Sta.= 15 λ / L=1.4, ζ_a=7.720 cm

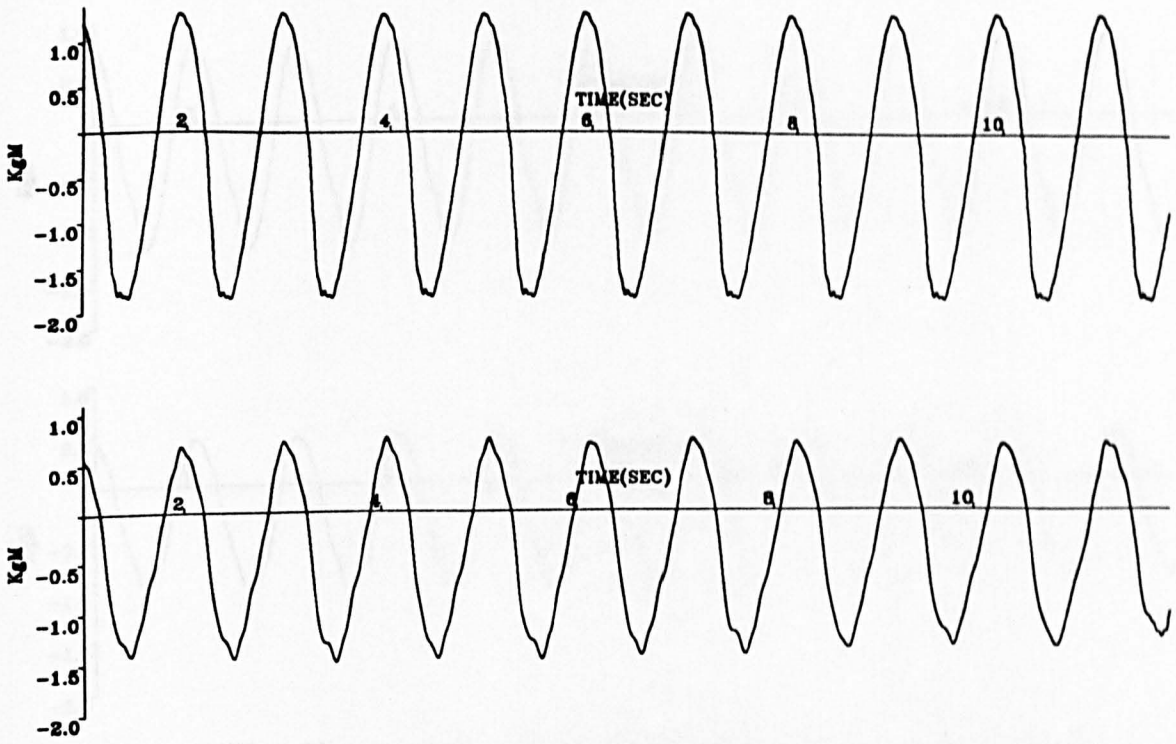

Fig.A.4.101 Time History of Global Bending Moment in Theory and Experiment

Fn=0.15 Sta.= 10 λ / L=1.2 ζ_a=4.083 cm

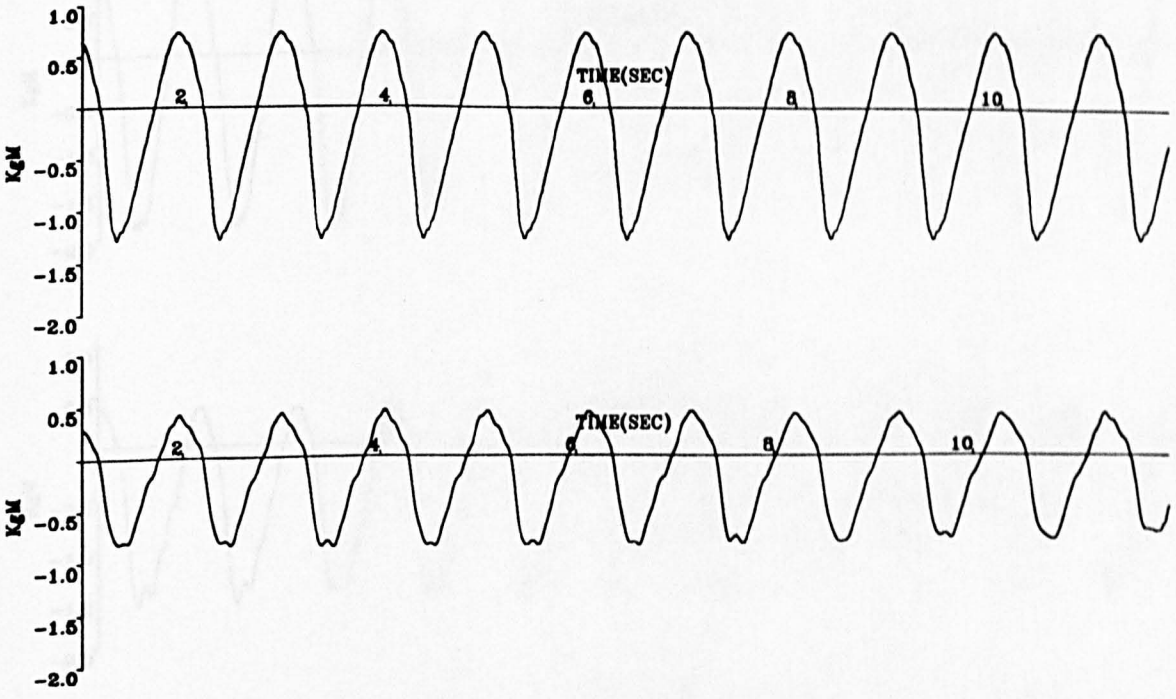

Fig.A.4.102 Time History of Global Bending Moment in Theory and Experiment

Fn=0.15 Sta.= 7 λ / L=1.2 ζ_a=4.083 cm

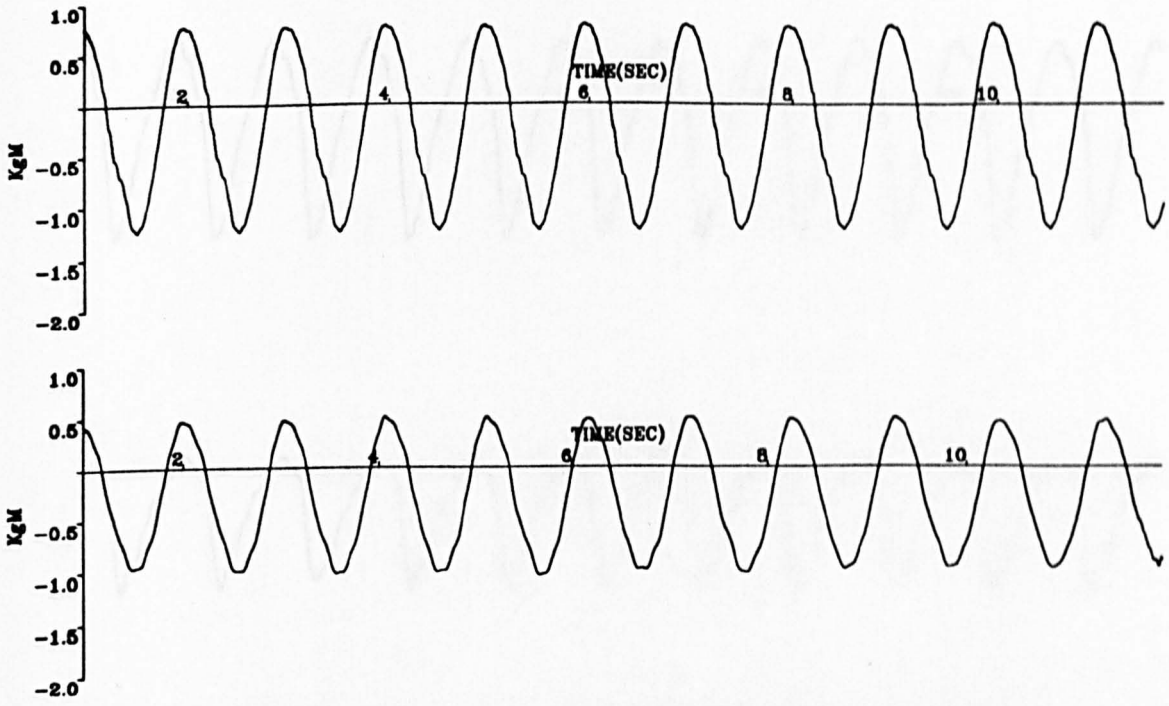

Fig.A.4.103 Time History of Global Bending Moment in Theory and Experiment

Fn=0.15 Sta.= 15 λ / L=1.2 ζ_a=4.083 cm

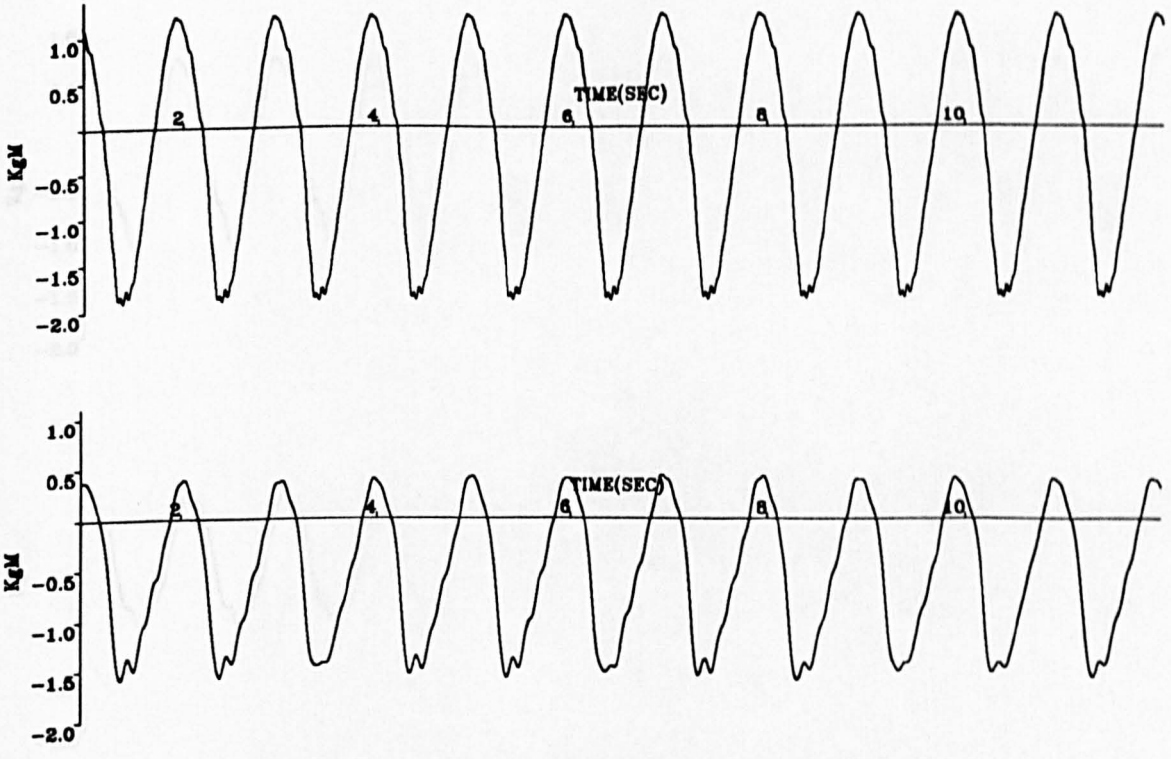

Fig.A.4.104 Time History of Global Bending Moment in Theory and Experiment

Fn=0.25 Sta.= 10 λ / L=1.4 ζ_a=4.050 cm

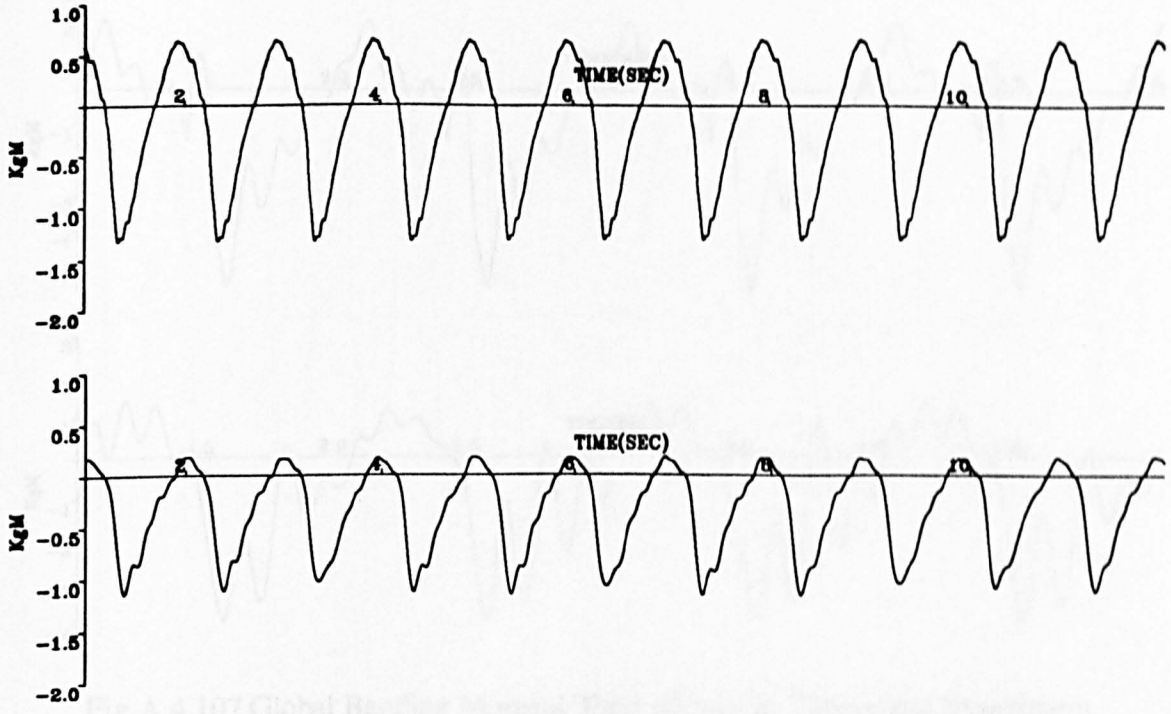

Fig.A.4.105 Time History of Global Bending Moment in Theory and Experiment

Fn=0.25 Sta.= 7 λ / L=1.4 ζ_a=4.050 cm

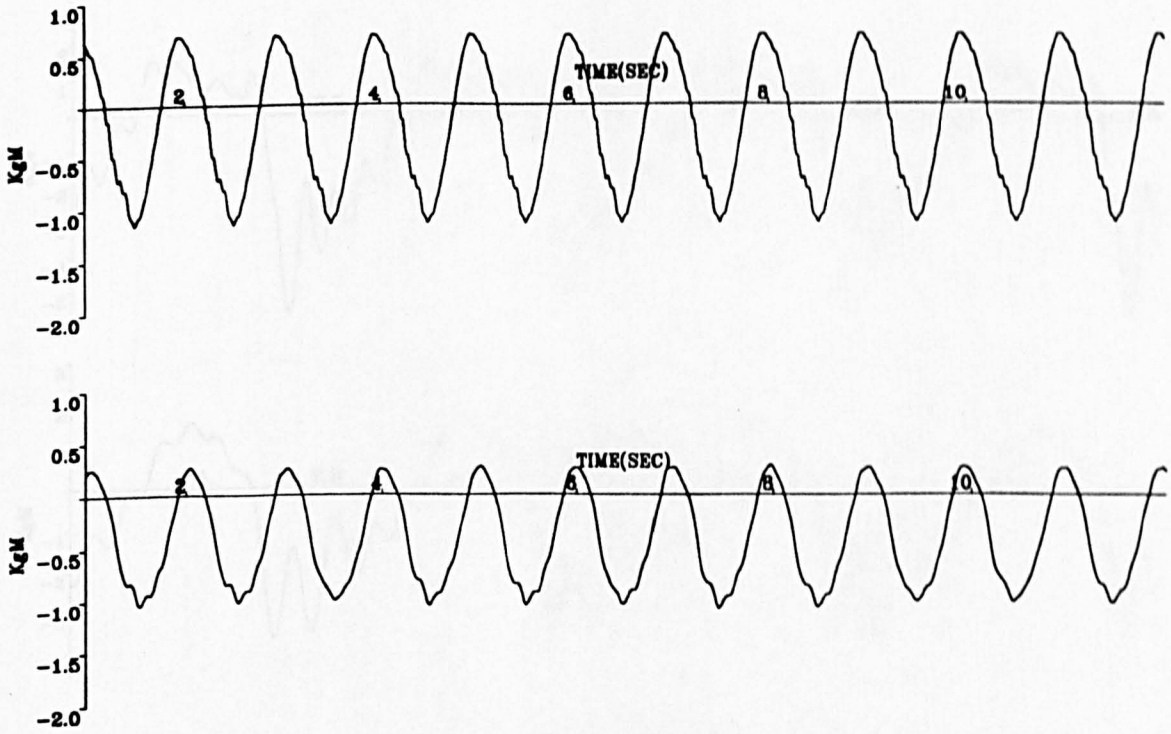

Fig.A.4.106 Time History of Global Bending Moment in Theory and Experiment

Fn=0.25 Sta.= 15 λ / L=1.4 ζ_a=4.050 cm

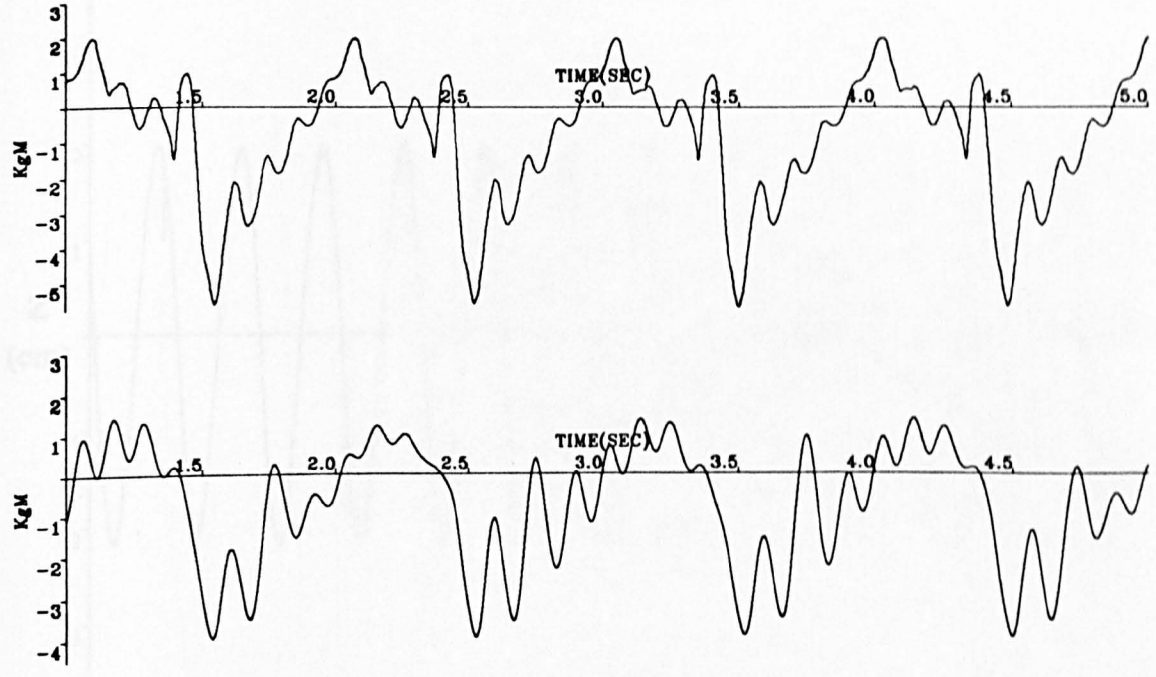

Fig.A.4.107 Global Bending Moment Time History in Theory and Experiment

Fn=0.15 Sta.=10 $\lambda / L = 1.2$ $\zeta_a = 7.786$ cm

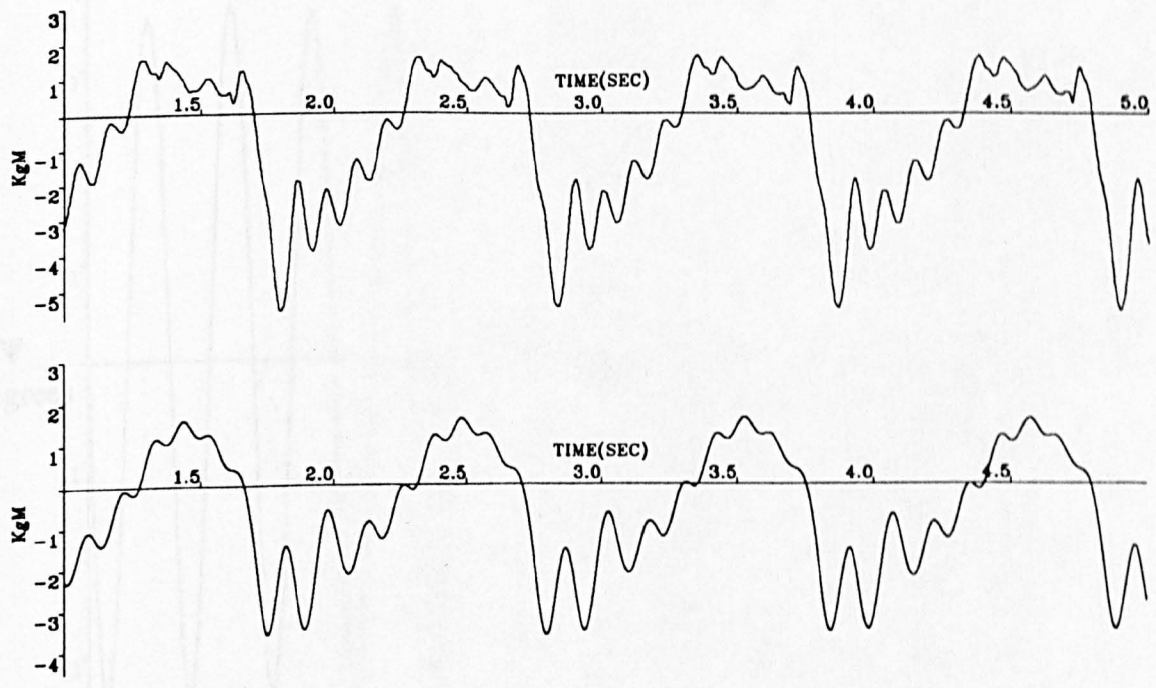

Fig.A.4.108 Global Bending Moment Time History in Theory and Experiment

Fn=0.25 Sta.=10 $\lambda / L = 1.4$ $\zeta_a = 7.720$ cm

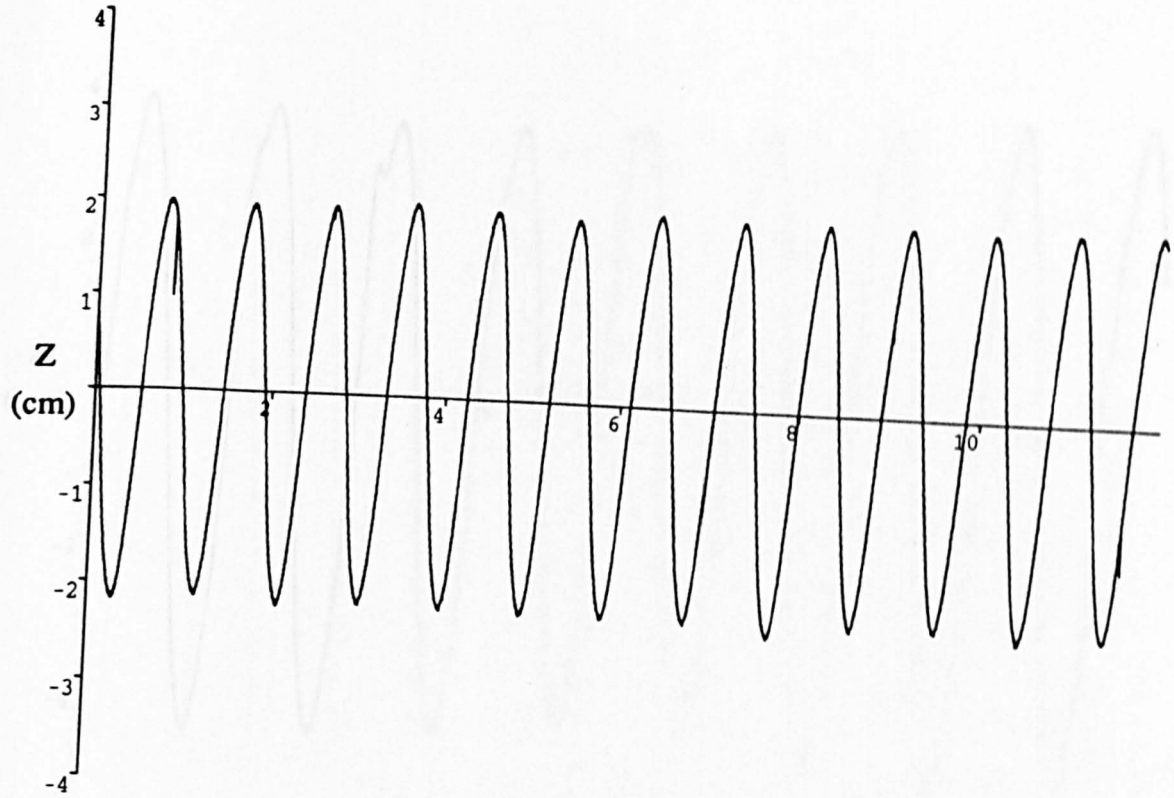

Fig.A.5.1 Heave Time History in Experiment

Fn=0.15 λ / L=1.0 ζ_a=3.775 cm

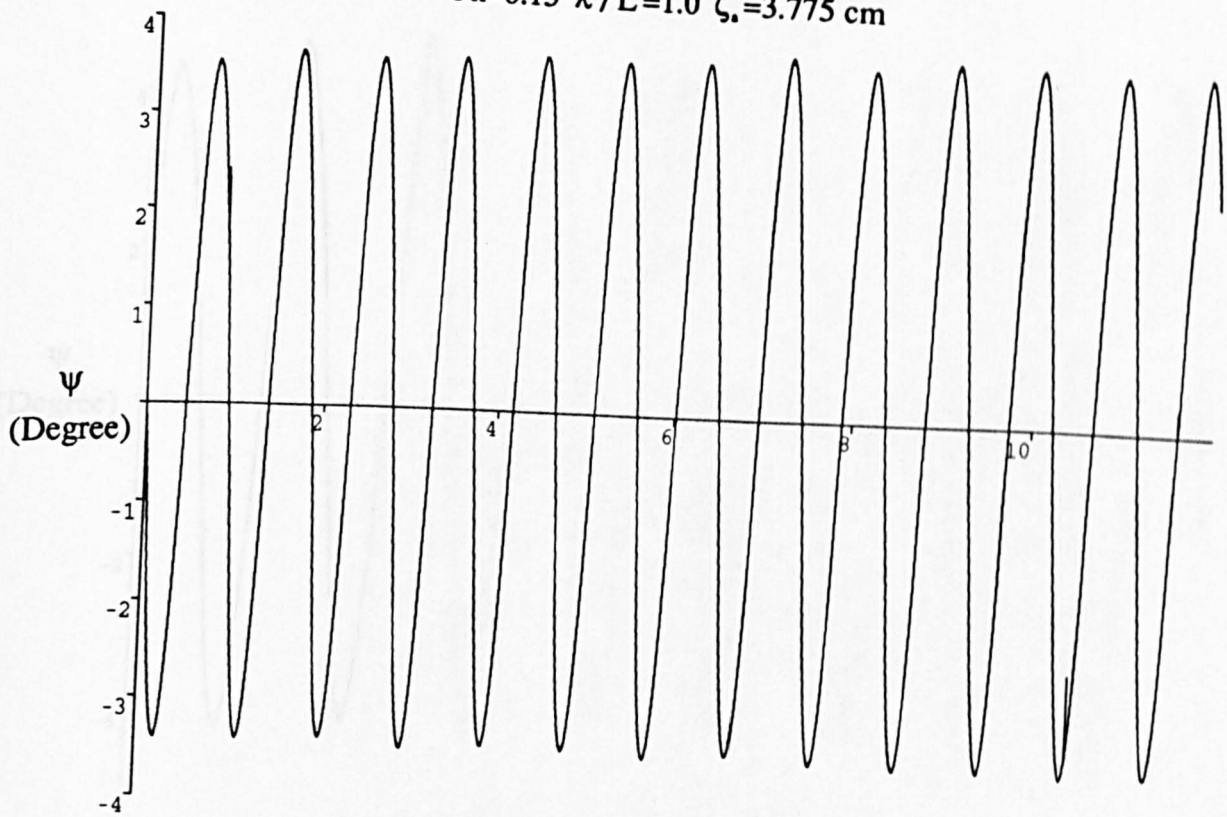

Fig.A.5.2 Pitch Time History in Experiment

Fn=0.15 λ / L=1.0 ζ_a=3.775 cm

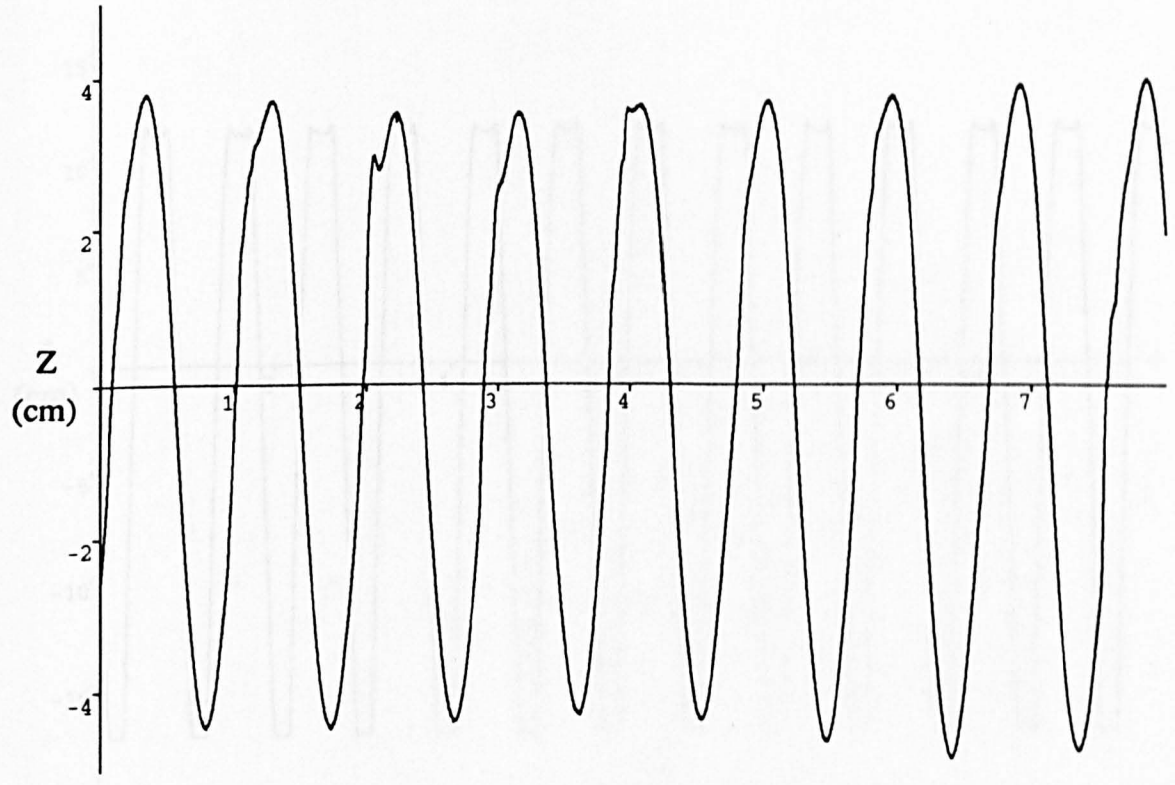

Fig.A.5.3 Heave Time History in Experiment

Fn=0.25 λ / L=1.3 ζ_a=3.965 cm

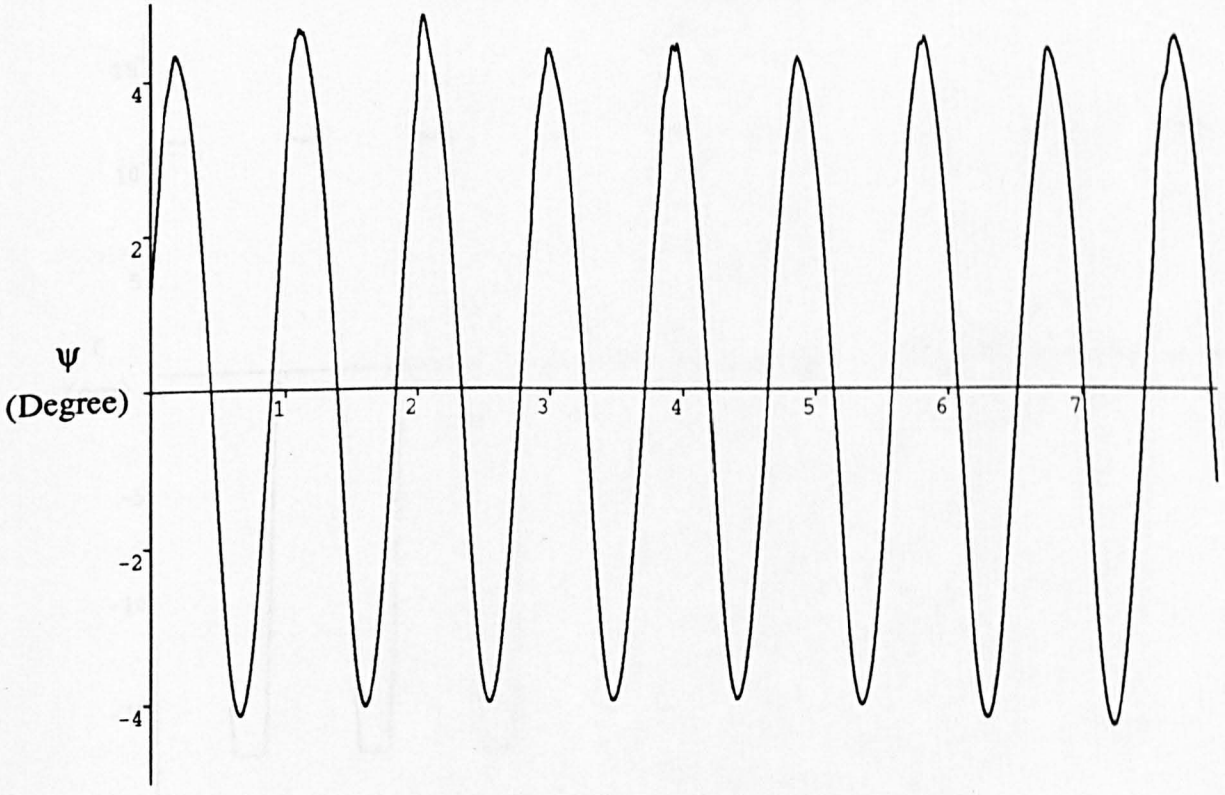

Fig.A.5.4 Pitch Time History in Experiment

Fn=0.25 λ / L=1.3 ζ_a=3.965 cm

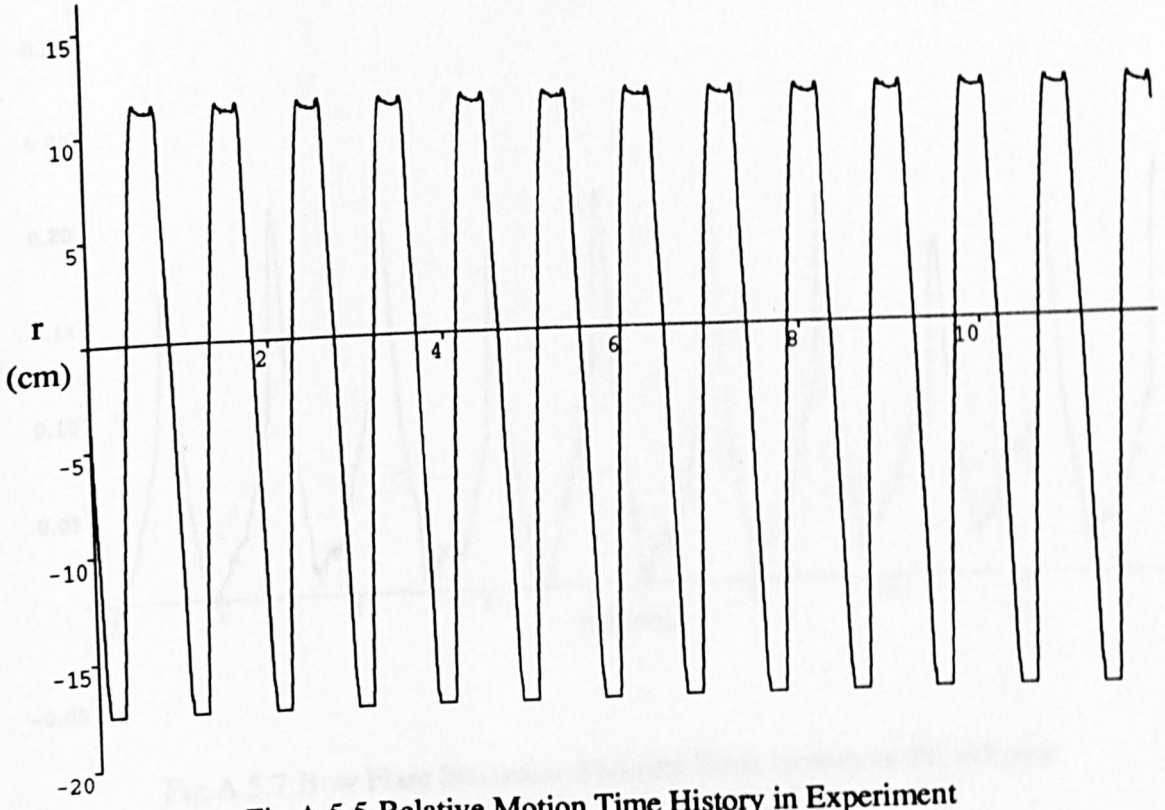

Fig.A.5.5 Relative Motion Time History in Experiment

Fn=0.15 λ / L=1.0 ζ_a=3.775 cm

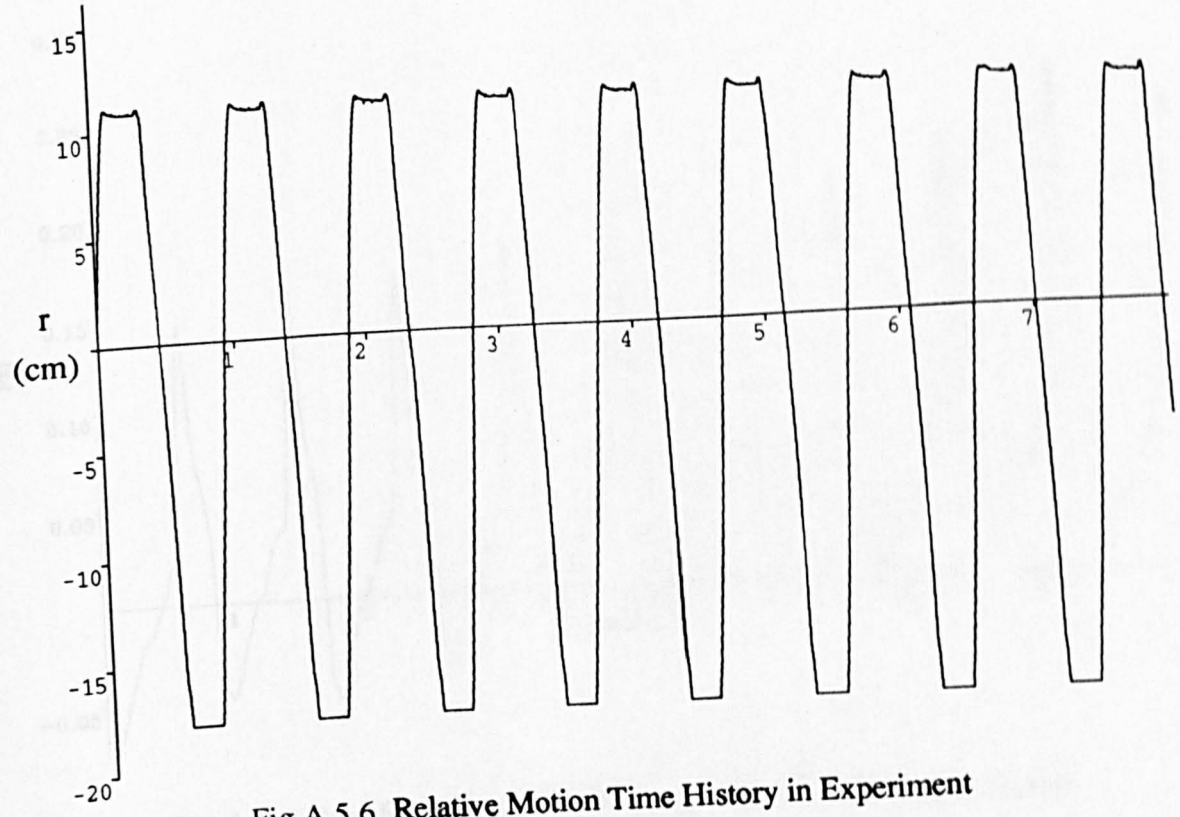

Fig.A.5.6 Relative Motion Time History in Experiment

Fn=0.25 λ / L=1.3 ζ_a=3.965 cm

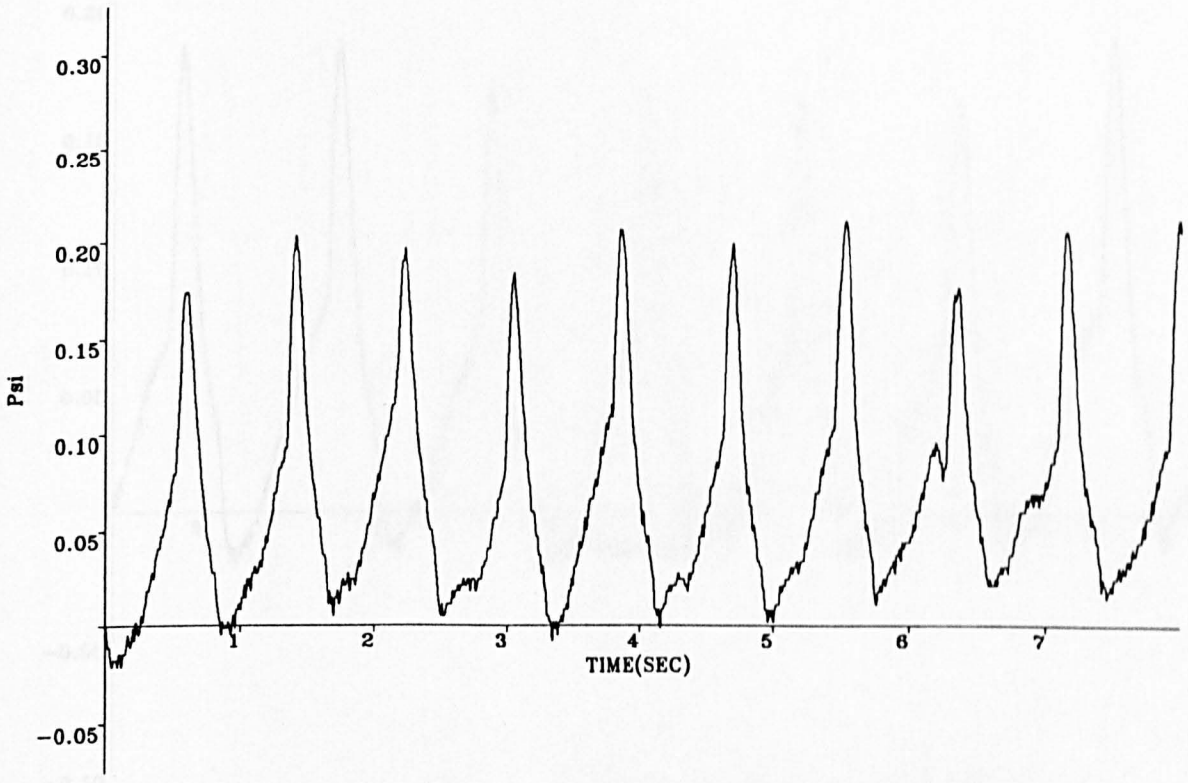

Fig.A.5.7 Bow Flare Slamming Pressure Time History in Experiment

Fn=0.25 Sta.= 2 $\lambda / L = 1.1$ $\zeta_a = 3.82$ cm

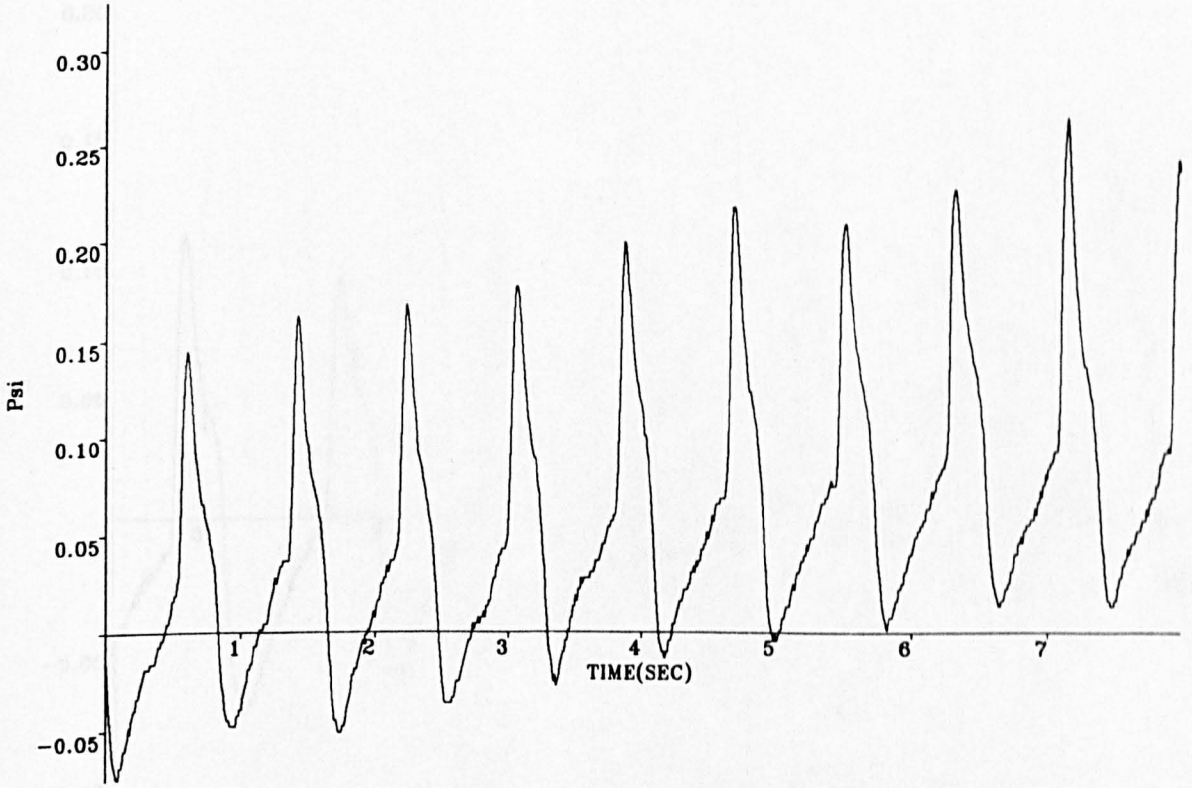

Fig.A.5.8 Bow Flare Slamming Pressure Time History in Experiment

Fn=0.25 Sta.= 3 $\lambda / L = 1.1$ $\zeta_a = 3.82$ cm

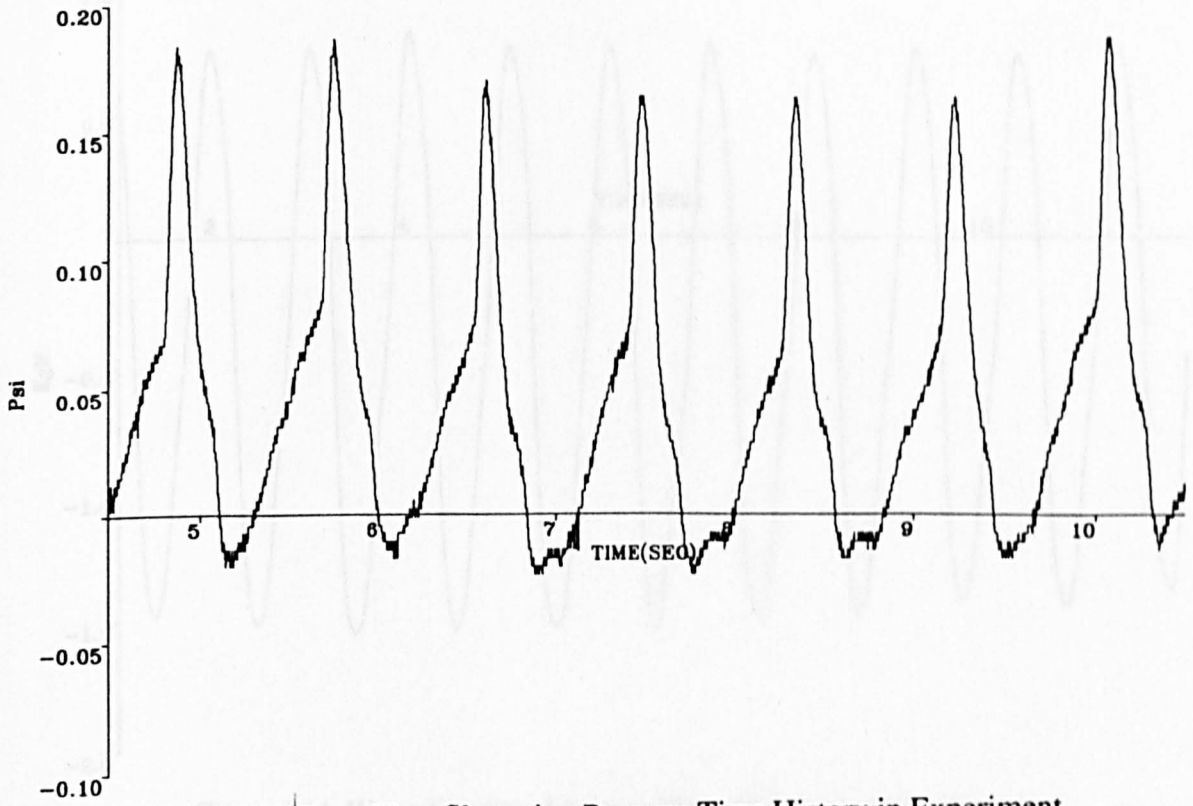

Fig.A.5.9 Bow Flare Slamming Pressure Time History in Experiment

Fn=0.15 Sta.= 2 $\lambda / L = 0.9$ $\zeta_a = 4.22$ cm

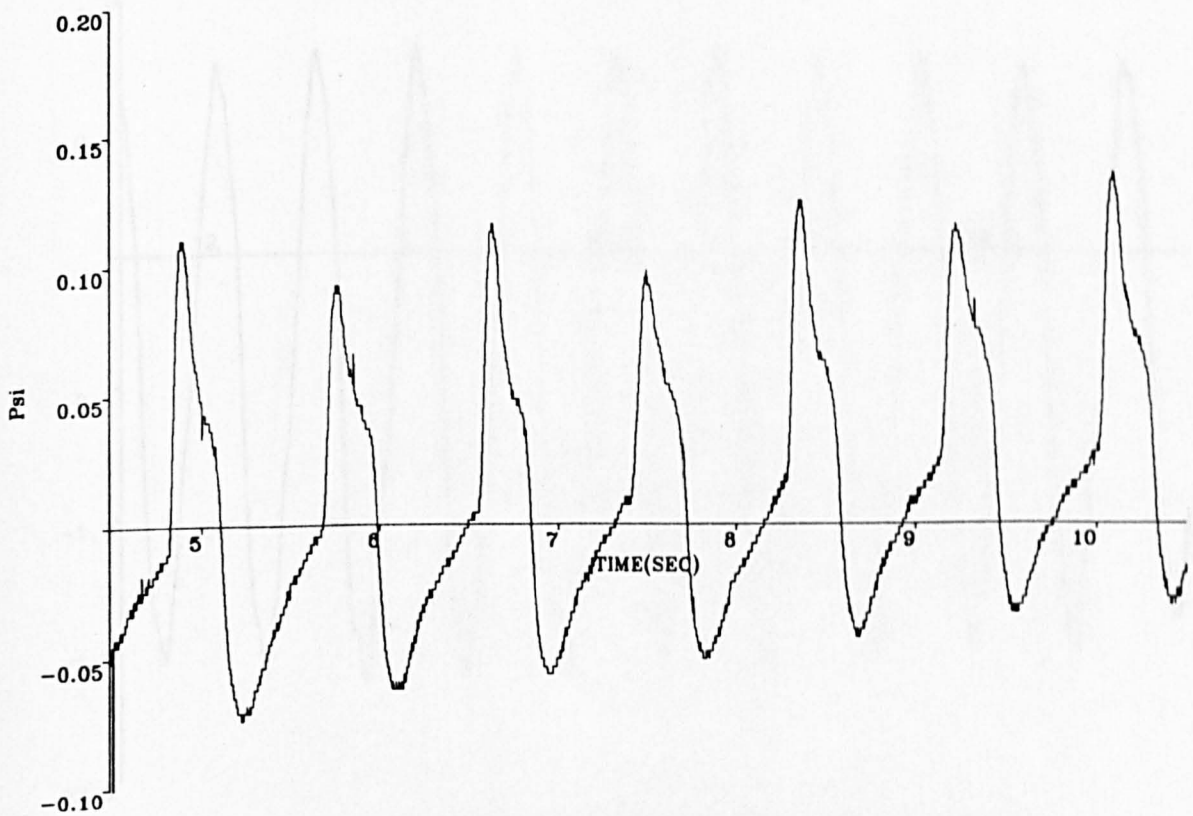

Fig.A.5.10 Bow Flare Slamming Pressure Time History in Experiment

Fn=0.15 Sta.= 3 $\lambda / L = 0.9$ $\zeta_a = 4.22$ cm

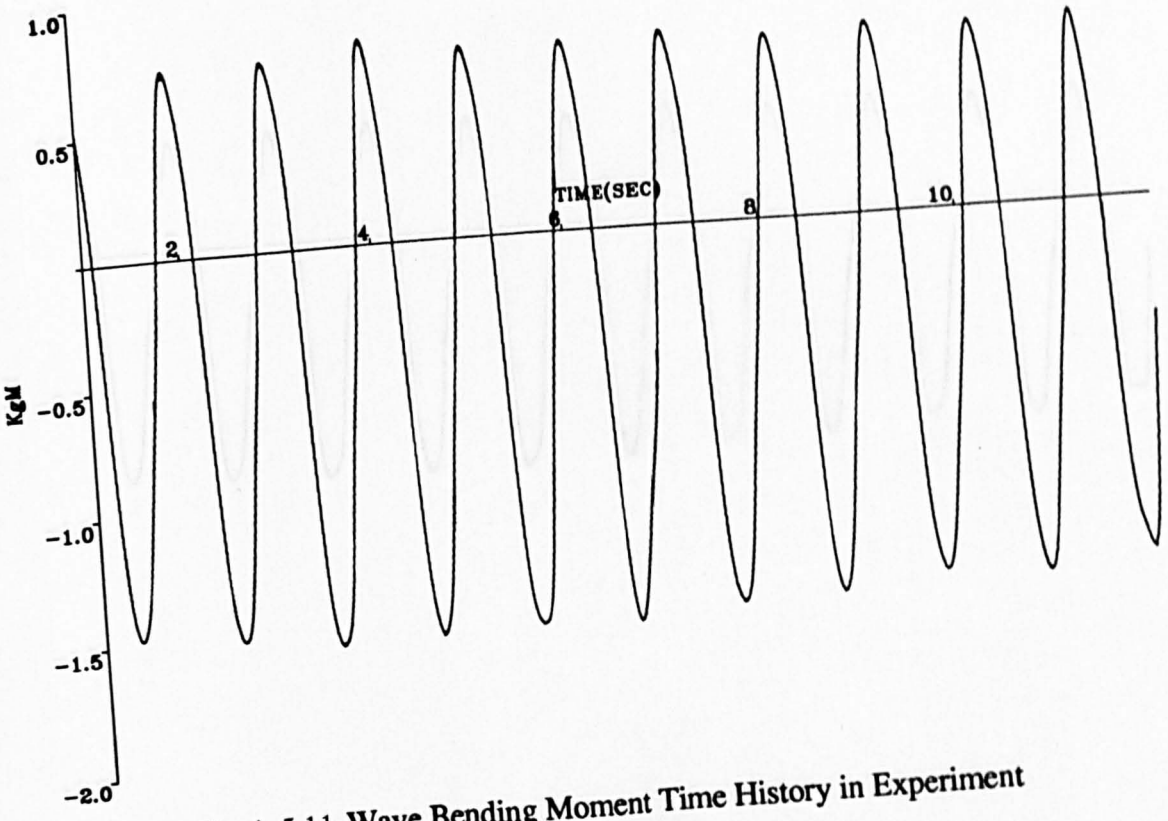

Fig.A.5.11 Wave Bending Moment Time History in Experiment

Fn=0.15 Sta.=10 λ / L=1.2 ζ_a=4.083 cm

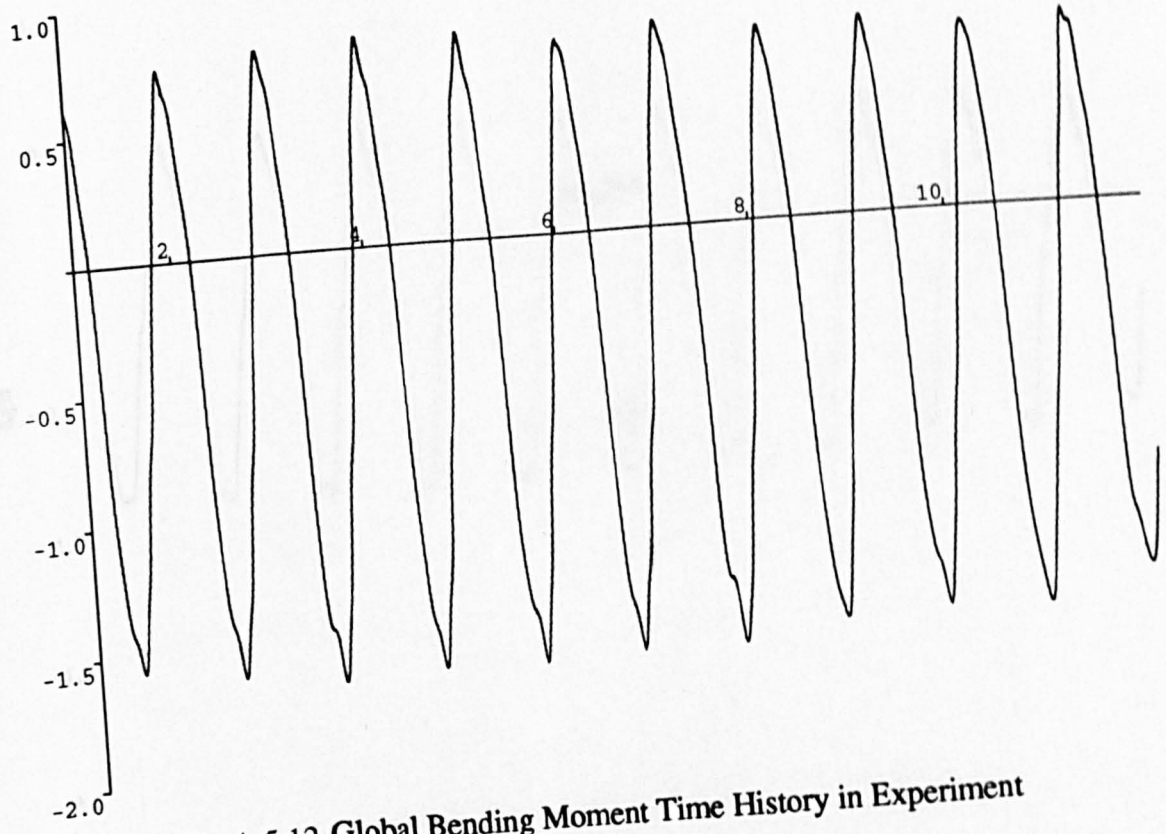

Fig.A.5.12 Global Bending Moment Time History in Experiment

Fn=0.15 Sta.=10 λ / L=1.2 ζ_a=4.083 cm

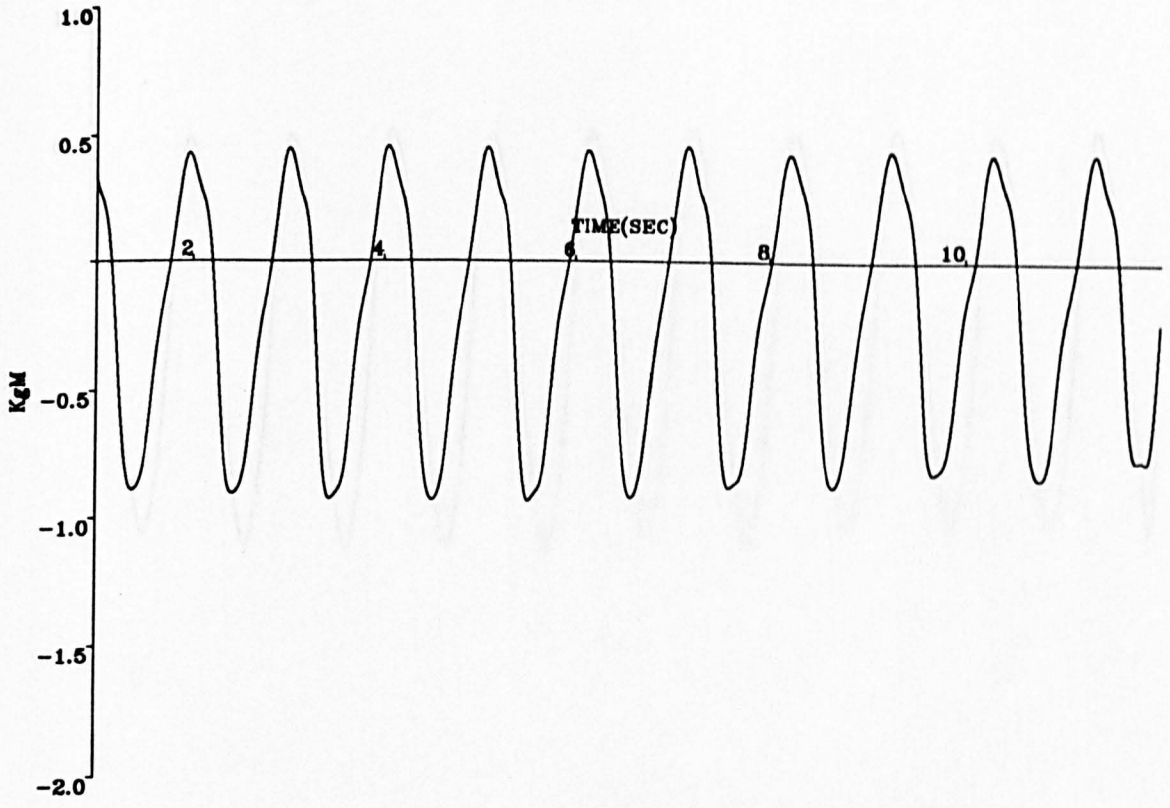

Fig.A.5.13 Wave Bending Moment Time History in Experiment

Fn=0.15 Sta.=7 $\lambda / L = 1.2$ $\zeta_a = 4.083$ cm

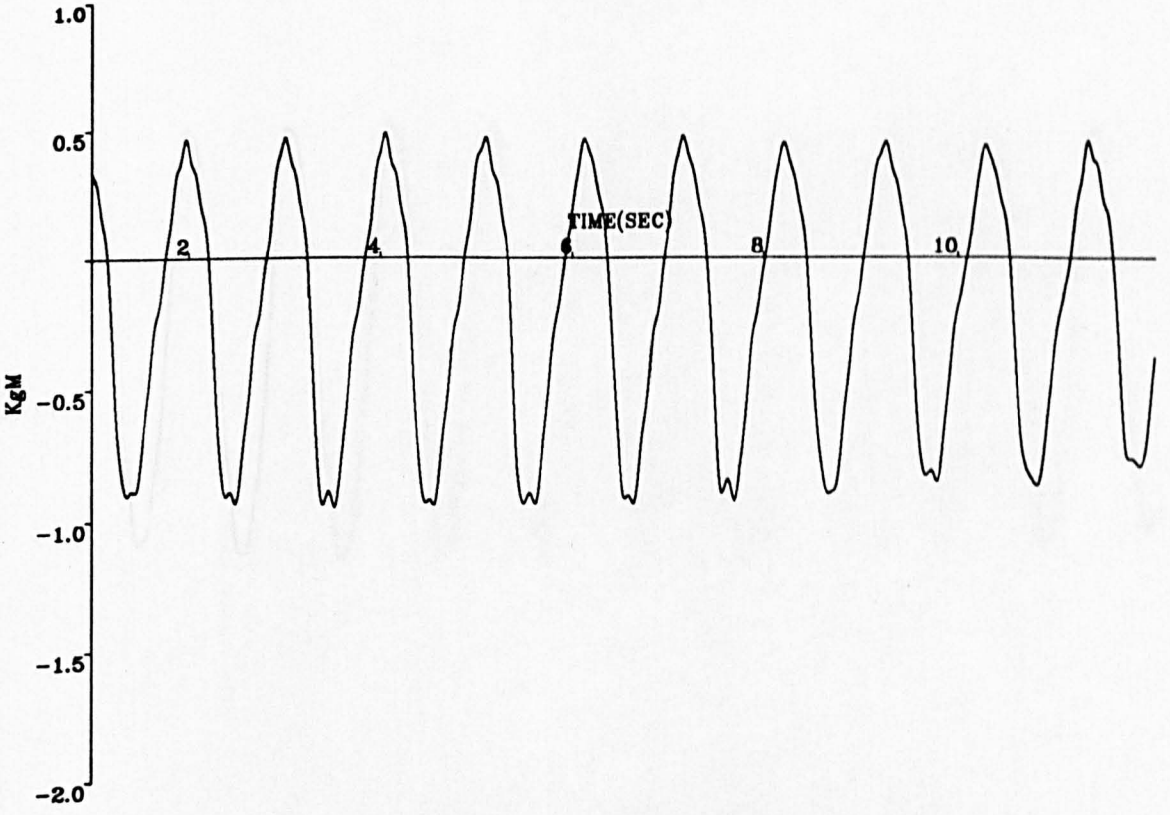

Fig.A.5.14 Global Bending Moment Time History in Experiment

Fn=0.15 Sta.=7 $\lambda / L = 1.2$ $\zeta_a = 4.083$ cm

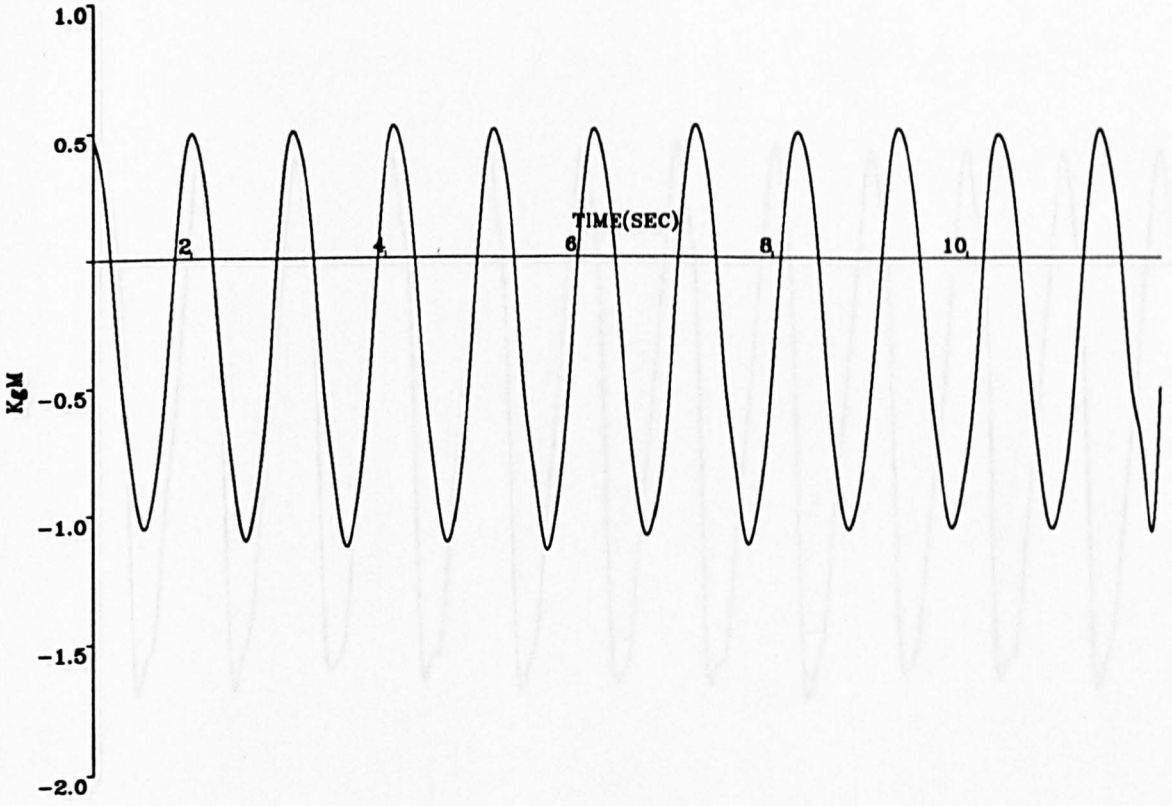

Fig.A.5.15 Wave Bending Moment Time History in Experiment

Fn=0.15 Sta.=15 $\lambda / L=1.2$ $\zeta_a=4.083$ cm

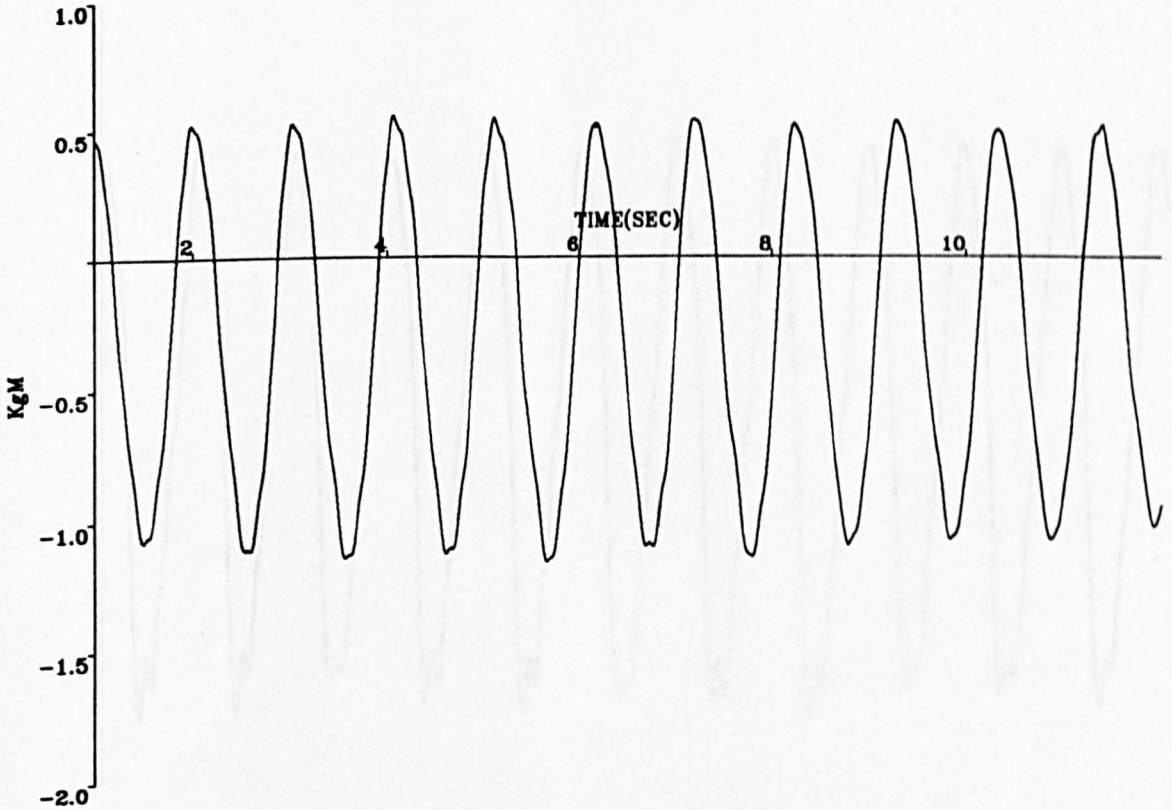

Fig.A.5.16 Global Bending Moment Time History in Experiment

Fn=0.15 Sta.=15 $\lambda / L=1.2$ $\zeta_a=4.083$ cm

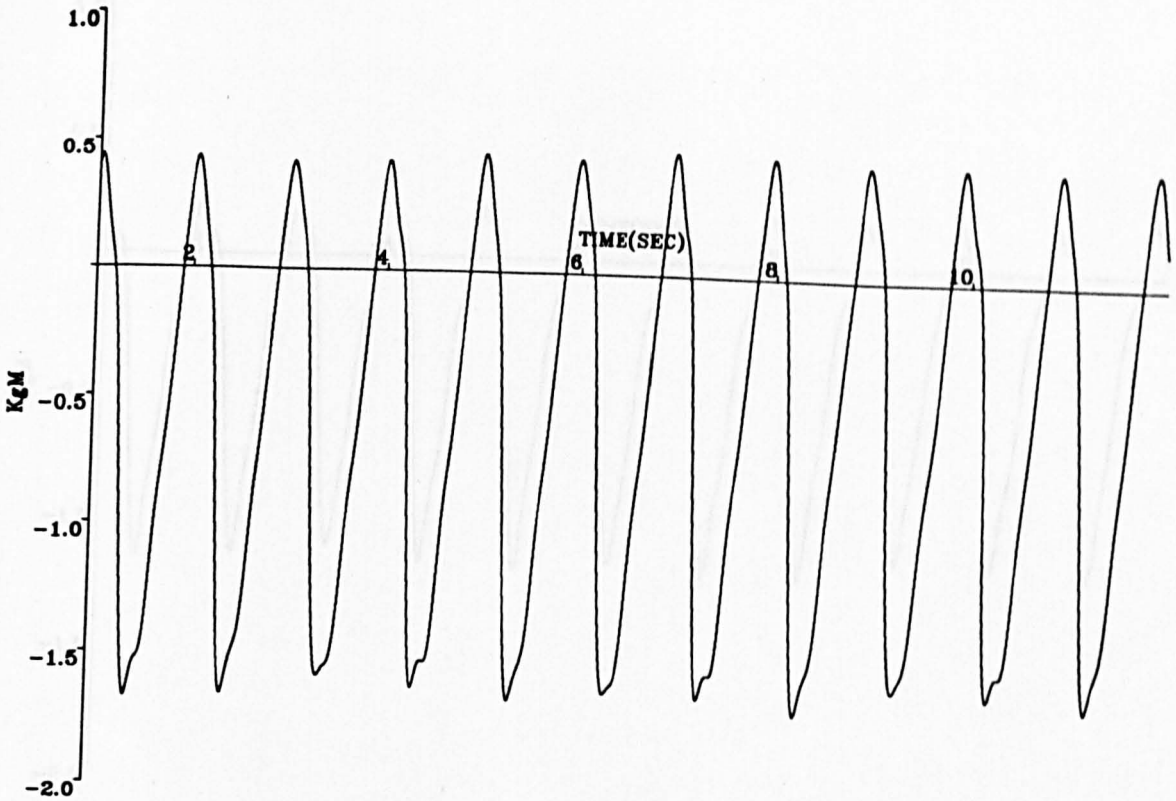

Fig.A.5.17 Wave Bending Moment Time History in Experiment

Fn=0.25 Sta.=10 λ / L=1.4 ζ_a=4.050 cm

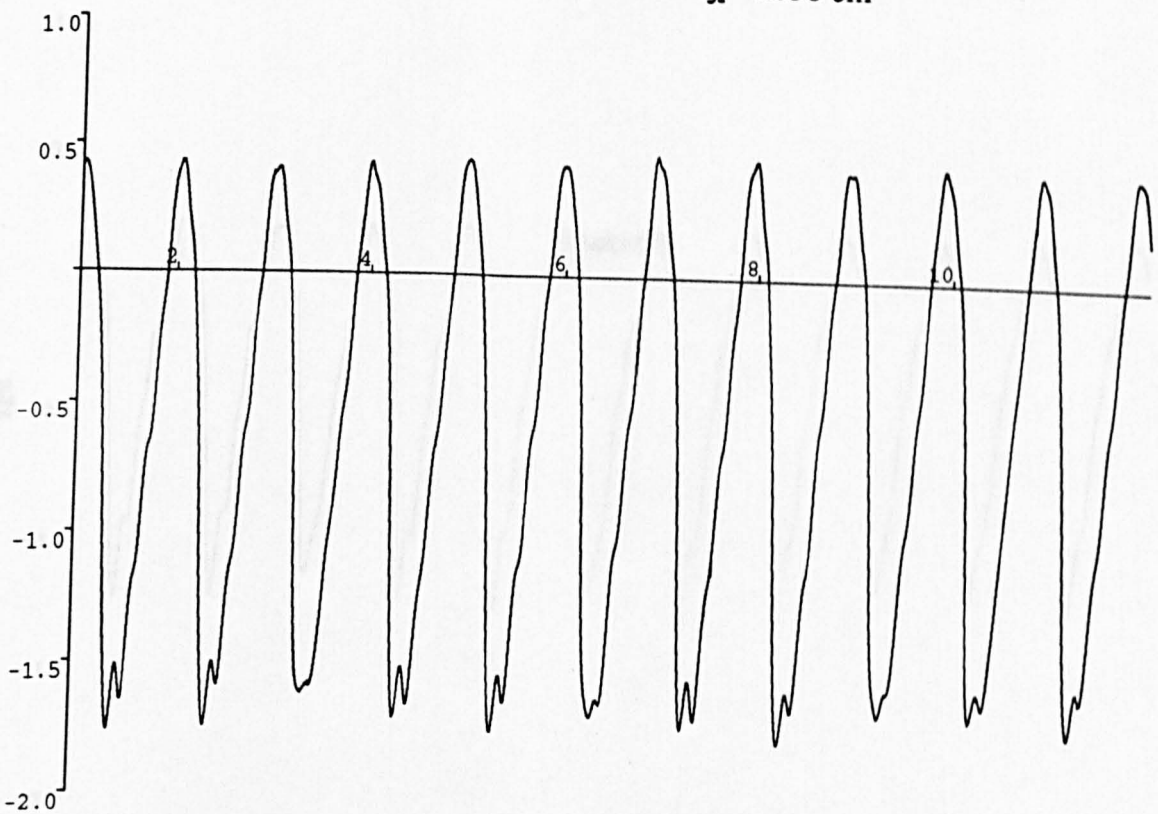

Fig.A.5.18 Global Bending Moment Time History in Experiment

Fn=0.25 Sta.=10 λ / L=1.4 ζ_a=4.050 cm

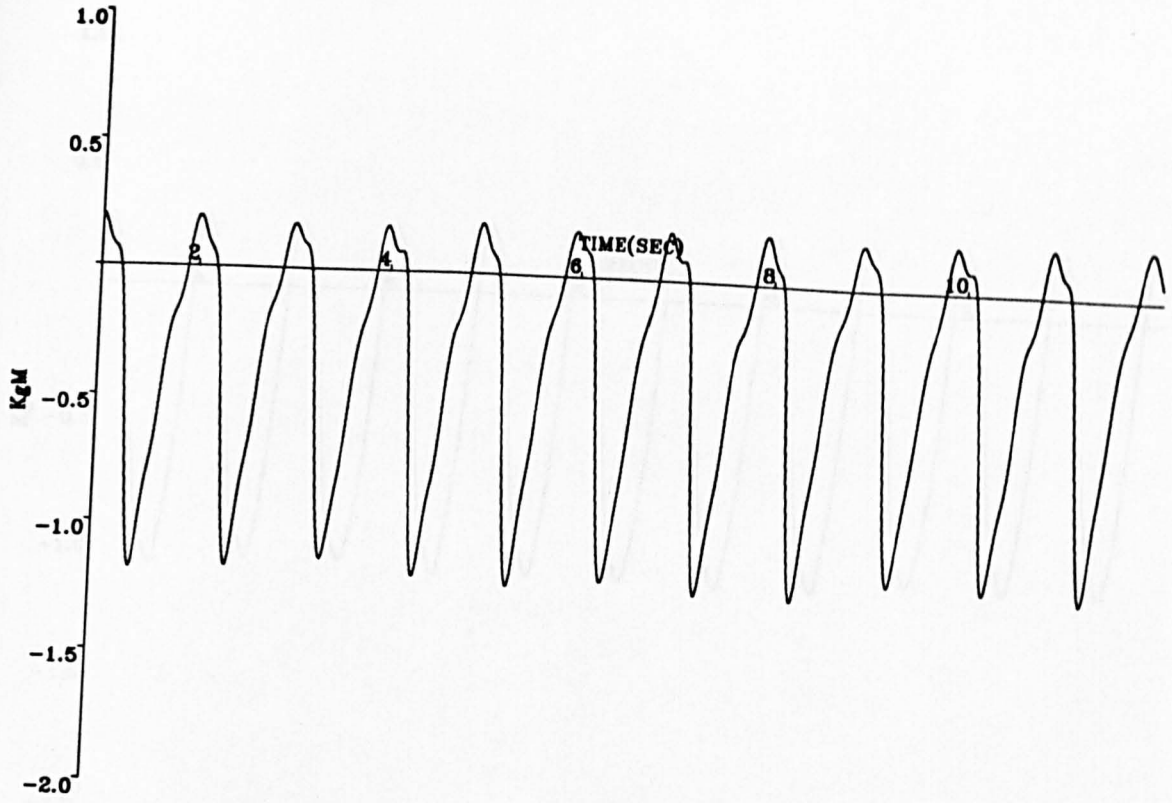

Fig.A.5.19 Wave Bending Moment Time History in Experiment

Fn=0.25 Sta.=7 $\lambda / L = 1.4$ $\zeta_a = 4.050$ cm

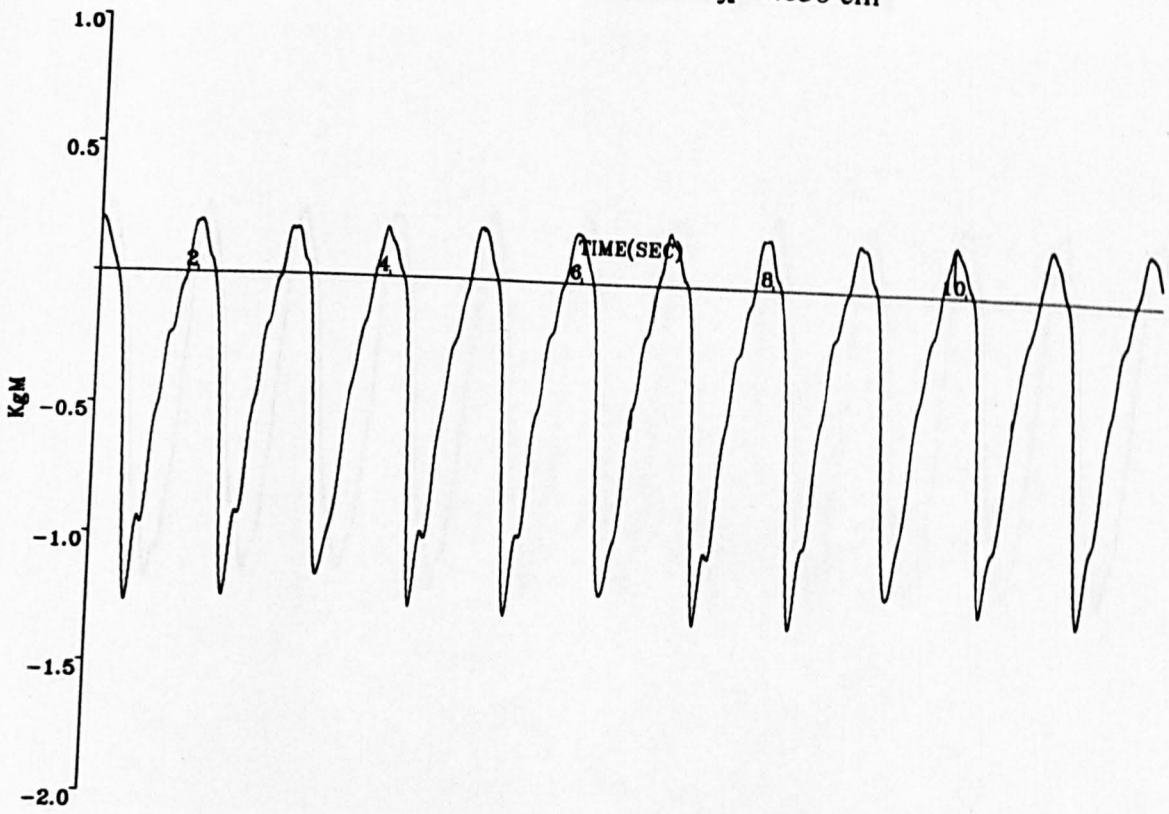

Fig.A.5.20 Global Bending Moment Time History in Experiment

Fn=0.25 Sta.=7 $\lambda / L = 1.4$ $\zeta_a = 4.050$ cm

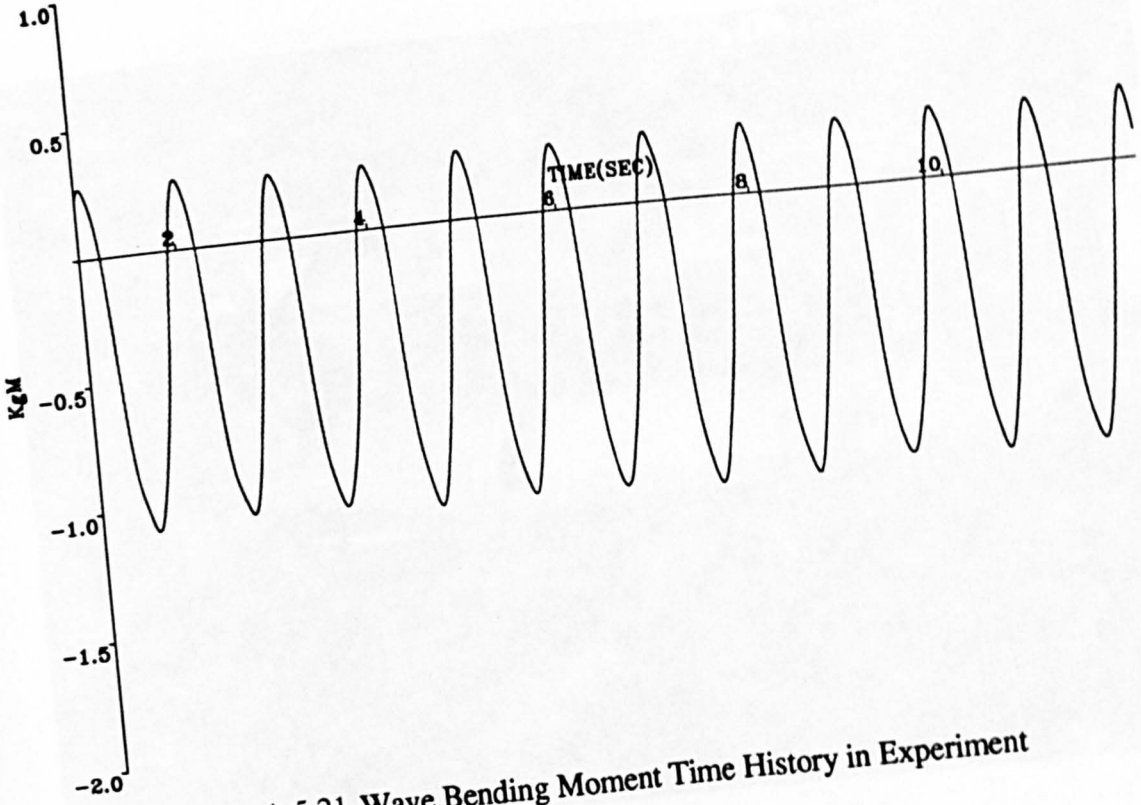

Fig.A.5.21 Wave Bending Moment Time History in Experiment

Fn=0.25 Sta.=15 $\lambda / L=1.4$ $\zeta_a=4.050$ cm

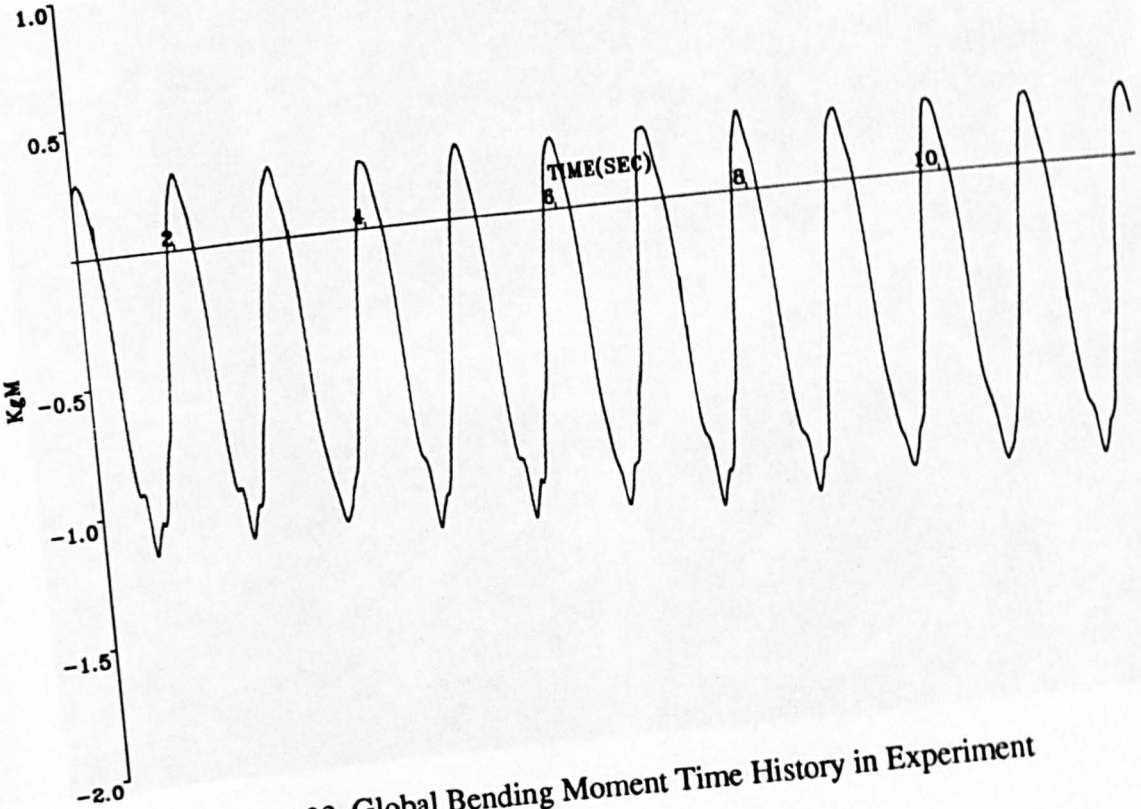

Fig.A.5.22 Global Bending Moment Time History in Experiment

Fn=0.25 Sta.=15 $\lambda / L=1.2$ $\zeta_a=4.050$ cm

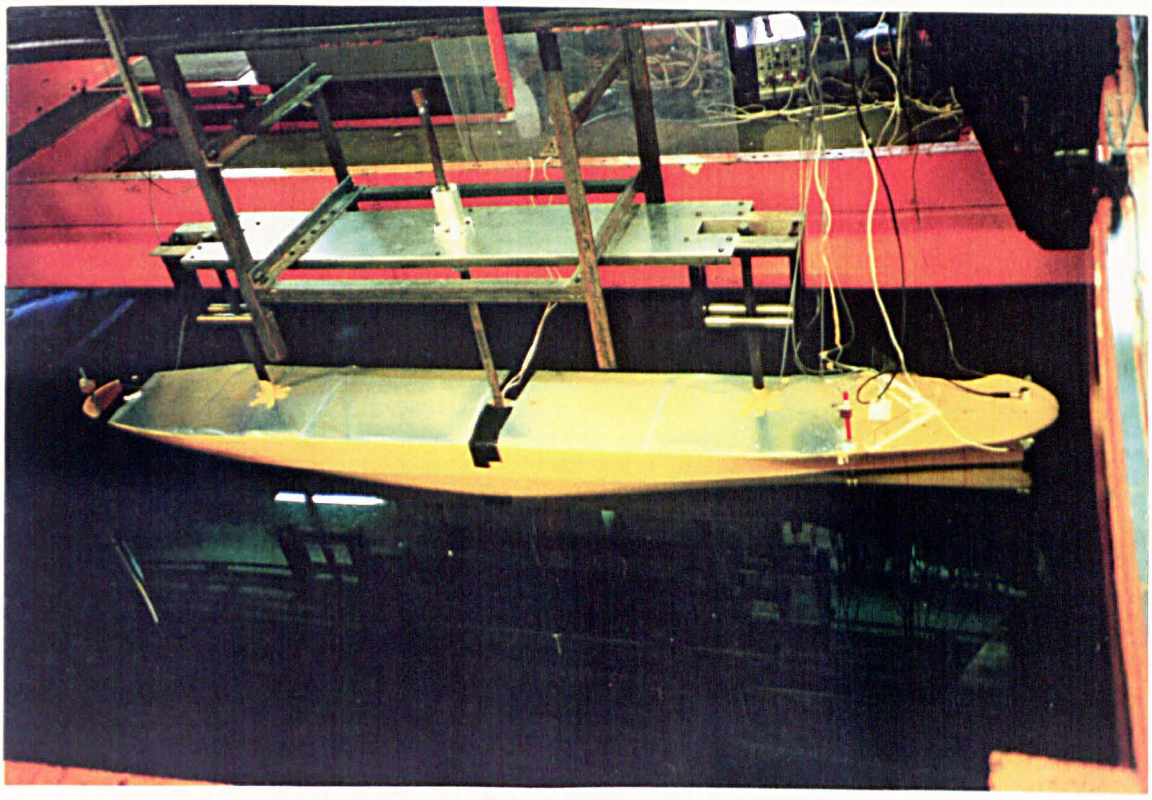

Photo 1 The Model Set up in the Carriage

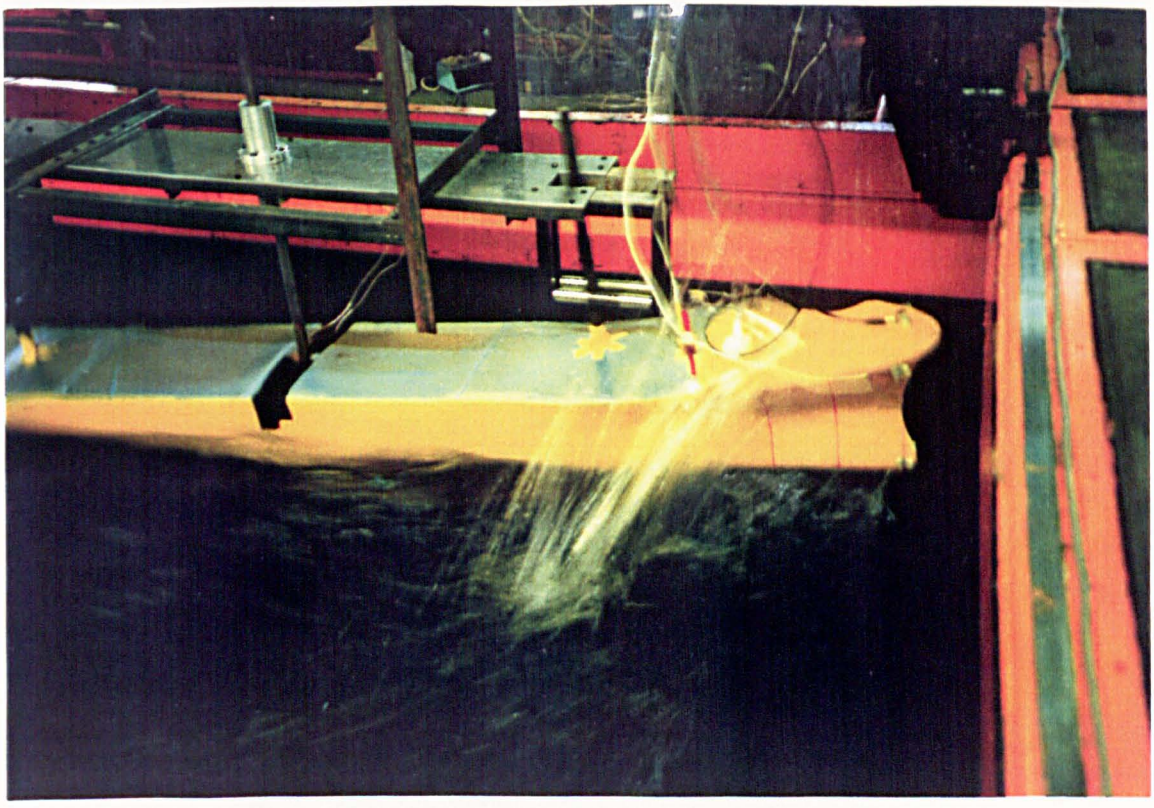

Photo 2 The Model in the Wave -- Out of the Water (Bow)

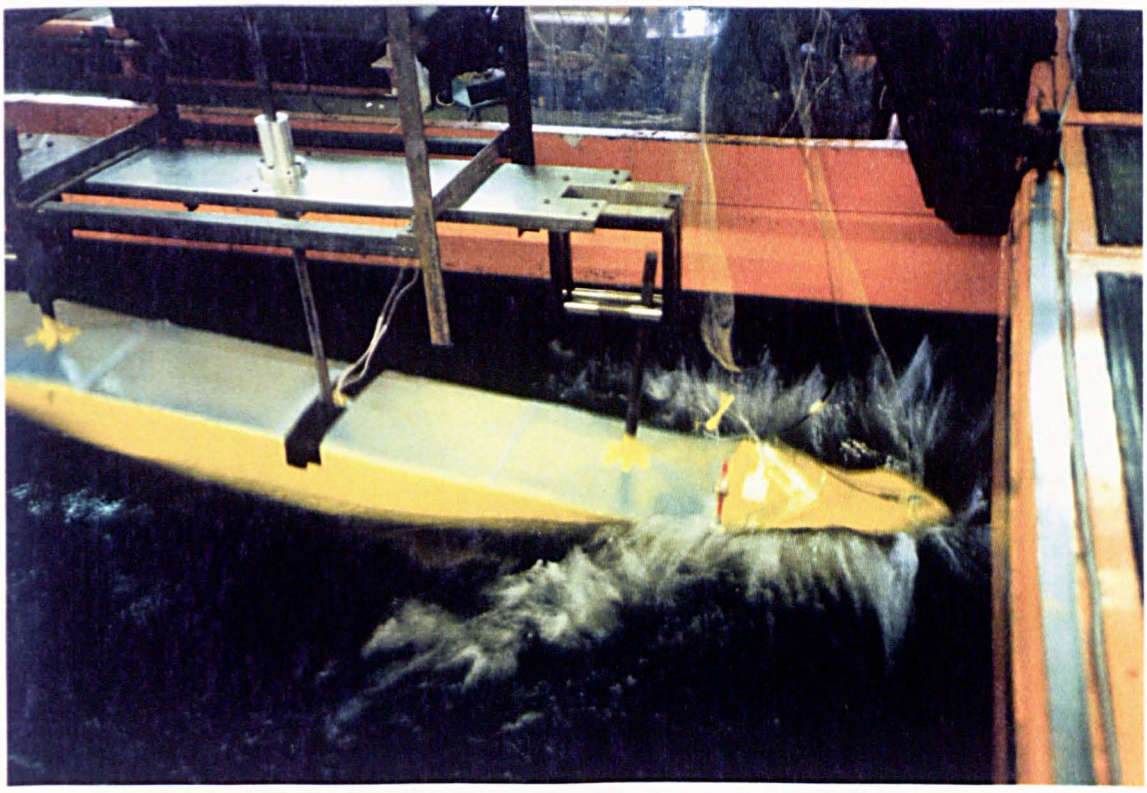

Photo 3 The Model in the Wave -- Slamming

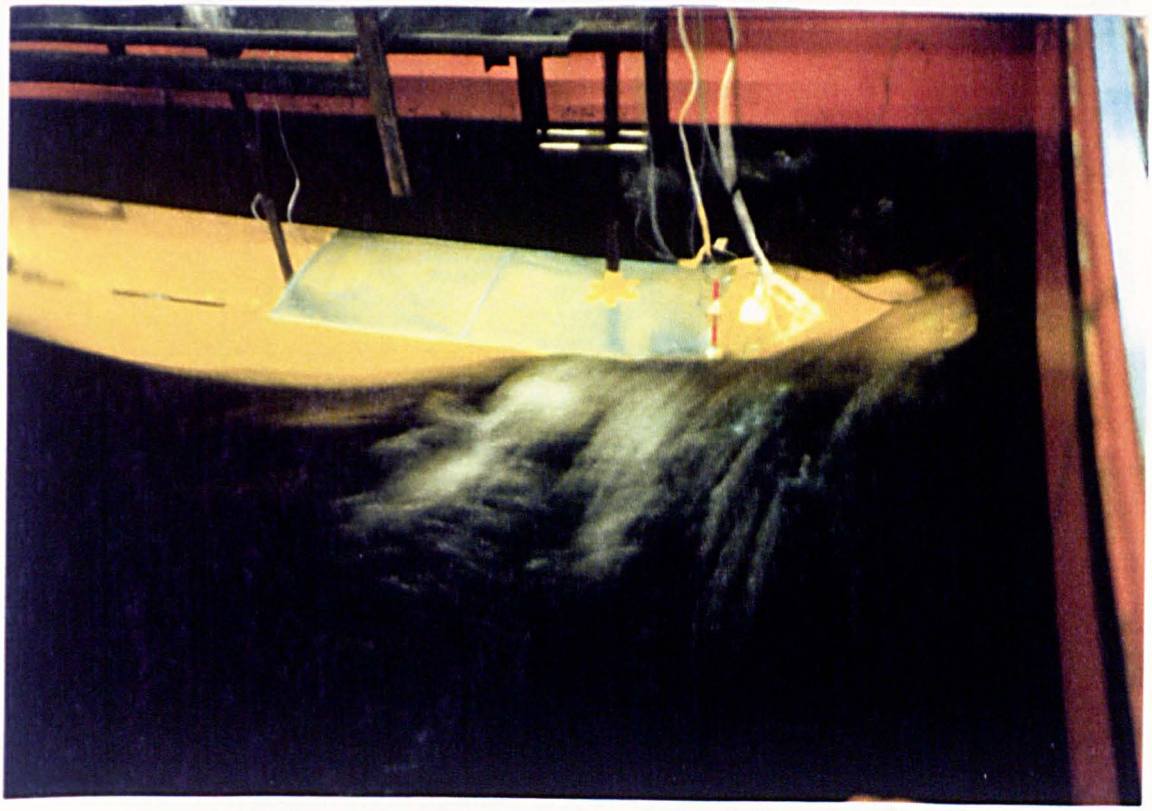

Photo 4 The Model in the Wave -- Deck Wetness

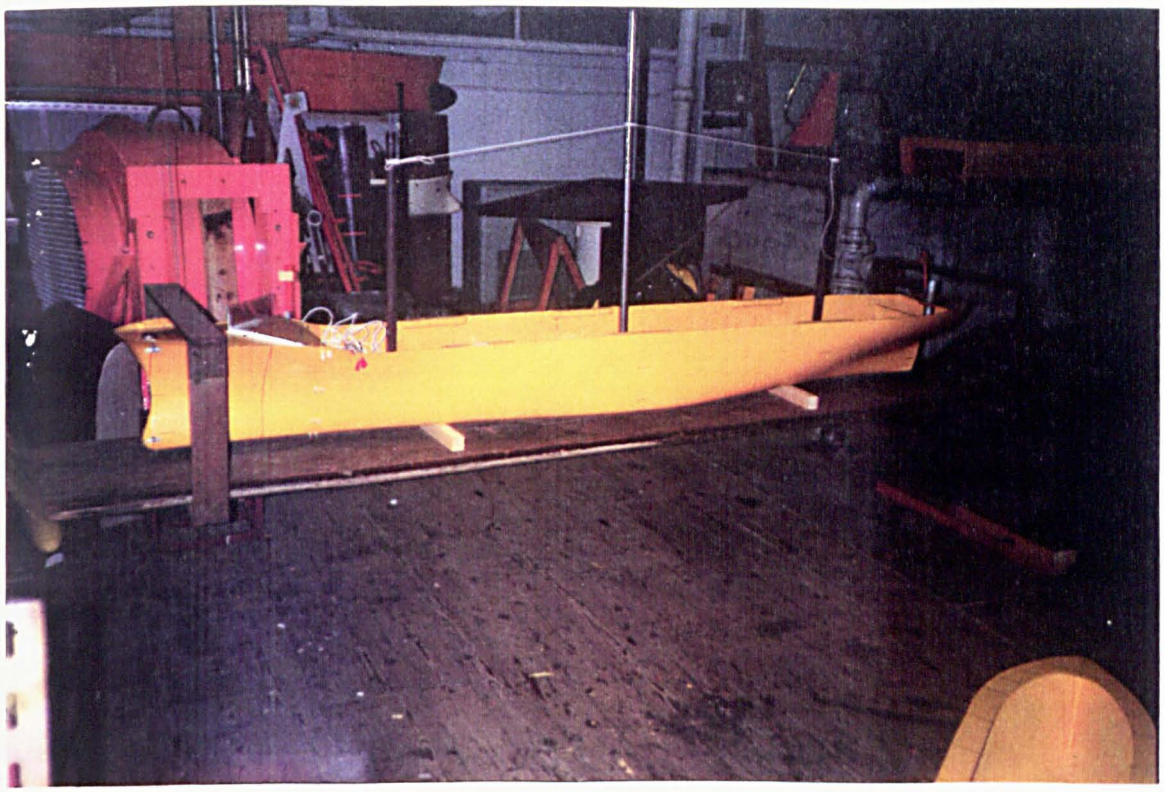

Photo 5 Radius of Gyration Measurement by Bifilar Suspension Method

Photo 6 Adjacent Segments of Model Sealed with a Flexible Tape